Indira Gandhi Centre for Atomic Research

2008

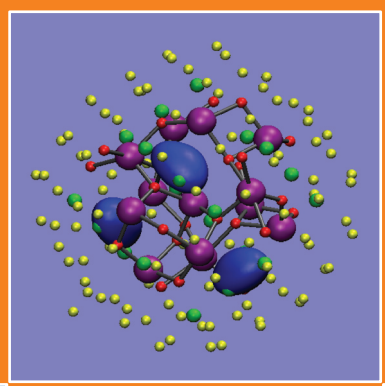

ANNUAL REPORT

Government of India
Department of Atomic Energy
Indira Gandhi Centre for
Atomic Research
Kalpakkam 603 102

Dr. Homi Bhabha Centenary Year - 2008-2009

IGCAR

2008

Indira Gandhi Centre for Atomic Research

ANNUAL REPORT

Government of India
Department of Atomic Energy
Indira Gandhi Centre for
Atomic Research
Kalpakkam 603 102

"Actions today mould our tomorrows"

- Indira Gandhi

"The scientist must be free to think and put forward whatever ideas he considers right"

"Ideas are some of the most important things in life and men are prepared to suffer and die for them"

- Homi Jehangir Bhabha

"....we are convinced that if we are to play a meaningful role nationally, and in the community of nations, we must be second to none in the application of advanced technologies to the real problems of man and society"

- Vikram Sarabhai

Address for Correspondence
Dr. P.R. Vasudeva Rao
Chairman, Editorial Committee
Director
Chemistry and Metallurgy & Materials Groups
Indira Gandhi Centre for Atomic Research
Kalpakkam - 603 102
Phone : +91-44-2748 0229 / 0222
Fax : +91-44-2748 0222 / 0065
Email : cmmg@igcar.gov.in
dcg@igcar.gov.in
Website : www.igcar.gov.in

Published by:
Scientific Information Resource Division
Indira Gandhi Centre for Atomic Research
Kalpakkam - 603 102

February 2009

Contents

Front Cover Legend

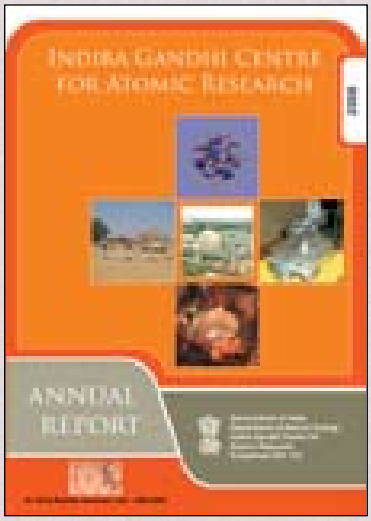

From top clock wise:

- Model system of Y_2O_3 nanoclusters in bcc iron for interpreting positron experiments
- CORAL Mobile Vehicle
- Erection of Safety Vessel on the inner wall of reactor vault (PFBR)
- Time domain Electromagnetic system developed at IGCAR

Center:

- Fast Breeder Test Reactor

Back Cover Legend

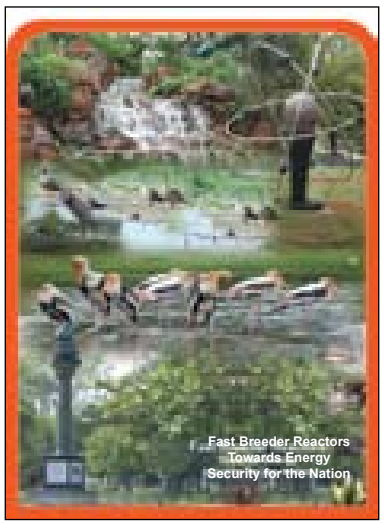

- Bio-diversity - Flora and Fauna at Kalpakkam including prominent landmarks of the Centre

Foreword

I am delighted to write the foreword note for the Annual Report for the year 2008, highlighting the significant and diverse research and developmental activities carried out at the Centre.

We have achieved all round progress during 2008, which is very gratifying. The flagship of our Centre, the Fast Breeder Test Reactor (FBTR) was successfully operated during the current year and the indigenous fuel has continued to perform well, without any fuel pin failure in the core. The comprehensive Post-Irradiation Examination (PIE) conducted on the fuel, clad and structural materials, as well as the modelling of the fuel and material behaviour have given us the confidence that the fuel can be taken to further higher limits of burn-up. The Mixed Oxide (MOX) test fuel of 500 MWe Prototype Fast Breeder Reactor (PFBR) has reached a burn-up of about 80 GWd/t in FBTR.

This year saw our department crossing an important milestone in the construction of PFBR, namely the erection of the safety vessel in the reactor vault. IGCAR has played a key role in this activity by way of realising manufacture of the vessel to close tolerances, and finalisation of the erection sequence, besides being involved in important steps such as precise measurement of the as-installed coordinates of the vessel. IGCAR has continued to provide inputs towards design, R&D, regulatory review and manufacturing aspects of PFBR components and systems to ensure timely completion of many of the crucial components. IGCAR has closely worked with BHAVINI in the manufacture of important components like grid plate and core support structure. These components have been realized with high precision and quality. The rich experience of IGCAR in sodium technology was also a key factor in the successful charging of liquid sodium into the storage tanks at PFBR. The prototypes of the Diverse Safety Rod (DSR) and Diverse Safety Rod Drive Mechanism (DSRDM) have been tested in air, water and sodium, confirming their good performance.

The entire fast reactor community in the world is keenly looking forward to the commissioning of PFBR. It is now the time to enhance comprehensive R&D towards the next four FBRs, which would be primarily based on the design of PFBR, but with significant design improvements that would enable us to reduce the cost of the reactor and at the same time enhance the safety. Key R&D programmes to be undertaken in this regard have been identified and the work has started in full earnestness. We can look forward to a challenging and exciting period ahead.

Closing the fuel cycle is a crucial element of our fast reactor programme, without which we cannot achieve the growth in fast reactors that we have targeted. We have made significant progress in achieving a robust fast reactor fuel cycle. With respect to the fuel reprocessing, based on the fruitful experience of the earlier campaigns, the reprocessing of 154 GWd/t burn-up FBTR fuel has been accomplished. ***This is an important milestone as the reprocessing of high plutonium bearing carbide fuel with such a high burn-up has been carried out for the first time in the world***. The pre-project activities for Fast Reactor Fuel Cycle Facility (FRFCF), which would cater to the fuel cycle for PFBR, are gaining momentum. Simultaneously, we are embarking on test irradiation of mixed oxide fuel fabricated through sol-gel route and also metallic alloy fuel, mechanically bonded as well as with sodium bonding. These experiments would constitute important steps towards advanced fuel and fuel cycles for fast reactors, the engines for growth of nuclear energy in India.

One of the targets that we have set ourselves is to push the fast reactor fuels to higher and higher levels of burn-up towards reducing fuel cycle cost. A number of steps have been taken to fulfil this objective. On the materials front, the development of oxide dispersion strengthened Ferritic/Martensitic steels with yttria dispersion has been vigorously pursued, resulting in the trial manufacturing of the clad tubes with desired specifications. This indigenous experience involving inter-DAE and inter-institutional collaborations will pave way for the ODS clad tubes for future FBRs.

The comprehensive range and intensity of R&D that we have been pursuing has provided us with many significant breakthroughs. With multidisciplinary strengths and a wide range of relevant sophisticated

experimental facilities, we have an unique opportunity to extend our support to a variety of national mission programmes. Our expertise and experience in materials development and charaterisation has given us the confidence to embark on the development of Reduced Activation Ferritic-Martensitic steels for the Indian test blanket module of International Thermonuclear Experimental Reactor (ITER). It is also a matter of pride that we have also contributed to the Chandrayaan mission in terms of neutron radiography of the pyro-devices used for the launch using our KAMINI reactor. Our success in deployment of SQUIDs for magnetoencephalography (MEG) has a potential to make a significant impact on healthcare in the country.

Our performance in meeting the milestones with regard to budget and S&T achievements has been appreciated. On human resources development front, the Training School at IGCAR has added Materials Science specialisation in the training programme from this year onwards, which shall provide valuable manpower in the domain of materials research. The programmes of Homi Bhabha National Institute have entered into the second year of academic session, with a significant addition of research scholars. The University Grants Commission-Department of Atomic Energy Consortium for Scientific Research (UGC-DAE CSR) node at IGCAR has made rapid progress in identifying the infrastructure, experimental facilities and relevant research programmes.

A large number of scientists and engineers in IGCAR have been recognized in the year 2008 with prestigious national awards in the category of individual as well as group awards. This is a reflection of the excellent R&D work being done in the Centre in various domains of science, engineering and technology development.

The year October 30, 2008 – October 30, 2009 marks the birth centenary of Dr. Homi Jehangir Bhabha, the architect of the Indian nuclear programme. The vision of the three stage programme enunciated by Dr. Bhabha is an enduring one, and is in fact, engaging the attention of the international community. We at IGCAR are committed to the development of the second stage of the nuclear programme, and we take inspiration from his visionary approach. We focus on doing relevant science to shape much needed indigenous development of relevant technologies in our Centre.

The strength of the Department is its talented manpower with diverse specializations, working in the areas of physics, chemistry, metallurgy, mathematics, biology, engineering sciences as well as interdisciplinary research. Harnessing and enhancing capacity, confidence and capability of manpower has been a key reason for the success of the Centre to realize robust and innovative technologies. Dr. Bhabha stated **"…*The relative role of indigenous science and technology and foreign collaboration can be highlighted through an analogy. Indigenous science and technology plays the part of an engine in an aircraft, while foreign collaboration can play the part of a booster. A booster in the form of foreign collaboration can give a plane an assisted take-off, but it will be incapable of independent flight unless it is powered by engines of its own. If Indian industry is to take-off and be capable of independent flight, it must be powered by science and technology based in the country*.."** We follow this Mantra as our philosophy of growing science and technology. We have the enthusiasm and confidence to grow indigenous technology, which is essential to implement the approach of Dr. Bhabha.

I would like to complement the new editorial committee (Dr. M. Sai Baba, Dr. G. Amarendra, Shri R.V. Subba Rao, Shri C. Jayakumar, Dr. Vidya Sundararajan, Dr. Saroja Saibaba, Shri S. Varadharajan, Dr. K. Ananthasivan, Dr. K.K. Satpathy) under the chairmanship of Dr. P.R. Vasudeva Rao for their committed efforts in bringing out the annual report with many improved features. They have reflected the traditions and enhanced the content and presentation with their innovative approaches.

I wish the readers successes and bliss during the year 2009. With the large and crucial mandate of the Centre towards providing energy security for the country through fast reactors, it is obvious that we would need to harness the excellent infrastructure, expertise and knowledge base available in various academic and research institutions as well as the enthusiasm and commitment of the industry, to meet our goals. I hope that this Annual Report provides a good overview of our programmes, capabilities and commitments for further catalysing and strengthening our collaborations.

With my best wishes,

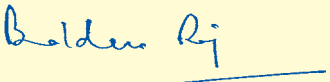

(Baldev Raj)
Director, IGCAR

Editorial

The year 2008 has seen many achievements in the Centre in several areas of science, engineering and technological developments. The precise lowering of the safety vessel into the reactor vault was a unique event in the fast reactor programme, symbolizing the indigenous design, fabrication and installation capabilities. Sodium has also been received at site, and fuel fabrication is on. Our synergy with BHAVINI is working well in terms of providing many important design inputs and co-ordination with many industries and quality control etc. We have achieved commendable progress in operation of FBTR, Post Irradiation Examination of high burn-up carbide fuel, reprocessing of the carbide fuel, and also several frontier R&D areas including ODS clad tube development, welding methodologies, safety issues etc. All this has made the task of bringing out this issue of Annual Report an enjoyable one.

A number of dignitaries and delegations have visited the Centre during the year 2008, and their visits and their interactions with our young colleagues have added further momentum and vibrancy to the lively spirit of the R&D community at Kalpakkam. It is obvious that the Centre is receiving the attention of the international community, thanks to the significant impact it has made in the fast reactor arena. We can be proud of the fact that our country is now considered as one of the leaders in fast reactor science & technology. It is the aspiration of the Editorial Committee that the perusal of the Annual Report would also underline these facts. Thus, the technical articles have been pruned, edited and classified with due attention so as to ensure that only significant achievements of the Centre are depicted in this volume in a comprehensive way. A new team of editorial committee has taken over the publication of the IGC Annual Report from this year. Readers can perhaps discern the difference in terms of the lay out as well as content, and we hope the issue is more readable and enjoyable.

I would like to express our sincere thanks to Dr. Baldev Raj for his guidance and support. He always encourages us to achieve higher than what we have already achieved, both with respect to technical excellence and elegant presentation style. Successive improvements in Annual Reports in the last few years are a testimony towards this.

I would like to thank the authors of the articles in this issue for the valuable technical contributions. I acknowledge with thanks the enthusiastic efforts of the members of the Editorial Committee. The Editorial Committee would like to convey its special thanks to the Scientific Information Resource Division for coordinating the publication process, and especially, the hard work put in by Shri G. Pentaiah, Shri A. Rangarajan and Shri K. Varathan of SIRD in putting together this issue.

We welcome any comments and suggestions from the readers for improving the annual report further.

Wishing all the readers a Happy and Prosperous New Year 2009.

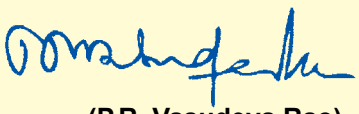

(P.R. Vasudeva Rao)
Chairman, Editorial Committee
Director, Chemistry, Metallurgy & Materials Groups

I

Fast Breeder Test Reactor

I.1 The 14th Irradiation Campaign - A Milestone for FBTR

The 14th irradiation campaign started at 14.59 hours on 17th February, 2007 and ended at 16.15 hours on 26th January 2008. The six MK-I Sub-Assembly (SA) in the second ring inner radius reached the limiting burn-up of 155 GWd/t. The PFBR test fuel SA has reached a burn-up of 78.67 GWd/t, as against the target burn-up of 100 GWd/t. The 14th irradiation campaign was the dream run of FBTR, with the plant having the longest continuous operation of 72 days with TG synchronized to the grid. This campaign is also unique in terms of the number of experiments carried out, which were of relevance to PFBR and the life extension of FBTR (Table 1).

In the 15th irradiation campaign, it is proposed to raise the operating temperatures close to the design levels with the current small core. Several modifications were completed in the plant between February - December 2008. The current mission irradiation of PFBR test fuel to the target burn-up of 100 GWd/t and D-9 alloys to 80-100 dpa would be continued in the 15th campaign to repeat the DND experiment at two diagonal locations and taking up trial production of Sr^{89} from yttria. Sr^{89} has therapeutic value in the treatment of bone cancer and is not available in India. For this purpose, a special irradiation subassembly (called IFZ-100) was loaded in the reactor for the first time. Fuel Handling for the 15th irradiation campaign (Fig. 1) has been completed.

Table 1: Salient features of the 14th irradiation campaign

Number of fuel handling campaigns during the campaign	7 (FHC#54A,B,C,D&E, 55 & 56)
Average Power	16.6 MWt
High Power Operation	2401 hours
Peak Burn-up Mark I (MK-1) Fuel	155 GWd/t
PFBR Test Fuel	78.67 GWd/t
Longest continuous operation	1719 hours (71.6 days) (From 18:00 on 6th Nov 2007 to 06:43 on 17th Jan 2008)
Cumulative Thermal Energy generated	38524 MWh
TG operating time	2199 hours
Electrical Energy Generated	3.669 Million Units
No. of scrams	Nil
No. of forced outages	3

Experiments carried out:

1.Validation of DND (five locations)	2. PFBR single pin irradiation
3.Grid plate flux measurement	4. Grid plate material irradiation
5.Testing of Kalman filter technique	6. PFBR neutron detector testing in detector pit

7.PFBR test fuel irradiation (continuing)

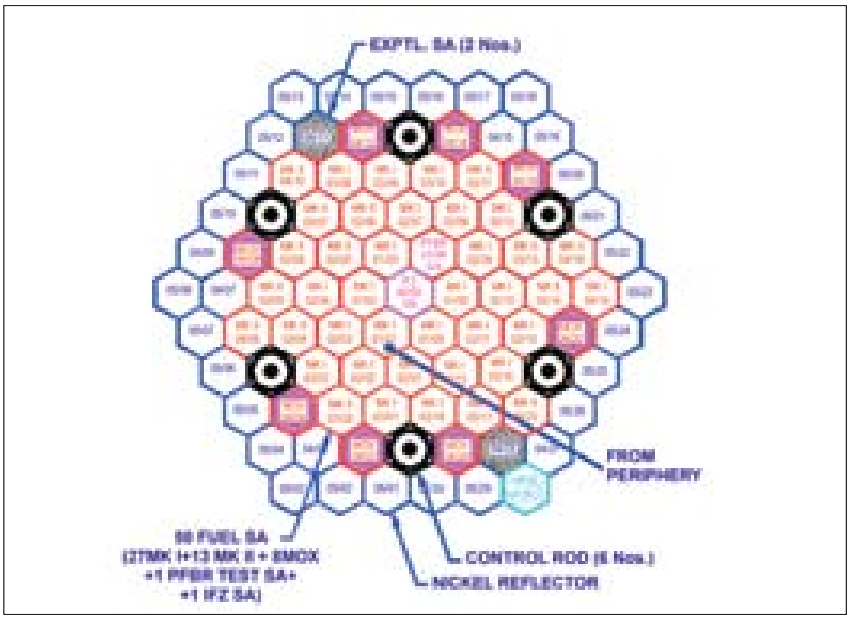

Fig. 1 *Core configuration for the 15th irradiation campaign*

I.2 Fission Gas Release Behaviour of Mixed Carbide Fuel at various Burn-ups

Fission gas release was estimated in the fuel pins of FBTR fuel subassemblies that have attained peak burn-ups of 25, 50, 100 & 155 GWd/t. Fission gas release behaviour of high plutonium content carbide fuel is not available in the literature. Fission gas extraction and analysis was carried out on a few selected fuel pins of different burn-ups. A single end, low dead volume, fission gas extraction chamber with a mechanically driven puncture tool was used initially for extraction of fission gases from the fuel pins. Since closure of fuel-clad gap was observed in 100 GWd/t burn-up fuel pins, a new double end fuel pin puncture chamber was designed, fabricated and used to enable collection of fission gases from both the plenum regions of high burn-up fuel pins (Fig. 1). Fission gas analysis was carried out by gas chromatography technique using hydrogen as the carrier gas to estimate the percentage of fission gas release, plenum pressure, Xenon to Krypton ratio and helium content in the fuel pins.

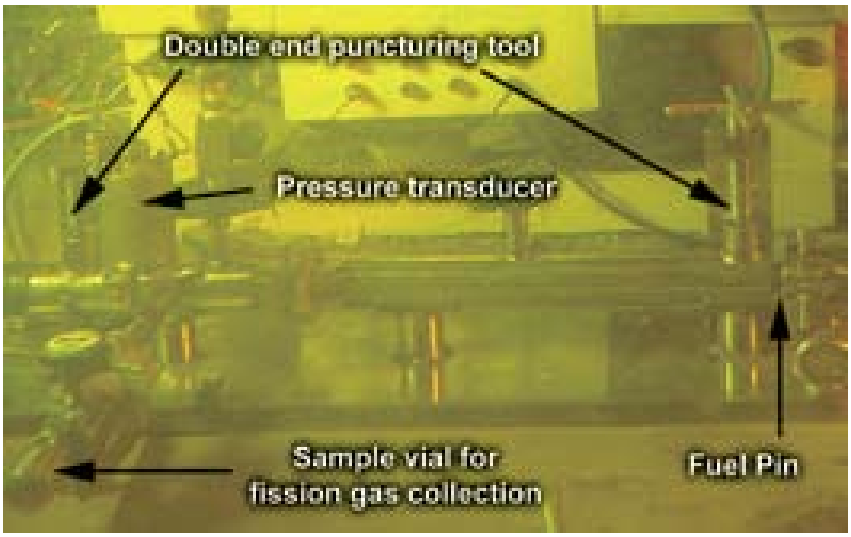

Fig. 1 *Double end fuel pin puncture chamber for fission gas extraction*

Percentage of fission gas release on fuel pins after 25 GWd/t burn-up was found to be less than 1 %. Considerable variation in fission gas release was observed in the fuel pins after 50 GWd/t burn-up ranging from 8 - 22%. Fission gas release measurements after 100 GWd/t burn-up indicated a gas release in the range of 4–14 %. The reduction in percentage of fission gas release in 100 GWd/t burn-up fuel pins is attributed to the reduction in fuel operating temperatures due to the closure of fuel-clad gap. Maximum fission gas release estimated on 155 GWd/t burn-up fuel pins was 16% and the corresponding internal pressure in the fuel pin was measured to be 2.1 MPa. Maximum fission gas pressure as a function of burn-up is shown in Fig. 2. Xenon to Krypton ratio was estimated to be around 13 in all the fuel pins. The fission gas release measurements at various burn-ups have indicated that the FBTR mixed carbide fuel has very low fission gas release and it is not a constraint in extending the fuel burn-up.

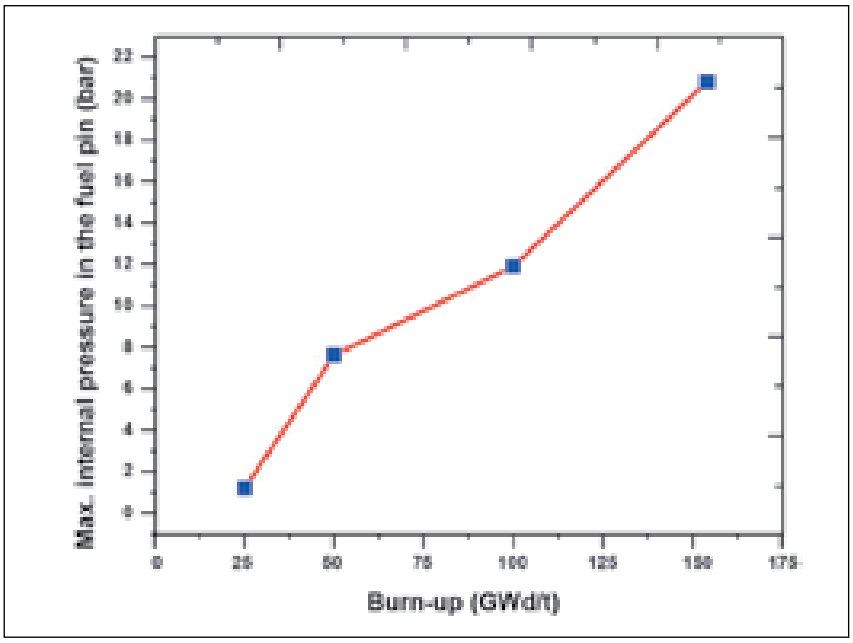

Fig. 2 *Maximum internal pressure in the fuel pins as a function of burn-up*

I.3 Preparations for taking FBTR to Higher Operating Temperatures

The maximum reactor outlet temperature reached by FBTR so far has remained at 703K except for a short spell of about sixty days in the year 2002, when the reactor outlet reached 719K during reactor operation at 17.4 MWt in the 10th irradiation campaign. In order to study the performance of the systems at design temperatures, and to conduct meaningful irradiation of fast reactor materials, it is required to raise the system temperatures closer to the design values. To achieve this with the current constraints on core size and reactor power, three options were studied- viz. operation with reduced feed water flow to the Steam Generator (SG), isolation of one SG module from each secondary loop and blanking of three water tubes from each SG module. The last option was considered best from considerations of decay heat removal capability, ease of carrying out the modification and ease of restoration when the core is enlarged to 40 MWt core. With this, it will be possible to realize reactor inlet & outlet temperatures of 653K & 763K with the present core.

Considering the critical nature of the work and intervention on safety critical equipment, detailed mock-up of the work with site constraints, strict adherence to all fabrication and testing procedures followed during manufacture of SG, third party inspection by QAD and final quality assurance by ROMG were stipulated by Safety Committee during the review.

The SG is made up of Nb stabilized 2.25Cr-1Mo ferritic steel. Welding procedure and welder performance qualification for this material were carried out as per FBTR standards. A full fledged mock-up set up simulating the site constraints was erected inside the SG casing.

For confirming correspondence of the cut tube at top and bottom, water was poured from top end and exit from the bottom tube end was checked. Discrepancies were noted between the top and bottom in four tubes in the west modules. The correspondence was then established by pouring chilled water from the open end of the cut tubes at the top and feeling the chillness of the tubes at the bottom. This was then confirmed by gamma radiography of all headers.

The interchanged tubes were cut as per the radiographic interpretation and correspondence of the top and bottom tubes was again confirmed by water pour test. The other tubes which were cut wrongly as per drawing were normalized by welding piping spools. End caps were then welded. Post-Weld Heat Treatment (PWHT), Radiographic Test (RT) and Helium Leak Test (HLT) of all the weld joints were carried out. After this, the bottom ends of tubes were closed by welding caps (Fig. 1) after filling it with helium, followed by PWHT, RT & HLT of these joints. Finally, hydro testing of SG at 135bar was done by operating the Main Boiler Feed Water Pump. Thermocouples were provided in two of the SG module shells to monitor the shell temperature distribution.

Fig. 1 *Modified water sub-headers*

Fig. 2 *Scooping of frozen sodium from the SG inlet header*

Fig. 3 *Knife edge aided rupture disc (removed from steam generator)*

Based on the operational feedback, several modifications were also required in the plant to face the challenges of higher operating temperatures. Some of these entailed direct intervention in the secondary sodium system (Fig. 2), warranting draining of the loops.

The surge tank level maintenance circuit in each secondary loop was modified to avoid thermal striping. In the current design, there is a continuous flow of hot sodium from the surge tank into the cold pool of the expansion tank. It was reported that due to thermal striping, cracks had developed in the expansion tanks in Phenix reactor. The circuit in FBTR secondary loops was hence modified by changing the sodium line into a hot argon line, with suitable modifications to maintain the surge tank level as per the design intent.

As per technical specification, the rupture discs in the SG headers are to be replaced periodically. As FBTR was operating at low sodium temperatures and purity level of the sodium has been maintained extremely well, it was inferred that there is no concern from corrosion effect at elevated temperatures and hence there is no need to replace the rupture discs. However SARCOP recommended that rupture discs in one loop are to be replaced and the old rupture discs tested in order to ensure that there is no deviation in the set value due to ageing of the material. The existing knife edge aided type rupture discs (Fig. 3) on the inlet and outlet headers of the west SG modules were replaced with state of the art scored type rupture discs (Fig. 4) having the same settings in the west loop. The rupture discs removed from the circuit were pressure tested and found to rupture as per the design intent.

Fig. 4 *Scored type rupture disc*

Fig. 5 *Set-up for injecting the sealant*

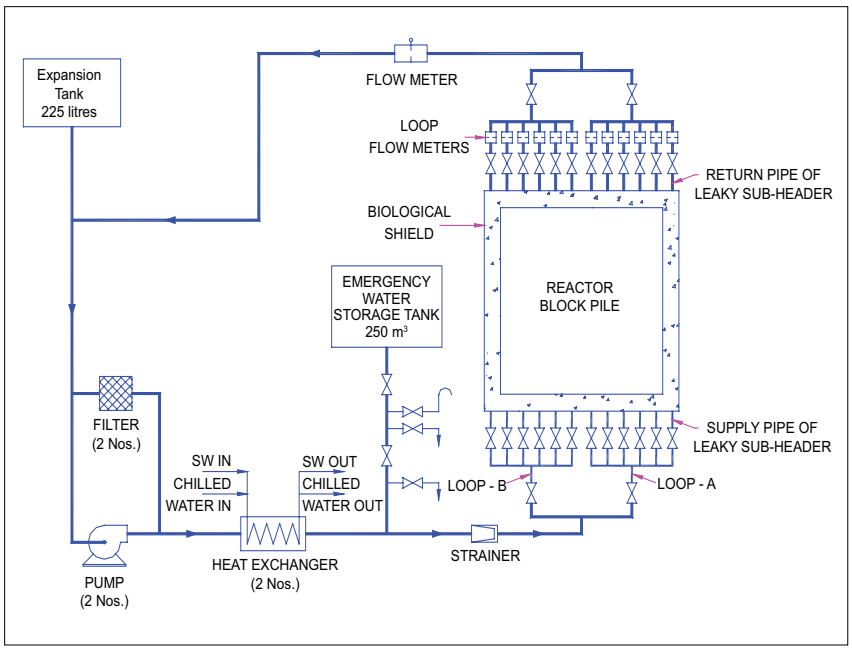

Fig. 6 *Schematic of the Biological Shield Cooling circuit*

In spite of all these major interventions in the sodium circuits, the sodium purity was found unimpaired, testifying to the efficacy of several precautionary measures taken.

Yet another major activity carried out was sealing of leaks from the "Biological Shield Cooling" circuits, using sealant, resin and hardener developed by BARC. The biological shield surrounding the reactor is a bottle of 600 mm thick borated concrete. The temperature of biological shield concrete is maintained using demineralised water as coolant passing through embedded pipes. There are twelve sub-loops (A1 to A6 and B1 to B6) divided into six sectors (Fig.6). Leaks had developed in some of the sub-loops earlier, and were chemically sealed in the years 2000 and 2005 by overseas contractor.

However, leaks of about 3l/h developed in each A4 & A6 sub loops in the year 2007. Pending sealing, reactor was operated with these sub-loops isolated. With the other sub-loops in these affected sectors, it was possible to maintain the temperatures during the 14th irradiation campaign. Concurrently, many in-situ sealing trials were conducted with test specimens in a test loop at FBTR, using sealant, resin and hardener indigenously developed by BARC. After gaining sufficient and satisfactory experience with these trials, actual leak sealing of A4 and A6 coils of Biological Shield Cooling loop were initiated.

Leak sealing operation was carried out in the A4 sub-loop in September 2008. The leak sealing procedure requires identification of the approximate location of the leak. The leak elevations in the sub-loop were identified by water manometer and air purge flow methods. Sealant formulation was mixed in demineralised water in predetermined proportion and injected into the sub-loop up to the required elevation by pressurizing the container (Fig. 5). Sealant was kept under pressure in the sub-loop with compressed air for a predetermined time to allow it to become sufficiently hard to seal the leaks but retain sufficient fluidity to enable draining of the sealant. Afterwards, the sealant formulation was depressurized and drained. The excess sealant formulation sticking to the pipe walls was flushed with demineralised water. The system was then cured for twenty four hours under positive air pressure. After normalizing, helium leak test was carried out and thereafter the loop was filled with water. The leak rate reduced to <0.2l/h in A4 sub loop. Based on these encouraging results, leak sealing was successfully carried out in A6 sub-loop in October 2008. The leak rate from A6 sub-loop was nil.

The other major jobs carried out for high temperature operation are: improving the concrete temperatures in A1 cell penetrations by adding chilled water cooled air handling units and improving the ambient temperatures at and elevation of 2.81 metres in Reactor Containment Building by using split units.

All these major shutdown activities were completed by November 2008.

I.4 Stand-alone Fine Impulse Test System

The Reactor Protection System (RPS) of FBTR is intended to protect the reactor against various incidents, which are neutronic & thermal in nature. RPS receives trip signals from neutronic channels, delayed neutron detection (DND) system, flow monitoring system and core temperature monitoring system. If any one of the parameter crosses its threshold limits, SCRAM logic, which is sub-system of RPS, initiates safety action to de-energize the electromagnetic coils and shuts down the reactor by dropping all the six Control Rods (CRs) simultaneously under gravity into the reactor core.

SCRAM logic is a safety critical system built with solid state devices. Solid state devices may get stuck at '0' or '1' i.e. they may fail in safe mode or unfortunately in unsafe mode also. Hence, the healthiness of SCRAM logic is continuously monitored by Fine Impulse Test (FIT) logic. FIT Logic is galvanically isolated from the SCRAM logic at both the input and output stages, so that it will not interfere with the normal functioning of the SCRAM logic.

At present the FIT function is carried out by the computer systems of Central Data Processing System (CDPS) of FBTR, wherein the FIT logic program runs along with the other plant application software. It was decided to remove the safety related and non nuclear safety functions from the system performing safety critical functions. Since FIT function is a safety related function, it was decided to implement it as an independent stand-alone system.

To achieve high reliability, the Stand Alone Fine Impulse Test (SAFIT) system has been implemented in hardware using programmable logic devices (PLDs). The design was done using VHDL language. Independent functional verification of the HDL design was carried out by IIT Madras using ***'e'*** Hardware Verification Language under Specman Elite verification environment to ensure functional correctness of the design.

Fine Impulse Test Logic injects short duration trip pulses at all the SCRAM logic inputs successively and verifies the propagation of these pulses up to the final stage of safety logic chain. There are sixteen trip parameters, which need to be tested periodically. Out of sixteen trip parameters, eleven trip parameters are with triplicated channels, whereas five trip parameters are with single channel. Triplicated trip parameters are tested with seven different combinations of trip pulses such as A, B, C (i.e., 1/3 mode, at a time one channel receives trip pulses), AB, BC, CA (i.e., 2/3 mode, at a time two channels receive trip pulses), ABC (i.e. 3/3 mode, at a time all three channels receive trip pulses) whereas single channel trip parameters are tested by injecting a single trip pulse. The FIT logic is capable of detecting both safe and unsafe failures in the safety logic of FBTR.

The SAFIT system has been designed to maintain compatibility with the existing interfaces to Control Room and SCRAM logic. The interface logic receives information from the SAFIT hardware and injects the test pulse to the selected input of the SCRAM logic. The fault information is sent to the control room to alert the operator for necessary action. The information is also printed and displayed on a terminal.

Testing is inhibited on start-up parameters (three triplicated parameters), whenever reactor power is higher than two KWt. The testing time is twenty one seconds for triplicated trip parameters and three seconds for single channel trip parameters. Therefore the minimum cycle time is one hundred eighty three seconds and the maximum cycle time is two hundred forty six seconds.

In online mode all the parameters are sequentially tested. In addition, the system has also got a maintenance mode where, individual trip parameters or a group of selected trip parameters can be tested. This mode is provided to help the reactor maintenance personnel to ensure the system healthiness before starting up the reactor.

After initial testing in the laboratory the system was installed at FBTR and the performance was observed round the clock for a period of two months, while the reactor was shut down. The performance of the system was found satisfactory.

I.5 Seismic Analysis of Primary Sodium System Components for the Seismic Re-evaluation

FBTR is a 40 MWt (13.5 MWe) loop type reactor operating with an unique plutonium rich carbide fuel. The first criticality was achieved in October 1985. After twenty years of successful operation, it is planned to extend the life of FBTR. Towards this, seismic reevaluation of structures, systems and components has been undertaken.

Geometrical Details

The main components of the primary sodium system are the reactor vessel, two intermediate heat exchangers (IHX) and two sodium pumps. Two primary sodium pumps deliver sodium into the reactor. The outlet sodium from reactor flows by gravity to the intermediate heat exchangers and then back to the pump suction. The entire primary sodium system is housed in the concrete cells below zero level in the Reactor Containment Building (RCB). The system is provided with a nitrogen-filled envelope called double envelope, to avoid sodium fire in case of main pipe leak. As far as sodium pipings are concerned, the hot pipe lines coming from the reactor joining to intermediate pipe line between IHX & pump, cold line running from pump to 'Y' junction, called 'cullotte' and finally reactor inlet pipe are the main sodium pipings. The main pipe is provided with double envelope, throughout its length. There are four hangers (two for east loop and two in the west loop), attached in the double envelope of the hot pipings and eight hangers (four per loop) in the cold line. There are six bellows in the double envelopes of hot line (three per loop), twelve bellows in the intermediate line (six per loop) and twenty two bellows in the cold loop (eleven per loop). At a few locations the double envelopes are welded to the main pipes. At few more selected locations, there are only guides which allow the axial sliding while constraining all the radial directions, between them. Thus, the system is complex because of strong coupling of components, pipelines and double envelopes. Hence, there is a need to analyse them together with appropriate boundary conditions, which need special kinematic relations to be implemented in the computer code. Fig. 1 depicts 3D graphical display of geometry developed by PDMS, which helps to confirm the accuracy of the geometrical data translated.

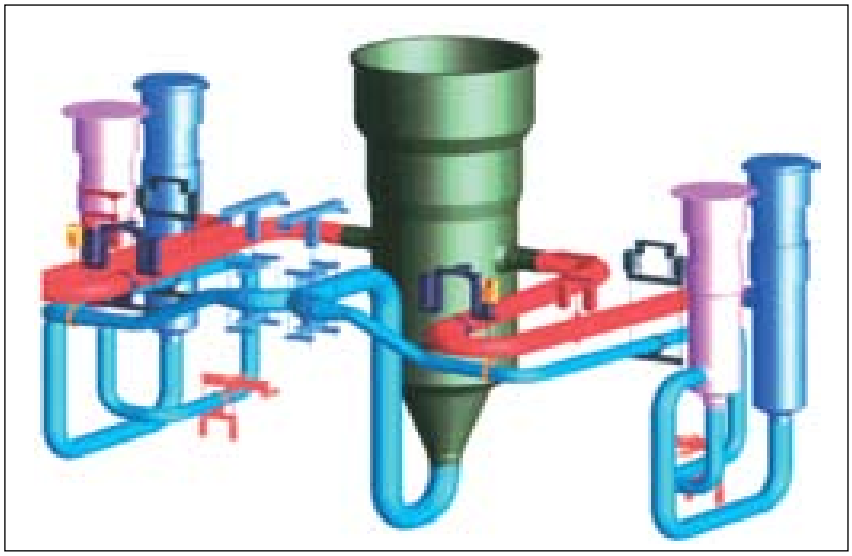

Fig. 1 *PDMS output of primary system*

Loadings

To comply the design code requirements, the analysis is carried out for the dead load, internal pressure and seismic excitations. Total self weight of main components including east and west loops and sodium is about eighty four tonnes. The total weight of double envelopes including east and west loops is about ten tonnes. Average temperatures vary from 653K to 793K for the main components and pipings. The temperatures of double envelopes are maximum 323K less than the temperatures of the respective components at steady state condition. The pressure for reactor vessel and main pipings is taken as 0.5 MPa under normal operating conditions, adding some margin

on the design pressure for pump (57 mlc). For the purpose of seismic reevaluation, review base ground motion (RBGM) spectra were generated at the ground level. The RBGM is similar to safe shutdown earthquake (SSE). Subsequently, floor response spectra (FRS) at the primary system support elevations are generated from the seismic analysis of civil structures. FRS generated at the elevation of reactor supporting elevation in two horizontal and one vertical directions corresponding to 5% damping are applied in such a manner to yield conservative results. Fig. 2 shows the floor response spectra used for the analysis.

Overall Analysis Approach

The analysis is aimed to determine displacements and stresses to check the functional and design code limits. For preventing mechanical interactions between main component/piping and their respective double envelopes, the relative radial displacements are limited to gap between main and double envelopes at respective locations. For ensuring the structural integrity of bellows, the effective axial deflections of bellow are limited to the respective limits prescribed by the bellow manufacturer. Stresses are limited by the primary stress limits recommended by RCC-MR (2002 edition).

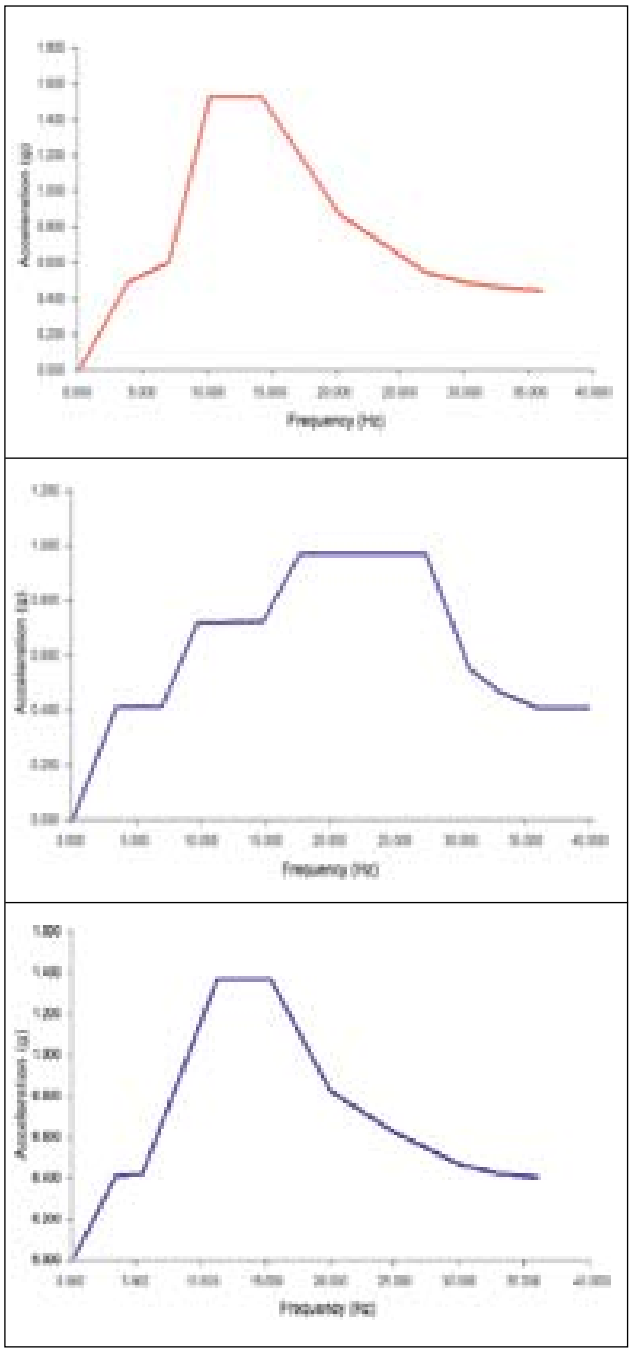

Fig. 2 *Floor response spectra (SSE 5 % damping)*

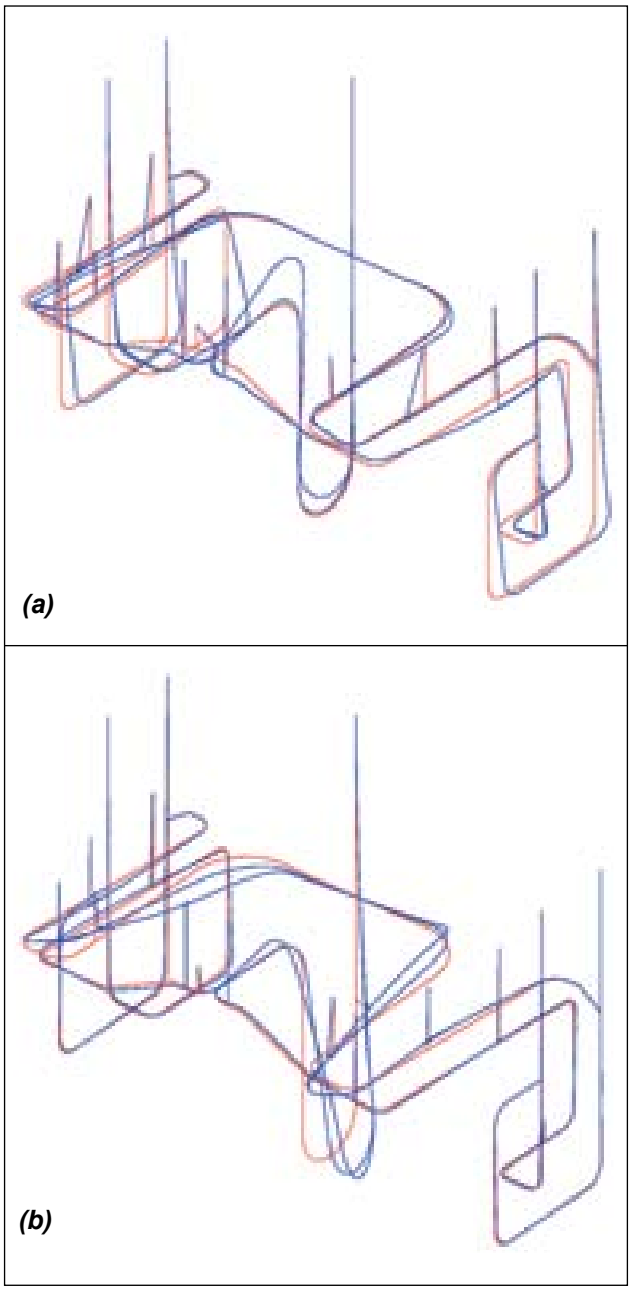

Fig. 3 *Mode shapes depicting*
(a) *Intermediate heat exchangers and pump vibrations at 9 Hz*
(b) *Reactor vessel vibration at 11 Hz*

While pipelines have 1D feature, components, especially at the junctions and branch pipes call for 3D treatment. Addressing these issues, seismic analysis is carried out by following an integrated approach. Finite element method is used for the entire analysis, with the computer code called 'CAST3M' issued by CEA France. The analysis is completed in three steps. In step-1, global analysis is carried out to determine the deflections, forces and moments due to dead load and seismic loadings using straight pipe elements and bends. The deflections are used for verifying the deflection limits. The forces and moments are used for the computation of P_m&(P_m+P_b), following either step-2 or step-3. In step-2, P_m&(P_m+P_b) are computed using the correlations recommended in RCC-MR for the pipes, bends and branch pipes. The correlations for the tees recommended in RCC-MR are used for the branch pipes by assuming that the dimensional restrictions for the fillet radius, etc. are respected, based on which critical branch pipes are identified for the detailed FEM analysis in step-3.

Summary of Results

As the first phase, natural vibration analysis is carried out to determine natural mode shapes and associated frequencies, which have been extracted up to 50 Hz. Fig. 3a and Fig. 3b show the critical mode shapes that are associated with the pumps, IHXs and reactor vessel contributions are predominant. Fig. 4 shows the 3D local deformations and von Mises stress distributions under combined pressure and seismic induced forces and moments in the Y junction at reactor inlet called 'Cullotte', the critical location in the reactor.

Based on the analysis, it is concluded that the seismic behaviour of components in east and west loops including double envelope are similar. The deflection limits to prevent the mechanical interaction between the main and respective double envelopes are met with comfortable margin. The maximum net axial deflections are found to be less than minimum acceptable values. The stresses induced in components namely, reactor vessel, IHX and pumps including their double envelopes are small. As far as pipings are concerned, the hot lines are critical, particularly the shell nozzle junctions. However, stress limits are met with detailed FEM analysis. The pipe bends including cullotte are meeting the design code limits.

In summary, all the main components in the primary sodium systems in the as built conditions meet the seismic design requirements.

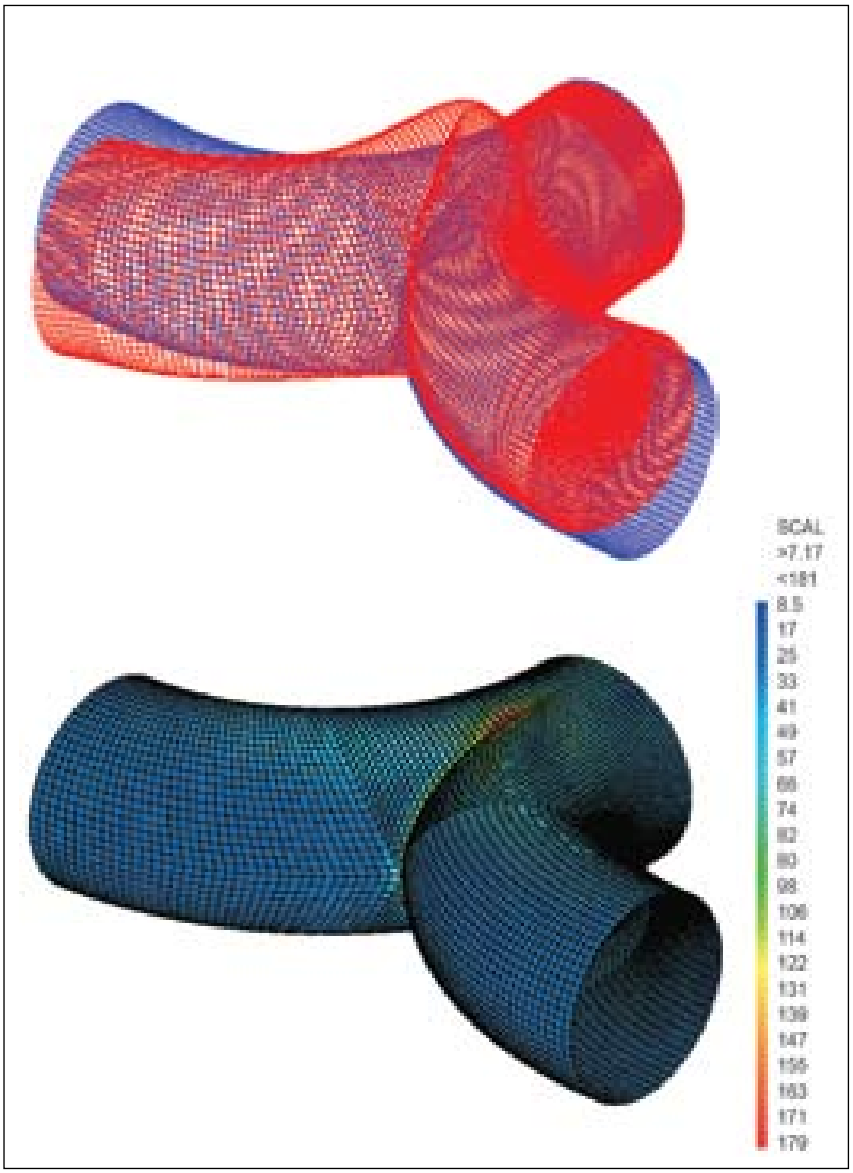

Fig. 4 *Deformation & Von Mises stresses in cullotte under combined loadings*

I.6 Investigative Analysis of Radioactivity Profile during Delayed Neutron Detection Experiments

Calibration and failed-fuel-pin localisation capabilities of the Delayed Neutron Detection (DND) system in FBTR have been assessed with a special perforated natural uranium fuel sub-assembly located at various locations in the core for few hours. During the experiments, gamma spectrometric analysis of Reactor cover gas (RCG) samples and also the gas samples collected from failed fuel localisation system (FFLS), continuous monitoring of clad rupture detection system (CRD) and general radiological monitoring were undertaken.

Immediate and delay counting of the gas samples at different time intervals were done and also the gamma spectra obtained. All the spectra indicated the presence of cover gas activation product ^{41}Ar, fission product noble gases (FPNG) such as ^{85m}Kr, ^{87}Kr, ^{88}Kr, ^{135}Xe, ^{138}Xe, ^{88}Rb, ^{138}Cs and trace quantity of ^{24}Na. Short-lived radionuclides ^{87}Kr, ^{138}Xe and ^{138}Cs were detected in the immediate counting only. RCG samples collected at the time of DND experiments did not indicate the presence of ^{133}Xe and ^{135}Xe in some cases because the formation and build up of these radio nuclides in the cover gas takes much longer time. ^{133}Xe is formed from the decay of ^{133}I with a half life of 20.8 h. Similarly ^{135}Xe is formed from the decay of ^{135}I with a half life of 6.61 h. Hence, the RCG sample collected on the subsequent day of the experiment revealed the presence of these radionuclides. The percentage of total fission product noble gases activity in the cover gas varied from 3 to 26 and this large variation is attributed to varying concentration levels of argon gas as well as time of collection of gas samples. Cover gas samples were also collected using FFLS. RCG is adsorbed in an activated charcoal bed and Kr and Xe gases were separately desorbed and collected in two samplers. The γ-spectrometry of the samplers showed the exact separation of Kr and Xe gases and all the expected radionuclides were present.

Gamma detection based CRD systems of the RCG circuit showed increase in readings by about a factor of 2 to 10 compared to normal values. Increase in the readings of CRD systems revealed a definite release of FPNGs from the special Sub-assembly into the cover gas as well as the capability of these monitors to detect it. The trend behaviour of CRD monitors was similar during all the five DND experiments.

Area γ-monitors in Reactor Containment Building (RCB) showed a marginal increase of ambient dose rate upto 2 μGy/h, and spot measurements, upto 10 μGy/h. The increase in the ambient radiation level in RCB is due to leakage of cover gas into the RCB atmosphere which is essentially ^{41}Ar with a specific activity of 0.18 MBq/m^3. Particulate air activity in RCB was closely monitored using six installed continuous air monitors (CAM) located at 'zero' and -2.81m locations and the trend of the deposited activity on the filter papers of the CAM is shown in Fig. 1. The deposited activity increased with time, reached the maximum value within few hours after reactor shutdown and thereafter showed decreasing trend. Gamma spectrometry of the filter paper samples revealed the presence of short-lived isotopes such as ^{88}Rb and ^{138}Cs, i.e., the daughter products of ^{88}Kr and ^{138}Xe. The maximum particulate activity has been found to be about 0.5 DAC. Surface contamination on the floor of RCB was observed to be about 50 Bq/100 cm^2 due to short lived ^{88}Rb and ^{138}Cs. Gas samples collected from the exhaust side of the RCB filter bank indicated ^{41}Ar in the range of 0.5-1.2 MBq/m^3. The total amount of gaseous activity released through the stack during the five experiments was 15.4 GBq.

In actual case of fuel clad failure in FBTR fuel, the amount of FPNG release is expected to be much higher and the installed monitors are definitely capable of detecting it at the early stage itself.

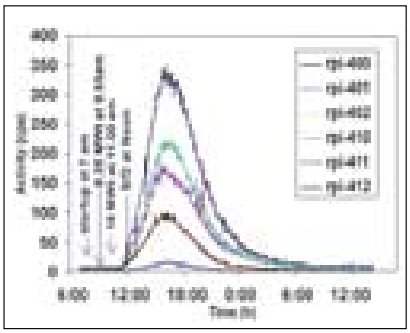

Fig. 1 *Trend of particulate activity monitors*

I.7 Theoretical Assessment of Peak Burn-up Limit for Carbide Fuel

FBTR uses mixed carbide as the driver fuel. The core structural material used for the clad and wrapper are SS 316M and 316L respectively. Carbide fuel burn-up has been increased progressively with periodic evaluation based on the Post Irradiation Examination (PIE). Presently one Sub-Assembly (SA) has reached a peak burn-up of 155 GWd/t which was based on the consideration of wrapper dilation. The burn-up is limited by structural material performance in the core which requires extensive modeling of the effect of neutron damages on these materials. The dimensional instability arising out of the thermal as well as neutron effects calls for the assessment of deformation of clad and wrapper in various burn-up stages.

Although the clad sees higher temperature which makes it swell more than the wrapper tube, the wrapper dictates the burn-up from the dilation of the same which reduces the gap between the SAs in the core giving rise to fuel handling concerns. The performance study requires the analysis to be performed at various axial levels of the core as the clad at active core centre sees relatively higher neutron flux but lower temperature than at the active core top where the neutron flux is low but the temperature is higher (Table 1). Assuming that there is no axial heat conduction, there is an option to separately analyze each axial segment only for the radial temperature profile.

The limiting factors for burn-up of the fuel are viewed with the perspective of the fuel, clad and the wrapper. The clad being the primary barrier has to qualify for its integrity during operation and the wrapper is to retain adequate ductility and deformation should be within limits for the safe handling of SA. The factors that influence the limitation of fuel burn-up of both clad and wrapper are listed in Table 2. The analysis has been performed by computing the clad and wrapper strains at various locations. The computed clad strain comprises thermal creep, irradiation creep and swelling strains. The total strain is shown in Table 3 which match very closely with the PIE results. At 155 GWd/t, the clad strain computed is 6.2% as against the PIE measured value of 5% at 154.8 GWd/t and the diametrical increase is 0.274 mm. The close comparison commends the validity of the swelling and creep correlations

TABLE 1: Parameters at various axial levels

Parameters	Active Core Bottom	Active Core Middle	Active Core Top
Coolant Temp (average)	613K	661.5K	713K
Coolant Pressure (MPa)	0.34	0.25	0.17
Neutron Flux (n/cm^2-s)	125×10^{15}	1.71×10^{15}	0.98×10^{15}

TABLE 2: Burn-up limiting parameters

Clad	Wrapper
Clad integrity	Swelling
Fission gas pressure & FCMI	Creep
Residual ductility	Ductility loss due to neutron irradiation
Dimensional instability arising out of clad deformation by swelling & creep	

TABLE 3: Comparison of predicted & PIE data on clad strains

Burn-up (GWd/t)	Total clad stain (%)		Clad diametrical increase (mm)	
	Predicted	PIE	Predicted	PIE
50	0.2	0.3	0.01	0.018
100	1.9	1.6	0.09	0.08
150	5.7	-	0.27	-
155	6.2	5 (154 GWd/t)	0.274	0.27 (154 GWd/t)
160	6.7	-	0.32	-
165	7.2	-	0.34	-

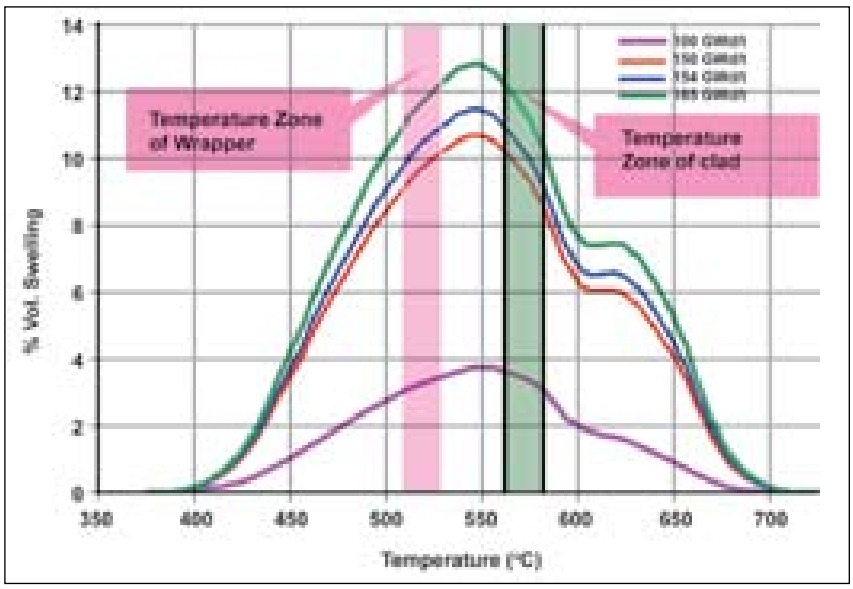

Fig. 1 *Swelling of 20% CW 316 SS*

used in the theoretical predictions. The swelling of 20% CW SS 316 material and the clad and wrapper operating temperature zones are shown in Fig. 1.

The wrapper strains are calculated from creep due to the coolant pressure and swelling. The wrapper at the end of 155 GWd/t is found to dilate 0.7 mm. This dilation was limited to the minimum gap available between the Sub-assemblies to prevent their interaction in any other location other than the intended contact pads. The Sub-assemblies surrounding the 155 GWd/t burn-up Sub-assembly are with different burn-ups as shown in Fig. 2 and accordingly dilatations for both Sub-assemblies (in position 01-02 & 02-04) worked out to limit it within the gap available. From this limitation, the projected burn-up achievable is found to be 169 GWd/t as seen from Fig. 3. From the ductility aspect, by comparing the swelling of the wrapper it is seen to have enough ductility to reach up to a burn-up of 175 GWd/t while limiting the volumetric swelling to 6% which is reported to be the limit for the wrapper to retain enough ductility for handling purposes.

Excessive swelling of the clad can give rise to bundle duct interactions and also can cause a severe coolant flow area reduction. The consequences will be on clad over heating and also excessive stresses on the clad and the wrapper reducing its life. Further, analysis was carried out to estimate the bundle expansion and the wrapper which shows a marginal over growth of the bundle with respect to the wrapper. The pins get readjusted within the void space thereby giving some force on the wrapper, which is also experienced in the PIE operations. It was also ensured through the analysis that the flow area reduction by the clad swelling is not of concern with respect to the coolant pumping power or any blockages.

The FBTR carbide fuel performance study done has been compared against the PIE to predict the burn-up limit which is computed as 169 GWd/t based on wrapper dilations by swelling and creep. The models used are progressively validated through the PIE results.

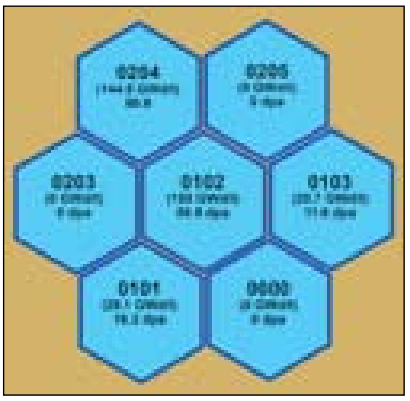

Fig. 2 *Present core burn-up map*

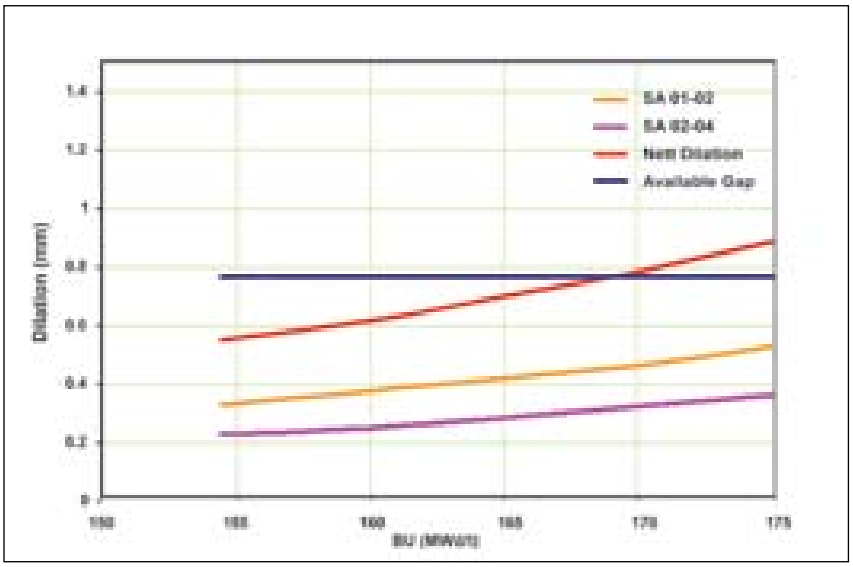

Fig. 3 *Achievable burn-up*

I.8 Development of Floor Response Spectra for the Reactor Building

The assessment of safety of a existing nuclear power plant is undertaken to determine the seismic risk of the plant with respect to a current seismic design specification. The seismic re-evaluation of an existing plant is prompted by the evidence of seismic hazard and revisions of standards in reinforced concrete and seismic design. FBTR is 40 MWt sodium cooled loop type reactor that was constructed 20 years ago and it is required to seismically qualify the plant as per current standards to extend its operating plant life. Seismic re-evaluation of FBTR is carried out jointly by IGCAR, AERB and SRI.

Seismic Re-evaluation

The Reactor Containment Building (RCB) of FBTR is cylindrically shaped and houses the reactor assembly, primary heat transport circuit, fuel handling equipment, rotating crane and auxiliary circuits. The containment ensures the safety of the plant personnel and the public under accident. The RCB is founded on bedrock and is supported on a 2.5 m thick base slab from where all the internal structures and the circular wall are constructed. The containment wall is of normal reinforced concrete and has a diameter of 25 m with a thickness of 900 mm. The dome of the RCB is constructed in two layers separated by PVC membranes.

The internal structures in RCB are divided into four zones A, B, C, and D according to their accessibility and geographic location. The cells designated as zone A, house and support the reactor vessel, sodium inlet and outlet pipes, steel vessel and thermal insulation. The zone B cells house the installation of primary sodium system and certain active pits. The zone C surrounds zone B and houses auxiliary systems and equipment. Zone D houses fuel handling flasks, rotating crane, control panel etc. and is above zones A, B and C. The floor response spectra are developed for seismic qualification of equipment that are not modelled with the primary structure.

Mathematical Model

The three dimensional mathematical model of RCB is developed using finite element software ANSYS. The 3D model consists of rigid assemblage of shear walls, beams and columns. The different elements used for modeling are described below.

Elastic Shell elements having both membrane and bending properties with six degrees of freedom at each node are used for modeling vertical Reactor Containment walls and Reactor Containment floor-slabs

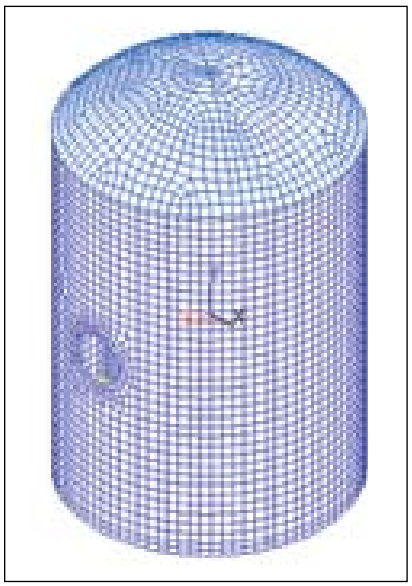

Fig. 1 *Finite element model of reactor containment of FBTR*

TABLE 1: Summary of predominant modes in FVA

Mode No	Frequency Hz	Mass participated (kg)		
		X	Y	Z
4	7.03	7813	6.47E-03	4.61E+06
5	7.32	4.77E+06	765	7707
46	18.67	1.83E+06	2.49E+06	708660
47	19.07	1.12E+06	2.17E+06	1.35E+06
48	19.22	2.91E+06	74	1.39E+06
49	19.61	39542	171052	1.97E+06
60	22.96	5344	1.87E+06	648
140	36.36	3845	1.86E+06	16635
144	37.95	27807	32483	543953
151	40.36	175297	590060	35959

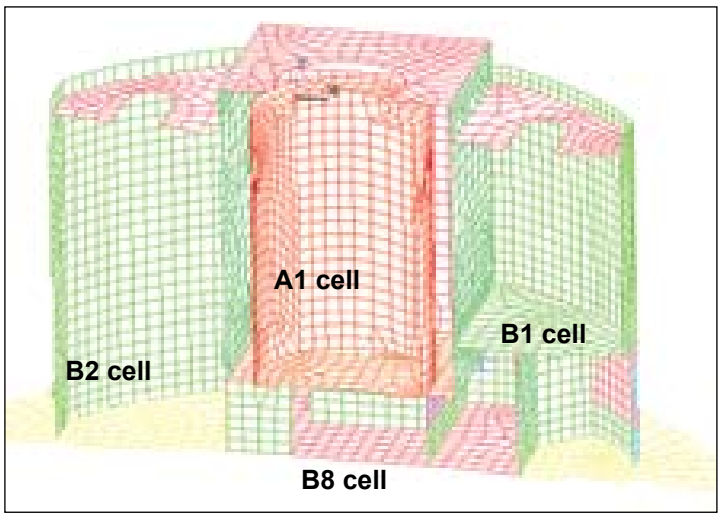

Fig. 2 *Section across RCB showing A1, B1, B2 and B8 cells*

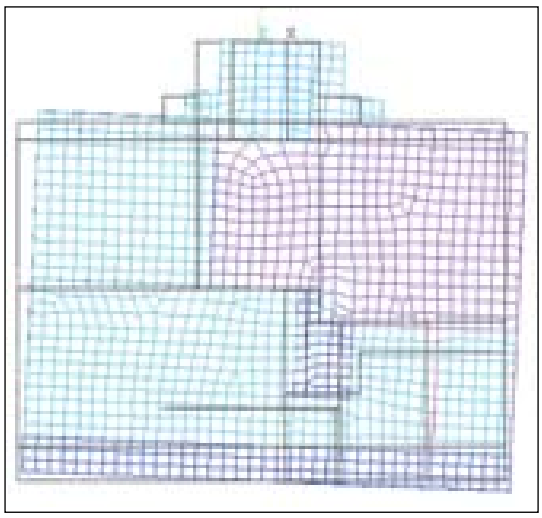

Fig. 4 *Mode shape 5, frequency 7.32 Hz*

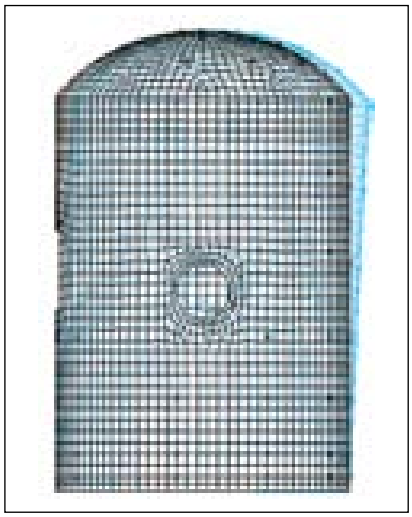

Fig. 3 *Mode shape 5, frequency 7.32 Hz*

and roofs. Elastic beam elements having six degrees of freedom at each node, are used for modeling beams and columns in the model. Spring-Damper element having longitudinal or torsional capability in 1-D, 2-D, or 3-D applications with up to three degrees of freedom at each node are used to model the soil medium. The mathematical model is presented in Fig. 1 and Fig. 2.

Free Vibration analysis or Eigen value analysis is carried out by Block Lanczos method to obtain the natural frequencies and mode shapes of the mathematical model of the containment building. Table 1 presents predominant modes from the analysis. The mode shape for a predominant mode is depicted in Fig. 3 and Fig. 4.

Floor Response Spectra

Time history analysis is carried out by modal superposition method with more than 90% mass accounted for in the modal analysis. For this, three independent spectrum compatible time histories corresponding to Review Level Earthquake are used as input. From the response histories at the respective nodal locations, the floor response spectra are obtained. The envelope of the floor response spectra at reactor vault location and at the steel platform supporting control panels at EL at 0.00 is presented in Fig. 5 and Fig. 6 respectively. In reactor vault support, maximum amplification is 13 m/sec^2 at around 19 Hz in "X" direction, 4.8 m/sec^2 at 21 Hz in Vertical direction and 11 m/sec^2 at 21 Hz in "Z" direction, all for 5% damping. The peak amplification in FRS in Steel Platform at EL 0.00 is 22 m/sec^2 at 6-7 Hz in "X" direction, 17 m/sec^2 at 6-7 Hz in vertical direction and 20 m/sec^2 at 6-7 Hz in "Z" direction.

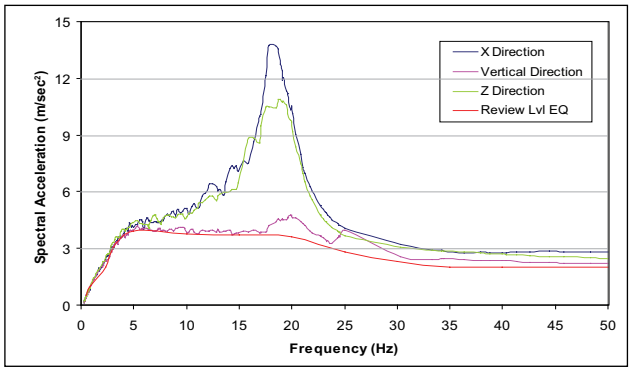

Fig. 5 *Floor response spectra for reactor vault support (5% damping)*

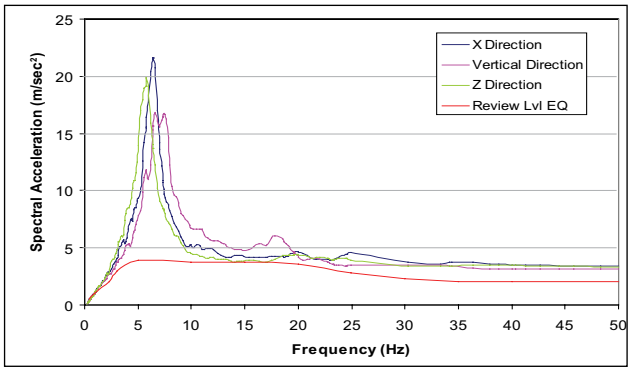

Fig. 6 *Floor response spectra for steel platform supporting control panels (5% damping)*

I.9 Development of Gas-gap and Sodium filled Capsules for Irradiation of Specimens at Higher Temperatures

In the design of instrumented irradiation capsule, the specimens will be kept in an inner container filled with sodium and surrounded by outer container with an uniform annular gap in between the containers. Helium-argon gas mixture is filled in the annular gap to adjust the heat transfer characteristics of the gap. Thermocouples will be attached to measure the irradiation temperature on-line. As part of development of instrumented irradiation capsule, a sample capsule was fabricated with outer container (20 mm outer diameter and 1 mm wall thickness) and inner container (16 mm outer diameter and 1 mm wall thickness), filled with specimens and sodium in the inner container and helium-argon gas mixture in the annular gap between the containers. One stainless steel sheathed chromel-alumel thermocouple was attached to the centre of the capsule by laser welding to measure the temperature of specimens immersed in sodium during exposure of the capsule to high temperatures. Two other thermocouples were attached to the surface of outer container to measure the ambient temperature respectively. This capsule was heated in an electrical furnace up to 200°C and temperature of specimens indicated by thermocouple was recorded using a data acquisition system along with temperatures indicated by other thermocouples. Fig. 1 and Fig. 2 show the photograph of the sodium filled capsule with thermocouple attachments and its exposure in electric furnace respectively. It was found that the temperature profiles shown by the thermocouples were smooth thereby verifying the feasibility of attaching thermo-couple to the irradiation capsule to measure the temperature. A theoretical model was developed to simulate the transient temperature distri-bution in the capsule when exposed in the furnace at different temperatures. Temperature values measured by thermocouples during exposure of the capsule in the furnace and theoretically predicted values match well. Fig. 3 and Fig. 4 show the measured temperature profiles and the predicted values respectively.

Fig. 1 *Sodium filled capsule with thermocouple attachments*

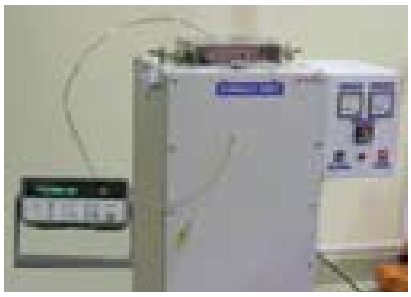

Fig. 2 *Exposure in electrical furnace*

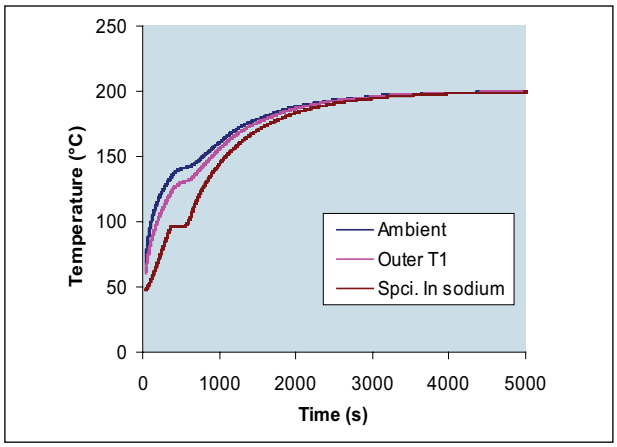

Fig. 3 *Temperatures indicated by thermocouples*

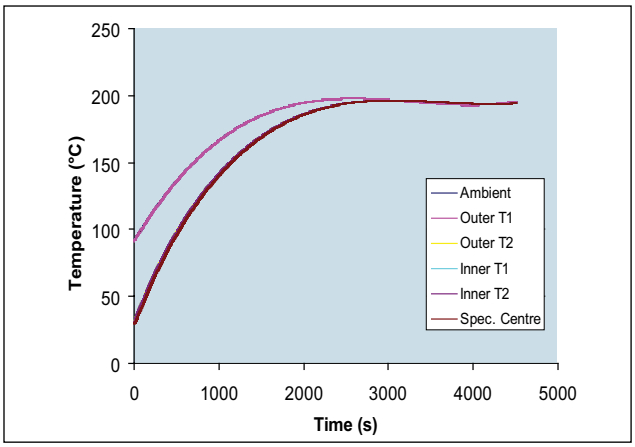

Fig. 4 *Results of temperature distribution by theoretical analysis*

I.10 X-ray Radiography of 154 GWd/t Irradiated Fuel Pins

During the fuel irradiation to higher burn-up levels, the important characteristics that have influence on the fuel pin integrity in the reactor are fuel pellet cracking, fuel densification, fuel pellet swelling, fission gas release from the fuel matrix, fission product migration, clad creep, clad swelling, fuel column growth, clad corrosion and crud deposition and the resultant change in thermal conductivity of the fuel/clad gap and fuel itself. The total length of fuel column (stack length) in the fuel pin is important, as it gives insight into fission gas release and subsequent changes in the pin internals (i.e. plenum and spring). Deformation of fuel pins in the fuel assembly affects the thermal hydraulic characteristics of the coolant and efficiency of cooling. X-ray radiography of fuel pins is aimed at estimation of variation in the fuel stack length, spring and plenum length with respect to pre-irradiated conditions. Image analysis has been employed on the radiographs to assess pellet to clad gap, pellet to pellet gap, cracks etc in the fuel columns. Radiography was carried out in RML hot cells, employing a specially designed fuel pin carriage with tungsten markers embedded at periodic intervals for the purpose of calibration. The radiography system used was 420 kV Philips industrial X-ray unit. A special carriage drive for high speed positioning and retrieval of films was setup to minimize the effect of high gamma fogging. In addition, various strategies such as increasing the applied voltage, applied current (mA) and minimum exposure time have been adapted to minimize the effect of gamma fogging. Dimensional measurements on the radiographs were carried out axially (for stack length) using a three dimensional non contact coordinate measuring instrument (MONDO) and by using image processing methodologies.

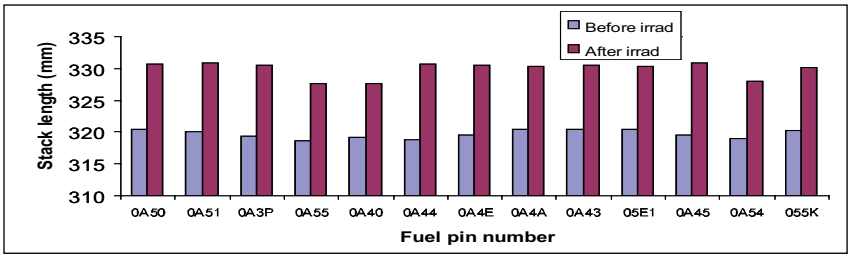

Fig. 1 *The variation in fuel stack length for various fuel pins after 154 GWd/t burn-up*

Fig. 1 shows the variation in the stack length of various fuel pins, after 154 GWd/t burn-up. The fuel column stack length is found to increase in all the fuel pins and it varied from about 8.47 mm to 11.71 mm. (2.7% to 3.7%). The average increase in stack length is 10.20 mm. It is observed that the spring length varies from 98.6 to 102.6 mm as against the nominal value of 106 ± 2 mm. It is obvious that the axial increase in the stack length resulted in the compression of the spring. The spring compression is clearly seen in all the radiographs. The digitized radiography image of a portion of the fuel column of one of the fuel pins is shown in Fig. 2. A linear indication is seen across the pellets spreading axially.

Fig. 3 shows the radiography image of the spring side fuel region of pin 0A45. It is observed that the fuel pin is bent in the spring side of the fuel column which is indicated by arrows.

The steep increase observed in stack length measurements beyond 100 GWd/t burn-up and complete closure of the fuel-clad gap indicates that the fuel column has entered the restrained swelling regime. From the X-ray radiography images, it has been observed that clad tube has not breached and also the restrained swelling behavior of carbide fuel. These results indicated no constraints to increase the fuel burn-up beyond 154 GWd/t.

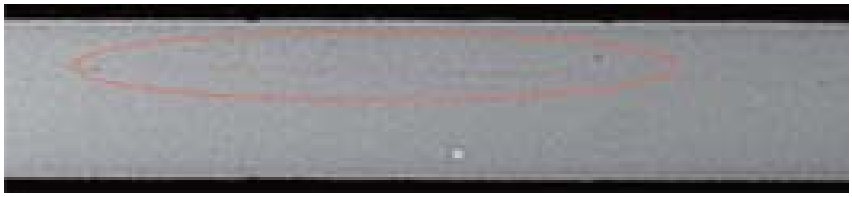

Fig. 2 *A linear indication seen in the pellet region of pin 0A45*

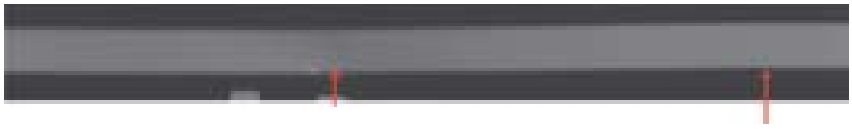

Fig. 3 *Spring side fuel column of pin 0A45 (bend on the pin is clearly seen)*

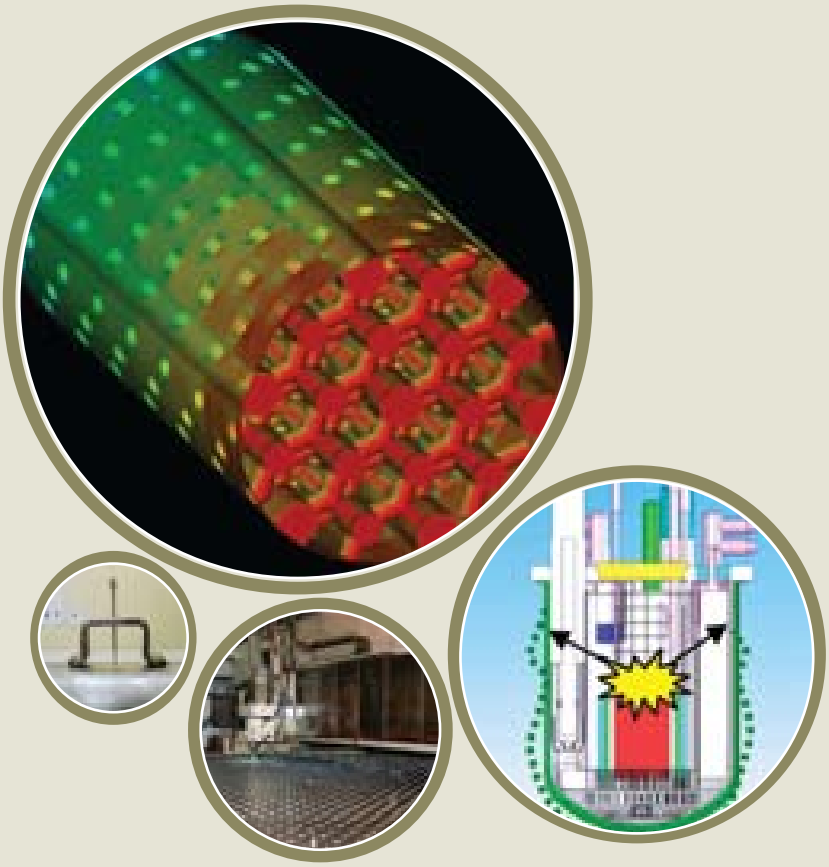

II

Prototype Fast Breeder Reactor

II.1 Construction Status of PFBR

The construction of PFBR has progressed well during 2008 (Fig. 1). The safety vessel of 13.5 m diameter and 13 m height, which was manufactured at site with close fabrication tolerances, has been lowered to its position in the reactor vault (Fig. 2). Manufacturing of main vessel, grid plate, core support structure, primary piping, steel shielding, outer boron carbide subassemblies and a number of shutdown mechanisms has been completed.

Manufacturing of long delivery mechanical components of Nuclear Steam Supply System (NSSS), viz fuel and blanket subassemblies, rotating plugs, control plug, IHX, sodium pumps, steam generators, inclined fuel transfer machine and decay heat removal exchangers is in different stages of progress in Indian industries. Manufacturing of inner vessel and top shields is in an advanced stage of completion at site assembly shop.

Construction of eight numbers of Nuclear Island Connected Buildings, diesel generator buildings, turbine building, sea-water intake and outfall, ventilation stack, simulator building, raw water / fire water pump house is in progress at various elevations. Turbo-generator package, 230 kV switchyard package, 6.6 kV switchgear package, plant cranes, diesel generator sets, variable speed drive for pumps, I&C system packages, and sodium service valves contract are under execution by the Indian industries. The contract for sodium piping package has been awarded. Sodium has been filled into the reactor sodium tank from six sodium tankers. The project has achieved 40% overall physical progress as of December 2008.

The successful manufacturing of nuclear components viz main vessel, grid plate (Fig. 3) and safety vessel has demonstrated the capability of Indian industries to manufacture fast reactor components comparable to international standards.

Fig. 1 *Overall view of nuclear buildings*

Fig. 2 *Erection of safety vessel*

Fig. 3 *Grid plate*

II.2 Ab-initio Computational Fluid Dynamics Simulations of Flow and Temperature Distributions in Fuel Subassembly

In PFBR, the fuel subassembly (FSA) is a 217 pin bundle generating a high heat flux of ~1.5 MW/m^2. The spacing between the fuel pins is maintained by helically wound spacer wires over each pin. The spacer wires also induce cross stream flows that promote mixing of sodium among the various sub-channels of the fuel subassembly. There are significant flow and temperature variations around the fuel pins with local hot spots beneath the spacer wires. The life of the fuel pin is a strong function of the peak temperature seen by the clad, which in turn is affected by the sodium flow distribution. In conventional thermal hydraulic analysis of the fuel subassembly, the peak value of the clad temperature is estimated by the use of hotspot factors. This approach leads to a conservative estimate of the temperature. Unfortunately, it is impossible to measure this temperature in any operating reactor. Realistic estimate of this temperature requires detailed knowledge of flow and temperature distributions within the fuel pin bundle.

The fuel pin assembly forms a tight triangular lattice with helically wound spacer wires, forming over 514 sub-channels with free mixing of sodium from one sub-channel to the other. The hydraulic diameter of the sub-channel is very small (~3.5 mm) and it offers little scope for small scale experiments. Experimental determination of local flow and heat transfer characteristics is very difficult due to the miniature nature of the sub-channels that demand non-intrusive-type of instruments. Since the Prandtl number of sodium is very small (0.005), water cannot simulate the heat transfer behavior of sodium. Experiments need to be conducted only in sodium. Due to the violent exothermic reaction of sodium with air/moisture, compounded with opaque nature of sodium that offers no possibility of flow visualization, sodium experiments are very difficult to perform.

Traditionally, sub-channel approach is followed for the thermal hydraulic analysis of the fuel pin bundle. This approach is used in the codes like SUPER-ENERGY, wherein porous body formulation is adopted and the exchange of mass, momentum and energy among the various sub-channels is defined explicitly based on limited experiments performed on fuel pin bundles. This approach provides only a global picture of the thermal hydraulics within fuel subassembly without much detail on pin-to-pin circumferential variations. Contrary to this porous body formulation, computational fluid dynamics (CFD) based approach has more maneuverability to capture intricate details of the flow physics, which are very difficult to measure in a tightly packed pin bundle. In this approach, complex thermal hydraulic characteristics of the FSA are predicted from fundamental principles by numerically solving the conservation equations of mass, momentum and energy.

Due to the advances in the computing technology and innovations in CFD solution methodologies, CFD simulation of thermal hydraulics from fundamental principles is becoming increasingly possible. In order to accomplish this task a collaborative project has been initiated with IIT-Bombay. In the CFD adventure for a complex fuel subassembly, generation of a structured mesh with adequate refinement around the clad and spacer wire surfaces is a challenging task, requiring concerned efforts. A customized mesh generation tool has been developed for this purpose. A part of the CFD mesh generated for 217 pin PFBR FSA is depicted in Fig. 1.

The mesh requirement for a complete simulation of entire pin bundle is highly demanding in terms of memory and computational

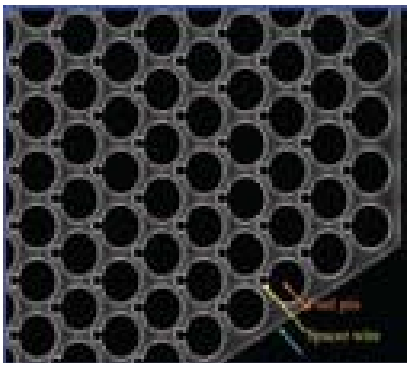

Fig.1 *Part of the structured finite volume mesh for 217 pin fuel subassembly*

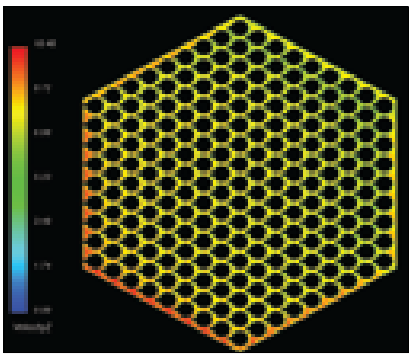

Fig.2 *Axial velocity distribution in the cross section of the central FSA (m/s)*

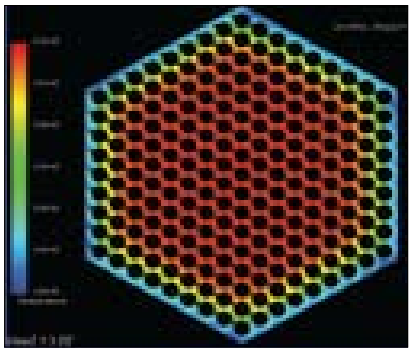

Fig.3 *Sodium temperature distribution at the top of active zone in central FSA (°C)*

time. To circumvent this difficulty, the rotational periodicity in the velocity and pressure distributions has been judiciously utilized. In this novel approach, detailed velocity and pressure distributions are estimated only for 1/6th length of the spacer wire pitch. Then the flow and pressure fields for the entire length of the fuel pins are established from the simulation results corresponding to 1/6th pitch. This flow field is utilized in the energy equation to determine the temperature distribution of sodium in the entire pin assembly, taking into consideration the axial variation of the heat generation rate.

The axial velocity and temperature distributions at the exit of the active zone are depicted in Fig. 2 and Fig. 3. The velocity is highly non-uniform in the wall sub-channels, varying from 10.5 m/s to 8 m/s. The velocity is maximum in the sub-channels housing the spacer wire, despite a larger hydraulic resistance. Since the spacer wire revolves around the pin, the location of the sub-channels of the wall revolving with more velocity is around the inner periphery of the hexcan. It is evident from the temperature contours that the mixing induced by the spacer wires is insufficient. At the top of the active zone, there is a temperature difference of over 100 K between the central and wall sub-channels, with wall sub-channels being colder due to flow by-pass. This temperature difference reduces in the top axial blanket region to 60 K. The value of non-dimensional peak clad temperature (ξ) defined as equation,

$$\xi=(T_{Peak\text{-}Clad}-T_{Na\text{-}Bulk})/(T_{Avg\text{-}Clad}-T_{Na\text{-}Bulk})$$

where $T_{Peak\text{-}Clad}$ is the peak clad temperature at any axial location, $T_{Na\text{-}Bulk}$ is the bulk sodium temperature at that level and $T_{Avg\text{-}Clad}$ is the average clad temperature. ξ is found to vary from 2 to 5, providing valuable information for use in the safety analysis.

Another hallmark of this collaborative project with IIT, is the development of integrated models for CFD analysis of entire FSA starting from orifices at the foot to top of the pin bundle considering pin-to-pin variations in the power generation. A customized mesh generator has been developed for generating tetrahedral mesh for complex honey-comb orifice plates. The pressure distribution in the honey-comb orifice plates in a typical FSA is depicted in Fig. 4. The pressure drops predicted by the CFD code has been found to compare within 20% of the experimental data.

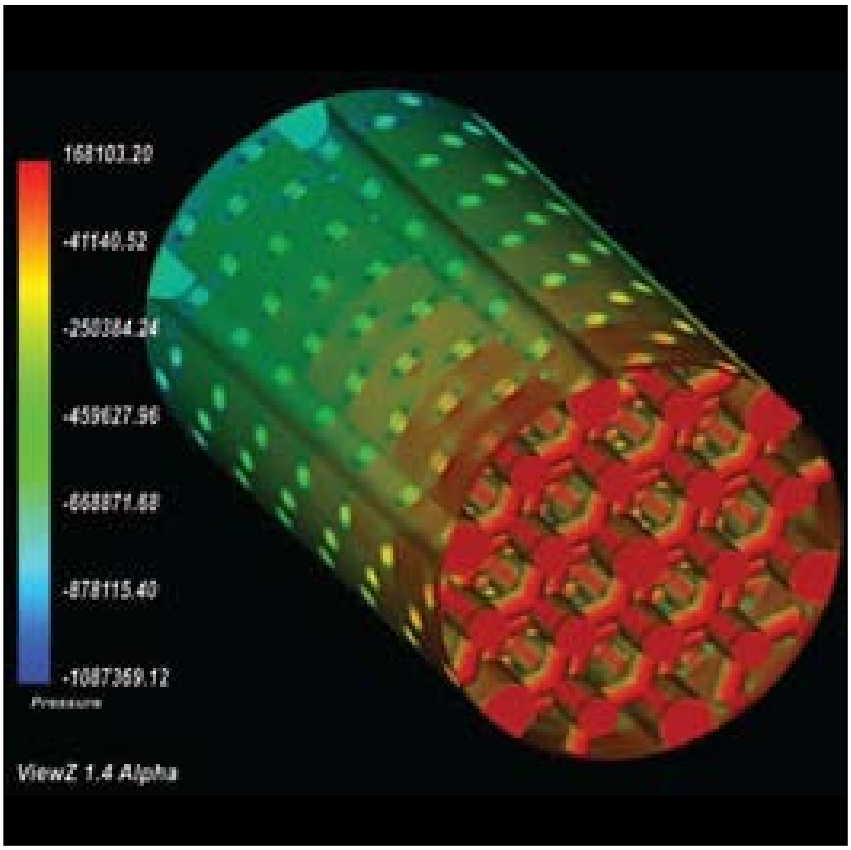

Fig.4 *Isometric view of pressure distribution in honey-comb orifice plates (Pa)*

II.3 Fuel Subassembly Lift Force Experiment

In PFBR, subassemblies are mounted in the grid plate sleeve and cold sodium enters the subassembly through the slots provided on the foot of the subassembly. Top and bottom labyrinths are provided on the foot of the subassembly. The function of the top labyrinth is to minimize the leakage flow of cold sodium into the hot pool and the function of the bottom labyrinth is to ensure the minimum flow required for main vessel cooling. Tests were conducted in water test loop at Engineering Hall-II to investigate the hydraulic lifting/floating of maximum rated dummy fuel subassembly. Full scale model of subassembly was manufactured incorporating top and bottom labyrinths, dummy fuel bundle and grid plate sleeve.

In order to allow the rated flow through the subassembly and leakage flows, subassembly should have sufficient hold down force to prevent hydraulic lifting. It has been theoretically estimated that the hydraulic lift force acting on maximum rated fuel subassembly is 8.095 kN against the hold down force of 9.980 kN.

The test loop consists of grid box assembly with four inlet water connections as shown in Fig. 1. Full scale model of Zone-1 grid plate sleeve was machined and assembled with grid box for mounting the test sub assembly and this arrangement simulates the support condition and flow path for subassembly as in the reactor. Perspex embedded SS window was assembled in the test loop to view the movement of top end of subassembly during experiments.

In the present study, overall subassembly pressure drop measurements with grid plate sleeve were carried out. Pressure tapping points are provided in the pipe of grid box assembly, subassembly exit location and bottom collection chamber for the measurement of pressure (Fig. 2). Experiments were conducted for a maximum loop flow of 190.1 m^3/h and cold plenum pressure below the grid plate is simulated in bottom collection chamber for each flow tested. The temperature of the demineralised water was maintained at 343 K. Loop flow rate was measured using orifice flow meter. Bottom leakage flow is sent to the main tank via bottom collection chamber. A marking on the top of subassembly was made and it was clearly visible through the perspex window provided in the test loop. A reference marking was provided on the outer surface

Fig. 1 *Test loop*

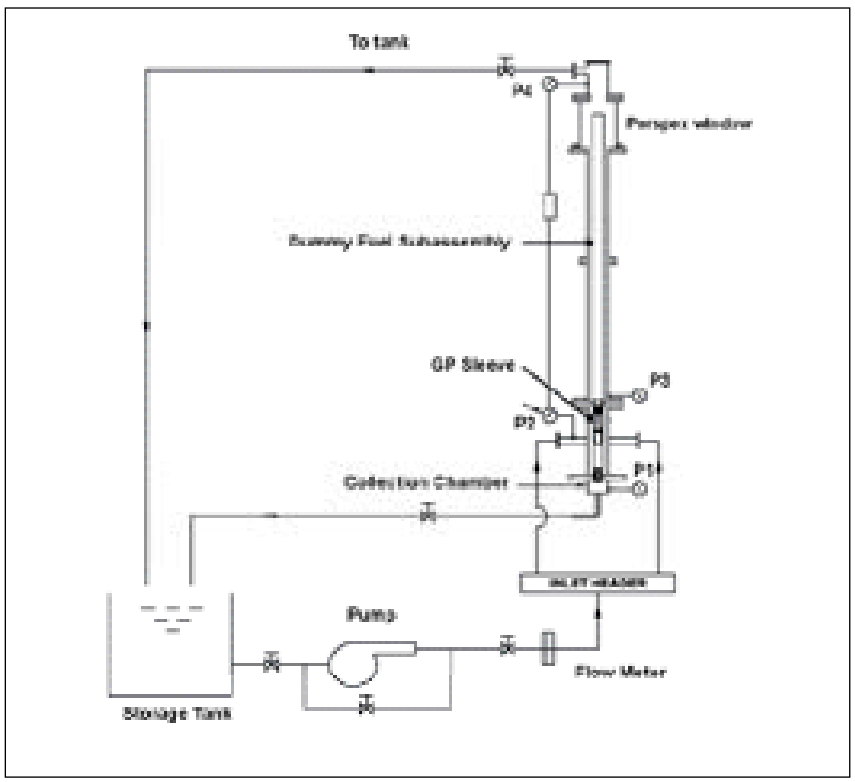

Fig. 2 *Schematic of test loop*

of the perspex window. When the flow was sent through the test loop these markings were carefully monitored for any lifting/floating of subassembly.

Fig. 3 shows the pressure drop characteristics of subassembly with grid plate sleeve. From the studies it is found that the overall pressure drops of subassembly with grid plate sleeve is 63.43 mlc of sodium at nominal sodium flow of 36 kg/s against the theoretically estimated value of 64.23 mlc of sodium. From the experiments it is observed that subassembly was not lifted from the grid plate sleeve for maximum loop flow of 190.1 m^3/h at 343 K.

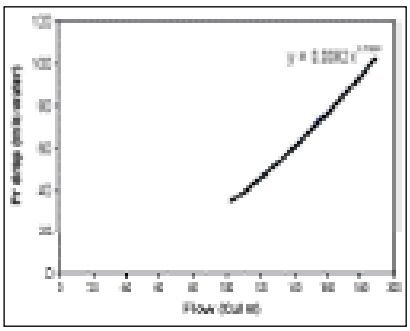

Fig. 3 *Pressure drop of sub assembly (Model)*

II.4 Testing of Back-Up Seal

Elastomeric seals are provided in PFBR to seal the annular gap between rotating and stationary parts of the rotatable plug support arrangement. This comprises of two numbers of inflatable seals and one back-up seal. During reactor operation, the annular gap is sealed by one of the inflatable seals along with the back-up seal. Before starting plug rotation, the second inflatable seal is inflated and the back-up seal is disengaged and kept in raised condition.

The back-up seal is a static seal with sealing achieved by the compression of the seal. A trapezoidal shape seal has been selected to reduce the compression load required to seal the surfaces. The seal is fixed to a seal holder and a compression load is applied uniformly over the seal surface.

To validate the design, a one metre diameter prototype backup seal (manufactured by M/s. Hasetri, Rajasthan) was tested at room temperature as well as at a higher temperature of 383 K. The operating conditions are shown in Table 1.

During the room temperature testing of seals, the effectiveness of sealing was checked for three different clamping loads of 500 N, 1000 N and 1400 N per clamping point and the axial seal displacement (compression) was measured for the loading case. These tests were carried out for three axial level differences of 0, +1 and -1 mm and for a radial gap of 5 mm. Test results show that for all the three axial level conditions the leak rate was found to be less than the maximum acceptable leak rate of $1x10^{-3}$ std cc/s per m length of seal at 1400 N clamping load for an inter seal pressure of 250 mbar. The compression of the seal at the load was 5 mm.

High temperature test facility consists of cylindrical heater shell with tape heaters and hot air blower. The Backup seal test rig assembled inside heater shell is shown in Fig.1 and the heater shell in boxed up condition is shown in Fig. 2. After reaching the steady temperature of 383 K around the seal region, the effectiveness of sealing was checked with three

Table 1 : Operating conditions of seal

Parameters	In reactor	In test facility
Pressure inside the sealing surface	20 kPa (200 mbar) (normal condition)	25 kPa (250 mbar)
Temperature	363 K max	383 K max
Fluids in contact	Air on one side and argon on other side	Air on one side and argon on other side
Material in contact	Carbon steel surface	Carbon steel surface
Radial gap to be closed	5±2 mm	5±2 mm
Axial mismatch between two surfaces	±1 mm	±1 mm
Average amount of seal compression in axial direction	5 mm	4.5 to 5 mm

Fig. 1 *Back-up seal test rig inside heater shell*

Fig. 2 *Back-up seal rig with heater shell in boxed condition*

different axial levels of 0, +1, -1 mm and radial gap of 5 mm. All these tests were carried out for a seal compression of 5 mm.

Test results show that required leak tightness (< 1 x 10^{-3} std cc/s per m length of seal) can be achieved even for differential level difference of $\pm$1 mm for a radial gap of 5$\pm$2 mm at room temperature as well as at an elevated temperature of 383 K for 250 mbar inter seal pressure. The testing of backup seal at room temperature and at elevated temperature has given confidence to the design of the backup seal for PFBR.

II.5 Design and Analysis of Handling Structures for Erection of Large Vessels

Handling of large diameter thin walled shell structures, such as safety vessel and main vessel without causing any change in geometrical shapes is a truly challenging task in the erection of reactor assembly components of PFBR. The erection methodologies of the main vessel and safety vessel have been finalized in novel ways. The safety vessel (SV) has been first erected inside the reactor vault (RV) successfully in June 2008. Subsequently, it is planned to lower the main vessel assembly with core support structure (CSS) and core catcher (CC) inside the safety vessel. During this erection, four lugs are attached to the core support structure. The main vessel will be lifted through four ropes attached to the lugs. The ropes will be connected to a spider at the top and subsequently to the crane hook. During this process the lifting ropes will support the weight of main vessel along with CSS and CC. There are twelve equally spaced aluminium pads of diameter 400 mm placed in the safety vessel for the seating of main vessel inside the Safety vessel. Once the main vessel is placed on the safety vessel, the load is transferred to safety vessel. While resting on the safety vessel a box type ring will be attached to the main vessel top portion with thirty six stiffeners. The main vessel will then be lifted through the box type ring with seventy two rods attached to it. The rods will pass through the sleeves present in outer wall of RV. Grid plate, thermal baffle, main vessel cooling pipes, primary pipes and inner vessel will then be placed in the main vessel, in the hanging condition. Finally, the roof slab will be brought to the RV and supported on the outer wall of RV. The main vessel will be lifted further to bring in position to the roof slab and will be welded to it.

Since the main vessel and safety vessel are large size thin shell structure and should not undergo any plastic deformation during erection, these are analysed with CAST3M FE software for the loads appearing on them during,

- Lifting of safety vessel through 12 lugs along with the spider
- Seating of main vessel with CC and CSS at the base on

aluminium pads in safety vessel

- Lifting of assembly (Main vessel, CC, CSS, GP, IV and primary piping) through 72 rods.

Inner diameter of safety vessel is fixed as 13.5 m. The self-weight of safety vessel along with the weight of insulation is 155 t. The lugs for lifting the safety vessel are designed. The safety vessel is analysed for erection load with six lifting lugs attached to its support flange. Conservatively, the total load of safety vessel along with insulation is taken as 180 t for analysis purpose. The stresses on the different parts are found to be within the elastic limit (yield stress), thus avoiding any plastic deformation. However, considering possible uncertainties in load distribution in the actual site condition twelve supports are recommended. The analysis is carried out with twelve lifting lugs also. The radial deflections at the conical support to safety vessel junction are found to be smaller than 0.4 mm, which are insignificant. Hence, there is no requirement of putting spider at that location during erection.

A lifting spider is designed to facilitate the vertical lifting of the safety vessel i.e. the lifting lugs are connected to spider with vertical ropes. Two designs are considered, one with single point lifting at the centre and another with four point lifting. Based on ease of manufacturing the design with four point lifting is suggested. The spider is made of twelve radial beams which are interconnected by tangential beams. The beams are made of ISMB 600 with additional plates in some sections to increase the rigidity. Lifting blocks are attached to the beams as box type structure at 90° apart. To adequately transport the safety vessel from the site assembly shop to reactor vault location a base frame is designed and the safety vessel is supported on this base frame through four vertical supports and support blocks.

Stress analysis of the base frames, for transporting safety vessel and main vessel from site assembly shop to RV location, has been done to verify the support carrying capacity and to find the deflection levels at the loading points. For easy and safe transport the maximum deflection are limited to less than 25 mm. Fig. 1 shows

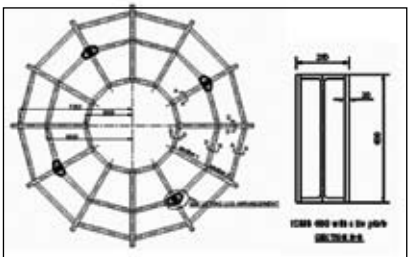

(a) Spider arrangement for four point lifting

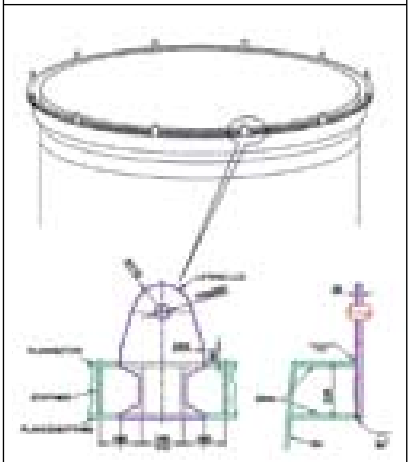

(b) Lifting lug arrangement for safety vessel

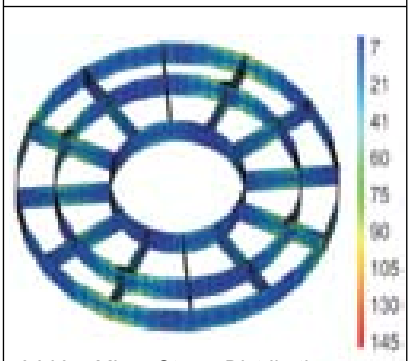

(c) Von Mises Stress Distribution

Fig. 1 *Design and analysis of space spider structure used for handling safety vessel erection*

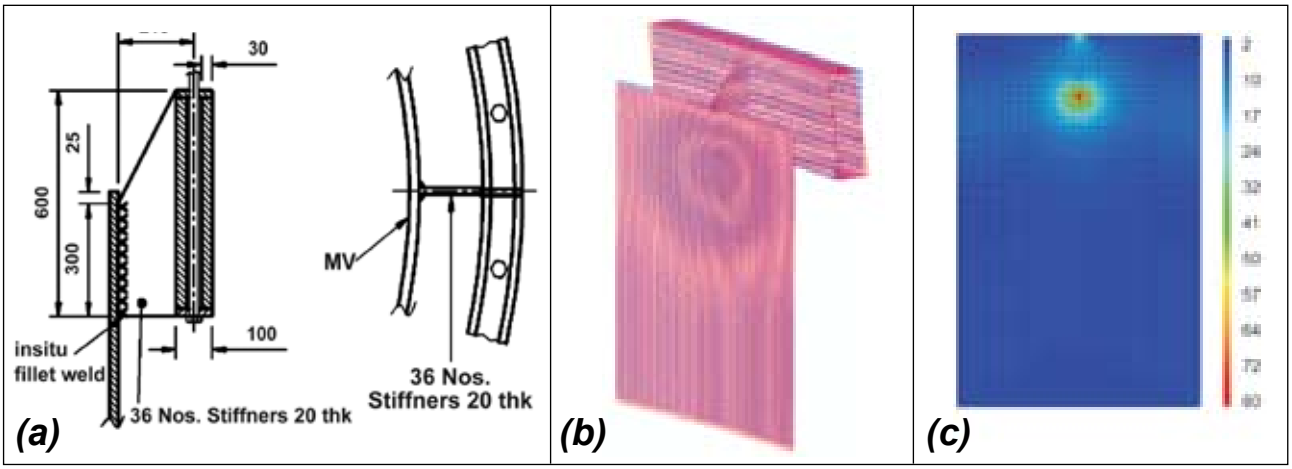

Fig. 2 *Analysis of box type support structure conceived for erection of main vessel (a) Schematic of the box ring attached to top of main vessel (b) Deformation on main vessel while lifting through 72 rods (c) Von Mises Stress intensities on main vessel*

the design and analysis of space spider frame used for erection of safety vessel. Fig.2 shows the design and analysis of a novel box type support structure for lifting of main vessel.

Analysis while main vessel rests on the safety vessel

When the main vessel is resting on the safety vessel, it is assumed that all the pads may not take load. So, the analysis is carried out for four cases viz. (i) all pads sharing equal load, (ii) one pad not sharing load (iii) two pads not sharing load and (iv) three adjacent pads not sharing load. 180^0 sector of the safety vessel with six pad locations is used for the analysis. The weight of main vessel with internals is applied as a uniformly distributed load at the pad locations. The Von Mises stress intensities for all four cases are found to be within the limit. It is found that the load on any pad has a local effect i.e in the vicinity of the pad. A box type ring is attached to the main vessel through thirty six stiffeners. The material for the stiffeners is same, as of the main vessel i.e. 316 LN, while the ring is made up of carbon steel. The main vessel will be lifted through rods attached to the ring. The grid plate, primary pipes, thermal baffle, inner vessel, etc. will be mounted inside the main vessel in hanging position. Seventy two rods are to be used for lifting the main vessel. So a 10^0 symmetric sector with one stiffener and two rods is used for the analysis. The total weight of the main vessel along the above components is 440 t, but for analysis ~10% margin on the weight is added. So the load used for the analysis is 480 t.

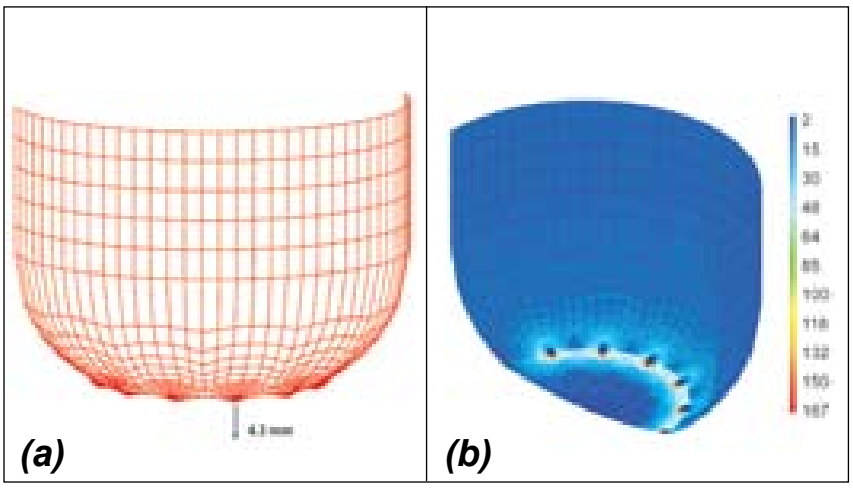

Fig. 3 *Local stresses on safety vessel while main vessel is rested during intermittent stage, (a) Deformation on safety vessel, (b) Von Mises stress distribution on SV (one pad not sharing load)*

The maximum stress intensities on main vessel and the stiffeners connecting main vessel and support flange are found to be within the limits (i.e less than yield strength). Also these stress intensities are local in nature (Fig. 3).

II.6 Development of Methodology for In-situ Marking on Main Vessel and Safety Vessel for aiding In-service Inspection

A marking scheme on the main vessel (MV) and safety vessels (SV) of PFBR has been formulated and established to facilitate the location of the in-service inspection device in the MV-SV interspace. The main vessel and safety vessel of PFBR are provided with a number of permanent reference marks on their external and internal surfaces respectively and coded with alphanumeric coding system. Using these reference marks, it will be possible to locate and position the in service inspection (ISI) device on the welds of the MV or SV surface in the MV-SV interspace during the ISI. These reference marks are marked along the welds at a pitch of 1000 mm and other areas in between the weld seams and associated coding are marked above these reference marks.

Each character size will be 6 x 10 mm and the depth of the

marking would be less than 0.2 mm on the SV. The gap between the characters in each marking will be 2 mm. The number of reference marks on SV will be ≈750 and associated set of coding will be ≈3614. The number of reference marks on MV will be eighteen and associated coding will be thirty six.

Reference marks and coding have been carried out by dot-matrix method in which the characters are marked by series of dots on the surface. A portable and programmable electromagnetic marking machine was used for carrying out the markings in situ on the vessel. Contour of the marking is necessary to have smooth and rounded edges. Since the machine is computer-controlled and programmable, all parameters relating to the depth of the marking and impact force for marking can be controlled to get uniform marking. Since the markings are to be carried out on the vessel in upright posture, it is essential to position the marking machine with respect to the identified and temporarily marked location on the vessel and clamp it onto the wall. For proper locating and clamping operations, a suction cup-based fixture has been designed and developed. The fixture has four suction cups with two cups on each side of the fixture housing.

Prior to the field use, extensive trials were carried out with this machine to arrive at the best methodology and final size of the letters to be marked on stainless steel plates. The depths of the markings were characterised by replica technique and were found to be around 125 micron and the width was around 1 mm. Marking was carried out on three test coupons of SS 316 LN of size 250 X 100 X 4 mm to study effects of pickling and passivation and their sequence of implementation. Pickling and passivation were carried out as per PFBR specification. Replicas were taken on all the plates and the depth & width of the numbers were measured on the cross section of the replicas by using digital microscope. Irrespective of loss of depth, the markings were readable and hence standardised. Readability of the markings were evaluated using the visual examination module developed for the ISI of PFBR and is found to be satisfactory.

First twenty five markings on the safety vessel at site in BHAVINI was demonstrated to the contractor who was entrusted with this work and subsequently other markings on the vessel were carried out by the contractor under our supervision. Random sampling of the markings was done to characterise the markings using replica technique and measurements by videoscope. Presently all the markings have been successfully completed on the safety vessel in BHAVINI before erection. Markings on the main vessel have been taken up and mock-up trials have been completed. Fig. 1 shows the marking on the safety vessel, Fig. 2 shows the marking machine with fixture clamped on to the safety vessel during the marking operation. Fig. 3 illustrates the removal of the replica being taken from the marking for characterisation.

Fig. 1 *Marking on the Safety vessel*

Fig. 2 *Marking machine with fixture clamped on to the Safety vessel during the marking operation*

Fig. 3 *Replica being taken from the marking for characterisation*

II.7 Qualification of Equipment Layout over the Top Shield

In PFBR, the top of the vessel is covered with a closure known as Top Shield that includes roof slab, large rotatable plug and small rotatable plug. Apart from forming a primary sealing boundary and supporting all the components that pass through it such as, primary sodium pumps, intermediate heat exchangers, control plug, transfer arm etc., the top shield also provides thermal and radiation shielding from the sodium pool in top axial direction. In addition, sodium pipes from heat exchangers, top shield cooling pipes, argon pipes, complementary shields and other auxiliaries/accessories including power, control and signal cables are routed through or located over top shield. Owing to a number of equipment and service pipings, it is a challenging task to optimize the layout of equipment over the top shield. A compact layout is necessary to minimize the overall diameter of top shield and to achieve an economically viable design for the reactor as a whole. This necessitates the verification of the layout from the point of view of easy access for operation, maintenance, handling and replacement of equipment through various component handling flasks as well as optimization of space available over top shield for location of few other components on temporary basis.

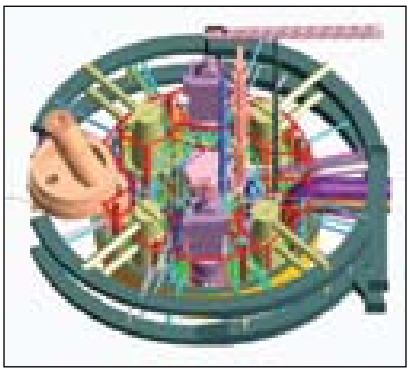

Fig. 1 *PDMS model of complete equipment layout over top shield*

To achieve the above goals, 3D modeling of the entire equipment over the top shield was carried out using sophisticated PDMS package. The layout was checked for possible interferences. The modeling has helped in 3D visualization of the complex layout of the equipment above Top Shield area (Fig. 1).

For further understanding and optimization of space, construction of 1:1 scale, top shield equipment layout model with the equipment projecting/mounted over top shield was undertaken and the same has been completed (Fig. 2 and Fig. 3). In the 1:1 scale physical modelling, the outer surfaces of the equipments projecting out of the top shield is being modelled using sheet metal of 3, 5 and 10 mm thicknesses. The overall diameter of the model is 20 m and the maximum height is 12 m.

This facility will be useful for planning the location of complementary shield around the components, accessing the space available for maintenance along with carrying out mock-maintenance to reduce the personnel radiation exposure on reactor, mock-up assembly and handling of components over top shield, planning of cable routing over top shield etc.

Fig. 2 *Side view of top shield layout model*

Fig. 3 *Top view of top shield layout model above platform level*

II.8 Qualification Testing of Diverse Safety Rod and its Drive Mechanism

The main function of Diverse Safety Rod Drive Mechanism (DSRDM) is to SCRAM the reactor at off-normal conditions (due to fast transients) by rapid insertion of Diverse Safety Rod (DSR) in to the core. Considering the high demands for reliable performance of DSR and DSRDM, thorough qualification of the system was carried out involving detailed design and analysis, subsystems testing, full scale prototype manufacturing, performance testing and endurance testing simulating all reactor operating conditions.

Photograph of DSRDM is shown in Fig. 1. The overall length of DSRDM is 13.5 m and maximum diameter is 250 mm. The mechanism mainly consists of an upper part and a lower part. The lower part is partially immersed in hot pool sodium and the upper part is in the Reactor Containment Building environment. Electromagnet (EM) at the lower end of DSRDM holds the head of DSR. DSR is parked above the core during normal operation and is always contained within its sheath.

Motor drive sub-assembly rotates the screw in either direction to raise or lower mobile assembly. When DSR is held by EM, it moves up or down based on the direction of rotation of motor.

On receiving the SCRAM signal, EM is de-energised and the DSR alone is released to fall under gravity. At the end of free fall travel of 825 mm, it is decelerated by a sodium dashpot for the remaining 250 mm travel.

Qualification testing consists of the performance testing followed by endurance testing, in simulated operating conditions. During the performance testing, all the functional characteristics were checked initially in air and then in sodium at 473, 573, 673 and 773 K, with 30 mm misalignment between the axes of DSRDM and the DSR. Upon successful completion of performance testing, endurance testing was carried out to check and ensure the intended performance for the design life of DSRDM.

For testing in the sodium, the mechanism was assembled in a vessel, called inner vessel and the prototype DSR was mounted at the lower end of the same vessel. The inner vessel with the mechanism was lowered in a 1.0 m dia x 12.6 m long sodium vessel, called Test Vessel-1 (TV-1). Sodium was filled in TV-1 to a specified height and maintained at different temperatures so as to simulate reactor operating conditions.

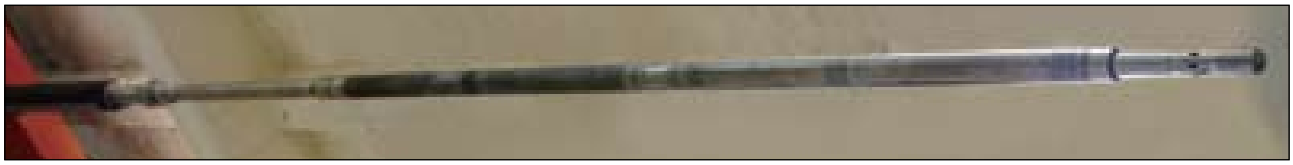

Fig. 1 *Photograph of DSRDM*

Table 1: Summary of results in sodium testing

Measured parameter	Testing in						
	Air	Argon at 473 K[a]	Sodium at				
			473 K	573 K	673 K	773 K	773 K[b]
Maximum frictional force (N)	235	205[c]	157.5	185	227.5	190	282.5
Minimum holding current (A)	0.6	-	1.42	1.1	0.85	0.85	0.8
EM response time (ms)	45/50	-	45/50	40/45	40/45	40/45	40/45
Free fall time (ms)[d]	610	-	564	539	535	531	–
Braking time (ms)[d]	414	-	217	215	219	209	–

Note: ***(a)*** *No SCRAM testing in hot argon*
(b) *Measured after 186 SCRAM operations*
(c) *Frictional force measured with out DSR*
(d) *Freefall time and braking time were measured using acoustic technique*

Problems were encountered due to insufficient clearance in the universal joint and also the failure of screws that fix the ultrasonic sensor to the dashpot body during the testing. They were sorted out and endurance testing was carried out to qualify the DSRDM for ten years of reactor operation.

Summary of the salient test results obtained in sodium testing is given in Table 1. The response time of the Electromagnet was less than 50 ms and well within the specified limit of 100 ms. Maximum free fall time and braking time were found to be 547 ms and 230 ms respectively.

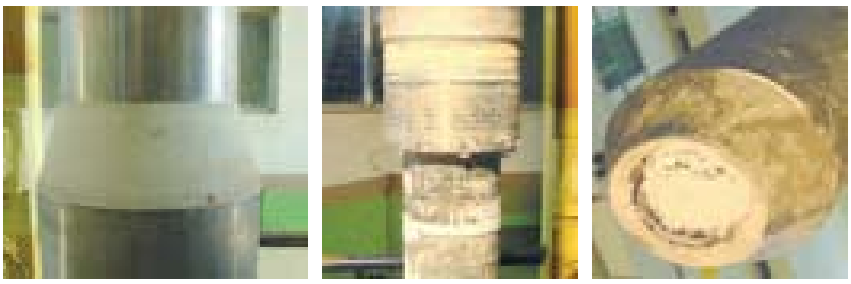

Fig. 2 *DSRDM lower part with reaction products after sodium cleaning*

After completion of sodium testing, DSRDM & DSR were dismantled from sodium test set up and cleaned in sodium cleaning facility. Fig. 2 shows the photographs taken after the sodium cleaning of DSRDM.

The testing has enhanced the confidence level of safe and reliable operation of DSRDM and DSR. Testing has qualified the system for use in reactor for a period of ten years. DSRDM will be further tested to qualify the remaining life of operation.

II.9 Experiments with Diverse Safety Rod Drop Time Measurement using Acoustic and Ultrasonic Techniques

PFBR has three numbers of Diverse Safety Rods (DSR) for the safe shutdown of the reactor during any off-normal operation. To measure the travel time of DSR inside the subassembly, acoustic method was employed during the sodium testing of DSR in DSRDM test facility. The acquired signals were analyzed and free fall time, braking time and total travel time were calculated from the characteristics of the impact signals produced during the entry of DSR into the subassembly dashpot. In order to validate and cross-check the methodology followed in acoustic technique, measurements were also carried out in DSRDM test facility using ultrasonic sensors. The position of DSR inside the subassembly with time after a SCRAM was also plotted from the experimental results.

During the normal operation of the reactor DSRs will be held outside the core using electro-magnets (EM). During the SCRAM, the DSR starts its travel to the core for a safe reactor shutdown. Inside the DSR subassembly, a dashpot is provided to decelerate the DSR and finally it is brought to rest (Fig. 1). The free fall time is defined as time between the instant at which the EM holding the DSR gets de-energized and the instant at which the dashpot action is initiated. Due to the dashpot action DSR will be brought to rest at the final rest position inside the subassembly and the corresponding time is referred to as the braking time. The designed total travel time of DSR is less than one second.

Experiments were carried out in sodium at 473K. DSR was dropped from a height of 1065 mm. Piezo-electric accelerometer mounted on the DSR mechanism was used as the primary sensing element and ultrasonic transducer was fixed on the dashpot bottom end. There was a gap of around 20 mm between the Ultrasonic sensor and the DSR bottom surface, when DSR is in its rest position inside the dashpot.

In order to validate the methodology followed in the acoustic detection technique, signals were recorded from both sensors. The ultrasonic instrument's gate location was fixed at the bottom most position (corresponding to the total drop time). The EM de-energizing signal, accelerometer signal and ultrasonic gate output signal were monitored continuously and DSR was dropped from a fall height of 1065mm. From the recorded time plot (Fig. 2), the total fall time from

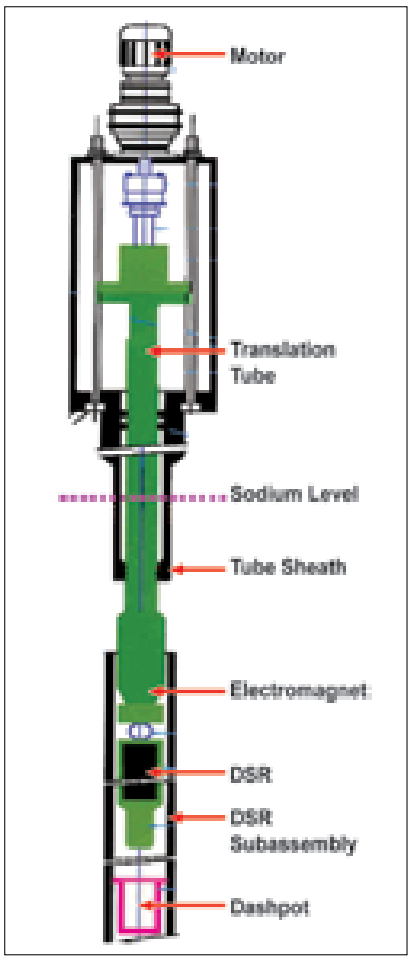

Fig. 1 *DSRDM mechanism*

Fig. 2 *Time signal during DSR dropping (1075 mm)*

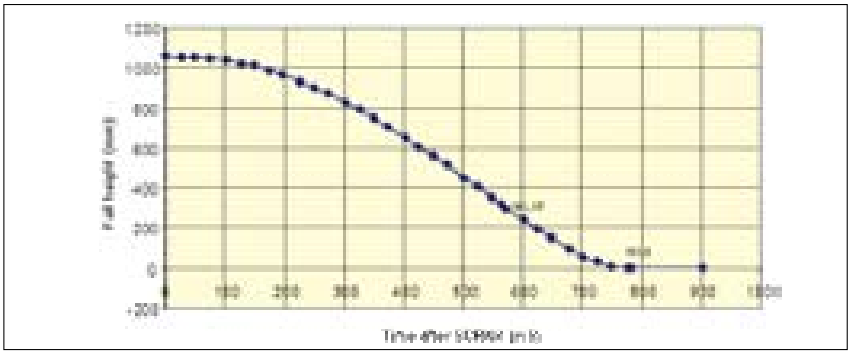

Fig. 3 *DSR position versus time graph*

the ultrasonic signal was observed to be 774 ms whereas from the acoustic sensor it was 781 ms. The difference of 7 ms may be attributed to the fact that the acoustic sensor picks up the impact signal at an elevation of around 11 m from the impact location and a slight delay can occur due to the propagation of the shock waves through the sodium and the structural material. Moreover, the limitation in setting the minimum possible height of the gate can also add to this difference.

In order to determine the position of DSR over its entire travel inside the subassembly after a SCRAM, the ultrasonic pulses and its echoes were continuously measured along with EM signal and accelerometer signal during the dropping of DSR. The time delay between the transmitted pulse and the received echo were continuously recorded and the height of DSR at various instants were calculated. Fig. 3 shows the DSR position versus time graph. The slope of the curve represents the velocity of DSR inside the subassembly. As expected the velocity slowly increases once DSR is released from the electromagnet and it reaches the maximum velocity and again as it enters the dashpot, the velocity starts decreasing and finally it is brought to rest by the dashpot action.

From the experimental results it can be seen that the free fall time, braking time and the total travel of DSR measured using acoustic technique and ultrasonic technique is in good agreement with each other. This proves that the methodology followed in acoustic detection technique is accurate and can be used in the detection of proper insertion of DSR during a SCRAM.

II.10 Design and Manufacturing Challenges of the Long Shaft of Primary Sodium Pump

PFBR is a 500 MWe sodium cooled pool type reactor designed with two Primary Sodium Pumps (PSP). Primary sodium pump (Fig. 1) is a mechanical, centrifugal, vertical type pump with a single stage, top suction impeller having a free sodium level and running at a nominal speed of 590 rpm. Pumps are supported at roof slab and extending down. The removable pump assembly is

located inside a standpipe in inner vessel, penetrating into the cold pool. The top flange of the pump is supported on the roof slab and the pump discharge nozzle plugs into the receptacle in the spherical header, which is connected to the grid plate through two primary pipes. This necessitates a pump shaft of around eleven meter length.

The pump shaft transmits the torque from the drive motor (3600 kW) to the impeller. The shaft is a stepped one, made up of three forged parts welded together i.e., two solid ends joined with a central hollow tube having an overall length of 11.307 m and a maximum diameter of 630 mm. The weight of the shaft is approximately 5900 kg. The shaft is supported in the pump by tilting pad thrust bearing with a sleeve bearing at the top and guided by a hydrostatic bearing at the bottom.

The diameters at the various sections of the shaft are fixed based on torque and critical speed considerations in addition to the requirement that weight and size should be minimum. To meet these simultaneous requirements, the shaft (Fig. 2) is made of composite construction having a hollow portion of 630/590 mm (length of 4.95 m) welded to solid portions of around 200 mm at either ends.

As the shaft is designed to operate

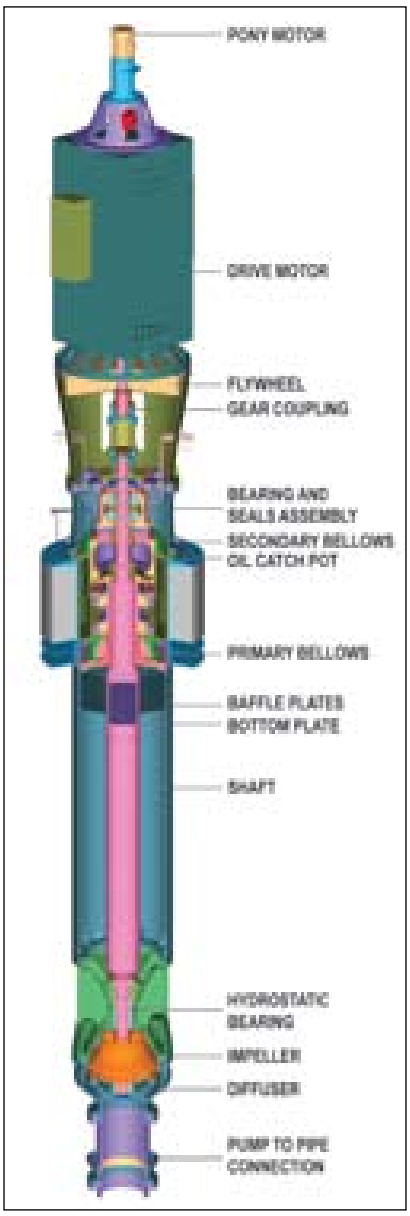

Fig. 1 *Primary sodium pump assembly*

under close running clearances at the bottom hydrostatic bearing level, it must be made to high standards of manufacture meeting various tolerances. Similarly, the welding process for joining the three parts of the shaft must ensure that the distortion is kept to a minimum as no machining on the hollow part and also no straightening of the shaft are permitted after welding.

Stresses are likely to buildup during various stages of manufacturing (i.e., rough machining and welding). Hence, it becomes mandatory that the shaft is stress relieved at a desired temperature under controlled conditions to ensure dimensional stability and relieve residual stresses. Uniform heating, soaking and cooling cycle at slow rate and scale free surface after heat treatment are the prime requirements of effective stress relieving. The shaft is stress relieved in vertical condition under gravity in an inert atmosphere of argon + hydrogen (8 to 10%) to avoid any scale formation. Further, the heat treatment in vertical condition also ensures straightness of the shaft.

An important requirement for all rotating parts is that the rotating axis coincides with one of the principal axis of inertia of the body. This requirement is difficult to satisfy exactly in the process of manufacturing and hence balancing becomes necessary to avoid excessive vibration at higher speed. After finish machining, the shaft alone is balanced dynamically and the residual unbalance is made to less than

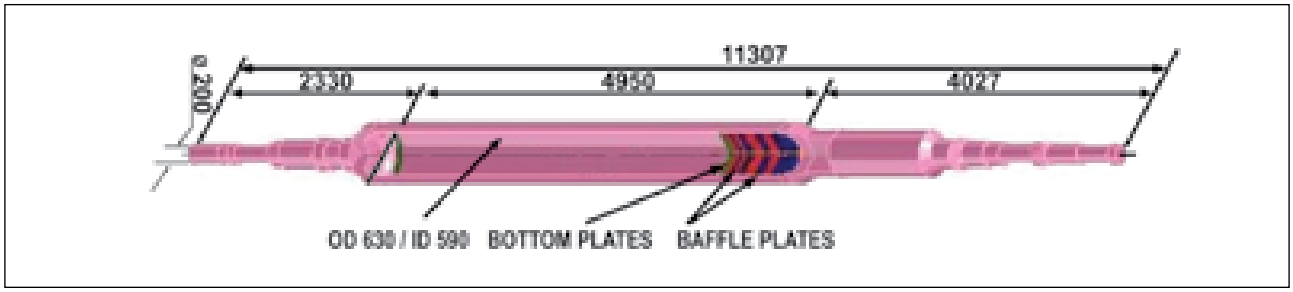

Fig. 2 *Shaft of primary sodium pump*

ISO Grade 1.0 (total unbalance of 0.096 kg-m). The shaft is subsequently assembled with all rotating parts in the pump like impeller, bearing journal, sleeves, half coupling etc. and final balance is made to ISO Grade 0.4 (total unbalance of 0.055 kg-m).

The hollow portion of the shaft is evacuated after welding of the solid ends and subsequent heat treatment. On the inside of hollow shaft, thermal baffles are incorporated to minimize the radiation heat transfer from the sodium surface to the upper side of the pump. Also, the baffles reduce the convection currents inside the hollow portion in case the vacuum inside the shaft is lost over a period of time during the reactor operation. The baffles (eight numbers) are welded to twenty mm rod attached to the top solid portion of the shaft with M 20 threads over a length of 40 mm (Fig. 3). The bottom of the rod is inserted into the plate (attached with the hollow portion of the shaft) through a clearance fit (maximum length of engagement is 5mm). The natural frequency of the baffle arrangement should be away from the entire operating range of pump speed to avoid any noise or vibration.

Towards this, the natural frequency of this baffle arrangement was estimated using a detailed finite element analysis. The geometry is modeled with plate and shell elements. The results of the analysis indicated that owing to the inherently available margin, the running speed can be further increased without any noise and vibration of the shaft. Further,

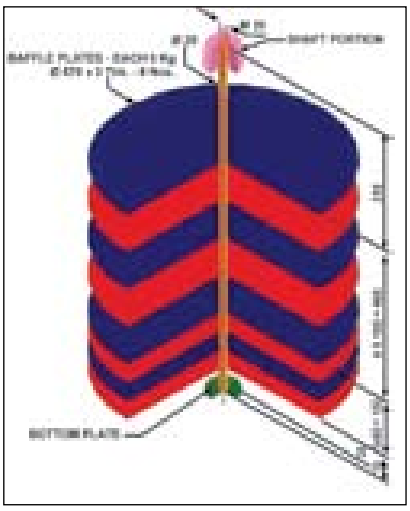

Fig. 3 *Existing design of the baffle in sodium pump*

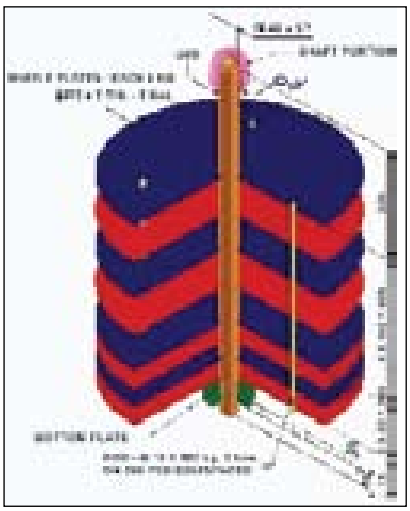

Fig. 4 *Revised design of the baffle in sodium pump*

based on the preliminary analysis, certain design improvements (Fig. 4) were carried out to ensure support of the baffles arrangement inside the shaft as well as to improve the natural frequency of the baffles and rod. These include;

- Increasing rod diameter from 20 mm to 50 mm.
- Tightening the variations in the threaded length to within ± 1 mm
- Welding the rod at the top end to the solid portion of the shaft by 8 mm fillet to improve the fixity condition at the support.
- Increasing the contact length between the bottom support and the rod by extended length of the rod (40 mm) to eliminate unlikely possibility of the baffles coming out of the support. The total length of the support for the rod at bottom is 60 mm including the bottom support plate thickness of 20 mm.
- Three 10 mm rods are connected through the baffle plates and welded to the baffle plates to reduce the possibility of any flapping of baffles during pump operation.

Subsequent to the design improvements, a detailed theoretical analysis was carried out and the typical vibration mode shapes for the baffles are shown in the Fig. 5. The results indicate good margin between the natural frequency and running speed of the pump i.e. 590 rpm.

Further to confirm the theoretical results and also to ascertain the structural integrity of the baffles, a detailed experimental study was carried out with the baffle arrangement in 1:1 scale. For this purpose, the hollow shaft up to the total baffle length (around 1 m) was simulated. Both the initial and improved design arrangements were tested at three different speeds of 200, 350 and 600 rpm. The results confirmed the availability of better margin and total absence of noise and vibration during the entire range of running speeds of the pump with the improved baffle support design.

For the PFBR, the shaft and the baffle arrangement was manufactured with all the specified

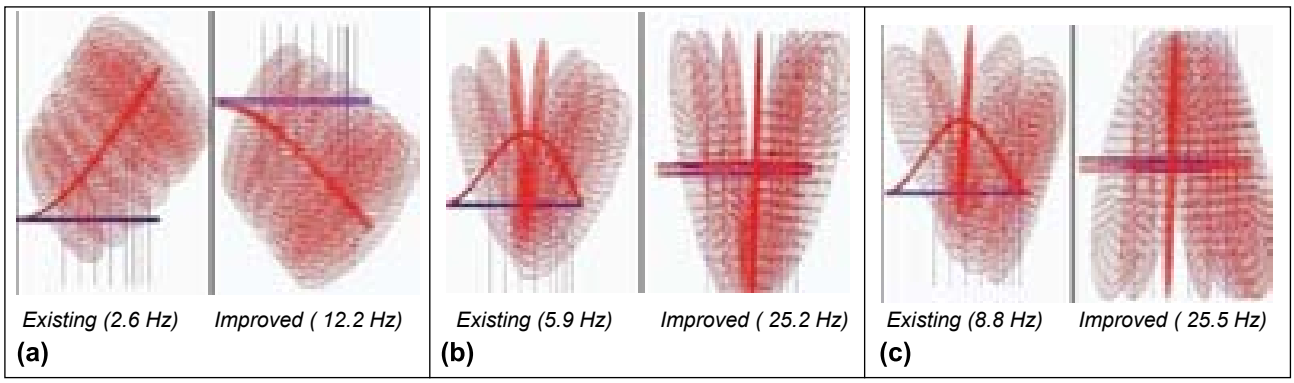

Fig. 5 *Various vibration mode shapes of baffles*
(a) Cantilever mode shapes (b) Simply supported mode shapes (c) Fixed mode shapes

tolerances. Subsequently it was heat treated and dynamically balanced to the required grade.

The detailed theoretical analysis and subsequent experimental confirmations have lead to robust design for the shaft and the baffle arrangement inside the shaft.

II.11 Core Flow Measurement

Eddy current flowmeter (ECFM) is used in PFBR for monitoring flow (Q) to the core. This flow signal is used in combination with reactor power (P) to trip reactor as P/Q. Eddy current flowmeter signal is used to protect the reactor against primary pipe rupture event. In addition, this also helps in protecting the reactor in case of events such as transient over power, one primary sodium pump trip, one primary pump seizure and class-IV power failure.

In PFBR, two centrifugal pumps are operating in parallel to maintain sodium flow in the primary circuit. These two primary sodium pumps (PSP) suck sodium from the cold pool and pump it to the grid plate. ECFM is located in a bypass line from pump discharge to suction. In each primary sodium pump, four flowmeters are provided.

Eddy current flowmeter consists of one primary coil and two secondary coils. Primary coil is at the middle. Secondary coils are

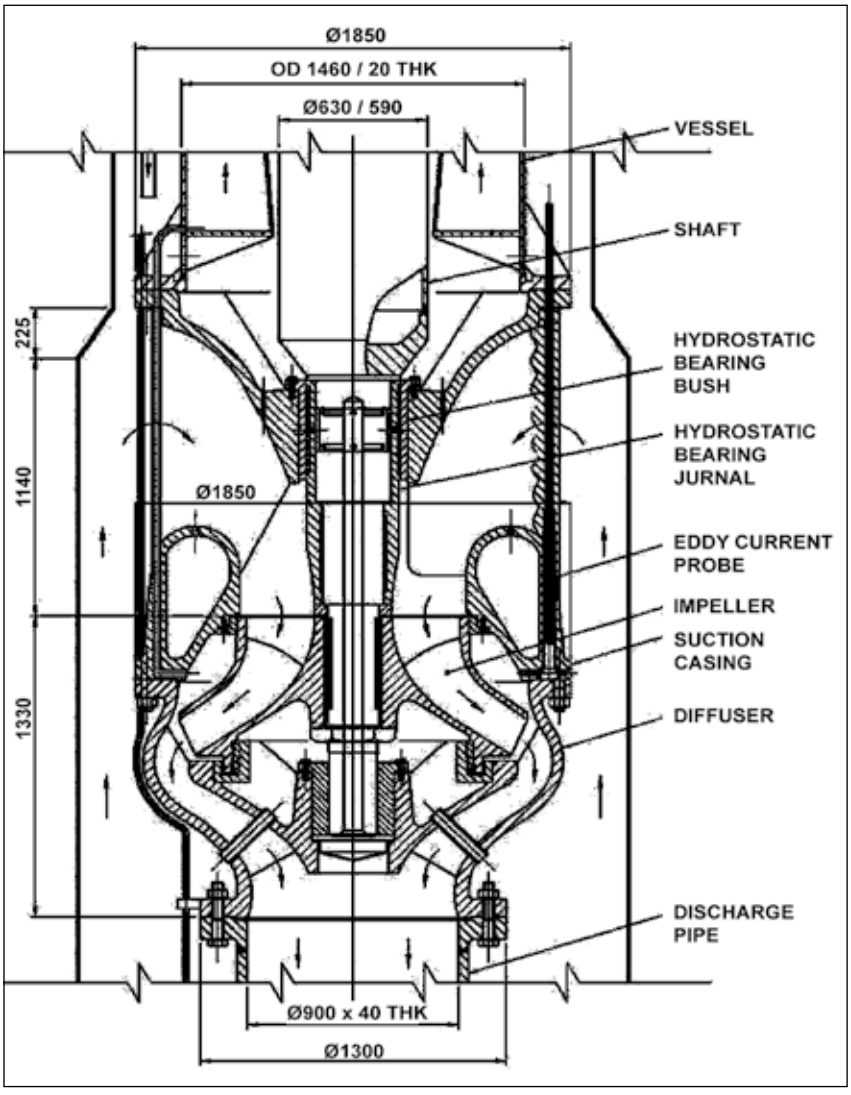

Fig. 1 *Location of eddy current flow meter in primary sodium pump*

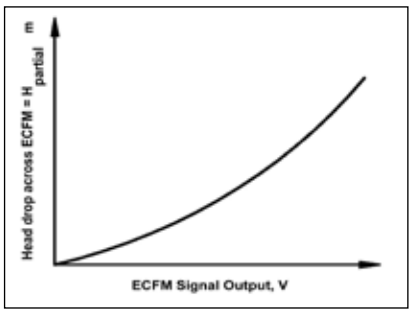

Fig. 2 *Head drop across ECFM Vs ECFM output*

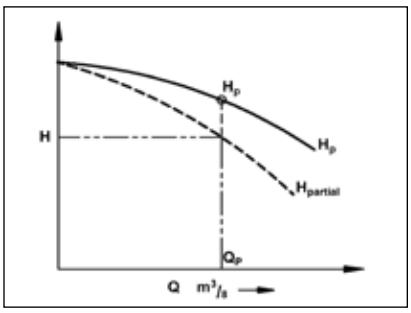

Fig. 3 *Pump characteristic*

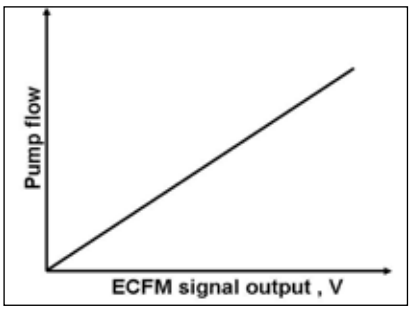

Fig. 4 *Pump flow calibration curve*

wound symmetrically on either side of the primary coil on the same core. Primary coil is excited with a constant current (200 mA) source at a constant frequency (~400 Hz).

Due to magnetic flux generated by the primary coil, secondary coils will have induced voltages, due to transformer action. When this flowmeter is inserted in flowing sodium, magnetic field interacts with sodium and produces eddy current which influences signal output. When the flow is established across the flowmeter, voltage induced in the upstream secondary coil is less than downstream secondary coil. The difference between two secondary coil voltages is proportional to the sodium velocity.

ECFM probe assembly consists of flow sensor and guide tube assembly. Each probe consists of two sensors. The guide tube assembly consists of inner guide tube and outer guide tube. Inner guide tube passes through the outer guide tube provided in the pump flange and enters the hole in the pump suction casing. Inner guide tube is supported at the bottom on a support tube. This inner guide tube is surrounded by Fe-Ni tube that is part of the pump. High pressure sodium enters the Fe-Ni tube through an opening of 30mm dia and flows through the annular space between inner guide tube and Fe-Ni tube and exits through the holes provided at the top of the suction web to the pump suction (Fig. 1). ECFM probe is inserted in the inner guide tube. This probe is replaceable. In each primary sodium pump two such assemblies are provided.

Hydraulic studies were carried out on 1:1 model to establish the head drop across ECFM and flow through ECFM. Studies were carried out in sodium to establish the voltage output of the ECFM for various flow rates. Tests were repeated at various temperature. Using the hydraulic studies and sodium studies, relation between the head drop across ECFM and ECFM signal was established (Fig. 2). The pump characteristics and signals to flow relations are shown in Fig. 3 and Fig. 4 respectively.

During plant operation, this flowmeter will be calibrated against the reactor thermal balance at steam water circuit. Through thermal balance, the estimated accuracy of the flowmeter is ± 2%. In case of pipe rupture, the flow reduction in the ECFM passage is very large. Reactor trip is generated from the reduction in flow.

II.12 Qualification of Wire Type Leak Detectors

Wire type leak detectors are used for detecting sodium leak in sodium circuits of PFBR. It is required to assess the performance of these detectors and confirm that they are meeting the requirements. LEENA (LEak Experiments in NAtrium) facility was set up to test wire type leak detectors by simulating sodium leaks of different rates.

Test facility consists of sodium dump tank, a test vessel, associated pipe lines with valves, micro filter and leak simulators. In the facility there are three different test sections of length 1000mm each. Test section-1 is a horizontal test section of diameter 790 mm. This test section is provided with three wire type leak detectors which are positioned 90°, 180° and 270° apart by taking top as 0°. In this test section two leak simulators are provided one at the top 0° position and other

at the side, 110° position. Test section-2 is a horizontal test section of diameter 210 mm. This test section is provided with one wire type leak detector located at bottom and leak simulator at the top. Test section-3 is a vertical test section of diameter 265 mm. In this test section wire type leak detector is wound with a pitch of 500 mm and leak simulator is provided just below one turn of leak detector. A leak simulator consists of a hole of size one mm drilled in the test section and closed with a tapered pin. The pin is moved up and down by a screw mechanism and there by the annular gap area is varied for getting different leak rate (Fig. 1).

Test facility was filled with sodium and twenty experiments were completed at 623 K and 823 K. Lowest leak that could be simulated was 214 g/h and it was detected in fifty minutes. Maximum quantity of sodium leaked out was 1.3 kg which was detected in six hours (leak rate of 222 g/h). A relationship between leak rate and detection time was established and found that sodium leak of 200 g/h and above can be detected within six hours (Fig. 2). By extrapolation it can be seen that a leak rate of 100 g/h likely to be detected within twenty hours which meets the requirement in ASME code. Fig. 3 and 4 show the test section and after leak experiments.

Fig. 1 *Leak simulator*

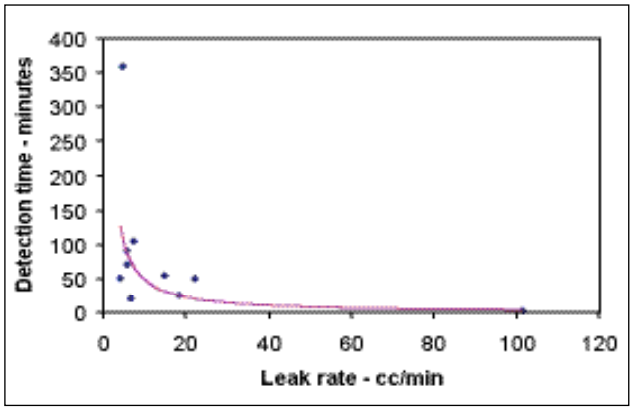

Fig. 2 *Leak rate Vs detection time curve*

Fig. 3 *Test section-1*

Fig. 4 *Test section-1 - after experiment*

II.13 Manufacture of Electromagnet Assemblies

Three numbers of Electromagnet assemblies (Fig. 1) were manufactured for diverse safety rod drive mechanism of PFBR. The electromagnet assembly is a critical component of DSRDM. Overall size of the Electromagnet assembly is 102 mm (dia) x 314 mm (height). It consists of an inner core and an outer core made of ASTM A 848 Alloy 1(Midhani Soft Iron), stopper rings and transition piece made of SS 316 LN material. The inner core and outer core of electromagnet assemblies were assembled and welded using a non-magnetic filler material (Inconel82). M/s. MTAR, Hyderabad has carried out mock-up welding, welder performance qualification (WPQ) and it was referred to Central Workshop Division of IGCAR to use the expertise and weld the critical dissimilar weld joints.

Fig. 1 *Welded electromagnet assembly*

The job was taken up at CWD, the mock-up welding with the designed weld configuration was carried out to establish the WPQ as per Welding Procedure Specification (WPS). Prior to commencement of welding process, all machined components were subjected to 100% dimensional inspection and L.P inspection of weld joint bevel edges.

First, the stopper rings were fillet welded with the inner core and subjected to L.P inspection. E.M coils were wound over the inner core. Outer core ID was increased 0.5 mm radially by machining to accommodate the inner core oversized during the coil winding Butt welding of electromagnet cores with narrow gap in 1G position was critical feature of welding. Three sets of electromagnet cores were welded by gas tungsten arc welding process using Inconel-82 filler wire with three passes successfully. Segmental welding technique was used to minimize and control distortion. Argon purging was given beneath the side of core to prevent oxidation in the root pass of weld joint during welding.

Weld joints were subjected to U.T, H.L.T, 100% dimensional inspection and found satisfactory.

II.14 Environmental and Qualification Tests of Real Time Computer Systems

Versa Module Euro (VME) bus based Real Time Computer (RTC) systems have been designed and developed for Safety Class 1 (SC1), Safety Class 2 (SC2) and Non-Nuclear Safety (NNS) I&C systems of PFBR. These RTC systems have to work properly among themselves as well as along with other systems in plant. Hence, electromagnetic emissions from these systems shall be within the limit as specified by standards and these systems shall perform its intended function in the electromagnetic environment. Also, these systems shall withstand the temperature and humidity conditions as specified by the standards. Hence, performance of RTC systems was evaluated by conducting environmental and EMI/EMC tests as per the test requirements listed below and these tests are regarded as type tests.

- Environmental Test Requirements for Instrumentation and Control System PFBR/60000/SP/1013, Rev. 1
- EMI/EMC Test Requirements for Instrumentation and Control System PFBR/60000/SP/1014, Rev. A

Two identical RTC systems and a SOLS were chosen as a typical test system. Each RTC system consists of VME bus based CPU card, thirty channel analog input cards, four channel analog output cards, thirty channel digital input cards, thirty channel digital output cards, fifteen channel relay output cards, three channel synchro to digital converter (SDC) card and counter timer card (CTC) along with VME bus backplane and I/O backplane. These cards were housed in a 19" 6U chassis. The SOLS consisting of switch over logic circuit card and ORing logic cards were mounted in a 19" 6U chassis. Further, EMI/EMC qualified power supplies were used to supply the required DC voltages to the VME chassis and Switch Over Logic Systems (SOLS) chassis.

Environmental Testing

RTC system along with SOLS have been qualified for environmental tests as per IS 9000 standards listed in the above test requirements. The Environmental tests comprises of dry heat, dry cold, damp heat and temperature cycling have been carried out using environmental test chamber (Make - WEISS TECHNIK). During the entire tests, the test system was subjected to a minimum temperature of 288 K and a maximum temperature of 328 K and relative humidity was varied from 50% to 95%.

Context diagram of this system is shown in Fig. 1 and the environmental test set up is

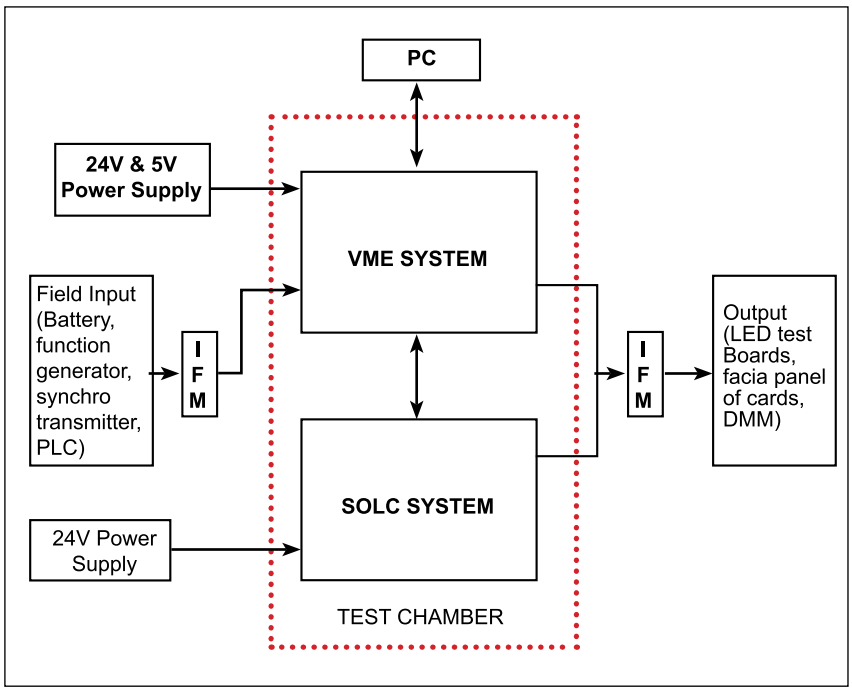

Fig. 1 *Context diagram of environmental test system*

shown in Fig. 2. The required field inputs were simulated using programmable logic controller, synchro unit, set of batteries, function generator and the outputs were monitored using LED test boards and digital multimeter.

Software to check the functionalities of each card was written in 'C' language using tasking 'C' cross compiler, fused into EPROM of CPU card. All I/O cards were scanned periodically every thirty seconds and the scanned data were sent to a logging PC through RS232 serial port. The SOLS system was tested to ensure the switch over function of the system. During each test, the system performance was monitored and logged at predefined nodal points. A post data analysis was carried out to find the performance of the system. It was found that the RTC system was performing within the design limits during the environmental tests.

Fig. 2 *Environmental chamber & test setup*

EMI/EMC Testing

EMI is defined as the unwanted coupling of signals from one circuit or system to another circuit or system which may degrade the performance of the system. EMC is defined as the ability of equipment or system to function as designed without degradation or malfunction in an intended operational electromagnetic environment due to EMI.

EMI/EMC tests are broadly classified into Radiated Emission (RE), Radiated immunity/ susceptibility (RS), Conducted Emission (CE) and Conducted Susceptibility (CS). Emission tests were carried out as per CISPR 11/22, and susceptibility tests were carried out as per IEC 61000 standards. These tests were conducted at SAMEER-Centre for Electromagnetics, Chennai, during June 2008.

Test system comprises of two identical RTC systems, Switch Over Logic System, associated power supplies and exhaust/ cooling fan modules was mounted in a 48 U height cabinet. This test system (shown in Fig. 3) is replica of the system which will be used in PFBR for safety class 2 applications. Inputs from simulator were connected to respective input cards via interface modules (IFM) and outputs from cards were routed through ORing logic cards. Software to test each card was fused into EPROM of CPU card. During tests, all cards were scanned in ten seconds scan interval.

Fig. 3 *EMI / EMC test setup (rear view)*

RE/RS tests were carried out inside the shielded semi anechoic chamber. For RE test, equipment under test (EUT)/test system was rotated from 0 to 360º and the emissions from the EUT were captured using ultralog antenna. For RS test, 10 V/m field strength was applied to EUT and the performance of the same was monitored.

For conducted emission test, the conducted emissions from the EUT sent back to AC power supply input were coupled using line impedance stabilization network (LISN) and measured using an EMI receiver. The conducted emissions from EUT sent back to telecommunication/ethernet port were coupled using RF current probe and measured using an EMI receiver.

For CS test, performance of the system was monitored by applying electrical fast transient (nanosecond pulse disturbance), surges (microsecond pulse disturbance) on AC power lines. Performance of the system was also monitored, by applying electrostatic discharge (ESD) disturbance, by varying power supply voltage, frequency and by introducing power supply voltage harmonicity.

After completing the above mentioned tests, it was observed that the emissions from the test system were within the limit and the system performs its intended function in the electromagnetic environment.

II.15 Development of a New VME Central Processing Unit Card

Versa Module Euro (VME) bus (IEEE Std P1014) based Real Time Computer (RTC) was chosen for safety critical, safety related and non-nuclear safety Instrumentation and Control (I&C) systems of PFBR. Accordingly, a central processing unit (CPU) card, analog input & output, digital input & output, counter timer and synchro to digital converter cards were designed and developed incorporating testability & fail-safe features as per AERB Safety Guide D-25.

The CPU card features Motorola MC68020 CPU, MC68882 Floating Point Processor, 2 MB of Static RAM, 1 MB of EPROM/EEPROM, 10/100 Mbps Ethernet LAN, VME bus interface and Timer/Real Time clock and Testable watchdog timer. In safety critical and safety related applications, the data and the thresholds are stored in Static RAM. As the densities of the memories have increased, they are prone to soft errors, wherein a bit in the memory is temporarily upset which may lead to reduction in availability and have a safety implication. Hence, it is imperative to employ Error Detection and Correction (EDAC) on the memories. Modified Hamming code, capable of detecting & correcting single bit error and detecting double bit errors, are commonly employed in memories and is transparent to the user. This makes the system tolerant to single bit error in memories, detect double bit errors and initiate fail-safe action.

The CPU card was designed using VME bus interface (VIC) logic and EDAC logic with commercially available off the shelf components. This card was manufactured by Electronics Corporation of India Limited and successfully passed the EMI/EMC & Environmental tests as applicable for PFBR. A photograph of this card is shown

Fig. 1 *ED-20 ver 3.2*

in Fig. 1. This board has been successfully deployed in central data processing system of FBTR and operator information system for augmented boron enrichment plant.

But, the above two major components were declared obsolete by the respective manufacturers and since VME CPU card is the backbone of PFBR instrumentation & control systems, it is imperative to design a new CPU card, with the above components designed in house using VHDL (Very High Speed Integrated Circuit Hardware Description Language) without sacrificing any of the functional specifications with respect to the earlier design. Further application level software portability is also ensured.

As the designs are implemented using VHDL, verification of the designs becomes mandatory. The goal of verification is to discover any hidden bugs in the design using constraint random testing and coverage analysis. IIT Madras carried out the functional verification of the above designs independently. The results of verification gave the confidence to build a prototype and test the design.

In order to validate the VIC design, which is more complex, the VIC IC in the earlier CPU card was replaced by a piggyback PCB, containing the in-house developed VIC logic implemented in a complex programmable logic device (CPLD). Then, this CPU card with the piggyback VIC, was tested with the same VME I/O cards and found to be working satisfactorily.

Once confidence was obtained in the VHDL design, a new CPU card (Fig. 1) ED-20 ver 3.2, incorporating both VIC as well as EDAC logic implemented in two field programmable gate array (FPGA) devices was designed, developed, tested and found to meet all the functional specifications as per the old design. Further, the VME interface logic of the card was also analyzed using VME bus analyzer tool to gain additional confidence of the design.

Thus, the problem of component obsolescence of VME CPU card was successfully tackled with the design of a new CPU card, in order to support PFBR for a long period.

II.16 Basis of Specified Tolerances for Erection of Reactor Assembly Components

Primary sodium and all internals of Reactor Assembly, such as Core Support Structure, Grid Plate, Reactor Core, Inner Vessel, Thermal Baffles, Primary Pipes, etc., are housed inside Main Vessel. Reactor Core is supported on Grid Plate, which in turn is supported on Core Support Structure. Bottom of Core Support Structure is welded to Main Vessel. Inner Vessel surrounds the Reactor Core and is supported on grid plate. Inner Vessel acts as a barrier between hot and cold pools of primary sodium. 'Inner Vessel bottom flange' is bolted to grid plate, which in turn is bolted to core support structure. Top Shield, consisting of Roof Slab, Large & Small Rotatable Plugs (LRP & SRP) and Control Plug, forms the top closure for Main Vessel. Main Vessel is welded to the Roof Slab. At the top, Roof Slab is supported from Reactor Vault. Control Plug is supported on SRP that in turn is supported on LRP. Similarly, LRP is supported on Roof Slab. Various major safety, functional and interface requirements of Reactor Assembly that govern the specification of tolerances for erection of Reactor Assembly components are briefly discussed below.

Control and safety rod drive mechanisms (CSRDMs), diverse safety rod drive mechanisms (DSRDMs) are supported on control plug. Transfer arm is supported on SRP. For proper operation of CSRDMs & DSRDMs and transfer arm, they are to be properly positioned with respect to the corresponding locations in core, which is supported on grid plate. This requires close control on the following inherent and interface features of various components:

(a) Positioning of CSRDMs & DSRDMs within the control plug / positioning of Transfer Arm within SRP and their verticality

(b) Relative positions of top shield components, namely, control plug, SRP, LRP and roof slab

(c) Horizontality of LRP, SRP & roof slab and verticality of control plug

(d) Concentricity between core and grid plate

(e) Verticality of 'grid plate sleeves' that support core subassemblies

(f) Concentricity between various components of vessels & internals, namely, grid plate, core support structure & main vessel

(g) Horizontality of grid plate & core support structure and verticality of main vessel

For meeting the above mentioned safety and functional requirements, appropriate dimensional & geometric tolerances are apportioned and specified for manufacture and erection phases. These manufacturing and erection tolerances are based on the permissible misalignment between CSRDMs/DSRDMs/Transfer Arm and corresponding core locations. During the course of manufacture, tolerances close to the specified values are achieved. The erection tolerances are updated based on the tolerances achieved during manufacture.

Components such as Primary Sodium Pumps (PSPs), Intermediate Heat Exchangers (IHXs), etc., are supported on the Roof Slab. PSPs and IHXs pass through the penetration / stand pipes provided in Roof Slab / Inner Vessel. Proper positioning of 'Stand Pipes of Inner Vessel' with respect to 'Penetration Shells in Roof Slab' is an important interface requirement for smooth erection of PSPs & IHXs and to avoid their mechanical interaction with 'Stand Pipes of Inner Vessel' at all reactor conditions. For achieving this, the following features are to be controlled suitably.

i) Co-ordinates of 'PSP & IHX stand pipes of inner vessel' with respect to 'bottom flange of inner vessel' that is bolted to grid plate

ii) Perpendicularity of 'stand pipes of inner vessel' with respect to 'inner vessel bottom flange'

iii) Concentricity between 'inner vessel bottom flange', grid plate, core support structure & main vessel

iv) Horizontality of grid plate & core support structure and verticality of main vessel

v) Co-ordinates of 'PSP & IHX penetrations in roof slab' with respect to 'outer shell of roof slab'

vi) Verticality of IHX

Concentricity between inner vessel, grid plate & core support structure is achieved by control on bolt hole co-ordinates of these components with respect to the axis of the components during manufacture. After accounting for the 'concentricity between main vessel & core support structure observed during manufacture', the co-ordinates of 'penetrations in roof slab' with respect to the 'centreline of roof slab' obtained during the course of manufacture of roof slab are suitably transferred to inner vessel (with respect to the centreline of 'inner vessel bottom flange') for cutting the openings for welding stand pipes in order to achieve proper relative positioning of 'penetrations in roof slab' and 'stand pipes of inner vessel'. While transferring the co-ordinates, a calculated inward radial offset for the centrelines of 'standpipes of inner vessel' with respect to the centrelines of corresponding 'penetrations in roof slab' is chosen

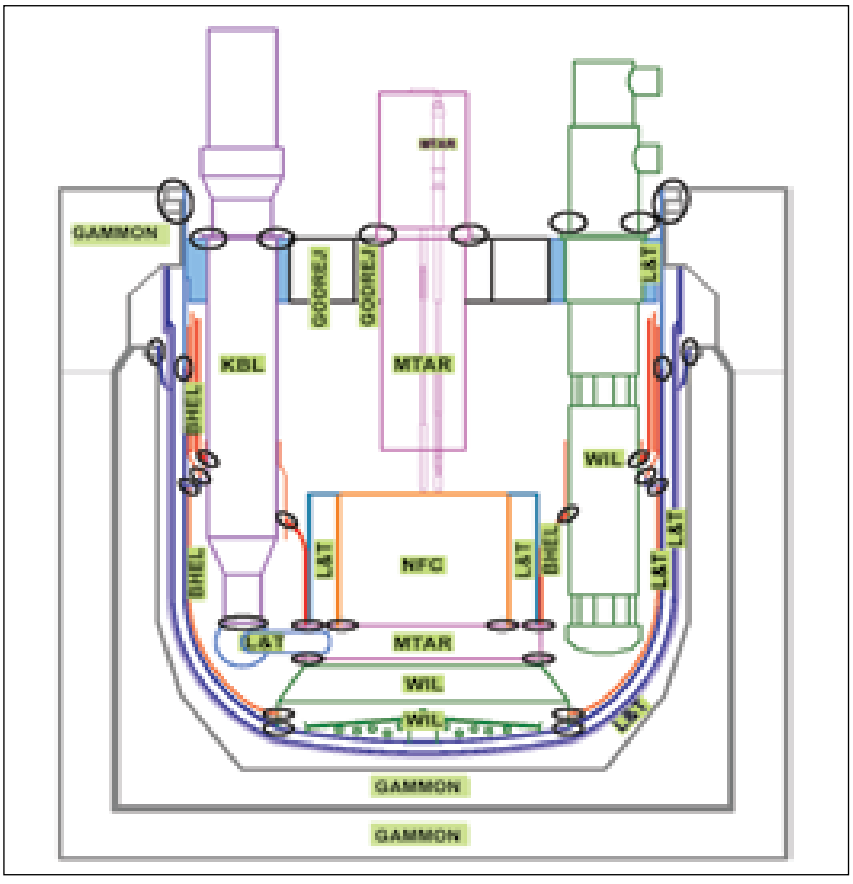

Fig. 1 *Industries involved in the manufacture of various components*

such that mechanical interaction at the interface (IHX-inner vessel seal) between IHX and inner vessel is avoided at all reactor conditions.

Safety vessel concentrically surrounds Main Vessel for containing the radioactive primary sodium in the unlikely event of leak in Main Vessel. The radial gap in the inter-space between Safety Vessel and Main Vessel is optimised as a trade off between two conflicting requirements such as (a) minimising the inter-space gap for maintaining safe level of sodium inside Main Vessel, in case of leak and (b) providing sufficient radial gap for entry and passage of ISI vehicle in the inter-space between Safety Vessel & Main Vessel. The factors that affect the inter-space gap are as follows.

1) Relative elevation of Main Vessel & Safety Vessel
2) Verticality of Main Vessel & Safety Vessel
3) Concentricity between Main Vessel & Safety Vessel

For meeting the above requirements, appropriate erection tolerances are specified based on (a) the tolerances achieved during manufacture and (b) the permissible variation in the inter-space gap.

For a smooth erection of all the Reactor Assembly components, many complex interfaces with varied requirements between individual components are met through close follow up of manufacture of various components and active interaction with different industries indicated against each component in Fig. 1.

II.17 Design and Qualification of Sliding Joint for Inclined Fuel Transfer Machine

Inclined Fuel Transfer Machine (IFTM) (Fig. 1) is one of the fuel handling machines of PFBR fuel handling system, which transfers the core subassemblies from in-vessel transfer position (IVTP) to ex-vessel transfer position (EVTP) and vice versa. Primary Ramp (PR) and Primary Tilting Mechanism (PTM) are two important components of IFTM. Both are subjected to high temperature environment, as they are located inside the hot pool of sodium. PR is fixed at the top of the roof slab whereas PTM is fixed on the grid plate. Both are connected with a sliding joint to facilitate the smooth movement of transfer pot. PR and PTM have differential thermal movements with respect to each other as they are fixed at two different locations. Movement parallel to their axis is allowed at the sliding joint and hence no restriction of axial differential thermal movement is considered. Due to differential thermal movements of their support locations there will be significant movement perpendicular to their axis which is restricted in the sliding joint. Due to this restriction, bending of PR or PTM may occur and localized deformation of the component at the edge inside the sliding joint may occur.

The Primary Ramp (PR) is of about 6.63 m in length and 10 mm thick. The outer radius of the PR is 270 mm and the inner radius is 260 mm. The PR & PTM are

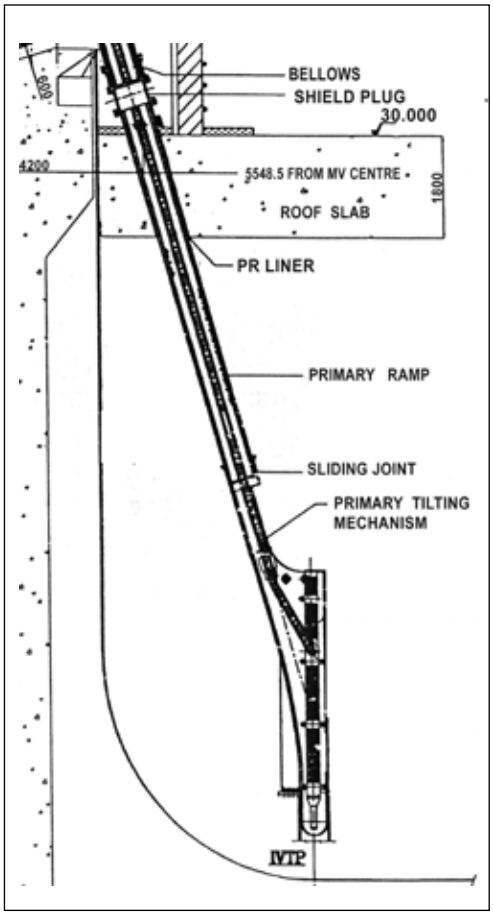

Fig. 1 *Schematic of inclined fuel transfer machine*

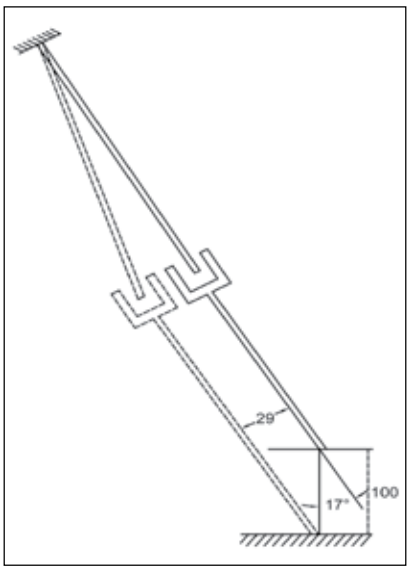

Fig. 2 *Schematic of primary tilting mechanism movement*

tilted at 17^0 from the vertical axis. The engaged length of the PTM and PR is 150 mm. The material of PR & PTM is SS 316 LN. The normal operating and safety grade decay heat removal (SGDHR) temperature at the junction is 825 K. During fuel handling the temperature reduces to 473 K.

The PR is hanging from the top of roof slab. The lowermost part of the ramp is having a sliding joint with PTM. PR is freely hanging and hence no stress in the lower part is induced due to the self weight. PTM is bolted on the grid plate at the bottom. Hence no stress is induced on the upper part of PTM due to self weight. Differential thermal displacement occurs between PR and PTM due to following:

- Radial displacement of the grid plate at the PTM location is more than that of roof slab at ramp location. So the PTM is moving radially outward with respect to PR.
- The PTM base on the grid plate moves downward w.r.t the ramp fixation location. Due to this there is a movement of PTM perpendicular to the PR in outward direction (Fig. 2).
- Due to cellular convection in the penetration gap of PR into the roof slab, the ramp is tilting towards the centre of the reactor. The displacement of the ramp tip is 3 mm perpendicular to the PTM in inward direction.

If PR & PTM are free to move, a gap will occur between them. But PR & PTM are connected together with a sliding joint. The PTM is moving outward with respect to the PR, it will try to bend the PR in outward direction, whereas the PR will try to pull back the PTM thus bending it in inward direction. The displacement for fuel handling, normal operation and SGDHR condition are calculated as 15 mm, 35 mm and 50 mm respectively.

Elastic analysis of PR/PTM sliding joint had been carried out using CAST 3 M for different reactor operation conditions. The maximum Von-Mises stress intensities at the sliding joint are found to be 82, 192 and 274 MPa for cold shutdown, normal operation and SGDHR conditions respectively. These stresses are demonstrated to have compliance with design code RCC-MR, 2002. The maximum local strain in the component was found to be 0.13% (with the help of the Neuber's rule applied to the elastic results). This result is validated by detailed non-linear analysis involving both geometrical and material non-linearities.

The sliding joint in actual component is modelled similar to the model adopted for validation problem, and elasto-plastic analysis is carried out. By detailed elasto-plastic analysis the strain obtained is 0.12% for SGDHR condition which is matching with Neuber's rule prediction. Also after unloading the PR gains its original shape and ovality is negligible.

Validation method

To study the deformation of edges of the PR and PTM inside the sliding joint, analytical and experimental investigation of a simplified sliding joint is carried out at room temperature. Two pipes made up of SS 304L of same size (900 mm length, 150 NB Sh 40) are used. Both pipes are stepped (machined on OD/ID) to 170 mm length and then engaged to 150 mm length.

Load is applied at two points, 600 mm apart. The pipes are simply supported and the supports are 1200 mm apart. The model of sliding joint is subjected to pure bending moment (Fig. 3). The elasto-plastic analysis of the model is carried out to understand the local deformation, ovality, plastic strain etc. The analytical prediction and experimental observations are compared.

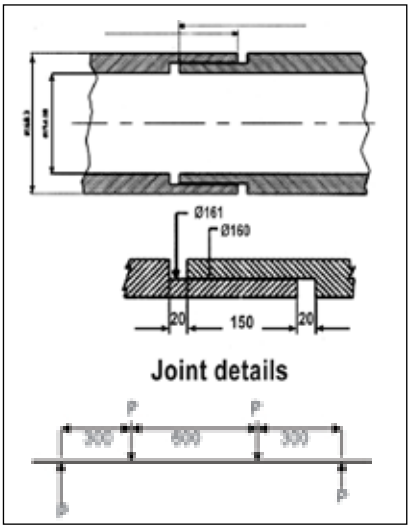

Fig. 3 *Joint and loading detail*

FEM analysis of the above joint as simulated in the experiment is carried out using CAST3M FE code. Four noded thin shell elements are used for analysis. The analysis comprises of both loading and unloading, to get residual strains.

Comparison of experimental and analytical results for the simplified model

Load versus displacement curve at different locations of the pipe for loading and unloading, the deformation pattern, strain at strain gauge location has been compared. A good match between the experimental and analytical results is found. The deformation pattern of the pipe (at section AA) at the end of the unloading is matching in both experiment and the analysis (Fig. 4A, Fig. 4B, Fig. 4C and Fig. 4D).

Ovality calculation has been done for the experimental setup (11.3% ovality) and the analytical model (10.1% ovality) at the end of the unloading and the results are found to be approximately same. Experimental values of the peak strain are less than that of analysis result.

Elasto-plastic analysis has been carried out to find out the maximum inelastic strain at the location of the sliding joint for 50mm relative displacement between primary ramp and primary tilting mechanism. The maximum local strain obtained is 0.12% which is well within allowable limit of 5% (local). The ovality on the primary ramp after applying relative displacement is found to be negligible.

The analysis methodology has been validated with experiments and analysis on simplified coaxial pipes with sliding joint subjected to bending moment. The results are well matched between analysis and experiment. The same methodology has been applied to PFBR IFTM where there is a sliding joint between PR and PTM.

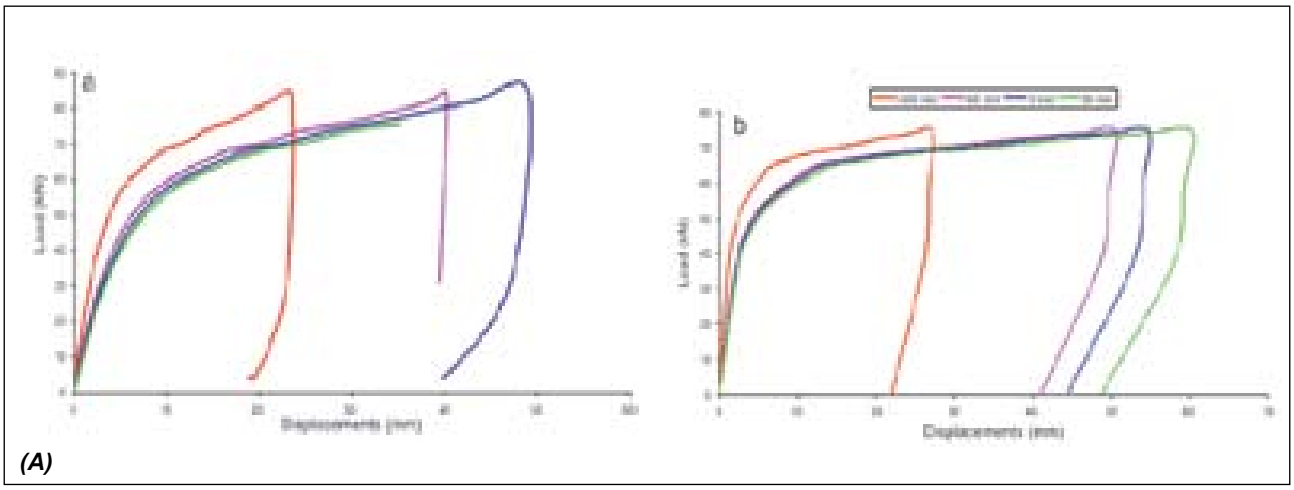

Fig. 4A *Load Vs displacement a) Experiment b) Analysis*

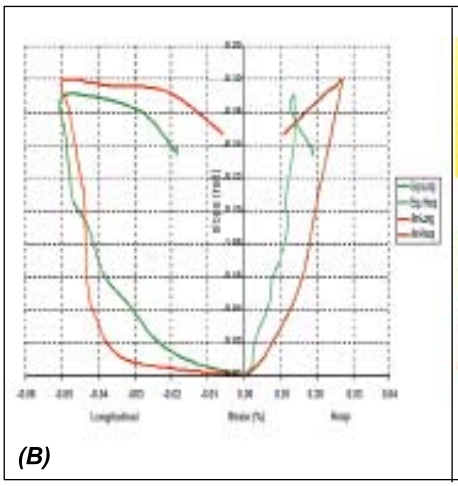

Fig. 4B *Variation of strain Vs slop at strain gauge location*

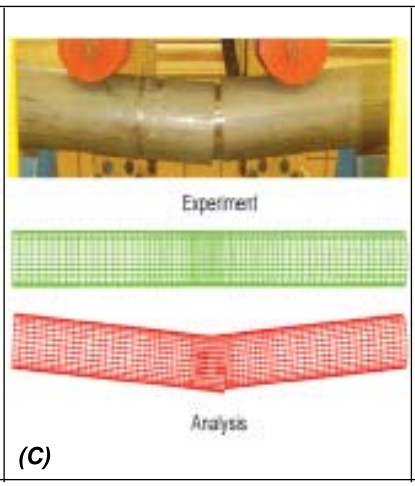

Fig. 4C *Deformation of pipe joint after unloading*

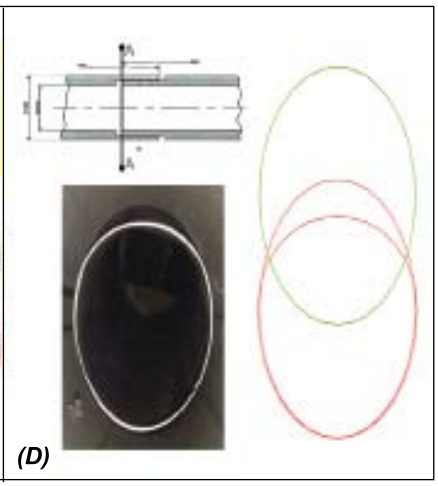

Fig. 4D *Deformation at section A-A*

II.18 Thermal Analysis of Reactor Vault Temperature under Loss of Cooling

The reactor vault (RV) is a concrete structure which supports the main vessel and the safety vessel of the reactor. This structure, built around the safety vessel, gets heated due to the heat emanating from the outer surface of the safety vessel insulation. The reactor vault consists of two walls, viz. the inner wall and the outer wall. The inner wall supports the safety vessel while the outer wall supports the main vessel. The inner and outer walls are separated by expanded polystyrene insulation. From design considerations the temperature limits on the reactor vault are (i) 338 K during steady state operation, (ii) 363 K during safety grade decay heat removal (SGDHR) condition and (iii) 450 K during a station blackout condition.

The vault is lined on the inner side by 6 mm thick carbon steel liner and is cooled by water flowing through square pipes embedded in the concrete and welded continuously to the liner (Fig. 1). Complete loss of cooling to vault is considered as a category - 3 event. Evolution of vault temperature during this event has been analyzed and the safety action required has been finalized.

The thermal hydraulic analysis has been carried out in two parts: (i) Global analysis for the bottom shield, lower lateral shield and upper lateral shield, and (ii) Local analysis for the safety vessel support embedment (SVSE). For the global analysis, the computer code HEATING5 has been used while for the local analysis, commercial CFD code has been employed. Both the analyses consider heat conduction in the walls, radiation heat exchange among the various structures through the transparent nitrogen gas and natural convection of nitrogen gas in the annuli between the main vessel, safety vessel and the reactor vault, simultaneously.

Two extreme scenarios of loss of vault cooling have been considered. They are: (i) controlled shut down of the reactor within a short time after the occurrence of the event and (ii) station blackout in the plant extending for 14 h. In the first scenario, the main vessel temperature does not exceed 693K and it is brought down

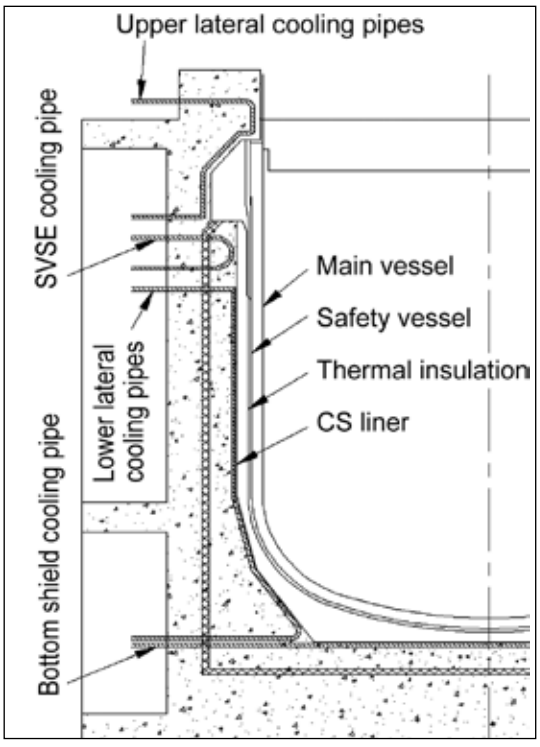

Fig. 1 *Reactor vault & cooling system*

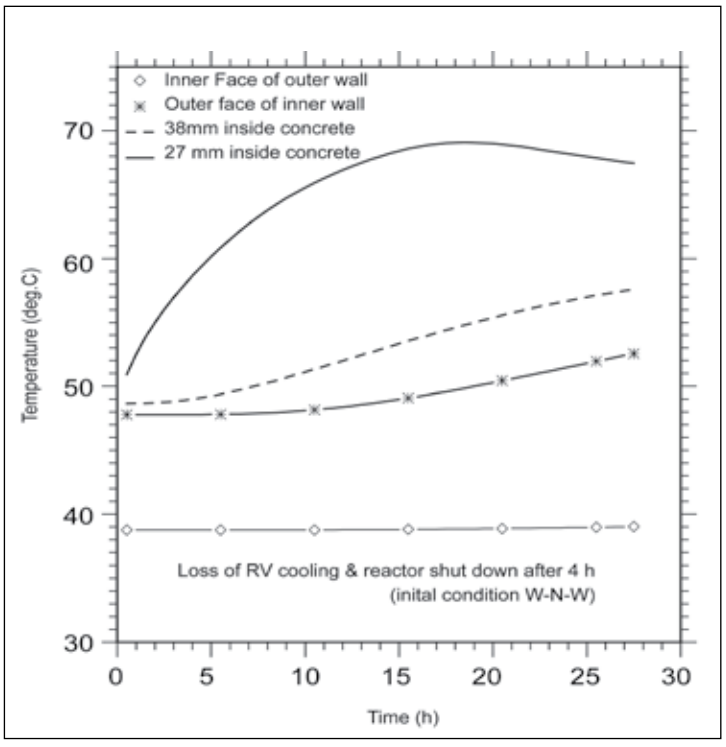

Fig. 2 *Temperature in vault after loss of cooling (loss of RV cooling and reactor shutdown after 4 hour (initial condition W-N-W))*

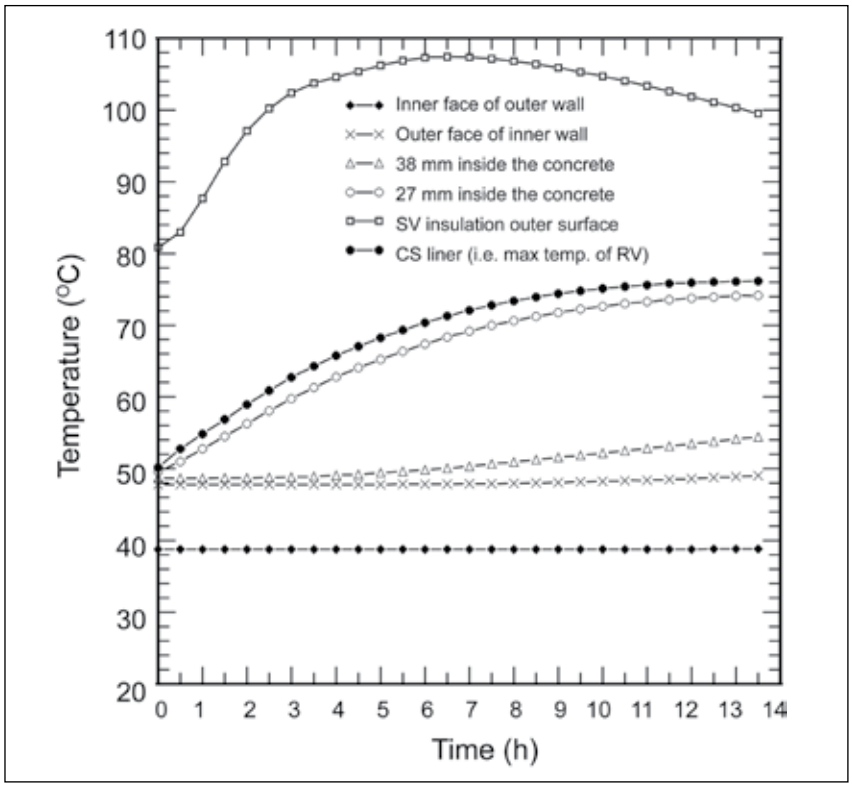

Fig. 3 *Temperature evolution in vault during station blackout*

gradually by controlled cooling of the primary sodium system to 473 K. In the second scenario, the main vessel temperature increases from nominal value to a maximum value of 893 K during the transient as the rate of cooling is very slow, due to the low decay heat removal capability of the SGDHR system.

The predicted temperature evolutions in the vault at various depths are depicted in Fig. 2. It can be seen that the maximum temperature of the liner is only 343 K at the end of eighteen hours. After this instant, the peak temperature reduces as the heat coming into the vault inner surface reduces while heat diffusion inside the concrete continues at a faster rate. Thus, it is clear that the peak temperature on the inner surface of the vault for a major part of the vault surface is only 343K, which is acceptable. The evolution vault temperature during a station black out is depicted in Fig.3. The thermal response of the reactor vessel is sluggish due to its large thermal inertia. Even fourteen hours after the loss of cooling, the liner temperature is only 349 K. As in the earlier transient, the thermal effect is limited very close to the liner.

The predicted temperature evolutions in the local zone around safety vessel support embeddment at various instants during the station black out are depicted in Fig. 4. It is clear that the peak temperature attained is 395 K, which is much less than the allowable value of 450 K. Thus, based on these investigations, it has been established that the event of loss of cooling to vault is easily manageable in the case of PFBR due to relatively large thermal inertia of the concrete structure. The operator action recommended for this event is controlled shut down of the plant, in about half an hour after confirmation of the event.

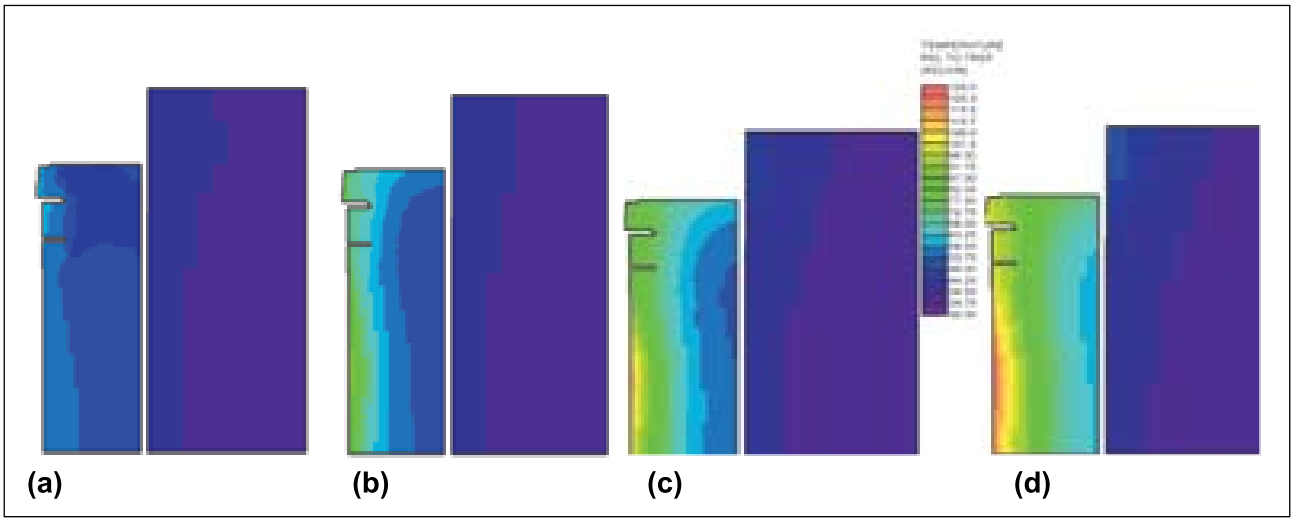

Fig. 4 *Vault temperature around support embeddment during station black out (a) 0 hours (b) 4 hours (c) 8 hours (d) 14 hours*

II.19 Characterization of Inter-Wrapper Flow in Core Thermal Hydraulics

Decay heat removal after reactor shutdown is one of the important safety functions which must be accomplished with a very high reliability. In PFBR this is achieved by two independent systems viz. Operation Grade Decay Heat Removal System (OGDHRS) and Safety Grade Decay Heat Removal System (SGDHRS). During incidents like electrical power failure, the steam-water system becomes unavailable leading to non-availability of OGDHRS. Subsequently, the decay heat removal function is transferred to SGDHRS which is a highly reliable, almost passive system. This consists of a sodium to sodium heat exchanger (DHX) and sodium to air heat exchanger (AHX). DHX removes heat directly from the hot pool and AHX dissipates the heat to atmospheric air which is the final heat sink.

The decay heat generated in the core is transported to hot pool by circulating primary sodium with the help of sodium pumps. Following some design basis events like off-site power failure or primary sodium pumps trip, the pumps coast down eventually leading to natural circulation of the sodium through the core. Even though there are backup power supplies for primary sodium pumps, the reactor is designed to meet all the design safety limits even under natural circulation mode.

Under this condition natural convection currents setup both inside the subassembly (SA) as well as outside of it. The outside flow through the narrow gaps between SA is known as Inter-Wrapper Flow (IWF). The former is supported by the buoyancy forces generated by the heat transfer from primary sodium to secondary sodium in the IHX and the heat transfer in core, while the latter (IWF) is due to the complex thermal hydraulic interaction amongst the inter-wrapper space, hot pool and DHX. International studies indicate that the heat removed by the IWF is significantly large having a strong potential to reduce core temperatures. Studies based on 1-D thermal hydraulic models also predict considerable reduction in the core temperatures.

The IWF gaps are narrow (~3 mm) compared to the length and width of the SA (~4 m and 130 mm respectively). Also a large number of SA (1758), stacked vertically in a voluminous pool of sodium (~12 m diameter) makes the IWF path complex. One-dimensional models are inadequate for the purpose as the flow is three dimensional in nature. Due to the vast difference in the length scales of various zones, a complete 3-D model for the IWF integrated with hot and cold pools calls for a high fidelity analysis involving billions of computational grids. One of the options to circumvent this difficulty is use of porous body model for the IWF linking it with hot pool. This calls for detailed knowledge of pressure drop and heat transfer characteristics of the IWF. Since the IWF path is very complex and the flow is induced by buoyancy, established correlations are not available in open literature to predict the pressure loss and heat transfer coefficient. Hence, these parameters need to be established from first principles by detailed

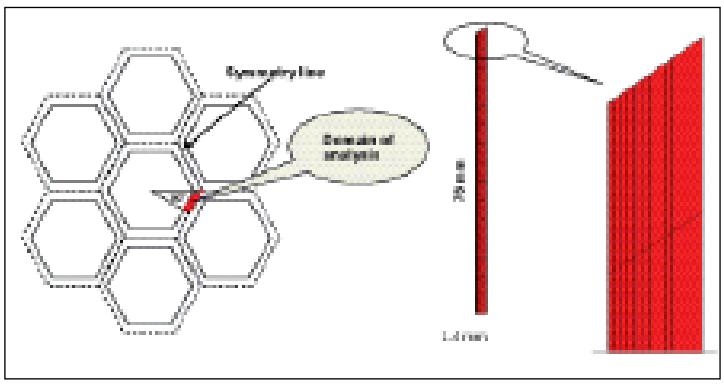

Fig. 1 *Hexagonal subassemblies, Inter-wrapper space and CFD mesh*

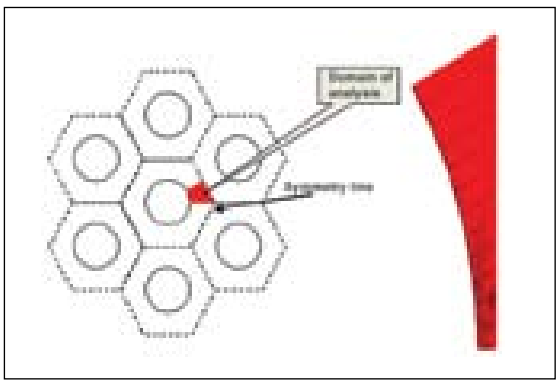

Fig. 2 *Circular subassemblies and CFD mesh for IWF space*

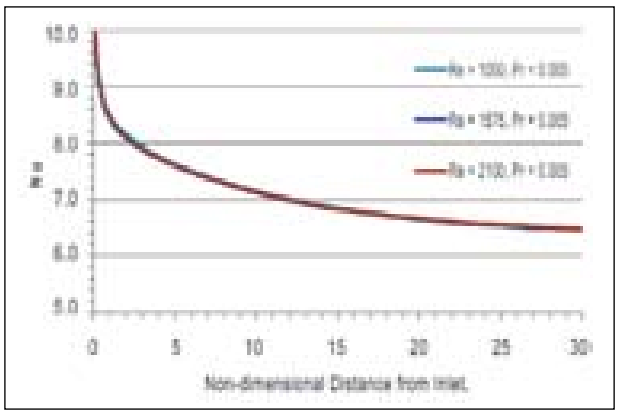

Fig. 3 *Nusselt number during axial flow between hexagonal subassemblies*

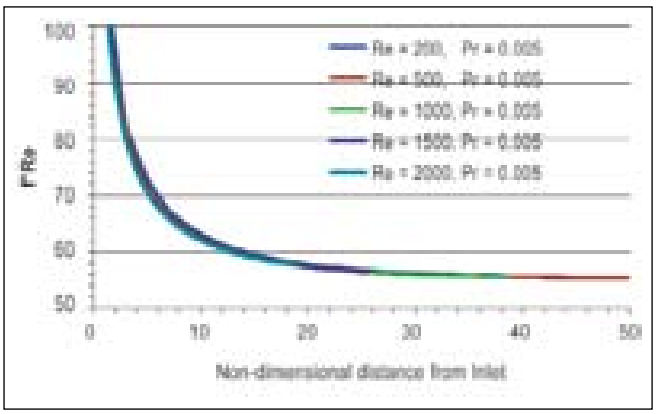

Fig. 4 *Friction factor during axial flow between circular subassemblies*

local 3D computational fluid dynamic (CFD) based studies.

The IWF has two components viz. axial flow and cross flow over the SA. The flow regime can be laminar or turbulent. The axial flow pressure drop and heat transfer coefficient are influenced by the heat generation in the SA, whereas the cross flow characteristics are mainly a function of only the Reynolds number. The fuel and blanket SA are hexagonal in cross-section and the shielding SA are circular in cross-section. The inter-wrapper gap has a 30° symmetry in the angular direction and also symmetric about the line passing through the center of the annular gap. The geometry and CFD mesh used for the hexagonal and circular SA are shown in Fig. 1 and Fig. 2 respectively.

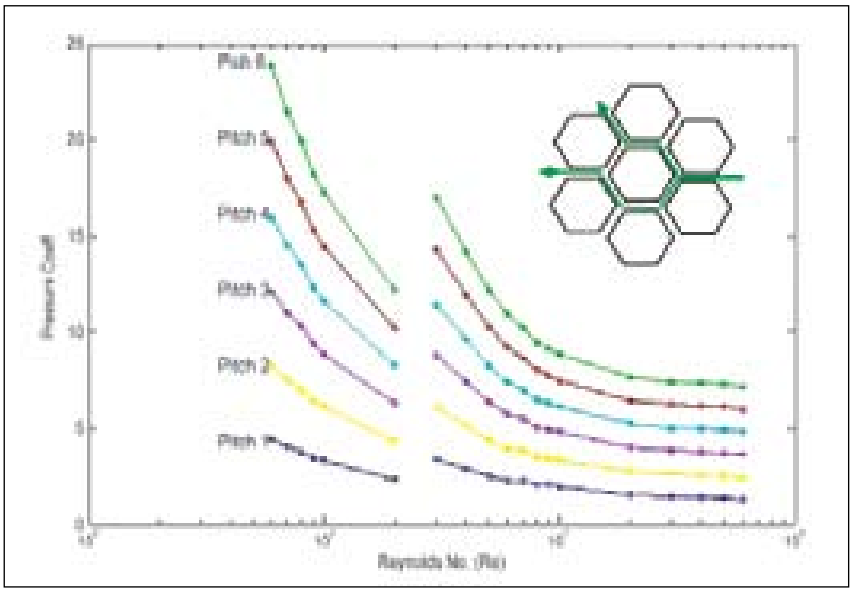

Fig. 5 *Pressure loss coefficient during cross flow over hexagonal subassemblies*

Typical data of friction factor (f*Re) and heat transfer coefficient (Nu), predicted by CFD studies for axial flow between SA are depicted in Fig. 3 and Fig. 4. Similarly, the predicted pressure loss coefficient for cross flow over hexagonal subassemblies in the laminar and turbulent regimes are presented in Fig. 5. These data would form input for the 3D porous body model of the inter wrapper flow.

II.20 Pool Thermal-Hydraulic Studies during Safety Grade Decay Heat Removal Condition

Even after shut down of the reactor, heat is generated inside the core due to the decaying process of the fission products. This heat must be removed to keep the maximum temperature inside the core within the specified safety limit. Under normal condition the core is cooled by forced convection using the operational grade decay heat removal system (OGDHR). But in case of total station black out

condition when no active system is available, safety grade decay heat removal system (SGDHR) has been provided to cool the core by free convection. SGDHR system of PFBR consists of four independent loops of each 8 MWt heat removal capacity. Each loop consists of a sodium to sodium shell and tube heat exchangers (DHX), secondary sodium loop, sodium to air heat exchanger, chimney and damper. The whole SGDHR system works on the principle of natural circulation system and hence does not require any active system except dampers provided on the airside. The DHXs are immersed inside the hot pool. Primary sodium flows in the shell side and the secondary sodium in the tube side.

Simulation of whole SGDHR system in a single model experiment is expensive and complicated. Therefore, it has been planned to split the whole study into two different experiments, one is primary pool thermal hydraulic studies and the other is natural convection studies in the secondary loop. The DHX – Core – Hot pool interaction during SGDHR condition can be revealed from primary pool thermal hydraulic studies carried out in SAMRAT model (1/4 scale model of PFBR primary circuit) using water as simulant. The establishment and behaviour of natural circulation path in the secondary loop can be studied in greater detail in sodium loop. In the SAMRAT model, immersion type rod heaters were fixed inside the fuel subassemblies and storage subassemblies to represent the generation of decay heat in the prototype after reactor shut down. In the secondary side of DHX, water has been circulated with the aid of an external pump to simulate the heat removal by DHX. The heat removal rate by DHX for various secondary side flow rate was estimated from earlier experiments. The shell side of DHX and the whole primary pool is cooled by natural convection. The possible major natural circulation path that may be established in the primary pool during the course of this study has been shown schematically in Fig. 1. Various parametric studies have been carried out to study the core coolability using the SGDHR system. One of the important finding is that the DHX which are immersed inside the pool is able to remove the heat generated inside the core effectively. This has been explained in Fig. 2 where,

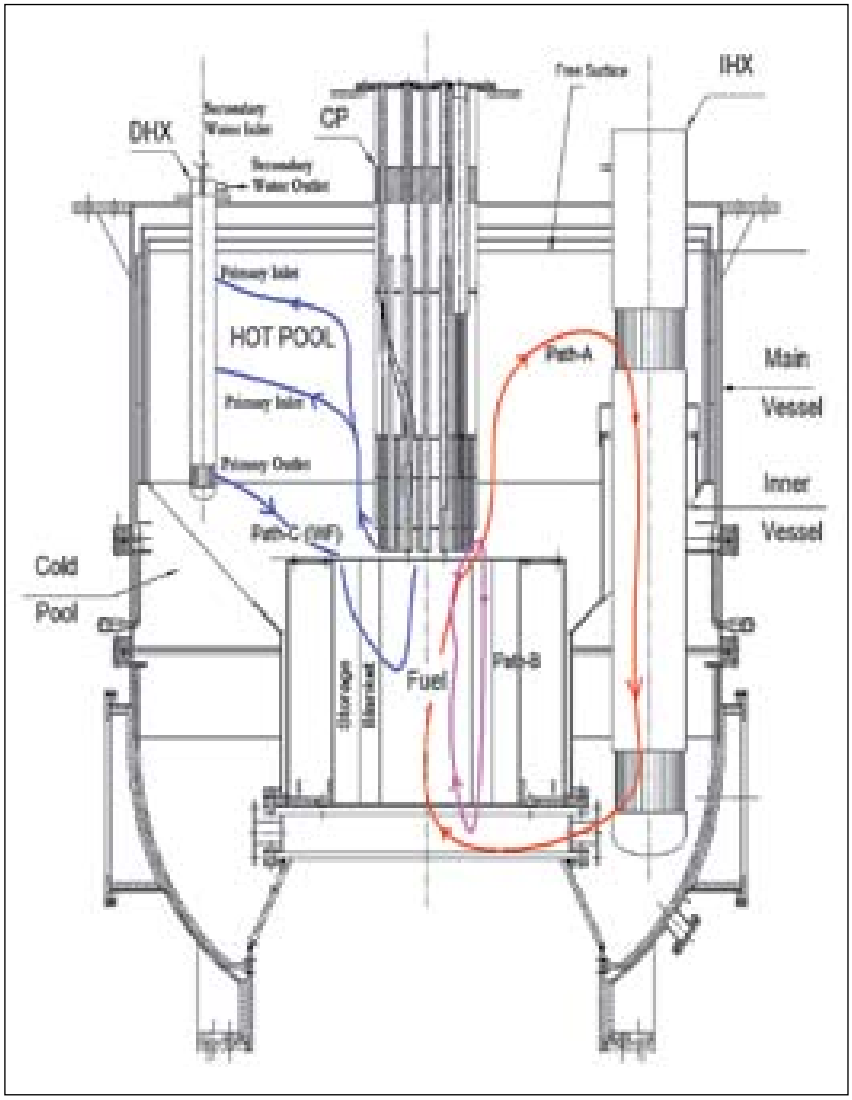

Fig. 1 *Possible natural circulation path in the primary pool during SGDHR condition*

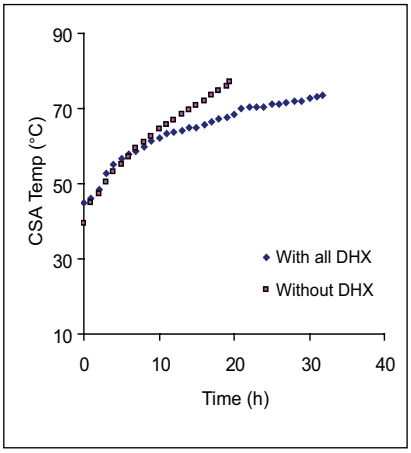

Fig. 2 *Effect of DHX on the CSA outlet temperature*

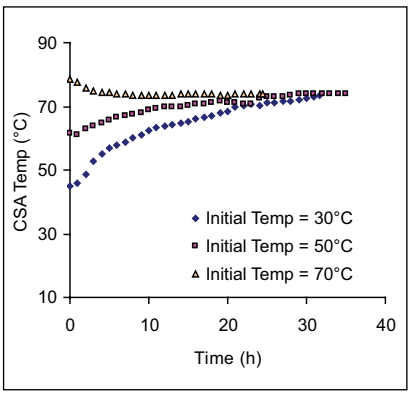

Fig. 3 *Central subassembly outlet temperature history with various initial pool temperature. Power = 60kW*

central subassembly (CSA) outlet temperature has been compared for both the conditions. It can be seen that, with the operation of DHX, the outlet temperature of CSA is stabilized at lower temperature. In another experiment, the effect of initial pool temperature on pool thermal hydraulics has been studied. In this case, the core power and the flow rate in the secondary side of DHX were kept constant. The result is shown in Fig. 3. It can be seen that the steady state temperature of the pool is same and does not depend on the initial temperature of the pool. Therefore, the important conclusion can be drawn that for a fixed decay power, there exists a unique solution of temperature field in the primary pool. These studies have given confidence to the establishment of natural convection in the reactor assembly for effective removal of decay heat.

II.21 Development of Ultrasonic Guided Wave Based Methodology for Inspection of Hexcan Seal Welds of Fuel Subassemblies

Inspection of seal welds in fuel subassemblies of PFBR is critical as failure of these welds in service may result in the separation of fuel pins from the subassemblies and difficulties in discharging of fuel subassembly and/or consequent pin failures leading to contamination of the coolant with the fuel and radioactive fission products. Due to the complex geometry of the hexcan seal welds, radiography testing of the weld cannot provide required sensitivity during the fabrication stage. Because of the geometry and less thickness of the weld, a new methodology based on ultrasonic guided wave is developed for inspection of the seal welds. This methodology is fast and can be used for detection of both axial and circumferential defects of about 300 µm or more in the seal welds.

The developed methodology involves testing the weld from the sheath side using 2.25 MHz guided wave. The sensitivity of the methodology was established using the reflection from a 300 µm deep back surface (ID) defect on a stainless steel plate of 3 mm thickness. In order to evaluate the back surface defects in the hexcan seal welds showing amplitude more than the reference defect, a calibration study was also carried out on the stainless steel plate having defects of depth in a range of 300 to 1100 µm.

Evaluation of an actual hexcan weld was carried out using the methodology developed based on the set reference level. A typical ultrasonic signal showing weld noise obtained from a defect-free region is shown in Fig. 1(a). Evaluation of hexcan welds revealed defect indications in a few of the faces. A typical signal corresponding to a defect in one of the faces is shown in Fig. 1(b). Based on the calibration study, the defect was found to be of about 1.1 mm depth. In order to confirm these observations, other techniques such as radiography and *in-situ* metallography were

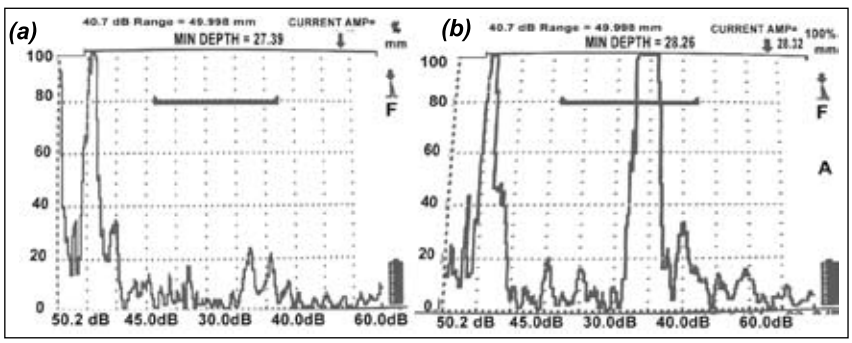

Fig. 1 *Typical A-scan signals corresponding to (a) a defect free weld and (b) a weld defect.*

employed. As the complex geometry is not amenable for radiography with required sensitivity, the face of the Hexcan with defective weld was cut and machined to a flat plate by removing the excess material from the ID side. The flat specimen of approximately 8 mm thickness was then radiographed, and the continuous ultrasonic indications could be correlated to the presence of a continuous discontinuity along this face (Fig. 2(a)). Though, the ultrasonic indications in the weld in this face could be revealed by the radiography, a detailed step wedge calibration study indicated that the defect obtained in the weld by radiography corresponds to a defect of depth about 150 µm only, in contrast to ~1.1 mm deep defect evaluated by the ultrasonic technique. In order to understand this discrepancy, in-situ metallography was carried out across the weld in this face. Fig. 2(b) and Fig. 2(c) show the macro-structures at low and high magnifications respectively, corresponding to a region identified to have a defect by both ultrasonics and radiography. Macrostructure of a defect-free weld is also shown (Fig. 2(d)) for ready comparison. It can be inferred from Fig. 2(c) that two types of defects exist in the weldment, i.e. cavity like defect below the fused location marked as "A" and an inclined tight lack of fusion like defect marked as "B". The total depth of the defect is ~1 mm, which is in good agreement with that evaluated by the ultrasonic technique (~1.1 mm). By comparing Fig. 2(a) and Fig. 2(c), it can be seen very clearly that the defect revealed by radiography corresponds to defect "A" shown in Fig. 2(c), which is only ~200 µm deep. As the tight inclined defect (marked as "B") observed in the macrostructure results in negligible material loss in radiography direction, in comparison to overall thickness of the material in that region, such defects do not produce appreciable contrast to be registered in the film during radiography. However, these defects could be reliably detected by the developed ultrasonic guided wave based methodology.

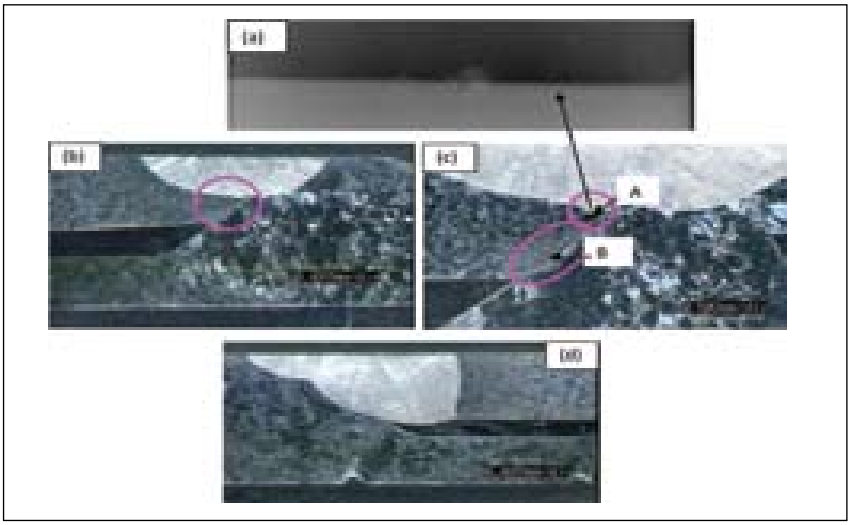

Fig. 2 ***(a)*** *Radiograph of the face of the Hexcan with defective weld showing a linear indication throughout the weld except at the centre of the weld, (**b**) Corresponding macrostructure at low magnification (**c**) At high magnifications and (**d**) Macrostructure of a defect free weld is also shown for ready comparison.*

II.22 Kalman Filter Based System for Measurement of Drop Time Performance of Diverse Safety Rods Drive Mechanisms

The Diverse Shutdown System of PFBR consists of three rods called Diverse Safety Rods (DSRs) and associated drive mechanisms, sensors, etc. During normal operation of the reactor, these rods are held out of core by means of electromagnetic clutches kept energized. A potentiometer indicates the continuous position of DSR when it is being driven in or out. Sets of top and bottom limit switches, actuated by the electromagnetic clutch / drive mechanism provide sensing of electromagnetic clutch top and bottom positions. However, design does not provide for direct sensing of top and bottom positions of DSRs due to physical restrictions on layout and unfavorable environmental conditions. On actuation of the trip system for DSRs, the electromagnetic clutches are de-energized, the rods leave the

clutches and drop in the core under gravity. Under such a situation, the time instant when the rods leave the top is known immediately but it is not possible to ascertain whether the rods dropped fully and also to measure the rod drop time. In view of this, an alternative means for inferring the rod position and drop time would be required.

A reactivity meter, based on Kalman Filtering Technique, has been designed and developed by BARC. The unit is capable of showing the reactivity in different operational regimes of reactor including shutdown. It makes use of the neutron flux signal taken from neutronic channels and estimates the instantaneous value of reactivity. It is proposed to use the reactivity meter for the purpose of DSR drop time measurement in PFBR (Fig. 1).

Table 1: Comparison between rod R_A drop time inferred from estimated reactivity with actual drop time

Position (mm)	Rod drop time inferred from estimated reactivity t_1 (s)	Actual rod drop time, t_2 (s)	Delay, t_1-t_2 (s)
322 (Initial)	1.141	1.141	0.000
300	1.236	1.208	0.028
275	1.286	1.243	0.043
250	1.319	1.269	0.050
225	1.352	1.291	0.061
200	1.384	1.312	0.072
175	1.420	1.330	0.090
150	1.449	1.343	0.106
125	1.475	1.361	0.114
100	1.501	1.375	0.127
75	1.556	1.387	0.168
50	1.610	1.403	0.207
25	1.663	1.426	0.237
16	1.696	1.437	0.259

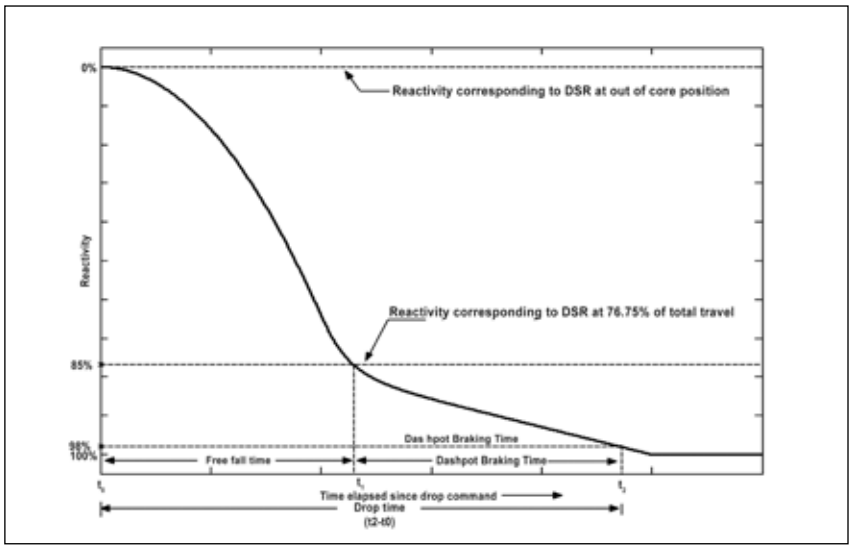

Fig.1 *Illustration of measurement of PFBR-DSR drop time*

Kalman Filter Algorithm

The system for estimation of reactivity based on the Kalman filtering technique consists (Fig. 2) of a state space model of the reactor which is a set of first order difference equations for neutron flux density *n*, precursors' concentrations C_1, C_2, C_m, reactivity ρ, and white noise sequence *w*.

The unit based on Kalman Filtering was qualified in FBTR, which was designed and developed by BARC (Fig. 2) are shown in Table 1 and Fig. 3.

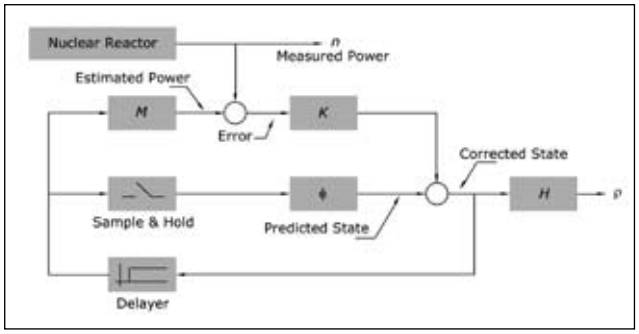

Fig.2 *Reactivity estimation using Kalman filter*

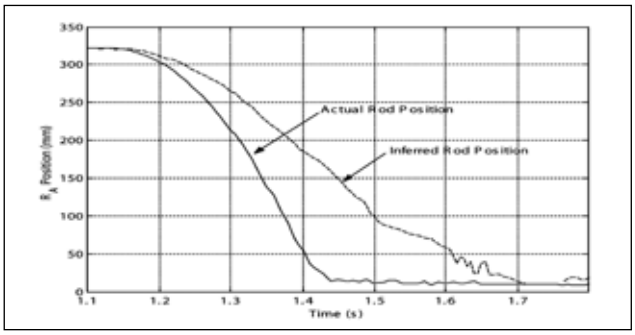

Fig.3 *Time variation of actual position of rods and rod position inferred from the estimated reactivity*

II.23 Structural Integrity of Main Vessel Under Revised Core Disruptive Accident Loadings

Core Disruptive accident is a beyond design basis event postulated for safety analysis of PFBR. This event has been analysed extensively at our Centre. Unprotected Transient Over Power Accident (UTOPA) and Unprotected Loss of Flow Accident (ULOFA) are the two events which are considered as having potential to release mechanical energy. Safety analysis has been revised considering the various aspects comprehensively towards meeting the requirements of peer reviews. As per the revision, the UTOPA does not have the potential to release the mechanical energy. However, ULOFA is energetic. It is postulated that it has potential of doing mechanical work up to 100 MJ. Under this postulation, reactor physics and thermal hydraulics computations were carried out for arriving at the status of core during pre-disassembly phase, which is the input for subsequent mechanical analysis. During pre-disassembly phase, the temperature of main vessel remains at 700K and the hot pool temperature rises to 855K. The analysis for the mechanical consequences were carried out for these revised conditions.

The scenario of release of mechanical energy is defined conservatively. The heat generated during pre-disassembly phase melts the core, to the extent of saturated liquid state. Subsequent heating generates the vapor phase, which is having high potential to do mechanical work in view of its high temperature and high pressure (Fig. 1a). The mechanical energy release is due to expansion of vapor phase from initial pressure (P_o) which is at saturated condition to the final pressure (P_f) equal to ambient condition prevailing in the reactor. During this rapid expansion of core bubble in the liquid sodium environment which is considered as isoentropic, the pressure/ shock waves are generated which deform the shell structures surrounding the core. Mechanical straining of main vessel and its internals, impact of sodium slug on the bottom of the top shield are the main mechanical consequences during the first phase (Fig. 1b).

Theoretical analysis is carried out using the finite element code called 'FUSTIN' which uses arbitrary lagrangian eulerian co-ordinate system for describing fluid motions and convected co-ordinate system for modeling

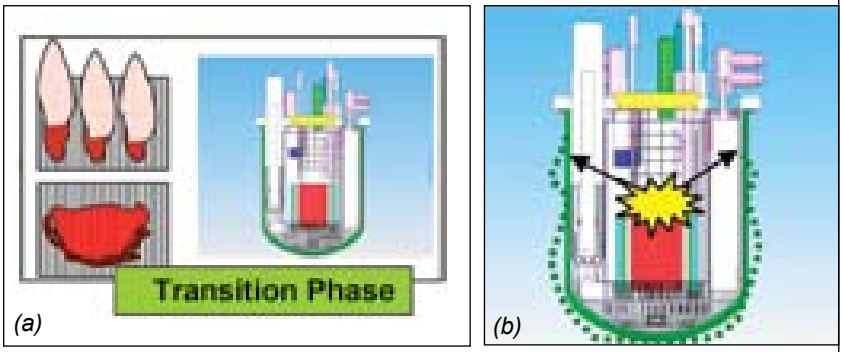

Fig.1 *Mechanical consequences of CDA (a) Melting and vapourisation of core (b) Mechanical energy release*

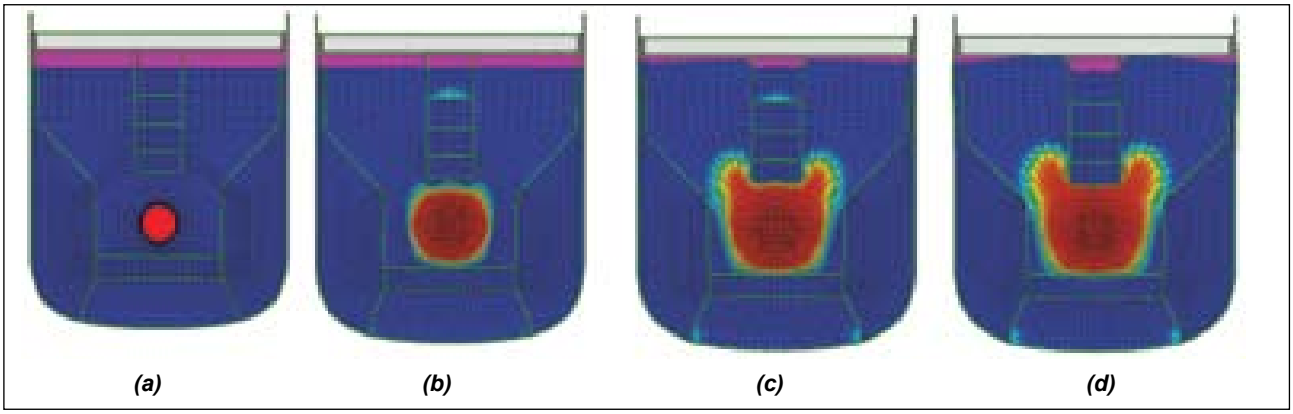

Fig.2 *Evolution of core bubble and vessel deformations during CDA (a) 0 ms (b) 60 ms (c) 120 ms (d) 200 ms*

the geometrical non-linearity of structures. The core bubble has been idealized as homogenous phase obeying ideal gas law: PV^{γ} = constant, where γ=0.72 and is derived from the pressure volume obtained from molten core behavior in association with initial pressure (4 MPa) and initial volume (2.56 m^3). Similarly the argon space is treated as ideal gas, obeying the relation: PV^{γ} = constant, where γ = 1.67. The finite element model consisting of core bubble, argon, sodium, main vessel and its important internals have been generated. The analysis is carried out up to 200 ms wherein all the important events are depicted. Temperature dependent material properties are used for structural elements. Fig. 2 shows that no evolution displacements of core bubble and structures, which depicts the sequence of events such as upward bowing of core cover plate of control plug bulging of inner vessel, downward displacement of main vessel at bottom portion, core bubble crossing the control plug, sodium slug impact on the top shield, reflection of pressure waves from top shield and downward bowing of core cover plate and downward displacements of sodium free levels. The figure also shows that the sodium impact is restricted to a small zone on the top shield around the control plug and no impact of sodium slug exists within the control plug on the top shield and the overall deformations of internals and main vessel are nearly uniform.

From the energy balance diagram shown in Fig. 3, it is seen that due to constraints of main vessel and internals, the maximum energy released by the core bubble is 60 MJ during transient condition. Under quasi-static condition when the kinetic energy is ignored, the energy released by core is fully absorbed by vessels and cover gas space. The total energy would be 45 MJ. The main vessel absorbs the energy in two phases: at about 25 ms due to initial impact of pressure waves propagated in sodium at about 25 ms. The displacement evolutions are shown in Fig. 4. The core cover plate oscillations, bending upwards (~70 mm) and bowing downwards (~ -110 mm) are seen clearly in the figure. The peak main vessel bottom displacement is 160 mm and the radial bulging is 103 mm. The triple point moves down by 36 mm (maximum). The important strains are peak strains on the main vessel surface. There are two critical locations: one is triple

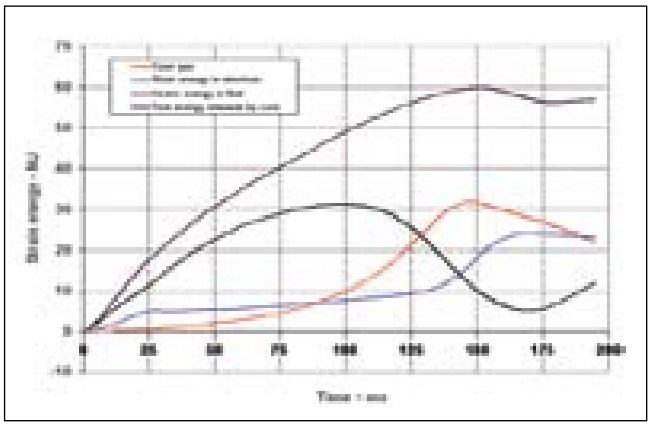

Fig.3 *Evolution of energy distribution*

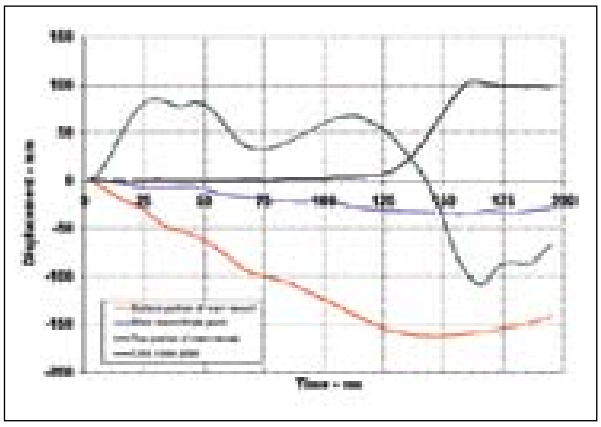

Fig.4 *Evolution of displacements of structures*

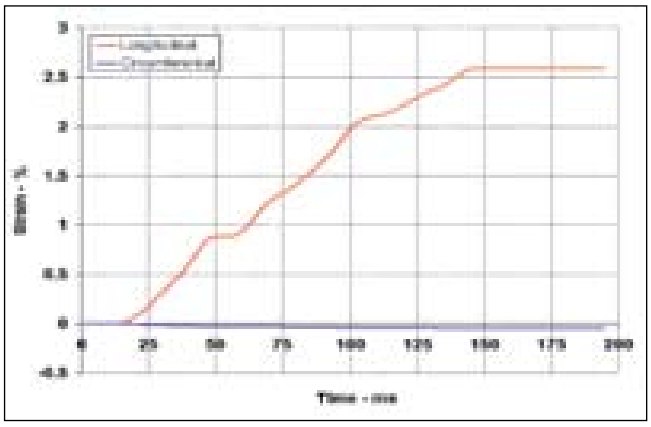

Fig.5 *Strains at MV triple point*

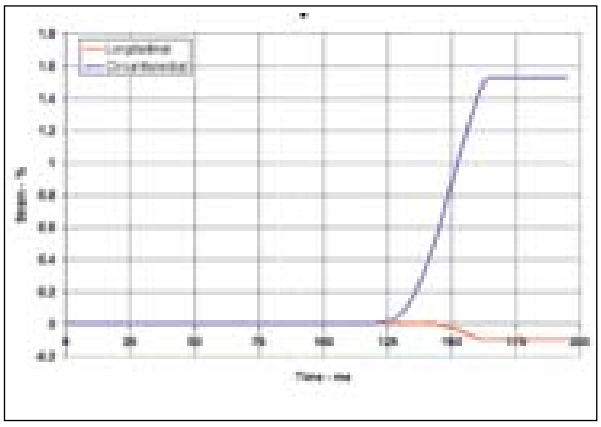

Fig.6 *Strains at upper portion of MV*

point and another is the upper cylindrical portion above sodium free level. Fig.5 and Fig.6 show the strain evolution at these two critical locations. The peak strains are: 2.6% (longitudinal) and (-0.1 % hoop) at the triple point (Fig. 5) and 1.53 % (hoop) and -0.1 % (longitudinal) at the upper portion (Fig. 6).

The peak equivalent strains (Von Mises Based) are computed as 1.54% and 2.6% respectively for the upper cylindrical portions and triple point. These values are very much lower than the allowable strain limit of 15%, recommended for PFBR. Further, the maximum displacements of main vessel are 165 mm at the bottom portion and 103 mm at the upper portion, which are less than the limit of 250 mm recommended. Hence the structural integrity of main vessel is demonstrated with comfortable margins.

The improved results have enhanced the confidence on the structural integrity of main vessel under CDA.

II.24 Development of High Temperature Fission Chambers

High Temperature Fission Chambers (HTFC), now under development by BARC and our Centre, are used in PFBR for core monitoring. Six numbers of HTFC with a neutron sensitivity of 0.2 cps/nv are provided in the control plug. These detectors are installed in the housing tubes provided in the control plug and are replaceable with the handling cum shielding assemblies. These detectors are used in pulse mode during source range and in Campbell mode during intermediate range (upto 5% power), as part of neutron flux monitoring.

Twenty four numbers of HTFC with neutron sensitivity of 0.2 cps/nv are provided in eight thimbles (three detectors in each thimble) near four intermediate heat exchangers (IHX) for delayed neutron detection (DND) as a part of failed fuel detection. The assembly of 0.2 cps/nv high temperature fission chamber is shown in Fig.1 The principal material of construction of fission chamber is Inconel 600.

The assembly consists of two concentric cylindrical electrodes. The inner cylindrical electrode is to be coated with LEU on outer surface whereas the outer cylindrical electrode is to be coated with LEU on inner surface. The annular spacing between the two electrodes is maintained at 0.8 mm within ± 50 micron tolerance.

The concentric electrodes are located inside a cylindrical inner housing, which is connected to instrumentation ground. This housing has top and bottom closures. The top closure has ceramic feed through, whereas the bottom closure has a tube for filling (argon (95%) + nitrogen (5%)) gas mixture to a pressure of six bar. A cylindrical chamber surrounds the inner housing and is the outer housing which is connected to the chassis ground. The outer housing is filled with Argon (95%) + Nitrogen (5%) gas mixture to a pressure of four bars (abs).

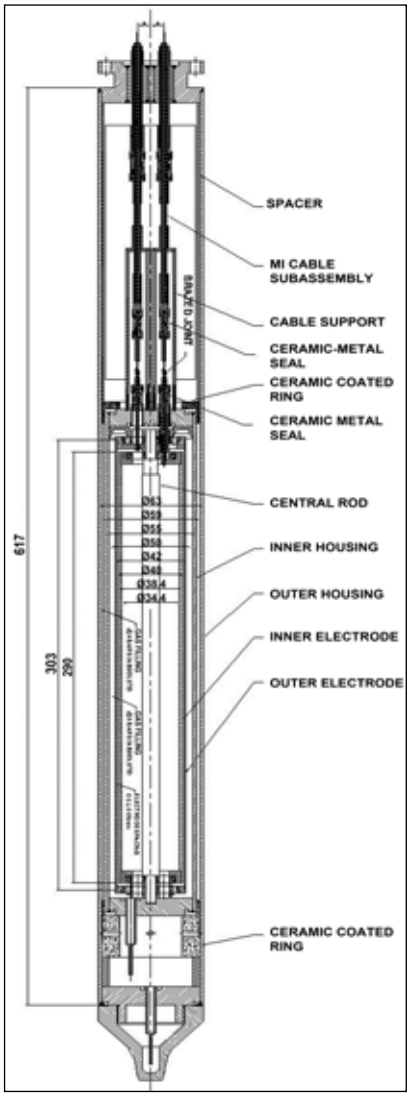

Fig.1 *High temperature fission chamber*

The manufacture of high temperature fission chambers (HTFC) is carried out as per ASME Section III, Class I components. Earlier, a prototype detector was fabricated with normal cables and tested at APSARA & FBTR at room temperature and a neutron sensitivity of 0.18 cps/nv was measured. A detector with twelve meter length of MI cables is ready for testing at APSARA.

II.25 Behaviour of AISI Type 316LN Stainless Steel and Modified 9 Cr-1 Mo Steel in a Bi-metallic Sodium Loop at 798 K

Fast Breeder Reactors (FBRs) are designed with two heat transport circuits to contain radioactivity. In the primary circuit, sodium transports the heat generated in the core to the intermediate heat exchanger (IHX).The sodium from the IHX then transfers heat to the water in the steam generator (SG). In PFBR, the low nitrogen varieties of types 304 and 316 stainless steels are used as construction material for the primary circuit and the IHX. Modified 9Cr-1Mo steel is used as the construction material for steam generators. The compatibility of these materials with liquid sodium is of utmost importance for the safe operation of the reactor. Liquid sodium when in contact with ferritic steels and austenitic stainless steels at high temperature can function as an agent for transport of alloying elements such as nickel, chromium, molybdenum and carbon. Transport of carbon causes the two steels to either carburize or decarburize depending on the direction and extent of carbon transport which is decided by the prevailing carbon potential gradient across the steel-sodium interface. Therefore, to assess the long term integrity and performance of structural materials in flowing high temperature liquid sodium environment, it is essential to know the extent of carbon transport. In the primary circuit which is made of entirely one type of material, the direction of the transport would be from the high temperature region to the low temperature region. In the secondary circuit, where the materials are different, the carbon transport depends on the relative carbon activities of the steels at their respective temperatures of operation. A bi-metallic (BIM) sodium loop was constructed to get a clear concept of the long term carburization / decarburization behaviour of the steels in the simulated environment of the secondary circuit of PFBR. The BIM loop is designed such that it simulates the secondary circuit of PFBR with respect to sodium velocity, temperature gradient, material sequence and area ratios. In this article, we report the changes in microstructural and mechanical behaviour of AISI type 316LN stainless steel and modified 9Cr-1Mo steel after 16000 hours of sodium exposure at 798K.

Microstructures of type 316LN stainless steel and Modified 9Cr-1Mo steel are shown in Fig. 1 and Fig. 2. The matrix of the sodium exposed material had a sensitized microstructure and also exhibited a degraded layer of about 5 μm

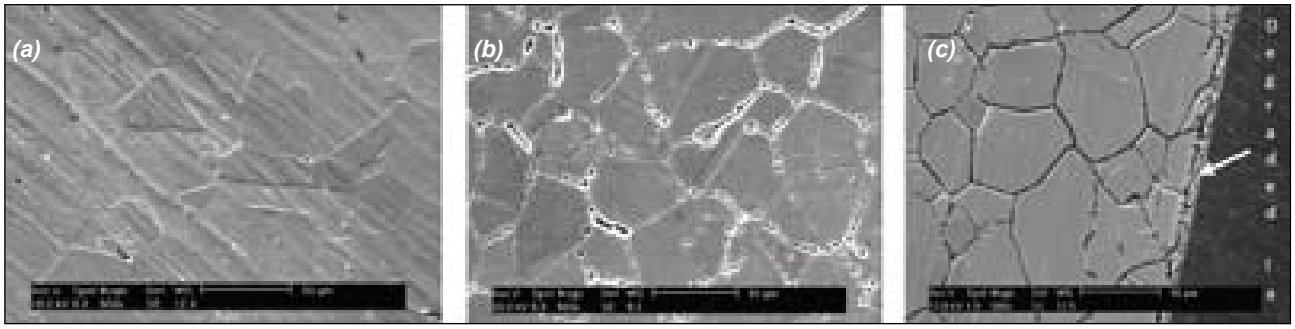

Fig. 1 *Micrographs of AISI type 316LN stainless steel (a) In the mill annealed, (b) Thermally aged and (c) Sodium exposed condition*

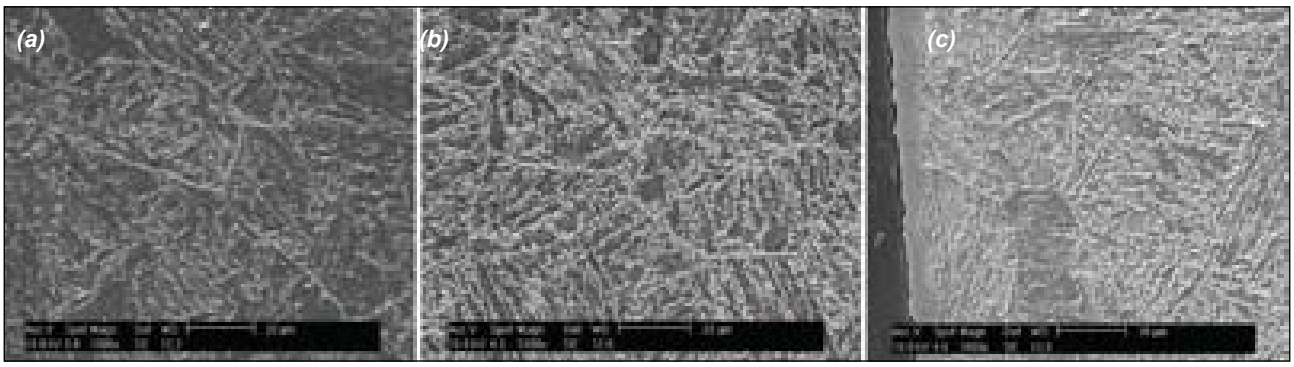

Fig. 2 *Scanning electron micrographs of Modified 9Cr-1Mo steel, (a) In the mill annealed, (b) Thermally aged and (c) Sodium exposed condition*

depth (Fig. 1c). The degraded layer was confirmed to be ferrite by GIXRD analysis. Tempered martensitic microstructure with abundant precipitates along prior austenite and martensitic lath boundaries was observed in the normalized and tempered condition (Fig. 2a). There was a slight increase in the density of carbides for the thermally aged (Fig. 2b) and sodium exposed (Fig. 2c) materials, and the tempered martensitic structure and lath morphology with prior austenite grain boundaries was retained in them. The carbides are usually Cr rich $M_{23}C_6$ and monocarbides of vanadium and niobium in the normalized and tempered state.

In the case of sodium exposed type 316LN stainless steel, the surface hardness was measured to be around 275 VHN. The hardness values decreased along the depth and reached the annealed matrix hardness (187 VHN) at around 70 µm. In the case of sodium exposed modified 9Cr-1Mo steel, an enhanced surface hardness to 259 VHN was observed which gradually reduced down to the matrix value (220 VHN) at around 70 µm. Thus, a hardened layer of 70 µm depth was measured in both the steels.

Tensile test results for type 316LN stainless steel in the mill-annealed and sodium exposed condition are given in Table 1. The yield strength (YS), ultimate tensile strength (UTS), uniform elongation (UE) and total elongation (TE) were evaluated. On sodium exposure, the YS increased by 11% and TE reduced to 34% due to carburization and thermal ageing effects. Table 2 shows that sodium exposure of modified 9Cr-1Mo steel had not caused much change in the YS and ductility of the material, while significant increase in UTS was observed. The results of the impact tests, given in Table 3, for type 316LN stainless steel and mod. 9Cr-1Mo steel indicated no significant changes in the impact energy of the sodium exposed material when compared to the mill-annealed material for type 316LN stainless steel; while normalized and tempered modified 9Cr-1Mo steel showed a decrease in impact energy on sodium exposure.

Table 1: Tensile test results of type 316LN stainless steel

Material condition	YS (MPa)	UTS (MPa)	UE (%)	TE (%)
Mill-annealed	324	627	60	66
Sodium exposed	356	657	39	43

Table 2: Tensile test results of modified 9Cr-1Mo steel

Material condition	YS (MPa)	UTS (MPa)	UE (%)	TE (%)
Mill-annealed	510	629	14	20
Sodium exposed	514	711	14	17

Table 3: Impact energy in joules for type 316LN stainless steel and modified 9Cr-1Mo steel

Material condition	316LN SS	Modified Cr-1Mo steel
Mill-annealed	144	99
Sodium exposed	136	56.5

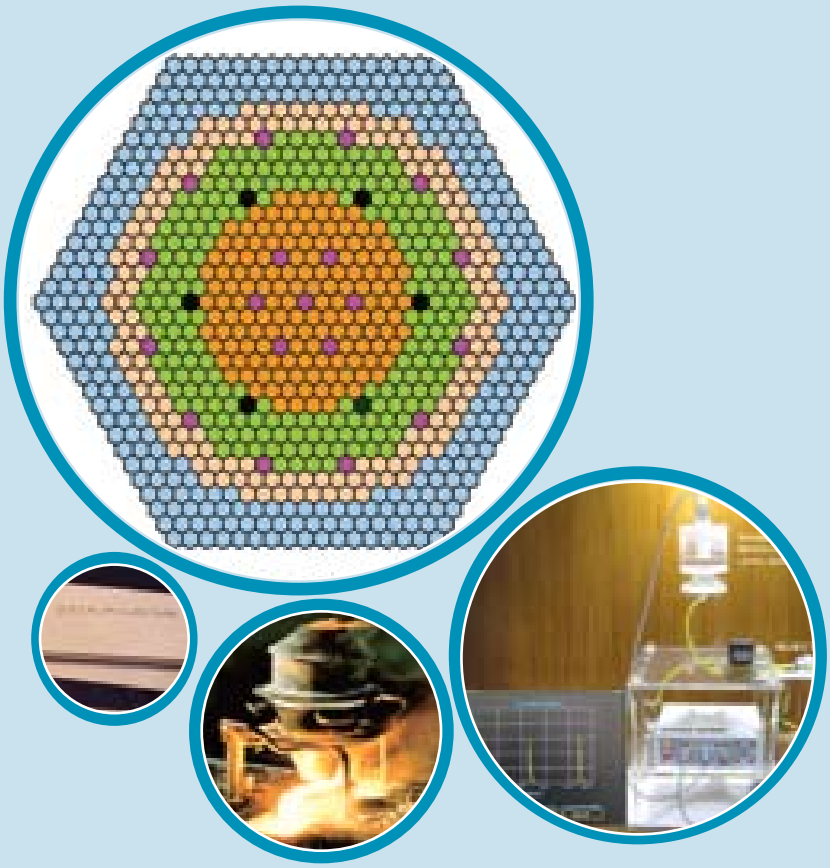

III

Research & Development for FBRs

III A Component Development & Testing

III A.1 Design Optimisation and Qualification of Large Diameter Bearing for FBRs

In PFBR, to facilitate in-vessel handling of core subassemblies, small & large rotatable plugs (SRP & LRP) and one offset transfer arm (TA) machine are provided. By a combined rotation of the plugs and TA, it is possible to access all the subassemblies located within the handling diameter. To enable the rotation of SRP and LRP, they are supported on large diameter bearings known as slewing rings. As the name suggests, these bearings are meant for slewing operation i.e., oscillatory type of movement with integral drive gear arrangement for the rotation. The bearing support arrangement is shown in Fig. 1.

Design Optimisation

Based on the physical limits, temperature difference between the raceways, large amount of axial load in comparison to radial load, small amount of moment loading, manufacturing capabilities of Indian industries, angular contact thrust bearing is selected among several options for the application. Further, considering the amount of load transmitted, case hardenable medium carbon alloy steel (42CrMo4V or AISI4140) is selected as material for bearing raceway, which is commonly used in large diameter bearings and is available as ring forgings As axial loads are predominant with minimum radial loads, higher contact angle under operation is preferred. The presence of differential temperature between the races tends to increase the contact angle and is estimated to be around 10^0-15^0. Hence, while selecting initial contact angle, the expected change due to thermal expansion should be kept in mind. Table 1 gives the final recommended values based on optimisation studies done with respect to contact angle, ball diameter & number of balls. Fig. 2 and Fig. 3 give the cross section details of SRP and LRP bearings respectively.

Table 1: Results of optimisation study towards design of large diameter bearing

Sl. No.	Parameters	SRP	LRP
1	Ball diameter (Db)	60	90
2	Number of balls	120	120
3	Mean diameter (mm)	4505	6690
4	Contact angle	60	60

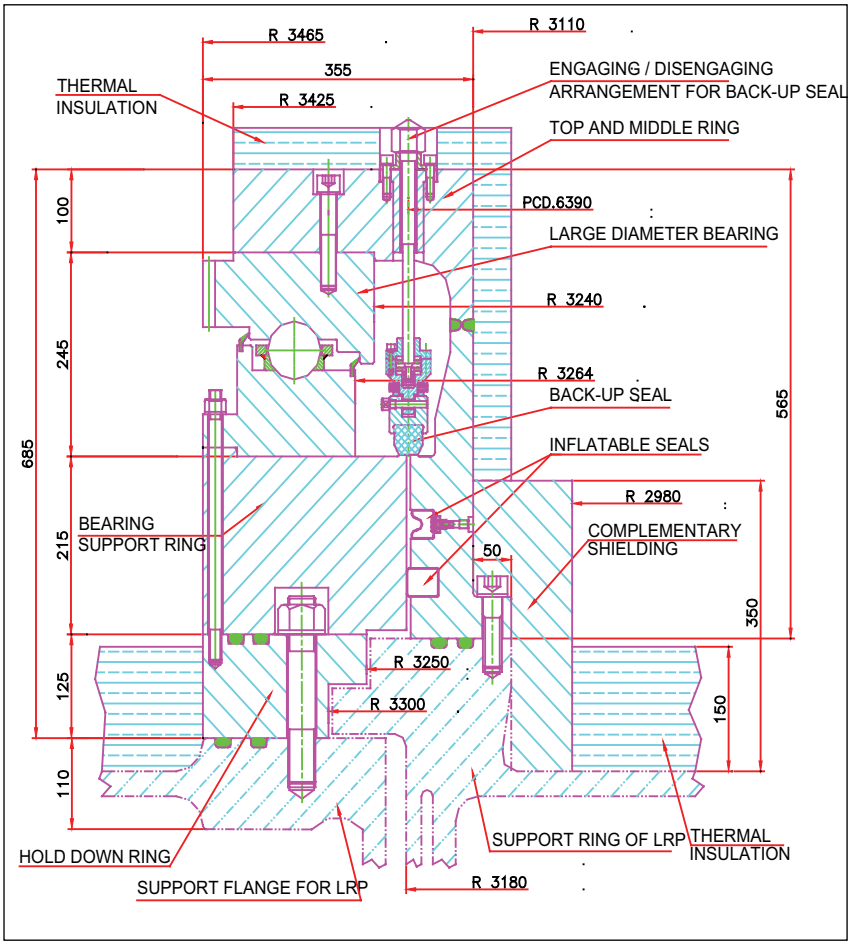

Fig. 1 *Support arrangement for bearing*

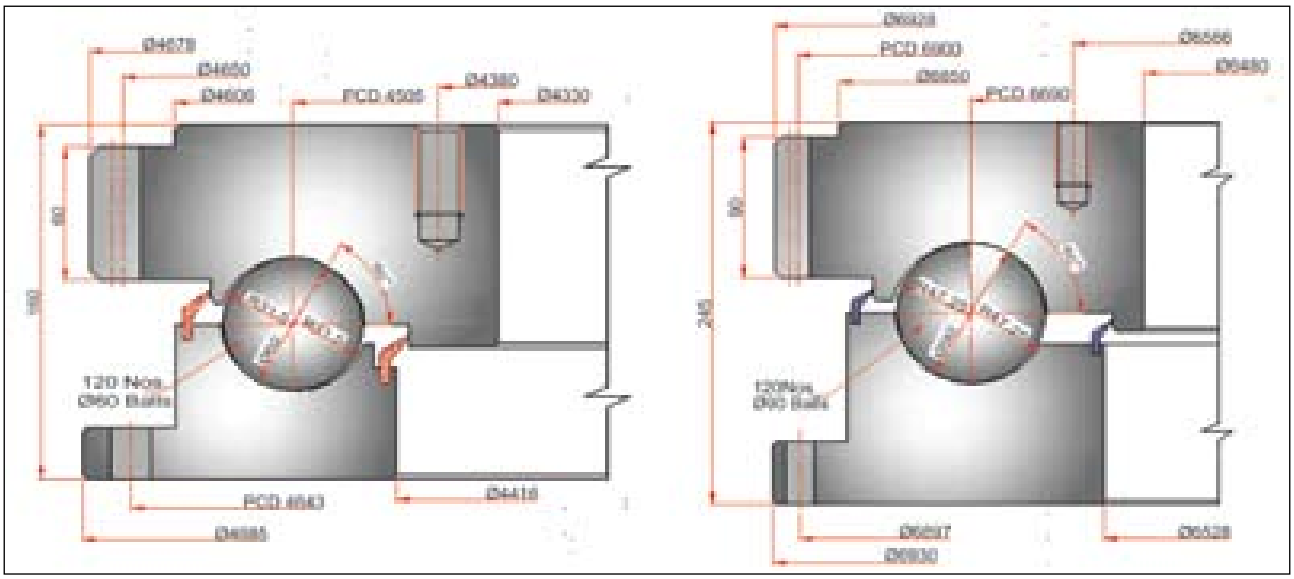

Fig. 2 *Geometrical details of large diameter bearing for SRP & LRP*

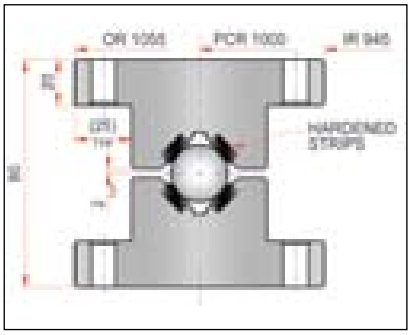

Fig. 3 *Bearing for seismic qualification*

Qualification

In order to understand the behaviour of large size bearings under seismic events, a bearing of 2 m diameter was manufactured. As the goal was to generate input data for further analysis and study, a simple 'V' shaped groove geometry was selected for this bearing. In place of hardening the surfaces, hardened strips were embedded at the contact surfaces (Fig.3). The steps followed towards seismic qualification are :

- Determination of stiffness of one typical ball along with the contact surface based on 3D non-linear contact analysis
- Integration of individual balls with the bearing assembly
- Natural frequency analysis with random variation of point of contacts
- Establishing the points of contact by comparing experimentally determined natural frequencies
- Comparing the results of seismic analysis of bearing assembly with that of experimental shake table tests

Fig. 4 shows the experimental set-up erected on shake table for testing. The bearing was loaded with lead shots and along with the load of the top structure and lead shots, the total load on bearing was 4 t. The seismic analysis of the bearing was carried out (Fig. 5a) to obtain the frequency of the bearing versus number of balls in contact (Fig. 5b). The natural frequency of 20 Hz obtained during shake table testing for the experimental bearing was plotted on this curve to obtain number of balls in contact which is found to be ~20 compared to the total

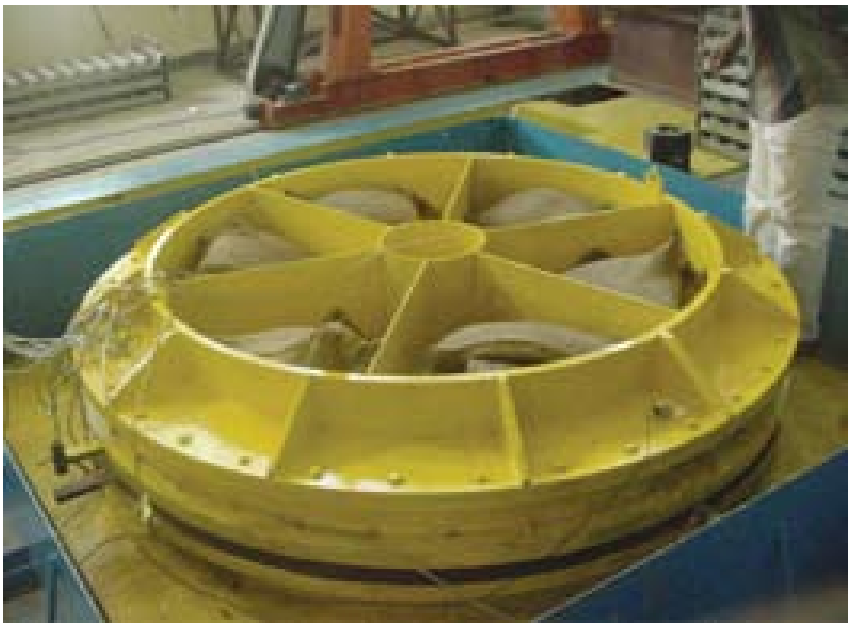

Fig. 4 *Shake table testing of model bearing*

number of 120 balls present. This clearly indicates non-uniform load distribution among bearing balls. The same was verified by opening the bearing which showed the presence of dents at few locations indicating sharing of total loads by few balls only.

The design and qualification studies performed are the important milestones towards indigenous development of large diameter bearings for the future FBRs.

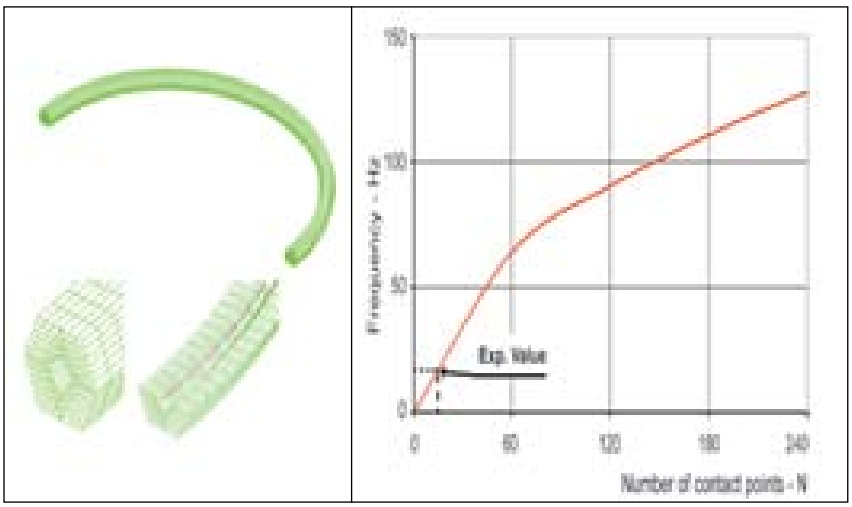

Fig. 5a *FE model of raceway*

Fig. 5b *Plot of frequency vs. No. of balls in contact*

III A.2 Fabrication of Thermal Shock Test Pot-1

Test pot-1 assembly (Fig. 1) is used as sodium storage vessel, having provision for holding electromagnet of PFBR-DSRDM and temperature sensitive magnetic switch for thermal shock testing. The overall size of the assembly is 1190 mm diameter and 3540 mm height, and are made of SS 316 / 304 materials. It consists of cylindrical shells, concentric reducer, U-type heaters, electromagnet (EM), EM guide tube, brackets, cover flange, top flange, lug support brackets, etc.

The top and bottom cylindrical shells of different diameters are joined with concentric reducer in between by welding. As the diameter of cone ratio was high, four equal segments were formed using press brake and welded. The bottom end of the test pot was covered with a torispherical dished end (600 mm ID) fabricated by progressive cold forming process, solution annealing and passivation carried out as per the specification. The cover, ring flanges of diameters 1190 mm, 37 mm thick, nozzles for connecting electro magnet and level probe for sodium level measurement were precisely machined and subjected to 100% dimensional inspection.

Fig. 1 *Fabricated thermal shock test pot*

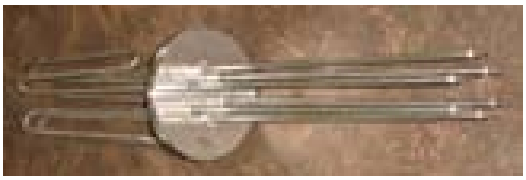

Fig. 2 *Fabricated heater subassemblies*

'U' type heaters (Fig. 2) are provided at the bottom of the shell to heat the sodium to the required temperature. Bending of SS sheathed heaters to 453 K in two different planes was a critical task and has been achieved successfully. Heater tubes were welded with heater support plate and sleeves. GTAW process was used for root / stabilizing passes and SMAW process for subsequent passes in 1 G position. Distortion control techniques were adopted to minimize distortion and achieve the geometrical tolerances within limit.

All weld joints were subjected to Liquid penetrant inspection, 100% radiographic testing and the final assembly was subjected to Pneumatic test as per SEC. VIII and found satisfactory.

III B Thermal Hydraulics

III B.1 Thermal Striping Studies in Fuel-Absorber Rod Subassembly Interface

The phenomenon of thermal striping is characterized by random temperature fluctuations in structural material, when flowing fluids at different temperatures mix in its vicinity. The mixing process is random, due to turbulence and jet instability and the resulting temperature fluctuation is also random. This random temperature cycling leads to repeated straining of the metal surface which is in contact with the fluid. This will lead to crack initiation and growth, eventually leading to the structural damage of control plug components like shroud tubes, lattice plate, skirt etc. An experiment has been carried out in SAMRAT model (1/4 scale model of PFBR primary circuit) using water as simulant to understand the mixing behaviour and to determine the extent of thermal fluctuation in the above core area of PFBR. It has been established by earlier researchers that water can be used as analogous fluid to simulate the mixing phenomena of non-isothermal sodium jets if Reynolds number (Re) and Peclet number (Pe) are sufficiently large (Re > 20,000 and Pe > 600).

In the present work, mixing in the fuel-absorber rod interface region was studied. The affected structural components of the CP are shroud tubes. These are provided to protect the absorber rod drive mechanism (ARDM) from flow induced vibration. Hot water at 343 K was sent through the fuel subassemblies (FSA) and cold water at 308 K was sent through absorber rod subassemblies (ASA). To measure the fluid thermal fluctuations, fast response thermocouples (time constant better than 15 ms) were used.

Fig. 1 shows the thermocouple locations in the shroud tubes. Tip of all thermocouples are located approximately 2 mm away from the surface to ensure that measurement is taken above the thermal boundary layer. The flow rate in FSA was monitored by annular flow meter (accuracy ≈1%) and in the ASA by glass tube rotameter (accuracy ≈2%) of suitable range. Parametric studies were carried out by varying the Re ratio between FSA and ASA keeping minimum Re as 20000. From the statistical analysis of data the mean temperature and the standard deviation as seen by each thermocouple was estimated. The temperature data are presented in a normalized form based on the

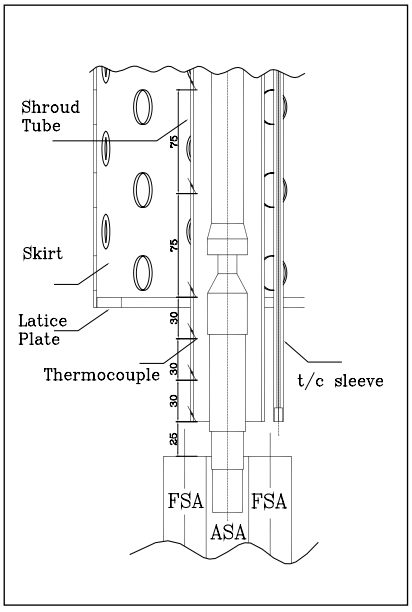

Fig. 1 *Schematic of thermocouple location*

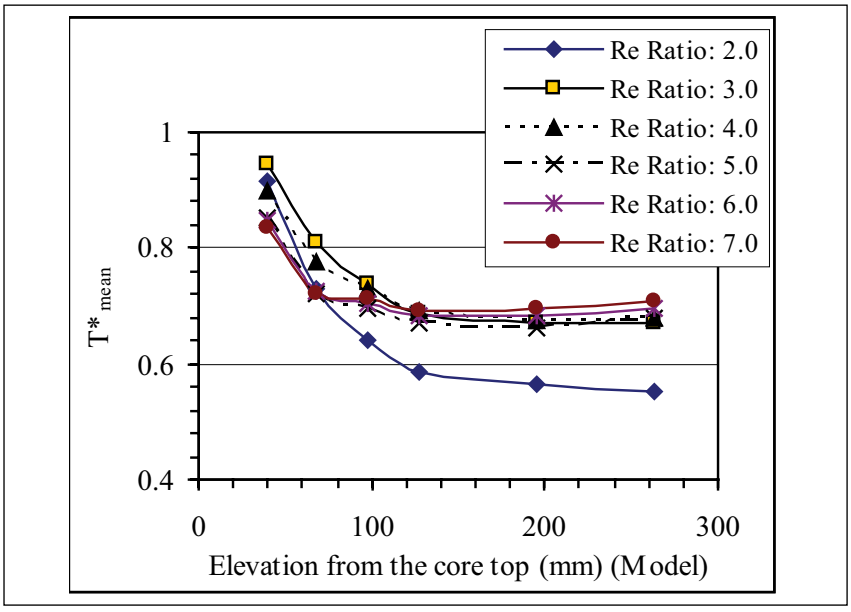

Fig. 2 *Typical variation of T^*_{mean} Vs. height*

maximum temperature difference between hot and cold jet. This normalization helped to transpose the result for reactor condition. Two parameters have been used to characterize the thermal mixing phenomena. They are T^*_{mean} (normalized mean temperature) and NSD% (normalized SD of temperature fluctuation).

Typical variation of T^*_{mean} versus height above the core top along the shroud tubes at various *Re* ratio (Re_{FSA}/Re_{ASA}) keeping Re_{ASA} = 20,000 is plotted in Fig. 2. The typical variation of maximum NSD% (as found from the various plots between NSD% vs elevation) is plotted against *Re* ratio and is shown in Fig. 3. With maximum temperature difference between hot and cold jet of 423 K in prototype and Re ratio of 1.0, the maximum fluctuation is predicted as ±298 K within 95% confidence level. Further it can be seen that the magnitude of fluctuation decreases as the *Re* ratio (or velocity ratio) increases. This is an important observation because in prototype, *Re* ratio is higher than the maximum tested *Re* ratio in the model experiment. Therefore, the maximum fluctuation is expected to be less at higher *Re* ratio. FFT analysis was carried out for all temperature signals to find out the dominant frequency and the corresponding amplitude. It is found from the FFT analysis that the dominant frequency of fluctuation ranges from 0.2 to 0.6 Hz and corresponding maximum amplitude ranges from 275 to 279 K.

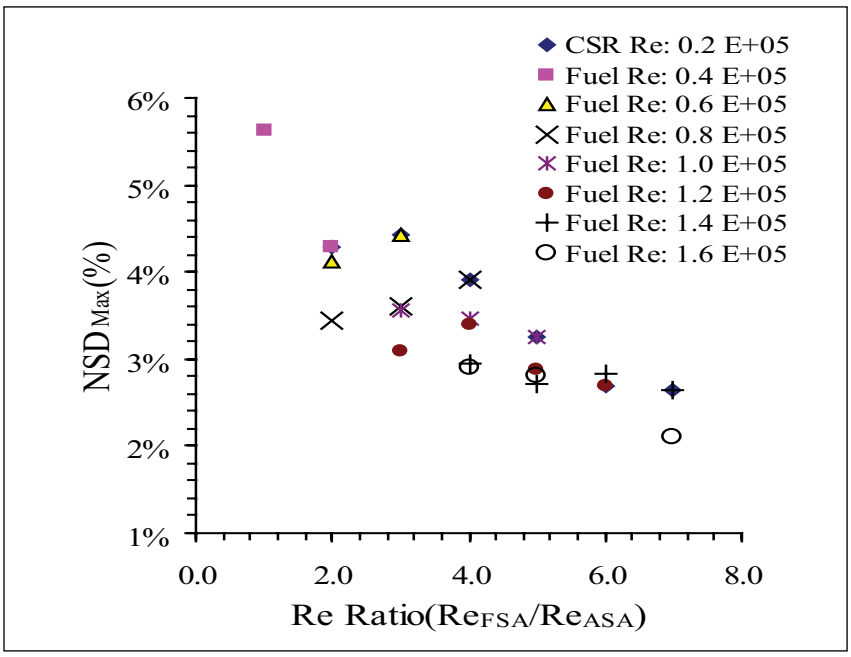

Fig. 3 *Typical variation of NSD_{max} with Re Ratio*

III B.2 Thermal Striping Limits for Future FBR Components

In almost all liquid metal cooled fast breeder reactors, designed so far, liquid sodium is used as the coolant. High boiling point of sodium implies that sodium remains in liquid state up to a temperature of 1175 K at atmospheric pressure and excellent heat transfer characteristics bring many advantages for the sodium as coolant. Higher boiling point permits high operating temperature for the reactor, still ensuring sufficiently high margin to avoid boiling of the coolant under all the design basis events. Sodium remains in liquid state during operating conditions without calling for any pressurization and hence design pressure for components is nearly atmospheric, in turn requiring lower wall thickness for structures. The excellent heat transfer properties provide high natural heat removal capability, particularly in the pool type concept. While pool type concept has many distinct advantages from the point of view of safety, there are certain critical structural mechanics issues, especially with the austenitic stainless steels (ASS), commonly used structural materials in view of its excellent compatibility with sodium and high strength at elevated temperatures. In the pool type concept, both hot sodium pool which is about 820 K and cold pool at about 670 K co-exist, which imposes high ΔT (150 K-maximum) in sodium in the narrow transition regions of hot and cold pools, during operating as well as transient conditions.

This is termed as 'thermal stratification'. With the ASS as structural material which has low thermal conductivity and high coefficient of thermal expansion and the sodium with its inherently high heat transfer coefficient, the adjoining structural wall surface is subjected to high ΔT, created in sodium without any significant film drop and time delay. This causes high thermal stress range ($\Delta\sigma$) in the structural wall. Further concern of thermal stratification is steady oscillations, relatively at lower frequencies (< 1 Hz), which is one of the sources of high cycle thermal fatigue damage for the metal wall. Apart from this mechanism, high thermal fatigue cycles are caused by a special phenomenon called 'thermal striping'. Thermal striping is a complex thermal hydraulics phenomenon, which generates random fast temperature fluctuations, originating from the incomplete mixing of hot and cold jets of fluid, sodium in the present context, in the vicinity of adjoining structural wall surface (Fig. 1). The range of frequency of oscillations under thermal striping is reported as 1-10 Hz. Thermal striping occurs at a few locations in the hot and cold sodium pools in the reactor assembly, predominantly on the core cover plate of control plug and at mixing 'Tee' junctions in the secondary sodium pipelines. It is worth mentioning that apart from thermal striping, oscillations of thermal stratification layers and sodium free level do cause temperature fluctuations in certain locations in the sodium pools. Fig. 2 shows a few potential areas of level fluctuation, thermal stratifications and thermal striping.

Rigorous design rules have been established to define thermal striping limits reflecting the latest creep-fatigue design criteria, based on the analytical solutions for the representative plate geometries, of uniform wall thickness 'δ', having a part through wall crack size *'a'*, and subjected to random surface temperature history (PSD has a constant value up to 10 Hz and zero beyond 10 Hz) with the peak value ΔT_{max}. The plate has accumulated fatigue and creep damage values due to normal and design basis thermal transients. With these idealizations, the temperature, stress components and stress intensity values are derived analytically with the objective of determining permissible temperature range (ΔT_p) as a function of D_{eff}.

An important aspect which has been brought out is the attenuation of sodium temperature on the metal wall surface as a function of frequencies in Fig.3. It is seen that, in the case of constant temperature on the wall surface (frequency = 0), the stress is constant across the thickness. When the frequency increases from 0 to 1 Hz, the stress decays rapidly across the thickness, till 1 Hz, beyond which, the decay is smaller and it reaches nearly saturation at the frequency of about 10 Hz. Hence at higher frequencies, the stresses are concentrated in the vicinity of surface without significant penetration, implying that thermal striping can only initiate cracks and does not have potential to cause growth. However, once cracks are initiated by high cycle fatigue cycles (accumulate quickly within a few years), other major load cycles causing creep-fatigue damage can cause propagation and ultimate rupture.

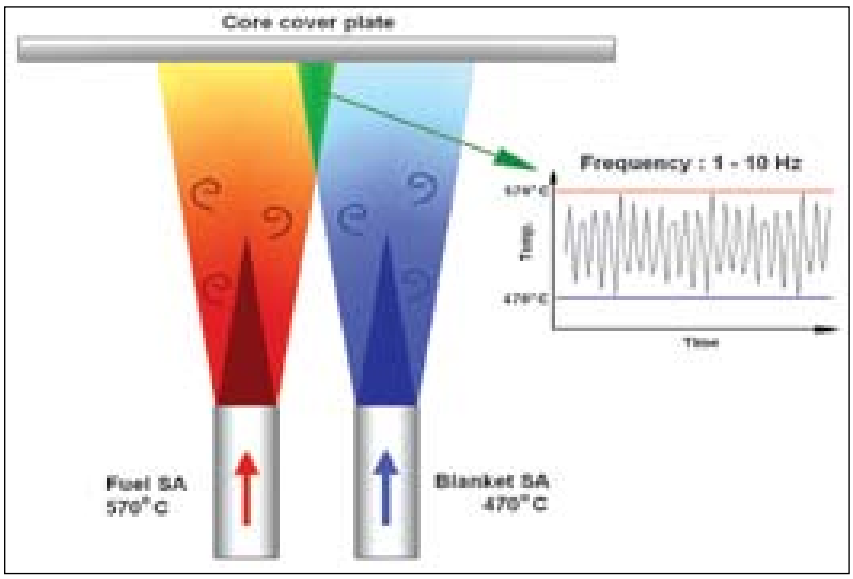

Fig. 1 *Thermal striping phenomenon in the vicinity of core cover plate in FBR*

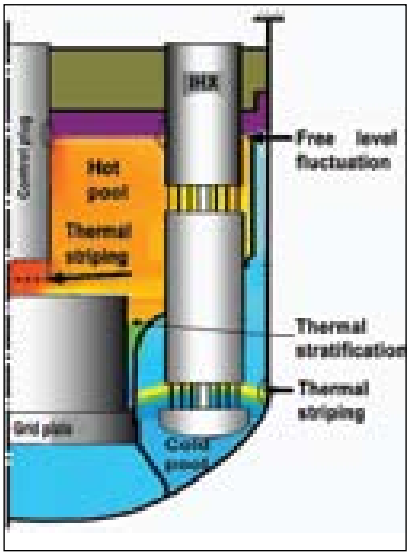

Fig.2 *Thermal striping, thermal stratification and level fluctuations in FBR*

Subsequently, permissible thermal striping limits (ΔT_p) are derived as a function of accumulated creep-fatigue damage based on random analysis approach where the power spectral density of temperature fluctuation in sodium is used as input. By this, the effects of the frequencies up to 10 Hz are accounted systematically. For quantifying the effects of attenuation, two cases are analysed: (1) there is no thermal attenuation on the surface wall temperature ($h \rightarrow \infty$) and (2) there is thermal attenuation depending upon the frequency (h = 40,000 W/m^2/K). The results are shown in Fig. 4. It is noted that the ΔT_p reduces significantly with the increase of creep-fatigue damage: 39 to 26 K under the assumption of no attenuation and 75 to 46 K with attenuation. This also indicates that the effect of attenuation due to high frequency components of temperature spectrum is very significant.

The recommended limits are assessed based on international experiences of test loops and large size reactors, which are compiled in Table 1. The values are extrapolated for prototype situations.

Table 1: Operating experiences

Reactor/facility	Geometry	ΔT – K	No. cycles
Operating reactors			
PHENIX	Expansion tank	170	5.50×10^6
PHENIX	Mixing tee	90	3.24×10^8
SPX	Mixing tee	220	1.44×10^4
BN 600	Cold trap	160	2.20×10^7
International test facilities			
FAENA	Cylindrical tube 1	378	1.60×10^4
	Cylindrical tube 2	192	1.05×10^6
SUPERSOMITE	Cylindrical tube 1	210	3.60×10^6
	Cylindrical tube 2	180	3.60×10^7

The corresponding extrapolated values are: 68, 63 and 144 K based on Phenix, FAENA, SUPERSOMITE data respectively. It is worth mentioning that at all the failure locations in the operating reactors, creep-fatigue damages due to major cycles were present. Hence, the extrapolated values are on lower side (63 K). For SUPERSOMITE, failure has been detected after certain crack propagation and hence it yields a higher value (144 K). This exercise provides good confidence on the thermal striping limits arrived.

Based on the above, the permissible limits considering thermal attenuation are less pessimistic and are recommended for the future FBRs, which are designed for long design life (60 y) and with high capacity factor (85%). As per this, at the location such as core cover plate where the accumulated creep damage is insignificant and fatigue damage is small (< 0.1), ΔT_p can be 70 K. At the control plug lower portion where the D_{eff} is < 0.3, ΔT_p can be 62 K and at the main vessel near IHX outlet, where D_{eff} is < 0.5, ΔT_p can be 55 K. Further, minimum ΔT_p of 45 K can be acceptable at any location (e.g. typical tee in hot secondary sodium pipeline) where the creep-fatigue damage can be as high as 0.9.

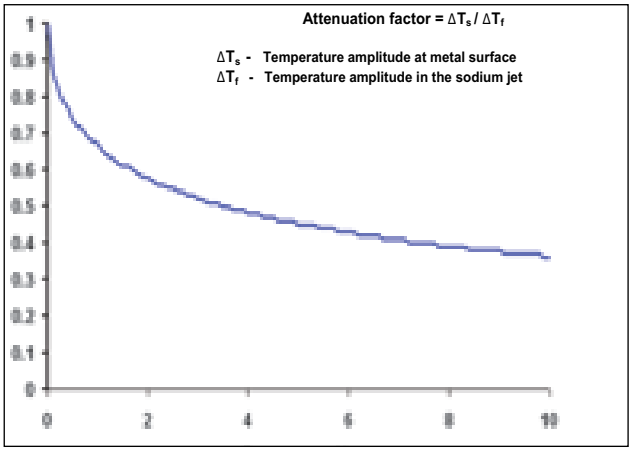

Fig. 3 Attenuation of thermal striping temperature on the metal wall surface (Attenuation factor = $\Delta T_s / \Delta T_f$)

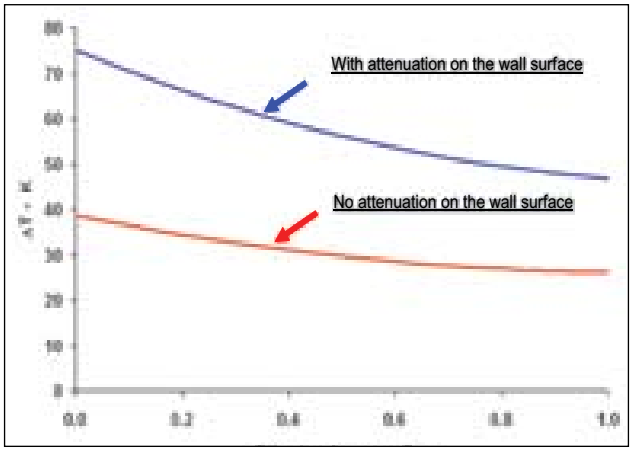

Fig. 4 Permissible thermal stripping limits for the FBR structures, made of SS 316 LN

III C Inspection Techniques

III C.1 Time of Flight Diffraction Technique for Evaluation of Austenitic Stainless Steel Weldments at Elevated Temperatures

Ultrasonic examination is a mandatory requirement during In-Service-Inspection (ISI) of the welds in the main and safety vessel of PFBR. Presently, conventional ultrasonic techniques have been proposed for this . Two of the main challenges likely to be encountered during inspection is the high temperature of the vessels (around 423 - 473 K during shut down) and the background radiation. Ultrasonic time of flight diffraction (TOFD) technique is now a well established technique and codes of practice such as ASME, recommend it for regular inspection of thick weldments (>12.5 mm). It is applicable for both pre-service and in-service inspection. Two main advantages of TOFD compared to conventional ultrasonic techniques are (a) TOFD can characterize the dimensions of linear defects with better accuracy compared to conventional UT and (b) The entire weld can be scanned in a single pass with great reliability and within very short times. The above mentioned points are highly relevant especially in the context of ISI. The second advantage is particularly attractive since the probes and electronics would be exposed to the effects of radiation and high temperatures for lesser periods of time. In view of this, it was decided to explore the feasibility of application of TOFD for the examination of such welds. The temperatures likely to be encountered during ISI would be of the order of 423 K – 473 K. One of the main problems during ultrasonic examination at high temperatures is the decrease in the signal to noise ratio resulting in poor sensitivity. A survey of literature indicated that while TOFD has been extensively applied for thick carbon steel weldments at ambient temperatures, its application for evaluation of stainless steel weldments especially at high temperatures is sparse. Compared to carbon steel, examination of stainless steel is more complicated due to the anisotropic nature of the material and the weldment.

Systematic work was undertaken at our Centre to evaluate the feasibility for application of TOFD for evaluation of thick austenitic stainless steel weldments with temperatures upto 473 K and also ascertain the possible errors likely in quantitative defect characterisation at these temperatures. Austenitic stainless steel weld pads of thickness 25 mm and with defects such as lack of penetration and slag inclusions were used for experimentation. A hot plate with provisions to vary the current using a variac setup was used for heating the weld pads. The temperature distribution on the steel plate surface especially in the weld region could be maintained within ± 4 K during the scanning by adjusting the variac. Special probe holder and scanning arrangement was designed and developed for this study (Fig.1). High temperature 45° longitudinal wave probes were used along with high temperature couplant and cable. Initial calibration was carried out using a reference specimen of thickness 30mm

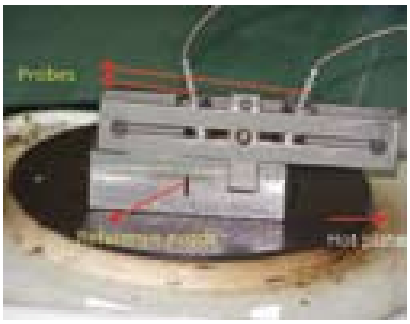

Fig. 1 *Set up for a reference specimen with a side notch*

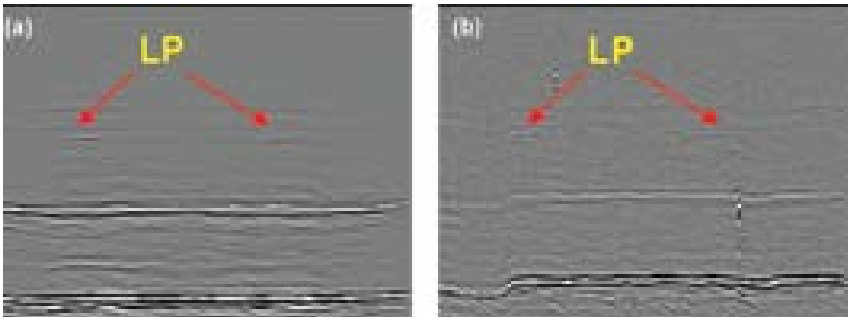

Fig. 2 *Lack of penetration detected by TOFD at constant gain at a temperature of (a) 298 K and (b) 423 K. Note increased noise in image (b)*

with a side notch of dimension 10 mm×10 mm×1 mm.

Analysis of the TOFD images (Fig. 2) revealed that the peak amplitude of the diffracted signal decreases as the object temperature increases. The decrease in signal amplitude could be attributed to increased attenuation and also increased scattering with increase in temperature. Scattering is the most important cause of decreased signal amplitude at higher temperatures. As the temperature increases, the inter atomic vibrations increases and this would produce large amount of scattering. Scattering is also the sum of several effects like reflection, refraction and mode conversion, which depends on the frequency and polarization of the vibrations, the grain size and degree of anisotropy of the grain. An increase in elastic anisotropy (this can be achieved by increase in temperature) also causes an increase in scattering. An additional gain was necessary to compensate for the decreased signal amplitude. In the case of reference specimen, the increase in gain varied linearly with temperature while for welds it was non linear. For the case of welds, this increase in gain with temperature could be described by the constitutive relation

$$\Delta g = aT^2 + bT + c$$

The non linear variation in case of welds could be explained by the fact that the weld has a different grain structure compared to the parent material and the anisotropy in the weld region especially in the case of stainless steel is much more pronounced compared to the base material.

An important requirement of ISI is dimensional measurement of defects. A study was made to estimate the error in defect dimension measurement at higher temperatures by comparison with actual physical dimensions in the case of reference notch (length and width obtained through microscopy) and radiographic images in the case of slag and Lack of penetration (Fig. 3). The errors in the defect dimensional measurement were observed to be less than 5%. The 200 mm long weldment could be scanned by

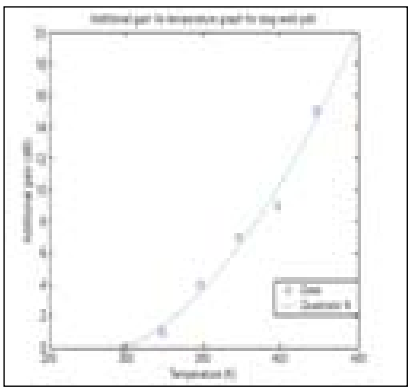

Fig. 3 *Additional gain required at different temperature for welds with slag inclusion*

TOFD within 10 secs after initial setup while in the case of pulse echo technique the scanning could be completed only in one hundred and twenty seconds. Thus, to scan a weld of length about 3 m in the main vessel or safety vessel, TOFD would require about three minutes while pulse echo techniques would require about thirty minutes.

Overall the study clearly established that TOFD is better suited for in-service inspection of stainless steel weldments at high temperatures due to its better defect characterisation capabilities and also faster scanning times compared to pulse echo techniques.

III C.2 Non-destructive Detection of Magnetic Flux Leakage from Sub-surface Defects in Steel Plates using Giant Magneto-resistive Sensor

Magnetic flux leakage (MFL) technique is widely used for non-destructive evaluation of ferromagnetic steels. In this technique, the object is magnetized and the magnetic flux that leaks out of defects is detected using magnetic field sensors such as Hall sensor. In comparison to Hall sensors, Giant magneto-resistive (GMR) sensors are attractive, as they offer high sensitivity for low magnetic fields, good signal-to-noise ratio (SNR), room temperature operation and high spatial resolution. The GMR sensor has been used for detection of leakage magnetic fields from sub-surface and deeply located defects in carbon steel plates.

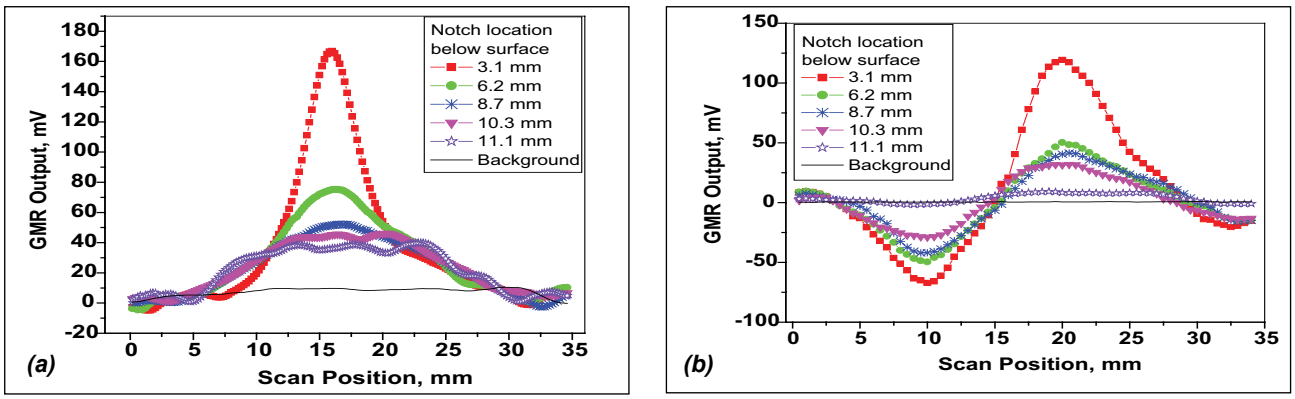

Fig. 1 *GMR sensor response for subsurface notches in 12 mm thick carbon steel plates*
(a) *Tangential component* ***(b)*** *Normal component*

The GMR sensor consists of a few nanometer thick multilayer structures such as Fe/Cr/Fe and Co/Cu/Co, in which ferromagnetic layers are separated by a nanometer thick non-magnetic layer (Cr or Cu). It works based on the GMR effect in which there is a large change in electrical resistance of the multilayer, exposed to an incident magnetic field, due to the spin dependent scattering of electrons at interfaces between ferromagnetic films and nonmagnetic interlayer.

In typical GMR sensor, four GMR resistors are configured in the form of a Wheatstone bridge to measure the differential output to enhance sensitivity and cancel noise. The sensitivity of the GMR sensor is found to be 260 VT^{-1} at 5V biasing voltage. The GMR sensor exhibits linear response within the range of 0.2 to 1.3 mT.

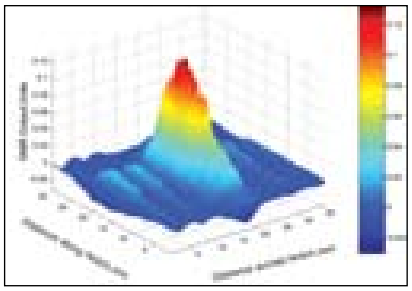

Fig. 2 *Magnetic flux leakage image (tangential component) of a subsurface notch located at 6.2 mm below the surface in a 12 mm thick carbon steel plate.*

An in-house developed MFL testing set-up consisting of a C-core electromagnetic yoke, GMR sensor, carbon steel plate with defects, X-Y scanner, amplifier and personal computer has been used. The specimens used in this study are five carbon steel plates of dimensions 450x150x12 mm^3, each having EDM notches (15 mm length, 1 mm width) of 3.1, 6.2, 8.7, 10.3 and 11.1 mm depths. Finite element modeling has been carried out to optimize the spacing between the legs of the yoke and the GMR sensor position. Keeping the yoke centered over the notches, the tangential (along the measurement surface) and normal (perpendicular to the measurement surface) components of the leakage, magnetic flux are measured at discrete points by scanning the GMR sensor across the notches. The sensor output is amplified, digitized and stored in computer for further analysis.

The tangential and normal components of the leakage magnetic field for sub-surface notches located at different depths below the surface in 12 mm thick steel plates are shown in Fig. 1. As can be seen, unique Gaussian type signals and dipolar type signals have been observed for tangential and normal components of leakage magnetic fields, respectively. The GMR sensor could reliably detect the sub-surface notch located at 11.1 mm (depth 0.9 mm) below the surface. The reduced detectability by the normal component of leakage field is due to higher lift-off (0.8 mm) of the GMR sensor as compared to tangential component measurements carried out at a lift-off of 0.3 mm. Both the tangential and the normal components of the GMR sensor output are found to decrease with increase in the notch location below the surface due to the divergence effect.

MFL images of notches are obtained by scanning the GMR sensor in a raster manner**.** Fig. 2 shows the MFL image of a sub-surface notch located at 6.2 mm below the scanning surface in the plate. The MFL image readily provides the spatial extent of the notch. In order to enhance the images, Eigen value based approach has been developed and a significant increase in SNR has been observed.

This study revealed that GMR sensors can be effectively utilized for detection of feeble leakage magnetic fields from sub-surface and deeply buried defects in ferromagnetic steel materials.

III C.3 Lock-in Thermography for Characterisation of Colmonoy Coatings

Hard facing alloys like Colmonoy are overlaid on nuclear components to provide corrosion, wear and galling resistance under high temperature service conditions. Gas tungsten arc welding (GTAW) and plasma transfer arc (PTA) processes are used to deposit these alloys, at various locations on the components. Typical reactor components on which overlays are provided include the grid plate, diverse safety rod drive mechanism etc. The thickness of the overlay ranges from 0.5 to 3 mm. Defects likely during the process of deposition include lack of bonding between the substrate and overlay, cracks and porosities. Conventionally ultrasonic normal beam technique, liquid penetrant examination and radiography (depending on the nature of coating) have been used for the process qualification and on the actual components. This experimental work explores the feasibility of using an advanced NDE technique - Lock in thermography, for the detection of defects especially lack of bonding which is more serious and not permitted.

Thermography or thermal imaging is an advanced non-destructive test method based on the detection of infrared radiation emitted by the object. The technique is an indispensable tool for predicitive condition management in industries and also finds extensive applications in a variety of fields such as materials science, energy management, civil engineering, quality assurance etc. Lock-in thermography is an advanced active thermography technique that uses a continuous sinusoidal heat wave rather than a pulsed heat source. The object is illuminated by a harmonically modulated (sinusoidal) heat source. The absorbed heat generates a thermal wave at the surface of the object, which propagates inside and gets reflected from interfaces where the physical heat propagation parameters are changing (e.g. at voids or delaminations). The interference of incoming and reflected waves leads to a harmonic oscillating radiation pattern on the object surface, which is detected by the infrared camera. By analysing the phase and amplitude lock in images, one can clearly differentiate between the good and defective regions. The main advantage of lock in thermography compared to other active thermography techniques is that problems due to emissivity and non-uniform heating are minimized.

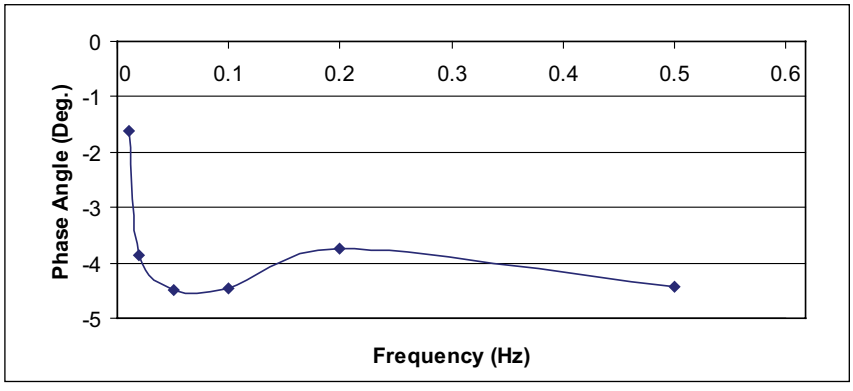

Fig. 1 *Variation of phase angle as a function of frequency*

Colmonoy overlays laid using Plasma Transfer Arc (PTA) welding on AISI 316 LN substrate with thickness varying from 2 mm - 3 mm were used for the studies. For purposes of initial calibration, a 5% notch, 2 mm φ flat bottom hole and 2 mm φ side drilled hole was used. A Silver- 420 system with pulsed and lock in thermography was used for the study. Success of lock in thermography depends on the frequency of excitation. Fig.1 is the plot of variation of phase angle with frequency in case of reference specimen. A sinusoidal signal was used and the frequency of modulation varied from 0.01 - 0.5 Hz. Based on these studies the optimum frequency of the excitation was determined.

The lock-in images on the actual samples were acquired at a frame rate of 50 Hz and the integration time was 1600 µs. The phase and the amplitude images were analysed. The amplitude image clearly revealed the notch and flat bottom hole in the reference specimen. Apart from these, all the surface variations manifested making interpretation difficult. The phase image on the other hand revealed not only the notch and the hole but also a debonded region (Fig. 2). The phase angle value at the notch and debonded region

was measured and observed to be almost same (-81.47 and -81.57° respectively). Compared to a good region, the phase angle value in the debonded region had a large difference of about 41.25°. Through appropriate image processing techniques, the extent of debonded region was also quantitatively determined.

For validation of the results obtained using lock-in thermography the specimen was also subjected to ultrasonics and radiography. The area predicted by ultrasonic technique matched well with the dimensions predicted by lock in thermography (within <3%)(Fig. 3).

Experiments clearly revealed that lock in thermography is a very sensitive and reliable technique for the detection of debonds in colmonoy overlays. The main advantage as compared to other active thermal imaging techniques is that emissivity and surface variations do not manifest and the phase angle variation is a clear indicator of the defective regions. Compared to other NDE methods such as ultrasonics, the main advantage of lock-in thermal imaging is that it is a whole field technique and an entire area can be covered in a single step. Further, it is quantitative, gives a visual image that can be evaluated and the nature size of the defects can be more accurately determined and it can be applied on the field.

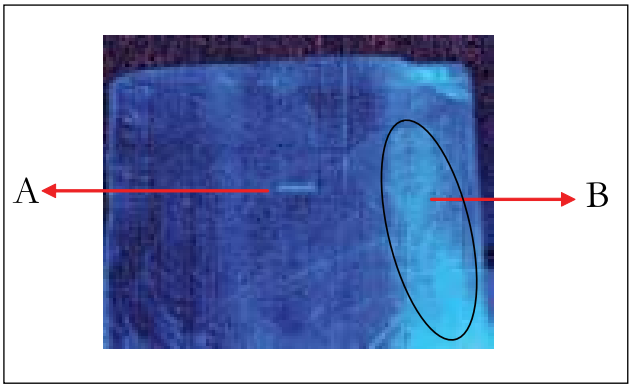

Fig. 2 *Phase thermal image. Apart from the notch, the debonded region indicated by the ellipse can be clearly seen. A = 5% Notch; B = Debonding.*

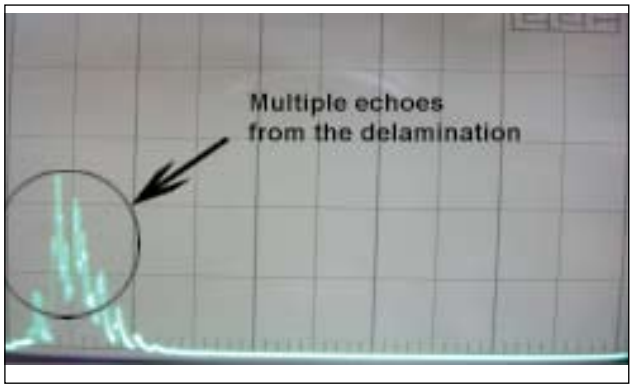

Fig. 3 *Ultrasonic (pulse echo) indication of debonded region.*

III C.4 Neutron Radiography as a Quality Control Tool for Pyro Devices of Chandrayaan-1

Neutron radiography is a valuable Non-destructive testing (NDT) tool, complementary to X-radiography, with unique ability to image low density hydrogenous materials embedded in high density materials. It takes advantage of the difference in the attenuation behavior of neutrons, which is primarily controlled by the nuclear properties of the interacting medium.

Neutron radiography was carried out using the KAMINI neutron source facility located at our Centre. The radiography facilities at Kamini consist of three beam ports with a high degree of neutron collimation. The facility has also adjustable aperture control device, beam shutters, radiographic rig and cassette drive mechanism. The cross-sectional view of the radiographic facility is given in Fig. 1. The neutron radiographic facility at Kamini has the capability to carry out neutron radiographic inspection of highly irradiated fuel materials from (FBTR) and non-radioactive components from Defence and Aerospace departments.

In a space launch, hundreds of pyro devices are used in the launch vehicle as well as in the satellites. Pyro devices are basically pyro-chemical based mechanical devices, which contain a small amount of explosive mixture inside thick metal casing, and are extensively used in all the stages starting from ignition of the strap-

on motors up to positioning of the satellite in the required orbit. Pyro devices are also used to shear, very thick fasteners to sever burnt out stages and for jettisoning the heat shields from the launch vehicle after it has cleared the dense atmosphere. In the satellite, pyro devices are used to deploy solar panels, antennas and for parking the satellite in the desired orbit. Pyro devices are also required for de-orbiting a spacecraft to bring it back to the earth. Hence, their reliability is highly critical for the success of any space mission. Neutron radiographic inspection of pyro devices are carried out to ensure the presence of explosives, continuity and uniform charge density and presence of "O" rings inside the sealed metal casings of the devices, to ensure cent percent reliability.

Neutron radiography examination of pyro devices used in the Indian Space Programme for launching PSLV and GSLV rockets are being carried out at Kamini. The pyro devices are pre-loaded in front of the neutron beam tube of reactor, at the radiography site on a remotely operated stepper motor driven cassette drive mechanism, which can carry many pyro devices at a time. Most of the components are radiographed at a reactor power of 15 kW(T) and a flux of 10^6 n/cm^2/s at the radiography site. Due to the excessive primary γ-rays originating from the reactor core, the indirect / transfer method using dysprosium metal foils was adopted for imaging of pyro devices using neutrons. The transmitted neutrons from the object activates the converter screen by (n,γ) reaction producing a latent image of the object radiographed. After exposure, the activated dysprosium converter screens are removed from the cassette drive mechanism and then kept in contact with X-ray films to transfer the image and obtain the radiograph. The dysprosium converter screen has a half life of about one hundred and forty minutes and hence the converter screens are kept in contact with the X-ray film for about twelve hours. The exposed films are then developed as per normal procedure to produce a permanent record. Fig. 2 shows photograph of an array of pyro device and a typical neutron radiograph.

In the recent launch of PSLV-C11 rocket, for Chandrayaan-1 space craft, one of the payloads was a moon impact probe (MIP) intended to make a landing on the moon. MIP pyro thruster and MIP cartridges were qualified for Chandrayaan-1 mission using Kamini neutron radiographic facility, in addition to other pyro devices used in the launch vehicles and space craft. The pyro thrusters were used in the Chandrayaan-1 space craft to transfer the space craft from the earth's gravitational orbit to the lunar orbit. The MIP cartridges were used for de-orbiting the MIP from the Chandrayaan space craft. The cartridges were used to spin/de-spin the MIP so as to land it perfectly on the lunar surface. The cartridges that were handled and tested at Kamini are now resting in the lunar soil. The contribution of neutron radiography in the quality control of the pyro devices has ensured the successful placement of our tricolour on the moon.

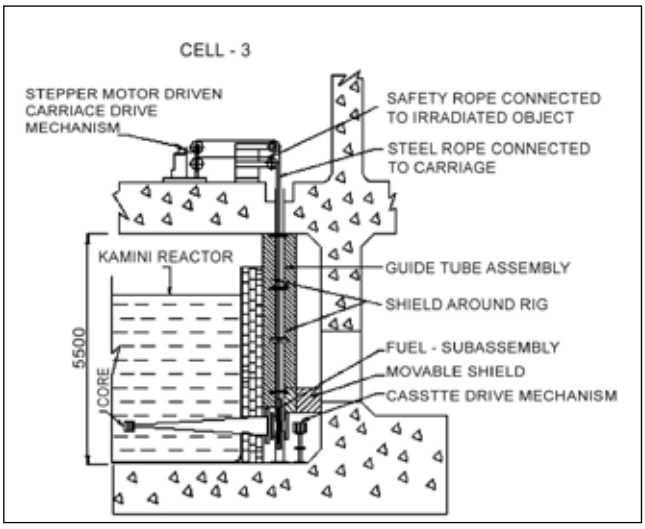

Fig. 1 *Cross-sectional view of the neutron radiography facility at RML*

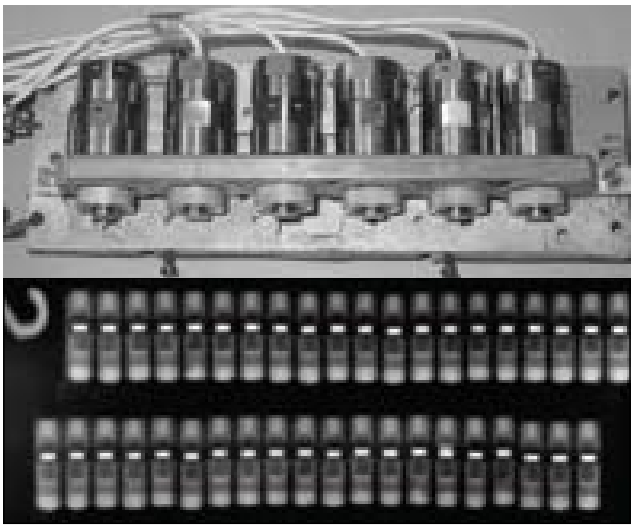

Fig. 2 *Array of critical component cleared by neutron radiography for use in the Chandrayaan mission and a typical neutron radiograph of a pyro device*

III C.5 3D Finite Element Modeling of Remote Field Eddy Current Testing for Detection of Localized Defects in PFBR Steam Generator Tubes

Remote field eddy current (RFEC) technique has been developed for in-service inspection of modified 9Cr-1Mo ferritic-martensitic steam generator (SG) tubes. The RFEC probe consists of circumferentially wound exciter and receiver coils which are axially separated by two to three tube diameters. The electromagnetic fields from the exciter coil travel through the tube wall in the axial direction and enter back at about two to three tube diameters to be picked up by the receiver coil. The amplitude and phase of the induced voltage in the receiver coil enable the assessment of the condition of the tube wall. The circumferential receiver coil exhibits limited sensitivity for detection of localized defects. In this regard, miniaturized receiver coils are attractive. In this study, 3D finite element modeling has been carried out for design and development of radial array and axial array types of receiver coils. RFEC signals for through hole and flat bottom holes (FBH) have been predicted and performance of receiver coils have been compared.

The 3D finite element model employed for simulation of RFEC phenomenon in modified 9Cr-1Mo steel SG tubes, has been developed in-house. This model is based on the A-V formulation (magnetic vector potential (A) and electric scalar potential (V)). Eight noded hexahedral 3D finite elements with linear shape function have been used in this model. An optimized mesh for the RFEC geometry consisting of SG tube with defect and exciter coil has been employed after systematic trials. Quasi-minimal residue (QMR) iterative solver has been used to solve the global matrix to obtain the scalar and vector potentials at the nodal points of the mesh. A preconditioning technique based on incomplete lower-upper (LU) decomposition scheme, has been used to approximate the solution matrix (prior to QMR) to minimize the computational time and resources.

The SG tube having a through hole (1.5 mm diameter), 60% and 20% wall loss FBH (1.5 mm diameter) has been modeled. RFEC signals have been predicted for radial array and axial array type receiver coils at each angular position along the circumferential direction inside the tube, as shown in Fig. 1. The computed signal peak amplitude and phase difference relative to the baseline for through hole, 60% FBH and 20% FBH for axial and radial coils are given in Table I. It can be observed from Table I that the detection sensitivity of radial coil is better than that of the axial coil. This enhanced detection

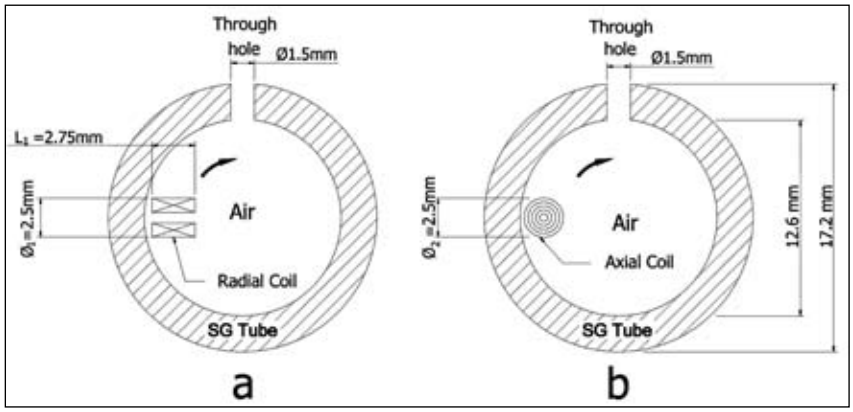

Fig. 1 *Cross-sectional view of receiver coils in SG tube having a localized through hole*

Table I: Comparison of performance of axial and radial type receiver coils

Defect type	Axial receiver coil		Radial receiver coil	
	Peak amplitude (µvolts)	Phase difference (degrees)	Peak amplitude (µvolts)	Phase difference (degrees)
Through hole	31	10	154	136
60% FBH	13	1.7	28	43
20% FBH	4	0.25	5	7

sensitivity of radial coil is attributed to larger radial leakage fields entering from the tube wall by the presence of localized defect. The model predictions have been experimentally validated for the case of 1.5 mm diameter hole and the deviation has been found to be less than 20%.

A unique two-peak behavior has been observed in the amplitude signal of the radial coil for the through hole, as shown in Fig. 2. This has been attributed to the large perturbations in the magnetic field due to the presence of hole which extends over a conical region and spreads in both axial and radial directions inside the tube without any change in the direction. The variation in the radial component of this magnetic flux density extends even beyond the central axis of the tube starting from the inner surface of the tube below the hole. The two-peak amplitude is an unique feature of hole type defects and can be used advantageously for reliable detection of holes and other leak paths in SG tubes. However, for sizing localized defects, phase lag information would be used. Utilizing the predictions, design and development of a radial type eight array receiver probe is underway.

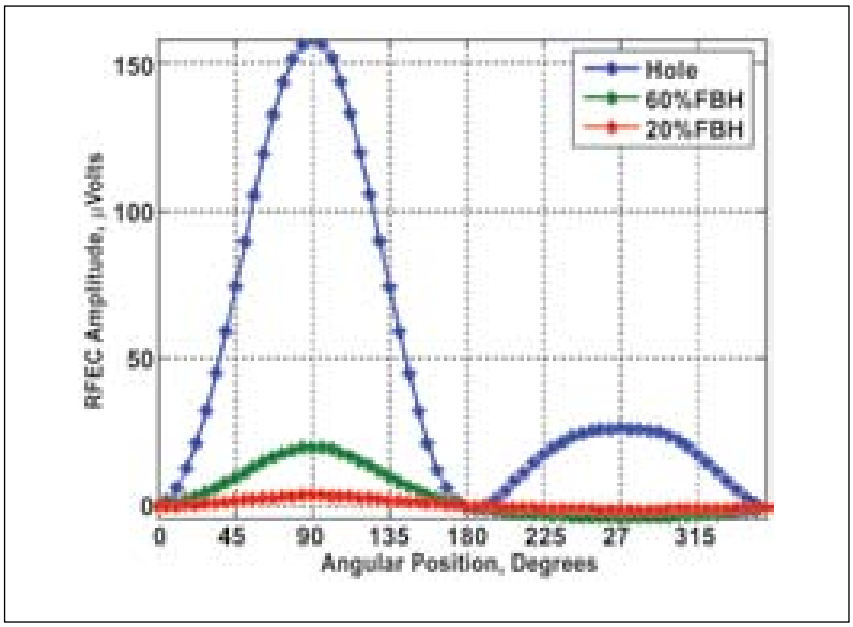

Fig. 2 *Predicted remote field eddy current signals for radial type receiver coil for a through hole, 60% and 20% flat bottom hole*

III D Sodium Technology

III D.1 Development and Testing of High Sensitivity Permanent Magnet Flowmeter

Based on the expertise and technological development at our centre, a sodium injection set up is being constructed by a private company in Mumbai. In this facility it is required to measure low sodium flow rates of the order of 20 lph. Presently sodium flowmeters to measure flow up to 100 lph have been designed and manufactured (Fig. 1). High sensitivity with low flow is achieved by modifying the magnetic circuit so as to get a high flux density of the order of 0.7 Tesla. Duct is made flat so that the air gap length can be minimized and length of the conductor can be increased. This flowmeter consists of duct assembly and magnet assembly. Magnet assembly consists of two ALNICO 5 permanent magnet blocks of U shape and mild steel pole faces joined by bolting. Flattened duct with electrode plates welded on either side is used as duct assembly. Movement of the duct is arrested by providing clamp and stud pin arrangement. Two pairs of electrodes are welded to the electrode plates and routed to the terminal connector. Electrode pair 1 is located at 5 mm upstream side from the magnetic central axis and electrode pair 2 is located 10 mm down streamside of the magnetic central axis. One such flow meter was fabricated and introduced into sodium sampler circuit of *b* loop for calibration along with the existing sampler flowmeter. Testing of High sensitivity permanent magnet flowmeter (HSFM) was done at different temperatures of 523, 573

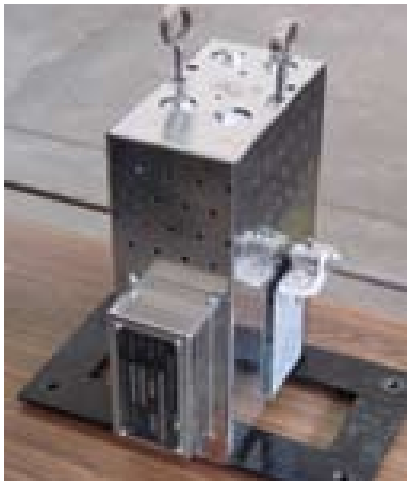

Fig. 1 High sensitivity permanent magnet flow sensor

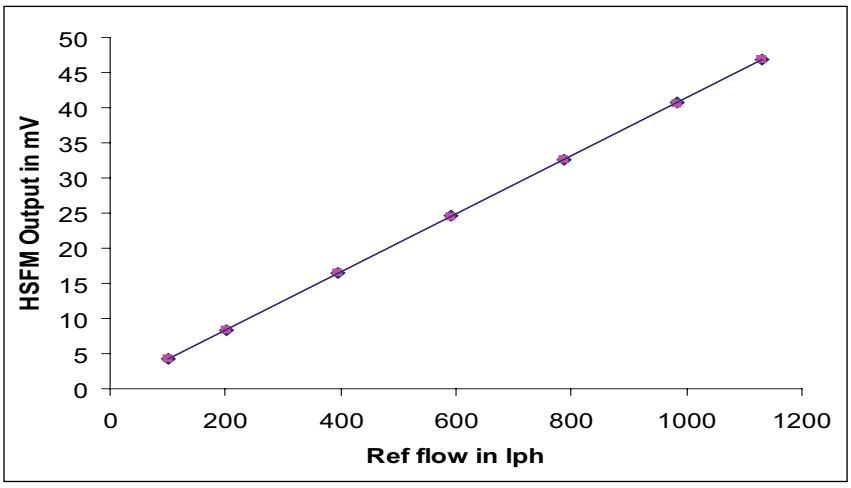

Fig. 2 Variation of output of high sensitivity permanent magnet flowmeter as a function of flow

and 623 K and at different flows up to 1176 lph.

Outputs of sampler flowmeter and HSFM were monitored and compared. The sensitivity of the HSFM was estimated based on the flow read by the reference flowmeter and the millivolt given by the HSFM (Fig. 2). Sensitivity of the HSFM was found to be 41 mV/m^3/h. Maximum non-linearity of the sensitivity with respect to flow was found to be 2.11% and maximum non-linearity of the sensitivity with respect to temperature at a flow rate of 983 lph was found to be 0.75%. It was also found that downstream side electrode pair of the flowmeter is more sensitive than upstream side electrode pair.

III D.2 Validation of Temperature Compensation Method for Mutual Inductance Type Level Probe

Mutual inductance (MI) type continuous level probe works on the principle of variation of mutual inductance between two windings when they are immersed in an electrically conducting fluid such as sodium. It is used for monitoring the sodium level in sodium tanks and vessels of PFBR. The probe has a primary winding and a secondary winding, wound in a bifilar fashion on a stainless steel former and kept inside a stainless steel pocket. When the primary winding is excited with a constant AC current at a fixed frequency, an *emf* is induced in the secondary coil. The liquid sodium surrounding the probe acts like a short-circuited winding. Hence an *emf* is induced in sodium which causes an eddy current to flow through it. The flux due to this eddy current opposes the main flux produced by primary winding. Hence the net flux linked with secondary winding decreases and thereby the secondary voltage reduces when the sodium level increases. When the sodium temperature increases, the resistivity of sodium increases, hence the eddy current decreases and the induced voltage in secondary winding increases at a given sodium level in the tank. This voltage variation is presently compensated electronically to reduce the error in the output because of the temperature change, which results in an error of ± 3%.

A new method of temperature compensation is found out for accurate measurement. It makes use of the variation of internal resistance of secondary winding with temperature to compensate for the variation of induced emf due to temperature. At any given level, the internal resistance, R_i, of the secondary coil increases with temperature. By connecting an external resistance, R_{ext}, across the secondary, there is a current, i, through R_{ext}, such that the voltage drop, (R_i * i) in the internal resistance of the secondary coil compensates the increase in the

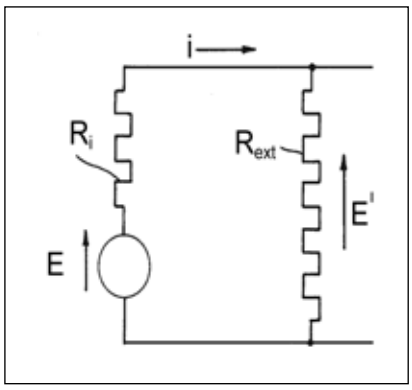

Fig. 1 *Equivalent circuit of secondary winding for temperature compensation*

$$R_{ext} = \frac{E \times \Delta R_i}{\Delta E} - R_i$$

R_i = *Internal resistance of secondary.*

E = *Secondary output.*

ΔR_i = *Difference in internal resistance at 473 and 823 K*

ΔE = *Difference in secondary voltage at 473 and 823 K.*

induced emf due to temperature rise. The schematic diagram is shown in Fig.1.

The external resistance required at zero and full level was calculated using the available experimental data of a 6.0 m active length probe at different frequencies and plotted in Fig. 2. The optimum frequency of operation was found to be 2.5 kHz.

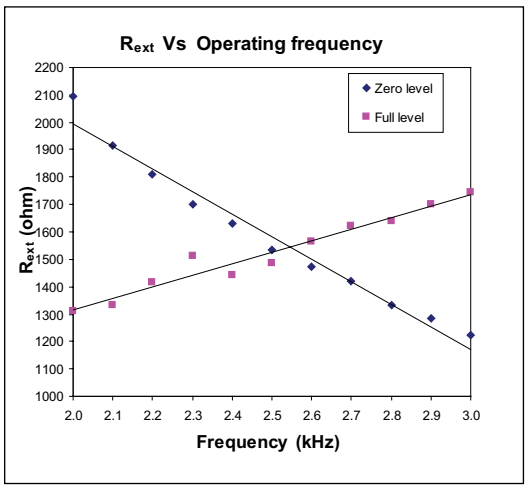

Fig. 2 *The external resistance calculated for zero and full level at different frequencies*

An experiment was conducted at this optimum frequency of operation, to find out the external resistance required. This resistance was connected across the secondary of the probe and the secondary voltages were measured at different sodium levels and temperatures between 473 to 823 K. A dip stick type level probe was used as a reference probe to cross check the level.

Table 1 shows the comparison of %variation of secondary output w.r.t average change in secondary output without compensation and with new method of compensation. Using this method, the temperature effect on level is reduced from 10.15 to 1.73% over a temperature range of 473 - 773 K.

Thus the new temperature compensation technique was validated experimentally for 9600 mm long MI type continuous level probe. This technique not only improves the accuracy but also simplifies the electronic circuitry by eliminating the temperature compensation.

Table 1. Sensitivity variation with temperature

Freq: 2.5kHz	**Experimental values without compensation**		**Experimental values with new method of compensation**	
Average change in secondary output over 473-823K (in mV)	30.53		29.42	
% temperature variation with respect to ΔE_ave	11.72	Zero level	1.46	Zero level
	10.15	Full level	1.73	Full level

III D.3 Application of Fusible Plug Concept in Sodium Leak Collection Tray System

Sodium-water reaction is one of the concerns in sodium cooled fast reactors There are many mechanisms/provisions to handle small to large sodium leaks. To handle the large leaks in the sodium components and piping, one of the passive protection devices used is the leak collection trays (LCT). These are positioned below the secondary sodium pipelines in the steam generator building (SGB). They collect the leaked sodium in a hold up vessel, suppress the sodium fire due to oxygen starvation and guide the sodium to an inerted sodium transfer tank located at the bottom most elevation of the SGB. This later procedure of draining the leaked sodium into a transfer tank has been envisaged as a defence in depth measure against the messy handling of un-burnt

sodium and to guard against larger leak rates than what the LCT can handle effectively. Towards this, a network of carbon steel pipelines are laid out connecting all the LCT and the transfer tank through headers in strategic locations, each having a fusible plug, which separates the argon and the ambient. Woods metal is the preliminary choice for the fusible plug. It is an alloy of 50 % Bi, 25% Pb, 12.5% Sn and 12.5 % Cd with a melting point of 395 K.

Normally the transfer tank is filled with argon at ~ 0.03 bars-g pressure. Both the header and the tank are at room temperature during normal conditions. Leaked sodium by virtue of its high temperature has to heat up the fusible plug to melt the same and drain into the transfer tank. Melting of the fusible plug and drainability of the leaked sodium is a function of the leak rate and initial temperature of sodium. On its passage through the network of pipes and header and before it reaches the fusible plug, the sensable heat in the sodium is transferred to the pipeline and gets cooled. In order to demonstrate the concept, a conservative and simplified two dimensional transient conduction heat transfer with phase change analysis, without consideration of any impurity in sodium has been carried out. Minimum operating temperature of sodium in any condition of the plant is 423 K. For sufficiently large leak rates when the sodium can reach the headers where the fusible plugs are installed, it can be assumed that the fusible plug is subjected to a sudden column of sodium and pipe at 385 K above it, where the later temperature is the thermodynamic equilibrium temperature of the spilled sodium and the 3 mm thick 100 mm NB schedule-10 pipe material. The pipe header is insulated with 25 mm of mineral wool. Convective boundary condition of 5 W/m^2/K is assumed over the insulation. Fusible plug, flanges, the portion of pipe header considered below the fusible plug and all the insulation are assumed to be at the ambient temperature of 303 K.

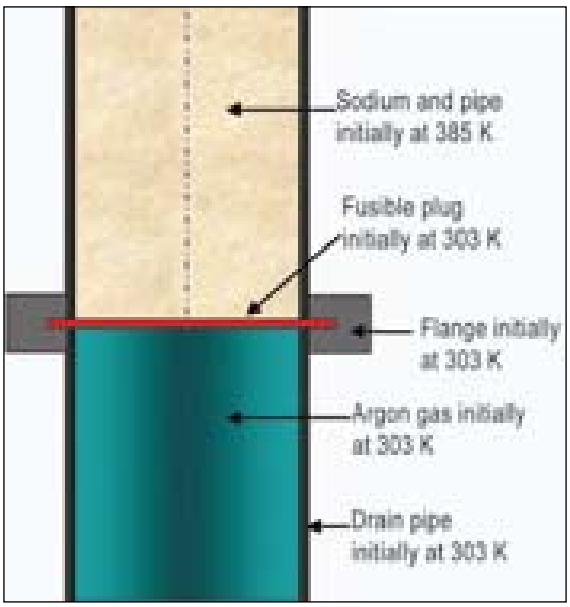

Fig. 1 *Physical model of the system*

Thermal and mechanical analysis is carried out to arrive at the optimum thickness required for the plug to meet the structural and functional requirements. Fig. 1 shows the computational domain. Analysis has been carried out for two cases – 6 mm and 3 mm thick fusible plugs, to bring out the relative advantage. Isotherms obtained at two different times are

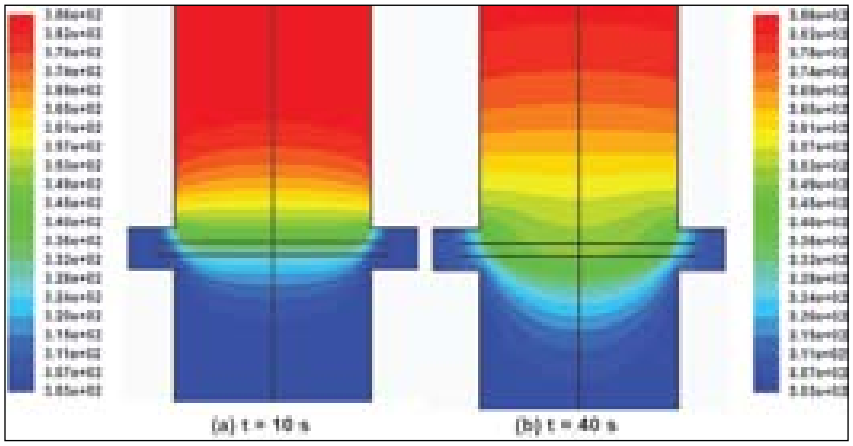

Fig. 2 *Isotherms in the header with 6 mm thick plug (Temperature scale in K)*

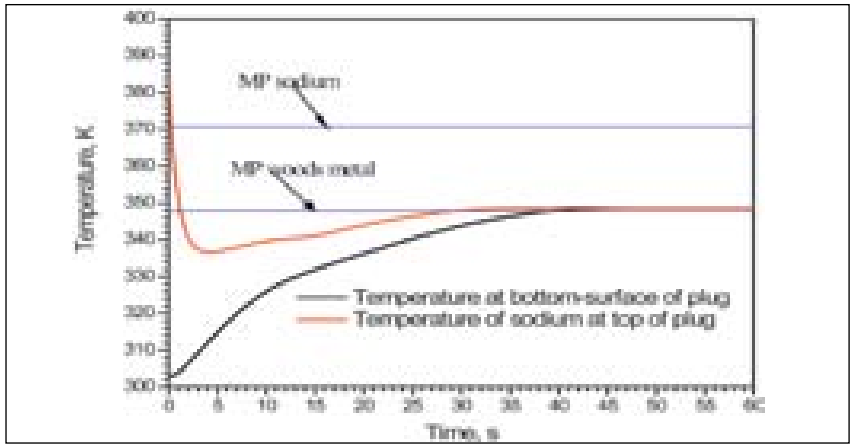

Fig. 3 *Sodium and plug temperature at the plug center (6 mm thick fusible plug)*

depicted in Fig. 2(a) and Fig. 2(b). Fig. 3 shows the transient evolution of the sodium and fusible plug bottom region temperatures just above the center of the fusible plug. It is clear from these figures that the sodium temperature falls much below the solidification temperature of sodium (371 K). Time taken for at least 3 cm radius of the fusible plug to melt completely is estimated as 40 s and by this time solidified sodium of 9 cm is found to be present over the plug and continuing to grow. It is also important to notice that the sodium temperature just above the fusible plug is at least 293 K lesser than its melting point and its evolution has become flat, indicating that with any amount of time (read with any amount of further sodium arrival at 385 K above the sodium column) the sodium plug formed will not re-melt. Isotherms obtained at the end of 5 s and 10 s are shown in Fig. 4. Transient evolution of the sodium and fusible plug bottom region temperatures just above the center of the fusible plug are shown in Fig. 5. It is evident from these figures that the fusible plug melts completely within five seconds, and at the same time only a 3 mm thick sodium layer solidifies momentarily. However, within about ten seconds, the sodium re-melts and increases beyond the sodium melting point, indicating the possibility of trouble free draining of the sodium into the transfer tank.

Finally, it is established that effective melting of the fusible plug and trouble free draining of the leaked sodium is possible for a 3 mm thick fusible plug. Further, the structural integrity of plug with 3 mm thickness has been demonstrated. Experimental demonstration is planned to qualify the design in a comprehensive way involving all system components.

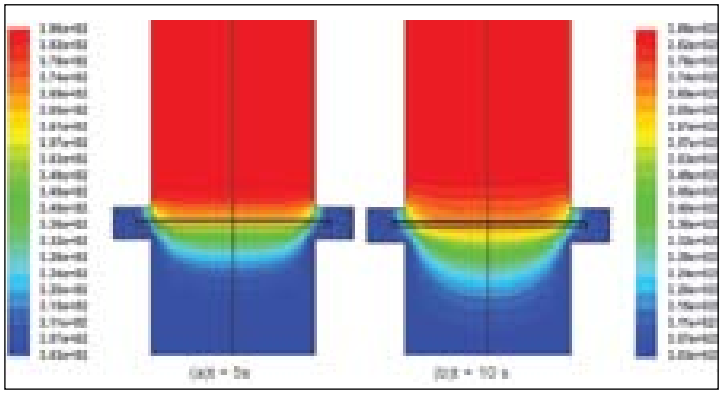

Fig. 4 *Isotherms in the header with 3 mm thick plug (Temperature scale in K)*

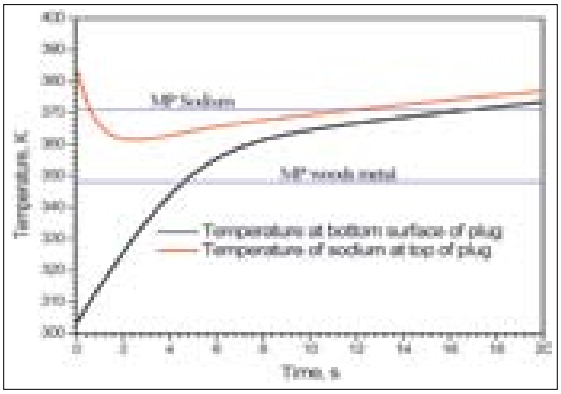

Fig. 5 *Sodium and plug temperature at the plug center (3 mm thick fusible plug)*

III E Materials Development

III E.1 Development of Reduced Activation Ferritic-Martensitic Steel for Fusion Energy Application

Reduced activation ferritic-martensitic (RAFM) steels are being considered as a viable structural material for the test blanket module (TBM) of International Thermonuclear Experimental Reactor (ITER). The indigenous development of RAFM steel has been taken up in co-operation with MIDHANI, Hyderabad for Indian Test Blanket module of ITER.

The chemical composition of conventional P91 steel (9Cr-1Mo-0.06Nb-0.2V-0.05N (wt%)) has been modified with the substitutions for highly radioactive Mo by W and Nb by Ta. The strict control has been exercised on radioactive tramp elements (Mo, Nb, B, Cu, Ni, Al, Co, Ti) and elements that promote embrittlement (S, P, As, Sb, Sn, Zr, O). These elements have been restricted to ppm levels. The RAFM steel has been produced by proper selection of raw materials and employing VIM and VAR melting routes with strict control over the

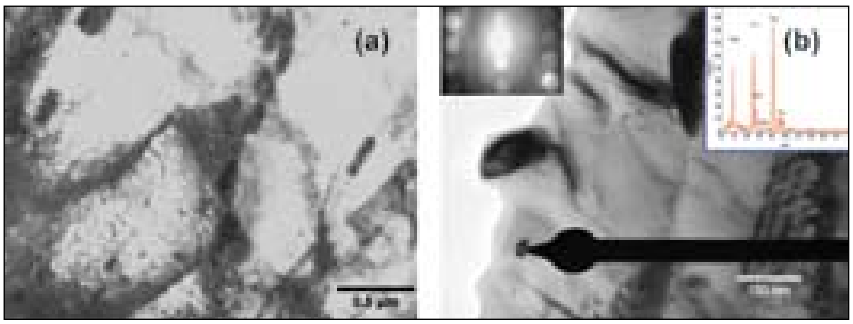

Fig. 1 *TEM micrographs showing* ***(a)*** *tempered martensite structure;* ***(b)*** *fine MX type precipitates (arrow marked) rich in Ta and V.*

parameters of forging, rolling and heat treatments. Optimization of normalizing and tempering heat treatments were conducted on the rolled products. The optimum normalizing and tempering heat treatment conditions of the steel were arrived at 1253 K for thirty minutes and 1033 K for sixty minutes respectively considering the austenitic grain growth and hardness. Microstructure characterizations for evolution of precipitates and identification of the different critical transformation temperatures (M_s, M_f, Ac_1 and Ac_3), and specific heat of the steel were carried out using SEM, TEM and DSC techniques. Steel has a tempered martensitic structure with intergranular $M_{23}C_6$ and transgranular MX (M = Ta, V) type of precipitates (Fig.1).

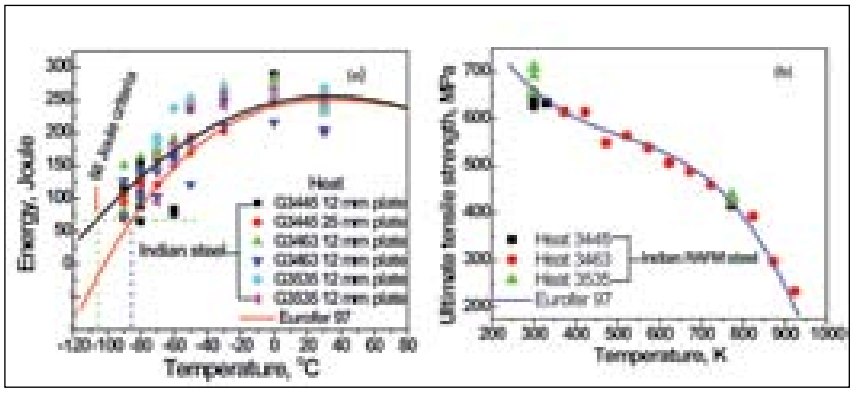

Fig. 2 (a) *Charpy impact energy and* ***(b)*** *tensile strength of Indian RAFM steel, compared with those of Eurofer 97 steel.*

Charpy V-notch impact, hot tensile, creep and fatigue tests have been conducted on these alloys. Impact property of the different heats of the steel are shown in Fig. 2(a) and compared with those of Eurofer 97. The ductile brittle transition temperature (DBTT) (based on 68J criteria) is estimated to be less than 173 K compared to around 193 K for Eurofer 97 having comparable upper shelf energy. The variation of ultimate tensile strength of the steel with testing temperature is shown in Fig. 2(b). The indigenously developed RAFM steels have tensile strength and ductility comparable to the Eurofer 97 steel. Initial results shows that the developed steel has creep rupture strength slightly higher than the Eurofer 97.

III E.2 Characterisation of Nano Sized Yttria Dispersoids in a Model Oxide Dispersion Strengthened Ferritic Alloy and Feasibility Studies on ODS Clad Tube Manufacturing

Future Liquid Metal Cooled Fast Breeder Reactors need to be operated at higher temperatures of ~923K for improved economy and cost of power. This requires significant improvements in the materials that are to be used for fuel cladding in such reactors. Ferritic / Martensitic alloys (9-12%Cr) exhibit higher void swelling resistance (under irradiation) than austenitic stainless steels used for clad tube applications in current FBRs. However, creep resistance limits operating temperatures to ~823 K. This limitation can be overcome by dispersion strengthening of the steel using dispersoids such as yttria in the ferrite or ferrite/martensite matrix. The dispersed fine oxide particles improve creep strength by impeding dislocation motion and retard irradiation swelling by trapping irradiation induced point defects at the dispersoid – matrix

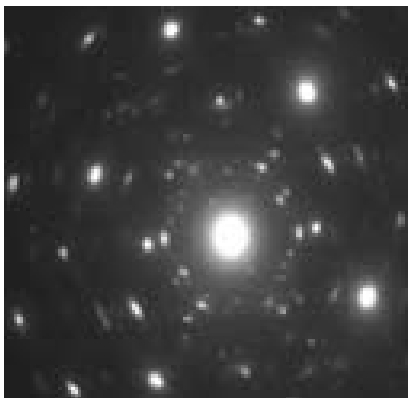

Fig. 1 *Selected area electron diffraction pattern from the ODS alloy showing matrix diffraction spots along with those from the dispersoids. The innermost spots help identify the dispersoids as being the bcc form of* Y_2O_3 / $Y_2Ti_2O_7$

interfaces. Addition of a small amount of titanium results in the formation of very fine mixed oxide particles of yttrium and titanium thus significantly improving creep rupture strength.

Based on these principles, a development effort was initiated to synthesise yttria strengthened 9Cr ferritic steel and to fabricate clad tubes using this oxide dispersion strengthened (ODS) steel. The alloy development involves mechanical milling of powders, consolidation by hot extrusion and tube formation by cold pilgering. The different process parameters in each of these stages need to be optimised. Model Fe-Ti-Y_2O_3 alloys have been synthesised and characterised for size and distribution of yttria dispersoids in the ferrite matrix.

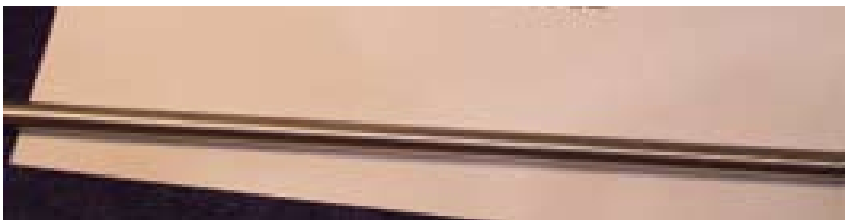

Fig. 4 *Fabricated ODS clad tube*

Elemental Fe and Ti powders with an initial particle sizes of 150 µm and 105 µm respectively, mixed with 10 – 20 nm sized Y_2O_3 powder in the weight ratio corresponding to a final composition of Fe-0.2Ti-0.35Y_2O_3, was milled for various times in an attritor mill under an Argon cover gas. The powder was degassed at 723 K and sealed in a mild steel can which was hot isostatically pressed at 1323 K under 1000 MPa and subsequently upset in an extrusion press and forged at 1323 K. Thin foils were prepared for transmission electron microscopy (TEM) from this sample, in order to characterise the resulting microstructure with emphasis on the identification of dispersoids and a determination of their size and distribution in the matrix. Fig. 1 shows a typical diffraction pattern from this alloy showing diffraction spots from the matrix and multiple dispersoids. The presence of the 0.433 nm (211) spot enables identification of the dispersoids as *bcc* Y_2O_3 or Y_2TiO_7. Fig. 2 shows a fairly uniform distribution of dispersoids in the ferrite matrix, imaged in dark-field TEM mode. The smallest dispersoids measurable in this mode are ~ 20 nm (61%) with a much smaller size fraction (5%) at ~ 80 nm. High-resolution TEM was taken up to image individual dispersoids that were too small to be imaged by diffraction contrast mechanisms. Fig. 3 is a typical lattice image where the central polygonal region with broad fringes is a single dispersoid ~ 5 nm in size while the relatively finer fringes surrounding it correspond to the lattice planes of the ferrite phase.

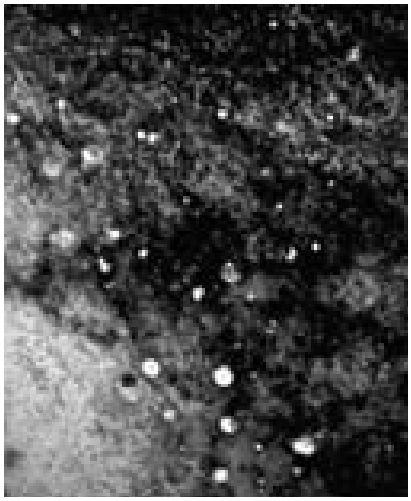

Fig. 2 *Dark-field TEM image showing a fairly uniform distribution of dispersoids in the ferrite matrix*

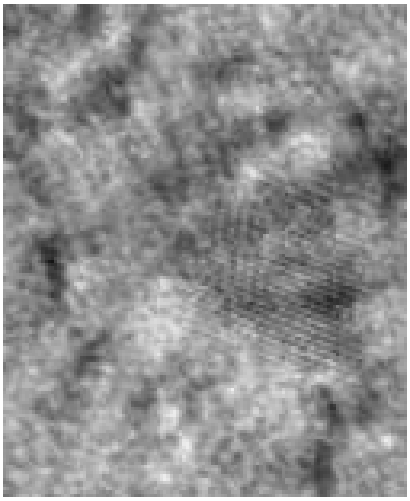

Fig. 3 *High-resolution TEM image from the ODS alloy showing a single dispersoid ~ 5 nm in size embedded in the ferrite matrix.*

The above results show that the required ferritic alloy with a fine dispersion of yttria-based particles can be synthesised by the powder metallurgy route that has been adopted above. Further fabricability studies have been carried out at NFC, following which a clad tube of outer diameter 6.6 mm and a thickness of 0.48 mm has been obtained (Fig. 4).

III E.3 Thermomechanical Processing and Hot Cracking Susceptibility Studies of Alloy D9 and its Variants

Modification of microstructural topology through thermo-mechanical processing is the emerging concept to develop the desired microstructure in austenitic stainless steels to alleviate radiation induced segregation. A one step strain annealing approach has been adopted to optimize the grain boundary character distribution (GBCD) in alloy D9. The experimental methodology adopted in this investigation was based on the strain annealing approach in which small amount of strain (5-15%) was imparted on solution annealed sample. Cold rolling operations were carried out on 3mm thick rectangular plates on a laboratory rolling mill. The cold deformed samples were subsequently annealed at various temperatures (1173-1273 K) for different time periods (0.5-2 h). The microstructure of the 'as received' material is shown in Fig. 1. The grain boundaries are identified as one of the following categories: Σ1, Σ3, Σ9, Σ27 and other low Σ CSL or random high angle boundaries (HABs). The as received material contained 45% of Σ3 boundaries. The proportion of Σ1, Σ9 and Σ27 boundaries are 3.5, 2.9 and 0.8% respectively. The total percentage of special boundaries (SBs) in the 'as received' specimen is ~ 55%. It should be noted that SBs refers to coincidence site lattice (CSL) boundaries with $\Sigma \leq 29$. Fig. 1(b) shows only the random HABs in the as-received sample. It could be seen from the figure that the random HABs are well connected and provide a potential path for percolation.

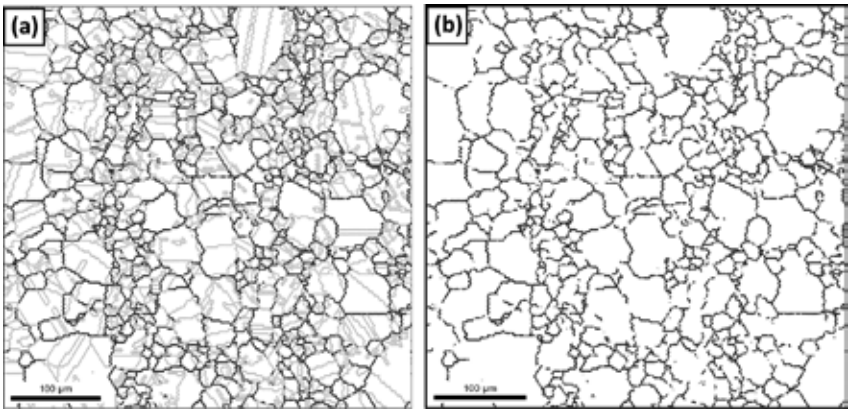

Fig. 1 *Microstructure of the solution annealed (SA) sample (a) Grain boundary reconstruction from EBSD data, the thick black and thin gray lines represent random high angle boundaries (HABs) and special boundaries (SBs), respectively (b) only HABs are shown to assess the random boundary connectivity*

It has been observed that annealing after 5% deformation induces anomalous grain growth with a moderate increase in number fraction of coincidence site lattice (CSL) boundaries. However, a 10-15% strain followed by annealing at 1273 K for 0.5-2 h was found to be a suitable thermo-mechanical processing schedule to optimize the GBCD in alloy D9. The representative microstructure is shown in Fig.2(a). The frequency of Σ3, Σ9 and Σ27 boundaries are 62.0, 8.7 and 4.7% respectively. The proportion of SBs, in this condition, is ~ 80%. The random HABs map shown in Fig.2(b) reveals a significant disruption of random boundary connectivity due to direct incorporation of Σ3 and its variants. The evolution of microstructure in these samples could be understood as follows. The combined strain and thermal energy is insufficient to trigger recrystallization. However density of lattice dislocations is sufficient enough to promote strain induced boundary migration. In this

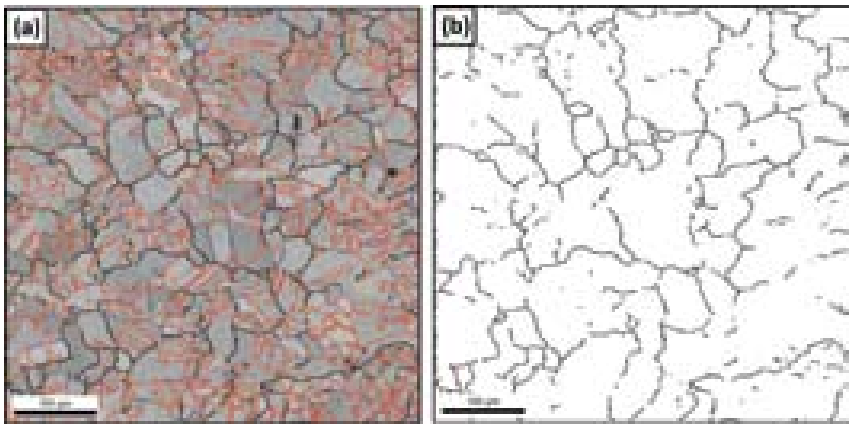

Fig. 2 *(a) OIM map in the optimized GBCD condition (Color code: Σ3 – red; Σ9 – blue; Σ27 – green; Σ1 – yellow; other low Σ CSL – purple, random HAB – black) (b) grain boundary map showing only the random boundaries*

condition, grain boundary moves at an optimal rate, which is ideal for twin multiplication.

Hot cracking behavior of alloy D9 is an important consideration during welding as this material solidifies without any residual delta ferrite in the prior austenitic mode and also contains titanium. Both Varestraint and Hot ductility tests were used to evaluate its hot cracking susceptibility. Hot crack studies using Longitudinal Varestraint Test (LVT) and Trans-Varestraint Test (TVT) were carried for the heats of an improved version of alloy D9 containing controlled amounts of P (0.022-0.025 wt%), Si (0.75-1.00 wt%) and Ti (0.21-0.29 wt%). These tests were done on specimens of 3 mm thickness in 20% cold-worked condition at four strain levels of 0.5, 1.0, 2.0 and 4.0%. Brittleness temperature range (BTR) was also evaluated during testing. These Varestraint tests indicated that these alloy heats have very high hot cracking susceptibility during autogenous welding to itself, as the total crack length (TCL) and maximum crack length (MCL) in both the weld and heat affected zone as also the BTR values were very high compared to that of D9. The test results for TCL and BTR for these heats are shown in Figs. 3(a) and 3(b) respectively. Hot ductility tests were also conducted on these variants using thermo-mechanical simulator to determine the Nil Ductility Temperature (NDT). The simulation comprised heating to temperatures below their melting point to temperatures above 1573 K and applying tensile load to fracture the specimens. The NDT for 316 L SS, D9 and its variants were 1591-1643 K, 1619-1638 K and 1580-1601 K respectively. These results confirmed that the hot cracking susceptibility of these variants is higher than that of D9 and SS 316 L. It has been proved by the recent study using autogenous weld between SS 316 LN versus D9-variants showed less cracking tendency than D9-variants versus D9-variants during the autogenous welding. Hence, for autogenous end-cap welding of the D9-variants clad, a suitable SS 316 LN end-cap material has to be chosen to ensure sufficient dilution of P, Si and Ti in the weld zone for imparting adequate hot-cracking resistance.

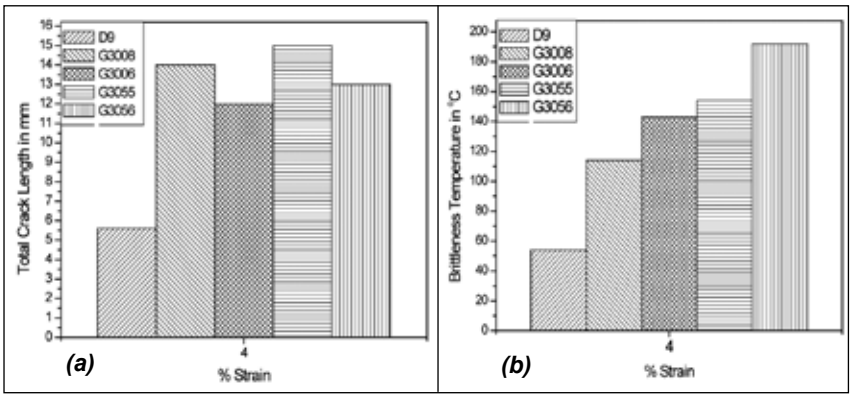

Fig. 3 *Total crack length and brittleness temperature range of D9 and its variants at 4 % strain levels. Test results of (a) total crack length and (b) brittleness temperature*

III E.4 Determination of Effective Vacancy Migration Energy from Positron Annihilation Studies on Proton Irradiated D9 Steel

D9 steel is envisaged for use as clad and wrapper in PFBR. Intense neutron flux in the nuclear reactor causes void swelling in the structural components. The basic understanding of defect production due to the irradiation and their thermal stability would pave the way to gain better insight into macroscopic dimensional changes of the material. The study of defect recovery during annealing of irradiated samples yields information regarding the occurrence of defects, migration, clustering, growth and annealing of various defect species. Among various parameters that determine the void swelling behavior, the effective vacancy migration energy is the most critical and fundamental and hence, it is important to determine the same experimentally in D9 alloy. Positron annihilation studies have been carried out on proton irradiated D9 steel to identify the annealing stages due to defect recovery, while isothermal studies have been carried out

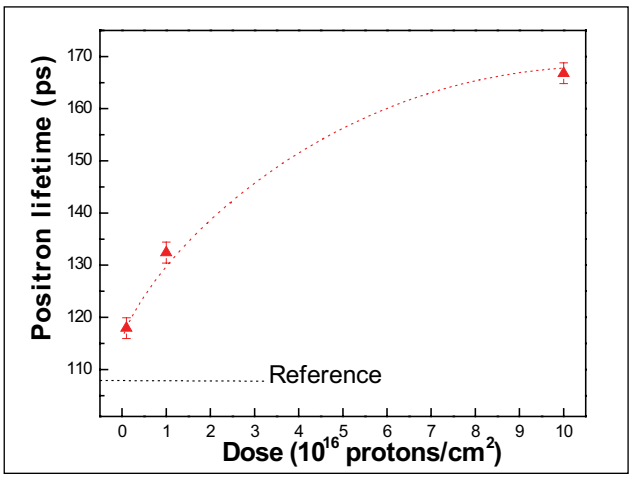

Fig. 1 *Variation of positron lifetime as a function proton dose. Reference values taken on un-irradiated sample are shown.*

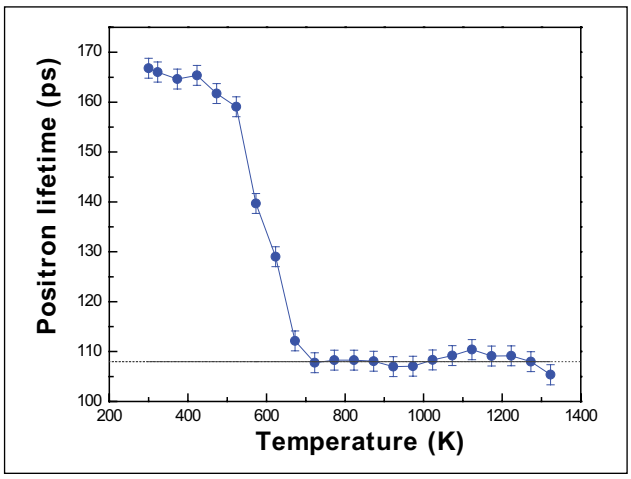

Fig. 2 *Isochronal study - positron lifetime verses annealing temperature for sample with proton dose of 1x10^{17} cm^{-2} . Reference value of un-irradiated sample is shown as horizontal dashed line.*

to investigate the migration kinetics of vacancy defects. The solution annealed and 20 % cold worked D9 have been irradiated at room temperature with 3 MeV protons using 1.7 MV Tandetron accelerator, with proton dose of 1×10^{15}, 1×10^{16}, 5×10^{16} and 1×10^{17} protons/cm^2.

Isochronal annealing results in terms of the variation of positron lifetime as a function of irradiation dose in annealed D9 sample is shown in Fig. 1. The defect-free lifetime of the solution annealed D9 is 108 ps. Upon irradiation, the positron lifetime is found to increase indicating the presence of radiation induced vacancy-type defects. As the proton dose is increased, there is a significant increase in positron lifetime. This observation is also supported by similar increase of complementary Doppler line shape S-parameter. Based on the consistent variation in both positron lifetime and S-parameter, the observed increase is attributed to the increase in the concentration of vacancy defects at higher irradiation doses. Annealed D9 irradiated to a dose of 1×10^{17} ions/cm^2 was subjected to isochronal annealing and the results are shown in Fig. 2. During the initial annealing at lower temperatures, there is not much change in the lifetime but beyond 500 K the lifetime exhibits steep reduction, and attains defect-free values beyond 700 K. In the temperature range of 500 to 700 K, vacancies are highly mobile, they get rapidly annealed out due to migration to sinks and finally they disappear beyond 700 K. Positron lifetime is found to attain the defect-free value above 700 K annealing temperatures. This stage indicates the complete recovery of steel from radiation-induced vacancy-defects. Corresponding to the maximum change seen in isochronal curve (shown in Fig. 2), isothermal annealing was carried out at 623 K to study the kinetics of vacancy defect migration. An exponential decay of the positron lifetime as a function of annealing time was observed as shown in Fig. 3. The method of combination of isochronal and isothermal studies was applied to deduce an effective activation energy for vacancy migration to be 1.13±0.08 eV. This information is useful in modelling void swelling behavior of the D9 steel.

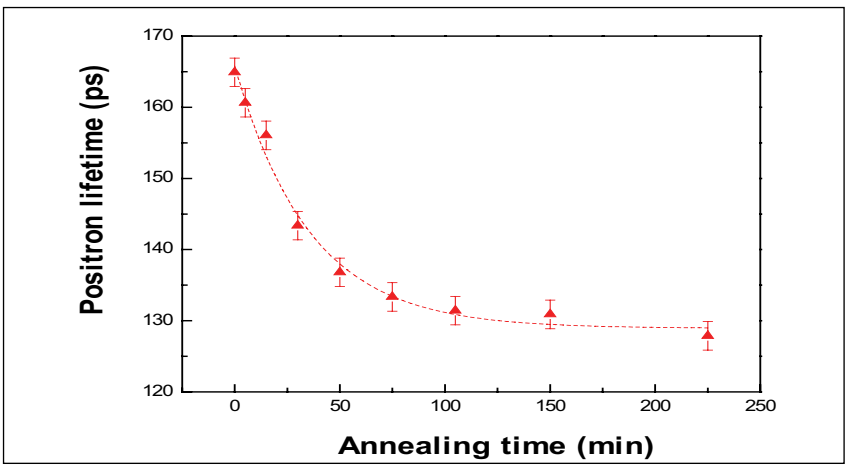

Fig. 3 *Isothermal study - positron lifetime verses annealing time at 623 K for sample with proton dose of 1x10^{17} cm^{-2}*

III E.5 Durability and Thermal Cycling Behaviour of Thermal Barrier Yttria-Stabilized Zirconia Coating on 9Cr-1Mo Steel

For the pyrochemical reprocessing of spent metallic fuels of future fast breeder reactors, molten chloride salts will be used for the electrorefining process. The molten salt preparation for electrorefining involves impure salts and high temperature producing highly corrosive conditions. In order to overcome the corrosion of metallic materials like type 316 L SS, Inconel 625 and 9 Cr-1Mo steel in molten chloride environment it is proposed to apply thermal barrier coating (TBC) of yttria stabilized zirconia over the surface. The TBC coating provides inert surface to the molten salt and enhances the useful life of components. However, the loading and unloading of salts and increase and decrease in operating temperature of the salt vessel may lead to build up of thermal strains associated with cracking and spallation of coating during prolonged service. In order to study the influence of thermal cycling on the integrity of TBC, coating facility was established and systematic study was initiated to understand the phenomenon.

The YSZ (92 wt% ZrO_2 and 8 wt% Y_2O_3) thick top coatings (300±10μm) and CoNiCrAlY bond coating (30 ± 10μm) were applied by air plasma spray (APS) on 9Cr-1Mo steel disc specimens. The durability of plasma coated 7-8% YSZ 9Cr-1Mo steel were tested in static air at 923, 1123 , 1223 and 1323 K with 10 minutes heating and cooling thermal cycling condition. Similarly, the material degradation behavior of plain 9 Cr-1Mo was tested at different temperatures of 473, 673, 873, 1073, 1123 and 1323 K under similar thermal cycling condition. Failure was defined when significant area of the TBC larger than 10 mm in one direction has spalled off.

The material degradation behavior of plain 9 Cr-1Mo steel that sustained the maximum number of cycles was tested for long thermal cycling condition at different temperatures. It was observed that the surface of the plain 9Cr-1Mo steel substrate oxidized and changed in color, depending on the treatment conditions (Fig. 1). However for the TBC-YSZ coated 9Cr-1Mo steel, spallation of YSZ from the substrate was observed at 1223 K and 1323 K and the average cycles sustained by these coatings were up to 30 cycles at 1223 K (Fig. 2). The weight/gain losses observed during the thermal cycling of plain 9 Cr-1Mo steel at 473 and 673 K (Fig. 3(a) and Fig. 3(b)) shows no significant change, however, at higher temperatures of 923 K gradual weight gain with increase in cycling time could be observed. The increase in weight is attributed due to increase in oxidation and scale formation associated with oxygen transport during cooling and heating at different temperatures as indicated by the change in the color. The top coat YSZ do not show any spallation even after 500 cycles at 923 K. This demonstrates the excellent thermal cycling properties of the YSZ-TBC at temperatures below 923 K. Though higher weight gain was observed at 1073 K compared

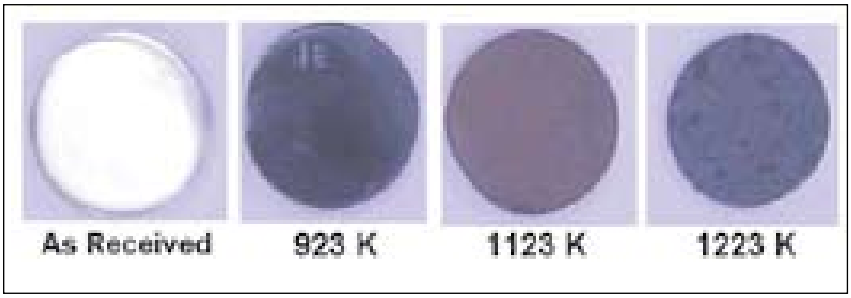

Fig. 1 *9Cr-1Mo steel specimens after undergoing different thermal cycling treatment at RT, 923, 1123 and 1223 K*

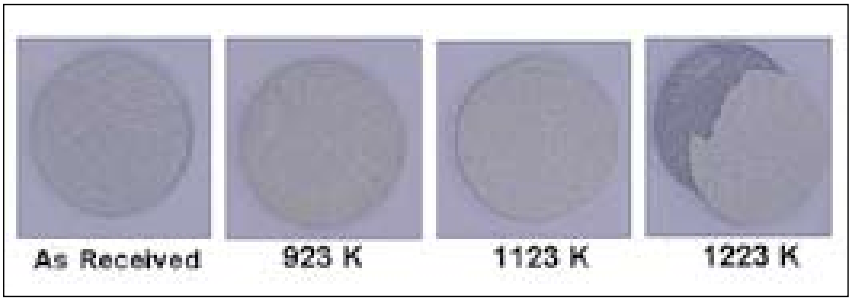

Fig. 2 *TBC coated YSZ specimens after different thermal cycling treatment at RT, 923, 1123 and 1223 K*

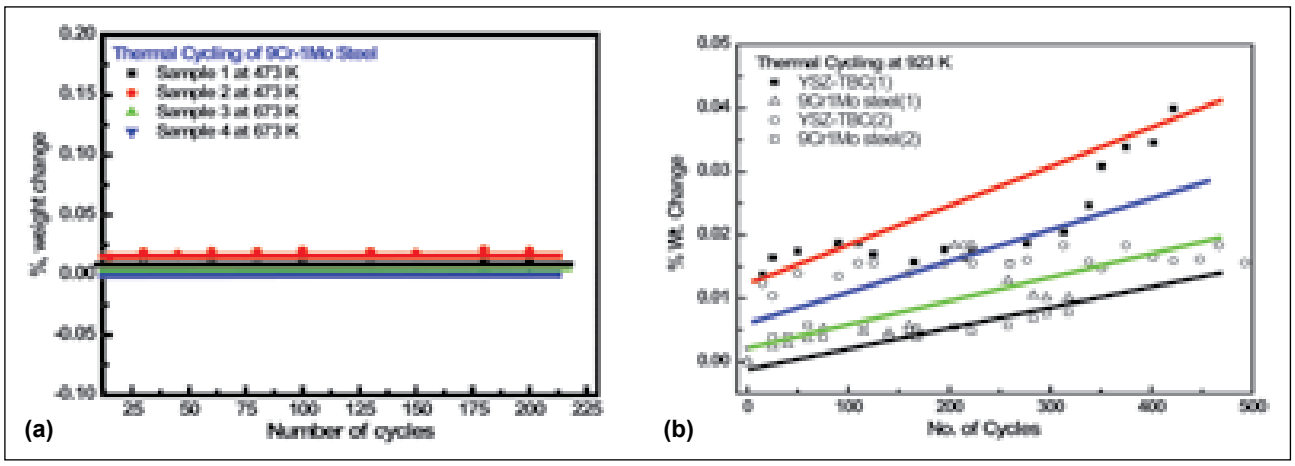

Fig. 3 *The weight changes of (a): 9Cr-1Mo steel at different thermal cycling temperatures of 473 and 673 K and (b): plain 9Cr-1Mo steel and TBC-YSZ at 923 K during the thermal cycling test*

to measurements carried out at 873 K no cracks or spallation was observed even after 180 cycles indicating good integrity. However, increasing the temperature to 1223 and 1323 K showed cracking, spallation and detachment of YSZ coating (Fig. 2).

The GIXRD pattern of the as-sprayed YSZ-TBC contained predominantly ZrO_2 and Y_2O_3, tetragonal (t) and cubic (c) phases of ZrO_2. The plasma-spraying parameters used could cause most of the monoclinic ZrO_2 in the powder to transform to t-ZrO_2 and c-ZrO_2. The t-ZrO_2 was predominant throughout the YSZ layer in as-deposited TBCs and showed no transformation to the monoclinic phase after various thermal exposures. Dielectric Electrochemical Impedance Spectroscopy was used for characterizing the physical behaviour of the coating before and after thermal cycling studies. The typical Nyquist and Bode plots of YSZ-TBC coated 9Cr-1Mo steels after thermal cycling at different temperatures are represented in (Fig. 4(a) and Fig. 4(b)). The effect of different thermal cycling temperatures indicated that the overall resistance, which is represented by the intercept on the real impedance axis, increases sharply with decrease in thermal cycling temperatures. However, the semicircles corresponding to the untreated YSZ-TBC layer are larger than those corresponding to YSZ-TBC under different thermal cycling temperatures. The YSZ-TBC resistance and capacitance exhibited an initial increase and the corresponding decrease, respectively, with increase in cycling temperature. This may be due to the micro-cracks generated within YSZ during thermal cycling test or dissolution of porous oxide layer. Characteristic frequency dependences of the Bode plots presented in Figures are similar for all TBC-YSZ coated 9Cr-1Mo steel. It is known that the high frequency region of the impedance spectra reflects the properties of the porous layer, while the properties of the barrier layer are associated with the low

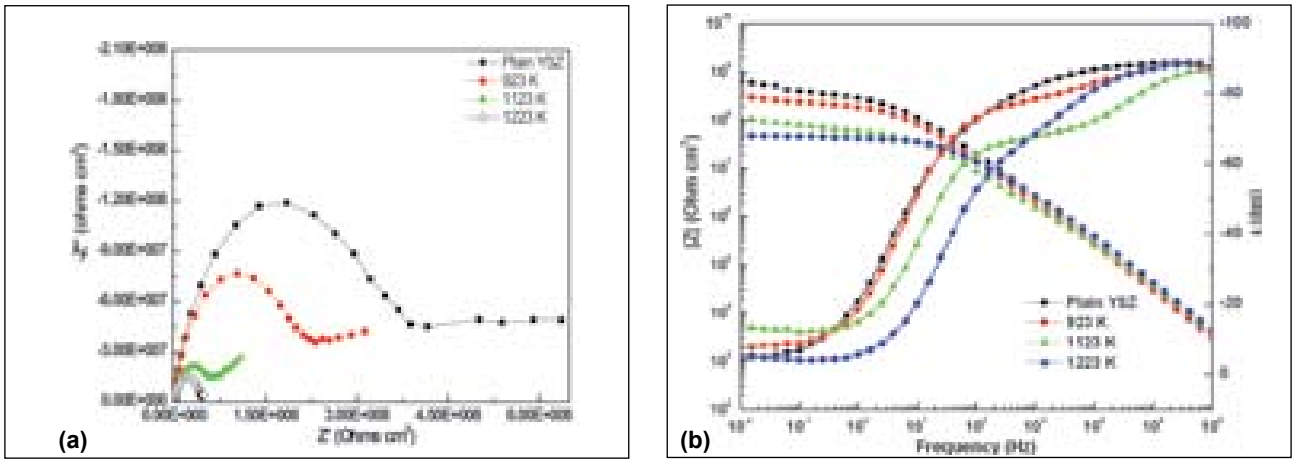

Fig. 4 (a) *Typical Nyquist and (b). Bode plots of YSZ-TBC coated 9Cr-1Mo steel specimens after thermal cycling at different temperatures*

frequency region. The magnitude of the impedance modulus for plain YSZ was greater than that for other TBC-YSZ at different temperatures in all frequency ranges. Higher impedance modulus observed for plain TBC-YSZ coated 9Cr-1Mo steel (order of 10^9 Ω cm^2) from medium to low frequencies suggesting higher coating resistance.

The present investigation shows that thermal cycling life of 9Cr-1Mo steel, bond coated and TBC-YSZ coated 9Cr-1Mo steel is better at temperatures below 923 K while at higher temperature range above 1223 K no transformation of TBC-YSZ phases could be observed in all the tested conditions.

III E.6 Effect of Grain Size Refinement on Ductile to Brittle Transformation Temperature in 9Cr-1Mo Steel

Ferritic steels are excellent materials for clad and wrapper applications of fast breeder reactors, as they exhibit excellent void swelling resistance. The irradiation/thermal embrittlement phenomena leading to increase of ductile to brittle transformation temperature (DBTT) or reduction of upper shelf energy (USE) poses a major obstacle in development of Ferritic steel for core applications of future FBRs. There are many factors that cause higher DBTT in steels, such as: low Mn/C ratio, high C and Cr content and presence of tramp elements (P, S, As, Sb). For a given alloy composition, grain refinement is a unique method that improves the strength as well as the ductility/fracture properties. The 9Cr-1Mo ferritic steel derives its strength from the tempered martensitic microstructure, obtained by Normalizing & Tempering (N&T) treatment. In 9Cr-1Mo steel, the prior-austenite grain size (PAGS) as well as size of the sub-structural features could determine the fracture behavior. In the present study, a two-step normalisation heat treatment has been developed to reduce the grain size, and thereby reduce the DBTT.

Since grain size is primarily a function of austenitisation temperature (T_γ), a lower temperature is beneficial in obtaining smaller grain size. However, a normalizing treatment at lower temperatures results in a martensite with incomplete dissolution of pre-existing carbides due to the sluggish dissolution kinetics. Thus, an austenitisation temperature of about 100-150 K above Ac_3 is generally employed to ensure complete carbide dissolution in steels. Accordingly, the 9 Cr-1 Mo steel ((in wt%) - 9.27 Cr, 1.05 Mo, 0.1 C, 0.75 Si, 0.63 Mn, 0.001 S, 0.02 P) in this study was normalized at 1323 K followed by a tempering treatment at 1023 K, which resulted in a uniform tempered martensitic structure with grain size of ~26 μm and an average hardness of 249 VHN.

In order to reduce the grain size and obtain the desired microstructure, a two-step normalisation treatment was developed. This consisted of an austenitisation at 1323 K

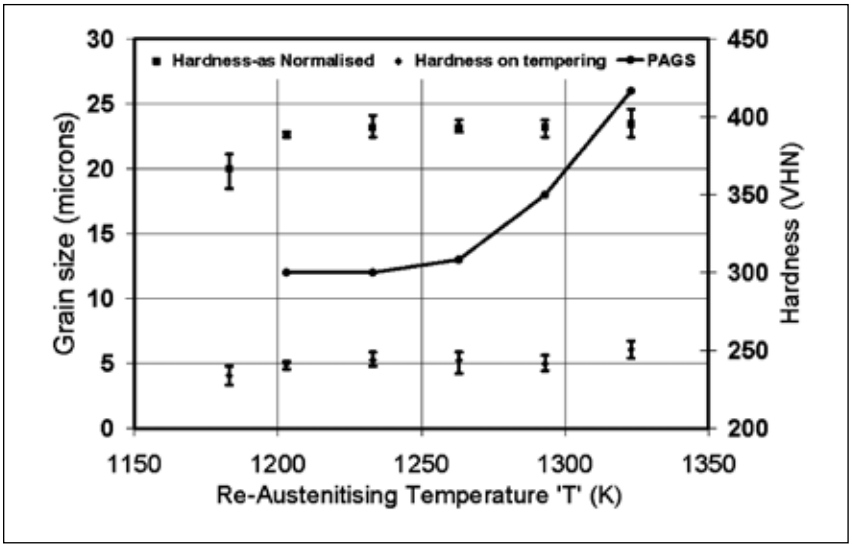

Fig. 1 *Variation of prior-austenite grain size and hardness with austenitisation temperature*

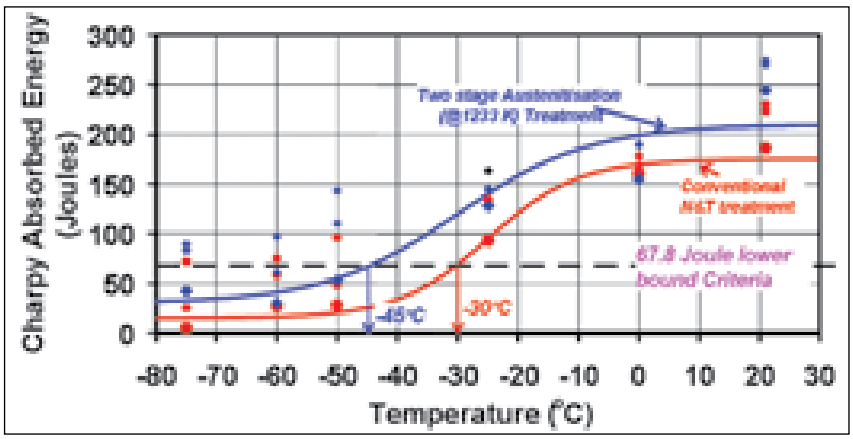

Fig. 2 *Impact energy-temperature curves for conventional N&T and the two step N&T treatment.*

to obtain a complete martensitic structure on cooling, followed by a second normalising treatment at lower temperature (1323 K > T_γ < 1183 K) using a high heating rate to avoid carbide precipitation during the heating, followed by the tempering process. This two-step treatment resulted in a uniform martensitic structure but with a smaller grain size, in contrast to a single step N&T at lower T_γ ~ 1233 K, which resulted in a mixed microstructure of soft ferrite phase and tempered martensite. The variation in PAGS and hardness (before and after tempering) as a function of re-austenitisation temperature is given in Fig. 1. The grain size decreased from 26μm for the conventional austenitisation treatment (1323 K) to 12 μm for re-austenitisation temperature of 1233 K and saturates for further decrease of re-austenitisation temperature. The hardness change was insignificant as the primary strengthening in this steel is due to the substructure.

The impact toughness of the heat treated 9 Cr-1 Mo steel was evaluated by Charpy tests using standard sized V-notch specimens for the two cases, namely coarse grained (26 μm grain size) obtained by conventional N&T treatment and fine grained (12 μm grain size) obtained by the two step treatment. Fig. 2 shows the Charpy absorbed energy as a function of test temperatures. The DBTT was evaluated based on 67.8 Joule lower bound criteria. The fine grained steel showed a reduction in DBTT by 15ºC and increase in USE by about 30 Joules. This study has demonstrated a method of reduction of DBTT by controlled heat treatments in the 9 Cr-1 Mo steel, which is now being studied systematically.

III E.7 Fracture Toughness and Fatigue Crack Growth Studies on Indigenously Developed Modified 9Cr-1Mo Steel and SS 316L(N) weld

For the damage tolerant design and integrity assessment (e.g., LBB analysis) of the components, the fracture toughness and fatigue crack growth (FCG) properties are necessary. An extensive campaign is underway to characterize the fracture behaviour of the structural steels modified 9 Cr-1 Mo steel and SS 316 L(N) under monotonic (both dynamic and quasistatic) and cyclic loading conditions including assessment of the effect of long term service exposure. Quasistatic and cyclic loading investigations are carried out under operating temperatures while dynamic fracture studies of ferritic steels are carried out in the ductile-brittle transition and upper shelf regimes. This article describes a few important results from these studies.

Crack Arrest Toughness of a Modified 9 Cr-1 Mo Steel

Crack arrest toughness (K_{1A}) is an important parameter for design against cleavage fracture of ferritic steels, as one of the measures of material toughness in the transition regime. However, the experimental determination of K_{1A} involves uncertainties in the determination of the load (P_A) and crack length (a_A) at arrest. In a recent study on modified 9 Cr-1 Mo steel with instrumented (precracked) Charpy V (PCCV) impact tests, crack arrest was observed, and a meaningful K_{1A} value was determined; P_A was identified from load (P) –displacement (d) plot (Fig. 1(a)) and a_A measured from the SEM

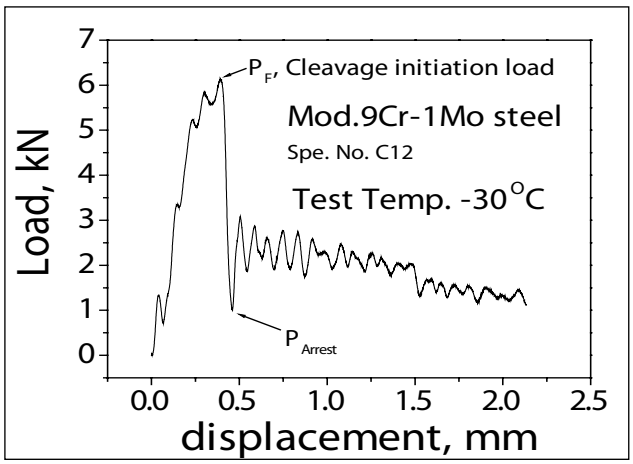

Fig. 1 *(a) P-d plot from PCCV tests*

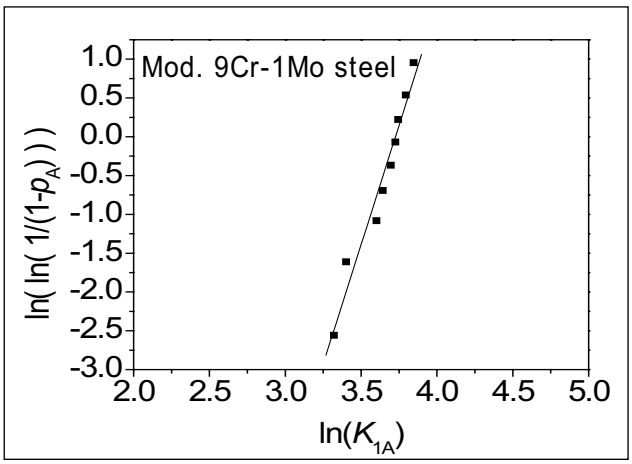

Fig. 1 *(b) Two parameter Weibull plot for arrest toughness*

fractographs. The scatter in K_{IA} due to the local microstructural variations could be described well using a two parameter Weibull distribution (Fig. 1(b)).

Quasistatic Fracture Toughness of a Modified 9 Cr-1 Mo Steel

Fracture toughness of the modified 9 Cr-1 Mo steel developed by our Centre in collaboration with Indian steel industry was characterized under quasistatic loading conditions at ambient and service temperatures 653 and 803 K. The J-R curves for the normalized and tempered material at all the three temperatures are presented in Fig. 2. While the crack growth was by cleavage at ambient conditions, stable ductile tearing was observed at higher temperatures. The J-R curve for ambient temperature is based on the data prior to the onset of cleavage. The J-R curves for 653 and 803 K are similar up to about 0.5 mm total crack growth; however, the tearing modulus is significantly higher for 803 K. The $J_{0.2}$ values were 128 and 160 kJ.m^{-2} at 653 and 803 K respectively which is higher than that suggested by RCC-MR (100 kJ. m^{-2}).

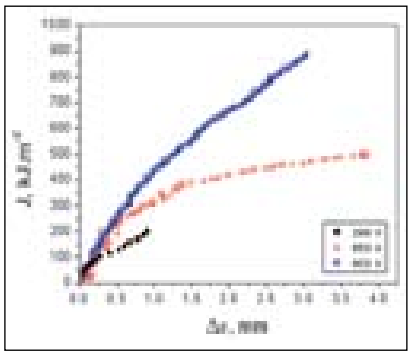

Fig. 2 *J-R curves for the normalised and tempered P91 for 298, 653 and 803K*

Effect of Ageing on Fracture Toughness and FCG Behaviour of SS 316(N) Weld

During long term service exposure of the welds to temperatures in the range 623 and 823K, the normal operating temperatures of the SS 316L(N) components, the δ-ferrite undergoes a variety of solid state transformations. A campaign was conducted to characterize the phase changes during ageing at low temperature (643-823 K) up to twenty thousand hours and their influence on the fracture toughness and FCG behaviour of SS 316 (N) welds prepared using indigenous consumables developed in collaboration with the Indian Industry.

Effect of Low Temperature Ageing on FCG Behaviour of SS 316(N) Weld

Room temperature FCG properties in Paris and threshold regimes were determined. For intermediate crack growth rates, FCG rate is related to the stress intensity factor range by the Paris equation $da/dN = C\Delta K^m$ ΔK_{th}. which is the threshold value of ΔK at which da/dN ostensibly equals zero. C, m and ΔK_{th} characterize the FCG properties of the material in the entire regime.

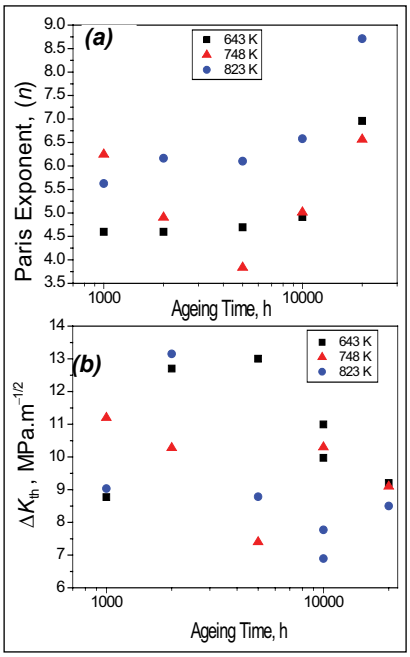

Fig. 3 (a) and (b) *Variation of the FCG parameters for SS 316(N) weld metal with ageing time*

The variations of the Paris constants *m*, and the ΔK_{th} with ageing time are shown in Fig. 3(a) and Fig. 3(b) respectively, for different ageing temperatures. The variation in C was complimentary to that of m for all the conditions. On ageing at 643 and 823 K, the Paris constants showed a slow variation up to ten thousand hours beyond which there is a rapid change. However, for ageing at 748 K, the variation is non-monotonic; the value of m decreases with ageing time up to five thousand hours after which it increases. Unlike in the case of Paris regime, the threshold regime FCG is significantly influenced by ageing at all the three temperatures, and the variation is not monotonic. There is an initial increase in ΔK_{th} with ageing time, beyond which the trend reverses; this trend reversal is faster at 823 K. However, for ageing at 748 K, there is an initial reduction in ΔK_{th} up to five thousand hours followed by an increase indicating that peak ageing at 748 K occurs at five thousand hours The effects of ageing on the FCG behaviour of SS 316(N) weld are complex due to the combined influences of the changes in microstructure and possibly residual stress distributions.

Effect of Ageing on J-R curves of SS 316(N) Weld

Fracture tests were carried out on SS 316(N) weld after ageing at (i) 923 K for four thousand and two hundred hours (advanced ageing according to RCC-MR) and (ii) 823 K for one thousand hours (minor ageing as per RCC-MR). Comparison of the J-R curves for the material in different ageing conditions with that for the as welded material is presented in Fig. 4. The J values are higher than the respective values reported in RCC-MR for this class of welds. While the $J_{0.2}$ values were in the range 200 - 250 kJ.m^{-2} for as welded and aged materials (not significantly affected by the ageing), a drastic reduction in the tearing modulus d*J*/d*a* was observed. Fractography revealed fine dimples characteristic of ductile fracture in the as-welded sample, and intermediate regions of brittle cleavage like facets in the aged material, indicating low energy crack propagation. Further investigations are in progress to confirm the nature of crack growth in the aged material.

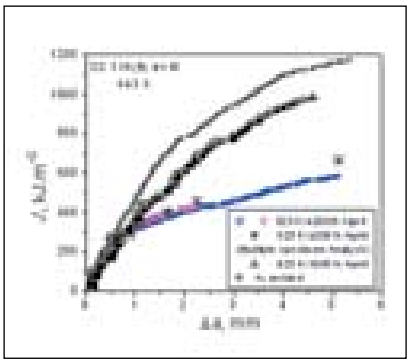

***Fig. 4** J-R Curves for un-aged welds*

III E.8 Irradiation Performance Assessment of Cold Worked SS 316 Structural Material upto 83 dpa

Twenty percent cold worked austenitic stainless steel is used as the wrapper and cladding material in FBTR. Neutron irradiation at high flux levels (>10^{15} n/cm^2/sec) coupled with high temperature of 673- 823 K induces dimensional change in the structural materials due to void swelling and irradiation creep. Degradation in mechanical properties also take place which are associated with microstructural changes. The performance of SS 316 in FBTR has been systematically studied through post-irradiation examination (PIE) at various displacement damages (dpa) corresponding to various burnup levels. PIE techniques used for characterizing the irradiation damage include dimensional measurements in duct and fuel pins, mechanical testing, void swelling measurement and transmission electron microscopy (TEM) studies.

Dimensional measurements carried out on the duct include (i) head-to-foot misalignment (bow) and (ii) changes in the flat-to-flat and corner-to-corner distances. The fuel pins after extraction from the duct are subjected to diameter and length measurements to evaluate the diametral strain and its length increase. The variations in these duct and fuel pin dimensions have a bearing on fuel handling operations and thermal hydraulics of fuel bundle respectively. The trends in the dimensional changes of duct and cladding as a function of fuel burnup are shown in Fig. 1(a) and Fig. 1(b). The void swelling of the cladding determined from

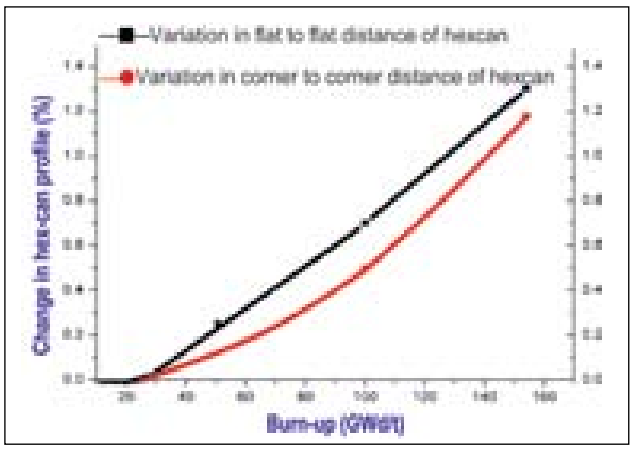

Fig. 1(a) *Changes in hexagonal duct dimensions with burn-up*

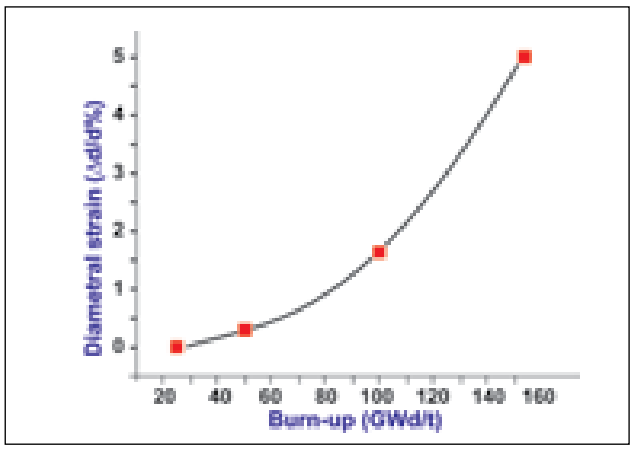

Fig. 1(b) *Diametral strain in fuel pins as a function of burn-up*

immersion density measurements shows a trend similar to that of diametral strain. The maximum volumetric swelling after 83 dpa corresponding to the burn-up of 155 GWd/t is estimated to be around 11.5 %. The higher swelling of the cladding as compared to that of duct is attributed to the higher temperatures seen by the cladding which is close to the peak swelling regime. The trends in the void swelling show a higher rate of increase beyond dpa> 60 which is also evident from the faster rates of dimensional increase in duct and cladding beyond a burnup of 100 GWd/t.

The trends in the ultimate tensile strength (UTS) and ductility of the irradiated cladding as a function of dpa and irradiation temperature are shown in Fig. 2. It is seen that the UTS of the cladding shows a significant decrease at displacement damages > 60 dpa both in high temperature and room temperature tests. The room temperature tensile properties of the duct evaluated using shear punch tests indicate significant hardening and a decrease in the uniform elongation.

Transmission Electron Microscopy (TEM) studies of hexagonal duct showed extensive void formation beyond 40 *dpa* in addition to precipitation and dislocation loops. Fig. 3 shows the TEM micrographs at different dpa superimposed on the swelling curve. The void density showed a progressive increase with displacement damage. The precipitates were identified to be mainly of nickel and silicon enriched M_6C type of η phase, whereas radiation induced G phase was also observed at 83 dpa. The precipitates were found to be associated with the voids which can be understood considering the growth of precipitates being achieved by diffusion of solutes, which in turn brings a vacancy surplus alongwith it. The retention of cold worked structure was unambiguously seen after 83 dpa irradiation which suggests that no recrystallisation has taken place and irradiation hardening is more prominent than the softening effects.

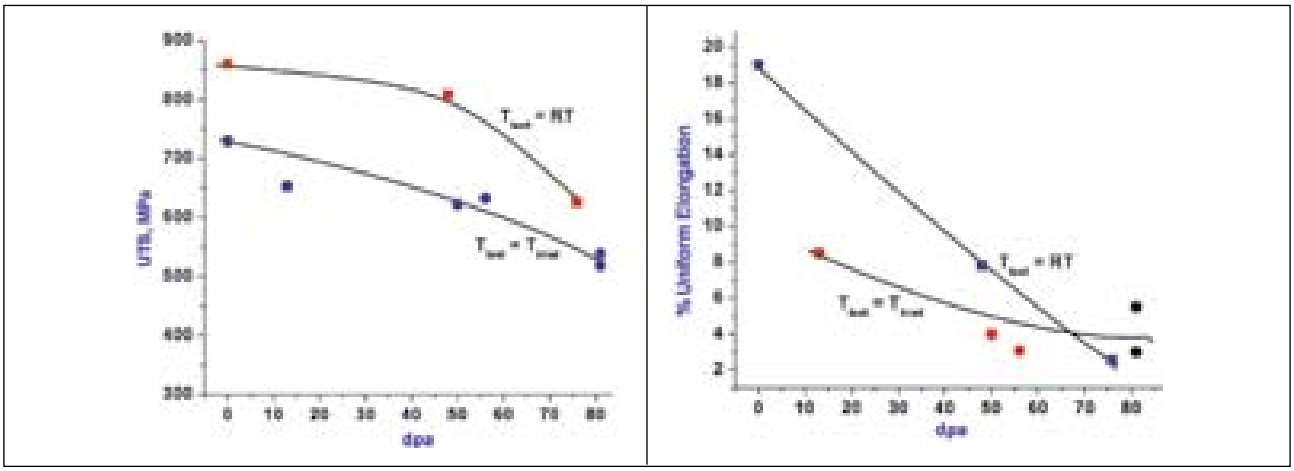

Fig. 2 *Trends in ultimate tensile strength and uniform elongation of SS316 cladding with dpa* T_{irrad} *– Irradiation temperature (703 -793 K), RT - Room temperature (298 K),* T_{test} *– Test temperature*

The PIE results indicate a faster rate of damage in the 20 % CW SS316 duct and cladding at displacement damages greater than 60 dpa. The performance assessment of the core structural material of FBTR by PIE was very useful in extending burnup of the fuel to 155 GWd/t. Based on the thermo-mechanical analysis and available margins for dimensional and ductility changes, it is planned to increase the burnup of one fuel subassembly beyond 155 GWd/t.

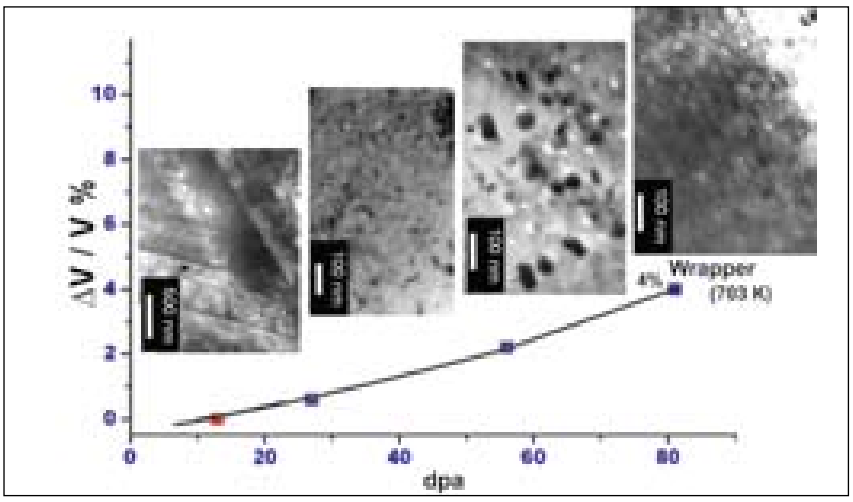

Fig. 3 *TEM micrographs of SS 316 hexcan at various dpa superimposed on the swelling curve.*

III E.9 Towards Development of High Nitrogen Steels as Structural Materials for Future FBRs

SS316 L(N) containing 0.02-0.03 wt% carbon and 0.06-0.08 wt% nitrogen has been used for high temperature structural components of PFBR. Although the current design life of FBRs is generally of the order of forty years, there is a growing interest to design future FBRs with a design life better than sixty years. As a part of the effort to develop structural materials with very long design life, the influence of nitrogen on high temperature mechanical properties at concentrations higher than 0.07 wt% has been evaluated. Four commercial heats of SS 316 L(N) containing 0.07, 0.11, 0.14 and 0.22 wt% nitrogen have been produced. The carbon content in these heats was maintained at 0.03 wt% (Table 1). Nitrogen was found to be beneficial with respect to tensile and creep properties. Yield and ultimate tensile strength were found to increase linearly with increase in nitrogen content in the temperature range of 298-1123 K as shown in Fig. 1(a) and Fig. 1(b). Equations have been established to predict yield and tensile strength as a function of nitrogen content and test temperature. Tensile ductility generally showed a decrease

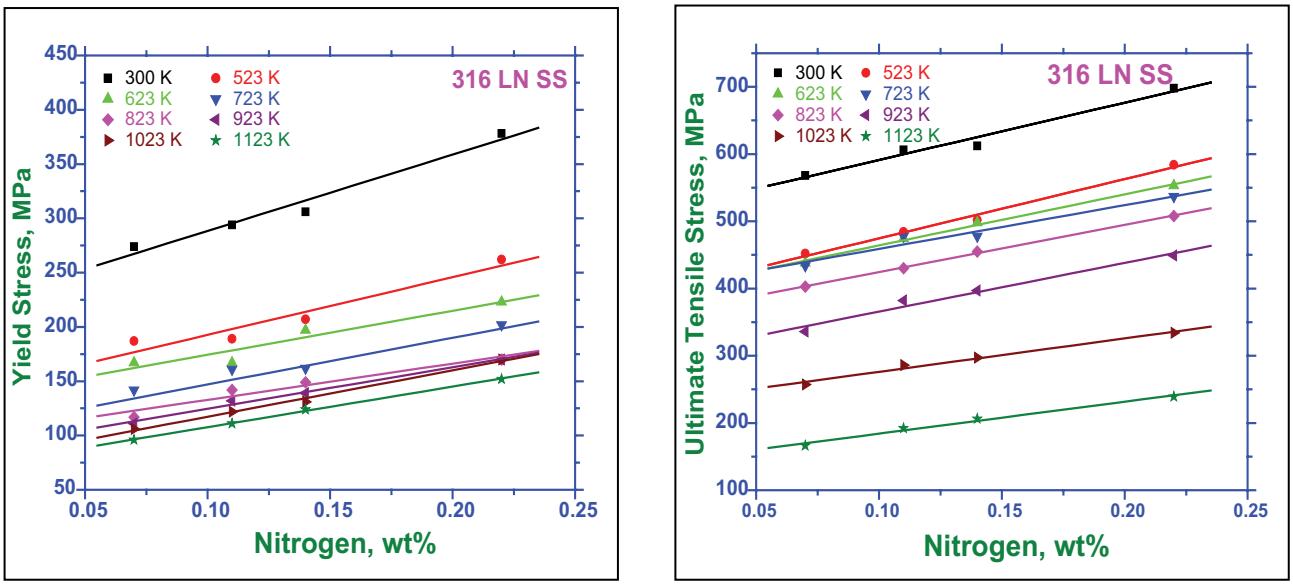

Fig. 1(a) Influence of nitrogen content and tensile test temperature on yield strength and (b) Ultimate tensile strength

with increase in nitrogen content. Creep rupture strength at 923 K increased substantially with increase in nitrogen content (Fig. 2). Steady state creep rate showed a corresponding decrease with increase in nitrogen content. The beneficial effect of nitrogen on the creep strength resulted from the combined effects of increased resistance to recovery of the dislocation substructure and from reduction in the creep damage.

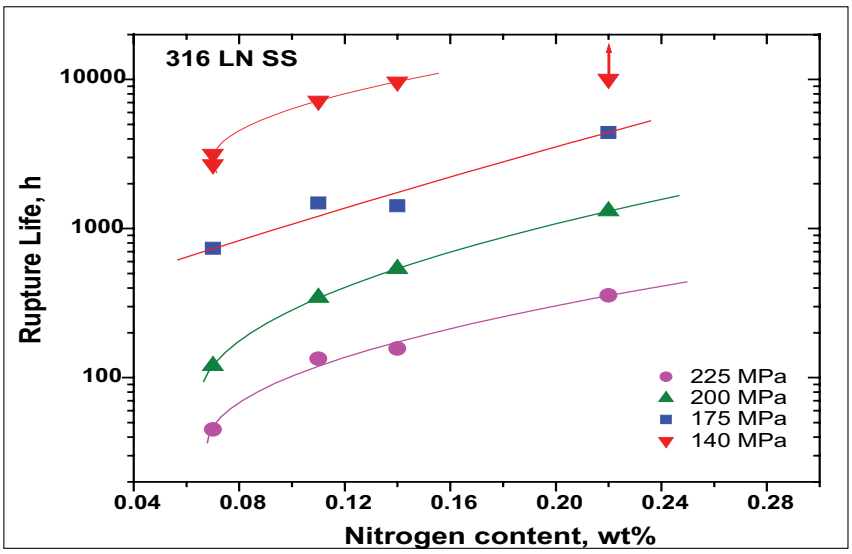

Fig. 2 Influence of nitrogen content on rupture life.

Table 1: Chemical composition of the four heats of 316L(N) SS (in wt%).

Designation	N	C	Mn	Cr	Mo	Ni	Si	S	P
7N	0.07	0.027	1.70	17.53	2.49	12.20	0.22	0.0055	0.013
11N	0.11	0.033	1.78	17.62	2.51	12.27	0.21	0.0055	0.015
14N	0.14	0.025	1.74	17.57	2.53	12.15	0.20	0.0041	0.017
22N	0.22	0.028	1.70	17.57	2.54	12.36	0.20	0.0055	0.018

III E1 Materials-Welding

III E1.1 Studies on Modified 9Cr-1Mo Ferritic Steel Weld Joints

Low Cycle Fatigue and Creep-Fatigue Interaction Behaviour

Low cycle fatigue (LCF) and creep fatigue interaction behavior of shielded metal arc welded modified 9Cr-1Mo similar weld joint in post-weld heat treated (1033 K/3h) condition have been evaluated at 823 and 873 K. Continuous cycling LCF tests were performed using a triangular waveform and creep-fatigue interaction tests were conducted by employing one minute hold at peak strain either in tension or compression. Both the base metal and the weld joint exhibited similar lives at 823K under continuous cycling conditions. At 873K the weld joints displayed lower lives than the base material due to the combined effects of oxidation and creep cavity formation in the soft intercritical heat affected zone. Introduction of hold either at peak tensile strain or peak compression strain reduced the fatigue life of the weld joint significantly at both 823 and 873 K. Application of one minute compressive hold period has a far more deleterious effect on the fatigue life than application of one minute hold under tension due to the different response of the oxide layer to load cycling. During tension hold in air, an oxide coating forms in the surface cracks and leads to crack tip blunting, but the cracks are shut during the compression hold and thus they stay sharp and cause more damage.

In order to quantify the effect of environment in this material, LCF tests were conducted in a pure dynamic sodium environment. The fatigue lives were significantly improved in sodium environment when compared to the data obtained under identical testing conditions in air environment

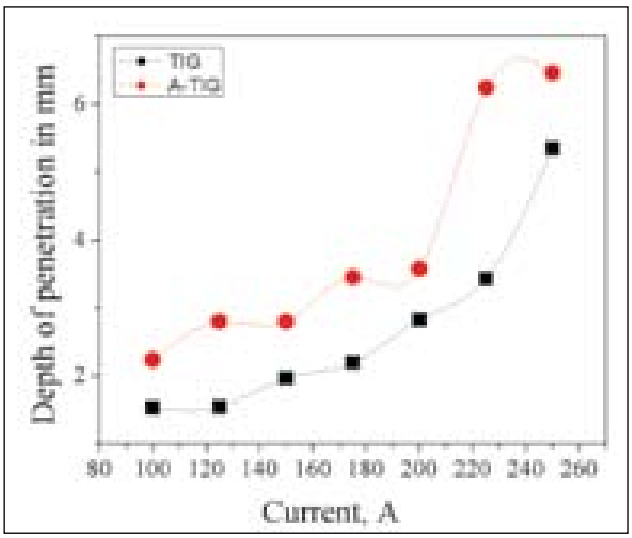

Fig. 1 *Effect of sodium environment on fatigue life of the weld joint at 823K*

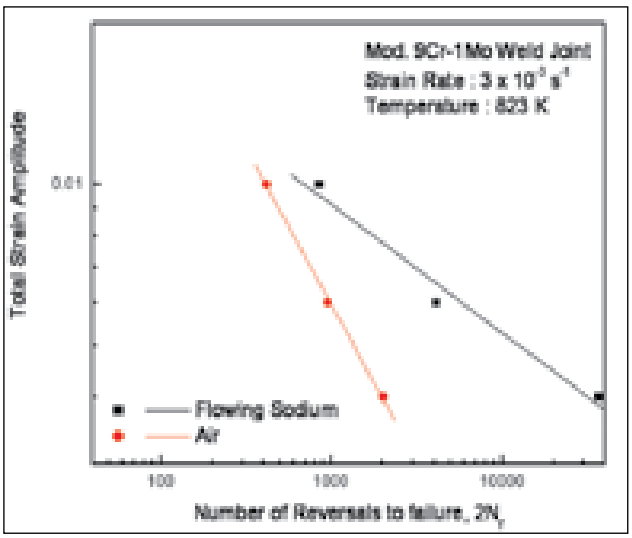

Fig. 3 *Effect of activated flux on depth of penetration as a function of current*

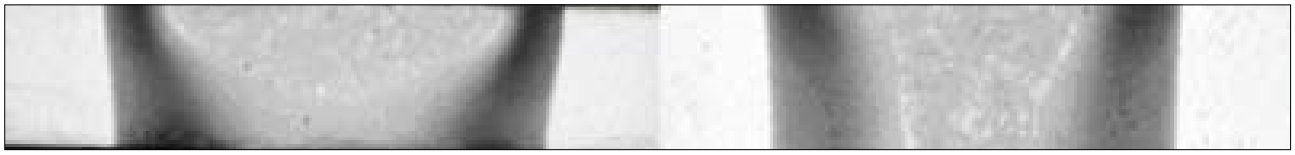

Fig. 2 *Weld bead shape of modified 9 Cr – 1 Mo steel weld (a) without flux and (b) with flux*

(Fig.1). The lack of oxidation in sodium environment is considered to be responsible for the delayed crack initiation and consequent increase in fatigue life.

Development of Activated Flux for Tungsten Inert Gas (TIG) Welding

Activated flux has been developed to improve the process performance of TIG welding of modified 9Cr-1Mo steel. Using the flux, square butt joint welds of 6 mm thick could be made in single pass at reduced heat input values. Fig. 2 compares the weld bead shapes of mod. 9Cr-1Mo steel welds on 6mm thick plate made without and with activated flux. Weld bead was found to be narrow and deep in the case of welds produced using the activated flux. Fig. 3 compares the depth of penetration that could be achieved in single pass TIG welding without and with activated flux in mod. 9 Cr-1Mo steel as a function of current at a torch speed of 16 cm/min. Effect of flux on the microstructure and hardness and tensile properties have been studied. During tensile testing failure was found to occur in the base metal region implying that weld metal is stronger than the base metal. A TIG weld exhibited strength and total elongation values higher than the minimum specified for the weld joints in codes and standards.

III E1.2 Corrosion Fatigue of AISI Type 316LN Stainless Steel and its Weld Metal

The corrosion fatigue behaviour of type 316LN stainless steel base metal was studied in boiling acidified NaCl solution using compact tension specimens by the fracture mechanics approach under different loading and environmental conditions. Also, the difference in corrosion fatigue behaviour of type 316LN stainless steel base metal and type 316N stainless steel weld metal was studied in boiling 45% magnesium chloride ($MgCl_2$) solution using smooth specimens. In the studies on type 316LN stainless steel base metal, carried out at a frequency of 0.1 Hz, with different stress ratios (R-ratios), adjusted by varying both the maximum and minimum stress intensity factors, K_{max} and K_{min} respectively, crack growth rate per cycle (da/dN) increased slightly with increasing R-ratio (Fig. 1). At

both these R-ratios, a significant rise in da/dN was observed at values of ΔK ($=K_{max}-K_{min}$) greater than K_{ISCC}($=27.5 MPa.^{0.5}$) of the material. This rise in da/dN beyond $\Delta K=K_{ISCC}$ decreased with increasing R-ratio. Contrary to the above, tests performed at a frequency of 0.1 Hz, with different R-ratios performed by keeping K_{max} constant and varying K_{min}, da/dN decreased with increasing R-ratio (Fig. 2). Only marginal increase in da/dN was observed with increasing temperature (Fig.3). In some of the crack growth tests at a frequency of 0.1 Hz, open circuit potential (OCP), acoustic emission counts and energy were monitored with respect to time. The results indicated a sudden increase in these parameters at about 7000 seconds and this was related to crack initiation. In the studies on base and weld metals at a frequency of 0.1 Hz and R-ratio of 0.25, type 316N stainless steel weld metal possessed better resistance to corrosion fatigue than type 316LN stainless steel base metal in boiling 45% $MgCl_2$ solution (Fig. 4). The difference in the corrosion fatigue resistance between the base and weld metals decreased with increasing mean stress. No fatigue limit was observed for both the weld and base metals.

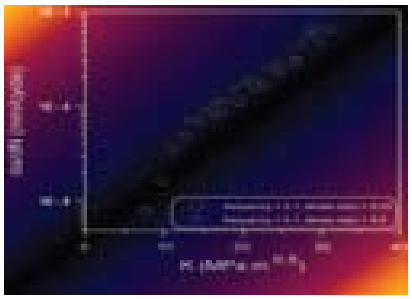

Fig. 1 *da/dN vs ΔK plots at R-ratios of 0.25 and 0.5 at a frequency of 0.1Hz in 5M NaCl + 0.15M Na_2SO_4 + 2.5 ml/l HCl*

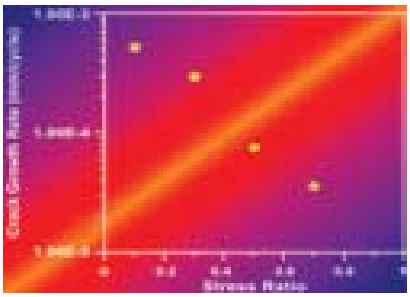

Fig. 2 *Effect of R-ratios on corrosion fatigue crack growth at a frequency of 0.1 Hz. R-ratio was varied by keeping K_{max} constant at a value of 30 MPa.m$^{0.5}$*

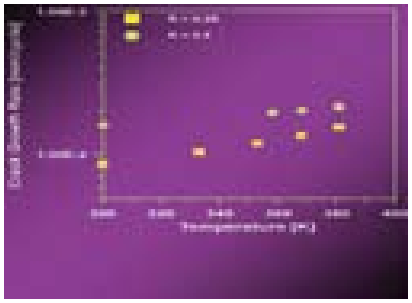

Fig. 3 *Effects of temperature on corrosion fatigue crack growth rate at R-ratios of 0.25 and 0.5 and frequency 0.1 Hz in 5M NaCl + 0.15M Na_2SO_4 + 2.5 ml/l HCl*

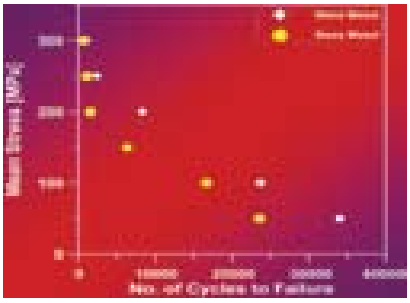

Fig. 4 *Corrosion fatigue behaviour of type 316LN stainless steel base metal and type 316N stainless steel weld metal at a frequency of 0.1 Hz and a stress ratio of 0.25 in boiling 45% $MgCl_2$ solution*

III E1.3 Modeling Methods to Predict Mass Transfer and its Confirmation using Electron Probe Micro Analyzer

Long term exposure of stainless steel to high temperature sodium leads to mass transfer and different forms of corrosion. The surface of the material is either carburized/decarburized depending on the thermodynamic activity of carbon in sodium as well as in stainless steel. Finite difference methods was used to predict the extent of mass transfer in AISI type 316 stainless steel exposed to reactor grade liquid sodium at 823K for 16,000 hours.

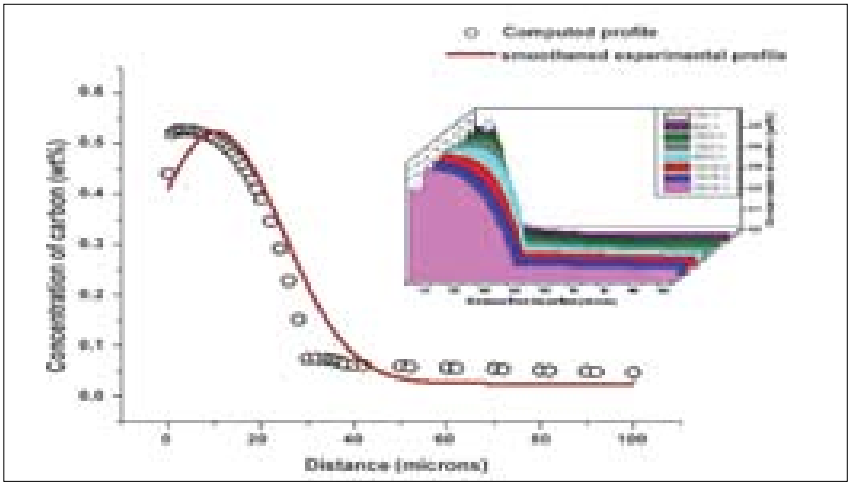

Fig. 1 *Carbon diffusion profiles*

Experimental evidence was obtained for the formation of a carburized layer upto 70μm from the surface in addition to the presence of a ferrite layer (~5μm) on the surface of sodium exposed stainless steel. Using the carbon calibration chart generated using EPMA it was possible to accurately determine the carbon content in the carburized layer. The carbon diffusion profiles simulated using the finite difference method showed reasonable agreement with experimental results (Fig. 1). Simulations predicted that change in the thickness of the carburized layer will reach saturation (max 70μm) after 10000 hours of operation itself at 823K (insert in Fig. 1). Hence, it is inferred that the width of the carburized layer would remain the same, after forty years of exposure to liquid sodium.

III E2 Control & Shielding Materials

III E2.1 Operation Experience in Augmented Boron Enrichment Plant

The augmented boron enrichment plant (ABEP) has been setup at our Centre with a capacity to produce five Kg of 90% enriched ^{10}B per year to meet the requirements of control rod material for FBTR. This plant utilizes the process of ion exchange chromatography for enrichment of this isotope of boron.

ABEP uses fine resin of particle size in the range of 0.075 to 0.150 mm compared to 0.3-1.2 mm in boron enrichment plant (BEP). ABEP was commissioned in April, 2007 and is in continuous operation. The plant has two streams, each having of five process ion exchange columns charged with fine resins. The displacement of borate band is being carried out with a band velocity of 10 cm/h. Whenever a column gets exhausted the resin in the column is hydraulically transferred to regeneration column and after regeneration it is brought back to the same ion exchange column. The average pressure drop observed during the plant operation at a band velocity of 10 cm/h is 1.2 bar per column. Periodically profile samples were taken from the rear end of the borate band and analysed for enrichment of ^{10}B. The 65 % enrichment level in ^{10}B has crossed in eleven months of operation without cut and feed BEP. When normal resin of size 0.3 to 1.2mm is employed for chromatographic operation, took four years to reach the same level of enrichment in ^{10}B with cut and feed. The profile sampling taken after fifteen months of operation shows a maximum enrichment level of 75 % in ^{10}B. The enrichment profile is shown in Fig. 1. The amount of ^{10}B having enrichment between 65 to 70 % and is 4.464 Kgs, between 70 to 75 % is 3.868 Kgs, and more than 75 % is 5.35 Kgs.

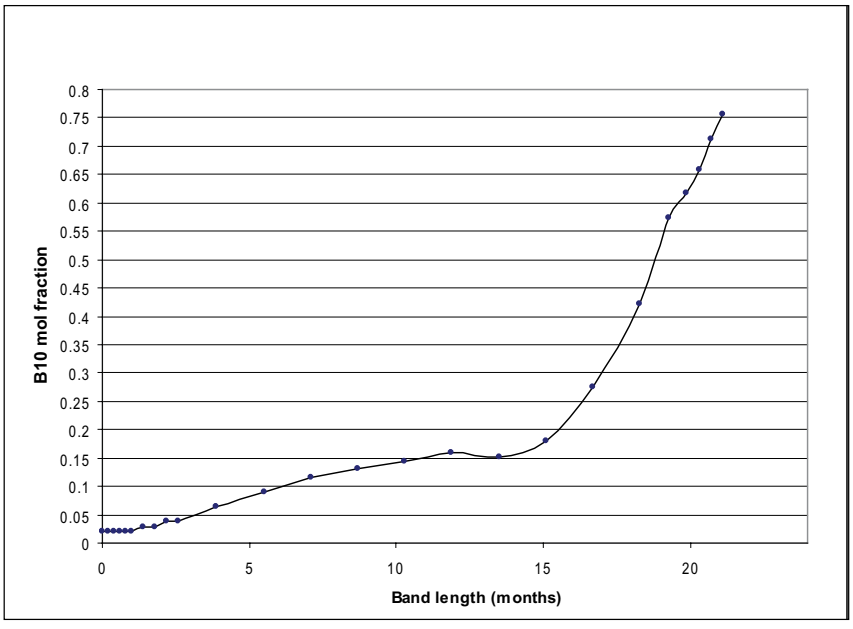

Fig. 1 *Enrichment profile in ABEP*

By using the fine resin, the equilibration time for reaching an enrichment level of 65% in ^{10}B, which is required for PFBR, is brought down to eleven months in ABEP from four years of operation in BEP. The plant is being continuously operated to reach the target level of 90% enrichment level.

III E2.2 Studies on the Ignition and Oxidation Behavior of Electrodeposited Boron Powder

High-density compacts of boron carbide, containing boron enriched in ^{10}B isotope, will be used in the control rods of the PFBR. The boron carbide will be fabricated by reacting elemental boron with carbon. Elemental boron, in turn, is prepared by high temperature electrolysis of potassium fluoroborate dissolved in a molten mixture of potassium fluoride and potassium chloride. A facility to demonstrate the feasibility of production of elemental boron by electrowinning process is being operated at our Centre. During electrolysis, boron is deposited on mild steel cathode. The electrodeposited boron is then powdered to facilitate easy removal of impurities such as iron, nickel, fluoride, chloride etc. However, elemental boron in powder form is pyrophoric and is susceptible to oxidation and hydrolysis. Therefore knowledge of the oxidation and ignition behaviour of elemental boron is important to understand the high reactivity of elemental boron with oxygen. This is also important in preventing loss of elemental boron during production and processing in the form of boric oxide. Hence investigations were carried out to understand the ignition and oxidation behavior of elemental boron using thermogravimetry (TG) and simultaneous differential thermal analysis (DTA) techniques.

Powdered boron can burn in oxygen at a favorable temperature resulting in an explosive combustion reaction. The ignition temperature (T_{ig}) of boron powder is the onset temperature in the differential thermal analysis (DTA) curve when a sudden escalation in the oxidation reaction takes place. The T_{ig} and the effect of heating rate, partial pressure of O_2 and particle size of the boron powder on T_{ig} were investigated. It was observed that the ignition temperature increases with the size of particles for a given heating rate. A powder with finer particles that provide greater surface area is thus more reactive. A low value of T_{ig} for powder with size <44 μm is due to the fact that this fraction contains particles which fall in submicron range also. It was observed that T_{ig} increases with heating rate as shown in Fig. 1. At lower heating rates the temperature gradient across the sample would be less, facilitating a thermal equilibrium. Thus, the measured values of the onset temperature would be closer to the minimum ignition temperatures observed for a given size fraction. Further the maximum gain in the weight due to ignition of boron, as expected, was observed when the sample was heated in a stream of oxygen, irrespective of the size of the constituent particles of the boron powder.

Isothermal TGA experimental data were used to deduce the mechanism of the oxidation of boron and to evaluate kinetic parameters. A plot of fraction reacted 'α' vs time 't' at various experimental temperatures is shown in Fig. 2. In oxidation

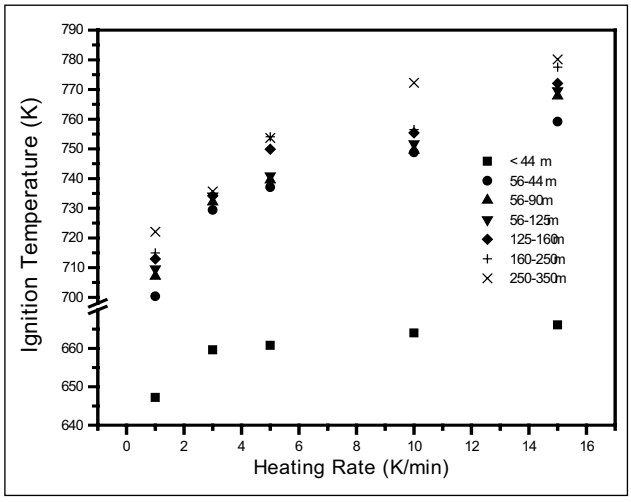

Fig. 1 *Variation of ignition temperature (T_{ig})with heating rate*

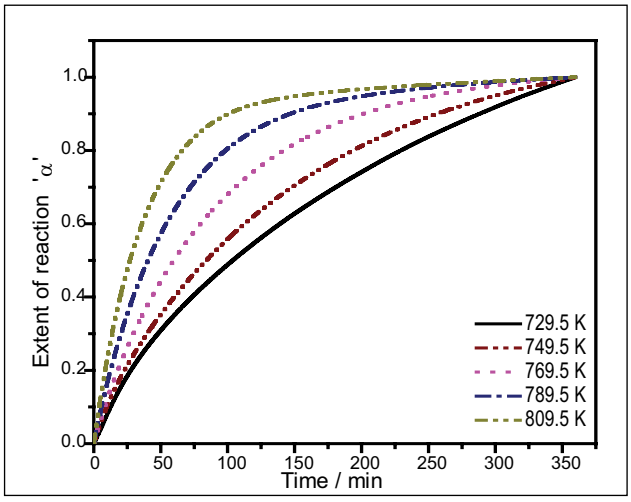

Fig. 2 *Extent of reaction vs time*

reaction, it was deduced that two types of mechanisms were in operation. First order rate law operates from α = 0 to 0.5 and the power law mechanism is operative from α = 0.7 to 1. This is because of the continuous decrease in the number of nucleation sites as the reaction progresses. Nucleation takes place with the formation of product phase on these nucleating sites. This is generally the slowest step in the reaction. Later the growth of the product phase takes place on these nuclei. The activation energies calculated from these rate laws were found to be 79.75 ± 0.62 and -129.45 ± 0.83 kJmol^{-1} respectively. This study establishes that elemental boron could be ignited at temperatures as low as 650 K if the particle size is less than 40 micron. However, the size range of elemental boron employed for the conversion of boron to boron carbide is 10 to 100 micron. Hence it is important to establish a procedure for handling and storage of boron powder with the use of these data.

III E2.3 Neutron Attenuation Measurements with Ferro Boron Slabs in KAMINI Reactor

Reactor core shielding constitutes an important part of fast reactor assembly. An important objective is improved economics and reduction of volume of shields. Ferro boron is identified as a promising shield material through scoping calculations. Experiments were conducted to study neutron attenuation behaviour in ferro boron slabs using the south end neutron beam of KAMINI reactor. The ferro boron slabs were cast with 10 % of boron. The dimensions of the slabs are designed to be more than the size of south beam end slit size to cover the neutron beam completely. The neutron spectrum at the south end of KAMINI reactor is fairly similar to the neutron spectra at the outer shield and sodium regions of PFBR. The experimental measurements are useful for further comparison with other prospective shield and regular materials contemplated for use in outer shield regions of future FBRs.

The experiment was conducted by stacking the ferro boron slabs of different thickness in front of south end neutron beam. The various activation foils were fixed in between the ferro boron slabs at required distances. The foils become activated when subjected to neutron flux and the measurement of their activities from different locations provided information on the neutron attenuation behaviour with respect to ferro boron slabs being used.

In this experiment three Ferro boron slabs of size 300 x 200 mm were used. Thickness of slab placed in the first position was 75mm. The second and third position slabs had thickness of 70mm and 50mm respectively. The overall thickness of the shield model was 195 mm. The bulk density of the Ferro boron slab is around 7.2 g/cc. The slabs were stacked in the south end beam path with the help of a fabricated special stand (Fig. 1). Activation of indium, gold, manganese-copper, rhodium foils and NaCl pellets was carried out. A total of thirty four foils and eight NaCl pellets were used for four different irradiation campaigns. The foils were irradiated at four different locations in the beam path. The first location was at the exit of the south end beam slit. The second, third and fourth locations were at a distance of 7.5 cm (after 1st slab), 14.5 cm (after 2 slabs) and 19.5 cm (after 3 slabs) respectively from the first location.

Measurements of attenuation of reaction rates representative of thermal, epithermal and fast neutrons were carried out in ferro boron slabs. Fig. 2 indicates the reduction factors observed in the activation of manganese, gold,

Fig.1 *Arrangement of Ferro boron slabs with foil holders in KAMINI south end beam path*

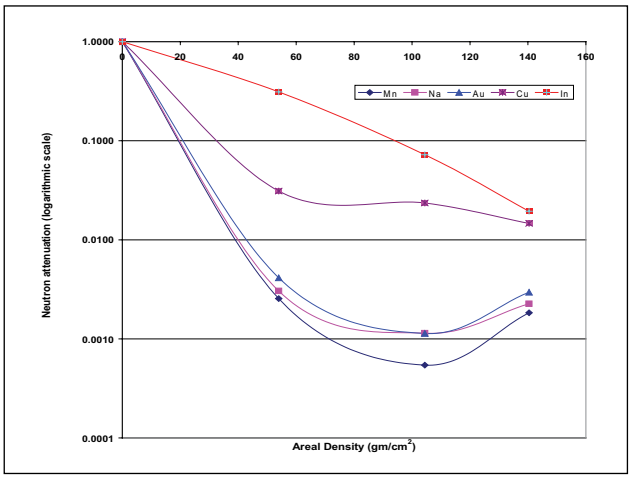

Fig. 2 *Thermal and epithermal neutron attenuation of measured reaction rates of ^{55}Mn (n,γ) ^{56}Mn, ^{197}Au (n,γ) ^{198}Au, ^{23}Na (n,γ) ^{24}Na and ^{63}Cu (n,γ) ^{64}Cu in ferro boron slabs.*

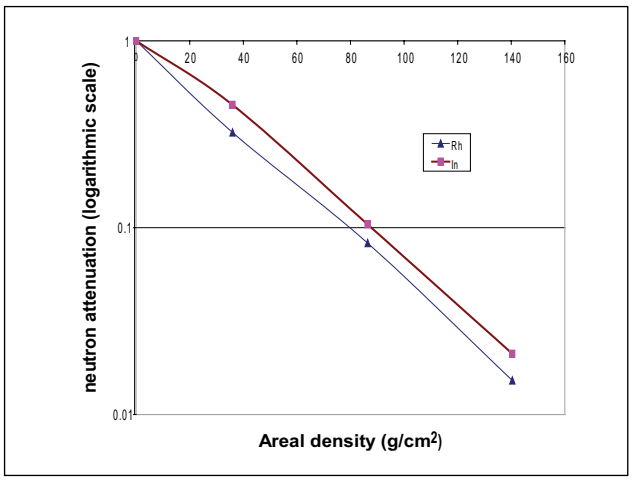

Fig. 3 *Fast neutron attenuation behaviour of $^{103}Rh(n,n')^{103m}Rh$ and $^{115}In(n,n')^{115m}In$ in ferro boron slabs.*

sodium and copper by thermal and epithermal flux attenuation. Reduction in activation of indium and rhodium shown in Fig. 3, represent fast flux attenuation. The attenuation factors observed for the measured reaction rates of Mn^{55} (n,γ) Mn^{56}, Au^{197} (n,γ) Au^{198}, Na^{23} (n,γ) Na^{24}, Cu^{63} (n,γ) Cu^{64} and In^{115} (n,n') In^{115m} through 14.5 cm thick ferro boron slab (equivalent to an aerial density 104.4 gm/cm^2 defined as product of density and thickness) are 1839, 877, 880, 45 and 14 respectively. The measurements in the last location (end of 19.5 cm thick slab (areal density 140.4 gm/cm^2)) of Mn, Na, Au and Cu (to some extent) showed higher values than expected because of reflection effects. But the effect of reflection on the threshold reaction rates of indium and rhodium are not appreciable in the last location. Measurements of activation of rhodium foils established the usefulness of the foils for measuring fast neutron attenuation. Attenuation of rhodium inelastic reaction rates is more than that of indium inelastic reaction because of lower threshold energy for the reaction. This experiment has demonstrated the potential of ferro boron as a shield material.

III F Safety

III F.1 Studies on Characterization of Sodium Aerosols for Fast Reactor Safety

Aerosols are produced in fast reactors in the hypothetical core disruptive accident and sodium leakage from the secondary loop. In the case of most unlikely event of core disruptive accident (CDA) in Liquid Metal Fast Breeder Reactor (LMFBR), the sodium slug may impact the reactor vessel head, and this provides a pathway for the escape of radioactive material (fission products and fuel material) and sodium into the containment. Fuel and fission product vapors will condense and form aerosols. In addition, sodium burning will give rise to various compounds of sodium aerosols. Thus reactor control building is bottled up with large amount of aerosols. The hot sodium burns in air and gives rise to large amount of aerosols. The aerosols generated are mainly sodium oxide (Na_2O) or higher oxides of sodium (Na_2O_2 and NaO_2) depending upon the ratio of sodium to oxygen available during the onset of fire. Since these oxides are highly reactive, they are further converted to sodium hydroxide and sodium carbonate or sodium bi-carbonate upon reaction with water vapor and carbon dioxide present in the environment. The dense

sodium fumes attack chemically vulnerable equipment such as gas blowers, heat exchangers, air filters and electrical components. It is to be noted that the threshold limiting value (TLV) for atmospheric concentration of soda is 2 mg/m^3. The aerosols can pose radiation hazard when they are released from RCB and inhalation health hazard to radiation workers and public when there is a large sodium fire in steam generation building. Hence the time evolution behaviour of sodium aerosols inside the RCB and the chemical speciation of sodium in aerosol phase are important properties to be studied.

In order to study the characterization of sodium aerosols, aerosol test facility has been designed, fabricated and commissioned at our Centre. It consists of an aerosol chamber of volume one m^3, a plasma torch for the production of aerosols of fission products and fuel equivalent materials, a sodium combustion cell for the production of sodium aerosols, aerosol measurement apparatus, humidity and auxiliary systems such as water cooling, air flow, gas flow, pneumatic control, vacuum, material handling systems and on-line data acquisition system for temperature, pressure and RH during experiments. Aerosol measurement apparatus are connected at various ports of the chamber.

Enhanced Brownian coagulation of sodium aerosols under gamma radiation field

During CDA, the Reactor Containment Building is bottled-up with large amount of sodium aerosols along with fuel and fission products associated with very high gamma radiation field. Due to the gamma radiation the aerosols acquire distribution of bi-polar charges. When the aerosols undergo Brownian coagulation while they are charged, the coagulation coefficient is enhanced due to the Coulomb force of attraction. In the present work, experiments were carried out by generating sodium compound aerosols in the aerosol test facility and exposing the chamber volume panoramically with gamma radiation source. By using a light scattering technique, the real time changes in number, concentration of aerosols and their volume-size distributions were measured (Fig. 1). From the data, the coagulation coefficient is derived with and without the presence of gamma radiation field. It is observed that the coagulation coefficient is nearly one order more in the case of gamma field than without gamma field. This result is a strong experimental evidence for the theoretical studies on enhanced Brownian coagulation. It is observed from the results that in the presence of gamma field there is an enhanced Brownian coagulation of sodium aerosols. The result is useful in the safety studies of fast reactors in that, in a confined environment, the enhanced coagulation induces gravitational settling and it is to be applied in the computer codes while predicting the behavior of suspended aerosols (activity) inside the RCB.

There is strong evidence from our experimental results that there is an enhanced coagulation of sodium aerosols when they are bipolarly charged by radioactive source and the enhanced coagulation induces gravitational settling. Further, it has been confirmed that in the case of sodium leakage in secondary loop, the composition of sodium compound aerosol during the transit time between the on set of fire and up to 500 s, before reaching the site boundary, would completely be converted to carbonate (Fig. 2).

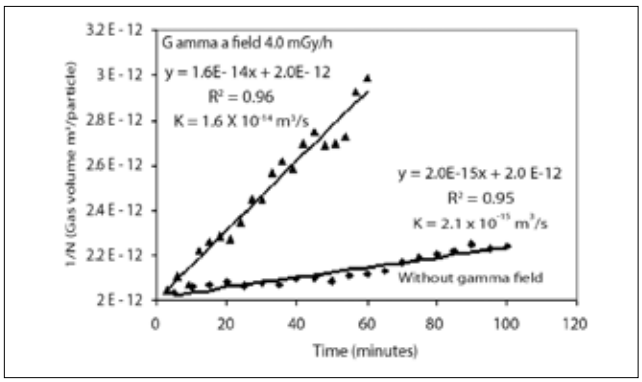

Fig.1 *Average gas volume per article (m^3) 1/N Vs Time graph*

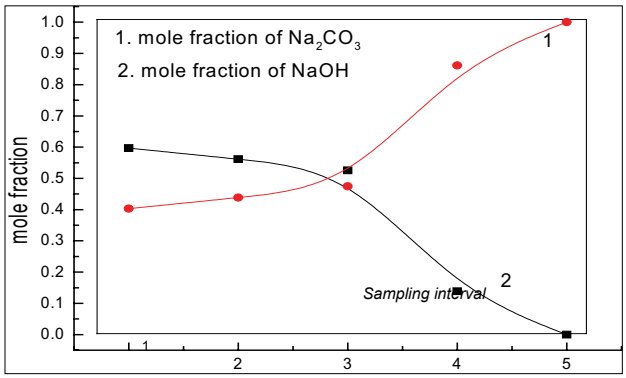

Fig.2 *The composition of sodium compound aerosol in the aerosol chamber at various time interval 50%RH. 1 represents 1st 100 s interval, 2 represents 2nd 100 s interval*

III F.2 IGSHIELD: A New Interactive Point Kernel Gamma Ray Shielding Code

An interactive gamma-ray shielding (IGSHIELD) code has been developed in Visual Basic. The computational methodology is based on the point kernel technique. In the point kernel technique, the large volume sources are divided into arbitrary predefined smaller volumes, which can be considered as a point source with appropriate source weight. The centroid co-ordinates of such small sources are calculated and these positions are considered as their location. From each such source point, optical path traversed in the source and shield media up to the detector location is estimated to calculate geometrical and material attenuations to get uncollided dose rate. Subsequently, this is multiplied with the appropriate dose buildup factor (accounts for scattered contribution) to get total dose rate. Finally, the dose rate for entire volume source is obtained by summing over all the sampled points.

The salient features of the code are: i) provision to declare point, line, plane, sphere, slab, cylinder, hexagonal cylinder and cone as sources ii) handling of multiple source shapes with accompanying energy distributions, iii) arbitrary orientation of sources and iv) provision to declare array of sources. The source bodies such as hexagonal cylinder and cone will be of immense use for calculations involving hexagonal shaped cylindrical sub-assemblies of fast reactors and cone shaped radioactive plume release from stack. The source array option will be of use for calculations involving stacked radioactive drums in vast storage areas. The code is validated by comparing the results for the standard shielding problems with analytical equations and Monte Carlo N-Particle (MCNP) code. Several sample problems encountered in nuclear industry and other useful information required for shield designers and analysts are the other highlights of the code. The input for any kind of situation can be prepared easily using the forms that flash with appropriate prompts. Since entry of data is the important part of the input, its validity is checked immediately and the user is cautioned against incorrect data. The input module accepts only the correct data. If the data happens to be an object, the code instantaneously displays the 3D view of all the objects built so far. Thus, the interactive gamma shielding code will cater to the needs of a shield designer as well as serve as an excellent educational tool. The main input source options are pictorially shown in Fig.1.

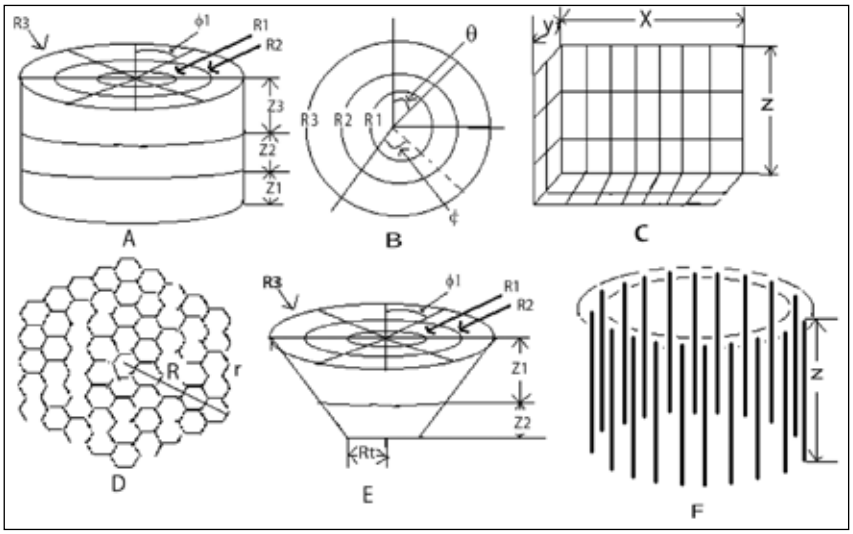

Fig.1 *Source options of IGSHIELD (A) Cylindrical source (B) Spherical source (C) Slab source (D) Hexagonal source, (E) Truncated right circular cone (F) Array of line sources*

This code can be applied only to situations where the basic point kernel technique is applicable. The user has to essentially select a medium for the buildup factor calculation based on the source shield configuration and knowledge regarding the selection of medium. The code is capable of handling upto 1000 zones constructed using basic bodies and 100 gamma energies in a single input. The accuracy of the code is governed mainly by the contribution of scattered dose component calculated using infinite medium buildup factor. The variation could be within few percent and only in unusual cases it will reach 20 to 30%.

III F.3 Design and Implementation of Mobile Radiation Survey System

Detecting and measuring radiation field is one of the primary concerns for any nuclear establishment. An efficient safety and monitoring system requires both stationary and portable units for radiation detection and measurement. While there are a number of monitoring devices and instrument for in situ applications in plants and in surrounding regions, there is a need for a reliable and rugged system for monitoring during mobile surveys. Such an instrument would have wide ranging applications in survey, detection and identification of hot spots of gamma contamination in the environment. It would also be a useful tool in radiation screening of wide areas in private and public domain during transport accident involving nuclear material or during untoward incidents in public domain in addition to surveys during routine and emergency situations. One such instrument has been developed at our Centre.

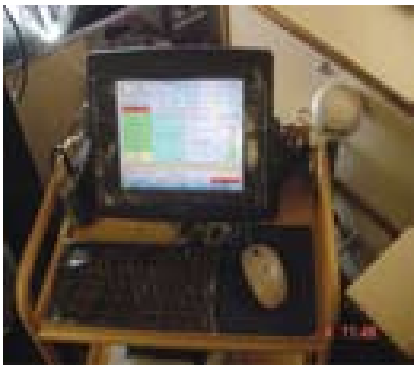

Fig.1 *Mobile Radiation Survey System mounted in a survey van*

Features

The system is based on an energy compensated GM, ZP1221/01 of M/s. Centronic Ltd, as the detector, which provides the real time data for assessment of environmental radiation at the location / point of interest (Fig. 1). The unit is also equipped with a GPS unit which provides the latitude and longitude of the location inaddition to time. A novel feature of the system is the real time navigational help on a geographical map of the region and archiving of data in the storage medium. A number of innovative features have been incorporated in the system to make it extremely rugged, versatile and easy to use during a field survey.

The software used for the data acquisition is DASYLab 9.0, a module based application software tool that does not need off line compiling before use. The data is archived in ASCII format as well as in an EXCEL file. A widely used navigation software is 'nRoute' which is provided by GARMIN. It has an in-built world map of reasonably high resolution which is used as a navigation aid during the field survey.

A very rugged vehicle mounted platform TREK-775 of ADVANTECH designed to withstand harsh environments has been used for this application.

Fig.2 *Navigational tool with real time track and satellite signal strength details*

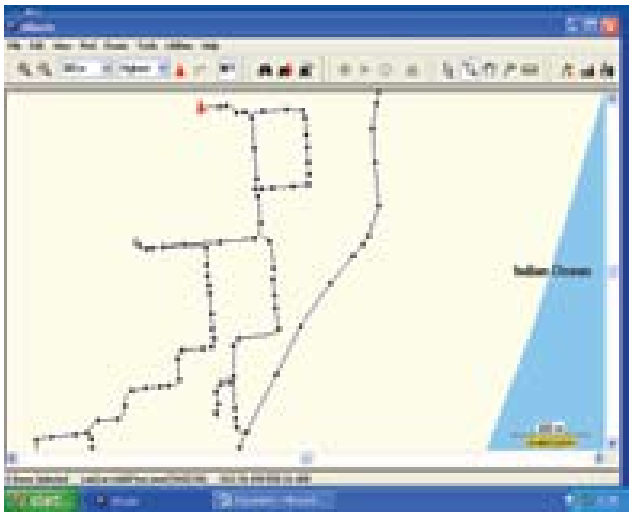

Fig.3 *The track shown on 300m scale*

Implementation and field survey

Fig. 1 shows the instrument mounted in a mobile monitoring van during one of the field surveys. Fig 2. shows the navigational map and the location of the instrument with real time track and satellite signal strength details during a field survey. The red triangle at a location on the map identifies the current location based on the GPS coordinates. The environmental radiation data averaged for the selected duration is continuously shown in nGy/h.

An initial field survey was conducted with the MRSS on 4th Sept 2008 inside the DAE complex at Kalpakkam covering a distance of 7 km in North South direction (KKM Gate in the North to Main Gate in the South) and about 1.5 km in East West direction. The survey was conducted along the major roads inside the site. The survey took about 75 minutes. Radiation data was gathered with an averaging time of five seconds and the vehicle maintained an average speed of about 35 km/h. The system performance has been excellent and the data archival has been 100%. The survey track can be seen in 1.5 km and 300m map scales (Fig. 3). These navigational screens are available in real time during the actual field survey. When the track is seen as an overlay on the sketch/map of the facility, it would appear as shown in Fig 4.

Fig.4 *Survey track shown over the facility map*

III F.4 GPS Sonde Ground Station at Kalpakkam for Atmospheric Profiling

Atmospheric observations are vital for understanding the vertical structure of the atmosphere, its stability, boundary layer wind field and its turbulence, modeling of air-borne effluent plume dispersion, and also for initialization/validation of numerical atmospheric codes used in site specific studies. GPS Sonde is a state of the art atmospheric profiler for probing both the lower and upper atmosphere (upto the stratosphere) using GPS navigation techniques. Ours is one of the nodal centers identified under the atmospheric boundary

Fig.1 *GPS Sonde payload and the balloon with He gas*

layer network and characterization (ABLN&C) project of ISRO. A GPS Sonde ground station is successfully set up at Kalpakkam in collaboration with ISRO as part of the ISRO-Geo-sphere Bio-sphere Programme (IGBP) for measurement of the atmospheric parameters in the atmospheric boundary layer at the coastal site and for atmospheric studies.

The GPS-Sonde was indigenously designed and developed by the Space Physics Laboratory of VSSC, Tiruvananthapuram at a comparatively low operational cost and high data precision. Unlike the conventional Radiosonde used at national weather stations, operation of GPS Sonde is quite simple and does not require radar tracking. The ISRO GPS Sonde named as the 'Dr.Pisharoty Sonde' has a GPS receiver and is operable with battery power (Fig. 1). The ground station receiver is a compact 2U system with frequency programmability and in-built rechargeable battery and data storage capabilities, The instrument can be easily carried and installed at any location for conducting field meteorological experiments. It has a payload of sensors for measurement of temperature, humidity, pressure in addition to having a twelve channel integrated patch antenna GPS module all packed in a compact low weight capsule. The novel feature of the ground station is that it has dual antenna (Quadrifilar and Monopole) to avoid the conventional mechanical tracking. The wind speed and direction are derived from the GPS tracked data.

Fig. 2 shows the vertical profile measured by the GPS Sonde

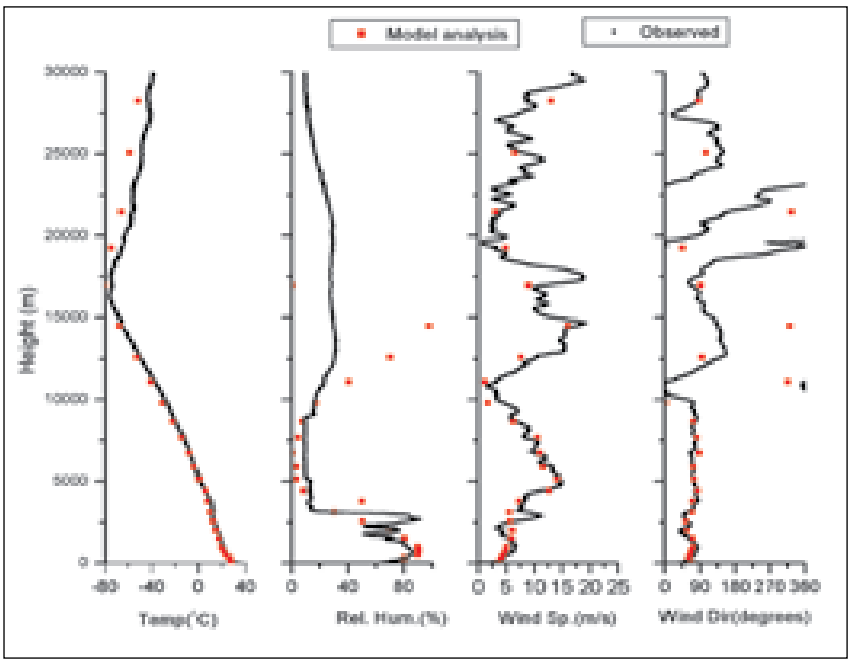

Fig.2 *Vertical profile of meteorological parameters from GPS Sonde and numerical model*

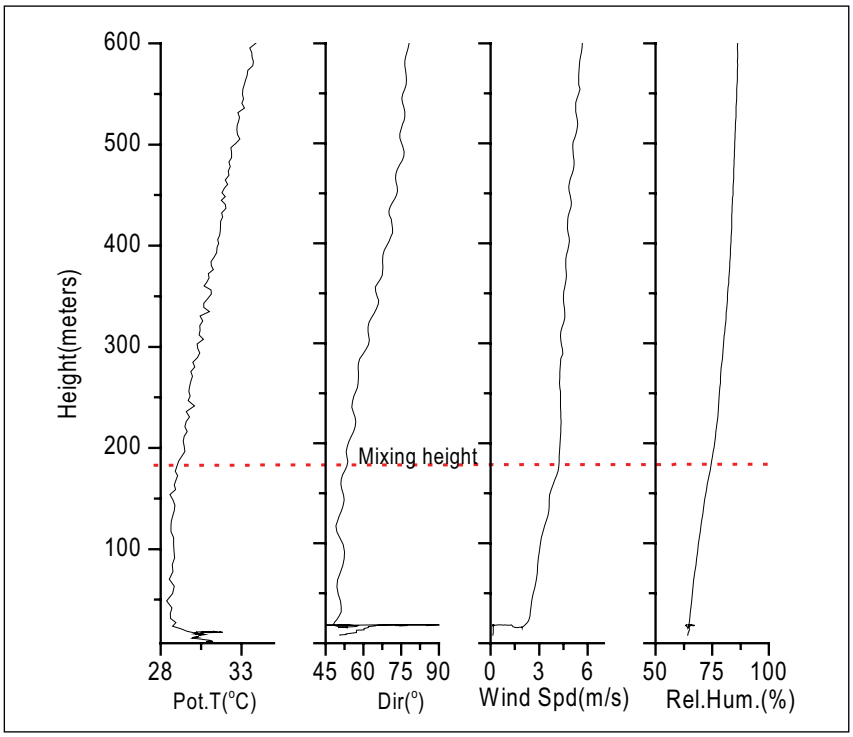

Fig.3 *Boundary layer profile from GPS Sonde*

on 10th November 2008. Balloon ascended at 5 m/s rate upto a height of 35 km. The data corresponds to a typical north east monsoon period and compares well with model prediction at standard pressure levels. The most interesting part is the lower atmosphere shown zoomed in Fig 3. A mixing height of about 180 m is discernible from the profiles that signify the vertical extent of pollution mixing at that instant of the day.

It is proposed to launch the balloon at regular intervals for a long period for site characterization and model validation studies.

III F.5 Development of Low Density Porous Carbon Foam – A Radionuclide Trap Material

In fast reactors, radioactive fission products like ^{131}I, ^{134}Cs, ^{137}Cs, ^{140}Ba, ^{144}Ce etc. get accumulated as the fission reaction progresses within the fuel pin. Any untoward failure of clad leads to the release followed by transport and deposition of these fission products at various locations of the primary circuit and cause high radioactivity burden to the operating and maintenance personnel. In order to reduce this activity burden, Radio Nuclide Traps (RNT) need to be incorporated in the primary sodium circuits thereby minimizing radiation field at other parts of the circuits. In order to remove the isotopes of cesium from sodium and carbon based trap material, viz., Reticulated Vitreous Carbon (RVC) is used. Owing to the difficulties encountered in importing this material, we attempted to indigenously produce the same. A low density home made porous carbon (HMPC) foam that could serve as a substitute to RVC, was synthesized and characterized by using various techniques. The effectiveness of RVC and HMPC in the removal of cesium isotopes were studied.

HMPC was synthesized from an acidic sucrose solution. The typical synthesis involved heating this mixture to 383 K under stirring to obtain a dark viscous resin. Subsequently, this resin was decomposed in air over a period of 48 hours in order to obtain the "green foam". This product was heated in the temperature range 573-1473 K under inert atmosphere to get the final product. Various analytical techniques such as infrared spectroscopy, powder X-ray diffraction, scanning electron microscopy and thermal analyses were employed to characterize and estimate the stability of this product.

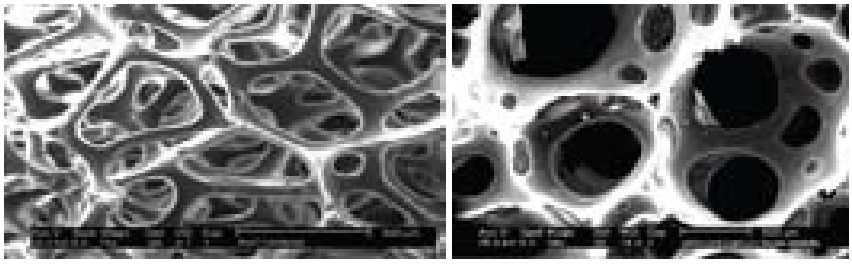

Fig. 1 *Scanning electron microscopic image of reticulated vitreous carbon and home made porous carbon*

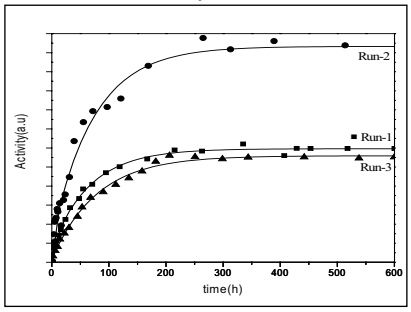

Fig. 2 *Cesium uptake by reticulated vitreous carbon*

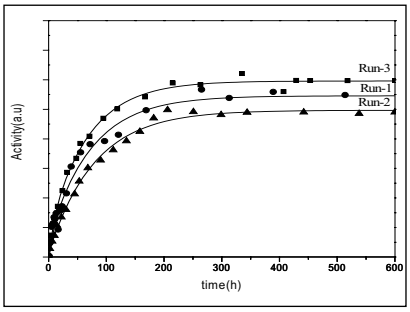

Fig. 3 *Cesium uptake by home made porous carbon*

Cesium trapping experiments were conducted in a static sodium system containing a known quantity of ^{137}Cs using cylinders of RVC and HMPC. ^{137}Cs uptake by RVC and HMPC at known intervals were estimated by using a NaI(Tl) detector.

Fig. 1 shows the secondary electron images of RVC and HMPC. From these SEM images, the average pore size of HMPC and RVC were comparable and was found to be 550 and 600 μm respectively. It was also found that the extent of graphitization of HMPC increased with the sintering temperature. The uptake kinetics of ^{137}Cs by RVC and HMPC are shown in Fig. 2 and Fig. 3. From these figures it can be seen that both these trap materials get saturated with cesium after about 200 h of exposure. The efficiency of cesium trapping and distribution coefficient (K_D) values obtained in the experiments using RVC and HMPC are given in Table 1. The K_D values were calculated by using the equation given below.

$$(K_D) = \left[\frac{\text{Mole of Cs in C}}{\text{Mole of C}}\right] \Big/ \left[\frac{\text{Mole of Cs in Na}}{\text{Mole of Na}}\right]$$

The trapping efficiency of a given materials is measured in terms of the (percentage) uptake of the radionuclide to be removed. The lower values for trapping efficiency and lower distribution coefficient observed with HMPC in comparison with RVC are attributed to the limited surface area (low porosity) and lesser extent of graphitization of HMPC.

Table 1: Experimental details of trap studies using RVC and HMPC

	Cesium activity (μCi)			Wt. (g) of		K_D	Efficiency (%)
	taken	trapped	remaining	trap material	sodium		
RVC							
Run-1	14	12.4	1.6	0.052	22	1.7×10^3	88
Run-2	30	28	2	0.047	23	3.5×10^3	93
Run-3	12	10	2	0.042	23	1.4×10^3	83
HMPC							
Run-1	15	11	4	0.066	23	4.9×10^2	73
Run-2	13	10	3	0.067	23	6.0×10^2	77
Run-3	16	12	4	0.072	23	4.9×10^2	75

However, the trapping efficiency of HMPC is high enough to satisfy the trapping criteria of ^{137}Cs from the sodium coolant circuits of fast reactors. Efforts are in progress to increase the porosity as well as the extent of graphitization of HMPC for use as a material for effectively trapping the isotopes of cesium.

III F.6 Comparison of Neutronics Parameters of a Carbide Core Benchmark with ERANOS 2.1 and FARCOB

Analysis of a 1500 MWe mixed carbide FBR benchmark was carried out using the European state-of-the-art code system ERANOS 2.1 and IGCAR code system FARCOB, under a collaboration in liquid metal fast reactor safety between CEA, France and our Centre. The acronym ERANOS stands for the European Reactor Analysis Optimised calculation System. It contains the nuclear data libraries, codes and calculation procedures, which have been developed within the European collaboration on fast reactors over the past twenty years or so. The IGCAR code system contains ABBN-93-CONSYST-EFCONSY1-COHINT-FARCOB.

The design of pin, subassembly and core of this benchmark was made at our Centre based on the design specifications from CEA, viz. burnup of 200 GWd/t, sodium void coefficient less than 2.5 $, core breeding ratio greater than one and maximum radiation damage of 200 dpa etc. The plutonium enrichments in core-1, core-2 and

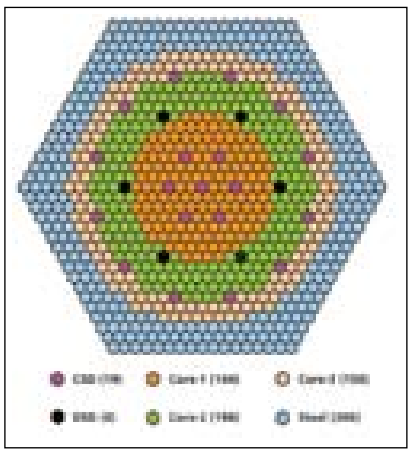

Fig.1 *Carbide core benchmark*

Table 1: Design data of carbide core

Parameter	Value	Parameter	Value
Smear density	80%	Linear power (Max)	500 W/cm
Pellet diameter	6.411 mm	Fuel column length	1000 mm
Pellet density	90% of TD	Plenum length	600 mm
Clad inner/outer dia	6.8 /8.0 mm	Axial blanket length	300 mm
Clad thickness	0.6 mm	Total pin length	2300 mm
Width across flats (outer)	151.4 mm	Pitch between pins	9.7 mm
Spacer wire diameter	1.65 mm	Number of Pins	217
Pitch between SA	155 mm	Thickness of wrapper	3.6 mm

core-3 were optimised as 15.1, 16.1 and 20.2% respectively. No radial blanket is provided. The upper axial blanket is replaced with a plenum to reduce the sodium void reactivity. There are two shutdown systems, viz. Control and Shutdown Systems (CSD) and Diverse Shutdown Systems (DSD). The CSD contains nineteen absorber rods of EFR type, whereas DSD contains six rods. The core configuration is given in Fig. 1. Table 1 summarises the important design parameters of this benchmark.

Three dimensional diffusion theory calculations were performed to estimate the neutronics parameters. The nuclear data used for ERANOS calculations was the latest JEFF3.1 based library called ECCOLIB-JEFF3.1. The results of this analysis is summarised in Table 2. It is seen that multiplication factor differs by 357 pcm between ERANOS and FARCOB, whereas a close agreement is seen for Doppler worth, Breeding ratio, burn-up loss of reactivity and sub-assembly-wise power distribution. However, in the present design the sodium void is worth about 4$.

Table 2: Results of carbide core analysis with FARCOB and ERANOS 2.1

Parameter	FARCOB	ERANOS 2.1
k-eff	1.00697	1.00340
Delayed neutron fraction (pcm)	400	373
Doppler worth (pcm)	-963	-971
Breeding Ratio	1.251	1.256
Sodium void worth (pcm)	+1547	+1813
Peak SA power	Deviation of 1.8 and 2.9% at BOC-1 and EOC-1	
Burn-up loss of reactivity	Close prediction for Cycles 1 & 2.	

III F.7 Evaluation of Alumina Lined Structural Concrete for Sodium Fire

A cubical structural concrete block (330 mm x 300 mm x 300 mm) with a central cavity (160 mm x 160 mm x 110 mm) lined with 6 mm thick alumina tiles (M/s. Jyothi Cermics, Nasik) was subjected to a pool sodium fire. The tiles were laid using ZIRCOAT binder. The block is provided with thirteen thermocouples in thermo-wells at various depths and locations as shown in Fig. 1, to monitor the temperature changes that occur during the progress of sodium (fire) concrete interaction.

About 1.3 kg of liquid sodium at 823 K was loaded into the lined cavity. Contrary to the expectations, the dumped sodium cooled down rapidly and there was little or no fire for the first half an hour. After this initial period, sodium pool temperature gradually increased, fire started and increased rapidly to a steady level. Sodium was allowed to burn until self-extinguishment took place (about an hour and a half). The temperatures recorded in the pool and the concrete block during the run are shown in Fig. 2 and Fig. 3 respectively. As indicated in Fig. 2,

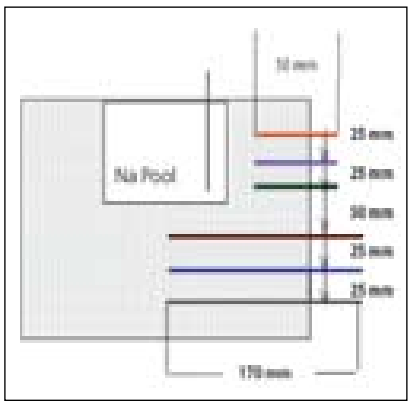

Fig.1 *Thermocouple positions in the concrete block*

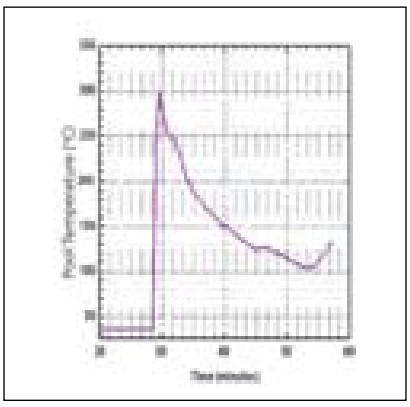

Fig.2 *Temperature in the Sodium pool during charging*

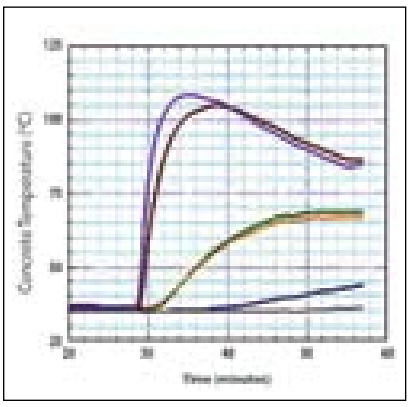

Fig.3 *Short time temperature evolution in the concrete block*

though the sodium temperature was measured as 773 K in the vessel, it experienced cooling immediately perhaps due to higher thermal conductivity and heat capacity of the tiles as compared to the concrete. Subsequent manual interference with the hot sodium resulted in the re-ignition of sodium causing the temperatures to increase as depicted in Fig. 4. The temperatures recorded in the concrete block are given in Fig. 5. It can be observed that the temperature of the concrete near the floor increased from 303 to 453 K while the corresponding increase along the walls of the cavity was in the range 373 to 423 K. The sodium fire debris inside the cavity were scooped out forty eight hours after the sodium combustion was over and the tiled surfaces were cleaned by mopping with methanol laden waste cloth. The tiles were found to be adherent to the concrete wall as it was placed originally. However, a week later the tiles peeled off the cavity walls with little or no effort. This shows that the damage on the concrete surface beneath the tiles has been slow and continuous.

Ultrasonic Pulse Velocity (UPV) measurements through in-direct transmission technique were carried out on the vertical outer surfaces of the block before and after the sodium fire interaction. Fig. 6 gives the relative change of the measured UPV at various heights on the outer surface of the concrete block, which was alumina tile lined and subjected to sodium fire. Post-experimental UPV measurements used in this figures are the values that were taken after the tiles were peeled off. It can be seen that the concrete has suffered about 20% deterioration on most locations with some localized severe damage in one or two locations.

In order to quantify the protection given by the tile lining, another bare structural concrete block was also subjected to sodium fire at the same initial conditions without the alumina lining and UPV measurements taken. The change in UPV in this block is shown in Fig. 7. It is evident from this figure that the damage sustained by this concrete block is two to three times more than that sustained by the tile lined block. Thus these experiments bring out clearly that the alumina tile lining could give good protection for structural concretes.

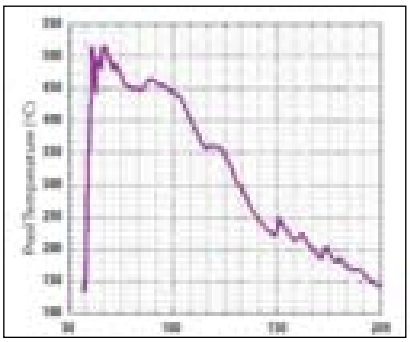

Fig.4 *Long time evolution of Sodium pool temparature in the concrete cavity*

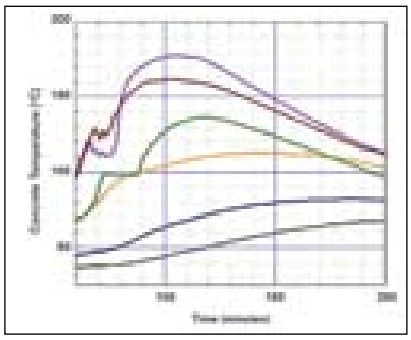

Fig.5 *Long time temperature evolution in the concrete block*

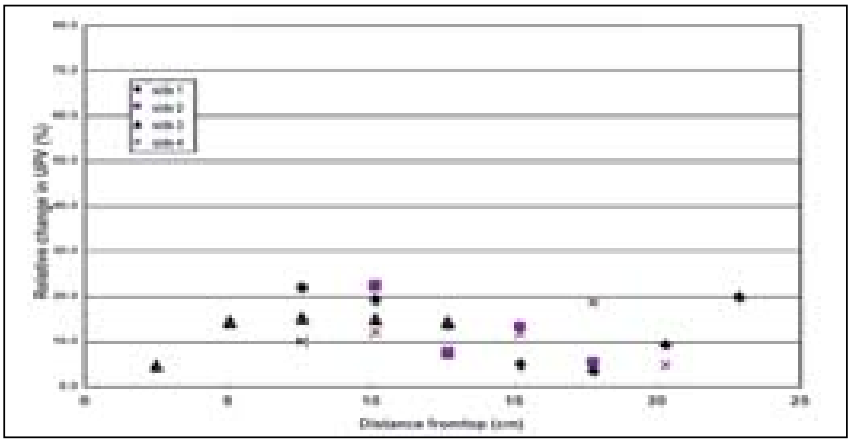

Fig.6 *Relative change in ultrasonic pulse velocity in titled concrete*

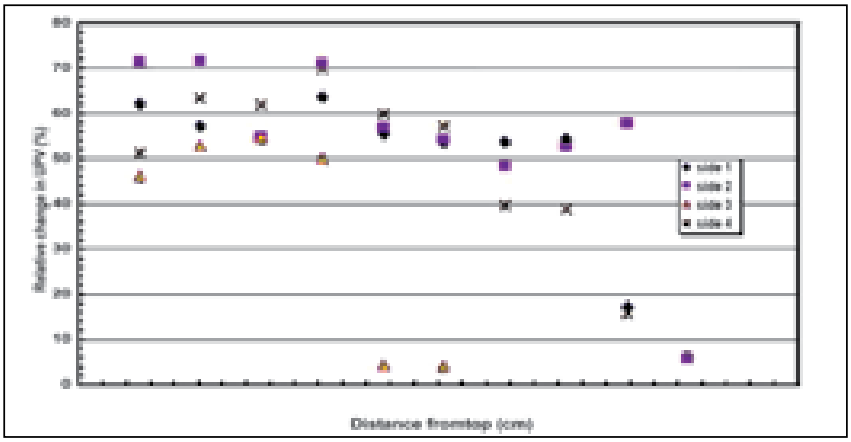

Fig.7 *Relative change in ultrasonic pulse velocity in bare concrete*

III F.8 Assessment of Iron - Alumina Thermite Melt for Simulation of Molten Fuel - Structural Interaction in Core Disruptive Accident Analysis

Analysis of core disruptive accident (CDA) is an important safety study in FBR. Unprotected Loss of Flow Accident (ULOFA) leads to melting of almost whole core, with simultaneous generation of vapour phase consisting of fuel, coolant and structural materials. The first phase of the accident is pre-disassembly phase, where the heat generated due to power excursion could melt the core, to the extent of saturated liquid state. Subsequent heating generates vapor phase, which is having high potential to do mechanical work in view of its high temperature and high pressure. Subsequent to completion of mechanical work, the vapor phase which is at ~ 5000K, condenses due to cooling of sodium pool which is at 855K and starts moving downwards melting the support structures, such as grid plate (GP) and core support structure (CSS) (Fig.1). Finally, the liquid settles on the core catcher and subsequently will be cooled by natural convection. Numerical simulation of molten fuel coolant interaction involves modeling of many complex phenomenon, heat transfer, melting of structural materials, phase change and fragmentation. The ultimate settling behavior of this mixture of solid particles in the molten fuel on the core catcher decides the post accident heat removal capability. The validation of such numerical tools is very important which involves complicated test facilities. The choice of material which can simulate the heat transfer characteristics of molten fuel with respect to melting of support structures is a key issue.

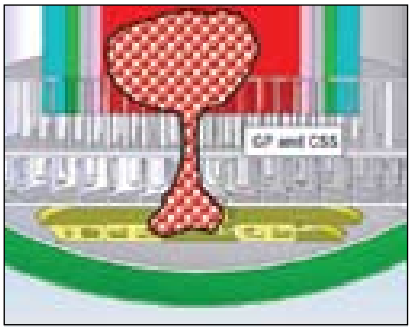

Fig.1 *Molten fuel relocation scenario*

Thermite reaction, an exothermic oxidation - reduction reaction between a metal having higher affinity for oxygen and another metal oxide is an attractive option to generate highly superheated molten metal in quantities required for laboratory scale experiments. The main advantage of this technique is that it requires no external power for producing the melt. The large exothermic energy release upon reaction itself caters to the need. The reaction rate, even at very high temperatures is much lesser than conventional explosives, thereby facilitating the conduct of controlled reactions. One such reaction is between ferric oxide and aluminium, where one can get elemental iron and alumina melt at a temperature of 3073 K under adiabatic conditions.

Fig.2 *Rail welding*

$Fe_2O_3+2Al=Al_2O_3+2Fe$ + 848.54 kJ (4.0 kJ/g of inventory)

The main challenge in using this technique is in containing the reaction products in an adiabatic manner to get maximum temperature of the melt and its controlled initiation and release from the container. Systems using this technique are in use for carrying out rail welding in a cost effective manner (Fig. 2). Another

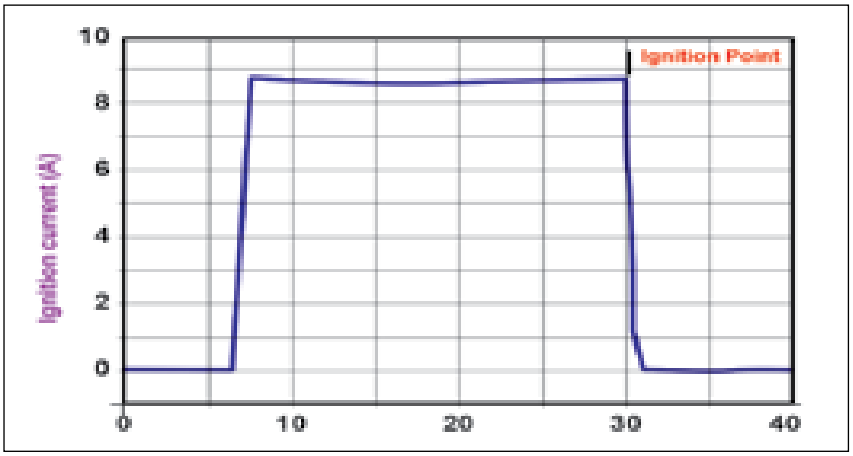

Fig.3 *Electrical ignition of thermite*

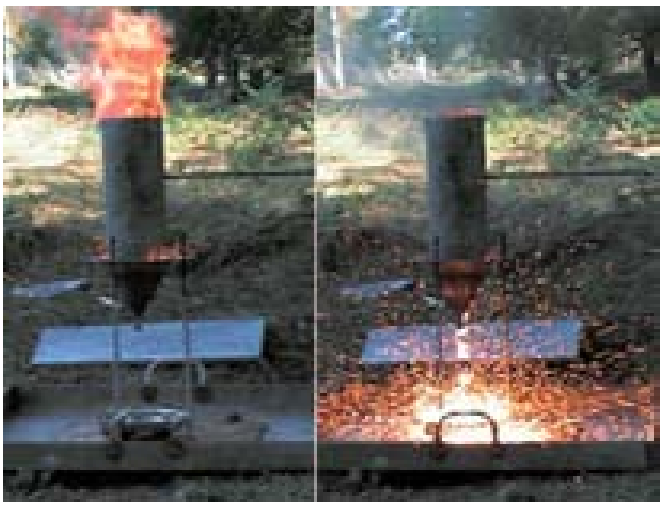

Fig.4 *Open vessel for thermite reaction*

Fig.5 *Conical reaction vessel*

problem with this specific reaction is that appreciable rate of reaction is reached and the reaction is self sustaining to completion only at temperatures greater than 773 K. Hence, it needs an ignition for initiating the reaction. Ignition through chemical means such as use of magnesium based wicks and seed reaction between glycerin and potassium permanganate and through electrical means have been tried out. It has been established that electrical triggering is safe and easily adapted for remote triggering. A twenty two AWG Nichrome wire having a resistance of about 2.8 Ω was used as the heating element. An optimum electrical current of nine Amperes was arrived at for heating this resistive element towards generation of 1073 K in about twenty four seconds (Fig. 3).

With the aim of standardizing the procedure: ignition, reaction containment and controlled melt stream release, scoping trials up to an inventory of four hundred grams have been carried out in a open reaction vessel (Fig. 4), conical reaction vessel with an inverted cone on top of it (Fig. 5), and in an internally MgO lined conical vessel. Generation of continuous downward melt stream is achieved with 25 mm release diameter. The measured melt temperature is ~2723 K using a two color ratio pyrometer (Fig. 6). MgO protective layer acted as internal insulation in limiting the rise in vessel temperature to 423 K (Fig. 7)

Further runs are planned for higher inventory thermite mixture with electric triggering. The outcome of the tests would provide an excellent insight on the melting of grid plate by molten fuel which has got strong link with the post accident heat transfer capability.

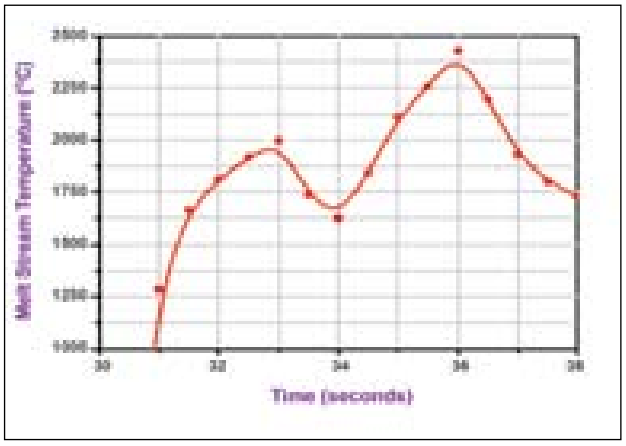

Fig.6 *Thermite melt temperature as measured by two color pyrometer*

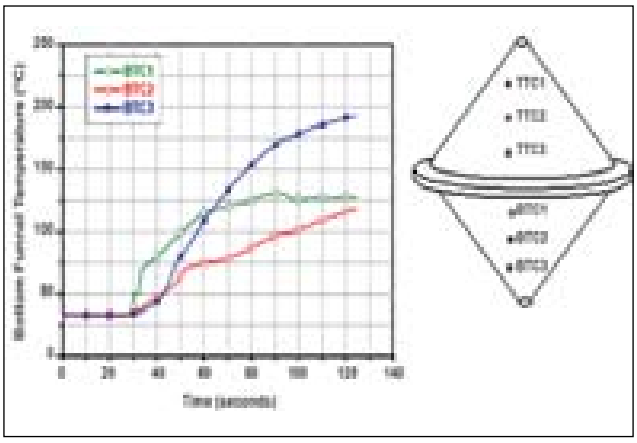

Fig.7 *Outer surface temperature of Thermite Reaction Vessel*

III F1 Electronics and Instrumentation

III F1.1 Development of Wireless Pressure Sensor using Non Contact Differential Variable Reluctance Transformer

A commercially available micro sensor, (*Microepsilon* make) non contact differential variable reluctance transformer (NCDVRT) is used for the accurate measurement of pressure with a wide dynamic range for industrial and R&D applications. A novel implementation of NCDVRT in a pressure port with a suitable stainless steel diaphragm provides a simple innovative pressure sensor which can work in any environment with good repeatability and with excellent resolution. The advantage of the developed sensor is that it can measure both positive and negative pressures and since there are no electrical contacts between the pressure port and sensing element, it can be used for remote applications. Fig. 1 shows the design of the developed pressure sensor. NCDVRT was rigidly fixed at the one side of one milli meter thick stainless steel diaphragm at a distance of 140 µm. This distance was selected in order to operate the sensor in its linear region. Teflon material was used to fix the sensor to avoid any spurious signal pickup. The other side of the diaphragm was used as pressure port.

This sensor can measure the positional movement of the stainless steel diaphragm with an accuracy of ± 2 µm corresponding to a pressure of 0.1 bar. Fig. 2 shows the calibration graph of the developed pressure sensor. PSoC microcontroller is used to generate an excitation AC signal to NCDVRT, synchronously measure the output AC signal depending on stainless steel diaphragm position, digitize it and transmit the same information to a personal computer through a wireless RF module. Fig. 3 shows the wireless pressure measurement system using single *PSoC* microcontroller chip (CY8C29466) and 2.4 GHz wireless RF Module.

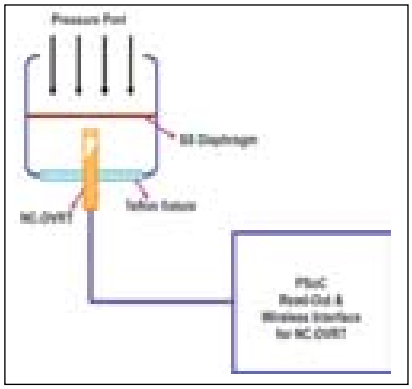

Fig.1 *Schematic of NCDVRT pressure sensor*

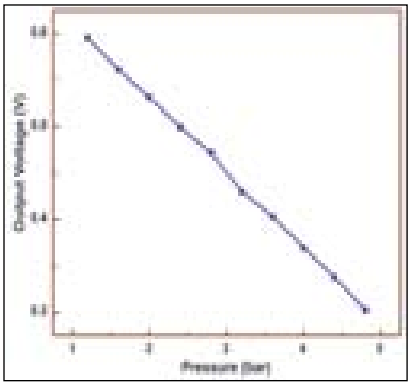

Fig.2 *Sensor calibration chat for stainless steel diaphragm*

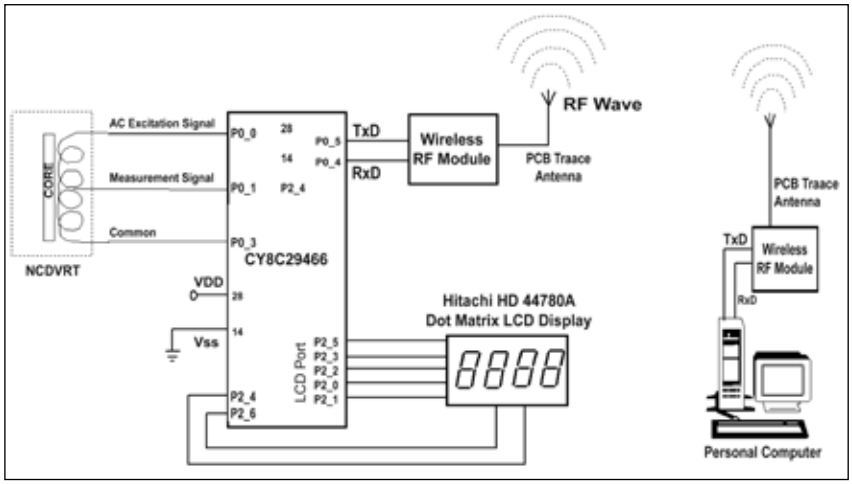

Fig.3 *Wireless pressure measurement system using PSoC and NCDVRT*

Microcontroller, was also programmed for a LCD port and was connected to a dot matrix LCD display. Microcontroller was powered by a rechargeable Ni-Cd battery. Virtual instrument based graphical language software written in LABVIEW, acquires the wireless transmitted RF sensor signal, provides on-line plotting, saving data and analyzing the data as per the user requirement.

III F1.2 Automation and Control of the Thermal Ionization Mass-Spectrometer based on a Single Board Computer

In a series of endeavours aimed at the upgradation and life extension of expensive analytical instruments, a single board micro controller based PC interface had been fabricated for enhancing the performance of a thermal ionization mass spectrometer (TIMS). This development involves designing of programmes for the 89C668 (in system programmable) microcontroller, functional circuitry for controlling various mass spectrometric functions, layout preparation, PCB fabrication, writing user interactive programs, functional testing and commissioning of the instrumentation. The present control system which has been developed fully in-house, has not only enhanced the functional aspects of the mass spectrometer but also possesses other advantages like amenability to further automation, ease of maintenance etc. The block diagram (Fig. 1) of the instrument automation is shown.

The following mass spectrometric functions have been achieved:

Setting of magnetic field

It is essential to set the magnetic field to a desired value to capture the exact isotope of the sample species. A 16 bit digital-to-analog converter (DAC) circuitry had been addressed to control complete range of field up to five Kilo gauss with a resolution better than 0.1 gauss. This enables the user to distinguish between isotopes of closer masses. The instrument hardware has been modified to accept the input from the DAC.

Counting system for signal measurement

Counting system was developed for measuring the selected parameter from among the various mass spectrometric parameters viz. ion beam intensity, acceleration potential and magnetic field. In this system, the selected analog input signal is first digitized proportionally using voltage to frequency converter and then counted in microcontroller for achieving high resolution. The counting period is set at one hundred milli seconds to cancel effects of power supply pick up.

Input signal selection

The important mass spectrometric parameters such as acceleration voltage, magnetic field and ion beam currents are sampled suitably, buffered and selected through PC, multiplexed by using an analog multiplexer.

Selection of gain and ampere full scale ranges

The ion current measuring electronics has five ranges of full scale ie, 10^{-4}, 10^{-5}, 10^{-6}, 10^{-7}, and 10^{-8} amps. and an overall gain range of 1, 2 and 5. Depending upon the range of ion beam intensity, user has the choice of selecting the suitable gain combination to cover the entire range of ion beam currents from 10^{-17} to 10^{-9} Amps.

The upgraded and automated instrument has been commissioned and tested with National Institute of Science and Technology (NIST) standards of boric acid and the ratios were measured and were found to be within the agreeable limits.

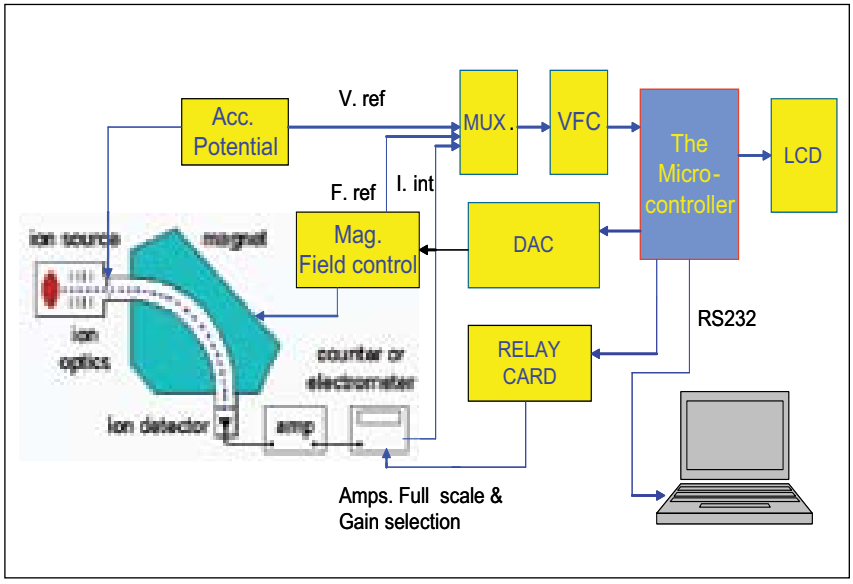

Fig. 1 *Schematic showing the thermal ionization mass spectrometer automation*

III F1.3 Time Domain Electromagnetic System

Our Centre is developing the time domain electro magnetic (TDEM) system suitable for an airborne survey for locating various minerals. The system will be used to map the location of sub-surface conductive layers. The methodology adopted was to design an initial system to be used for ground-based surveys and finally head towards the design modification to make the system worthy for airborne survey. In a typical airborne survey the transmitter-receiver coil assembly will be towed by a helicopter at a terrain clearance of thirty metres.

The system works on the principle of electromagnetic induction and eddy currents in nearby solid conductors. The changing magnetic field is generated by injecting a pulsed current through the transmitter coil. The field generated by the sub-surface layer eddy currents are captured by the in-loop receiver coil in the absence of the primary field. The final goal was to design and develop a transmitter coil with a diameter of twenty five meters through which a pulsed current of 300A peak amplitude will be injected. The final system will have the adequate dipole moment to map conductive layers to a depth of three hundred meters below the earth surface.

System Design and Development

The development activity started with the design of a laboratory scale model followed by the stage-1 (1/10th scale) model. In both stages extensive experiments were conducted with metallic sheet targets. The experimental results were verified by finite element method based electromagnetic simulations. The successful design of stage-1 system was followed by the design of the stage-2 (1/2 scale) industrial prototype, with a pulsed current source capable of delivering 200A into a sixteen meters diameter transmitter coil. The system was tested in known field geologies to validate the transmitter current source and the receiver electronics. The field experiments were organized by geophysicists and geologists.

Experiments conducted at site-1

The first set of experiments with the stage-2 system was conducted at site-1, where the rocky terrain had many parallel vertical conductive bodies made up of sulphides and graphites at an average depth of forty meters from the ground surface. Depth sounding and profiling studies were conducted over the target locations and the receiver coil voltage data was recorded in all the three axes. The receiver coil induced voltage exhibited a longer exponential decay, which indicated

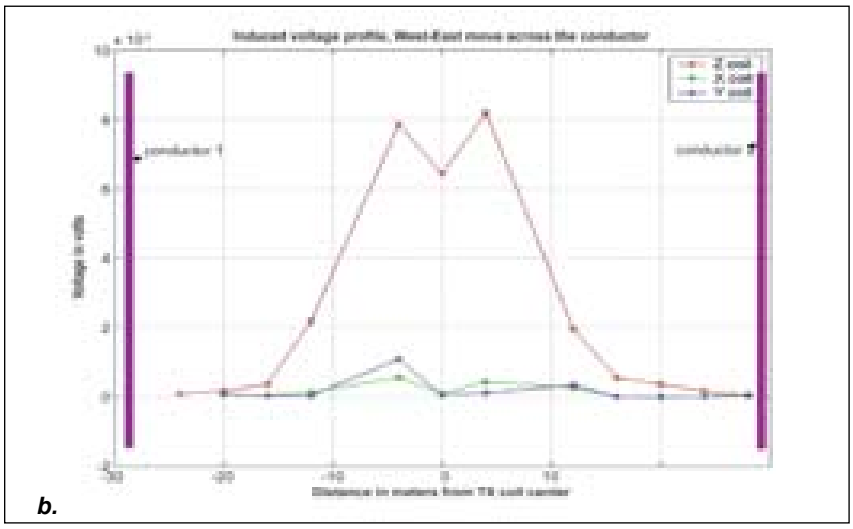

Fig.1 *Stage-2 system (a) experiment setup (b) results. experiment carried out at Rohil*

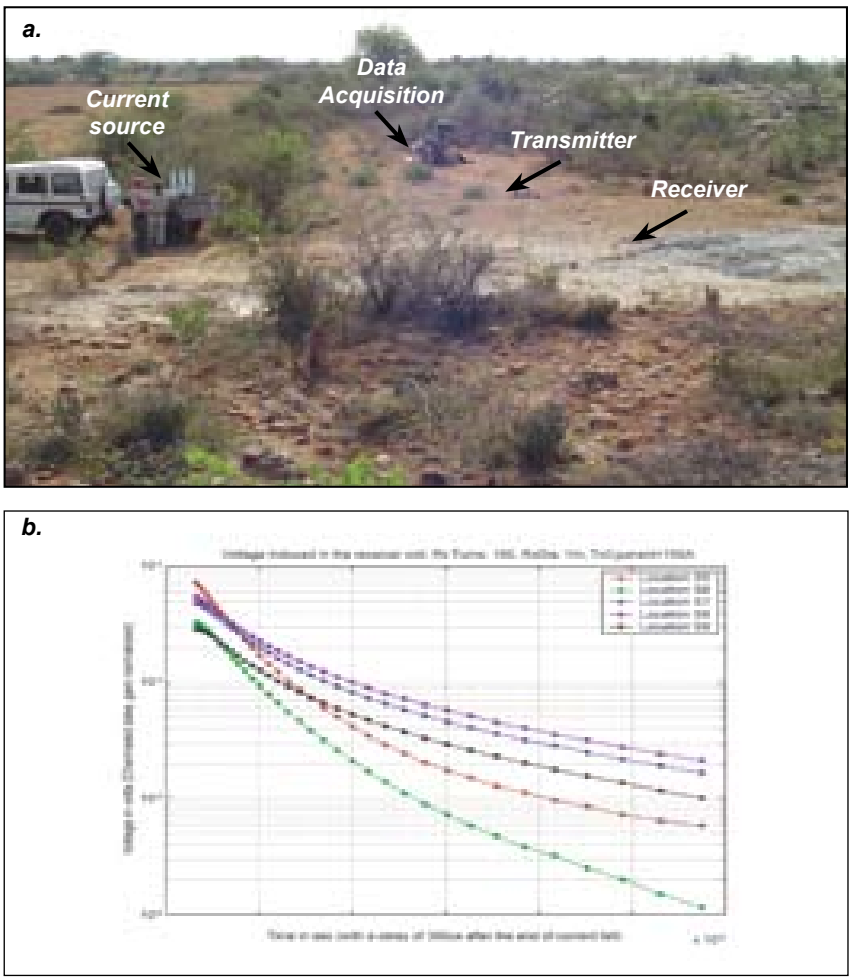

Fig.2 *Stage-2 system (a) experimental setup (b) results. experiments conducted at Koppanure*

the presence of a conductive body. For profiling studies the transmitter coil was fixed in a location and the receiver coil was moved along the traverse. From the profile graphs, information about the orientation of the conductive body was extracted. The stage-2 experimental setup along with a profile graph is shown in Fig. 1.

Experiments conducted at site-2

A second set of experiments were conducted at site-2 where the sub-surface was a layered earth. The targets were horizontal conductive layers sandwiched between resistive layers. Sounding studies were conducted at several locations wherein the conductive layers were at a varying depth of 50-100 metres from the surface. The receiver coil induced voltage data was recorded in all the three axes. The recorded voltage data exhibited longer decays which indicated the presence of the conductive layers. The pre-processed induced voltage data is being further analysed. The induced voltage sounding curves recorded at different locations is shown in Fig. 2 along with the experimental setup.

Airborne system development

The ground based TDEM experiments provided enough data to characterize the transmitter and receiver electronics. To upgrade the stage-2 system for an airborne survey, a new transmitter coil design and development has been initiated. The coil assembly will have an aerodynamically compatible structure with stabilizers. The tests to qualify the electronic systems to be placed on-board the helicopter is under progress.

III F2 Sensors

III F2.1 Studies on the Electrochemical Hydrogen Meter

Detection of hydrogen in liquid sodium circuits in Fast Reactors is elegantly accomplished with the help of an electrochemical hydrogen meter (ECHM) developed inhouse. These sensors have been installed at various facilities viz., FBTR, steam generator test facility (SGTF), the sodium water reaction test facility (SOWART) and were found to perform satisfactorily. These meters could reliably detect an increase of 15 ppb of hydrogen over a background of 50 ppb in these facilities. Based on this experience it is proposed to install ECHM along with its

instrumentation at the outlet of each steam generator (SG) unit of the PFBR for detecting leakage of steam. During the dumping of sodium the meter experiences a sudden change in temperature. Since the output of this sensor is temperature dependent, it could change its output. Some more experiments were carried out by simulating similar conditions that prevail in the actual operating plant. These experiments were carried out in the test loops in the laboratory as well as in FBTR. The ECHM was found to restore its output during such temperature surges within 10% (Fig. 1).

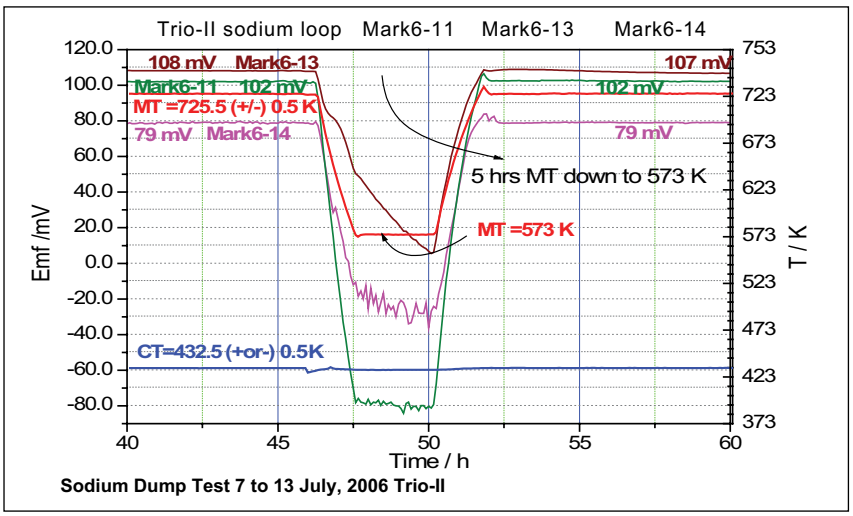

Fig. 1 *Restoration of ECHM output after temperature cycling between 723 K and 423 K. (Sodium dump test 7 to 13 July, 2008 Trio-II)*

The instrumentation necessary for detection and measurement of dissolved hydrogen concentration in sodium has also been developed. A specially designed preamplifier for the sensor, placed in the sensor cell housing, transmits a frequency signal corresponding to the dissolved hydrogen concentration. The control unit placed remotely in the local control centre (LCC) receives the signal and converts the same into concentration (ppb) and displays the value. A microcontroller manages the overall coordination of signal measurement, conversion into ppb units, system healthiness surveillance check and display of the hydrogen concentration values and the status in the panel. The reported values are quantified and are valid at 723 K ± 4 K as the EMF is sensitive to sodium temperature as well. In order to provide confidence of the validity of the value, the instrument measures the sodium temperature around the meter section and raises an alarm when the temperature differs by more than (±) 4 K from the operating temperature of 723 K.

The instrumentation includes the customized VFC based analog to digital converter (ADC) to provide better linearity, wide dynamic range and required resolution even at the high end of the hydrogen concentration. It also includes digital signal transmission and signal isolation to ensure reliable/ reproducible signal to noise (S/N) ratio. It provides appropriate analog signal and healthiness digital signal suitable for interfacing with the remote terminal unit in the plant back bone of the PFBR DDCS. The system is now qualified in different sodium experimental facilities of IGCAR like SGTF, SOWART and in FBTR.

In order to gain operating experience with the ECHM in a commercial power plant, an ECHM that was calibrated in our laboratory in mini sodium loop along with the instrumentation was installed in Phenix reactor as part of the Indo-French collaboration program on fast reactor safety during middle of September 2007. The response of the meter to H injections of ~10 ppb made on-line during the Phenix reactor operation was comparable to that of conventional diffusion type meter that uses QMS for H detection (Fig. 2). The test results established the facts that (i) the ECHM gives a very clean signal (Fig. 3), (ii) the typical response time (including transport time) is about ninety seconds (similar to the conventional meter in nearby location) (iii) even after a gestation period during the dumping and refilling of liquid sodium the signal could be restored to within 10% of the original value.

Instrumentation for the ECHM

A microcontroller based instrumentation for hydrogen detection in argon cover gas (HAD) has been developed for continuous monitoring of hydrogen levels in the argon cover gas and detecting the steam/water leaks. When the reactor is under start-up and low power operations, the temperature of the sodium coolant would be around 523K and at these temperatures, the hydrogen in sodium detectors (HSD) would not respond as the dissolution of the reaction products into sodium is kinetically hindered. Hence, a large fraction of hydrogen gas

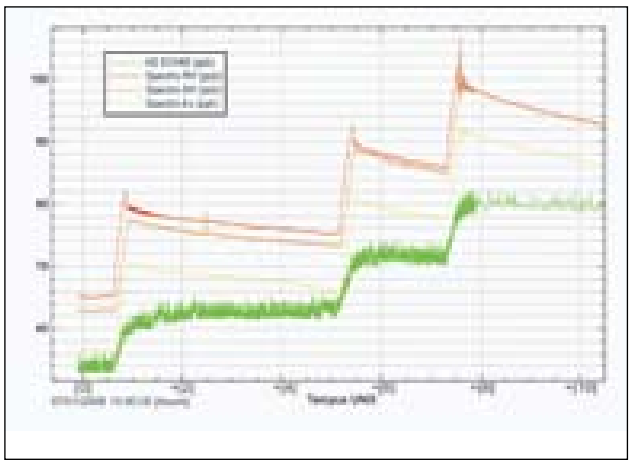

Fig. 2 *Response of ECHM to hydrogen injections into sodium during plant operation conditions in Phenix reactor in France*

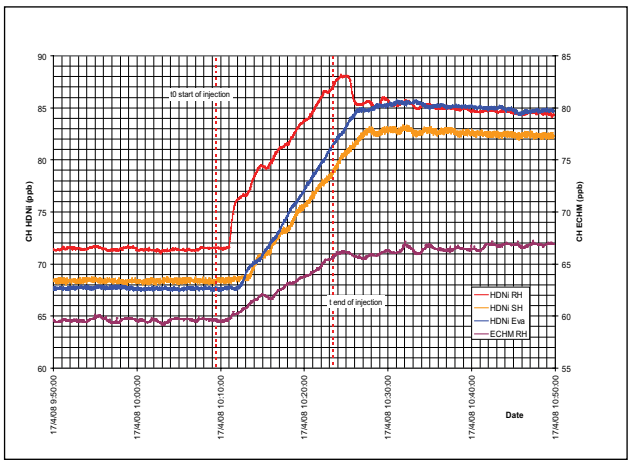

Fig. 3 *Response of ECHM to on-line H injections in Phenix reactor*

formed during sodium/water reaction bubbles through sodium and escapes into cover gas plenum.

The HAD is made of a thin walled nickel membrane in the form of a coil for separation of hydrogen from argon cover gas. Hydrogen that is separated from cover gas is subsequently measured by a thermal conductivity detector (TCD). Hydrogen that diffuses into the coil from the cover gas at the operating temperature is carried by a stream of high purity argon to the TCD. Due to the difference in thermal conductivity of argon and argon-hydrogen mixture, TCD gives signal which is directly proportional to the hydrogen concentration in the argon carrier gas. The TCD and the signal preamplifier are housed in the argon gas manifold near nickel coil assembly. The photograph of the nickel coil assembly is shown in Fig. 4.

In the preamplifier, the TCD output and the TCD block temperature are measured, amplified and converted into corresponding frequency signals. The frequency signals are transmitted by RS422 differential driver to the signal processing module located in 19" rack. The microcontroller based signal processing unit receives the signal and calculates the hydrogen concentration in ppm units and displays in a DPM.

A suitable constant current circuit is designed to maintain the specified current through TCD bridge. The ambient temperature

Fig. 4 *Photograph of the Nickel Coil Assembly*

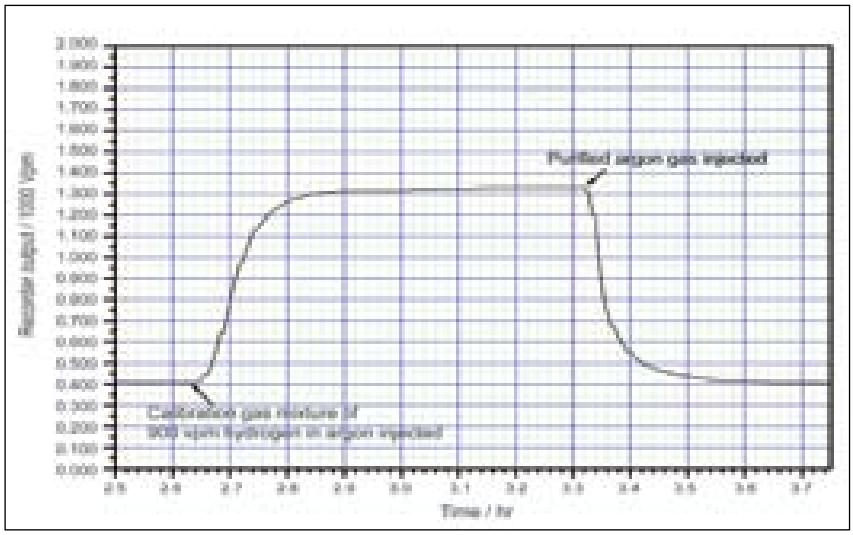

Fig. 5 *Response of the microcontroller based instrumentation for hydrogen injection*

data of TCD block is used to apply a suitable correction for any variation in TCD signal with ambient temperature. The temperature coefficient of the TCD output was experimentally found and fed to system for use in the calculation. The system also has a supervisory circuit that protects the TCD from any excessive current. The supervisory circuitry also generates a digital signal regarding the healthiness status of the system. The hydrogen concentration and the healthiness status signal are available in the rear panel that can be interfaced with the remote terminal unit in the plant back bone of the PFBR DDCS.

The instrumentation includes the customized VFC based ADC to provide better linearity, wide dynamic range and required resolution for measurement.

The minimum detection limit of 16 ppm of hydrogen in argon is realized. The range of the measurement is 2000 ± 4ppm (Fig.5).

III F2.2 A Pump-less Flow Injection Analysis Utility Based on Pulsating Sensors

Flow Injection Analysis (FIA) utility, which requires only a few micro-liters of sample volume for analysis in less than a minute has been developed. The FIA involves injection of a small volume of sample solution to a flowing carrier liquid within a narrow tube. Depending on the requirement, the carrier liquid could be one that reacts chemically with the desired species in the sample leading to advancement of the reacted solution front along the tube. The carrier liquid could even be a non-reactive one transporting the mixed front (mixed diluted zone) along the tube. As the reacted or mixed front passes through a tiny pulsating sensor (as the detectort)placed downstream, the response is followed in real time.

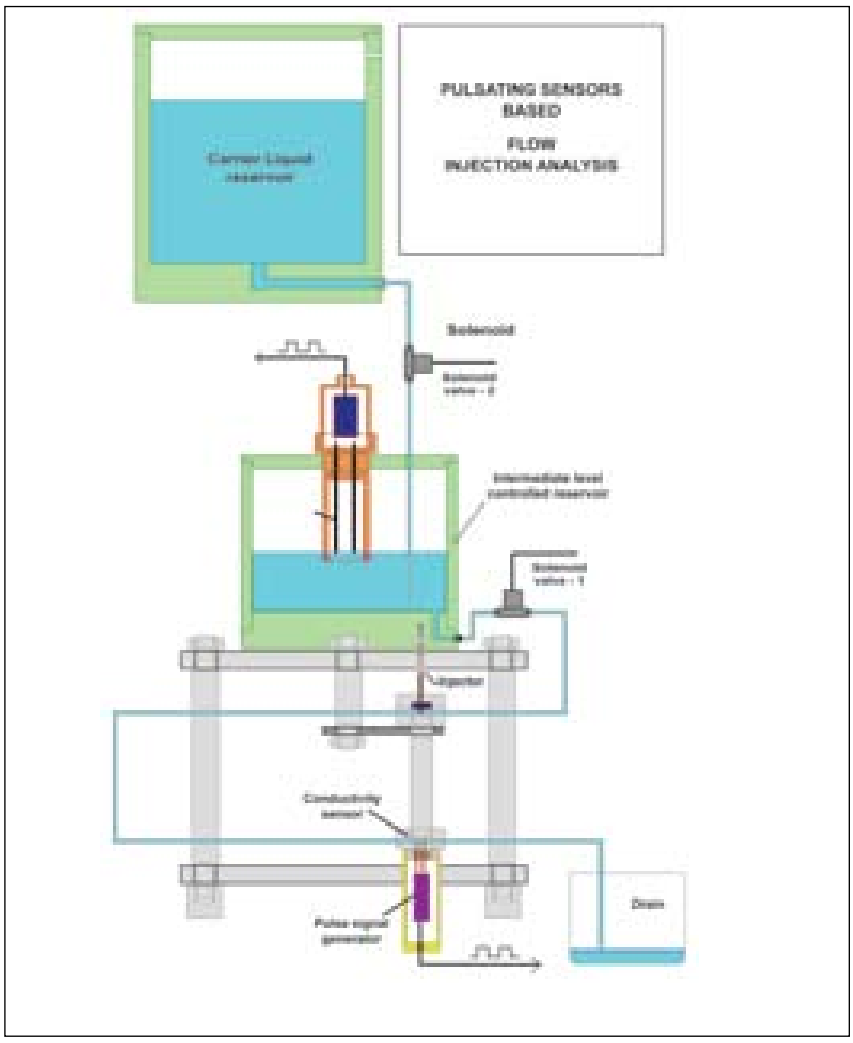

Fig. 1 *Schematic diagram of the laboratory built pump less Flow Injection Analysis utility*

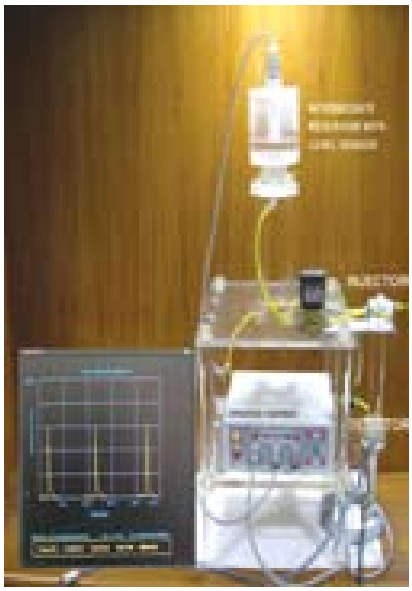

Fig. 2 *A photograph of the PC based rugged and automated prototype FIA instrument including all sensing, measurement & control hardware and software*

The desired analytical information is then derived from the detector response. Undisturbed flow path and identical flow conditions during every injection are essential conditions for reproducibility of the flow injection peaks. This FIA utility makes use of a flow type conductivity sensor for rapid monitoring of the changed conductivity profile in the affected moving zone. The carrier liquid flows under gravity instead of being driven by a pump.

Design of the pulsating conductivity sensor, choice of flow tube diameter, location of the sensor in the flow path etc. were optimised through separate laboratory studies. The prototype (Fig. 1) called for an appropriate provision for reproduction of flow condition during every injection and automation for flow control of the carrier liquid. Flow reproduction was realised through use of a medium sized reservoir between the main reservoir and the flow tube. This intermediate vessel is fitted with a specially developed pulsating level sensor that responds to the set level with sub-millimeter uncertainty for any conducting liquid starting from demineralised water to those with high conductivities. Operation of the solenoid valves are controlled by the PC based unit.

Prior to every injection, the upper solenoid valve is opened to transfer by gravity the carrier liquid from the main reservoir to the intermediate vessel till the set level is reached. The lower solenoid valve then opens for passage of the carrier liquid, again under gravity flow, through the flow tube and the system prompts the operator for injection. Following the injection the operator can visualise graphically in real time the profile being displayed progressively and, once the reacted or the mixed zone has gone past the detector, the system closes the lower solenoid valve on receiving the command from the operator. The system then automatically opens the upper solenoid valve for bringing the carrier liquid to the set level for the next injection at the same pressure head which reproduces the gravity driven smooth flow condition quite precisely. Time taken for recording data for one injection is only about thirty seconds which includes the time for the system to be ready for next injection. At the end of desired number of injections, the operator can quickly get the quantitative results immediately using the built-in user friendly navigational features.

A photograph of the FIA utility is given in Fig.2. It has a small detachable section, consisting only of the miniature injector and the detector, for housing within a fume hood or glove box for work with radioactive samples.

The utility has been used for optimizing the conditions for quick off-line assay of HNO_3 samples as expected from different sources in a reprocessing plant through simulation of impurities like fission products. Typical flow injection peaks on repetitive injections of 5 µl of sample in non-reactive (DM water) and reactive (very dilute NaOH) carrier liquids are shown in Fig. 3. The unit can be adapted as a general purpose utility for different chemical species and is now ready for deployment in a radiochemical plant.

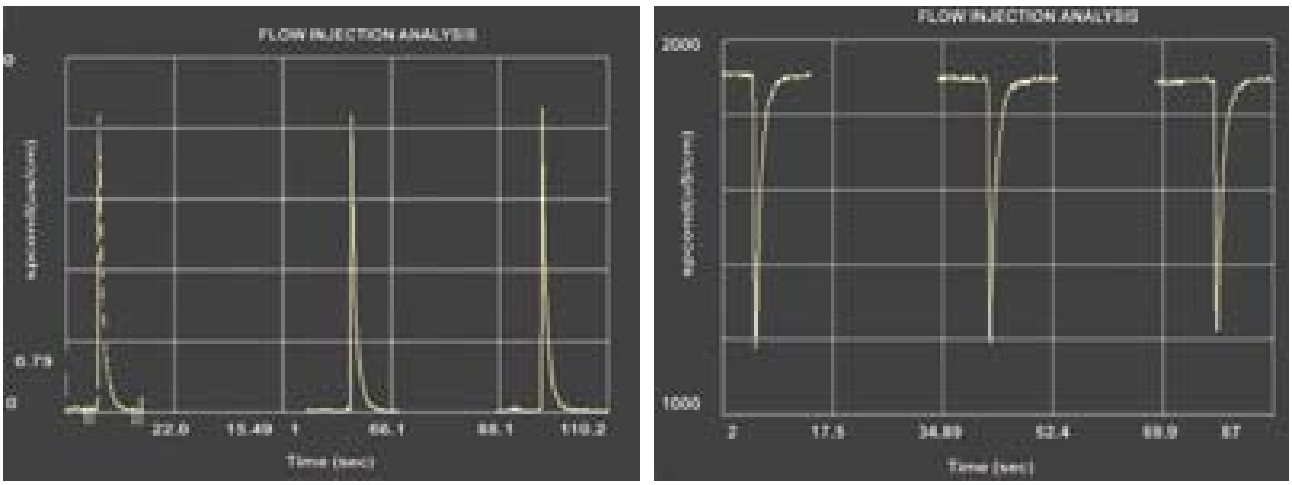

(a) ***(b)***

Fig. 3 *Typical flow injection peaks on injection of (a) 5 µl of 0.05 M HNO_3 in flowing DM water (b) 5 µl of 4 (M) HNO_3 in flowing reactive carrier liquid of 0.008 M NaOH.*

III F2.3 Differential Pressure Sensors for Environment Control in Radioactive Facilities

Sensitive differential pressure (ΔP) sensors are needed for control of atmosphere in glove boxes, hot cells and reactors. Air or inert gas flow patterns across the boundaries between different atmospheres have to be regulated in a desired manner. In view of above large scale requirement in highly sensitive and reliable differential pressure sensors of unique design have been developed at our Centre. The sensors are of pulsating type and are based on precise level sensing of a suitable non-conducting liquid of low vapour pressure within specially constructed manometer housing of different types. Several versions were made and tested and results have been highly satisfactory. The success prompted development of prototypes for various applications in different ranges: 0-10, 0-25 and 0-55 mbar. An example of such a prototype for possible application in fast reactors is given in Fig. 1. On application of a pressure differential, the level of the non-conducting liquid within the vertical narrow tube as "one arm" changes lot more in comparison with the corresponding change of oil level in the surrounding cylindrical section of much larger diameter at the bottom as the "other arm". The digital pulse frequency at the output of an appropriately designed pulsating oil level sensor within the narrow tube is governed by the prevailing differential pressure.

Fig. 1 *An in-house developed rugged ΔP sensor in the range 0-55 mbar with its schematic representation.*

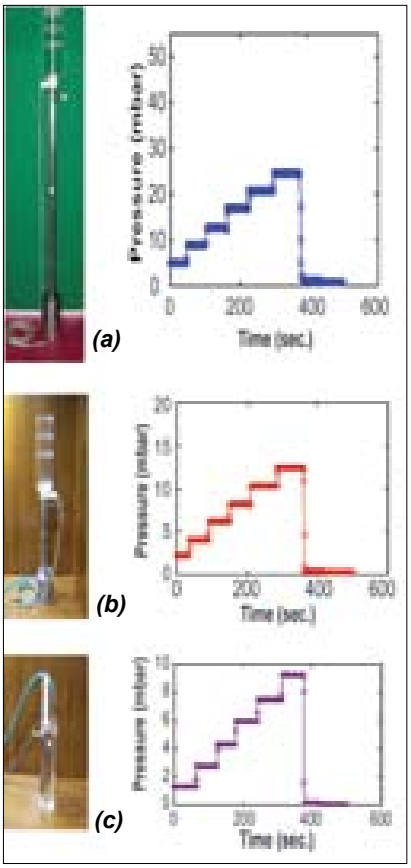

Fig. 3 *Recorded on-line responses to stepwise increase in ΔP for three sensors of different ranges made in the laboratory. The drops in ΔP to zero at the end are due to deliberate release of build up pressure differentials*

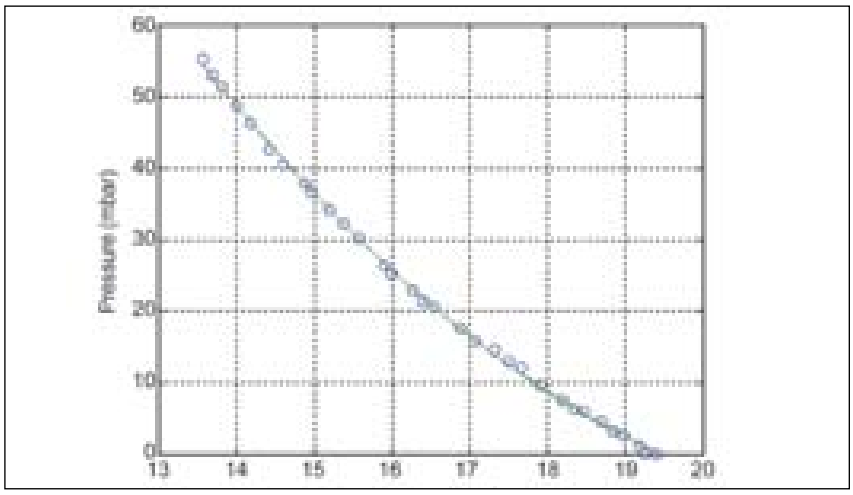

Fig. 2 *Output pulse frequency to ΔP relationship for a typical sensor. The numerically fitted two-degree polynomial equation, derived from the multi-point calibration data, is used as the working equation in on-line signal processors*

The rugged prototype devices have been constructed in-house. Suitable calibration utilities were made, which permitted easy and quick multipoint calibration with high reliability. The pulse frequency to ΔP relationship for a typical sensor is given in Fig.2. Appropriate passive features have been incorporated in some sensors for containment of the liquid within the devices in the

event of accidental excessive over pressurization or evacuation.

Simultaneously monitored differential pressure from three different sensors by the laboratory developed multi-channel pulse processors are given in Fig. 3. The figure shows the on-line response of stepwise change in differential pressure as a function of time for these sensors separately. Under the laboratory conditions of measurements at room temperature, the precision of differential pressures were within ± 0.1 mbar at every step.

III F2.4 Studies on Some Lithium Ion Conductors for use as Lithium Sensors

Pb-17 Li (at%) alloy is a candidate fluid for use as coolant as well as breeder in fusion reactors. Because of the depletion of lithium from the alloy owing to the nuclear reactions and also due to possible chemical interactions with structural materials, there is a need for continuous monitoring of lithium activity in this alloy. Lithium ion conducting Li_2ZrO_3 and $Li_{(2-4x)}Zr_{(1+X)}(PO_4)_2$ (where x=0, 0.35) were chosen as candidate solid electrolytes for this purpose. They were prepared by conventional solid state reaction between Li_2CO_3 and ZrO_2, and Li_2CO_3, ZrO_2 and $(NH_4)H_2PO_4$ and compounds were characterized by X-ray diffraction (Fig. 1). Their electrical conductivities were measured in the temperature range 300-723 K. The experimental results showed that the phosphozirconates possess a conductivity that is one to two orders of magnitude higher than that of lithium zirconates in this temperature range (Fig. 2). The transport number of lithium ion (t_{ion}) in $Li_{0.6}Zr_{1.35}(PO_4)_2$ was found to be 0.98, while that in Li_2ZrO_3 was 0.80. To assess the chemical compatibility of these solid electrolytes with Pb-17Li (at%) samples in the form of a pellet were equilibrated with the molten metal at 773 K for five hundred hours. XRD analysis of the retrieved samples after equilibration showed that $Li_{0.6}Zr_{1.35}(PO_4)_2$ was compatible with Pb-17Li (at%) alloy while Li_2ZrO_3 was not compatible.

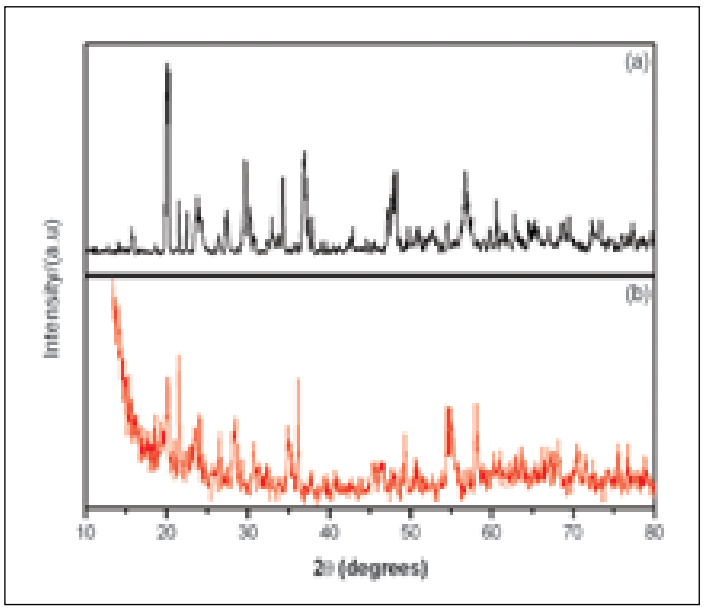

Fig. 1 *X-ray diffraction patterns of $Li_{0.6}Zr_{1.35}(PO_4)_2$ (a) before and (b) after equilibrating with Pb-17Li alloy at 723K for 500 h.*

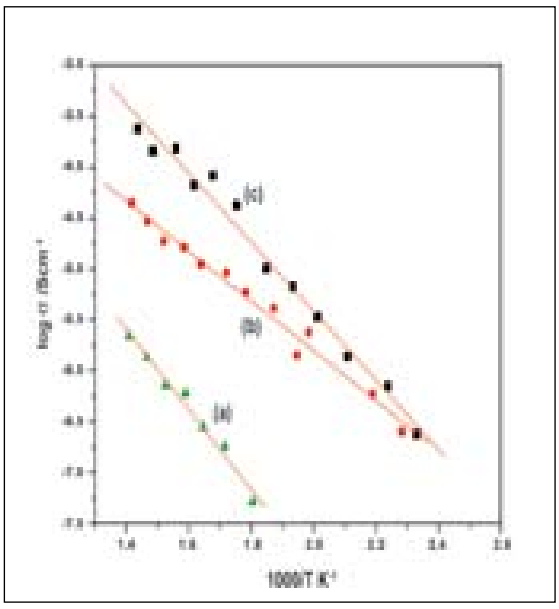

Fig. 2 *Arrhenius plots showing the conductivity as a function of temperature for (a) Li_2ZrO_3, (b) $Li_2Zr(PO_4)_2$ and (c) $Li_{0.6}Zr_{1.35}(PO_4)_2$ in air*

III F2.5 Proton Exchange Membrane Fuel Cell Based Electrochemical Hydrogen Burner

Many important components of a fast reactor like sodium pumps and heat exchanger need maintenance or replacement. The fuel sub-assemblies are routinely removed from the reactor for reprocessing of the spent fuel as well. Prior to carrying out maintenance or disposal of these components, the sodium sticking to their surface needs to be cleaned. Hydrogen evolves during the sodium removal using the water-based processes. The faster the cleaning process, the higher would be the concentration of hydrogen evolved and it could build up well beyond the explosion limit of 4% hydrogen in air. In order make this operation safer, the system is usually purged with an inert gas such as argon or nitrogen to keep the hydrogen concentration well within its explosion limits.

An attractive alternative to the above procedure is to burn the hydrogen liberated during the clean up. Such a burner when fitted at an appropriate location in the clean up circuit should bring down the concentration of hydrogen from a value as high as 50% v/v to a value well within the explosion limits. Usually catalyst based hydrogen removers are employed. Such systems pose the risk of the mix up of the reactive gases viz., hydrogen and oxygen.

A prototype "electrochemical burner" comprising proton exchange membrane (PEM) based fuel cell stack has been developed as an attractive alternative. In addition to being devoid of the explosion risks posed by the conventional systems, this burner brings down the concentration of hydrogen well below its lower explosion limit (LEL). Since the burner also facilitates the recovery of hydrogen in the form of water, it could also be used for recovering the precious deuterium and tritium from a gas stream. This hydrogen burner could also be used in the decontamination of PHWR components and for regulating hydrogen concentration in PHWR cover-gas within the safe limit.

A schematic of this electro-chemical burner is shown in Fig. 1. This comprises a modified fuel cell stack of optimal power, a load box for controlling the load drawn from the fuel cell stack and hydrogen sensors for monitoring the concentrations of hydrogen at the inlet and at the outlet of the fuel cell stack.

The performance of this burner was evaluated with test experiments in which a mixture of argon and hydrogen was let into the fuel cell stack. The current resulting from the electrochemical conversion of hydrogen to water was drawn from this stack using a load box and the concentration of hydrogen was measured both at the inlet and the exit of the stack using an indigenously developed PEM hydrogen sensor. The hydrogen concentration at the exit could also be estimated from the value of the inlet concentration and the current drawn using the load box. (The experimental set–up used is shown in Fig. 2). Fig. 3 depicts the results obtained in support of the efficacy of using the burner for the safe removal of hydrogen. It is evident from the results presented that when a stream containing 10% of hydrogen in argon was used, the hydrogen concentration got reduced to a near-zero value as the current drawn was increased to two ampere. When the hydrogen concentration was increased from 10 to 15%, there was an increase in the concentration of hydrogen at the exit since the rate of removal remains constant at a given current. On increasing the current to 2.9 ampere, the hydrogen concentration gets reduced to

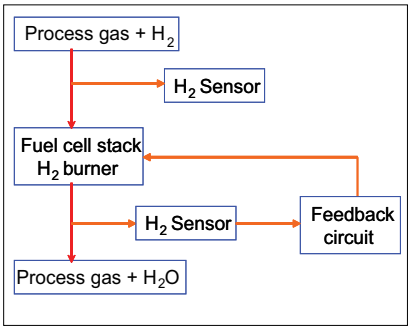

Fig. 1 *Schematic of the electrochemical burner*

Fig. 2 *Electrochemical hydrogen burner*

a near-zero value. Similarly the current drawn was required to be increased depending on the concentration of hydrogen in the gas mixture. Experiments were conducted at 20 and 30% hydrogen in argon. These studies clearly indicated the utility of this electrochemical burner for the safe and rapid removal of hydrogen. The necessity of a feed back system that regulates the current based on the feed back of the value of the measured concentration of hydrogen was also evident from these studies.

Proton Exchange Membrane Fuel Cell based Electrochemical Sensors

From the foregoing it is evident that monitoring the concentration of hydrogen during the clean up operations is an important aspect. In order to accomplish this, a fuel cell based amperometric sensor was developed in-house. The configuration of this hydrogen gas sensor could be expressed by using the standard notation as follows.

$$H_2/Pt//Nafion//Pt/O_2$$

Nafion was used as the electrolyte while the electrodes were made of platinum electrocatalyst. The catalyst film was coated on either side of the membrane by a transfer printing technique (decal method). A sample gas containing hydrogen was passed over the sensing electrode while the counter electrode was exposed to air. This sensor was operated in the fuel cell mode and the short circuit current was measured as the signal. A mechanical barrier was employed to limit the flux of hydrogen gas reaching the sensing electrode. Owing to this, the short circuit current was found to attain a limiting value at each concentration of hydrogen in the carrier gases like argon, nitrogen and carbon dioxide. This sensor functioned as a "self-breathing" device without any air flushing at the counter electrode side. Since the hydrogen flux at the sensing electrode was limited by a barrier, the limiting current measured using a sensitive current meter was found to be linearly dependent on the hydrogen concentration in percentage level. A direct read out device, developed for this purpose stored the calibration parameters and displayed the concentration of the measured hydrogen gas. This sensor has successfully been utilised for monitoring the hydrogen evolved during the sodium cleaning of the Failed Fuel Location Module (FFLM) and Diverse Safety Rod Drive Mechanism (DSRDM). Fig. 4 shows the position of the sensor in the sodium cleaning facility and Fig. 5 shows the time dependent response of this sensor during a sodium clean-up of FFLM.

PEMFC based NO_x Sensor

Nitrogen oxides (NO_x) are produced during the electrochemical acid killing stage in the reprocessing of irradiated fast reactor fuel. Either NO_x or a mixture of NO_x and hydrogen evolve. NO_x being toxic requires continuous monitoring. A polymer electrolyte based amperometric sensor in a "three electrode" configuration has been developed for monitoring the concentration of NO_x (% level) in an inert gas stream (Ar, N_2). This sensor uses Nafion as the proton conducting solid electrolyte. Schematic of this three electrode potentiostatic sensor is shown in Fig. 6. The construction and mode of operation were both identical to that of the hydrogen sensor, excepting that NO_x was sensed instead of hydrogen at

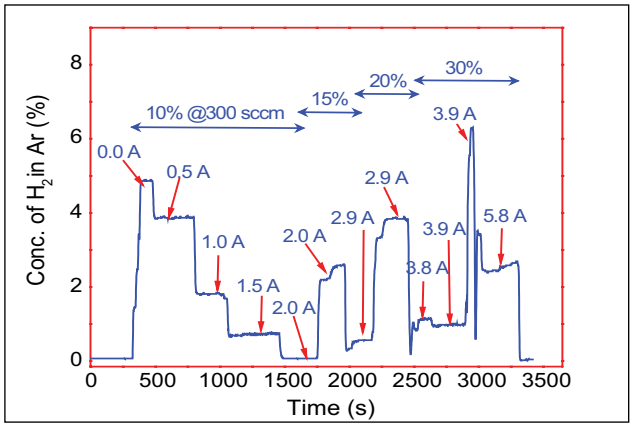

Fig. 3 *Hydrogen removal using electrochemical burner*

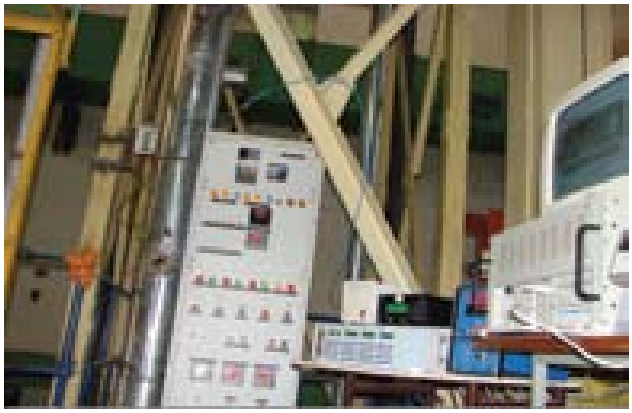

Fig. 4 *Hydrogen sensor used in Na cleaning of FFLM by H_2O-CO_2 process*

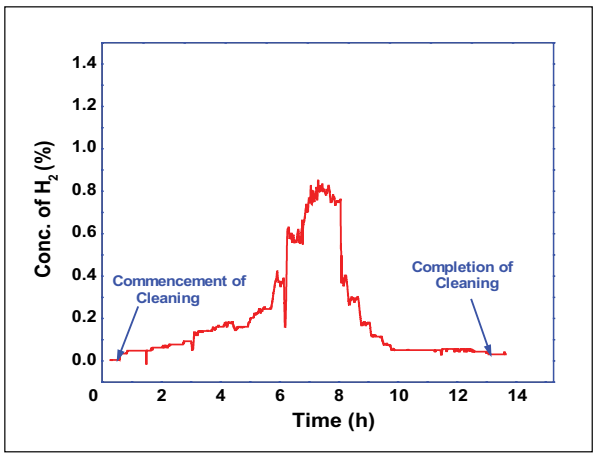

Fig. 5 *Hydrogen released during Na cleaning of FFLM by H_2O-CO_2 process*

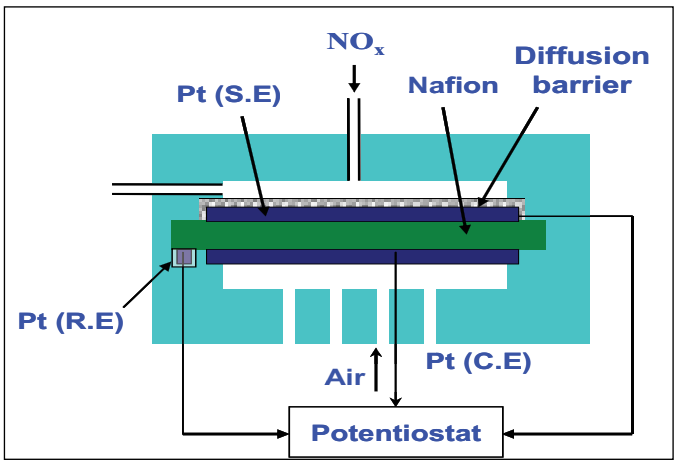

Fig. 6 *Schematic of PEMNS for NO_x in percentage range*

an appropriate potential. The configuration of this cell could be expressed by using the standard notation as follows.

NO_x/Pt//Nafion//Pt/air

This sensor was operated in chronoamperometric mode using a commercial potentiostat. Similar to the hydrogen sensor this sensor also attained a limiting current for each concentration of NO_x. The limiting current was found to vary linearly with the concentration of NO_x in argon as shown in Fig. 7.

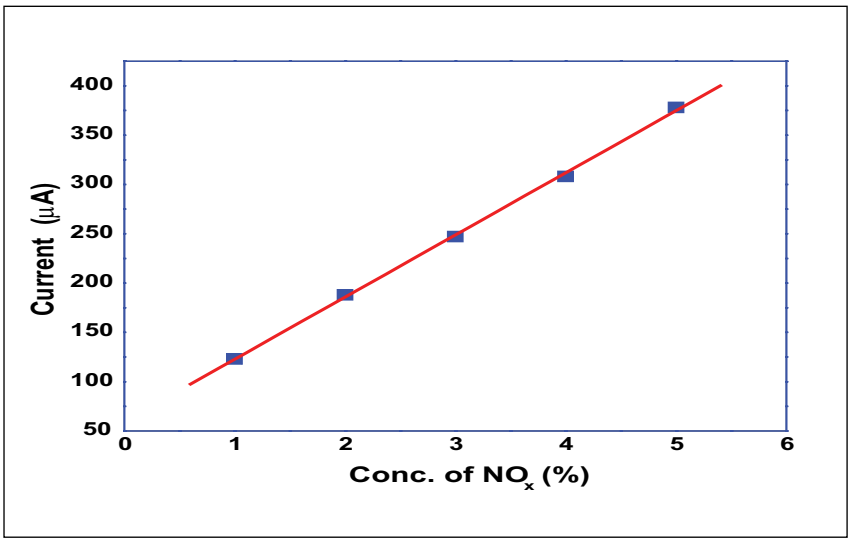

Fig. 7 *Calibration plot of PEMNS for NO_x in percentage range*

III F2.6 Optical Fiber Based Distributed Sensor for Sodium Circuits

Raman scattering based distributed temperature sensor (RDTS) system has been installed and calibrated. The system has a spatial resolution of one meter and temperature resolution of 273.1 K at room temperature with a temporal response of ten seconds.

A test loop for testing fiber optic distributed temperature sensor is erected (Fig. 1). The test loop is provided with base heaters along the axis, local heaters at desired positions and an air blower to obtain different heating/cooling patterns. The total heating system is controlled by PID controllers.

A fifty micron multimode gold coated fiber encapsulated in a protective stainless steel capillary has been used to measure high temperatures. Also, a polyamide coated fiber, which can withstand upto 573 K is laid directly in contact with the loop pipe, in order to study the effect of stainless steel sheath on the sensitivity of the sensor fiber. The stainless steel capillary/ fiber is placed in position using retaining shims spot welded to the body of the pipe (Fig. 1). The insulation and encasing is done in the usual way after the fiber is laid.

Using the gold coated fiber encased in SS, temperature measurements up to 923K have been demonstrated on the test loop (Fig. 2). At these temperatures the temperature resolution achieved is 293 K. Measurements on RDTS agree with

Fig. 1 *Test loop for testing fibre optic distributed sensor* and *SS encased gold coated optical fiber laid on the pipe*

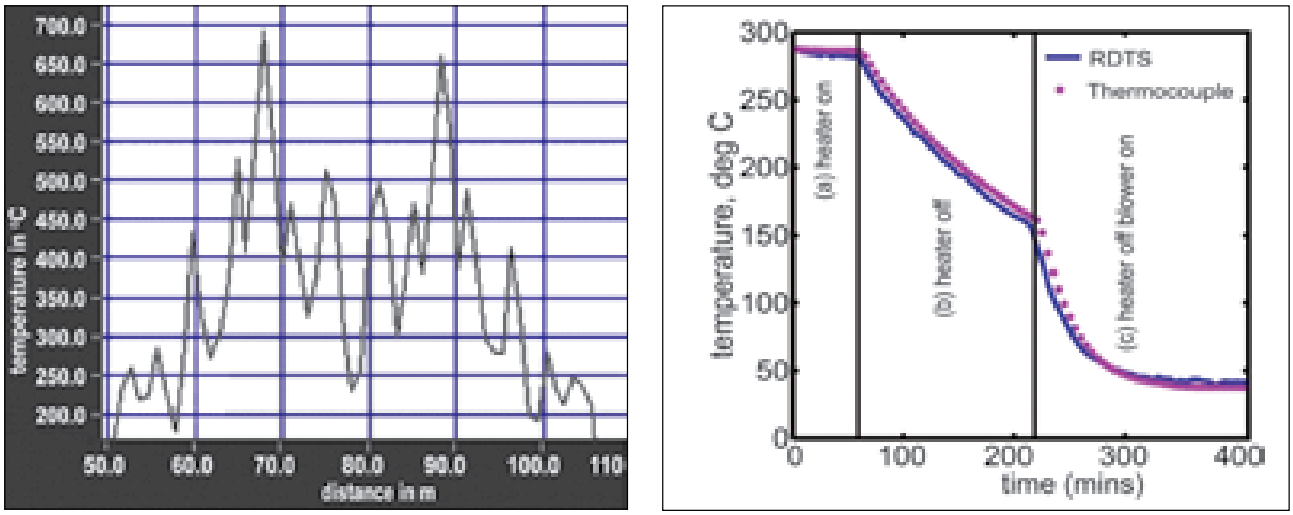

Fig. 2 *Temperature profile measured using RDTS and Dynamic response of RDTS compared with thermocouple*

those of conventional thermocouple based measurements.

Also, temperatures measured by stainless steel encased gold coated fiber and bare polyamide fiber are same at intermediate temperatures. This indicates that there is no significant decrease in sensitivity due to stainless steel capillary encasement of the gold coated fiber.

Fig. 2 shows the comparison of the dynamic response of RDTS with that of thermocouple. In Fig. 2, time period (a) corresponds to the period having temperature in equilibrium when the heater is on. Time period (b) corresponds to the time when the heater is switched off and undergoing natural cooling. Time period (c) corresponds to force cooling by using a blower. Further work is in progress to adopt RDTS system for leak detection.

III F2.7 Analysis of Eddy Current Flowmeter Developed for use in Phenix Reactor in France

Eddy Current Flowmeter (ECFM) is an electromagnetic device, which can be used for flow measurement of electrically conducting liquid metals at different operating temperatures. It consists of a central primary winding, energized from an AC. source, flanked on either side by two identical secondary windings connected differentially. When the flowmeter is immersed in

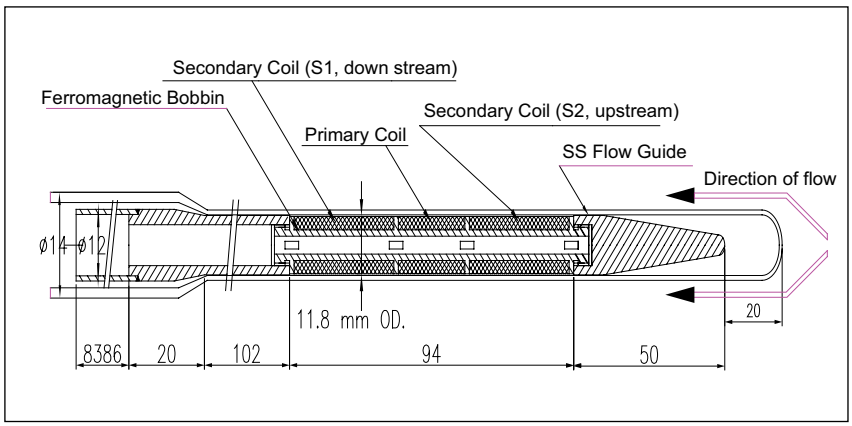

Fig. 1 *Eddy current probe assembly*

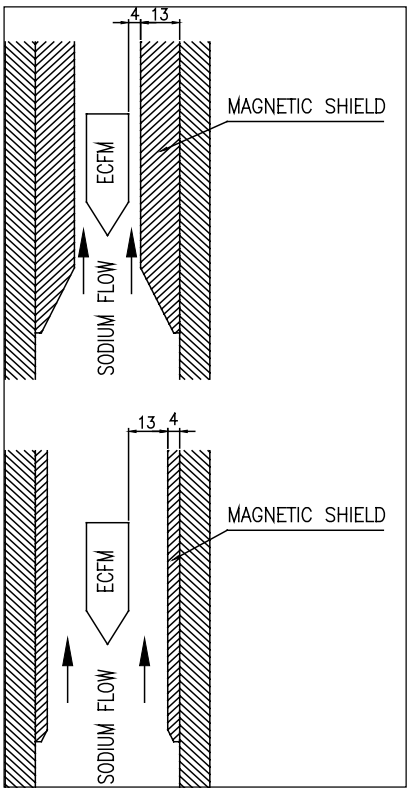

Fig. 2 *Existing Configuration in IGCAR of schematic of the test configuration*

static sodium the two secondary windings develop equal voltage and since both the secondary windings are connected in series opposition, the resultant output voltage is zero. The relative motion of sodium distorts the external field so that the electromotive forces generated in two windings differ by a magnitude proportional to the relative sodium velocity. The ECFM output is improved by providing a magnetic shield of high magnetic permeability surrounding the probe because influence of external magnetic field on secondary winding is blocked by magnetic shield. A magnetic shield of SS 410 has been used for this purpose. The eddy current probe assembly is shown in Fig. 1.

ECFM developed by our Centre will be used for measurement of sub-assembly flow in Phenix reactor in France. The annular gap which will be there for sodium to flow is 4 mm as against 13 mm in IGCAR design. For a given configuration of ECFM, the output signal is function of annular gap, frequency, resistivity and temperature of flowing medium. There exists an optimum frequency at which ECFM output signal is not influenced by variation in operating temperature. Therefore an analysis was done using finite element method (FEM) based software COMSOL 3.4 to determine the operating frequency and the expected voltage range for the test configuration. The schematic of the test configuration is shown in Fig. 2.

S1 and S2 are the output voltages of the two pick-up (secondary) coils. The sensitivity plot, i.e. ratio of differential signal output to the sum of signal output, (S1-S2)*100/(S1+S2) versus various operating temperatures is shown in Fig. 3 for the existing ECFM. The optimum frequency corresponds to the point where the temperature effects on sensitivity are minimum. From Fig. 3. it can be seen that the curves intersect at around 400 Hz which is also validated by the experimental operating frequency of 400 Hz and sensitivity of 1.7%. With this confidence, analysis for ECFM for PHENIX configuration was done for different temperatures and the optimum frequency was found to be 1500 Hz. This modeling has enhanced our confidence in the design of ECFM.

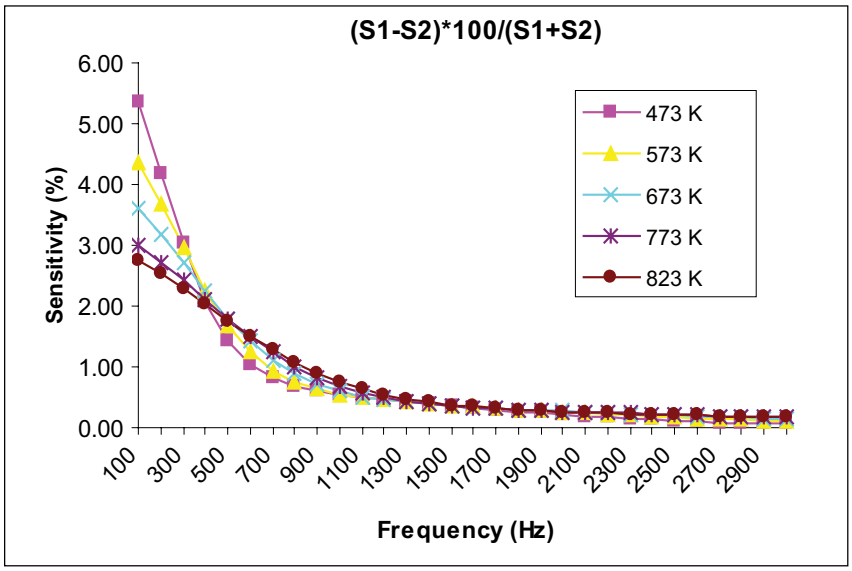

Fig. 3 *Sensitivity plot for the existing configuration in IGCAR*

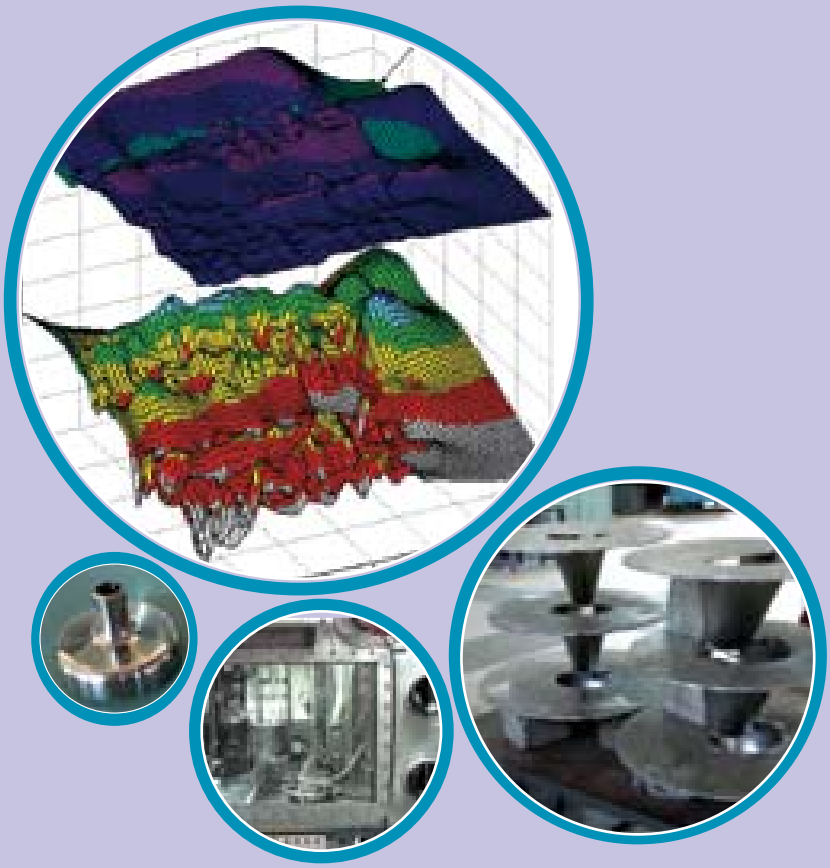

IV

Fuel Cycle

IV A Fuel Chemistry

IV A.1 Laboratory Scale Facility for the Fabrication of Sphere-pac Fuel Pins for Test Irradiation

The sol-gel route for the fabrication of fuel is a fuel fabrication technology that has significant advantages over the conventional process but is yet to be implemented on a larger scale. This procedure averts the handling of powders and many disadvantages associated with it. It is certainly an attractive alternative, for it involves lesser number of process steps and is also amenable for automation. Microspheres of mixed oxide prepared through the sol-gel route would be used to fabricate sphere-pac fuel pins by vibrocompaction. A laboratory scale facility has been set up for fabricating these test pins.

Fig. 1 *Sol-gel internal gelation set up in the containment box*

This facility has an interconnected array of special purpose glove boxes that house the equipment required for carrying out the various unit processes in the fabrication. This facility was designed such that it is best suited for remote operation through master slave articulated manipulators (AM) and for maintenance with gloves.

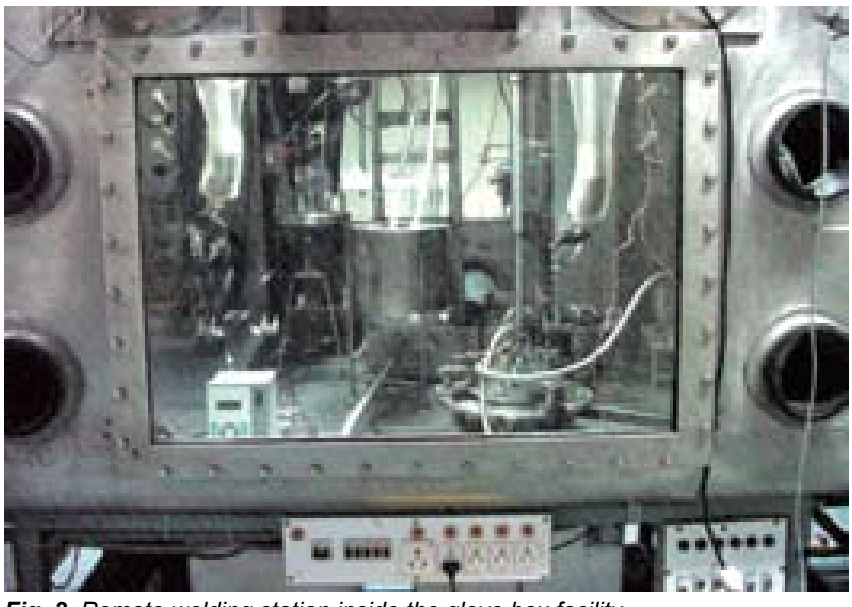

Fig. 2 *Remote welding station inside the glove box facility*

The larger MOX microspheres would be produced through an internal gelation process in a set up housed inside a glove box (Fig.1). Special equipment such as a vibrator lifting mechanism driven by chain-pulley counter weight arrangement, nozzle changing device actuated by quick release mechanism, calcination furnace lifting mechanism driven by gantry mounted three stage telescopic hoisting system etc., facilitate automated remote operation. The commissioning of these equipment was completed and UO_2 microspheres were produced successfully. The microspheres produced in this process would be sintered in a tungsten mesh furnace housed in another glove box.

The salient features of equipment inside the glove box include; top

dome lifting mechanism driven by ball screw-nut unit, pneumatically actuated dome indexing mechanism, high precision gantry mounted XYZ positioning system with pneumatic grippers for handling the charge carrier and suction transfer devices for loading-unloading microsphres from / into the charge carrier. Operations such as loading of microspheres in clad tube, vibrocompaction and end cap welding will be carried out in a double module special glove box.

This glove box also houses the equipment required for degassing and weighing and suction transfer of aliquots of the two fractions of microspheres for loading them in the fuel pin. After vibrocompacting the microspheres, the clad tube will be moved to another station where hardware such as insulation pellets, spring etc. would be loaded before finally moving it to a welding station (Fig. 2) In the welding station operations such as the end cap loading, evacuation, backfilling of helium bond gas at 6.2 bar and remote end cap welding in vertical position will be carried out. The entire process sequence was successfully demonstrated by fabricating dummy fuel pins with only UO_2 microspheres with an appropriate smear density (78%TD). This pin comprised of UO_2 microspheres of both coarse, fine fractions and other internals. These dummy fuel pins were subjected to quality control steps and were found to be meeting the acceptance criteria.

An internal gelation assembly was set up, commissioned inside a double module glove box and many batches of coarse fraction UO_2 microspheres of 98-99% TD were prepared for trial welding operations. Several batches of fine fraction of UO_2 microspheres were prepared using a jet-entrainment set-up. These microspheres were characterized and were found to meet the specifications for use in test fuel pins.

IV A.2 Applications of Modifier Free Delivery of Ligands for Supercritical Fluid Extraction of Actinides

Supercritical fluids possess the properties of gas-like diffusivity and viscosity, liquid-like density and low surface tension that help them to easily penetrate through the pores of a sample matrix and extract the components of interest more efficiently. Supercritical fluids provide faster, cleaner and efficient extractions, and they become gas at the end of extraction and escape leaving behind the dissolved solute. Thus the supercritical fluid extraction technique provides an excellent alternative to recover the actinides with minimum generation of secondary liquid waste. Carbon dioxide modified with ligands is used for the extraction of metal ions including actinides. However, the ligand delivery without modifier results in elimination of liquid secondary waste. It is also essential to minimize the phase perturbation by a modifier to safeguard the integrity of the supercritical fluid phase of carbon dioxide. Supercritical fluid extraction based procedures were earlier developed in-house using modified supercritical carbon dioxide for the recovery of uranium, plutonium and americium from various waste matrices (e.g.) tissue paper, removal of silicone oil from urania microspheres, separation of uranium from thorium etc.

The supercritical fluid extraction system comprised two reciprocating pumps i.e. one with a chiller head to liquefy and pump the supercritical fluid carbon dioxide and another for the delivery of ligand dissolved in methanol, ligand delivery vessel, extraction vessel for accommodating metal ions, a constant temperature oven (±0.1 K) and a back pressure regulator. Ligand delivery vessel (LDV) with a restricted geometry (LDV-RG, 10 mL) was employed for the delivery of ligands such as octyl (phenyl)-N, N-diisobutylcarbamoylmethyl phosphineoxide (CMPO) and di(2-ethylhexyl)isobutyramide (D2EHIBA). The design of a vessel with a restricted geometry involves inlet and outlet located beside each other i.e. in the same face of the ligand delivery vessel.

Supercritical fluid extraction of uranyl nitrate crystals, uranyl nitrate from tissue paper matrix and preferential extraction of uranyl nitrate from thorium nitrate was investigated using modifier

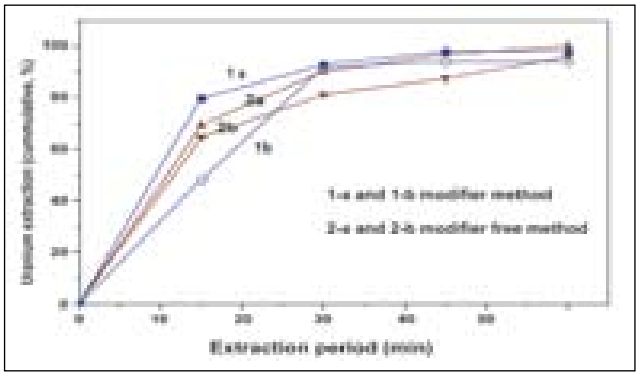

Fig.1 *SFE of uranyl nitrate (~5mg U) from tissue paper matrix. conditions: Super critical CO_2 2.5mL/min; Pressure 300 bar and Temperature 313 K*

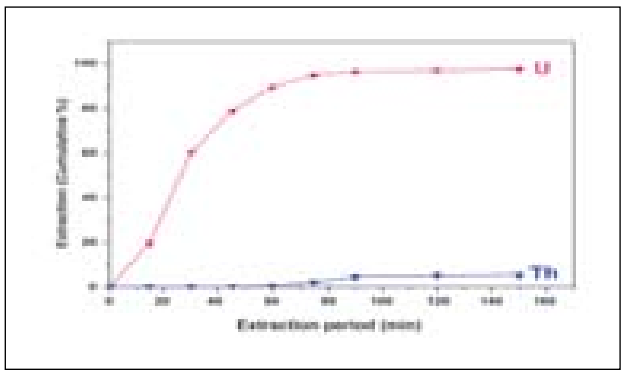

Fig.2 *Preferential extraction of uranium over thorium.*

free delivery of ligands. The ligand CMPO was employed for the extraction of uranyl nitrate. The modifier free mode of delivering CMPO was compared with the extraction of the same using CMPO in a typical modifier mode i.e. CMPO dissolved in methanol. In both these studies, the quantity of CMPO delivered was maintained at about 50mg/h. The extraction profile of uranium using CMPO delivered by modifier free mode established the extraction pattern, similar to the trend observed with the CMPO in methanol, in which a complete extraction of uranium was achieved (Fig. 1) (Super critical CO_2 2.5 mL/min; Pressure: 300 bar, Temperature: 313 K, 1a, 1b: CMPO in methanol flow rate of modifier 0.1 ml/min 2a, 2b: 500mg loaded to 10ml vessel). The comparable extraction of uranium in the typical extraction period of forty five minutes establishes the feasibility of achieving the extraction without incorporating the typical modifier methanol.

Thorium fuel cycle requires a method for the preferential extraction of uranium over thorium. D2EHIBA was delivered from a vessel of restricted geometry up to a period of ninety minutes. The results of the preferential extraction of uranyl nitrate over thorium nitrate are shown in Fig.2 (D2EHIBA (250mg) taken in 10ml vessel (LDV-RG) super critical CO_2: 2.5ml/min; Pressure 300bar and Temperature: 313 K, 50mg each uranium and thorium nitrates taken in 1ml extraction vessel). The preferential extraction of uranium over thorium was established in these studies.

The controlled delivery of ligands such as CMPO and D2EHIBA by this method results in the elimination of secondary liquid waste. Moreover, as the rate of extraction of the metal ion decreases towards the end, the amount of ligand required for complexation may also fall proportionally and hence the controlled delivery of ligand for complexation can effectively lead to waste minimisation.

IV A.3 Design and Analysis of Metallic Fuel Pins for FBRs

Metallic fuel is being developed for use in future FBRs. In order to acquire data and experience on the performance of the metal fuel pin it is proposed to load experimental pins in a sub assembly of FBTR.

Hence, it is decided to use the FBTR SA with pin length of MK-1 fuel pin (531.5 mm). To extrapolate the performance for future reactors, PFBR clad size of 6.6 mm OD with 0.45 mm thickness is considered. With these dimensions, a 37 pin subassembly is contemplated for this purpose. To assess the metal fuel performance, two design variants viz., sodium bonded and mechanical bonded designs are under study. In sodium bonded type, two design options viz., 6% Zr in fuel and fuel without Zr and incorporated as Zr-4 liner are conceived. In the alternate design, clad, liner and fuel are co-swaged together such that all of them are mechanically bonded in which fuel is designed with two grooves. To achieve higher burn-up, a low swelling material T91 is chosen as the clad material.

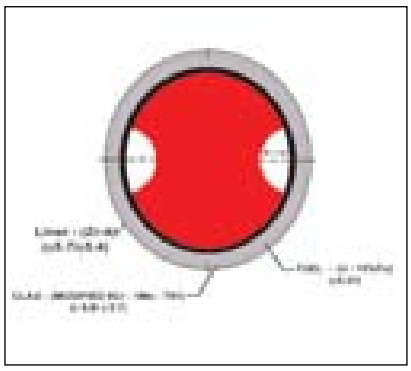

Fig.1 *Fuel pin showing geometry of various media*

In sodium bonded concept, it is expected that once pores in the metal slug get interconnected, fission gases will get released from the fuel matrix. In order to allow inter connection of pores, a lower smeared density of 75% theoretical density (TD) is chosen for both binary & ternary fuels. In the mechanical bonded concept, two grooves of 1.1 mm radius are provided longitudinally in the fuel slug. Since this groove is expected to act as a sink for early fission gas release, a higher smeared density of 85% TD for this type of fuel is considered. Fuel slug diameter is accordingly worked out. A plenum length of about 1.5 times the fuel column length is provided to accommodate fission gases released and axial elongation of the fuel due to thermal expansion and swelling. Location and length of plenum is decided in such a way to satisfy cumulative damage fraction (CDF) limit of 0.25. While plenum is distributed both at the top & bottom in the case of mechanical bonded pin, it is restricted only to the top of fissile column in the case of sodium bonded pin. Based on this requirement and the availability of pin length, fissile column length works out to be 160mm. Fissile column top is made to align with the middle of MK-1 core in the case of sodium bonded fuel and for mechanical bonded fuel, the middle of both fuel columns coincide. To improve breeding, a lower axial blanket is provided in all the pins.

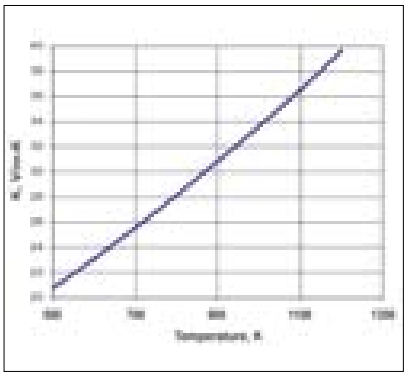

Fig.2 *Thermal conductivity of (U-15% Pu) Fuel*

In order to fix the operating parameters, thermal design was carried out based on the limitation to restrict the clad inside temperature under hotspot condition to 923 K and to avoid fuel melting at 116% power. Hot spot factors have been estimated and parameters have been grouped depending on

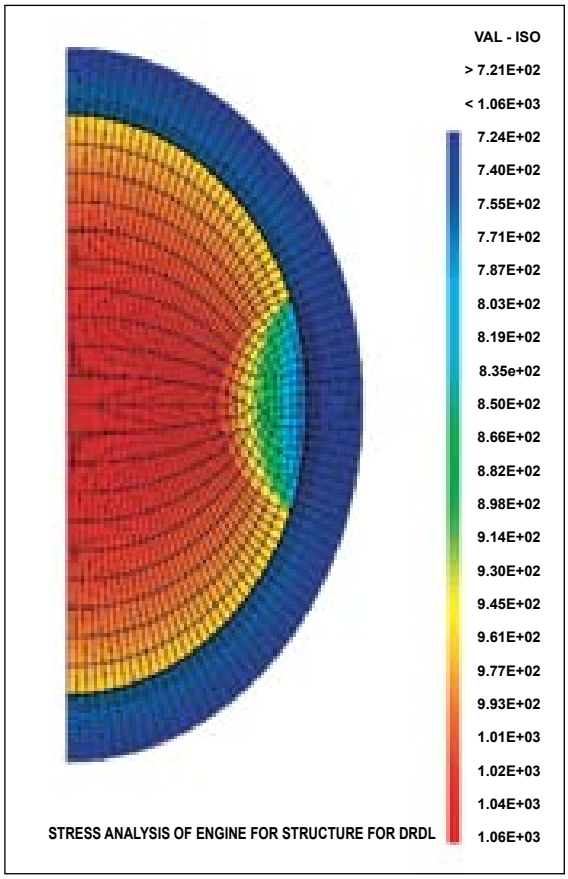

Fig. 3 *Temperature distribution in fuel pin*

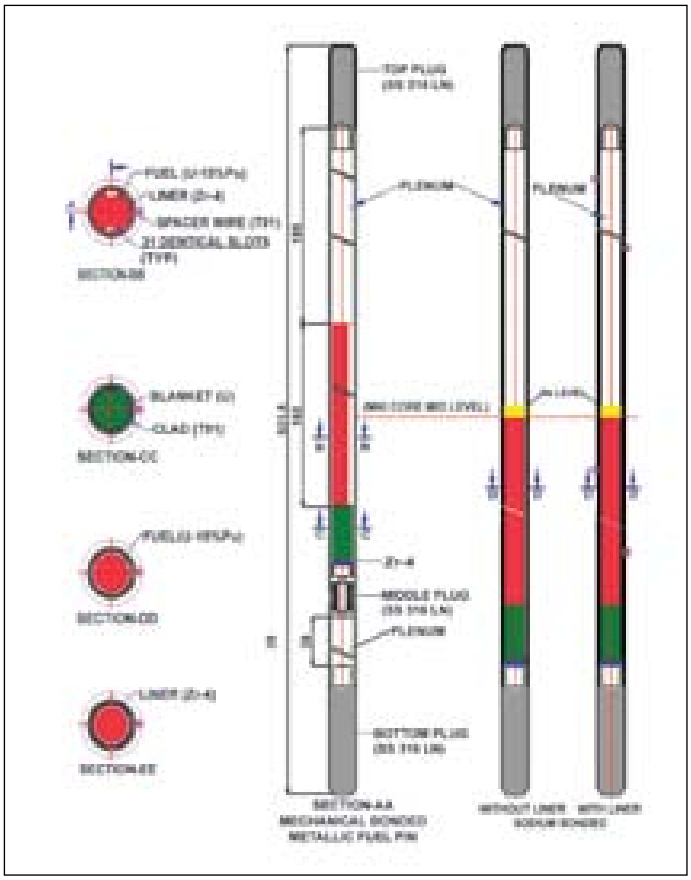

Fig. 4 *Metallic fuel pin*

the nature of their occurrences, statistical or direct. For the purpose of the experimental irradiation, inlet temperature of 653K is considered in FBTR and accordingly the subassembly is designed for a flow of 1.9 kg/s. Allowable linear power rating for each concept has been arrived at the beginning of life (BOL). The effect of the reduction in thermal conductivity with burn-up has also been considered while arriving at the limits. It is found that metallic fuel pin with both sodium and mechanical bonded concepts can be safely operated at 450 W/cm peak linear power and can sustain a burn-up of 150 GWd/t.

Fuel pins with all the three types of design will be tested in FBTR and fuel performance will be characterized. In order to compare the FBTR experimental pin with power reactor size pin for future FBRs, an estimate of temperature distribution in a metallic fuel pin has been made with core length of 1000mm. For this purpose, the helium bonded metallic fuel with liner and clad is modeled in 2-D and analysed with CASTEM code. The geometry of various media and thermal conductivity of fuel are shown in Fig.1 and Fig.2 respectively. The steady state temperature distribution in the fuel pin is shown in Fig.3. It is observed that fuel centre temperature is below its melting point for the design conditions. Fuel pins of two different types for the experimental program in FBTR are shown in Fig.4.

The design and analysis of metallic fuel pins marks an important phase in the metallic fuel development program.

IV A.4 Evolution of Carbon to Metal Ratio for MARK-I Carbide Fuel as a Function of Burn-up

The fuel used in the Fast Breeder Test Reactor (FBTR) is a bi-phasic mixture of the mono and sesqui-carbides of uranium and plutonium. Fuels with two different Pu/(U+Pu) ratio viz., 0.70 (Mark-I) and 0.55 (Mark-II) have been used in this reactor. The fission products bind the available carbon leading to a reduction in the effective carbon available per metal atom. The ratio of the total carbon to that of the (total) metal in the fuel (C/M) is used as an index for the availability of carbon. If the C/M drops below unity, the sesqui-carbide phase would disappear leading to the formation of a relatively low melting metallic phase. Hence, the evolution of the C/M as a function of burn-up needs to be evaluated.

The relative quantities of the various elements formed in the Mark-I fuel during fission (fission yields) under fast neutron flux, needed for the calculations were computed by using the KRIGEN code. The fission product elements could be categorized based on their similarity in their chemical behaviour, as shown in Table 1. Some of the fission product carbides dissolve in the fuel matrix. For example, ZrC, YC, NbC and mono carbides of the lanthanides 'LnC' dissolve in the mono-carbide phase of the fuel and the sesqui carbides of the lanthanides Ln_2C_3 dissolve in the sesqui-carbide phase of the fuel. The C/M is influenced by the dissolved fission products as well as the presence of oxygen. For instance Ba and Sr could also be bound by the residual oxygen present in the carbide. Thus the extent to which these elements consume carbon

Table 1: Categorization of fission products based on similarity in their chemical behaviour

Category	Elements	Carbide formed	C_{used}
Non-carbide formers	(Se+Te),(Br+I), (Xe+Kr),(Rb+Cs)	-	0
Noble Metals	(Ag+Cd+In+Sn+Sb), Ru	$MPgC_2$,M_2PgC_2	2/3
Mono-carbides	(Zr+Y+Nb),Mo,Ln	mono	1
Sesqui-carbide	Ln	sesqui	1.5
Di-carbide	(Sr+Ba)	di	2

would be rather lowered due to the presence of oxygen leading to an increase in the C/M. However, in order to estimate the maximum possible reduction in the C/M, the effect of oxygen is not considered in the present computations.

Once the carbon bound by various fission products is computed, C/M can be calculated by using for the following relation:

$$\left(\frac{C}{M}\right)_{\beta} = \left(\frac{C}{M}\right)_{o} - \left(\frac{C_{used} - \beta}{(100 - \beta + Yield_{(Y+Zr+Nb)} + Yield_{Ln})}\right) \quad (1)$$

Where β is burn-up, C_{used} is as described in Table 1 and the subscript 'o' is used for the fresh fuel (zero burn-up).

The carbon consumed by various fission products, forming mono-, sesqui- and di-carbides, as indicated in Table 1, is computed by using

$$C_{used} = 2*(\%Y_{Ba}+\%Y_{Sr}) + (\%Y_{Zr}+\%Y_{Y}+\%Y_{Nb}) + \%Y_{Mo} + 2(\%Y_{Pg})/3 + 1.25\ \%Y_{Ln}$$

where %Y is the percentage yield of the respective fission products. Lanthanides form both 'LnC' and $LnC_{1.5}$ and the carbon weightage per Ln is taken to be 1.25. The results obtained using the basic model are shown in Fig.1 along with the results from earlier work. These computations are in reasonable agreement up to about 100 GWd/t burn-up. The sharp increase in C/M when C/M falls below one, was attributed to the conversion of M_2PgC_2 to MPg_3 as shown below:

$$3\ M_2PgC_2 = 5\ MC + MPg_3 + C \quad (2)$$

where Pg refers to a noble metal. The contribution from the lanthanides to the C/M was corrected by incorporating two features in this computation. They were i) a correction for the contribution from the cerium and ii) for the relative quantities of the mono and sesqui carbides of the lanthanides. The details of these corrections are given below.

The metal Ru forms a stable compound $CeRu_2$. Earlier studies have revealed that almost all the ruthenium exists as $CeRu_2$ in the carbide fuel. Thus, the elements Ce and Ru would not bind carbon. Consequently the term C_{used} in the equation (1) becomes lesser to the tune of their yields. Thus the net contribution to the carbon consumption from the lanthanides excludes the contribution from Ce. The C/M computed after the incorporation of this feature was found to be higher than that predicted by the basic model as shown in Fig. 1. Further, the C/M was found to cross unity at a burn-up of about 185 GWd/t (~21 at%).

The basic model assumes that the fission product lanthanides form equal proportions of both the mono- LnC and sesqui-carbide $LnC_{1.5}$ phases. A mean weight factor of carbon demand for the lanthanides was assigned as 1.25. Based on a recent computation made in our laboratory it was found that a weight factor of 1.01 is more appropriate. The incorporation of this factor resulted in a further increase in C/M, (Fig. 1).

This study indicated that the C/M evolution predicted by the basic model proposed by Kleykamp and the new extended proposed model were in agreement for the Mark I FBTR fuel upto a burn-up of 100 GWd/t. The extended model revealed that the formation of the intermetallic $CeRu_2$ helps maintain the C/M of the fuel above unity upto a burn C/M of 185 GWd/t. Further amendment of the relative proportion of the mono- and sesqui- carbide formed by the lanthanides showed that the C/M of this fuel would fall below unity only at a burn-up as high as 220 GWd/t (~25 at %). These calculations did not consider the role played by oxygen in the evolution of C/M. Hence this is a conservative over-estimate of the reduction of C/M with burn up. The results obtained in this work served as valuable inputs for making a decision on the extended operation of the reactor with the above fuel.

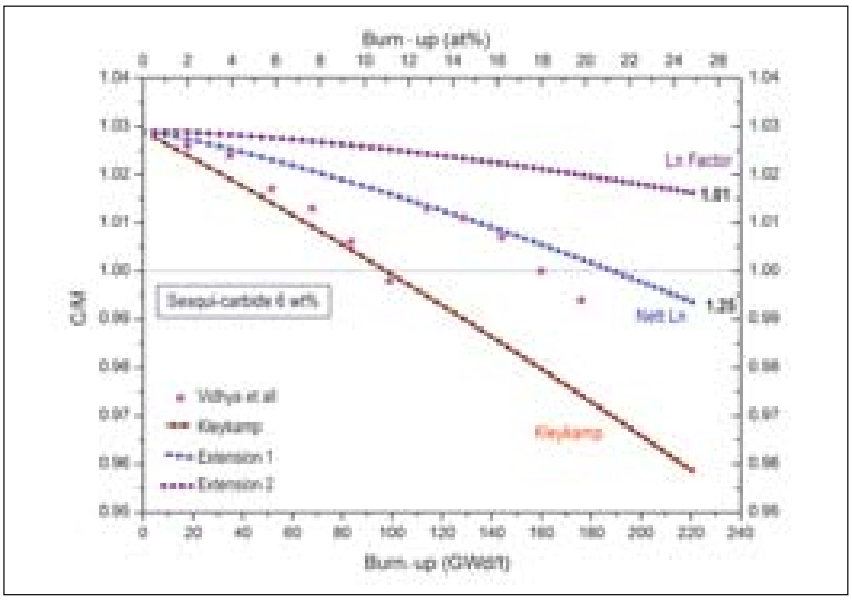

Fig. 1 *Variation of C/M with burn-up for the MarkI mixed carbide fuel for FBTR*

IV B Reprocessing & Waste Management

IV B.1 Reprocessing of Spent FBTR Fuel in CORAL

CORAL achieved a landmark of reprocessing of irradiated fuel from FBTR with a burn-up of 155 GWd/t. The campaign was successfully completed with the product meeting the specifications. Neutron flux measurements were carried out extensively inside the cell to assess the fissile material inventory in the facility.

A new process based on hydrazine carbonate was standardized and deployed in the spent solvent treatment facility to treat the lean organic on a routine basis. Though the treated organic was reused in the plant without any difficulty atleast three times, the raffinate losses are being closely followed to assess the performance. This exercise will aid in estimating the quantum of organic waste generated during the reprocessing of short cooled fuels.

Hulls from the 155 GWd/t campaign were taken up for estimation of plutonium by γ-scanning, using HPGe detector, (Fig. 1). Initial results show Ce^{144} peak which is indicative of Pu. Calibration using Ga^{72}/Na^{24} is being done to quantify the material.

CORAL continues to provide a test bed for optimizing the various process parameters and new techniques for measurement so that they can be deployed in future plants.

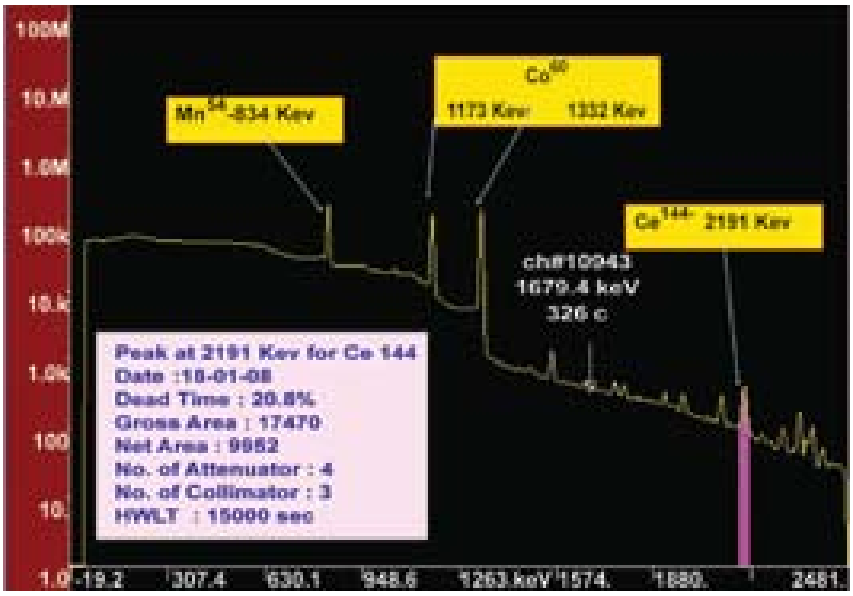

Fig. 1 *γ-spectrum of hulls from the 155 GWd/t campaign*

IV B.2 Current Status of Demonstration Fast Reactor Fuel Reprocessing Plant

Demonstration Fast Reactor Fuel Reprocessing Plant (DFRP) is construed as a vital link between the pilot plant CORAL and the commercial PFBR fuel reprocessing plant (PFRP). Successful demonstration of name plate capacity in DFRP by ensuring high plant availability factors is crucial for large scale launching of fast breeder reactor fuel reprocessing program. All the efforts are taken to incorporate design modifications required with respect to critical equipment such as chopper, dissolver, centrifugal contactors re-conversion equipment etc., (based on the invaluable operational experience gained through the several CORAL campaigns).

Piping engineering of all the cells and cell service area has been completed. Since severe space constraints exist, plant design system (PDS) piping software has been used (as a maiden venture) for cell service area piping engineering to ensure and facilitate interference free piping. A perspective view of the sampling cell is shown in Fig. 1.

Major site works viz., civil, mechanical, electrical, instrumentation and control are being executed through contracts in packages. Construction and geotechnical works of head end facility are in progress. Tenders have been released for all but two mechanical

works. All the major mechanical works are in progress. Purchase orders have been placed for all the critical and long delivery components such as chopper, dissolver, centrifuges, centrifugal extractors, in-cell cranes for sampling and contactor cells, assembly of radiation shielding windows and various types of manipulators.

Safety clearance for the plant by AERB is under progress. Seismic re-evaluation of all safety related buildings and systems are a pre-requisite for safety clearance for plant operation. The tender document prepared for floating consultancy tender for seismic reevaluation of DFRP safety related buildings and systems has been finalized.

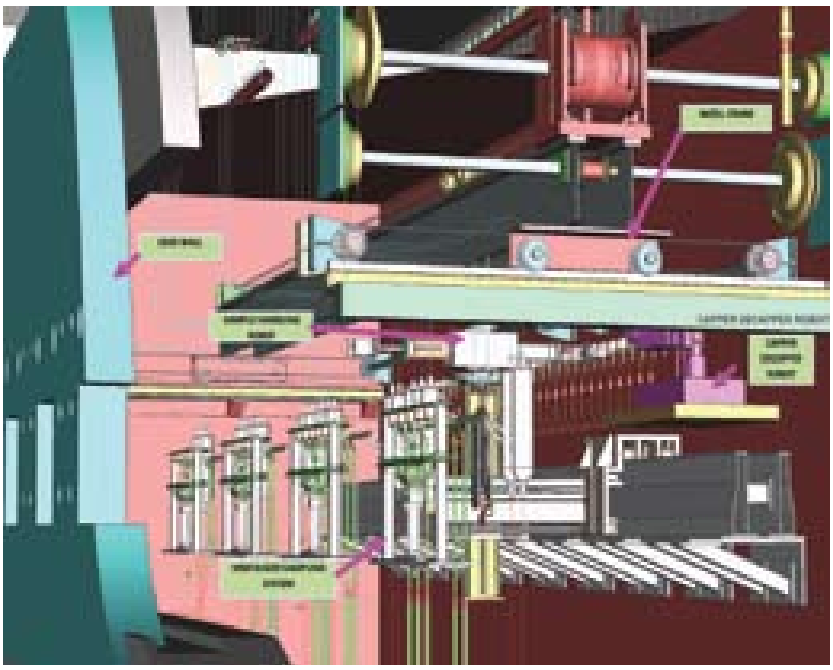

Fig. 1 *A perspective view of the sampling cell in DFRP*

Cold commissioning of the plant is slated for December 2009.

IV B.3 Status of Work on Fast Reactor Fuel Cycle Facility

Work on the design of the Fast Reactor Fuel Cycle Facility (FRFCF) to close the fuel cycle of PFBR is in progress (perspective view shown in Fig.1). The work is being piloted by IGCAR with technical support from BARC and NFC. Revised financial sanction for the preparatory project for development of site infrastructure and engineering of FRFCF has been obtained and the work is in progress. Approval of AERB for the site has been obtained. Technical investigations of the site like geotechnical investigations, hydro-geological studies and estimation of design basis flood level have been completed. Basic infrastructure like approach roads, construction power supply system, and storage/construction office space is being created at the site to reduce the lead time required

Fig. 1 *Perspective view of the planned Fast Reactor Fuel Cycle Facility*

to commence the construction work once the FRFCF project is sanctioned. The progress of work on stores building in FRFCF site is shown in Fig. 2. Review of the preliminary safety analysis report by project design safety committee for FRFCF and specialist working groups is in progress. The detailed project report and detailed design are planned to be prepared with assistance from consultants. Process of appointment of consultants is in progress. Detailed project report for FRFCF is planned to be submitted for financial sanction during the year 2009-10.

Fig. 2 *Work on stores building in progress at FRFCF site*

IV B.4 Environmental Impact Assessment for Fast Reactor Fuel Cycle Facility

Reactors with integrated fuel cycle facility, consisting of fuel reprocessing plant, fuel fabrication plant and waste management plant at a single site is the concept that is being adopted in India in the current phase of fast reactor programme. Integrated nuclear fuel cycle facilities restrict the movement of the fissile materials within the nuclear complex thereby completely avoiding transport of fissile materials in the public domain. An integrated Fast Reactor Fuel Cycle Facility (FRFCF) consisting of a Fuel Reprocessing Plant (FRP), a Fuel Fabrication Plant (FFP), a Reprocessed Uranium Plant (RUP), a Component Subassembly Plant (CSP) and a Waste Management Plant (WMP) is being planned at Kalpakkam (Fig. 1).

As per Environmental Protection Act 1986, obtaining prior approval for the project from Ministry of Environment and Forests (the competent authority in India) is a mandatory requirement. Carrying out a study of the environmental impact and prescribing the plans for the environmental management is a key element in the environmental clearance process. M/s MECON Limited was entrusted with the responsibility of carrying out the study, preparation of the report and for obtaining the necessary regulatory clearances. The tasks related to radiological assessment was excluded from the scope of the work and was done by RSD, IGCAR.

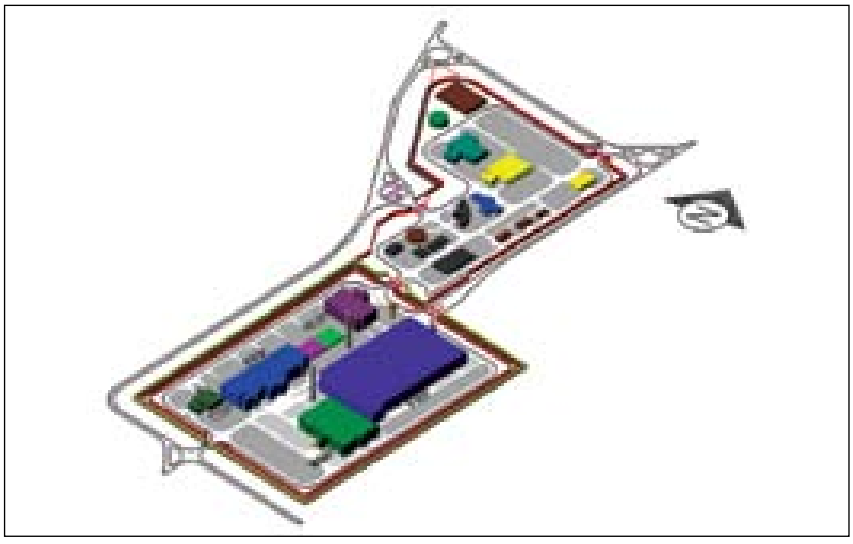

Fig. 1 *FRFCF complex – Layout of various plants*

Project activities responsible for environmental impact during the phases of siting, construction, operation and future phases were identified first. An impact matrix was generated with each column in the matrix referring to a particular activity and rows indicating the environmental factors that are influenced by the respective activity. Based on this, the parameters of the study were identified, sampling locations were finalized and field measurements were carried out for a period of three months. An Environmental Impact Assessment report highlighting the environmental

parameters studied, criteria for the choice of the sampling locations, sampling protocol and results of the analysis of the data collected during the first three months of the survey was prepared. The report with the results and analysis of data collected has been completed in May 2007. The report prepared as per the guidelines issued by Ministry of Environment and Forests contains eleven chapters viz.,

(i) introduction
(ii) project profile
(iii) impact identification
(iv) description of the environment
(v) prediction and evaluation of the impacts
(vi) mitigation measures
(vii) project benefits
(viii) additional studies
(ix) environmental monitoring programme
(x) disaster management plan and
(xi) environmental management plan.

The study has concluded that the construction of the project would bring-in a net positive benefit with implementation of the management plans suggested in the report.

IV B.5 Shear Wave Velocity Model at Fast Reactor Fuel Cycle Facility Site

Geotechnical investigations for nuclear facility sites vary widely in nature when compared to those for conventional infrastructure facilities. A complete and accurate site characterization of nuclear facility site is based upon an integrated approach, which includes both geophysical and exploratory geotechnical investigation. Benefit of geophysical measurements is to increase the spatial sampling density so that background and anomalous conditions can be accurately identified early in the investigation, thereby accurately positioning detailed measurements to critical areas of concern. Apart from mapping, geophysical investigations are used to develop the strength parameters of sub strata. Seismic refraction survey and site specific geotechnical investigations were carried out at FRFCF site to characterize the site. Subsurface

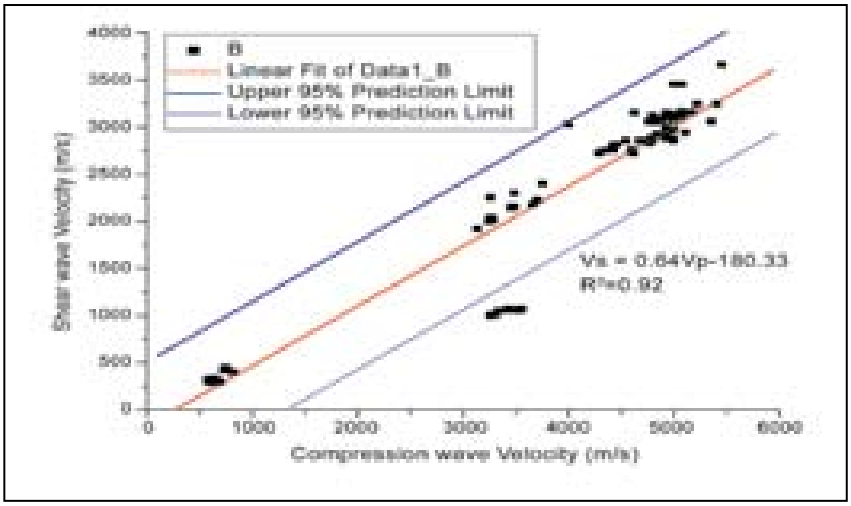

Fig. 2 *Relation between compression wave and shear wave velocity*

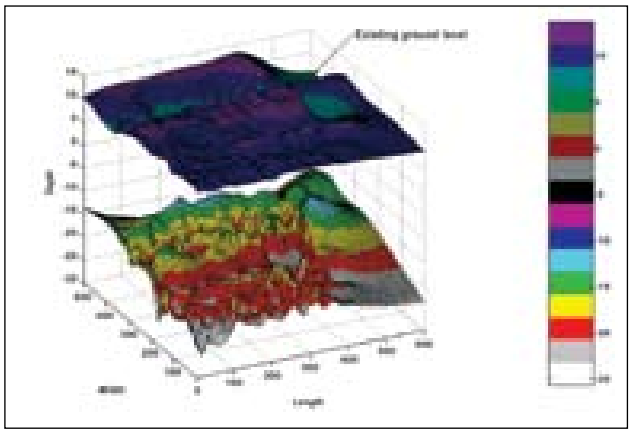

Fig. 1 *Soil model of FRFCF*

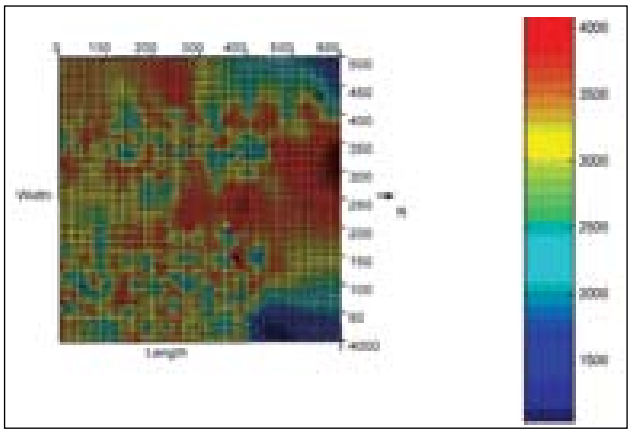

Fig. 3 *Shear wave velocity model*

model developed by integrating seismic refraction survey and site specific investigation is shown in Fig. 1. Determination of seismic wave velocity is important in evaluating engineering properties of sub soil material. Seismic compression wave velocity evaluated from seismic refraction survey varies from 4800 to 6000m/sec. However a few zones with velocity less than 3800m/sec were identified during the seismic refraction survey. For geotechnical engineering applications evaluation of shear wave velocity is important. Hence a site specific correlation was established between compression wave and shear wave velocity from site specific seismic cross hole test by carrying out a regression analysis which is given by the equation

$$V_s=0.64V_p-180.33\ (R^2=0.92)$$

Where V_s is shear wave velocity in m/sec and V_p is the compression wave velocity in m/sec. The relation is shown in Fig. 2. By using the above relation a shear wave velocity model was established at the bed rock level and found to be more than 2000m/sec, suggesting that the bed rock can be classified as hard rock. The shear wave velocity model obtained where RQD is more than 50 is shown in Fig 3. This shear wave velocity can be utilized for evaluating engineering properties of sub surface material.

IV B1 Process Development

IV B1.1 Electrochemical Studies Relevant to Pyrochemical Reprocessing

U-Pu-Zr alloy a candidate fuel for fast reactors, is reprocessed after attaining the target burn-up by using a pyro-electro-metallurgical process. This process is popularly known as molten salt electrorefining and involves the anodic dissolution of the spent U-Pu-Zr fuel followed by selectively depositing uranium on a solid cathode as well as recovering uranium and plutonium together by using a molten cadmium cathode. Zirconium, the third major constituent of this alloy fuel could exist in multiple oxidation states in the molten salt medium. The redox behaviour of zirconium in LiCl-KCl including the influence of the presence and absence of zirconium metal was studied and the redox couples involving Zr^{4+}/Zr^{2+} and Zr^{+}/Zr were identified by using transient electrochemical techniques.

The electrochemical reduction of the zirconium ions is also complicated by coupled homogeneous reactions and adsorption of the electroactive species. The cyclic voltammogram of $ZrCl_4$ in absence of zirconium metal shown in Fig. 1 indicates the presence of two redox

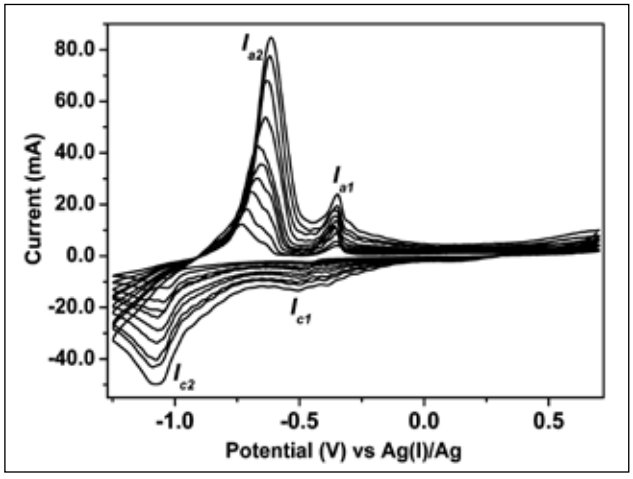

Fig. 1 *Cyclic voltammograms of $ZrCl_4$ in LiCl-KCl eutectic at 823 K (electrode W)*

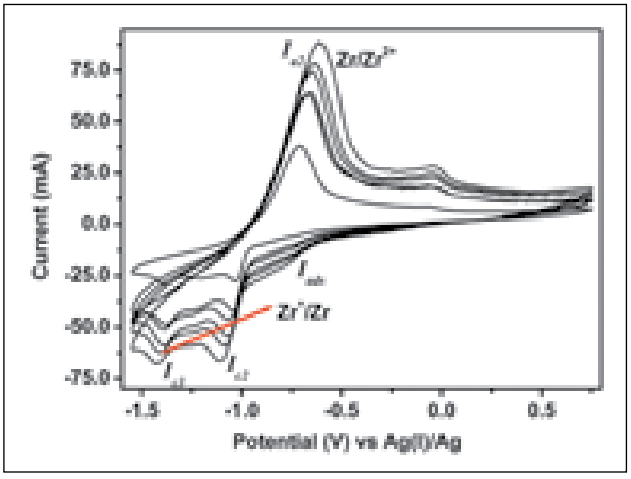

Fig. 2 *Cyclic voltammograms of $ZrCl_4$ + Zr metal in LiCl-KCl eutectic at 823 K (electrode W)*

couples, Zr^{4+}/Zr^{2+} and Zr^{2+}/Zr. The redox couple Zr^{4+}/Zr^{2+} is absent when zirconium metal is added to the melt as evidenced by the cyclic voltammogram depicted in Fig. 2. This clearly indicates that the addition of zirconium metal reduces Zr^{4+} to Zr^{2+}. (The prepeak I_{ads} in this figure corresponds to the adsorption of Zr^{2+} and the cathodic peak I_{c3} corresponds to the Zr^{+}/Zr couple).

It is necessary to develop in-situ analytical techniques for monitoring the concentration of actinides in the molten salt electrolyte during the electrorefining process. The concentration of uranium and plutonium in the electrolyte varies from 7-8 wt.% at the beginning of the electrorefining process and could be as low as 0.1 or 0.01 wt.% during the different stages in the process. Hence these analytical techniques should be capable of reliably measuring the actinide concentrations in mixtures in which a wide variation of concentrations of zirconium and other fission product elements prevail. In order to simulate such a scenario studies were carried out on the analysis of uranium using square wave voltammetry (SWV), normal pulse voltammetry (NPV) and differential pulse voltammetry of mixtures containing rare earth chlorides in which the concentration of the constituents spanned over a wide range. These experiments revealed that these electroanalytical techniques offer enhanced reproducibility, very low detection limit and are amenable for rapid analysis.

Fig. 3 shows the differential pulse voltammograms for the reduction of UCl_3 and the rare earth chlorides at two different modulation amplitudes. The optimum pulse amplitudes for SWV and Differential Pulse Voltammetry (DPV) was found to be 5-20mV. The results of DPV showed that the current varies linearly with the concentration of UCl_3 over the range 0.1 to 4 wt.%. The SWV results did not show a linear dependence on concentration of UCl_3 in the range between 0.5 to 4 wt.%. The non-linear behaviour in SWV at higher concentrations could be due to the fact that the surface area of the electrode during the reverse step current is larger than that during the forward step. The SWV output, which is obtained by subtracting the forward current from the reverse current at each step, would therefore be smaller than the actual at higher concentrations.

The reduction current of the NPV was differentiated with respect to the working electrode potential and the area of the corresponding peak was plotted against the concentration of UCl_3. A linear dependence of peak area with concentration was found in the range 0.5 to 11 wt.% UCl_3. The peaks in the differentiated NPV curve corresponding to the lanthanides were found to be distinctly resolvable from that of uranium.

The present results have shown that all the three techniques are highly selective and provide distinct peaks for each element and that presence of lanthanides had no influence on the estimation of uranium. Linear dependence of reduction current on concentration of uranium in the range studied is observed only in the case of NPV and DPV.

This study amply demonstrates the fact that pulse techniques could be applied for the online monitoring of concentration of actinides in presence of fission products during molten salt electrorefining. Further these studies have shown that while DPV is applicable at lower concentrations of uranium while NPV is suitable for monitoring higher concentrations.

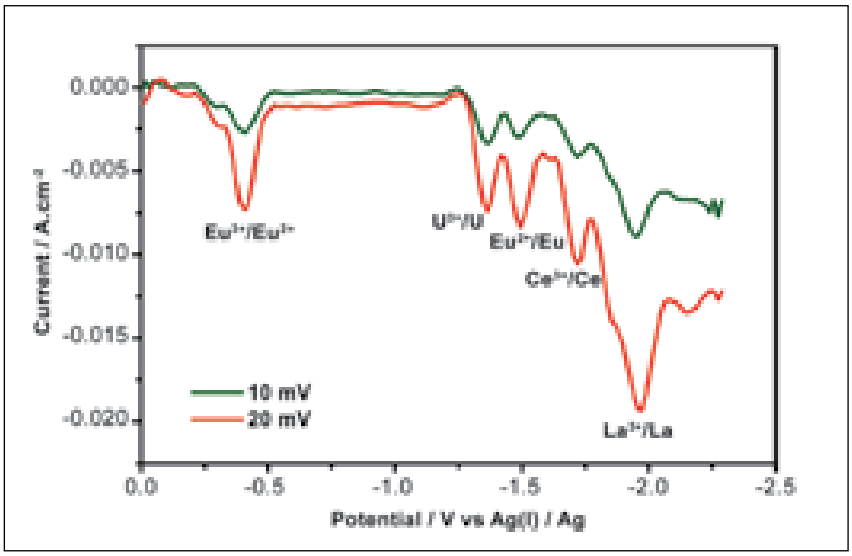

Fig. 3 *DPV curves of a LiCl-KCl eutectic melt containing 1 wt. % UCl_3, 0.7 wt.% $EuCl_3$, 1 wt.% $CeCl_3$ and 1 wt.% $LaCl_3$ at 773K [electrode W, modulation amplitude- 10 mV (green) & 20 mV (red)]*

IV B1.2 Application of Room Temperature Ionic Liquids in Fuel Reprocessing

Room temperature ionic liquids (RTILs) comprise of bulky organic cation and an inorganic or organic anion and have melting points below 373 K. Properties of RTILs such as, insignificant vapour pressure, high solubilising power, wide electrochemical window and tunability in synthesis have enabled their application in a variety of fields. For example, RTILs are considered as the substitutes for high temperature molten salt in pyrochemical reprocessing and as a diluent in aqueous reprocessing.

Significant quantities of platinum group metals (PGM) are formed during the nuclear fission and are rejected into HLLW in the PUREX process. Most of them are non-radioactive. At present, there is a huge demand of PGMs in various industries, while the PGMs available in the earth-crust are being consumed at a rapid rate. To meet the global demand of PGMs for future, it is desirable to recover the fission PGMs from HLLW.

There are several methods reported for the recovery of PGMs from HLLW. The electrochemical method is one of the easiest and promising techniques due to the simplicity and conducive reduction potential of palladium in nitric acid medium. It also avoids the addition of external reagents to HLLW. Therefore, the direct electrochemical recovery of palladium from simulated high-level waste that mimics the HLLW arising from fast reactor fuel reprocessing (FR-S-HLLW), corresponding to a burn-up 100 GWd/t, was studied.

Electrolysis of palladium nitrate from 1- 4 M nitric acid medium at stainless steel electrode resulted in the complete recovery of palladium with reasonably high faradaic efficiency. However, the recovery and Faradaic efficiency were significantly lowered to less than 40%, when direct electrolysis was attempted from simulated high-level liquid waste, possibly due to competitive reactions from other electroactive ions.

Extraction - Electrodeposition Process

To overcome the problems experienced, new process "extraction-electrode position (EX-EL)", using a room temperature ionic liquid, tri n-octyl methyl ammonium nitrate (TOMAN) for the quantitative recovery of palladium from FR-S-HLLW was developed and demonstrated. The process exploits the capabilities of TOMAN such as, the ion exchange and wide electrochemical window. The procedure is illustrated in Fig.1. More than 60% of palladium could be extracted using 0.5M TOMAN/$CHCl_3$ in a single contact and complete extraction was achieved in five successive contacts. The extracted palladium was quantitatively recovered by electrolysis of the organic phase using a stainless steel cathode. Under the experimental conditions, nearly twenty hours were required for complete recovery of palladium from organic phase which extracted palladium nitrate from 4M nitric acid medium, while more than 35hours were needed for recovery form organic phase, which was contacted with FR-S-HLLW. The process also demonstrated decontamination factor of ~10 during the extraction step and ~1000 during electrodeposition.

Electrodeposition of lanthanides and actinides

A new procedure for the dissolution of oxides of lanthanides and actinides using (bis(trifluormethylsulfonyl))amine, $HN(SO_2CF_3)_2$ ($HNTf_2$) followed by electrodeposition of them as metals in RTIL medium was developed. For this purpose, several ionic liquids that offer wide electrochemical window and extended cathodic stability such as, N-butyl-N-methylpyrrolidinium bis(trifluoro-methylsulfonyl) imide ($BMPyNTf_2$) and N-methyl-N-propylpiperidinium bis(trifluoromethylsulfonyl)imide, ($MPPiNTf_2$) were synthesised and used.

The europium and uranium oxides chosen as representative lanthanide and actinide oxides, were dissolved in required quantity of $HNTf_2$ in water. The metal-triflamides formed $M(NTf_2)_n$ (M = Eu(III) or U(IV) and n =3 or 4) were dried using rotary evaporation at 353K and diluted with ionic liquid. The electrochemical behavior of Eu(III) and U(IV) in RTIL medium at glassy carbon electrode was studied using transient electrochemical techniques.

The cyclic voltammogram of

$BMPyNTf_2$ recorded at glassy carbon working electrode at 373 K is shown in Fig. 2. Reduction of $BMPy^+$ cation occurs at a potential of -3.5 V (Vs. Fc/Fc^+) and the oxidation of NTf_2 anion occurs at 1.7 V (Vs. Fc/Fc^+). Therefore the electrochemical window of $BMPyNTf_2$ is 5.2 V, which may be sufficient for permitting the reduction of M(III) to metallic state. The cyclic voltammogram of Eu(III) in $BMPyNTf_2$ recorded at glassy carbon working electrode at 373 K is displayed in the same figure. The onset of cathodic wave occurring at a potential of -0.09 V (vs. Fc/Fc^+) which culminates in a peak at 0.45 V could be due to the reduction of Eu(III) to Eu(II). This is accompanied by an anodic wave at -0.07 V during the scan reversal. The cyclic voltammogram of Eu(III) is also accompanied by an irreversible cathodic wave occurring at -2.79 V (vs. Fc/Fc^+) due to the reduction of Eu(II) to metallic europium. EDXRF and XRD pattern of the deposited product obtained by the electrolysis of at -2.9 V confirmed the presence of metallic europium.

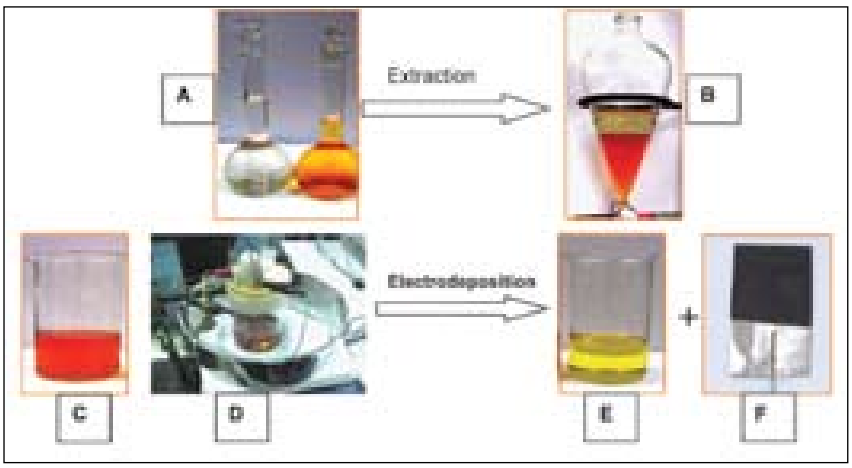

Fig. 1 *EX-EL process for the recovery of palladium from simulated fast reactor high level liquid waste (FR S-HLLW)*

A- The organic (pale yellow) and aqueous (orange) phases (100 mL each) taken for extraction
B- Extraction of palladium in organic phase (bottom)
C- The organic phase is taken for electrodeposition
D- Electrolysis of organic phase
E- Organic phase after electrolysis and is recycled for extraction
F- Palladium deposit

Similarly, uranium tetrakis[bis(trifluormethylsulfonyl)imide], $U(NTf_2)_4$, was synthesized and investigated at 373 K for the electrochemical behavior of U(IV) in $MPPiNTf_2$ at glassy carbon working electrode. The cyclic voltammogram of U(IV) in $MPPiNTf_2$ indicated that U(IV) undergoes a three step reduction to metallic form involving the redox conversions of U(IV) to U(III) at -0.4 V (Fc/Fc^+) U(III) to U(II) at -1 V and U(II) to U(0) at -2.47 V.

The studies demonstrated the feasibility of dissolving Eu_2O_3 and UO_2, in $HNTf_2$ medium and subsequent recovery by electrolysis in RTIL medium such as, $BMPyNTf_2$ or $MPPiNTf_2$.

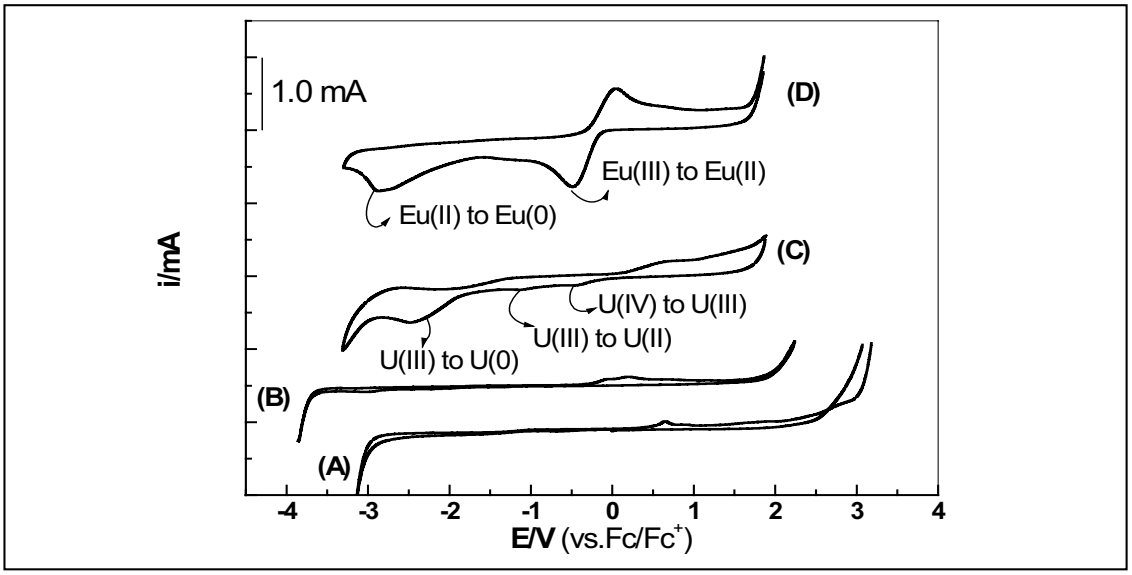

Fig. 2 *Cyclic voltammograms of $MPPiNTf_2$ (A) and $BMPyNTf_2$ (B), $U(NTf_2)_4$ in $MPPiNTf_2$ (C) and $Eu(NTf_2)_3$ in $BMPyNTf_2$ with glassy carbon working electrode at 373 K*

IV B1.3 Stripping Behaviour in TRUEX Process : Batch and Counter-Current Studies

Significant quantities of lanthanides and radiotoxic alpha emitting transuranium elements, also called as minor actinides are produced during nuclear reactor operation. Since all lanthanides and minor actinides such as americium and curium are essentially trivalent, they get rejected into the high level liquid waste(HLLW) during the PUREX operation. While converting the HLLW into waste forms, it is preferable to separate the alpha emitting minor actinides from lanthanides to reduce the load of the waste form that requires deep burial. Among the processes developed for the partitioning of lanthanides and minor actinides, the TRUEX process using a mixture of 1.2 M tri-n-butyl phosphate(TBP) - 0.2M n-octyl(phenyl)-N,N-diisobutyl-carbamoylmethyphosphine oxide (CMPO) in n-dodecane(n-DD), is a well tested one. Nevertheless the process suffers incomplete stripping of the co-extracted La/An metal ions, precipitation/ interfacial crud formation, and also phase separation problems while employing 0.01M nitric acid as strippant. The problem assumes greater significance in treating HLLW generated from fast reactor reprocessing and especially while recycling the solvent. Studies using a stripping composition containing several components of complexing agents, acids and reducing agents have been reported. The composition when tried in a system of simulated fast reactor waste solution gave phase separation problems and precipitate formation, possibly due to hydrolysis of the metal ions.

Hence studies were conducted to develop a simple stripping composition which is devoid of the abovementioned problems, suitable for the recovery of minor actinides and lanthanides especially from HLLW resulting from high burn up spent fast reactor fuel reprocessing.

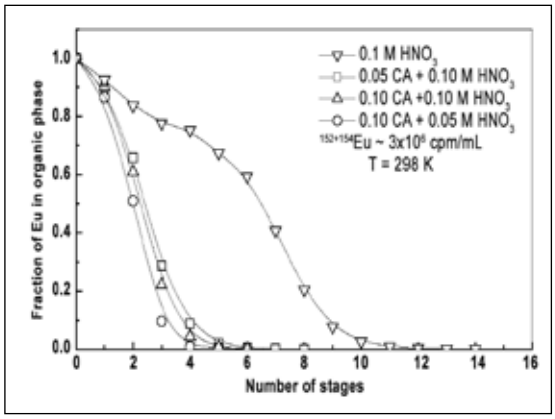

Fig. 1 *Stripping behavior of europium(III) loaded TRUEX solvent by various formulations of citric acid (CA) and nitric acid, A/O : 1, Temperature : 298K.*

Batch equilibration of TRUEX solvent with a simulated fast reactor high level liquid waste (FR-S-HLLW), corresponding a burn up of 100 GWd/T, spiked with $^{152+154}$Eu tracer, was carried out to optimize the extraction and stripping. Citric acid which is easily and commercially available in combination with nitric acid was found to be suitable after a series of scouting experiments. Fig.1 illustrates the results of stripping experiments carried out with different combinations of citric acid (CA), nitric acid (HNO_3) mixture in comparison with 0.1M HNO_3. It can be seen that 0.1M HNO_3 requires fourteen stages for complete stripping. Lowering the acidity to 0.01 M, resulted in crud formation. With compositions of 0.05M CA+0.1M HNO_3 and 0.1M CA+0.1M HNO_3 the stripping could be effected sans any crud/phase separation problem in respectively eight and six stages. The composition of 0.1M CA+0.05M HNO_3 could achieve complete stripping again without posing any problem in five stages. This indicates that the local hydrolysis of hydrolysable metal ions in the loaded organic phase could be prevented by the presence of complexing reagent, citric acid, during stripping and facilitates stripping of trivalents from organic phase by complexation.

Based on these investigations, the counter current extraction studies were performed with FR-S-HLLW by TRUEX solvent employing a novel 16-stage ejector mixer. The composition of 0.1M CA+0.1M HNO_3 was found to give quantitative and problem free stripping of loaded lanthanides in five stages.

IV B1.4 Recovery of ^{137}Cs from Simulated Acidic High Level Liquid Waste

Major goal of the radioactive nuclear waste treatment program is the selective removal of ^{137}Cs and ^{90}Sr. Reprocessing plants produce large volumes of these nuclides which have half-lives of 30.2 years (^{137}Cs) and 29 years (^{90}Sr). Removing these radioactive nuclides from nuclear wastes would result in a significant radioactivity and volume reduction.

It is well known that ammonium molybdo phosphate (AMP) is having high selectivity and capacity for removal of cesium from acidic waste streams generated during nuclear fuel reprocessing. However the microcrystalline structure of AMP makes it unsuitable for large column/industrial operations. Hence organic binders such as PAN (poly acrylo nitrile) are used to granulate for making it suitable for large scale applications especially for removal of radioactive cesium from nuclear waste streams. A novel resin is developed by M/s. Thermax Ltd., Pune, in which AMP is incorporated on PAN backbone. Work was undertaken in the laboratory to develop and demonstrate the technology for removal of cesium using AMP-PAN resin. Batch studies were carried with AMP-PAN resin for removal of cesium in 4N Nitric acid. The distribution coefficients (K_d) were calculated from the experimental data. Table.1 gives the results for equilibrium studies for removal of cesium using AMP-PAN resin.

Table 1: K_d value determination of cesium

Sl.No	Medium of the solution	Initial Concentration (ppm)	Final Concentration (ppm)	Distribution Coefficient Value(K_d) (ml/g)
1.	DM Water	9.79	0.143	1349
2.	4N HNO_3	9.9	0.161	1209

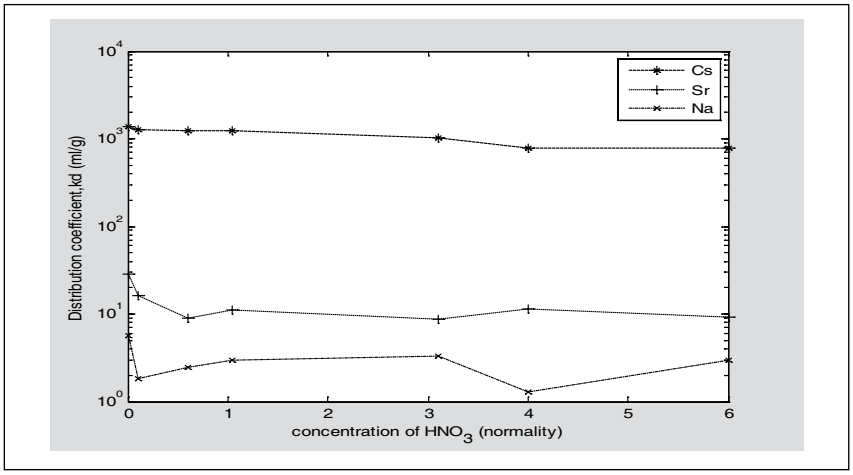

Fig. 1 *Comparison of K_d values of Cs in presence of Sr and Na at different concentration of Nitric acid*

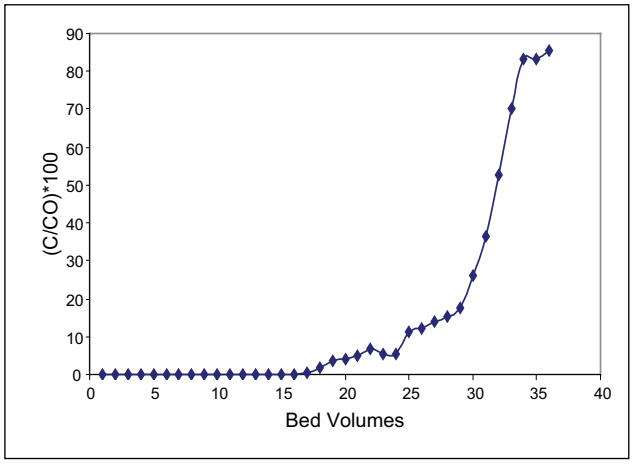

Fig. 2 *Breakthrough curve*

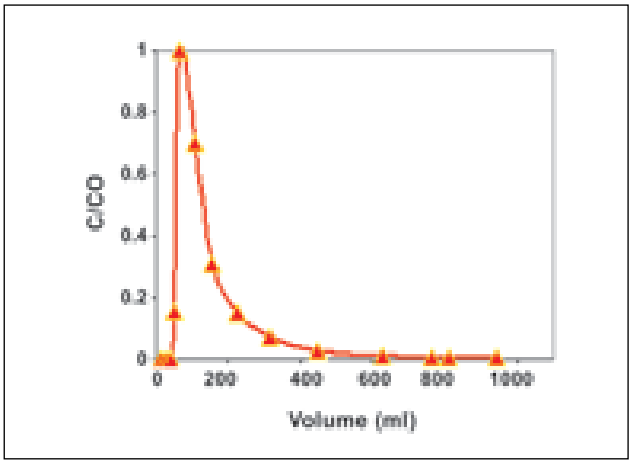

Fig. 3 *Elution Curve for cesium using ammonium chloride as eluant*

Uptake of cesium by AMP-PAN resin was tested in the presence of other important competing ions such as strontium and sodium. The effect of coexisting cations Sr^{2+} and Na^{+} did not show any significant effect on the distribution coefficient of Cs^{+}. The distribution coefficient of cesium was almost constant over a wide range of H^{+} concentration. The distribution coefficient for cesium is significantly higher than the Sr^{2+} and Na^{+}. Column experiment has been carried out to estimate the dynamic capacity of the resin and to obtain the break through curve.

Fig. 2 shows the break through curve for removal of cesium by AMP-PAN. The experiments showed that the capacity of the resin is approximately 57 mg of Cs per gram of dry resin. This value of dynamic capacity is higher than the literature value of 32 mg of Cs per gram of dry resin for similar resin. The adsorbed cesium from the resin is eluted using different ammonium salts. During elution the following reaction takes place,

$$(NH_4)_3\,PMo_{12}O_{40} + 3CsCl \longrightarrow (Cs)_3PMo_{12}O_{40} + 3NH_4Cl$$

-during adsorption

(AMP-PAN resin)

$$(Cs)_3PMo_{12}O_{40} + 3NH_4Cl \longrightarrow (NH_4)_3PMo_{12}O_{40} + 3CsCl$$

-during elution

Fig. 3 shows curve for the Cs elution from AMP-PAN resin using saturated solution of ammonium chloride as the eluent. Experiments were also conducted with radioactive ^{137}Cs for determination of distribution coefficient (K_d). K_d values obtained using ^{137}Cs are similar to those obtained in experiments using inactive cesium.

IV B1.5 Direct De-nitration of Uranyl Nitrate Solution using Microwave Heating

The final product solution from the reprocessing of spent nuclear fuel is in the form of plutonium nitrate and uranyl nitrate solution or uranium-plutonium (mixed) nitrate solution which, can be converted into oxide powders of these metals by using: precipitation process, fluidized bed direct de-nitration process or direct de-nitration using microwave heating. For a robust nuclear fuel cycle it is essential to establish a simpler conversion facility that converts plutonium and uranium nitrate solution to oxide powder. Overview of the literature indicates that conversion process using microwave heating method has several advantages over the other conventional method such as: good powder characteristic of the product, good homogeneity of U-Pu oxide powder, minimum liquid waste and simplicity of the process. A laboratory scale, 6kW output power microwave heating system (Fig. 1) has been developed for the direct de-nitration of U/Pu nitrate solution. The system is adaptable to glove box operation where electronics parts are isolated from the cavity through wave guide for ease of maintenance. It consists of microwave generator, waveguide, power supply, three stub tuner, chiller and a temperature sensing device (IR pyrometer). As can be seen from the Fig. 1 microwave power is transmitted through waveguide from generators that can be located safely outside a radioactive processing chamber (cavity) where routine system maintenance can be easily performed.

Experiment with the uranyl nitrate solution of about 300g/L has been conducted. The denitration proceeds through the concentration of the uranyl nitrate solution followed by thermal decomposition of the nitrate to UO_3 solid. The concentration of solution is caused by vaporization of nitric acid at ~383K. After the solution is concentrated to some extent, temperature increases gradually above ~573K, and the decomposition of uranyl nitrate proceeds as per the following reaction:

$$UO_2(NO)_3.6H_2O \longrightarrow UO_3 + NO_2 + NO + O_2 + 6H_2O$$

During the nitrate decomposition, NO_x gases are released which was scrubbed by water. As the solidification occurs, the oxide cake is obtained as a bulky and sponge like lump, which can be scraped easily. Further temperature is raised to about 723-773K for the conversion of UO_3 to U_3O_8 and it is maintained at this temperature for about half an hour. Fig. 2 shows a time vs temperature curve of the

de-nitration of uranyl nitrate solution. It is observed that more than 50% of the microwave energy absorbed is utilized in evaporating water and nitric acid. Final de-nitrated product was found to be U_3O_8 which was confirmed by XRD (Fig. 3) analysis.

Fig. 1 *Microwave generation and delivery system*

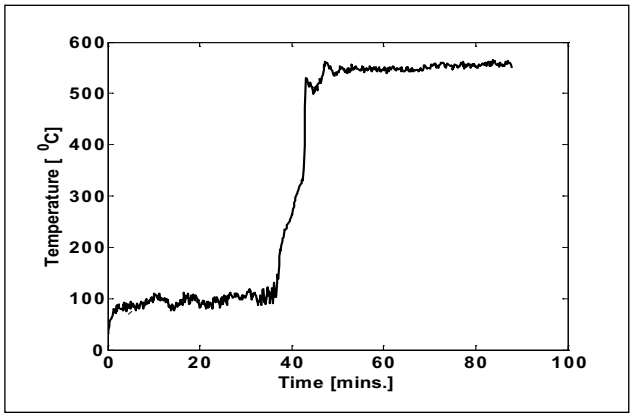

Fig. 2 *Time and temperature curve of the solution during de-nitration process*

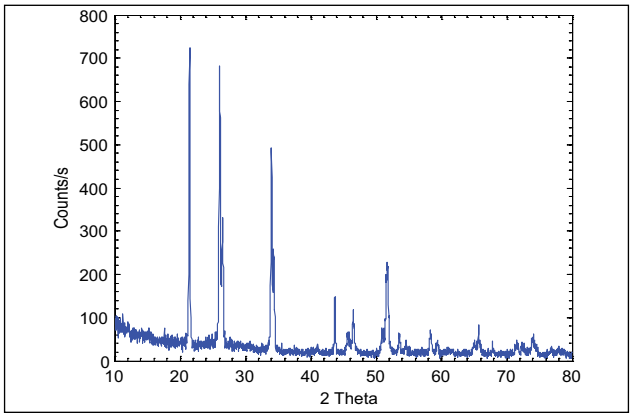

Fig. 3 *XRD pattern of the product obtained by direct de-nitration of uranyl nitrate solution*

IV B1.6 Development of Continuous Process for the Destruction of Nitric Acid by Formaldehyde

The aqueous phase resulting from the solvent extraction step of Fast Breeder Reactor fuel reprocessing plants constitutes the bulk of the high level radioactive waste in about 4M nitric acid, which is one of the major concerns as substantial amount of high level waste is generated during the reprocessing of spent nuclear fuels. To reduce the amount of high level liquid waste (HLLW) and to reduce the corrosion in waste tank during subsequent storage of concentrated waste solution, it is desirable to reduce the nitric acid concentration to a lower value. Among the various existing processes, the chemical reduction of nitric acid with formaldehyde or formic acid is widely engaged due to its efficiency.

A continuous process has been developed for the destruction of nitric acid using formaldehyde as reductant. For this, a reaction vessel (Fig.1) has been designed and experiments have been conducted with simulated solution as well as with nitric acid alone (~4M) in continuous and batch mode of operation. The reaction of HNO_3 with formaldehyde is initiated only after a certain induction period during which the auto catalyst HNO_2 accumulates in the solution up to a threshold concentration (ranging between 10^{-2} and 10^{-1} M) beyond which the reaction develops rapidly. This delay can be detrimental as the

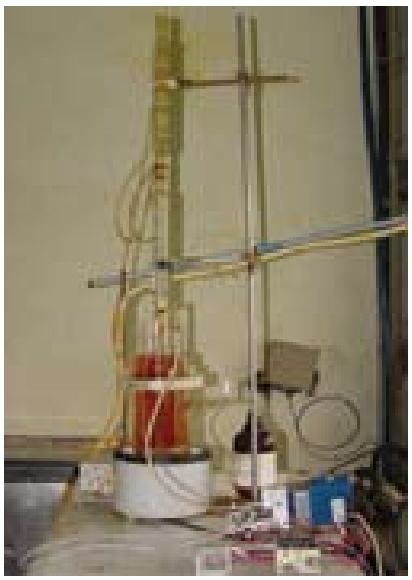

Fig.1 *Schematic diagram of experimental setup*

de-nitration following the induction period can be violent and lead to uncontrollable process conditions. However, in our experiments, when the formaldehyde was introduced into the reactor at about 371K reaction started instantaneously and no untoward incident occurred. De-nitration with formaldehyde is influenced by the concentration of nitric acid. For nitric acid concentrations between 2 and 8 M, the reactions involved are:

$$4HNO_3 + 3HCHO \rightarrow 4NO + 3CO_2 + 5H_2O - (1)$$

$$4HNO_3 + HCHO \rightarrow 4NO_2 + CO_2 + 3H_2O - (2)$$

$$2HNO_3 + HCOOH \rightarrow 2NO_2 + CO_2 + 2H_2O - (3)$$

At nitric acid concentrations below 2M, appreciable amount of the intermediate compound formic acid is produced and the reaction mechanism is dictated by reaction (3). Further addition of formaldehyde causes the build up of formic acid as the rate of formation exceeds the rate of destruction. When the concentration of nitric acid falls down to about 1.5 M, the de-nitration reaction is very slow and the reaction mixture requires to be refluxed for an hour or so to bring down the reaction to completion. Assuming the de-nitration with formaldehyde to be apparent third-order reaction, the rate of destruction of nitric acid was computed by solving mass balance equations (4 & 5) numerically for different feed rates of formaldehyde and HNO_3.

$$\frac{dc_A}{dt} = \left(\frac{F_A}{V}\right)C_{Ai} - \left(\frac{F_A + F_B}{V}\right)C_A - kC_A^3 C_B^{1.4} \quad (4)$$

$$\frac{dc_B}{dt} = \left(\frac{F_B}{V}\right)C_{Bi} - \left(\frac{F_A + F_B}{V}\right)C_B - kC_A^3 C_B^{1.4} \quad (5)$$

where, subscripts A & B represent HNO_3 and formaldehyde respectively. F, V and k are volumetric flow rate, volume of reaction vessel and rate constant and subscript 'i' inlet condition. The computed data are plotted along with the experimental results for the reduction reaction in Fig. 2. It is evident from the plot that the agreement between the two sets of data is reasonable. The results pertaining to an experiment conducted with simulated solution with fission products have also been shown in the same figure. A marginal decrease in the reduction rate for the simulated waste nitrate solution could be due to the reaction of metallic ions with formic acid to form insoluble residues. Some foaming was noticed during the de-nitration of a simulated feed solution containing degraded organic and fission products.

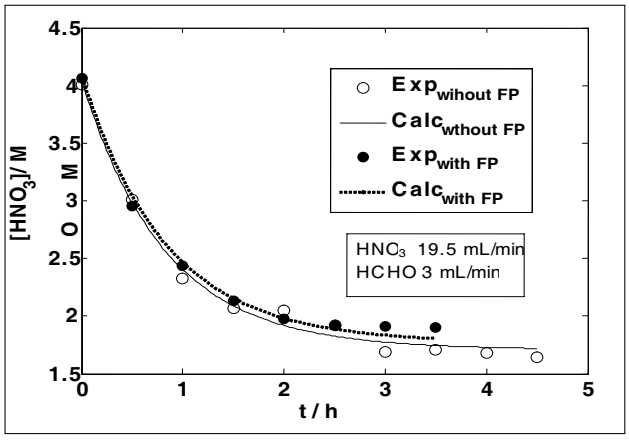

Fig. 2 *Vessel outlet concentration of HNO_3 with time*

IV B2 Component Development

IV B2.1 Fabrication of Continuous Dissolver Assemblies for Thermal Fuel Reprocessing

Fabrication of continuous dissolver mock-up assemblies of two different types were fabricated at central workshop division to assess and compare the performance. These assemblies will be used for fuel reprocessing to dissolve the spent fuels in nitric acid. The overall size of the assembly is 616 mm dia x 520 mm length and consisting of fifteen components made of SS304L material.

Partition plates (type 1 and 2) of dia 616 and dia 534 mm were precisely machined from 8mm thick SS304L plate. Achieving 1.6 µm surface finish and flatness of 0.20 mm on 5 mm thick partition plate during

facing operation in lathe machine was a critical feature of machining and machined satisfactorily. Partition plate has center opening with cam profile. Machining the cam profile at the centre of partition plate was a challenging task. Mock-ups were carried out in the CNC milling machine using special part programming. Optimum machining parameters were established to machine the partition plates with greater accuracy.

Unique layout was made to fabricate concentric and eccentric reducer cones (Fig. 1). Cones were formed by using a press brake machine and welded longitudinally. Opening for fall of fuel pellets in the next compartment was made manually on fabricated eccentric cones by hand plasma cutting machine. A rotary drum of dia 545mm, 3mm thick was fabricated using SS304 L material. SS bolts were machined precisely within the tolerance of +0.015/+0.002mm to suit the bearings. Fabricated components were assembled and stitch welded by GTAW process. MS supporting frame of size 351x784mm was fabricated to rotate the continuous dissolver. Both the assemblies (Fig. 2) were subjected to 100% dimensional inspection and found satisfactory.

Fig. 1 *Fabricated concentric and eccentric reducer cones*

Fig. 2 *Fabrication of continuous dissolver mock-up assemblies*

IV B2.2 Manufacture of Vent Pots for Demonstration Fuel Reprocessing Plant Sampling Cell

Seventy five numbers of vent pots (Fig. 1) were fabricated for demonstration fast breeder reactor fuel reprocessing plant (DFRP) sampling cell. These vent pots are used to separate gases and liquid from the samples in reprocessing of spent fuel. Each vent pot assembly comprises of six components namely main body, end cap, end plate, top pipes. The overall size of the assembly is 88.9 mm dia x 535 mm length, made of SS304 L material. Bottom end of vent pot is connected with liquid collection tank and top end is connected to stack through which gases will be vented out to atmosphere after filtration.

Fig. 1 *Machined end caps*

End caps (Fig. 2) were precisely machined in CNC Lathe. Machining of counter bore with 1 degree tapered face in the end cap and drilling dia 13 with an inclination of 125 degree on main body were critical features of machining and achieved successfully. Main body were machined from 80 NB schedule 40 pipe. All the machined components were subjected to 100% dimensional inspection.

To facilitate the welding and inspection process for mass production and to improve the productivity, assembly was classified into three different sub assemblies. Different activities were listed, process planning and scheduling were carried out to achieve the target schedule.

Fig. 2 *Vent pots in group*

All weld joints were carried out using GTAW process and extreme care was taken. Segmental welding technique was used to minimize the distortion. All the assemblies were subjected to 100% dimensional, HLT inspection and found satisfactory.

IV B2.3 Development of a Novel Mixer-Settler with In-line Static Mixer for Nuclear Solvent Extraction Applications

Solvent extraction also known as liquid-liquid extraction is a quite selective and economic technology. It finds extensive applications in a broader range of fields like chemical, petroleum, petrochemical, pharmaceutical and in nuclear chemical engineering applications. In general, solvent extraction is the most sought unit operation after distillation, utilized for separation of components using liquid solvents because these are generally designed to operate at ambient temperature, which makes them more attractive as compared to other separation processes in terms of energy conservation. As novel solvents are prohibitively costly, there is a need for the contactors operable with extreme organic to aqueous ratios. Recently at Reprocessing Group, a novel mixer-settler was visualized and developed for this kind of service. The mixer of the novel contactor is based on an in-line static mixer and does not involve any mechanical moving part. This mixer-settler was realized in a single stage prototype and tested for hydrodynamics in non-mass transfer region as well as mass transfer region. Fig. 1 shows a sketch of the experimental setup.

The hydrodynamic studies in the non-mass transfer region conducted include drop size distribution and holdup estimation. 30% tributyl phosphate diluted with kerosene was used as the organic phase. Acidified distilled water was used as the aqueous phase. Different runs were carried on at different phase ratios. In the non-mass transfer runs, the dispersed phase was checked first. If the dispersed phase was found to be organic then the sample was collected in a beaker, containing a small amount of surfactant. Surfactant was added to minimize coalescence. The samples were analyzed in a laser based drop size analyzer. Fig. 2 shows variation in drop sizes with the varying throughput.

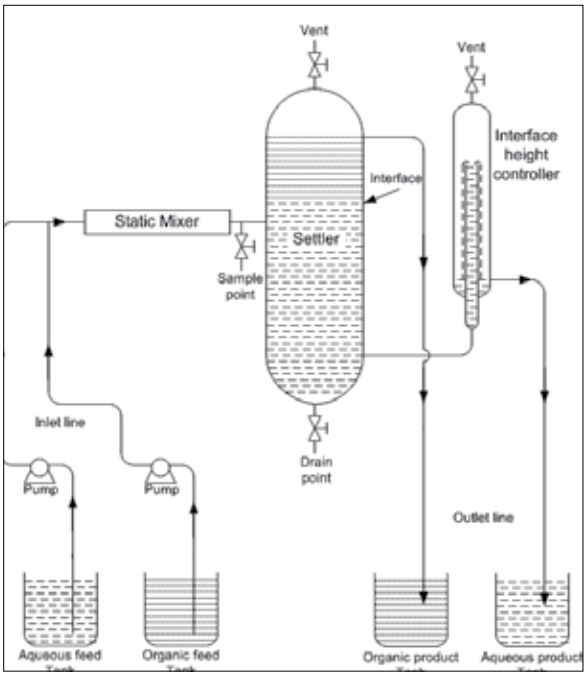

Fig. 1 *A Sketch of experimental setup for mass transfer run*

Mass transfer run was taken with 4N acid feed and an aqueous to organic flow ratio of 200. Fig. 3 shows a time dependent exit concentration profile. For the developed unit, the mass transfer efficiency was calculated on the organic phase basis and for the run with aqueous to organic phase flow ratio of 200; mass transfer efficiency of 92.6±0.6 was obtained on the basis of organic phase.

Additional benchmarking runs as well as design for multi-stage unit are in progress.

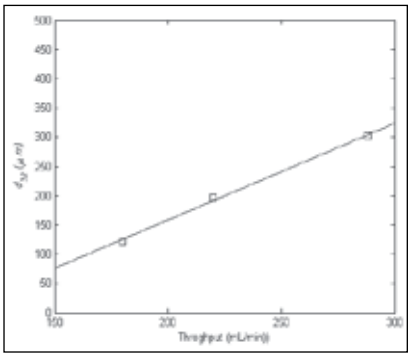

Fig. 2 *Variation of drop-sizes in Non-Mass Transfer Runs*

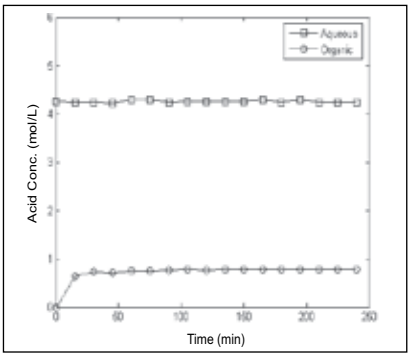

Fig. 3 *Temporal exit concentrations (mass transfer run)*

IV B2.4 Development of a Wireless Mobile Inspection Vehicle for the In-service Inspection of CORAL Waste Vault and In-service Inspection of Process Tanks below the Containment Box in CORAL

A wireless mobile robotic device has been conceptualized and developed for carrying out a global visual examination of the CORAL waste vault using a CCD based camera during in-service inspection (ISI). The mobile vehicle is completely remote controlled using Wi-Fi enabled system including the camera. The vehicle is configured with four wheels, in which front wheels have Ackerman's steering and rear wheels are driven. Permanent magnet DC motors have been used for the traction, steering and camera pan/tilt motions. The vehicle will run over special stainless steel guide rails laid along one of the walls of the CORAL waste vault. The motors of the vehicle are mounted on the base plate and gear trains are used to transmit the power to the drive wheels and steering wheels. With this arrangement, the vehicle can be moved and steered in a horizontal plane easily. On top of the base plate a camera holder with pan and tilt motion is kept. The overall size of this vehicle is 275 (length) X 215 (breadth) X 276 (height). The speed of the vehicle can be adjusted to 0-2 m/min. The vehicle can be remotely operated through a pendent and joystick. In view of the acidic atmosphere and radiation environment, SS 304 is chosen for the structural material of the vehicle.

The camera has a pan and tilt motions which will enable to see the trays below the waste tanks and pipelines above the tanks.

Fig. 1 *CORAL mobile vehicle for inspection of CORAL waste vault*

The resolution of the camera is 320x240 pixels. During the motion of the vehicle, the camera will aid in navigation along the guide rails. The on-board electronics include standalone embedded motion controller and a low power drives. The mobile vehicle has on-board controller which uses a 32 bit arm processor. It also has an embedded Wi-Fi module through which it can communicate with the control station. The vehicle uses on-board power supply using lithium polymer battery. Fig. 1 shows the photograph of the mobile vehicle and Fig. 2 shows the drive and control system for the vehicle.

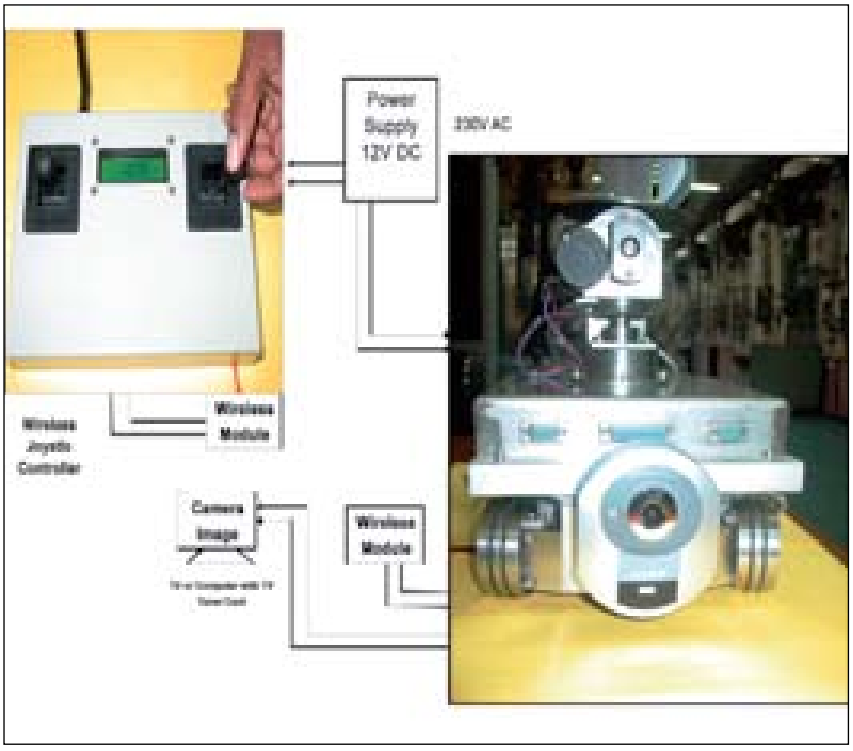

Fig. 2 *Electronic drive and control system schematic*

IV B2.5 Engineering Scale Demonstration Facility for Pyrochemical Process Studies

Molten salt electrorefining is a pyrochemical method that is considered the most suitable for reprocessing the spent metallic fuels. This process involves lesser number of steps, could be carried out in a compact plant and facilitates an easier waste management. Because of such distinct advantages it is preferred over the conventional aqueous process. In this method the alloy fuel is reprocessed by electrolysis after dissolving it in a molten salt (LiCl-KCl eutectic, 773K) wherein either a solid rod or molten cadmium serves as a cathode. (Since metallic fuels will be introduced in the commercial fast breeder reactors subsequently, development of this pyroprocessing technology assumes importance).

Laboratory scale studies on the electrorefining of uranium and plutonium alloys are being carried out in a special facility comprising a set of argon atmosphere glove boxes. In order to generate inputs for establishing a large scale reprocessing plant and to gain expertise in remotising the specialized equipment an inactive demonstration facility is being set up. The above facility is housed in a containment box maintained under argon atmosphere [5.3 m (L) x 2 m (W) x 2.5m (H)]. It also houses an in-cell crane of 500 kg capacity as well as a power manipulator for enabling remote handling and automating various operations. An electrorefining cell (Fig. 1 and Fig. 2) capable of processing 2 to 3 kg of alloys and an induction powered vacuum distillation system capable of generating a temperature as high as 1800K are incorporated inside this facility as well. This system would be used to distil off the occluded salt from the cathode deposit. This deposite would be a solid when the cathode employed is a rod or a liquid if the cathode is liquid cadmium. The uranium thus recovered would also be melted to from an ingot using the same equipment.

This facility would also incorporate an elaborate system for the purification and distribution of the inert argon cover. The system has been installed. In order to ensure radiological safety a special pressure control system has been designed and installed. In addition this system also ensures economical use of the inert gas. The moisture and oxygen impurities

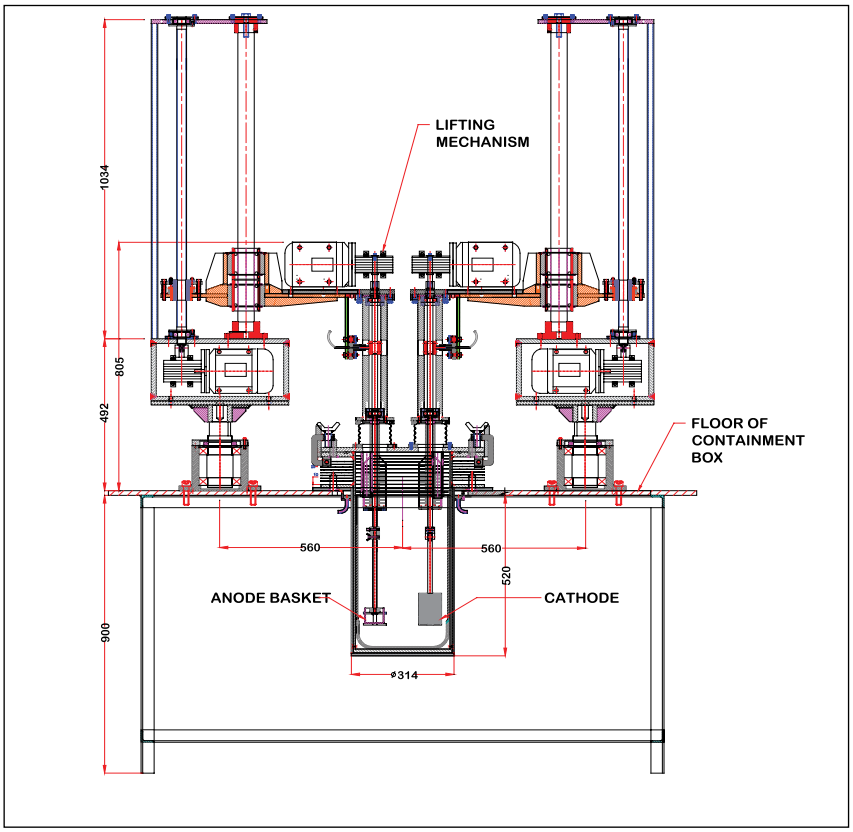

Fig. 1 *A schematic of the electrorefiner*

Fig. 2 *Electrorefiner*

would also have to be removed from three salts, while preparing the eutectic mixture. Since the LiCl, KCl and the eutectic mixture are all hygroscopic they need to be stored in an inert dry glove box. These salts are purified by a special procedure that involves melting, purging the melt with dry chlorine gas and finally cooling in a stream of argon. This is carried out in a batch mode with a batch size of about 15 Kg. In order to purify the salt a system comprising an inconel vessel with provisions for flowing the gas right through and a stainless steel receiving vessel has been designed and fabricated (Fig.3). The salt melt would be transferred from the inconel vessel to the receptacle through an insulated pipeline. In order to facilitate the handling and manipulation of these equipment a slewing crane is also incorporated in this facility. Currently trial runs are in progress.

Fig. 3 *Salt purification system*

IV B2.6 Fabrication of Zircaloy Based Components for FBR Reprocessing Applications

The excellent corrosion resistance of Zr in nitric acid has been known for over fifty years. Zirconium is highly resistant to nitric acid environments and is considered as candidate material for various applications in spent nuclear fuel reprocessing plants involving highly concentrated nitric acid medium. In France, eighty tons of zirconium and five thousand and five hundred meters of piping were employed in LaHague reprocessing plant for the manufacturing of various components like dissolvers, oxalic mother liquor evaporator and heat exchangers, vitrification dust scrubber, and liquid waste treatment reactors. Zirconium and its alloys are thus considered as candidate materials for various applications in spent nuclear fuel reprocessing plants involving nitric acid of high concentrations at high temperatures. They exhibit excellent corrosion resistance in nitric acid and are insensitive to intergranular corrosion unlike stainless steels. Also, unlike titanium and its alloys, Zr is unaffected by vapour and condensate of boiling nitric acid.

Systematic R&D was pursued at to study the corrosion behaviour of zirconium and its alloys Zircaloy-2 and Zircaloy-4 in 11.5 M HNO_3 medium in wrought and welded conditions. The study revealed the excellent corrosion resistance of the material and the welding by TIG and Electron Beam processes did not deteriorate the corrosion resistance. Attempts were made to join Zircaloy-4 to type 304LSS by using friction joining process in collaboration with IIT Madras and the results favoured the dissimilar joints with adequate strength, ductility and corrosion resistance. The studies provided confidence in employing indigenous Zircaloy-4 produced at NFC in various forms for application in reprocessing plants.

In collaboration with NFC, attempts were made first to make a full scale large zircaloy testing system with liquid, vapour and condensate zones of 10 litres capacity (Fig. 1). From the cast billet of zircaloy machined body of the vessel was fabricated and the same was welded by electron beam and TIG processes to attach the other units. The testing system was successfully commissioned at CSTD and long term corrosion testing was initiated for Zircaloy-4 samples in 11.5 M HNO_3 medium.

Based on the experience developed during the fabrication of the testing system attempt was

Fig. 1 *Fabricated test assembly*

Fig.2 *Autoclaved Zircaloy-4 mock-up dissolver assembly*

made to fabricate a full scale mock up dissolver system similar to the design of electrolytic dissolver of CORAL plant at the Reprocessing Group (Fig. 2). The dissolver was made again using the main body from the machined ingot of ultrasonic qualification and the side limbs with large diameter cold pilgered pipes. Electron beam (five welds) and TIG (twenty four welds) welding processes were employed, quality inspection using radiography and liquid penetrant testing was performed, and quality audit was performed by IGCAR on materials, fabrication and welding. Finally double autoclaving was performed on the fabricated unit in order to perform a strong oxide layer of ZrO_2 surface free from contamination as well as with highest corrosion resistance. The vessel will be used for establishing NDT and quality inspection and long term corrosion using simulated dissolver solution of FBR reprocessing.

IV B2.7 Non-destructive Assay of Plutonium by Neutron Measurements using Bubble Detector and Monte Carlo N-Particle Code

Nondestructive assay (NDA) technique for assay of plutonium involves total neutron counting, (both spontaneous fission and (α, n) neutrons) by using a set of pre-calibrated bubble detectors and deducing the quantity of plutonium using Monte Carlo N-Particle (MCNP) code.

Neutron Measurements

The important requirement for a neutron detector is that it should have high sensitivity to neutrons of wide energies and totally insensitive to gamma radiation. Indigenously developed Bubble Detector (Fig.1) which is compact, reusable and passive has been used for in-situ detection of neutrons. They were calibrated at 298K with 185 GBq Am-Be neutron source. Their neutron sensitivities are uniform and is 1.0 ± 0.1 bubbles per μSv. Number of bubbles nucleated in the bubble detector is counted using an optical image analysis system (Fig. 2) which consists of a high resolution digital camera, light source for illuminating the bubbles and associated image analysis software developed in JAVA.

Neutron measurements with bubble detector involves (i) sensitization of bubble detectors by unscrewing the cap (ii) placing them at the location near to the container having the fissile material (iii) exposing them for desired time duration (iv) counting the number of bubbles nucleated using the optical image analysis system and

$$\text{Amount of Pu (g)} = \frac{\text{Measured neutron flux}}{(\%\ \text{of } Pu^{240}) \times \text{neutron yield from } Pu^{240} \times \text{flux per neutron from MCNP}} \quad (1)$$

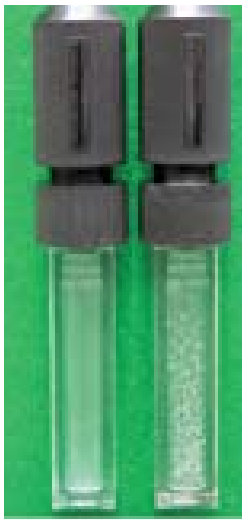

Fig. 1 *Bubble Detector*

Fig. 2 *Image analysis system*

(v) calculation of neutron dose rate and corresponding neutron fluxes.

Deducing the quantity of Plutonium using MCNP code

MCNP is a very versatile code which has a variety of standard source geometry options, collection of variance reduction techniques, an elaborate tally structure and an extensive collection of cross section data. As a result, it is the most widely employed code for radiation transport applications.

In the estimation of plutonium stored in a container, the geometry of the container was modelled and scoring of neutrons having energy greater than 0.1 MeV using F5 tally (point detector) was carried out. The quantity of plutonium was estimated by using the equation 1.

Table 1: The measured and estimated neutron fluxes in the bird cage

Distance (cm)	Time of irradiation (hours)	Measured Neutron dose rate (μSv/h)	Measured neutron flux (cm^2/sec)	Estimated neutron flux using MCNP (n/cm^2/sec)
On contact	2	138	99.4	112
25	5	13.5	9.79	7.41
50	5	3.0	2.59	2.96
75	5	2.0	0.82	1.18
100	5	1.0	0.29	0.73

Validation of the Technique

This technique was validated by measuring the neutron flux using pre-calibrated bubble detector at the surface of a bird cage containing known quantity of plutonium. The neutron flux at the surface of the bird cage was calculated using MCNP by taking into the account of the geometry of the bird cage, quantity and isotopic composition of plutonium. Experiments were repeated with measuring the neutron flux at various distances from the bird cage and compared with calculated values from MCNP.

The measured and estimated neutron fluxes from the plutonium source (with known isotopic composition and quantity) at various distances are provided in Table 1.

The total plutonium content in the bird cage measured in terms of neutron flux by this technique was found to be in agreement with the estimated value. The NDA technique developed using bubble detector and MCNP code holds promise as a practical approach to assay plutonium in any stage of fuel cycle facility. This technique is sensitive, simple and reliable and could be applied for nuclear material accounting, process control and criticality control in fuel cycle facilities.

IV B2.8 Indigenous Development of Systems and Components for Fiber Optic Aided Spectrophotometry

A fiber optic assisted spectrophotometric method was developed for the determination of oxidation states and concentrations of uranium and plutonium in process streams. The utility of the method was proved by its application during reprocessing of FBTR fuels of progressively increasing burn up at CORAL. Further the method was validated and qualified for in-line monitoring of plutonium in various process streams of DFRP. Encouraged by these results, a collaborative exercise was taken up by Reprocessing Group, IGCAR with RRCAT, Indore and ECIL, to indigenize and develop systems and components for fiber optic aided spectrophotometry with an object to achieve complete self-reliance. A complete fiber optic aided spectrophotometric system (Fig. 1) was indigenously developed and validated. The spectrophotometric part of the system was made at ECIL and the fiber optic probes were developed at RRCAT. The spectrophotometer has a tungsten-halogen lamp as light source and silicon diode as detector and its wavelength range is 380-900 nm. The completely indigenous system is deployed for remote analytical applications at process control laboratory of CORAL. This met the immediate analytical requirements of reprocessing campaigns involving fuels irradiated to 100 and 150 GWd/T and at the same time provided an opportunity to test the robustness and utility of the equipment for plant control analysis.

Improved fiber optic probes of path lengths up to 100 mm (Fig. 2), as also tips of various path lengths for use with probes (Fig. 3) were realized. Based on the improved design, probes of different path lengths from 10 to 100 mm were fabricated and were deployed for regular use. A stainless steel fiber optic probe of 100 mm path length is developed for the first time with an improved optical design for in-line monitoring (patent applications under process). These probes are essential for chemical analysis using remote spectrophotometric measurements and are resistant to nitric acid attack and radiation.

Such spectrophotometric systems are needed for in-line process monitoring, in chemical laboratories (in industry, educational institutions, research organizations), wherever in-situ measurements are required to monitor chemical reactions/ reaction products, and in pharmaceutical manufacturing units, hospitals where measurements need to be made in sterile environment or on any contaminated sample etc.

Fig. 1 *Fiber optic aided spectrophotometric system for remote application*

Fig. 2 *Fiber optic probe of 100 mm fixed path length*

Fig. 3 *Tip for variable path length fiber optic probe*

Fig. 4 shows a typical calibration curve for the determination of U (VI) in 3M nitric acid medium obtained using the completely indigenized fiber optic spectrophotometric system equipped with 50 mm path length probe.

Complete infrastructure and expertise is now available for the manufacture and validation of fiber optic aided spectrophotometric systems and components and thus the object of self reliance in this field is achieved.

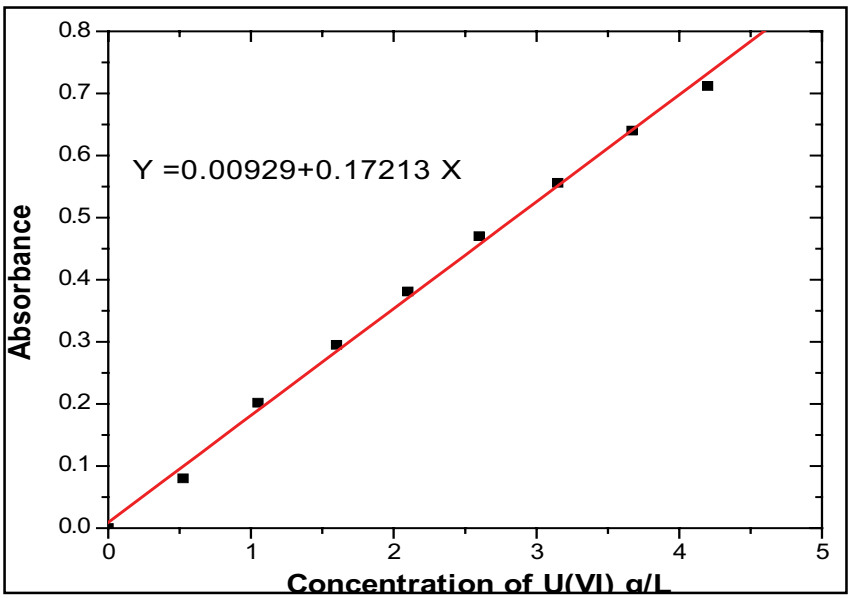

Fig. 4 *Calibration Curve for U (VI) in 3M HNO_3*

IV B3 Modelling & Material Development

IV B3.1 Apparent Molar Volumes of Key Solutes in Purex Process

The density of the solution is a very important parameter for solvent extraction operations. The use of density as a parameter is required at several places in the nuclear solvent extraction viz. design of settlers (decanters) for separation of organic and aqueous phases, as a major parameter in the remote operation and nuclear material accountability. In addition, density equation plays an important role in the prediction of fissile atom ratios during the criticality calculations involving radioactive solutions. The aqueous system of interest has several key and non-key components. The major key components are U(VI), Pu(IV) and nitric acid. The minor key components are U(IV), Pu(III) and Pu(VI). The reductants, stabilizers and fission products are non-key components in the system of interest.

In this work, apparent molar volumes at infinite dilution were estimated for $UO_2(NO_3)_2$-water binary solution, imaginary $Pu(NO_3)_4$-water binary and nitric acid-water binary solution. The experimental work was conducted for binary uranyl nitrate as well as nitric acid solutions. Fourteen solutions of aqueous uranyl nitrate,

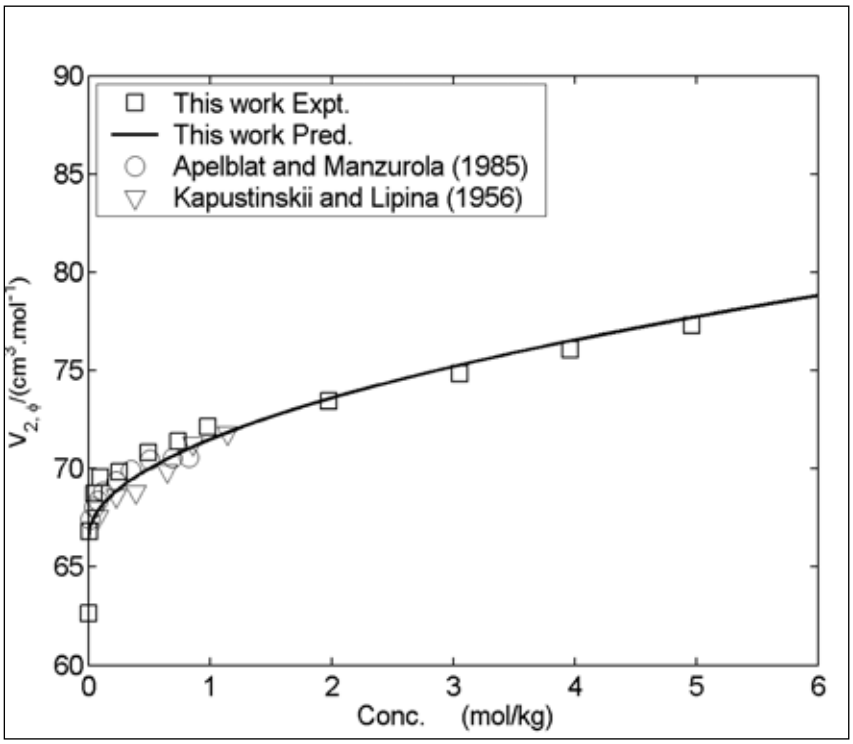

Fig. 1 *Apparent molar volume of $UO_2(NO_3)_2$ at 298.15K and 0.1 MPa*

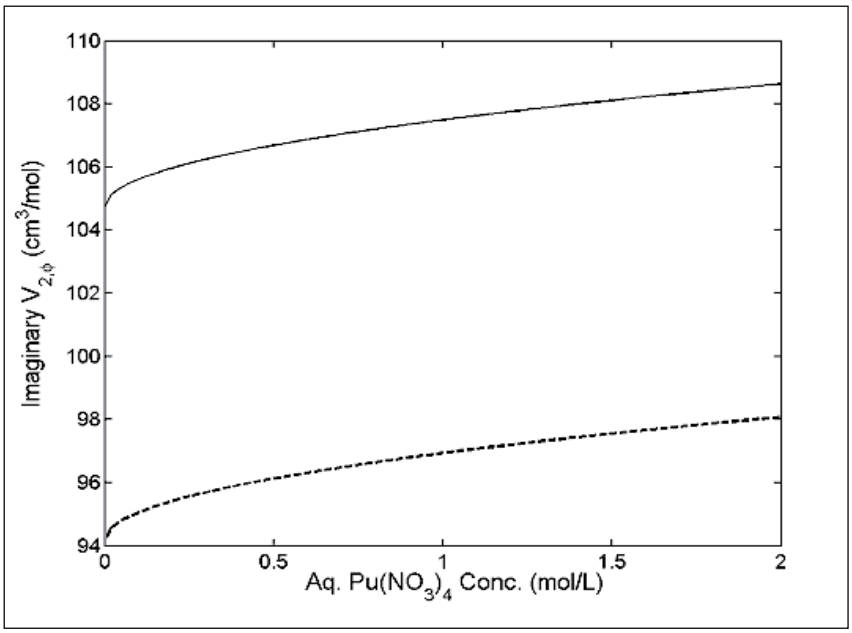

Fig. 2 *Apparent molar volume of $Pu(NO_3)_4$ at 298.15K and 0.1 MPa. Solid line for complete data base. Broken line for limited database*

ranging from ~0.0005m to ~5.0m, were made and densities were measured with a precision vibrating tube densitometer as per ASTM D-4052. From the experimental data, the determined $V^0_{2,\varphi}$ value was 66.4337 ± 0.0466 cm^3/mol, which is in close agreement with the literature reported value of 66.68 cm^3/mol. Fig.1 shows variation of apparent molar volume with the concentration.

After deducting the contribution of nitric acid density from the density of nitric solutions of Pu(IV) nitrate, the apparent molar volume of the $Pu(NO_3)_4$ in imaginary binary solution is obtained as 94.46 cm^3/mol (for smaller set consisting of French data) and 104.7 cm^3/mol for the complete data bank at IGCAR as shown in Fig. 2. The density of pure $Pu(NO_3)_4.5H_2O$ crystal is reported as 2.90 g/cm^3. This would correspond to a hypothetical Pu concentration of 5.0251 mol/L or 1201 g/L assuming isotopic composition of plutonium as 100% Pu^{239}. From the density values (assuming temperature of 298.15 K) the apparent molar volume of $Pu(NO_3)_4$ in the crystal is obtained as 108.67 cm^3/mol. Researchers at IGCAR recommend a $V^0_{2,\varphi}$ value of 104.7 cm^3/mol for $Pu(NO_3)_4$ in imaginary aqueous $Pu(NO_3)_4$ binary solutions.

Twenty seven solutions of aqueous nitric acid, ranging from 0.01N to 15.6N, were made by appropriate dilution of analytical grade nitric acid with ASTM grade-1 water. Densities were measured with a precision vibrating tube densitometer. Acidities of aqueous solutions were analyzed with an automatic titroprocessor. Fig. 3 shows variation of apparent molar volume with the concentration. Agreement of the estimated $V^0_{2,\varphi}$ value of 29.04 cm^3/mol for HNO_3 with reported values (29.00 cm^3/mol) was excellent.

Additional work on other non-key solutes is in progress. These results are being utilized in the development of a novel group contribution approach for predicting the density of aqueous solutions of interest to reprocessing.

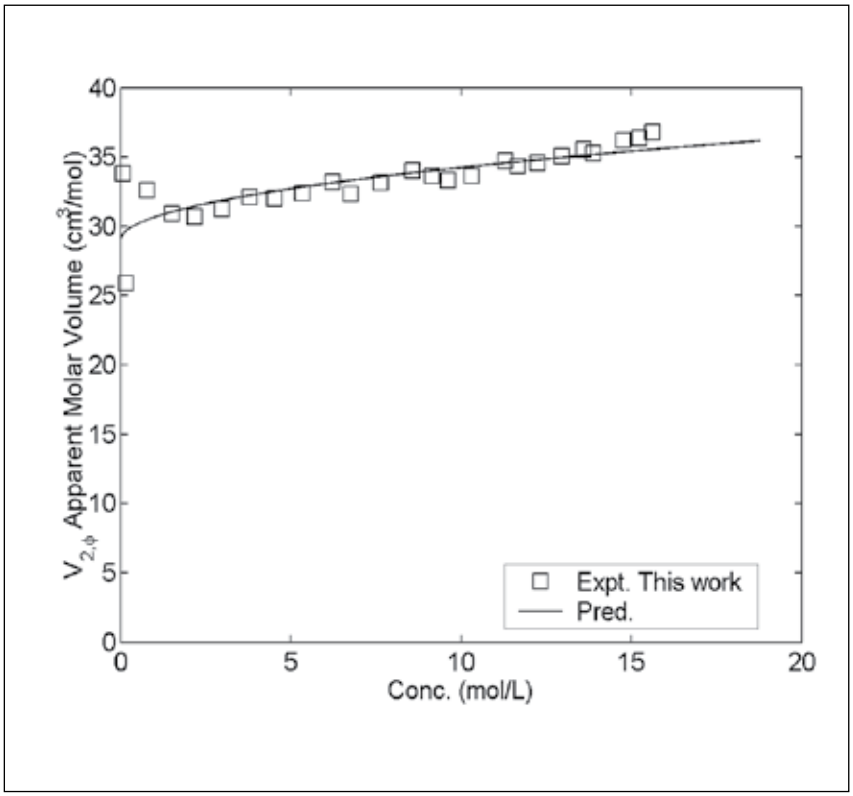

Fig. 3 *Apparent molal volume of nitric acid at 298.15K and 0.1 MPa*

IV B3.2 Development of Metal Waste Forms and their Characterization for Microstructure and Corrosion Behaviour

Metallic fuel is envisaged for application in future fast breeder reactors, and pyro-chemical route is the best option proposed for the reprocessing of spent fuel. Pyrochemical reprocessing involves electro-refining in molten chloride medium, cathodic processing, and alloy casting as the main unit operations. Subsequent to reprocessing operations, the metallic components left behind in the anode dissolution baskets of the electrorefining process are consolidated into a metal waste form (MWF), after distilling away adhering LiCl-KCl eutectic salt left in the anode dissolution baskets. Thus, the irradiated fuel cladding, zirconium from the alloy fuel, noble metal fission products (NMFP) (e.g., Tc, Rh, Ru, Pd, and Nb), and remnant actinides in the anodic dissolution baskets are melted together to make a "Metal Waste Form" intended for disposal in a geologic repository. The baseline waste form reported in the literature for EBR–11 spent metallic fuels was Stainless steel–

Fig. 1 *As-cast typical MWF alloy*

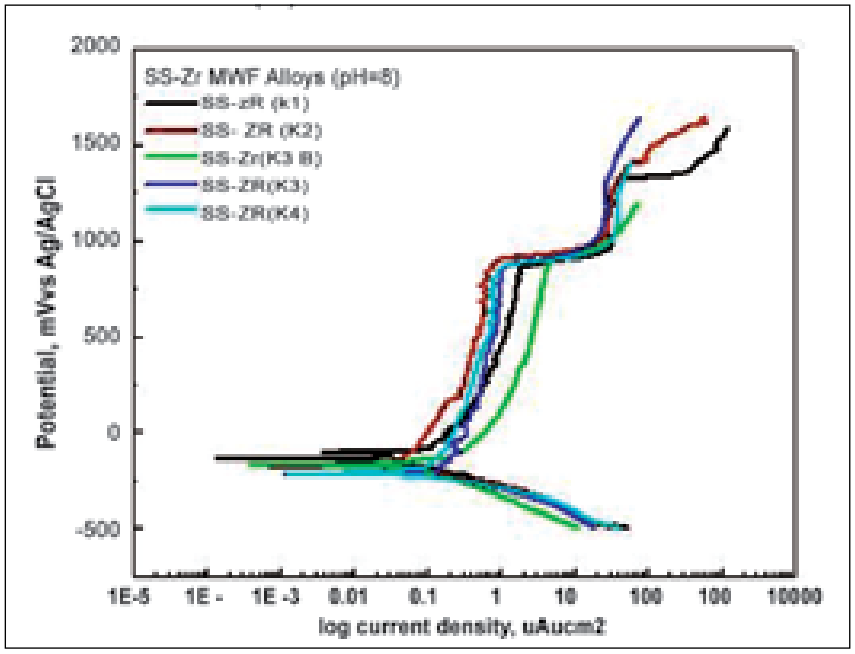

Fig. 2 *Potentiodynamic polarization curves of MWF alloys in simulated test solution*

15 wt% Zr alloy. However, the Zr content of MWF alloys may vary from 5 to 20 wt% depending on the composition of the starting fuel. The noble metal content of the waste form depend on the burn-up of the treated fuel and the actinide content on the efficiency of the electrorefining process; the waste forms may contain up to 4 wt% noble metal and up to 10 wt% actinides (mainly uranium).

Development and characterization of metal waste form (MWF) alloys of clad (D9 Alloy and 9Cr-1Mo) and zirconium was undertaken as a major project to understand the microstructure, phases developed and corrosion behaviour under simulated geological repository conditions. In the first phase Zr containing D9 MWF alloys were cast at DMRL, Hyderabad by using arc melting furnace under controlled atmosphere to produce each pancakes of 750 g weight (Fig.1). The chemical composition analyses for all MWF alloys have been made after the casting. In the first phase, MWF alloys of D9 Alloy (15Cr - 15Ni - 2.3Mo - Ti) stainless steel (SS) cladding with 5-20 wt% zirconium designated as K1 (SS-Zr5%), K2 (SS-Zr9%), K3B (SS-Zr12%), K3 (SS-Zr14%) and K4 (SS-Zr17%) (composition given in Table 1) were cast and investigated. The microstructure, microhardness, phase analysis, corrosion resistance and passive film properties were evaluated by scanning optical microscopy, electron microscopy (SEM), EDX (energy dispersive X-ray),

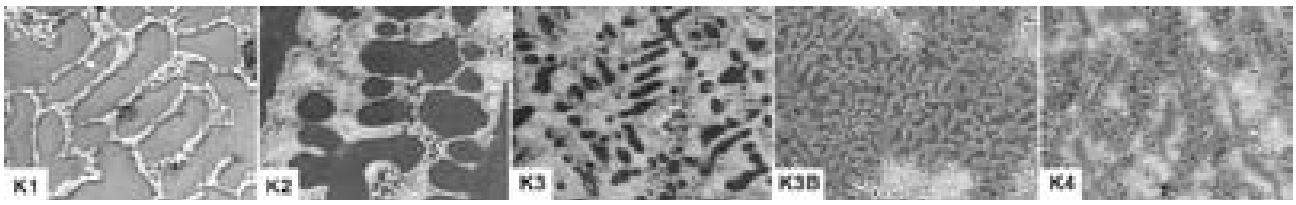

Fig. 3 *SEM micrographs showing surface morphology of tested samples*

glancing-angle X-ray diffraction (GXRD) and electrochemical methods. The long term corrosion behaviour under simulated repository conditions were carried out for leachability as per materials characterization (MCC) tests. The electrochemical polarization and impedance spectroscopy investigations of the different MWF alloys were carried out in de-mineralized (DM) water of pH 1, 5 and 8 to simulate the geological repository conditions. The results of the microstructural and phase analysis indicated that the identified phases are mostly the iron-based solid solutions of ferrite and austenite, $ZrFe_2$-type Laves and $Fe_{23}Zr_6$-type intermetallic. The typical microstructure of different as-cast MWF alloys showed the presence of ferrite (dark areas) and the Laves intermetallics (bright areas); austenite was observed along with the ferrite. Negligible quantities of zirconium were present in the ferrite and austenite; the element zirconium was present only in the intermetallic phases. Below 15 wt% Zr, the Fe solution phase with a mixture of α-Fe and γ-Fe was observed. At 15 wt% Zr(K4), near the eutectic composition, the Fe solution phase is essentially 100% α-Fe. The microhardness increased from 215 VHN for the alloy K1 to 445 VHN for the alloy K4.

The corrosion of MWF depends on three interrelated factors: alloy metallurgy, degradation mechanisms, and environmental conditions in the repository. The electrochemical test results showed that the corrosion behavior of MWF alloys is similar to that of stainless steels. The results of the corrosion potential indicated more active dissolution for SS-Zr(K1) in acidic pH 1, however, in higher pH 5 and 8 no systematic trend could be observed (Fig.2). In anodic polarization response of different MWF alloys, SS-Zr (K4 and K3) with higher Zr have better passivability and higher corrosion resistance. The structural and protective properties of passive oxide films formed spontaneously at the open circuit potential or during the anodic polarization studied by impedance spectroscopy showed a single semicircle of capacitance impedance that corresponds to well order of stability of passivity. However, variation in passive film resistance and capacitance were observed depending on the alloy composition and pH. The results of material characterization test (MCC-5) before and after leaching test for 120 days of all the investigated samples showed only a negligible weight loss (~0.0005 g). The corrosion resistance of different MWF alloys and its relations to the effects of pH, compositional variations, microstructures, phases and elemental profile are thus highlighted in the present work (Fig. 3). Further work is in progress to study the effects of different pH, simulated ground water, leachability, immersion, high temperature electrochemical and hydration test.

Table 1: Chemical composition of MWF alloy

Alloys	SS-Zr(K1)	SS-Zr(K2)	SS-Zr(K3)	SS-Zr(K3B)	SS-Zr(K4)
Element	Wt %	Wt %	Wt %	Wt %	Wt %
Cr	12.8	11.8	11.7	11.8	10.8
Ni	13.5	12.8	12.8	12.4	12.3
Mn	1.92	0.71	0.60	1.90	0.31
Si	0.46	0.5	0.50	0.45	0.52
Ti	0.12	0.2	0.17	0.12	0.2
Zr	4.4	8.5	12.2	14.1	16.8

IV B3.3 Development of Glass and Ceramic Matrices for Radioactive Waste Immobilization

Borosilicate glasses are the presently accepted host matrix for immobilization of high-level radioactive waste (HLW). However, they are not suitable for HLW containing high concentrations of heavy metals, platinum group elements and volatile fission products like Cs and Ru. Alternate glass and ceramic matrices thus need to be developed for the management of such types of wastes. One promising candidate is iron phosphate glass, commonly known as IPG, developed by the University of Missouri, Rolla (UMR group), USA. Among ceramics, monazite (a mixed rare-earth orthophosphate), is a natural mineral known to exist for billions of years. The fact that natural monazites contain appreciable amounts of thorium and uranium and possess crystal chemistry features suitable to contain these elements makes these minerals ideal hosts for the immobilization of HLW. Apatites are another group of naturally occurring phosphate minerals of very high durability. They have the unit cell formula of $M_{10}(PO_4)_6(X_2)$, M= Ca, Sr, Ba,Pb Cd and (X=OH, Cl or F). They can form solid solutions with various cations and anions such as Sr, Cs and Tc, and thus immobilize these important radioactive elements. In this context, a study was carried out on the synthesis and characterization of these three systems.

Laboratory scale synthesis of IPG was successfully carried out by melting iron oxide and ammonium dihydrogen phosphate at 1423K in air. The glass transition temperature (784K) and the density of the glass (2.9g/cc) match with the reported values. A systematic approach was carried out to load cesium into IPG. 36 mol% Cs_2O could be successfully loaded, whereas, the literature shows a maximum of only 29mol% loading. This Cs_2O loaded glass was molten at 998K and the volatilization loss was found to be less than 0.5 wt%. Hence this glass can be used as a source of radioactivity and used for medical purposes. The non-crystalline nature of the Cs loaded glass was confirmed by XRD (Fig 1). Glass transition temperature and density of this glass were found to be 743K and 3.69 g/cc respectively. Similarly, in separate experiments, 20wt% of a simulated waste composition was successfully loaded (at 1273K) into IPG, and the product examined by XRD and DSC (Fig. 1 and Fig. 2). The density of the glass (3.09 g/cc) and the glass transition temperature (813 K) were found to increase with waste loading. The increase in glass transition temperature shows that the waste loaded glass has better thermal stability compared to the bare glass.

The monazite $CePO_4$ was prepared by a solution chemistry route starting with aqueous solutions of analytical reagent grade $Ce(NO_3)_3{\cdot}6H_2O$ and $NH_4H_2PO_4$ in stoichiometric quantities at room temperature. $CePO_4$ with 10 wt% simulated HLW

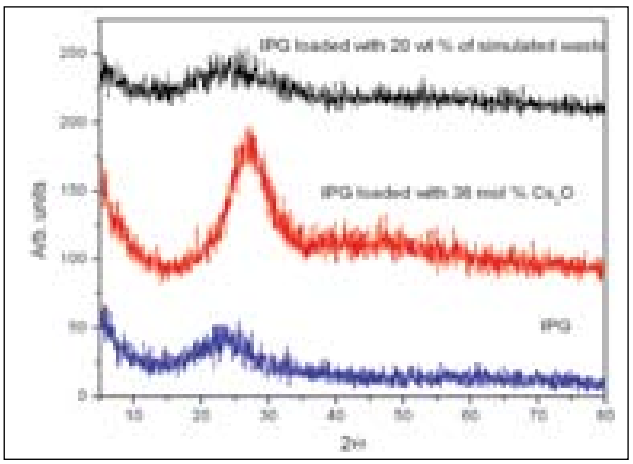

Fig. 1 *X-ray diffraction pattern of iron phosphate glasses*

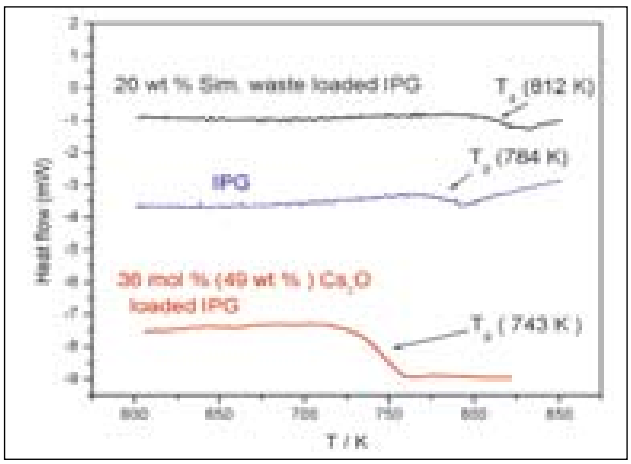

Fig. 2 *Glass transition temperatures (T_g) of the IPG type glasses*

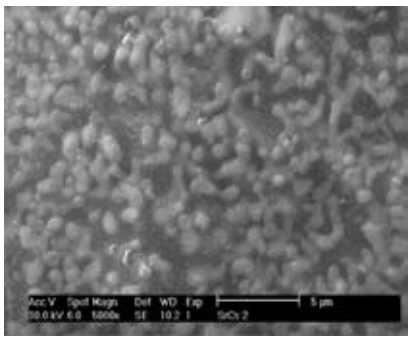

Fig. 3 *Microstructure of a typical apatite glass-ceramic*

expected from the FBTR fuel of 150GWd/t burn-up and one year cooling, was prepared in a similar way. The XRD patterns of the $CePO_4$ and $CePO_4$ loaded with 10 wt% simulated HLW sintered at 1473K are identical but for a trace impurity line of CeP_2O_7 in the latter (Fig. 3). The apatite compositions $M_{10-x}C_{s_x}(PO_4)_6X_2$ (M=Ca, Sr and Ba, X=OH and Cl) were synthesized by precipitation and sonochemical reactions at low temperatures. Ca and Sr chlorapatites were found to take up 5 mol% of Cs at the cation site on heat treatment below 1073 K, whereas $Ba_{10-x}C_{s_x}(PO_4)C_{l2}$ could accommodate 10 mol% of Cs. Glass-ceramic compositions were prepared by taking known amounts of the crystalline phase, mixing them with glass forming agents (e.g, 57 wt% SiO_2, 25 wt% B_2O_3 and 18 wt% Na_2O), and heating at 1123 K in air for three hours. The glass phase provides an additional immobilization barrier against leaching of the radioactive element from the waste form. In the glass-ceramic matrix with 50 wt% apatite, the crystalline phases were visible as buried under the glass in the SEM micrograph (Fig. 4).

Thermal expansion coefficient is an important thermophysical property of radioactive waste forms. The thermal expansion of the monazites was measured by high temperature X-ray powder diffraction in the temperature range 298 to 1173 K. The volume of the monoclinic cell was calculated from the lattice parameters measured at different temperatures. The average linear thermal expansion along the crystallographic axes, and the average volume expansion as a function of temperature were calculated from the measured lattice parameters. Fig. 5 shows the results for the waste-loaded monazite. The thermal expansion behaviour of the monazite with and without the simulated HLW is found to be very similar. The average linear (V/3) thermal expansion of $CePO_4$ at 1173 K is 0.73% which corresponds to an expansion coefficient of $8.3x10^{-6}$ K^{-1}, whereas, the average linear expansion of the same phase loaded with 10 wt% simulated HLW is 0.86% which corresponds to an expansion coefficient of 9.8 x 10^{-6} K^{-1}.

Thermal expansion property of the apatite ceramics was measured by thermo-dilatometry on high-density bulk specimens by using a home built dilatometer. The percentage linear thermal expansion of $Ba_{10}(PO_4)Cl_2$, $Ba_{9.5}Cs_{0.5}(PO_4)Cl_2$ and $Sr_{10}(PO_4)Cl_2$ is seen to be about 0.8 between room temperature and 800K. This indicates that the thermal expansion behaviour of the chlorapatites is not affected by moderate Cs-substitution.

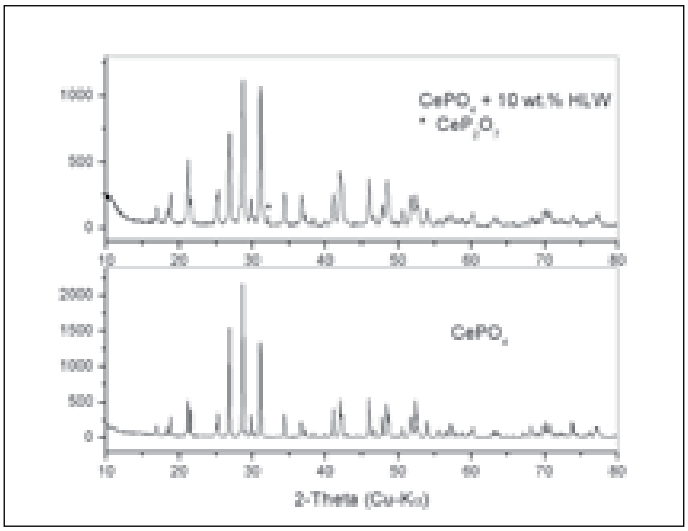

Fig. 4 *X-ray diffraction pattern of the $CePO_4$ monazite with and without the simulated waste*

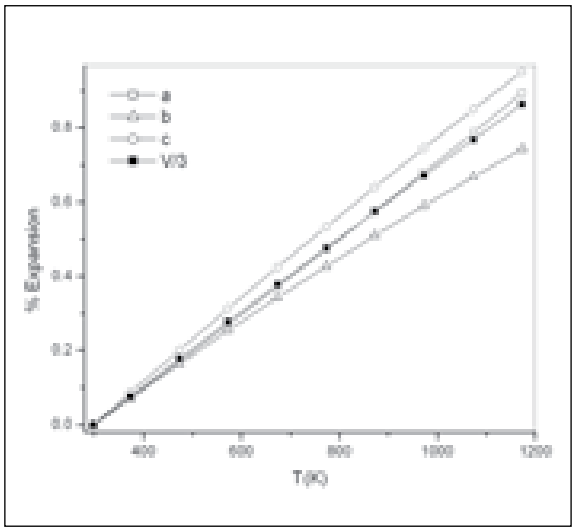

Fig. 5 *Axial and average thermal expansion of $CePO_4$ loaded with 10 wt. % simulated HLW. a,b and c are lattice parameters and V is the volume of the unit cell*

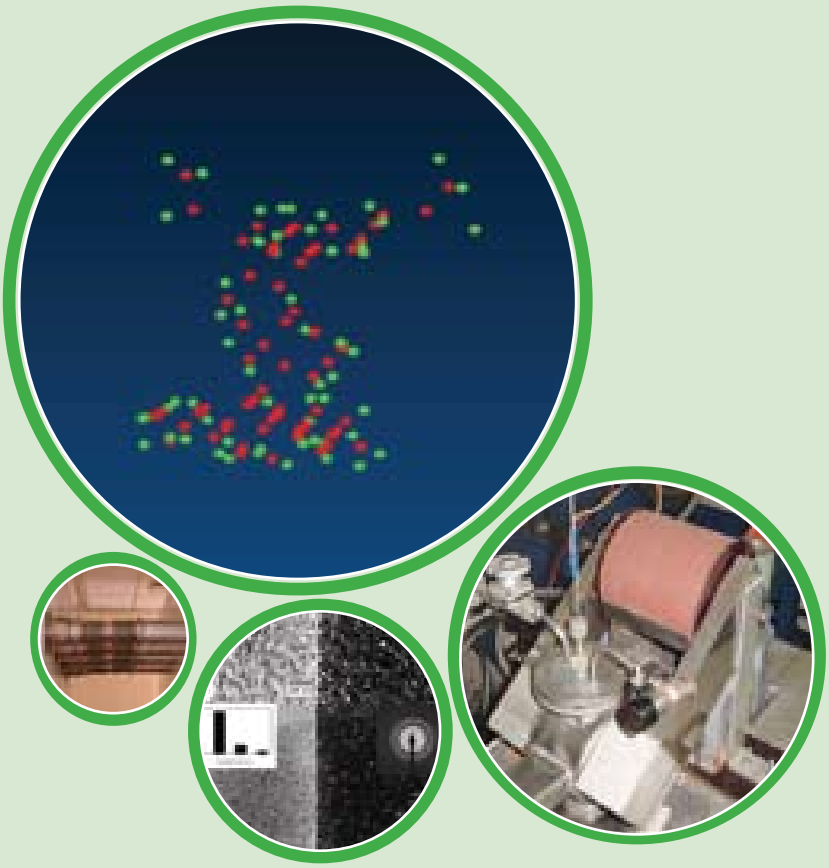

V

Basic Research

V.1 In-Silico Exploration of Material Properties through High-end Computation

The need to design, understand and control material properties arise in the context of basic research, material selection & design, reprocessing and a host of other contexts in the nuclear industry. The response of materials to radiation damage, phase stability of alloys, understanding chemical properties from an electronic structure point of view are some typical requirements. Many macroscopic properties of materials are influenced by processes which straddle huge dynamic range of length and time-scales. The mechanisms through which macroscopic material properties emerge through these scales are ill understood and are frequently inaccessible to even state of the art experimental tools. Hence, there is a compelling need for virtual materials laboratories. World-wide, the development of powerful multiscale models work is still under progress and provides the broad context for the computational initiative undertaken at our Centre. For this purpose, a modest Beowulf cluster consisting of 64 dual Xeon® CPU nodes with a peak performance of ~ 500 Gflops, was commissioned in April, 2008 at our Centre. Powerful packages for electronic structure and molecular dynamics calculations like *wien2k, vasp, siesta, pwscf, abinit, cpmd, dlpoly, lammps, moldy, gromacs* have been installed. Also the high-end terra-flop computing facilities at Computer Division are also being used for some of the work. A brief account of the research done is given below.

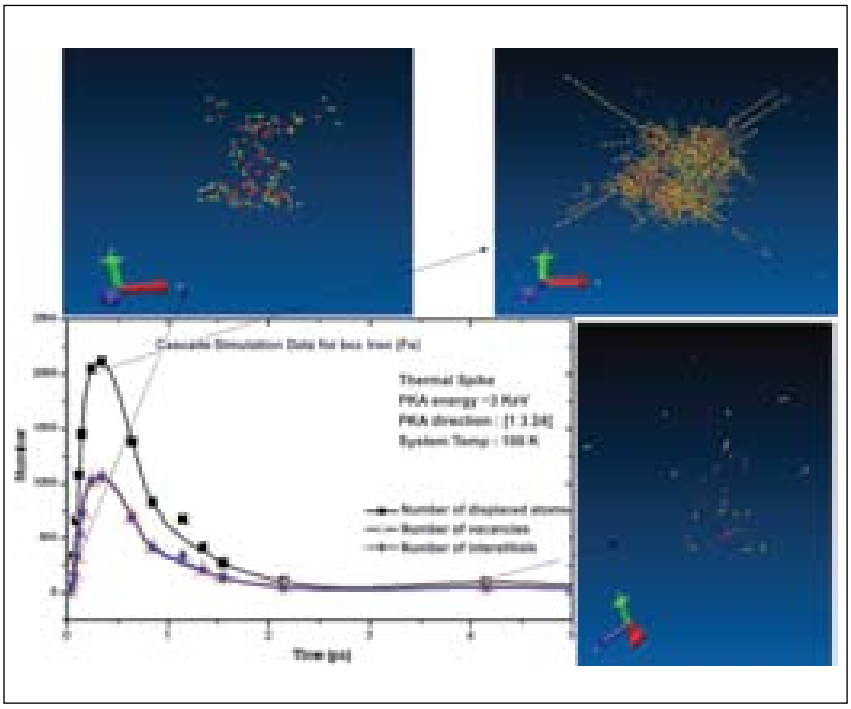

Fig. 2 *Time evolution of the number of primary defects and their spatial distribution in a radiation damage cascade produced by a 3 KeV primary knock on atom in Fe*

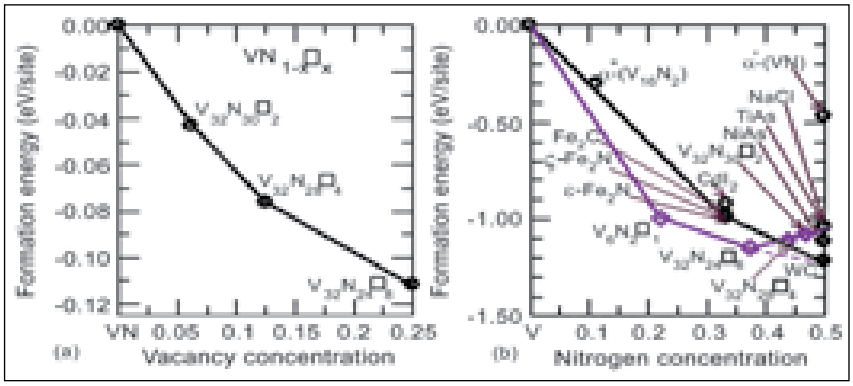

Fig. 1 *Calculated formation enthalpy of various vacancy stabilized vanadium nitrides as a function of concentration. (a) for the pseudo-binary $VN_{1-x}\square_x$ (□ represents Vacancy) in NaCl structure, and (b) $VN_{1-x}\square_x$ in various other structures. These graphs show that the vacancies on the nitrogen sublattice lowers the formation enthalpy of VN and V_2N in relation to the respective stoichiometric phases making the calculated phase stability to be in agreement with experiments*

The field of nanomaterials research and development is a current area of great promise. Nanomaterials have novel electronic, optical, magnetic and mechanical properties. As an example, in one study, it was

discovered that nanowires of Fe (as well as $Fe_{1-x}Co_x$) form a half-metallic ferromagnet, and hence are potentially useful as a spintronic material. In a related study, electron transport in magnetic tunnel junctions was computed as a function of applied bias and temperature using Green's function method. In another problem, *ab-initio* lattice dynamics calculations were used to obtain the phonon spectrum enabling interpretation of experimental data. In other studies, Density Functional calculations were employed to investigate phase stability of alloys and compounds. As an example, investigations on vanadium nitrides revealed the importance of vacancies for stabilizing the experimentally observed NaCl (δ-phase) in preference to the otherwise stable hexagonal WC and NiAs structures (Fig. 1). With the present tools even complex organic and biological molecules are amenable for investigation. For example, the selectivity of Metal Imprinted Polymer (MIP) Vinyl benzyl Imino Di Acetate (VbIDA) ($C_{26}H_{26}CoN_2O_8$:Na) to cobaltous ions as compared to ferrous ions was investigated a problem of relevance to waste management and decontamination programs. In the context of reprocessing, transport properties like the shear and bulk viscosities, thermal conductivity, etc, of hydrocarbons are being investigated using reverse non-equilibrium molecular dynamics. An ambitious program for the development of radiation resistant materials using *ab-initio* molecular dynamics, Monte Carlo simulations and continuum theories leading to seamlessly integrated multiscale models is envisaged. In this context, the formation energy of vacancies and self ion interstitials, and the binding between these, are studied. An in-house code for structural pattern recognition of defects is being developed. Fig. 2 shows the time evolution of primary defects in the cascade produced by a primary knock-on atom with 3 KeV energy in bcc Fe at 100 K. In metallurgy and materials selection study, the stability and response of oxide dispersion strengthened ferritic/martensitic steels under irradiation was investigated both experimentally and computationally. Fig. 3 shows the model system of Y_2O_3 nanoclusters in bcc Fe currently investigated, in this context, through computation to interpret positron experiments.

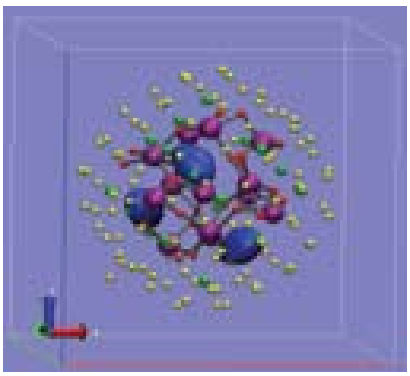

Fig. 3 *Positron density isosurface in blue color showing localization at interfacial vacancy cluster. Iron atoms at the interface are shown in yellow and remaining Fe atoms in super cell are removed for clarity. Green balls represent unrelaxed positions of 20 Fe vacancies distributed around Y_2O_3 cluster. Y and O atoms are shown in purple and red color respectively*

In summary, a broad based state of the art computational materials science activity with a rich repository of techniques is initiated which would be helpful in different areas of materials research and development undertaken by DAE.

V.2 Development of a New Quadrature Algorithm

Our Centre has contributed a variety of algorithms for functions of interest in physical sciences. These developments are byproducts of investigations in solving the integro differential equations of neutron transport. In particular, a variety of algorithms for the evaluation of the variants of Fermi-Dirac integrals have been introduced which are needed extensively in electron transport and stellar evolution. These routines are used throughout the world, particularly in semi-conductor device modeling, simply because they have phenomenal accuracy (stemming from analyticity properties) combined with the least computational cost. The latest edition of 'Numerical Recipes', the algorithm classic, published by Cambridge University Press carries this IGCAR algorithm.

In addition, several quadrature algorithms for the evaluation of regular, singular and hyper singular integrals have been introduced. These quadrature schemes are clever adaptations of recently introduced quadrature schemes like, TANH, IMT and DE methods. These three schemes are of very recent origin. TANH quadrature is an American invention while the other two, namely IMT and

DE have been contributed by the Japanese. For numerical quadrature, these newer schemes will slowly reach a utility level enjoyed by classical schemes like Gaussian and Clenshaw-Curtis. They are particularly useful for functions with end-point integrable singularities.

The above three new methods make an ingenious exploitation of the classical Euler-Maclaurin formula whereby the clustering of the quadrature nodes at the ends of the interval after a variable transformation guaran-tees an increased sampling of the function at the ends of the interval. But none of these quadrature schemes (including the Gaussian) has the capability to handle a singularity lying close to the line of integration within the interval of integration. These schemes can handle a singularity of the above type only after incorporating a correction for the singularity but without this correction, the convergence will be severely impaired. It is this problem that has been addressed by us. By suitably modifying the IMT scheme, the sampling around an interior singularity is sufficiently enhanced. We have proved that this new variant of IMT schemes still converges exponentially. Thus for the first time, a quadrature scheme has been introduced which can handle both end-point singularity and an interior singularity arbitrarily close to the midpoint.

V.3 Electron Cyclotron Resonance X-Ray Source

An Electron Cyclotron Resonance (ECR) based X-ray source has been developed and a schematic of this is shown in Fig. 1. The ECR X-ray source has a cylindrical cavity (diameter 130 mm, and thickness 85 mm) as a plasma chamber. Microwave (Magnetron, frequency: 2.45 GHz and power: 2000 W) is coupled to the cavity by a rectangular wave-guide (WR-284). In the diagonally opposite port X-rays are measured through an aluminum window (thickness: 2 mm). The cavity is connected to a vacuum pumping system, which can get a vacuum better than 10^{-6} torr in the cavity. In the fourth port, the target feed and the gas feeds are connected. The cavity is magnetized with a permanent magnet (superimposed with an electromagnet) and a yoke is provided for the magnetic field return path. The advantages of ECR X-ray source over the linear tubes are (i) it does not require high dc potentials and (ii) it can be made as a portable device. The ECR X-ray source differs from the conventional linear tube based X-ray sources because the electrons are accelerated by a simple principle of a cyclotron. The cyclotron frequency (ω_{ce}) of the electron is controlled by the magnetic field as $\omega_{ce} = eB/m_e$, where B is the externally applied dc magnetic field, *e* and *m* are charge and mass of the electron, respectively. When the frequency of the RF electric field is in resonance with the cyclotron frequency, the electron gets accelerated continuously. Further, in the ECR X-ray source, the Dees of the traditional cyclotron have been replaced with a resonant

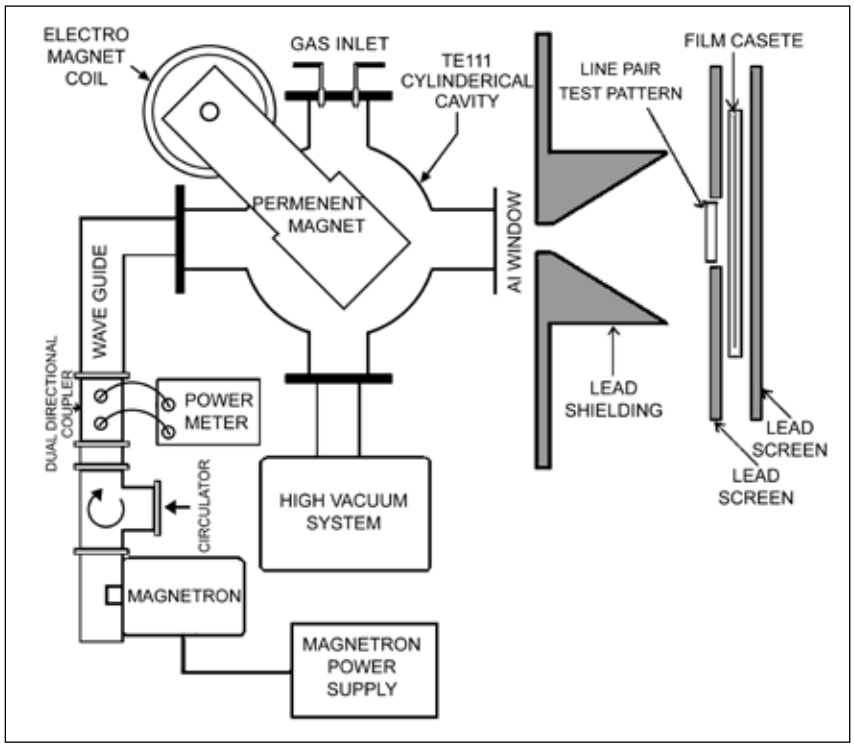

Fig. 1 *Schematic of the ECR X-ray source*

Fig. 2 *Photographs of ECR Plasma X-Ray Source*

cylindrical cavity. Fig. 2 shows the photographs of the facility.

Characterization of the Source

The X-ray energy spectra are obtained for various coil currents and gas pressures using a NaI(Tl) based spectrometer. From these spectral measurements, it is observed that the optimum gas pressure for maximizing the X-ray production is at 10^{-5} torr. When the gas pressure is increased (10^{-4} torr), the collision frequency increases and hence the number of electrons reaching higher energy is reduced. When the gas pressure is reduced, the number of electrons available for the acceleration is limited (the ionization becomes very weak at low gas pressure). The X-ray dose at the port is found to be nearly 8.85 mGy/h.

Application of ECR X-ray Source

(1) Variable Energy X-ray Source: From the experimental studies, it has been found that the effective energy of the Bremstrahlung spectrum can be altered by a inserting a high Z target disk inside the cavity near the port. Using this feature, the energy spectrum of the X-ray source has been modified for the calibration of TLD badges for personal monitoring in the low energy region (<150 KeV). The source was operated with and without a lead target disk and the effective energy of the spectra were obtained at 40 KeV and 70 KeV respectively. The TLD badges and the condenser-R meter are kept at a distance of nearly 25 cm from the port. The cumulative doses, obtained from the condenser-R meter and the TLD reader are compared.

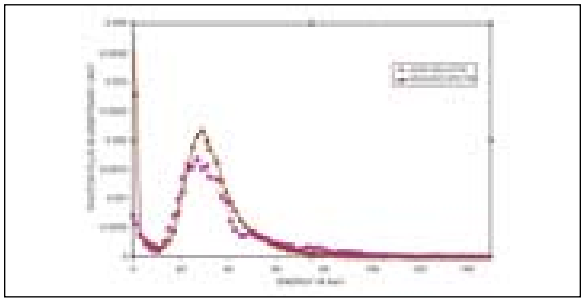

Fig. 3 *A typical X-ray spectrum from the ECR X-ray Source and the simulated spectrum*

(2) NDT and Soft Tissue Imaging: The potential use of the source for NDT and medical imaging application has been demonstrated. For the imaging application, the required dose has been estimated using a hospital X-ray machine. ECR X-ray source experimental parameters are tuned to get the required dose values. Lead collimation arrangement is made to get uniform flux. The flux profile is measured using a teletector at different distance from the port and uniform field region has been marked. The quality of the image resolution is estimated from the X-ray images of the line pair test pattern and the resolution is found to be comparable to that of commercial X-ray machine (better than 2 LP/mm). The images of

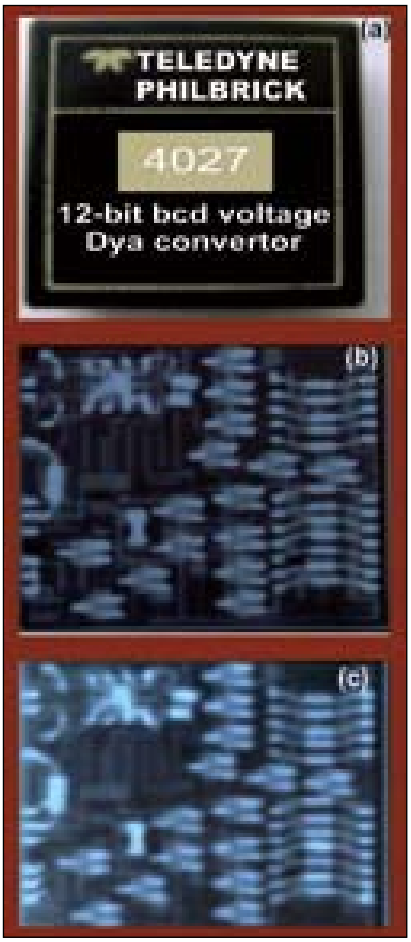

Fig. 4 *Comparision of images obtained using ECR X-ray source and medical diagnostic X-ray machine*

microcircuit pack, chicken leg and human palm are obtained from ECR X-ray source and compared with images obtained using a medical diagnostic X-ray machine. It is found that the image obtained from ECR X-ray source is suitable for imaging application.

Theoretical Study: The equation of motion of charged particles in the presence of an electric field (of TE_{111} mode) and the external magnetic field is modeled and used to analyze the electron trajectory inside the TE_{111} cavity. The electron trajectory simulation programme has been developed. Using is simulation programme, the energy distribution of the electrons hitting the cavity wall was calculated. The calculated electron energy distribution is used in the MCNP code for calculating the X-ray spectrum from the ECR X-ray source (Fig.4). The calculated X-ray spectrum matched well with the experimentally observed spectrum.

V.4 Nanofluids with Enhanced Thermal Properties

Magnetic nanofluid is a unique material that has both the liquid and magnetic properties. Many of the physical properties of these fluids can be tuned by varying the magnetic field. Such fluids are found to have several fascinating applications. In addition, they have been wonderful model systems for fundamental studies. Here, yet another fascinating application of magnetic nanofluid for thermal management has been demonstrated. Nanofluids are considered to be the future coolants for electronic devices and engines. Several nanofluids with enhanced thermal conductivity have been tailored during the past several years. The effective medium theory fails to explain the large enhancement of thermal conductivity in nanofluids and the temperature dependence of thermal conductivity. The possible mechanisms responsible for the enhancement of thermal conductivity in nanofluids still remain as a puzzle.

A stable colloidal suspension of magnetite nanoparticles of average diameter 6.7 nm, coated with oleic acid and dispersed in hexadecane has been used in this study. The size distribution of the nanoparticles measured using dynamic light scattering (DLS) experiment is shown in inset (a) of Fig. 1. The TEM image of the nanoparticles is shown in the inset (b) of Fig. 1. The thermal conductivity of the samples was measured by using a thermal property analyzer, which uses a single-needle sensor for heating, and also for monitoring of the temperature.

Fig. 1 shows the thermal conductivity ratio (k/k_f) of the nanofluid as a function of volume fraction of Fe_3O_4 nanoparticles, where k and k_f are the thermal conductivity of nanofluid and the base fluid respectively. No enhancement in thermal conductivity is observed up to a volume fraction of 1.5 % of Fe_3O_4 nanoparticle. At 2.6 vol %, the increase in k/k_f was marginal. The highest value of k/k_f observed was 1.23 at 7.1 vol % of Fe_3O_4 nanoparticles that corresponds to an enhancement in thermal conductivity of 23%. The data fitted with Maxwell model shows good agreement, especially at higher volume fractions. Slight deviation from the Maxwell fit is observed at lower volume fraction (below 4.5 %). The observation of

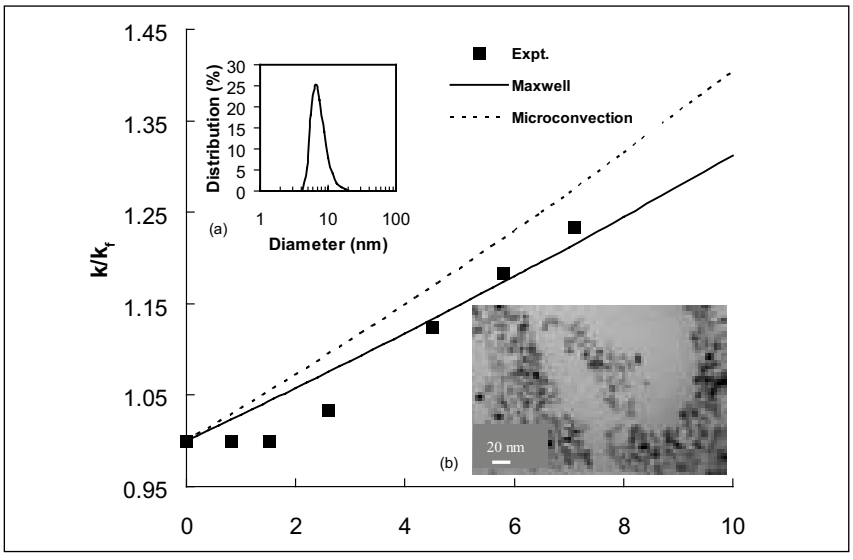

Fig. 1 *The thermal conductivity ratio (k/k_f) of the NF as a function of volume fraction of Fe_3O_4 nanoparticles. The size distribution of Fe_3O_4 nanoparticles (a) and the TEM image of nanoparticles (b) are shown in the inset*

thermal conductivity enhancement at low particle loading (<2 vol %) in presence of magnetic field (no enhancement without field) shows that aggregation is the main cause of thermal conductivity enhancement within Maxwell's limit. The enhancement above 1.76 vol% could be due to small clusters (dimers or trimers) formed in the nanofluid due to magnetic dipolar attractions. It appears that the wetting of nanoparticles is enhanced due to the organic sheath, which in turn leads to a lower interfacial thermal resistance. It is found that nanofluids with very small particles (~5nm) are also prone to settling when particles are uncoated. After repeating the magnetic cycles several times, the thermal conductivity comes back to the original value. The above experiments have been repeated in a variety of nanofluid samples with aqueous and non aqueous carrier fluids and the results obtained were similar.

Fig. 2 shows the thermal conductivity ratio (k/k_f) and the corresponding enhancement as a function of applied magnetic field in the nanofluid with 4.5 vol% of Fe_3O_4. The variation of k/k_f at three different magnetic cycles (rise and decay) shows that the enhancement is reversible, with a slight hysteresis. The maximum enhancement was 216%, at an applied magnetic field of 101 gauss. As the magnetic field is increased in a magnetically polarizable nanofluid, the nanoparticles align in the direction of magnetic field when the magnetic dipolar interaction energy $U_d(ij)$ dominates over the thermal energy k_BT, where, k_B is the Boltzmann constant and T is

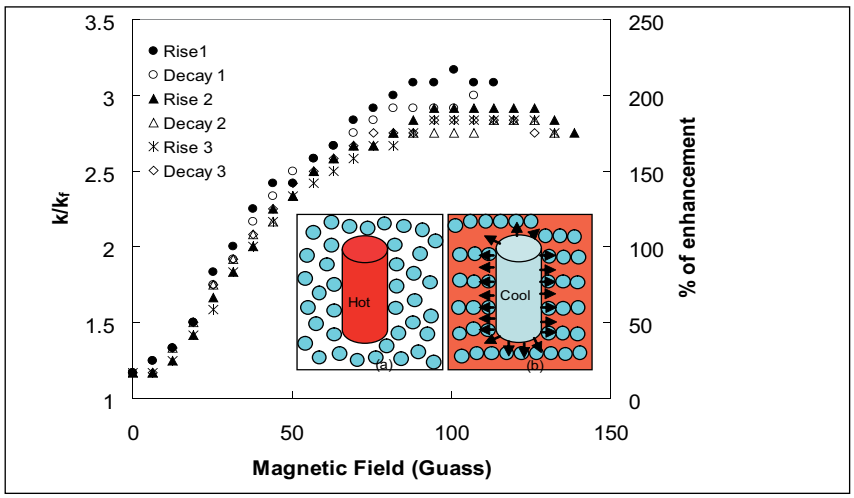

Fig. 2 *The thermal conductivity ratio (k/k_f) and the enhancement as a function applied magnetic field in the nanofluid with 4.5 vol % of Fe_3O_4 nanoparticles. The inset of figure shows the schematic of the mechanism of heat transport from a cylindrical device immersed in nanofluid without and with magnetic field*

the temperature. When the dipolar interaction energy becomes sufficiently strong, the magnetic particles form a chain like structure. Here, each magnetite particle is single domain super-paramagnetic with a magnetic moment **m**. Without any external magnetic field, the magnetic moments of the scatterers are oriented in random direction. With the increase in magnetic field, the moments of the magnetic particles start to align themselves along the direction of the magnetic field.

As nanoparticles starts to form chains, the convection velocity, ν

$$(\nu = \sqrt{\frac{18k_BT}{\pi\rho d^3}})$$

drops drastically due to the cube dependence of nanoparticle particle size *(d)*. ρ is the density of the nanoparticles. Therefore, the Brownian motion is severely arrested as the chain length increases. As the convection velocity decreases with increasing magnetic field, the observed enhancement in thermal conductivity cannot be due to the microconvection mechanism. In a nanofluid, series and parallel modes of thermal conduction through the base fluid and the nanoparticles can be visualized within the mean-field models. The parallel mode has the geometric configuration that allows the most efficient means of heat propagation. Extremely large thermal conductivity can be expected from such parallel modes. In the lower Hashin-Shtrikman (HS) limit, nanoparticles are well suspended and conduction is through series modes whereas in the upper HS limit, the conduction path is through dispersed particles. The clustering of nanoparticles can dramatically enhance the thermal conductivity. In the limit $(\varphi k_p/k_f)>>1$ (where φ is the volume fraction of nanoparticles), the predicted values of k/k_f for the upper HS and parallel modes are $(2\varphi/3)k_p/k_f$ and $(\varphi k_p/k_f)$ respectively. These values are comparable to $k/k_f=(\varphi/3)k_p/k_f$ predicted by the aggregation model. Using the experimental data, the expected values of enhancement for the upper HS and parallel modes

are 150 and 225% respectively. Strikingly, the observed enhancement of 216% is close to the predicted value for parallel mode conduction.

The observed reversible tunable thermal property of this nanofluid may find many technological applications for this fluid in nano-electromechanical systems (NEMS) and micro-electromechanical systems (MEMS) based devices. For example, depending upon the cooling requirement, the current or magnetic field can be precisely programmed to obtain the desired level of thermal conductivity enhancement or cooling. The mechanism of heat transport from a cylindrical devise immersed in such a nanofluid coolant without and with magnetic field is depicted in the inset of Fig. 2. When the magnetic field is off, the nanoparticles behaves as a normal fluid with random arrangement of particles. When the magnetic field is turned on, the parallel mode conduction leads to drastic enhancement of thermal conductivity. The slight decrease in thermal conductivity observed above the peak magnetic field strength is attributed to 'clumping' of chains and the subsequent distortion in the nematic like order.

In summary, the details of a magnetically polarizable nanofluid with tunable thermal properties are presented. It is demonstrated that, by controlling the linear aggregation length from nano to micron scales, the thermal conductivity of the nanofluid can be tuned from a low to a very high value. Further, it has been found that, under repeated magnetic cycling, the thermal conductivity is reversible. These findings offer promising applications related to thermal management.

V.5 Synthesis and Characterization of Nanocrystalline $Ti_{1-X}Al_xN$ by Reactive Magnetron Sputtering

Metastable solid solution $Ti_{1-x}Al_xN$ thin films have good oxidation resistance, erosion resistance, higher hardness and remain stable at high temperatures, compared to TiN, TiC, Ti(C,N) and CrN. The hardening mechanism is due to the substitution of Ti atoms in the TiN lattice by Al. Importantly, replacement of Ti atoms by Al atoms increases the oxidation resistance at elevated temperatures. The preparation technique and the control of deposition parameters have a significant effect on the stability of the cubic phase at higher concentrations of Al. The stability of $Ti_{1-x}Al_xN$ cubic structure decreases with Al concentration and finally it transforms in to the hexagonal AlN. The objective of this study is to synthesise $Ti_{1-x}Al_xN$ films with varying Al content and annealed in nitrogen atmosphere and characterize their structural and nanomechanical properties in order to understand the phase separation (spinoidal decomposition) behaviour.

The XRD profiles of $Ti_{1-x}Al_xN$ with different Al concentrations are shown in Fig.1. All these films exhibit signatures corresponding to TiN phase with a shift towards higher Bragg angle. In Fig. 2, the film with 64% Al splits into c-TiAlN and c-AlN where as the amorphous one with 81% Al becomes crystalline with hexagonal AlN phase (B4) and c-TiN phase after annealing.

The nanoindentation hardness of as-deposited and annealed $Ti_{1-x}Al_xN$ increases with Al concentration till the decomposition of cubic phase into hexagonal (Fig. 3). We have obtained maximum a hardness of 35 GPa and 38 GPa for as-deposited and annealed specimens, respectively due to the decomposition into cubic phases. The hardness of the ($Ti_{1-x}Al_xN$) films increased with x up to about 0.64, and decreased rapidly due to the presence of a B4 structure with second phase.

For understanding the structural properties, films prepared with

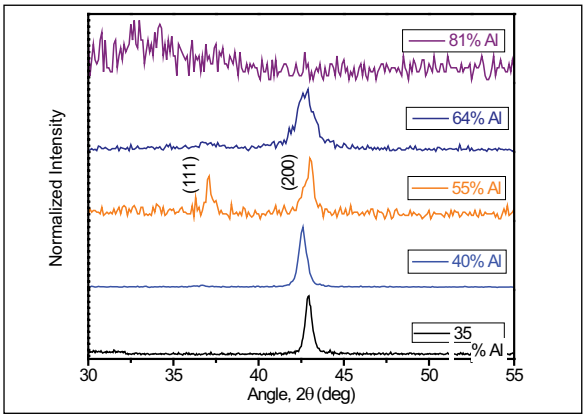

Fig. 1 *GIXRD profiles of $Ti_{1-x}Al_xN$ with different Al%*

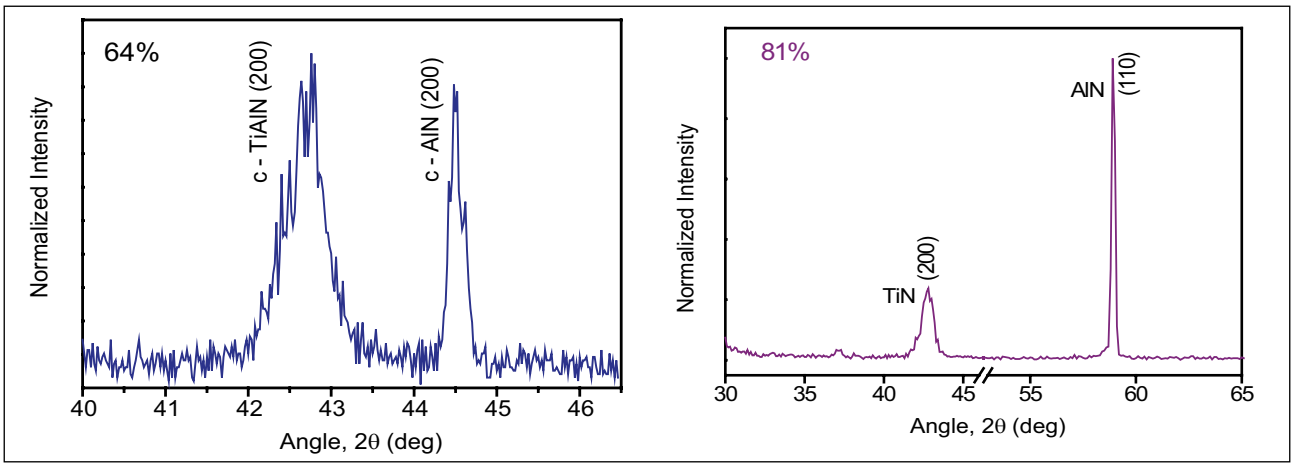

Fig. 2 *GIXRD profiles of $Ti_{1-x}Al_xN$ films with (a) 64% Al and (b) 81% concentration after annealing*

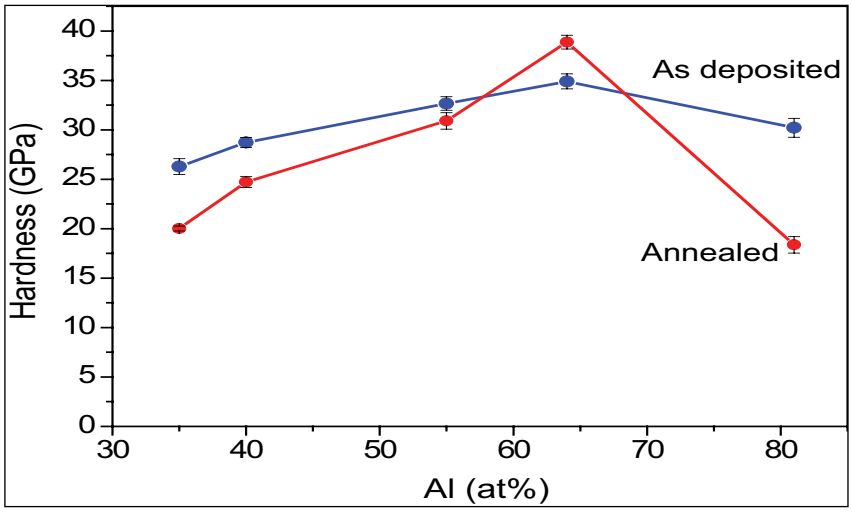

Fig. *3* *Indentation hardness of $Ti_{1-x}Al_xN$ with different Al%*

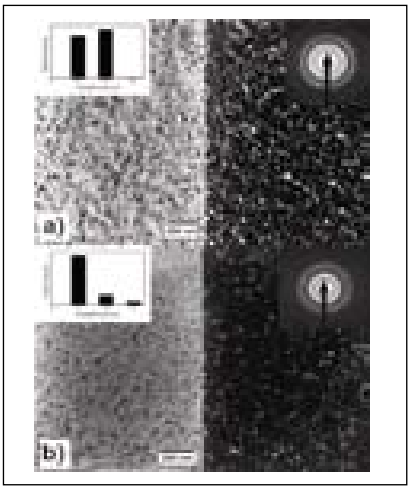

Fig. 4 *TEM micrographs (BF and DF) with crystallite size distribution histograms and SADPs of $Ti_{1-x}Al_xN$ films a) 64% Al and b) 81% Al*

64% and 81% Al were studied by TEM. It is seen from Fig. 4(a) that the TiN crystallites of size around 5 nm and 10 nm are embedded in an amorphous matrix. This is typical of nanocrystalline thin films. On the other hand, it can be seen from Fig. 4(b), that the crystallite sizes of 81% Al film are smaller in dimensions (~ 5 nm). By combining the GIXRD and TEM results, it can be said that as the Al content is increased, AlN replaces TiN as crystallites.

V.6 Electron-phonon Interaction in Zinc Oxide Nanostructures

There is considerable interest in zinc oxide nanostructures due to their potential applications in the areas such as photo-detectors, blue and ultraviolet lasers, optoelectronic devices, and radiation hard material. The controlled synthesis of ZnO nanostructures and a complete understanding of the physical properties are the key issues for the development of ZnO-based devices. In this context the electron-phonon interaction directly influences the carrier mobility and consequently determines the transport characteristics of an optoelectronic device. The electron-phonon *(e-p)* interaction is also responsible for the appearances of overtones of the longitudinal optic (LO) phonons in the resonance Raman spectra. In ZnO the LO phonon can have

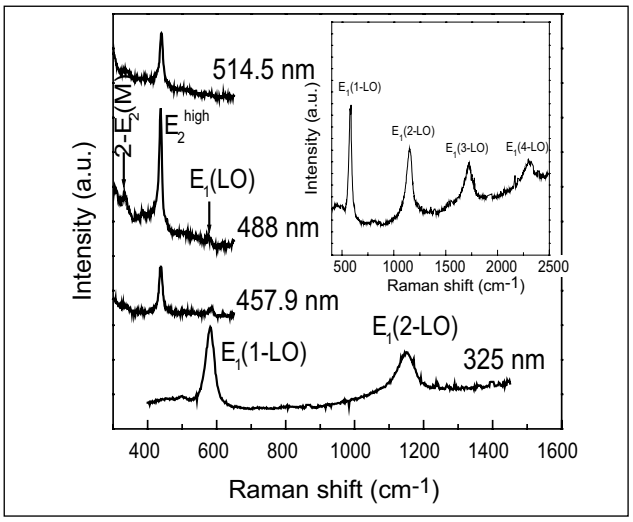

Fig. 1 *Raman spectra of ZnO nanoparticles obtained using different excitation wavelength. The inset shows the overtone spectra for 325 nm excitation*

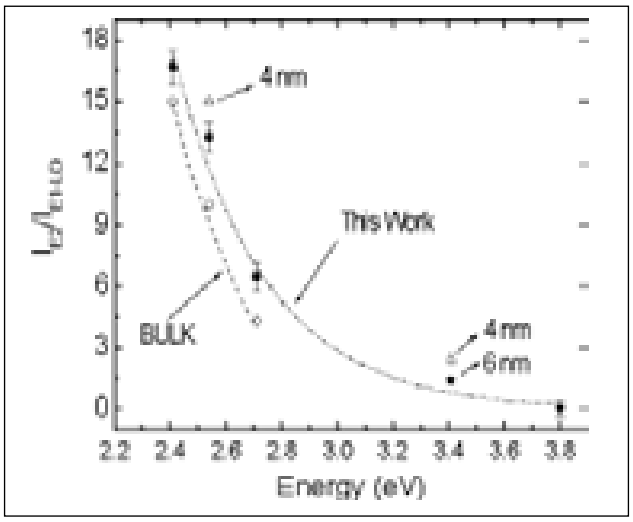

Fig. 2 *Intensity ratio $I_{E2}/I_{E1\text{-}LO}$ as a function of incident photon energy for ZnO nanoparticles*

E_1 and A_1 symmetries; however, A_1 mode exhibits negligible intensity. In view of this often the ratio of the intensity of the first overtone of the E_1-LO phonon to that of the fundamental is considered as a quantity that is proportional to the magnitude of the *e-p* interaction. This intensity ratio is found to be smaller in nanoparticles as compared to the bulk. However, the intensity of the Raman scattering from the LO phonons stems from the contributions from two processes: Frohlich interaction and the deformation potential. On the other hand, the Raman intensity of the non-polar phonon such as that of E_2 symmetry arises only from the deformation potential. Thus a study of the relative intensities of the E_1-LO and E_2 phonons gives an opportunity to evaluate the relative strengths of the two processes. Furthermore, how the *e-p* interaction gets modified in nanostructures is also of interest.

Zinc oxide nanoparticles of sizes around 8 nm were synthesized using precipitation in methanol. Raman spectra were measured using several excitation wavelengths using a Spex 14018 double monochromator. For measurements using 325 nm line a double-subtractive triple - monochromator (JobinYvon T64000) was used. Fig. 1 shows the Raman spectra of ZnO nanoparticle, excited using 514.5, 488 and 457.9 nm lines of a Ar^+ laser and 325 nm line of He-Cd laser. The spectra exhibits E_2 and 582 cm^{-1} E_1-LO modes at 438 and 582 cm^{-1} respectively. When excited under near-resonant condition (325 nm), E_1-LO mode exhibits overtone spectra (inset Fig. 1) up to 4-LO modes. The enhancement due to resonance can be explained based on a third-order perturbation calculation for the intensity for Raman scattering. When the incident photon energy is varied across an electronic transition, vanishing of energy denominators are expected to result in in- and out-resonances. Resonance Raman scattering in bulk ZnO has been well documented, whereas that in the nanoparticles is of current interest.

Fig. 2 shows the intensity ratio $(I_{E2}/I_{E1\text{-}LO})$ as a function of excitation energy. One can see that the ratio decreases rapidly as a function of incident photon energy. The reported data for other sizes and for the bulk ZnO are also included in the figure for the sake of comparison. Note that the ratio increases as particle size reduces. The intensity ratio was analyzed further in order to obtain insight into the *e-p* interaction. This represents the ratio of the matrix elements corresponding to the scattering mechanisms, i.e.

$$|Hep(E_2)/Hep(E_1\text{-}LO)|^2 = |DP(E_2)/\{DP(E_1\text{-}LO) + FI(E_1\text{-}LO)\}|^2$$

where DP and FI represent the deformation potential and the Frohlich mechanism of the *e-p* interaction respectively. Hence the present results suggest that the electron-phonon interaction is enhanced via Frohlich interaction as excitation energy approaches the resonance. Furthermore, a comparison of the ratio of E_2 and E_1-LO intensities with that of bulk suggests that the electron-phonon interaction for E_2 phonon decreases less rapidly than E_1-LO phonon with a reduction in size.

V.7 Crystal Structural Stability of Rare-Earth Sesquioxides Gd_2O_3 and Tb_2O_3 under High Pressure

The rare-earth sesquioxides (R_2O_3) are well known and widely studied due to their scientific and technological importance. In general, they are excellent host materials for powerful lasers and improved phosphors, and are also used as refractory materials and abrasives. Wing to its high neutron absorption cross section Gd_2O_3 is used in control rods. Its high refractive index makes it a very useful material in optics. When doped with rare earth ions like Eu^{3+} and Tb^{3+}, it shows good luminescent properties. This oxide may be subjected to extreme conditions in such applications. For example in the case of a nuclear reactor where Gd_2O_3 is used in the control rods, it is important to determine its equation of state and stability under high pressures and temperatures. These sesquioxides transform to several polymorphic forms under high pressure, namely, A-hexagonal, H-hexagonal, B-monoclinic, C-cubic, X-cubic, etc. Despite their high scientific and technological importance, high pressure studies on these oxides are very scarce. In order to determine the equation of state and structural stability of these sesquioxides under pressure, systematic investigations were carried out.

High purity Gd_2O_3 and Tb_2O_3 samples were characterized by X-ray diffraction technique using a high-resolution Guinier diffractometer. The in-situ high pressure X-ray diffraction studies were carried out using a diamond anvil cell (DAC) developed in-house and a high pressure Huber-Guinier diffractometer coupled to a rotating anode X-ray generator. The powdered samples were loaded into a 250µm diameter gasket hole of the diamond anvil cell. A ruby chip was loaded along with the sample for pressure calibration by ruby fluorescence method. Methanol, ethanol and water mixture (16:3:1) was used as the pressure transmitting fluid.

The present investigation reveals that Gd_2O_3 remains stable in its parent cubic or bixbyte (Ia3) phase up to a pressure of 12 GPa. At around 12 GPa, the compound undergoes an irreversible phase transformation to a hexagonal A-type structure. Fig. 1 shows the P-V data for both the parent and the high pressure phase. The large volume collapse between the two phases suggests that the phase transition may be of the reconstructive type. However Tb_2O_3 remains stable up to about 27 GPa, which appears quite unusual while considering the behaviour of other similar oxides.

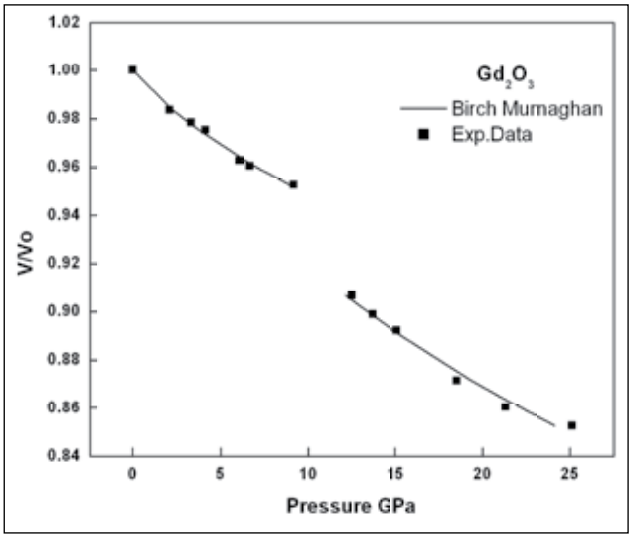

Fig. 1 *The P-V data for the parent (cubic) and high pressure (hexagonal) phase of Gd_2O_3 fitted to the Birch-Murnaghan equation of state*

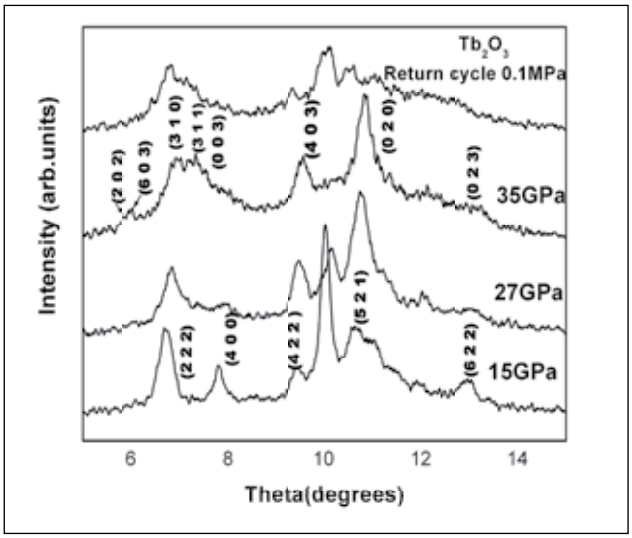

Fig. 2 *The X-ray diffraction patterns for Tb_2O_3 at various pressures up to 35 GPa including the return cycle at 0.1 MPa*

Above 27 GPa, Tb_2O_3 transforms irreversibly to a low symmetry phase which is identified as monoclinic, as shown in Fig.2. Usually, terbium occurs in the trivalent state. The large structural stability could be attributed to the presence of Tb^{4+} ions and the formation of covalent linkages using the additional 4f electron which is shared. The stability of this oxide under high pressure can have far reaching implications in several applications.

V.8 Synthesis and Magnetic Studies of Iron Substituted β-Ga_2O_3

Wide band gap semiconductors find application in a wide range of fields such as transparent conducting coatings, photocatalysis, smart displays and in the emerging and exciting field of spintronics. The central component in spintronics is a diluted (ferro) magnetic semiconductor (DMS) hosting a suitable paramagnetic ion at a magnetic dilution limit, such that the Curie temperature (T_c) is much above the room temperature. A search for a suitable semiconducting matrix was spurred by a concerted theoretical study which had predicted the T_c to scale with the band gap, albeit non-linearly.

Taking a cue from such a prediction, β-Ga_2O_3 (E_g = 4.9 eV) was chosen as a matrix. Gallia crystallizes in a monoclinic structure with two distinct crytallographic sites for Ga^{3+}; octahedral and tetrahedral in 1:1 ratio. Extrinsic magnetism due to the precipitation of paramagnetic ions, an annoying issue in these materials, was avoided by choosing a susbtituent (Fe) with well established solubility and solution combustion synthesis. Substitution of Fe ion at 1, 3 and 5 at % was carried out employing solution combustion synthesis using urea as a fuel in the fuel lean region. The resulting combusted product, identified to be metastable γ-Ga_2O_3, was annealed at 1273 K overnight to obtain stable β-Ga_2O_3 phase. High statistics XRD studies confirmed the monophasic nature of these materials.

Crystallographic data were estimated by carrying out Rietveld refinement of the XRD pattern and as a representative.

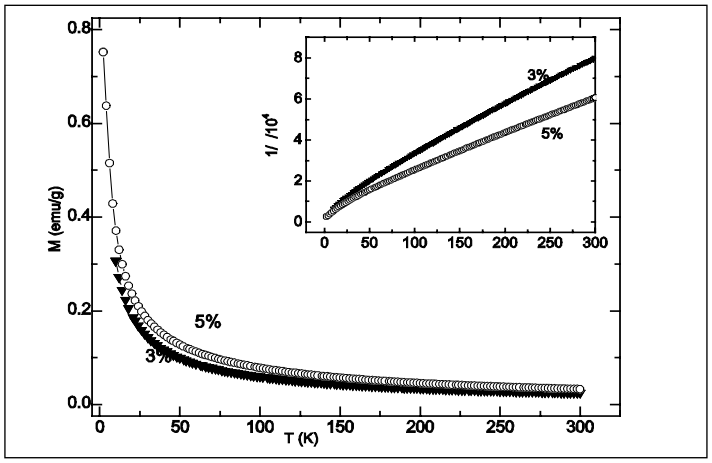

Fig. 1 *χ Vs T plot for 3 and 5 at % Fe substituted β-Ga_2O_3. Inset shows 1/χ vs T plots*

A small dilation of the lattice is observed with Fe, consistent with larger ionic radius of Fe^{3+} compared to that of Ga^{3+}. The thermomagnetization data of the samples with 3 and 5% Fe doped Ga_2O_3 shows paramagnetic behaviour down to 2K (Fig. 1). However, no satisfactory fitting to Curie law could be obtained. A plot of 1/χ vs T plot is shown as inset of Fig. 1. The curve strongly deviates from linearity to take a dip at low temperature and has negative intercepts along the temperature axis, reminiscent of ferrimagentic interaction. The paramagnetic state down to 2K implies a special case of ferrimagentic state, such that αβ=1, wherein α and β correspond to inter- and intra-sublattice interaction. A ferrimagnetic interaction implies two magnetic moments for Fe ions. The Mossbaüer measurement indicated two doublets, implying a paramagnetic state, in agreement with thermomagnetisation studies. The doublet with larger QQ split and low isomer shift could be unambiguously assigned to Fe^{3+} in high-spin state, substituting octahedral site. The other doublet with lower QQ and higher isomer shift, on the other hand, can be ascribed to Fe^{3+} in low-spin state or to Fe^{2+} in high-spin state. To resolve this, X-ray absorption studies are being planned.

Additionally, the intensity ratio of the doublet was 4:1, implying preferential substitution at the octahedral site. In order to elucidate preferential substitution of Fe, an ESR study was carried out at low concentration of Fe substitution, viz., 1 at% and the corresponding spectrum is shown in Fig. 2. The marked absorption signals arise from Fe^{3+} ions at the octahedral site alone. Also, the value of g=2.0006 implies non-interacting paramagnetic nature of the species.

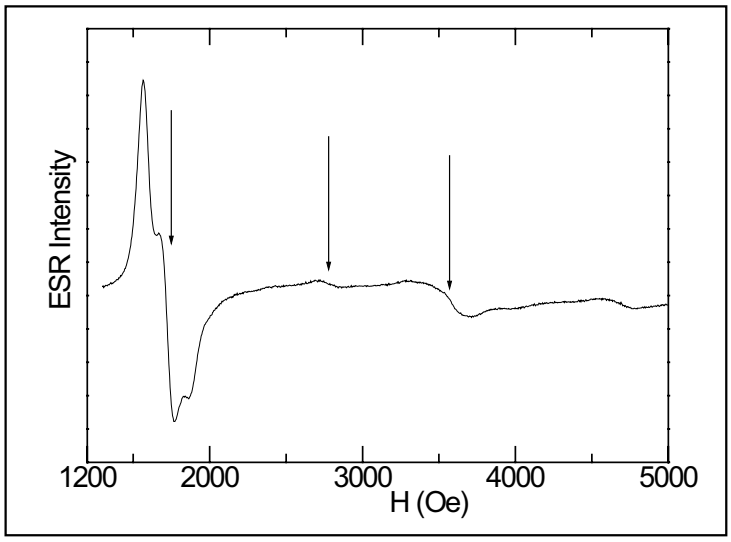

Fig. 2 *ESR spectrum of 1 at % Fe substituted β-Ga_2O_3*

V.9 Studies on the Pb-Cr-O System

Lead and eutectic alloys of lead and bismuth are candidate materials for spallation targets in the accelerator driven sub-critical systems. They could be used as coolants as well, owing to their favorable nuclear, thermal and physical properties. However, they are highly corrosive towards the structural steels. One method to circumvent this problem is to minimize the corrosion by controlling the dissolved oxygen content in these liquid metals which in turn leads to the formation of a protective oxide-film on the steel surface. In this context, detailed knowledge of the phase diagram of the systems Pb-M-O (M=Cr, Fe) are useful. Further, data on the thermochemical properties of the ternary oxygen compounds formed in these systems would serve as valuable inputs for understanding their compatibility with steels at high temperature. Hence, studies were undertaken to establish the phase diagram of the system Pb-Cr-O and determine the Gibbs energies of formation of $Pb_5CrO_3(s)$, $Pb_2CrO_5(s)$ and $PbCrO_4(s)$.

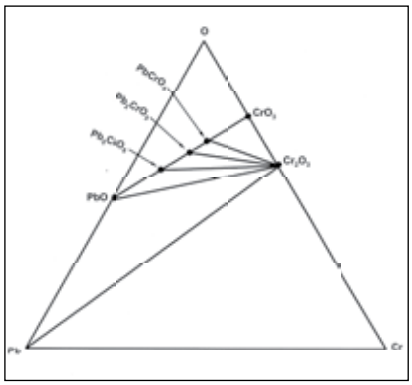

Fig. 1 *Equilibrium phase diagram of Pb-Cr-O system; isothermal section at 973 K*

This ternary phase diagram was established by equilibrating different constituent phases for a long duration followed by the analysis of the ensuing products by XRD. Based on these results, the isothermal section at 973 K of the equilibrium phase diagram was established and is shown in Fig.1.

The Gibbs energy of formation of the ternary compounds, namely $PbCrO_4(s)$, $Pb_2CrO_5(s)$ and $Pb_5CrO_8(s)$ were obtained by measuring the equilibrium oxygen pressures over the relevant phase fields either by manometry or by solid oxide electrolyte based emf cells. The oxygen partial pressures over $PbO(s)$-$Cr_2O_3(s)$-$Pb_5CrO_8(s)$ and $Pb_2CrO_5(s)$-$Cr_2O_3(s)$ - $Pb_5CrO_8(s)$ phase fields were measured by employing the following emf cells:

(-) Pt, $PbO(s)$, $Cr_2O_3(s)$, $Pb_5CrO_8(s)$ | YSZ | (O_2, 0.21 atm) Pt(+)

(-)Pt,$Pb_2CrO_5(s)$-$Cr_2O_3(s)$- $Pb_5CrO_8(s)$ | YSZ | (O_2, 0.21 atm) Pt(+)

Equilibrium oxygen pressures were measured over $Pb_2CrO_5(s)$-$PbCrO_4(s)$-$Cr_2O_3(s)$ by an experimental set up equipped with a sensitive capacitance manometer. Gibbs energy of formation of the ternary compounds was derived from these data and the auxiliary data on the Gibbs

energy of formation of Cr_2O_3(s) and PbO(s) reported in literature.

Gibbs energy of formation of Pb_5CrO_5(s), Pb_2CrO_5(s) and $PbCrO_4$(s)

$\Delta_f G^o_m$ <Pb_5CrO_8> ± 0.53 kJ = -1804.37 + 0.684 T (837-1008K)

$\Delta_f G^o_m$ <Pb_2CrO_5> ± 0.29 kJ = -1159.34 + 0.406 T (859-1021K)

$\Delta_f G^o_m$ <$PbCrO_4$> ± 0.18 kJ = -907.93 + 0.314 T (862-1092K)

The partial phase diagram of the ternary Pb-Cr-O system reveals that Cr_2O_3(s) would be the first phase to precipitate when the oxygen concentration in liquid lead is increased. Further increase in the oxygen concentration would lead to the precipitation of PbO (s).

V.10 Matrix Isolation Spectroscopy of Silanes

Understanding the conformational preferences of organic phosphates and the basic factors influencing such preferences is important, as it holds the key to unraveling the complex and interesting chemistry of the phosphates, in fuel reprocessing. However, the conformation picture of long chain phosphates, such as tri-n-butylphosphate, is rather complicated and for a study of this intricate problem, one has to resort to the study of smaller model compounds.

Towards this end, methoxymathanes were first chosen as model compounds, as these compounds have a similar backbone structure (C-O-C-O-C) as the organic phosphates (C-O-P-O-C). Matrix isolation infrared spectroscopy together with abinitio computations were employed to study the conformations of the methoxymethanes. A number of methoxymethanes, such dimethoxymethane (DMM), dimethoxyethane (DME) and dimethoxypropane (DMP) were studied. As a result of these studies, it has become clear that anomeric interactions, (which is the delocalization of the non-bonded electrons on the electronegative oxygen atom into the adjacent antibonding orbital), is an important factor in deciding the conformational preferences of molecules referred to above. The operation of the anomeric effect directs the lowest energy conformer in these molecules to have a $G^{\pm}G^{\pm}$ symmetry.

For an application of these results to phosphates, it is necessary to understand the role of anomeric interactions in molecules containing third row elements, such as Si and P. Hence, the above studies were extended to methoxysilanes. Conformations of dimethoxymethylsilane (DMMS), dimethoxydimethylsilane (DMDMS), trimethoxysilane (TMS) and dimethoxymethylphenylsilane (DMMPS) were studied using matrix isolation spectroscopy and *ab initio* computations. These molecules were trapped in nitrogen and argon matrices, using typical sample to matrix ratios of 1:1000. Computations were done at the HF and B3LYP levels of theory using 6-31++G** basis functions. As an example, the matrix isolation infrared spectrum of dimethoxymethylphenylsilane is shown in Fig. 1, together with the computed spectrum of the lowest energy conformer of this molecule. These studies showed that the lowest energy conformer in these silanes is again one with a $G^{\pm}G^{\pm}$ symmetry.

Comparison of the Conformational Picture in Methanes and Silanes

A comparison of the conformational picture in methoxymethanes and methoxysilanes reveals some interesting similarities and differences. As for the similarity, in both methanes and silanes, the lowest energy conformer has a $G^{\pm}G^{\pm}$ symmetry, which implies the dominant role played by the anomeric interactions in deciding the conformational preferences in both these systems. The difference is even more striking. The density of states, is higher in the silanes, than in methanes (Fig. 2), which essentially means that the energy differences between the conformers is smaller in silanes. This observation implies that the anomeric effect is less dominant in silanes, although still important enough to result in a $G^{\pm}G^{\pm}$ symmetry for this system. Fig. 2 shows a typical density of state picture for DMP and the silicon analogue, DMDMS. The

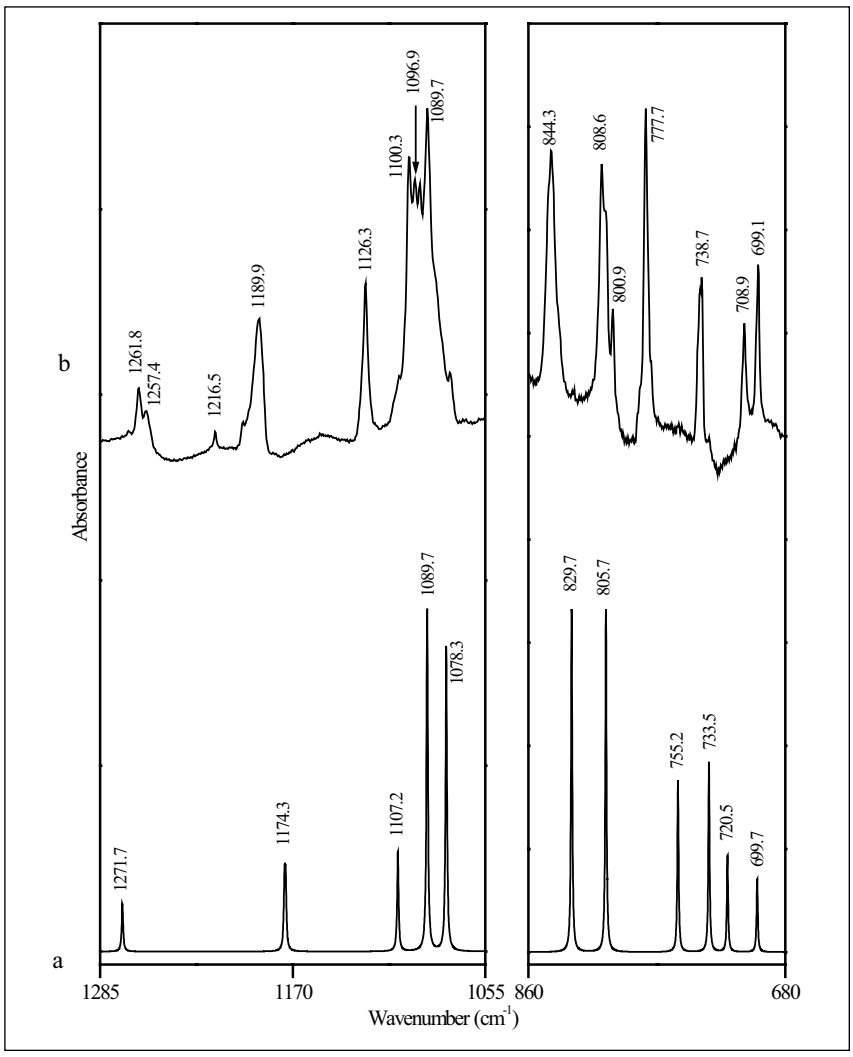

Fig. 1 *A comparison of the experimental and the computed spectra of DMMPS. (a) Computed spectra of G±G± conformer (b) matrix isolation IR spectrum of DMMPS deposited using room temperature effusive source; the spectrum shown is that recorded in the pre-annealed matrix*

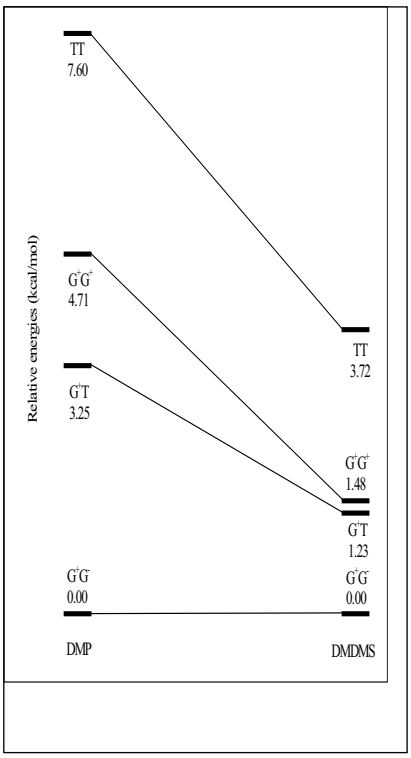

Fig. 2 *Diagram showing the correlation between the conformers of DMDMS and DMP. The energy of each conformer, computed at the B3LYP/6-31++G** level, relative to the ground state conformer of the corresponding molecule, are mentioned alongside*

same point is also corroborated by our natural bond orbital (NBO) analysis, which shows that the energies associated with the anomeric interactions (i.e. n-σ* interaction) is smaller in silanes than in methanes.

These studies have clearly established the role of anomeric interactions in deciding conformational preferences in the methanes and silanes, which can be extended to the phosphates. As a result of these studies, we now understand the conformational preferences and the factors influencing them in phosphates. These studies also throw open the possibility of these factors being perturbed through metal complexation and consequent alteration of the conformational pattern; results that can eventually shed light on the intricacies in the chemistry of reprocessing.

V.11 Superconductivity in Potassium Substituted $BaFe_2As_2$ System

The search for superconductivity in new materials has engaged several solid state chemists and physicists. Early 2008 has seen the discovery of yet another class of superconductors containing FeAs as the active layers. This class holds strong similarity to the cuprate superconductors in that superconductivity is induced by hole/electron doping in a magnetic

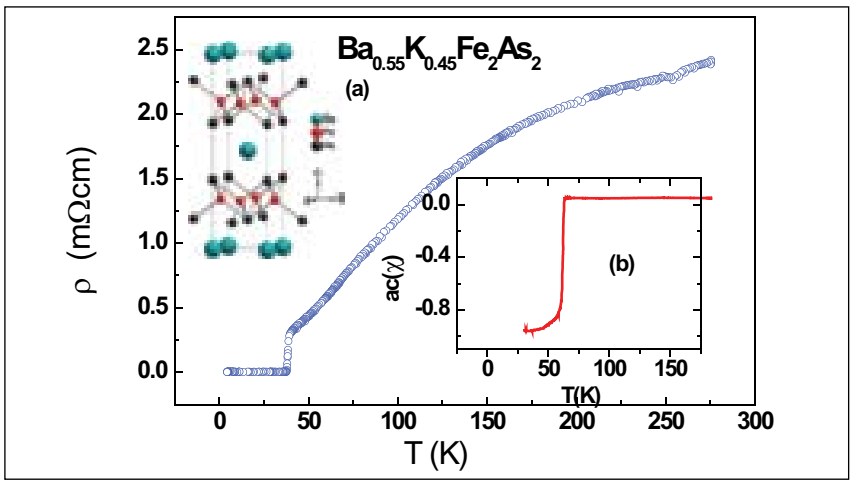

Fig. 1 *Variation of resistivity with temperature in $Ba_{0.55}K_{0.45}Fe_2As_2$. Inset (a) shows the crystal structure, Inset (b) shows the variation in ac susceptibility as a function of temperature*

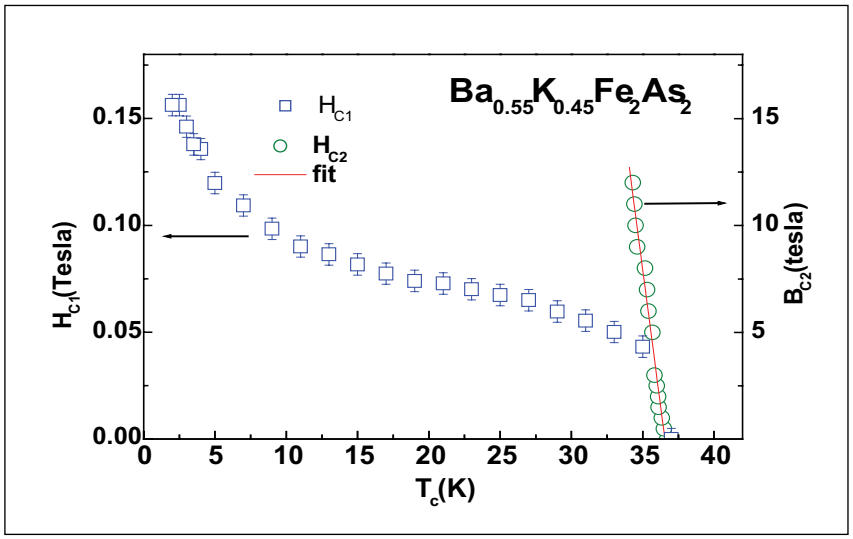

Fig. 2 *The variation of H_{C1} as a function of temperature obtained from low field magnetization measurements, H_{C2} versus temperature from magneto resistance measurements is also shown in the figure. The red solid line is the linear fit from which dH_{C2}/dT is obtained*

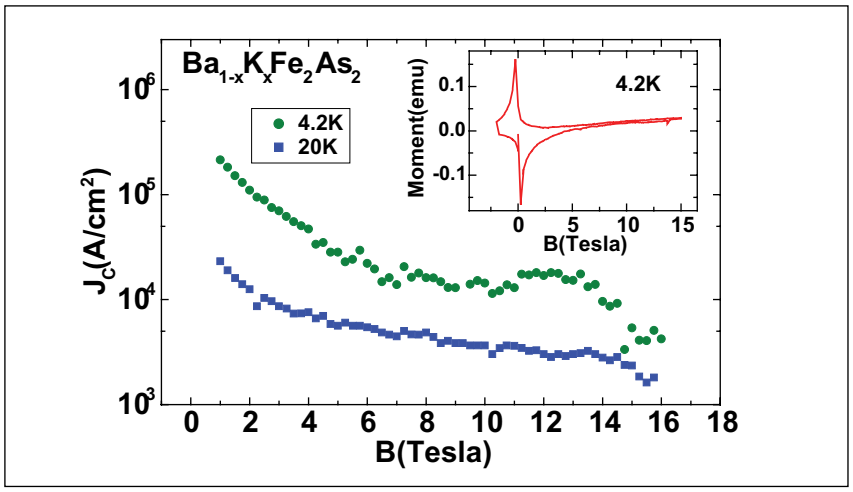

Fig. 3 *Inset shows the variation in magnetization obtained by cycling the sample from zero to 16 T to-2 T back to zero tesla at 4.2 K. The J_C obtained using Bean model for 4.2 K and 20 K is displayed in the main graph*

compound.

Synthesis of potassium substituted MFe_2As_2 systems, where M is an alkaline earth, was carried out in two steps, at first FeAs was synthesized at 873 K. Following this the air sensitive, K and Ba was loaded along with FeAs into Ta crucibles in a Ar/He filled dry box. The heat treatments were carried out by slow heating upto 1073 K following which the samples were removed out and pelletised and sintered at 1223 K for ~6 hours. All heat treatments were carried out in a stainless steel chamber under 50bar ultra pure Ar atmosphere. Inset a of Fig. 1 depicts the structure of the material, the resistivity in the potassium substituted $BaFe_2As_2$ sample is shown in Fig.1 and the diamagnetism exhibited by the sample is evident from inset b of Fig.1. The sharp drop in resistivity and ac susceptibility at 38 K is clearly visible indicating superconductivity in the sample. Having obtained the phase pure potassium substituted sample, magneto resistance and magnetization measurements have been carried out in fields upto 12 T and 16 T respectively. The decrease in the T_C onset obtained as a function applied magnetic field is shown in Fig. 2 The rate of change of T_C with applied field is ~5.07T/K, which implies a critical field at zero Tesla in accordance with conventional theory to be ~138 T. Magnetisation measurements were carried out in a vibrating sample magnetometer with field capability of upto 16 T and temperature range of 1.5 to 300 K. From the low field magnetization curves done on virgin samples the H_{C1} has been measured for several temperatures below T_C. H_{C1} versus temperature shown in Fig. 2, shows an anomalous upturn at

low temperatures. From the high field magnetization curves carried out at 4 K and 20 K, (shown for 4 K in inset of Fig. 3) the variation of critical current with applied field has been obtained by using the Bean model and is shown in Fig. 3. It can be seen that the critical current is larger than 104A/cm^2 at 4 K upto 14 T. This indicates the high suitability of this material for magnet applications; however the air sensitivity of the compound may hinder its actual application which is being investigated.

V.12 Establishment of Facilities for SQUID Based Magnetoencephalography

Magnetoencephalography involves the non-invasive measurement and characterization of magnetic fields associated with the physiological activities of human brain and represents one of the most challenging application of SQUID sensors. These magnetic fields, typically ~1p T or less, are indeed so weak that they are virtually immeasureable by any other sensor technology. Based on the earlier success in utilization of SQUID sensors in the development of systems such as SQUID magnetometer and SQUID based system for Non-Destructive Evaluation (NDE), facilities have been set up at our Centre for measurement of extremely weak magnetic fields associated with physiological activities of human heart and human brain using SQUID sensors. A survey of the ambient magnetic noise was conducted to pick-up a magnetically quiet site with a measured magnetic noise of 100pT/√Hz in the white noise regime and peaking at 6nT at 50Hz. A special building using stainless steel rods to reinforce concrete was constructed to minimize disturbances due to ambient magnetic noise; experiments showed that the influence of external magnetic disturbances was eight times lower in this SS reinforced building when compared to conventional building using ferromagnetic mild steel reinforcement. A special one metre deep concrete block reinforced with stainless steel weighing about fifty tonnes served as a foundation to erect the Magnetically Shielded Room (MSR) (Fig. 1) with a view to reduce vibration levels to under 10^{-4} ms^{-2}. MSR has two layers of μ metal (2mm and 3mm thick) and two layers of aluminum (8mm and 4mm thick) and provides a shielding factor of 70dB at 1 Hz, which improves to 100dB at 100Hz. The MSR is equipped with penetrations for stimulus presentation, helium gas recovery etc. and is connected to a Radio Frequency Shielded Room by four 100mm diameter shielded waveguides to route the SQUID cables. A Fibre Reinforced Plastic liquid helium cryostat housing the SQUID sensors is located inside the MSR while the measurement electronics is located inside the RFSR. The signal to be measured is coupled to the SQUID sensor via a first order superconducting gradiometer having a loop diameter of 15mm and a baseline of 50 mm. The SQUID output voltage was digitized with a 16 bit resolution and was recorded at a sampling rate of 300Hz. The system noise floor was measured to be 20-30 fT/√Hz, which is adequate for measurement of biomagnetic fields.

For the measurement of heart signal, the subject lay supine with his chest under the liquid helium cryostat and the component of magnetic field normal to the chest surface was measured. The SQUID output revealed the P wave related to depolarization of the atria, the QRS peak related to

Fig. 1 *MSR Coupled to RFSR via Shielded wave guides (Sheilding factor: 70dB @ 1Hz to improving to 100dB @ 100Hz)*

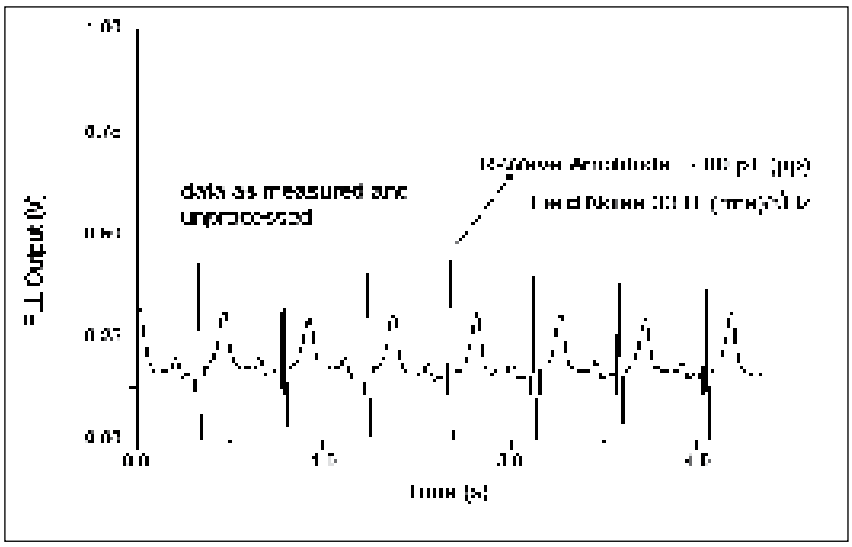

Fig. 2 *FLL Output shows MCG data of a 47 year old male recorded*

the depolarization of the ventricles and the T wave related to the repolarization of the ventricles. The signal strength of the R peak was over 50 pT and could be measured with a high signal-to-noise ratio. The results are shown in Fig. 2. Measurements were repeated at different positions on the chest to map the spatial distribution of the cardiac magnetic field. The signal could also be measured on the posterior back surface although with a slightly reduced intensity because of a higher stand-off distance.

For the measurement of MEG photography signal, the sensor was positioned above the scalp at the desired position. For the measurement of the alpha rhythm, the sensor was positioned on the occipital lobe of the brain and the SQUID output was measured with eyes open and with eyes closed. Signal in the eyes closed condition was observed to be larger in amplitude and revealed a peak at 9 Hz in the frequency spectrum as expected. For the measurement of the signal corresponding to the eyeblink, the sensor was positioned just above the eyebrow line and a signal amplitude of about 2pT was observed at each eyeblink. The results are shown in Fig. 3.

There are a number of advantages in the measurement of magnetic activity (MEG/MCG) as opposed to the more conventional measurement of electric activity (ECG/EEG). Electric activity measured on the skin by attaching leads is affected by the conductivity distribution of the tissues between the source and the measurement locations (which is often inhomogeneous and anisotropic with bones presenting very poor electrical conductivity) leading to distortions in the measured data. This problem is of much less concern in magnetic measurements since most tissues are weakly diamagnetic and do not distort the measured magnetic field distribution. The magnetic measurement is contactless and avoids the problem of skin potentials contaminating the data. Measurement of magnetic fields associated with a given physiological activity may also be expected to give complementary information not contained in the electrical measurements.

Based on the success in measuring biomagnetic fields using SQUID sensors, plans are underway to build a multi-channel MEG system. A ninteen channel system with a flat bottom cryostat is under design, which will be upgraded in the coming years to a sixty four channel system with a concave bottom cryostat. Efforts are underway to develop a multi-channel data acquisition system with a high sampling rate. Necessary signal processing techniques and computational algorithms are also being developed. These developments will help establish MEG technique in India as a reliable technique for probing the dynamics of human brain with a millisecond temporal resolution.

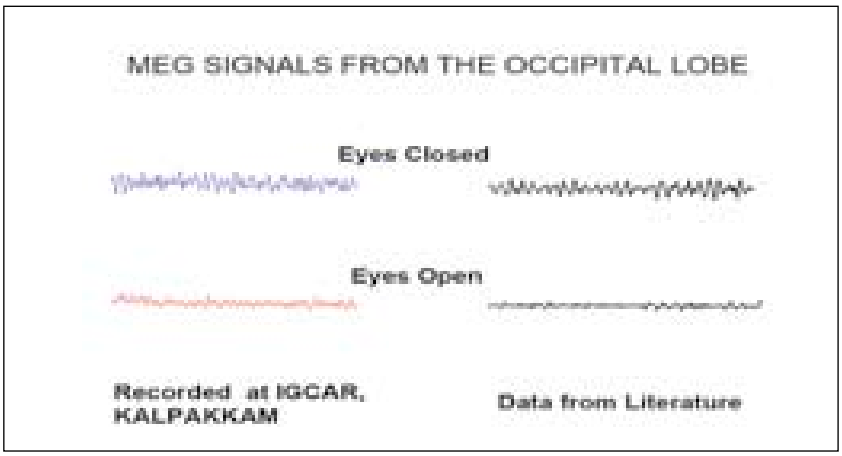

Fig. 3 *Results of Brain mapping - MEG signals from the occipital lobe*

V.13 Laser Induced Breakdown Spectroscopy

Laser induced breakdown spectroscopy (LIBS) is a technique wherein a focused laser beam is incident on the analyte sample. The power density of the laser that is used is sufficient to cause a breakdown and produce plasma. Optical emission from atoms and ions in the plasma is collected and focused by a lens onto the entrance slit of a spectrometer for data analysis. The emission from the plasma, in the first 500 ns or so after laser pulse, is dominated by the continuum emission that carries little information of the analyte. The latter part of the emission (>1 µs) after the plasma expands and cools, however, is dominated by atomic emission from the elements of interest, in the analyte sample. Hence to detect the emission from the analyte, the detection must be temporally delayed and gated.

The LIBS spectrometer consists of a Nd:YAG laser with a temporal pulse width of ~10 ns and typical pulse energies of 30 mJ. This laser pulse is focused on the sample using a fused silica lens to produce the laser plasma. The emission from the plasma is collected using another fused silica lens and focused onto the entrance slit of a spectrometer fitted with an Intensified Charge Coupled Device (ICCD) detector. Scattered light from the laser is imaged onto a fast photodiode, whose output after a suitably delay is used as a trigger pulse to initiate data collection by the ICCD detector. The data from the detector is acquired by a computer for further processing. During data collection, the sample was translated between laser shots so that a fresh surface was exposed for every laser shot; this was essential to obtain stable emission intensities.

A number of experimental parameters was found to influence the LIBS signal such as 1) laser frequency and energy, 2) speed of sample holder traverse, 3) focal length of lenses, 4) height of sampling zone of plasma from the surface of sample 5) sampling delay and gate width 6) distance of focusing lens from the sample surface and 7) purging with Ar gas. A systematic study was conducted to identify and optimize these parameters. Typical experimental conditions were the following: sample traverse speed - 1500 µm/s, laser repetition rate - 2 Hz, delay - 10 µs and 150 mm focal length lens. These experimental parameters yielded an RSD of ~6%, which compares well with other spectroanalytical techniques such as ICP-AES and AAS.

In order to evaluate the analytical performance of the method of LIBS, quantification of elements (Cr, Mo, Ni and Mn) has been done in steel standards, as test cases. The elements that were studied were Cr (1.16-19.06 %), Mo (0.47-3.55 %), Ni (0.95 - 5.66 %) and Mn (0.42-1.7 %). Ratio of the intensity of these analyte lines were taken with those from the emission lines of iron, which was used as an internal standard. This method minimizes the effects of laser shot-to-shot variations, on the LIBS signal and hence increases

Fig. 1 *LIBS facility showing the spectrometer with the ICCD detector and sample handling stage*

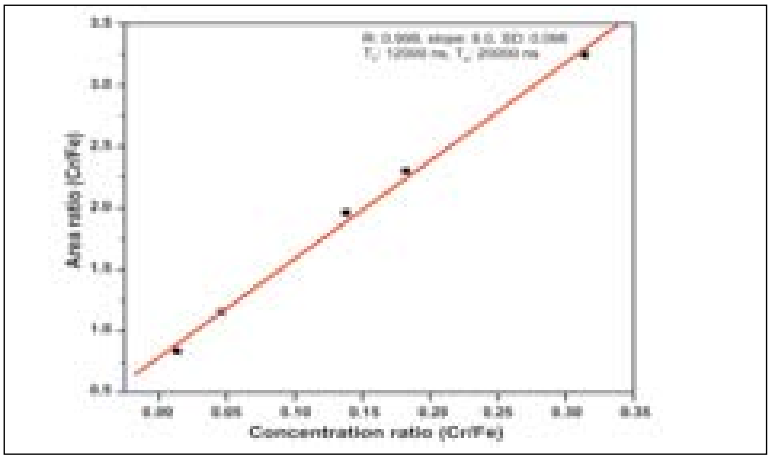

Fig. 2 *Plot of the intensity of the Cr emission in LIBS against concentration to demonstrate the linearity and analytical utility of the technique*

the measurement precision. The analytical lines that have been selected for calibration were Cr(I) (427.48 nm), Mo(I) (386.40 nm), Ni(I) (352.45 nm) and Mn(I) (403.07 nm), which were ratioed with the corresponding iron Fe(I) lines at 427.17 nm, 385.99 nm, 355.85 nm and 404.58 nm respectively.

Fig. 2 shows a typical concentration calibration curve for Cr to demonstrate the linearity of the analytical plots.

An increase in signal to noise ratio was observed when Ar gas was allowed to flow over the sample surface to create a quasi-inert atmosphere. A method has also been developed to use the LIBS technique to handle solutions, which has applications in handling radioactive solutions.

V.14 Thermophysical Property Measurements on Rare Earth Uranates and Chloroapatites

Rare earth elements are among the major fission products formed during irradiation of the oxide fuel in a nuclear reactor. Rare earth oxides are highly soluble in uranium oxide and form compounds with the formula RE_6UO_{12} (RE = rare earth). The thermophysical properties such as heat capacity and thermal expansion of these rare earth uranates serve as useful inputs for understanding the behaviour of the oxide fuel. The values of the heat capacity for these compounds RE_6UO_{12} (RE = La, Sm and Eu) have not been experimentally determined so far. Hence, the heat capacities of these compounds were experimentally determined for the first time using a Differential Scanning Calorimeter (298 - 800K) (Fig. 1). An interesting trend in the values of the heat capacity was observed. They were found to increase in the order Eu_6UO_{12}> Sm_6UO_{12}> La_6UO_{12}. Also, the difference in the values of the heat capacities of La_6UO_{12} and Sm_6UO_{12} is larger than that of Sm_6UO_{12} and Eu_6UO_{12}. Due to lanthanide contraction the ionic radii decreases from La(III) to Eu(III). This is reflected in value of the RE-O bond length in these ternary compounds. Values of the lattice parameters of these compounds (measured at room temperature) further support this argument. Also, the magnitude of the reduction in the values of the lattice parameter from La_6UO_{12} to Sm_6UO_{12} is larger than that observed from Sm_6UO_{12} to Eu_6UO_{12}. Shorter the RE-O bond length, higher will be the bond strength and consequently higher will be the heat capacity.

Apatites are naturally occurring minerals having hexagonal crystal structure (P63/m space group) with a unit cell formula of $M_5(PO_4)_3(X)$, M= Ca, Sr, Ba, and (X=OH, Cl or F). These apatites can immobilize highly radioactive and heat generating elements such as ^{90}Sr, ^{137}Cs, ^{99}Tc etc. Their ability to form substitutional solid solutions with chlorides render them appropriate to be considered as potential host matrices for immobilizing chloride wastes generated in the pyrochemical reprocessing. Another attractive feature is that the apatites could be easily prepared even at low temperatures.

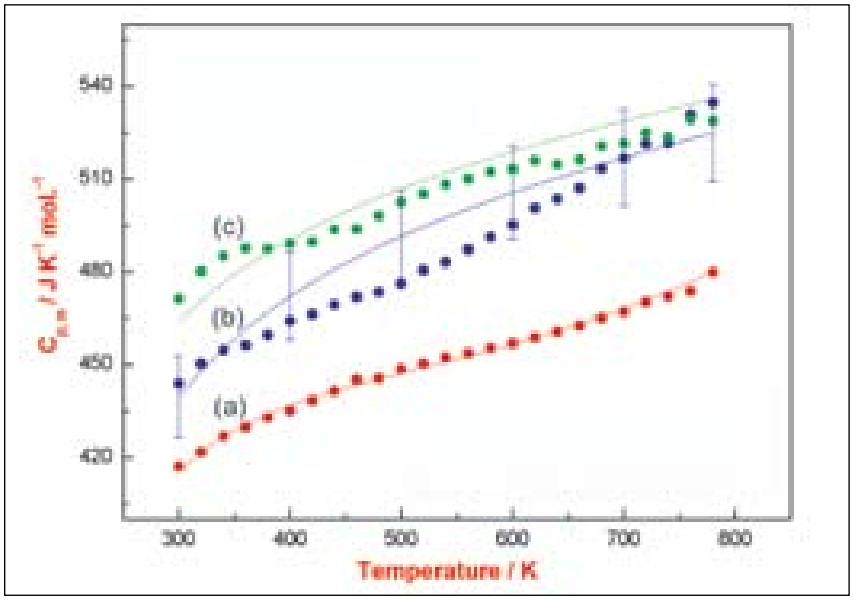

Fig. 1 *Heat capacity of rare earth urinates. The dashed line through the data points is a result of numerical fit (a) Measured $C_{p.m.}$ of La_6UO_{12} (b) Measured $C_{p.m.}$ of Sm_6UO_{12} (c) Measured $C_{p.m.}$ of Eu_6UO_{12}*

Thermophysical properties such as heat capacity and thermal conductivity of the chloroapatites are useful in understanding their phase behavior after immobilizing the chloride, alkali and alkaline earth fission products into the apatite structure. Experimentally measured values of the heat capacity of these compounds have not been reported so far. Calcium and strontium chloraptites, viz., $Ca_{10}(PO_4)_6Cl_2$ and $Sr_{10}(PO_4)_6Cl_2$ were synthesized, characterized and the values of their heat capacities were measured by using DSC in the temperature range 298 - 800K (Fig. 2). Heat capacity of $Sr_{10}(PO_4)_6Cl_2$ was found to be higher than that of $Ca_{10}(PO_4)_6Cl_2$ at all temperatures. It is in line with the expectation that as the cationic contribution to the heat capacity is known to increase with increase in atomic number between isotypical compounds of elements within the same group. This is because higher the mass, lower will be the phonon frequencies and hence higher will be the heat capacity. But as the temperature is increased, the vibrational energy levels become more closely spaced due to anharmonicity and therefore the difference between the heat capacity of $Ca_{10}(PO_4)_6Cl_2$ and $Sr_{10}(PO_4)_6Cl_2$ and decreases with increase in temperature.

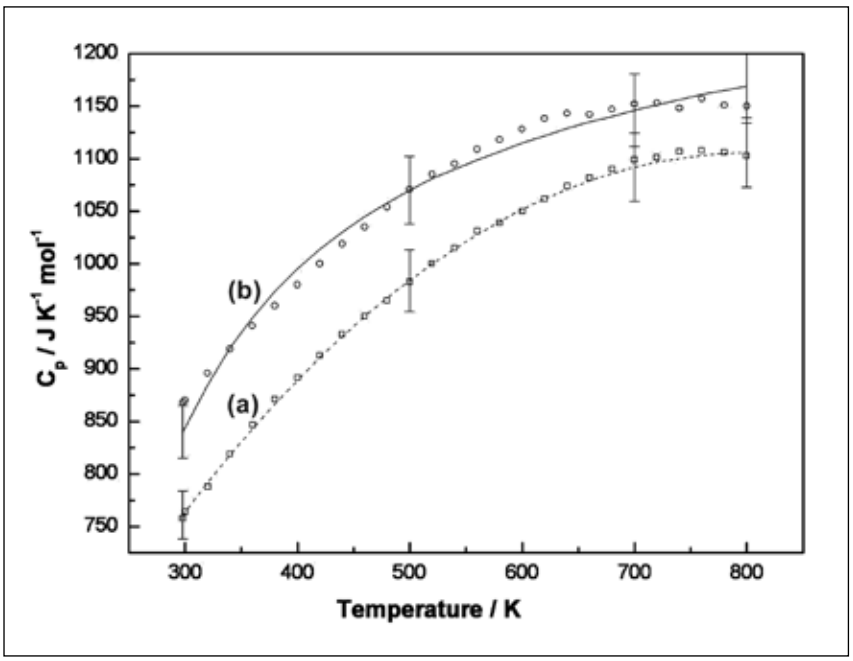

Fig. 2 *Heat capacity of Ca and Sr chloroapatites. (a)* $Ca_{10}(PO_4)_6Cl_2$, *(b)* $Sr_{10}(PO_4)_6Cl_2$

"There is no genuine knowledge of the universe that is not potentially useful for man, not merely in the sense that action may one day be taken on it but also in the fact that every new knowledge necessarily affects the way in which we hold all the rest of our stock"

- Homi Jehangir Bhabha

VI

Infrastructure Facilities

VI.1 Commissioning of Side Stream Filtration System at Central Water Chilling Plant

Central Water Chilling Plant (CWCP) is responsible for providing air conditioning and ventilation services to various buildings and radioactive laboratories of the Centre. The CWCP has an installed capacity of 3100 TR. It comprises of six centrifugal chillers and allied accessories like chilled water pumps, condenser water pumps, cooling towers, etc. The quality of circulating water through an evaporating cooling system has a significant effect on the overall system efficiency and the useful life of the system components. As, the water is cooled primarily by evaporation, the concentration of dissolved solids and other impurities in the water increases rapidly resulting in scaling in the condenser tubes. Also, it has been observed that appreciable quantities of air born impurities, such as dust, mud, dirt, suspended matter, etc. enter into the cooling water system through cooling tower and deposits on condenser heat exchanger surface resulting in reduction in heat transfer. The Quality of cooling water is shown in Table 1 and Table 2.

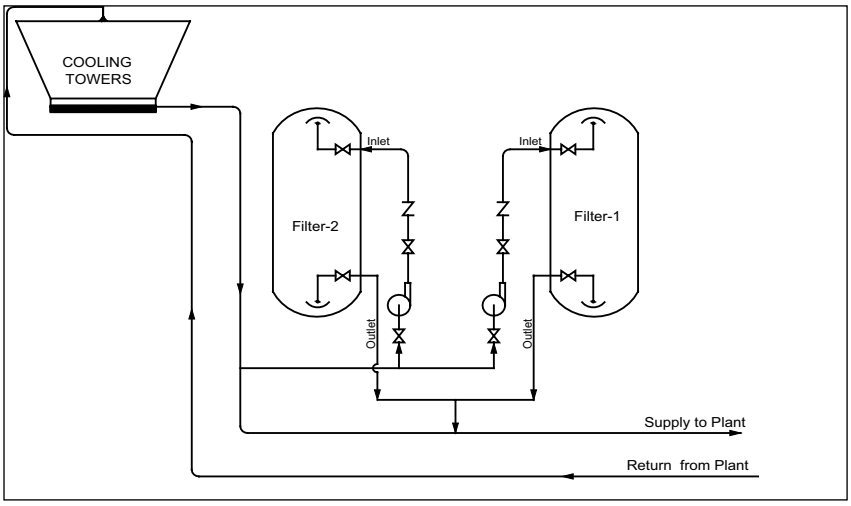

Fig. 1 *Schematic drawing of side stream filtration system*

In order to maintain the condenser cooling water quality with in acceptable limits, a side stream filtration system has been introduced in condenser cooling water system as shown in Fig. 1. The side stream filtration unit is filled with filtering media (fine sand) on top supported by layers of different size and grades of pebbles. Suspended solids collected in the filter are periodically removed from the filter by back wash with fresh water.

The filtered water was tested at water and steam laboratory and the test revealed that the level of total suspended solids are less than 5 ppm and turbidity less than 5 NTU.

Introduction of side stream filtration in the condenser cooling water circuit have helped in:

- Removing the total suspended solids and turbidity
- Reduction in the frequency of cleaning of tube
- Effective heat transfer and improved performance of the chillers
- Energy saving

Table 1: Quality of water before and after circulation

Sl. No.	Parameter water	Circulating value	Permissible
1	pH	8.4	7.0-7.5
2	TDS (ppm)	450	<500 ppm
3	Turbidity (NTU)	15.5	< 5

Table 2: Filter performance

Parameter	Permissible value	Filter Unit 1	Filter Unit 2
Turbidity (NTU)	< 5	0.8	0.8
Total suspended solids (ppm)	< 5	Negligible	Negligible

VI.2 Computational and Knowledge Management Systems

Parallel Cluster Supercomputer

A multi-purpose parallel high-performance computing cluster has been built using state-of-the-art components to cater the diverse computational requirements of users.

The parallel super computing cluster comprises of 128 Compute nodes and a management node interconnected by high-performance Infiniband and Gigabit networks.

The management/master node is the head node of the cluster which is used for cluster administration and providing user interface for job submission and management. The compute nodes are the cluster nodes where the users' jobs actually run. They are highly optimized to execute the parallel codes of the users. In addition, a console server is configured for hardware management of all compute nodes.

The cluster system has three interconnect networks and four storage nodes. It has also a backup server to take periodic backups of user data.

This parallel supercomputing cluster is designed to meet the large-scale numerical computing requirements of Scientists and Engineers of the Centre. Highly compute-intensive scientific applications in the areas of Computational Molecular Dynamics, Material modeling, Reactor Core cal-culations and safety analysis, Weather modeling and Engi-neering applications in the area of Finite Element Analysis, Comp-utational Fluid Dynamics can effectively make use of the cluster to vastly reduce their run times.

Intra DAE Grid Computing

The Intra DAE Grid Network facilitates sharing of computing power and information resources among scientific computing users coming under various geographically separated units of DAE family. As part of this project a grid site has been set up at IGCAR. The Grid Setup at IGCAR augments the Intra-DAE Grid computational resource by connecting the powerful computa-tional cluster located at IGCAR through the high bandwidth dedicated fibre optic leased line to other DAE Grid sites. The setup also facilitates the local scientific computing users at IGCAR to access the Grid resources available on the whole DAE Grid network.

The intra DAE Grid at IGCAR consists of two High-Performance Computing Clusters. Two separate PC based User Interface machines (UI) are configured which play the role of authorized access points to the DAE Grid services. Since resources from different DAE units are interconnected, universally accepted security standards and protocols are followed strictly on all the Grid services implemented.

The IGCAR Grid setup network diagram depicting the interconnection is given in Fig.1.

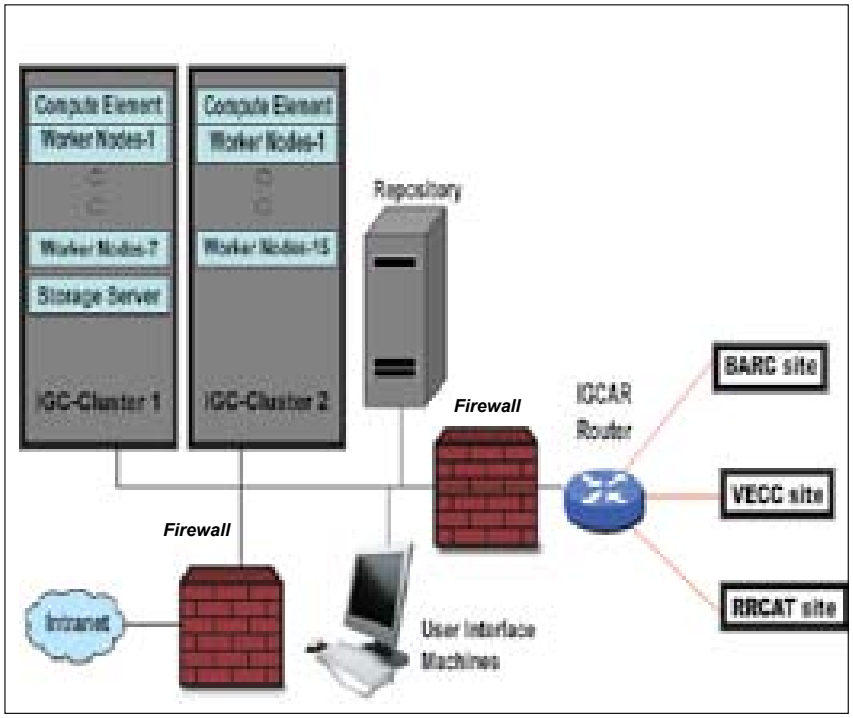

Fig. 1 *DAE Grid setup at IGCAR*

Implementation of Knowledge Management System

IGCAR has formulated and adopted a Knowledge Management Policy:

> *"IGCAR will consistently endeavor through concerted efforts of all it's employees to generate, archive, manage and disseminate the valuable Knowledge for improving it's productivity and achieve and sustain world class Leadership in all it's Scientific and Technological Research and Development activities"*

For the effective realization of the KM policy a Knowledge Management System (KMS) is developed and implemented .

It is intended to meet the needs of the entire organization, with the diverse activities like research, design, development, project execution, support services etc. by providing the right knowledge to the right person in right time in right form, irrespective of the place and time. Knowledge Management Servers are installed in all the Groups and are interlinked.

A task force consisting of knowledge officers from various groups was formed to oversee the progress in Knowledge Management System (KMS) implementation. Explicit Knowledge modules in the form of design reports, publications, presentations, activities, facilities etc. are made available in the server. A taxonomy scheme is being worked out at Divisional/Group level.

The experience gained while operating the FBTR is codified and stored in the server, which has helped in avoiding the reoccurrence of many incidents. Also the knowledge gained in many areas like reprocessing, materials development, engineering development, fuel & material chemistry, safety engineering etc. has given fruitful results in the design of PFBR, Fuel Cycle Facility etc. as depicted in Fig. 2.

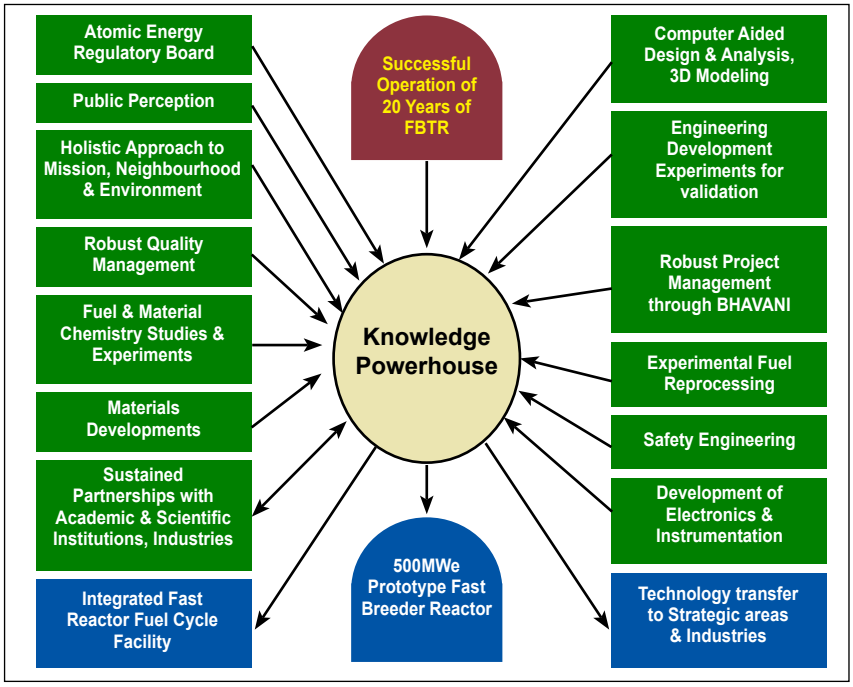

Fig. 2 *Knowledge melting pot*

Knowledge Management System for the preservation and utilization of the construction knowledge of PFBR is being developed. The utilization of the system is being monitored online.

Value Added Services at Scientific Information Resource Division

The digital library extends the breadth and scale of scholarly and cultural evidence and supports innovative research and lifelong learning. To do this, it mediates between diverse and distributed information resources on the one hand and a changing range of user communities on the other. In this capacity, it establishes "a digital library service environment"- that is, a networked online information space in which users can discover, locate, acquire access to and, increasingly, use information. To enhance the information resources usage, Scientific Information Resource Division (SIRD) has initiated many value additions in it's information services to patrons, including extention of Library timings. As advancement of RFID based circulation system, self check-in and check-out stations are introduced so that users can issue/return the books on their own.

To make the access to fast reactor related information much easier, a comprehensive web portal (Fig. 3) has been developed with three major disciplines namely Fast reactor technology, Reprocessing and Fuels. SIRD Holdings, Publications, E-resources and other useful links related to the respective subject categories were provided in a single window to enhance the information usage. As

Fig 3: *Fast reactor knowledge portal*

an initiative to switch to a paperless environment, online SIRD service forms were introduced.

Using the open source solutions of Linux, Apache, MySQL, PHP, an IGCAR Research Contribution (IRC) database has been developed, that contain the publications of our scientists and engineers from 1974. Full text links are provided to the available information sources. Search facility is provided based on various fields like author, subject, title, year etc. Reports are also being generated based on year wise summary, author wise listing etc.

VI.3 Biometric Access Control Systems for Radiological facilities

The Radiological Laboratories in IGCAR are provided with coded card based access control systems. The drawback of these coded card based system is that these cards can be duplicated or can be shared or lost (which can be used by adversary for entry). In order to overcome these drawbacks, it was decided to replace all these card based access control systems with Positive Personal identification by means of Hand Geometry cum RFID based access control systems for critical areas and only RFID systems for non critical areas.

The new Access Control Systems consist of conventional turnstiles and doors, which are controlled by means of hand geometry cum smart card readers. These turnstiles (Fig. 1) and doors are housed in various strategic locations spread over the entire center. All the transactions through these access control systems are logged on a computer system in Client server architecture. The network is isolated and independent for each facility with security features. The data is accessible only to authorised officials.

Fig. 1 *Entry with biometric access control system*

VI.4 Environment Development Activities at Site and Townships

Bio-Shield at Kalpakkam

After Tsunami hit the Kalpakkam coastal areas, Tsunami rehabilitation and livelihood programme as well as sustainable coastal area development were felt necessary, keeping the view “converting a catastrophe into an opportunity”. The rehabilitation project for Tsunami involves growing salt-tolerant plants as given below:

- Mangroves in sea-water
- Salicornia at the Shore
- Jatropha and other horticultural plants in the inland area

To achieve the above, expertise

Fig. 1 *Jatropha plant*

Fig. 2 *Simarouba plants in nursery*

from 'The Science Ashram' (TSA), a Non-Governmental organization, has been utilized.

Three sites have been selected to demonstrate Bio-shield project after conducting thorough survey at IGCAR and Township.

Salvadora, Jatropha and Castor have been planted at site-1.These saplings were grown in township nursery (Fig. 1 and Fig. 2). Survival rate & growth of these plants are found to be satisfactory. Simarouba were planted on the banks of rainwater canal. In addition seeds of Jatropa and Castor were also sowed.

Pump erection, fencing & electrification works are being carried out in site-2. Ploughing was completed and organic manure has been deposited. At site-3, two bore wells have been made. The water quality was analyzed and found to be suitable for Salicornia plantation. Leveling and fencing works have been taken up prior to the plantation. 7m x 5m bed was prepared at IGCAR nursery and Salicornia seeds were sown. 200 Salvadora saplings are being grown and their survival rate is good. Arrangements to feed brackish water for salicornia are made.

Biodiversity Assessment at DAE Campus, Kalpakkam

IGCAR has taken an initiative to create data base on the faunal diversity of its 2500 acres DAE campus at Kalpakkam. To achieve this objective the entire DAE campus at Kalpakkam was divided into four representative plots comprising of different landscapes namely; (1) undisturbed area with dense vegetation, (2) building area, (3) water bodies with riparian cover and (4) sandy area with meager vegetation for inventorying of charismatic terrestrial/semi-aquatic fauna viz., Mammals, Birds, Reptiles, Amphibians and Butterflies (Fig. 3). For birds, early morning surveys were made whereas for mammals evening and night surveys were followed. Mid-day sampling was followed for butterflies and other animals.

Totally 196 species of animals were identified during the survey and it has highlighted the potential magnitude of biodiversity on the campus. A monograph along with brief characteristics is available on IGCAR website.

Fig. 3 *Biodiversity at Kalpakkam*

Fig. 4 *View of the bridge from Sadras side*

Construction of New Bridge at Kalpakkam

Subsequent to review after TSUNAMI disaster, the need to have an additional bridge linking Puduppattinam and Sadras was felt. The earlier bridge was aged and it was not designed to withstand TSUNAMI force. Thus action was initiated to build an alternate bridge. The whole approach was departmental in terms of architectural layout, design, tendering and execution. Necessary support towards diverting services, electrical activities etc. was extended by GSO. The bridge has been architecturally engineered to blend with the natural serene landscaping and also keeping the old bridge in the background.

The bridge (Fig. 4) has special features to withstand earth quakes and was designed to ensure communication even under strong earthquake scenarios.

Environmentally-friendly Solid Waste Management at Townships

Prior to the implementation of Solid Waste Management at Townships, the garbage disposal was carried out through conventional method. The present system of solid waste management, implemented by M/s. Exnora Green Pammal and being monitored by Civil Engineering Division, GSO, is a Scientific method of disposing the wastes through environmentally acceptable manner. In this scheme baskets are issued to each house/public building. (Green colour basket for discharging bio-degradable wastes and Red colour basket for discharging non bio-degradable wastes) and wastes discharged by the residents at the respective baskets are being collected at each door step. The wastes collected above are being transported to segregation yards.

Finally wastes are disposed by converting the same in the forms of manure, recycling/reuse through environmentally acceptable manners.

"I know quite clearly what I want out of my life. Life and my emotions are the only things I am conscious of. I love the consciousness of life and I want as much of it as I can get. But the span of one's life is limited. What comes after death no one knows. Nor do I care. Since, therefore, I cannot increase the content of life by increasing its duration, I will increase it by increasing its intensity. Art, music, poetry and everything else that consciousness I do have this one purpose - increasing the intensity of my consciousness of life"

- Homi Jehangir Bhabha

AWARDS & HONOURS

Dr. Anish Kumar, NDED, Metallurgy & Materials Group has been awarded **"Young Scientist Award"** for the year 2008 by the Indian Society for Non Destructive Testing.

Dr. Baldev Raj, has been elected as **Member of German National Academy of Sciences**. He has been awarded the **Distinguished Alumni Award** for sustained excellence in Science & Technology by the Indian Institute of Science, Bengaluru. He has been elected as **Vice President, Materials Research Society of India (2008-2011)**. He has been appointed as **Adjunct Professor** of PSG College of Technology, Coimbatore and University Institute of Chemical Technology, Mumbai. He has been nominated as a **Member of the Governing Body**, Sree Chithra Tirunal Institute of Medical Sciences & Technology, Thiruvananthapuram. He has been invited by **'Global Energy'** to be a member of the **"Global Energy International Prize Committee for 2009-2013"** for selecting the awardees for research and development in the area of energy in the world along with other members which include Nobel prize winners in the field of Physics and Chemistry. He has been made as **Member, Nanotechnology Advisory Board**, Department of Science & Technology, Government of South Africa. He has delivered twenty fourth **Prof. Brahm Prakash Memorial Lecture** organized by Indian Institute of Metals, Bangalore Chapter. He has been awarded **Prof. Jai Krishna Memorial Award** by the Indian National Academy of Engineering for the year 2008. He has been selected as the **Vice President, Academia NDT International** and **Vice President (Academic, Professional & International Affairs)** in the Indian National Academy of Engineering (2008-2011). He has been designated as **Member, Editorial Board** of Steel Technology and Member, Editorial Board of Asian Journal of Professional Ethics & Management.

Dr. A.K. Bhaduri, MTD, Metallurgy and Materials Group has been awarded the **VASVIK award-2005** jointly with Dr.Gautam Kumar Dey of BARC for their contribution towards research in **Material & Metallurgical Sciences and Technology.**

Shri S.C.Chetal, Reactor Engineering Group has been awarded **VASVIK award-2003** for his contribution towards research in Mechanical & Structural Sciences and Technology.

Dr. John Philip, NDED, Metallurgy & Materials Group has been awarded **Indian Nuclear Society Medal-2007**.

Shri T. Karthikeyan, PMD, Metallurgy & Materials Group has been awarded **INAE Young Engineer Award** for the year 2008.

Shri M. Krishnamoorthy, CWD, Engineering Services Group has been awarded **"Best Welding Engineer-2008"** by the Indian Institute of Welding, Chennai Branch.

Shri G. Padmakumar, ST&HD, Fast Reactor Technology Group has been awarded with **Indian Nuclear Society Medal-2007**.

Dr. Shaju K. Albert, MTD, Metallurgy & Materials Group, **Shri R. Sritharan**, RCD, Reactor Engineering Group and **Shri C. Balasubramanian**, M/s Omplas Systems, Chennai have been awarded the **ISAMPE Outstanding Design and/or Process Development Award-2008** by the Indian Society for Advancement of Materials and Process Engineering (ISAMPE), Bengaluru.

Shri Sumantra Mandal, MTD, Metallurgy & Materials Group has been chosen as the recipient of the **"2009 SHRI RAM ARORA AWARD"** for Materials Science and Engineering Education from The Minerals, Metals and Materials Society (TMS), USA.

Dr. C.S. Sundar, MSD, Metallurgy & Materials Group has been awarded **"Tamil Nadu Scientist Award (TANSA)-2007"** under the discipline Physical Sciences by Tamil Nadu State Council for Science and Technology.

Smt. Uma Seshadri, PD, has received the **" Women Engineers Award"** for the year 2008 of Institution of Engineers (India) Tamil Nadu State Centre for her outstanding contribution in Engineering Profession.

Dr. P.R. Vasudeva Rao, Chemistry, Metallurgy & Materials Groups has been awarded **Indian Nuclear Society Award-2007 :** Nuclear Fuel Cycle Technologies, including Radiation Safety and Environmental Protection by Indian Nuclear Society. He has also been appointed as **Adjunct Professor** of University Institute of Chemical Technology, Mumbai and PSG College of Technology, Coimbatore.

AERB Green Site Award - 2007 has been awarded to the **Kalpakkam Site (IGCAR, MAPS, BHAVINI & Other Units)** by Atomic Energy Regulatory Board.

"HOMI BHABHA Quality Circle", CWD, Engineering Services Group led by Shri G. Kempulraj with members Shri T. Saravanan, Shri K. Narayanan, Shri Kumaran, Shri Chandrasekharan and Shri P. Shanmugam has won the **"PAR EXCELLENCE"** award, the highest in quality circle competitions at Quality Circle Convention (CCQCC-2008).

"Moon Quality Circle" C&IDD, Fast Reactor Technology Group led by Shri T.V. Maran with members Shri K. Mohanraj, Shri R. Rajendran, Shri A.T. Loganathan, Shri A. Ramamoorthy, Shri D. Kuppuswami and Shri A. Anthuvan Clement has won **Excellence Award** for their Project "ROBOA (Reduction of Breakdowns of all cut machine) at the National Convention for Quality Circles NCQC - 2008.

"SAMURAI Quality Circle", Maintenance & Inspection Section, Central Workshop Division led by Shri V. Praveen Kumar with members Shri C. Palani, Shri N. Chockalingam, Shri A. Magendran, Shri P.M. Ajithkumar and Shri Ramalingam got **"Distinguished Award"** during circle competitions at Quality Circle Convention (CCQCC-2008).

Adjunct Professorships

The following members were appointed as Adjunct Professors of PSG College of Technology, Coimbatore for the period of Feb 2008 to Feb 2010.

Dr. P. Chellapandi, Reactor Engineering Group

Dr. T. Jayakumar, NDED, Metallurgy & Materials Group

Shri S.A.V. Satya Murty, CD, Electronics & Instrumentation Group

Dr. K.S. Viswanathan, MCD, Chemistry Group

Dr. B. Venkataraman, QAD, Engineering Services Group

Dr. U. Kamachi Mudali, CSTD, Metallurgy & Materials Group

Dr. G. Amarendra, MSD, Metallurgy & Materials Group

Dr. P. Shankar, MSD, Metallurgy & Materials Group

Dr. M. Sai Baba, S&HRPS

Department of Atomic Energy Annual Awards for Excellence

Department of Atomic Energy has instituted annual awards for excellence in Science, Engineering and Technology in order to identify best performers in the area of Research, Technology Development and Engineering in the constituent units (other than Public Sector Undertakings and Aided Institutions). The Young Scientist, Young Engineer, Young Technologist, Homi Bhabha Science and Technology Award and Scientific and Technical Excellence Award fall under this category. Group Achievement awards for recognition of major achievements by groups have also been instituted. Life time Achievement Award is awarded to one who has made significant impact on the DAE's programme. They are the icons for young scientists and engineers to emulate. The awards consist of a memento, citation and cash prize.

Recipients from IGCAR for the year 2006 :

Homi Bhabha Science and Technology Award

Dr. G. Amarendra, MSD, Metallurgy and Materials Group

Scientific and Technical Excellence Awards

Shri V. Balasubramaniyan, RCD, Reactor Engineering Group

Dr. John Philip, NDED, Metallurgy and Materials Group

Dr. M. Joseph, FCD, Chemistry Group

Dr. Kinkar Laha, MMD, Metallurgy and Materials Group

Shri Shekar Kumar, RR&DD, Reprocessing Group

Dr. K. Velusamy, M&HD, Reactor Engineering Group

Young Engineer Awards

Shri V. Karthik, PIED, Metallurgy and Materials Group

Shri T. Karthikeyan, PMD, Metallurgy and Materials Group

Young Scientist Award

Dr. Anish Kumar, NDED, Metallurgy and Materials Group

Meritorius Services Awards

Shri N. Chinnasamy, MSD, Metallurgy and Materials Group

Shri A. Elumalai, RMD, Reactor Operation and Maintenance Group

Shri S. Ganesan, CWD, Engineering Services Group

Shri B. Ramachandran, CWD, Engineering Services Group

Shri S. Sundaramurthy, RR&DD, Reprocessing Group

Group Achievement Awards

Development of Compact Facility for Reprocessing Advanced Fuels in Lead Cells (CORAL)

Shri M.Venkataraman, Dr. S.B.Koganti, Shri P.Ramkumar, Shri V.Sundararaman, Shri A.Ravisankar, Shri N.Ramnath, Shri V.Vijayakumar, Shri B.M.Ananda Rao, Dr. R.V.Subba Rao, Shri Geo Mathews of Reprocessing Group and (former employees) Shri G.R.Balasubramanian, Shri M.S.Ilangovan, Shri R.Sudharsanam, Shri P.K.Verghese, Dr. A.Palamalai, Shri R.G.Diraviyam, Shri Joseph Benjamin, Shri E.Doss, Shri C.A.Dixit, (Late) Shri S.Dhanapal, Shri S.Shanmugam and Shri S.Arunachalam

Design of PFBR Main Vessel and Safety Vessel

Dr. P.Chellapandi, Shri V.Balasubramaniyan, Shri P.Selvaraj, Shri P.Puthiyavinayagam, Shri R.Srinivasan, Dr. K.Velusamy, Shri S.Jalaldeen, Shri T.Selvaraj, Shri A.Biswas, Shri R.Ravi Prasan, Shri U.Parthasarathy, Shri K.Natesan, Shri C.Raghavendran, Shri R. Sritharan, Shri R.Suresh Kumar, Shri Sriramachandra Aithal, Shri S.D.Sajish, Shri Bhuwan Chandra Sati, Shri Abhishek Mitra, Shri S.K.Pandey, Shri P.Ravi, Shri Gyanendra Prasad, Shri P.V.Sellaperumal, Shri Sebasti John, Shri G.Venkataiah, Shri D.Ajay Kumar, Shri A.Sivakumar and Shri S.Saravanan of Nuclear Engineering Group, Reactor Engineering Group

Penetration Enhancing Activating Flux Tungsten Inert Gas (PEAF-TIG) Welding of Dummy Fuel Subassemblies (DFSA) of PFBR

Dr. A.K. Bhaduri, Dr. M. Vasudevan, Shri M. Arul and Shri M. Munivel of MTD, Metallurgy and Materials Group and Shri A.S.L.K.Rao, Shri R.Veluswamy, Shri P.Sivaraman, Shri G.Kempulraj, Shri M.Krishnamoorthy, Shri T.M. Chandra sekaran, Shri M.Damodaran, Shri M.Kuppan, Shri V.Kodiarasan, Shri A.Padmanabhan and Shri N. Dhanasekaran of Central Workshop Division and Shri K. Loganathan of QAD, Engineering Services Group

The recipients of the same awards from IGCAR for the year 2007 are:

Homi Bhabha Science and Technology Award

Dr. B. Venkatraman, QAD, Engineering Services Group

Scientific and Technical Excellence Awards

Dr. N.V. Chandra Shekar, MSD, Metallurgy & Materials Group

Dr. K. Devan, RPD, Reactor Engineering Group

Shri V. Rajan Babu, RCD, Reactor Engineering Group

Dr. R. Sridharan, LM&SCD, Chemistry Group

Young Engineer Awards

Shri Chittaranjan Das, MTD, Metallurgy and Materials Group

Shri K. Natesan, M&HD, Reactor Engineering Group

Shri Sumantra Mandal, MTD, Metallurgy and Materials Group

Shri V. Vinod, SFD, Fast Reactor Technology Group

Young Technologist Awards

Shri Manoj Kumar Mishra, E&ID, Electronics & Instrumentation Group

Meritorius Services Awards

Shri G. Moorthy, AC&VSD, Engineering Services Group

Shri A.G. Sarangapani, CWD, Engineering Services Group

Shri N.S. Thampi, MMD, Metallurgy and Materials Group

Shri K. Victor Arulraj, ESD, Engineering Services Group

Group Achievement Awards

Design, Development, Manufacture & Qualification of Control & Safety Rod and its Drive Mechanism for PFBR

Dr. P. Chellapandi, Nuclear Engineering Group, Dr. D. Rangaswamy, Power Plant Control Division, Shri V. Rajan Babu, Shri P. Puthiyavinayagam, Smt. R. Vijayashree, Shri T.S. Paneer Selvam, Shri K. Krishnaprasad, Shri S. Jaisankar, Shri P.A. Sasidharan, Reactor Components Division, Nuclear Engineering Group, Reactor Engineering Group and Shri C. Meikandamurthy, Shri K. Gurumoorthy, Sodium Facility Division, Shri D. Ramdasu, Shri G.K. Pandy, Shri Ajesh Kumar, Separation Technology & Thermal Hydraulic Division, Shri R. Veerasamy, Shri S.C.S.P. Kumar Krovvidi, Shri Sudheer Patri, Shri S.K. Dash, Shri T. Logaiyan, Components & Instrumentation Development Division, Fast Reactor Technology Group, Shri E. Venkatesan, Quality Assurance Division, Engineering Services Group and Shri B. Saha, Electronics & Instrumentation Group

Development of Electrochemical and Solid State Gas Sensors

Dr. T. Gnanasekaran, Dr. R. Sridharan, Shri K.H. Mahendran, Shri S. Nagaraj, Smt. Kitheri Joseph, Smt. Manjulata Sahu, Dr. Rajesh Ganesan, Shri Sajal Ghosh, Shri G. Ravishankar, Liquid Metals & Structural Chemistry Division, Shri K. Dayalan, Shri A. Veerapandian, Shri V. Sureshkumar, Smt. S. Premalatha, Shri R. Parthasarathy, Shri K.C. Srinivas, Chemical Facility Division, Smt. K. Sujatha, Fuel Chemistry Division, Chemistry Group, Shri S. Bagavathiappan, Non-Destructive Evaluation Division, Shri C. Subramanian, Shri K.M. Natarajan, Shri P. Balakrishnan, Shri P. Shanmugam, Central Workshop Division, Engineering Services Group, Shri I.B. Noushad, Shri S. Kishore, Shri B. Muralidharan, Sodium Facility Division and Shri Vivek Nema, Sodium Technology & Thermal Hydraulic Division, Fast Reactor Technology Group

Post Irradiation Examination of Fuel & Structural Materials of FBTR

Shri K.V. Kasiviswanathan, Shri V. Venugopal, Shri N. G. Muralidharan, Shri N. Raghu, Shri C.N. Venkiteswaran, Shri V. Karthik, Shri V. Anandaraj, Shri M. Sekar, Shri R. Parthasarathy, Shri M. Ramanathan, Shri Jojo Joseph, Shri T. Johny, Shri Shaji Kurien, Shri A. Vijayaragavan, Shri T. Ulaganathan, Shri D. Ganesan, Shri V.L. Balakrishnan, Shri S. Maharajan, Shri N.P. George, Shri K. Satheesh Kumar, Shri R. Subramanian, Shri N. Kulasegaran, Shri Y. Ramaseshu, Shri B. Venugopal Naidu, Shri S. Kumaresan, Shri J. Seenuvasan, Shri R. Devarajulu, Shri P.R. Venkatesan, Group for Remote Handling, Robotics, Irradiation Experiments and PIE, Metallurgy & Materials Group and Ms. B. Sasi, Dr. T. Saravanan, Non-Destructive Evaluation Division, Metallurgy & Materials Group

Seismic Design and Qualification of PFBR Components, IGCAR

Dr. P. Chellapandi, Nuclear Engineering Group, Shri R. Srinivasan, Shri T. Selvaraj, Mechanics & Hydraulics Division, Shri S.D. Sajish, Shri C. Raghavendran, Shri P. Ravi, Shri Vankatiah, Shri V. Kothandam, Shri V. Devaraj, Shri R. Manu, Nuclear Engineering Group, Reactor Engineering Group and Shri Jagannath Mishra, Safety Research Institute, Atomic Energy Regulatory Board.

Publications during the year 2008

BOOKS / BOOK CHAPTERS

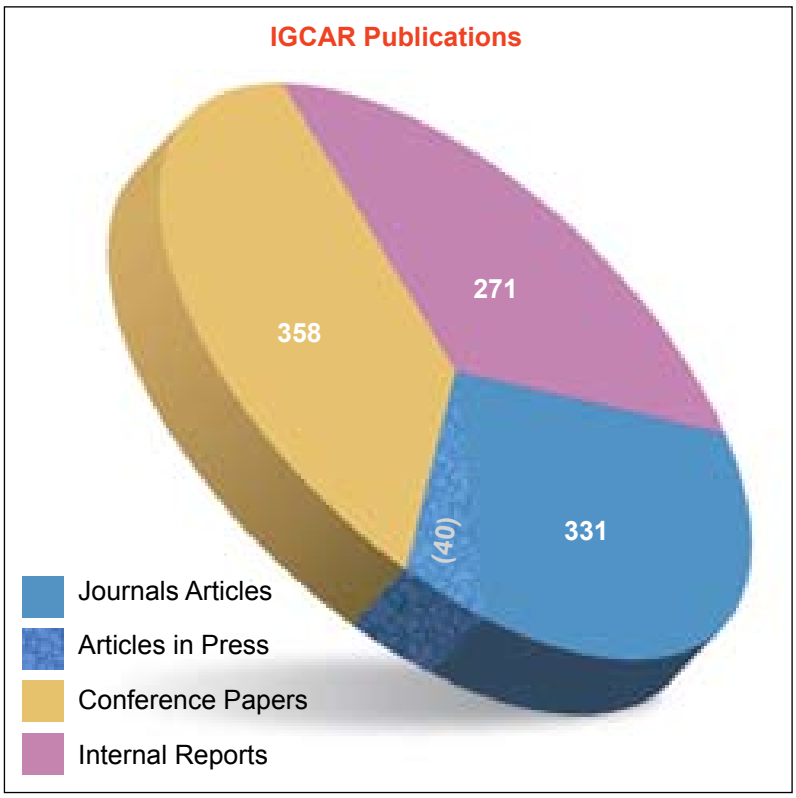

1. U. Kamachi Mudali and Baldev Raj, eds. **"***Corrosion Science and Technology: Mechanism, Mitigation and Monitoring",* New Delhi, India : Narosa Publishing House Ltd., 2008. Also, USA: CRC Press, 2008 & Europe: Alpha Publishers, 2008.
2. K. Jahir Hussain, K.K. Satpathy, M.V.R. Prasad, V.T. Sridharan, T. Ramesh and M. Selvanayagam, 2008. *Faunal Diversity Assessment at Department of Atomic Energy (DAE) Campus, Kalpakkam,* Kalpakkam, India: IGCAR.
3. S.K. Albert and S. Sundaresan, 2008, *"Using creep resistant steels in nuclear reactors",* In *Creep Resistant Steels*, edited by F. Abe, T.U. Kern, R. Viswanathan, 597-636, Cambridge, UK : Woodhead.
4. G. Amarendra and R. Govindaraj, 2008, "*Nuclear and Auger electron spectroscopic techniques for Corrosion studies*", In *Corrosion Science and Technology: Mechanism, Mitigation and Monitoring,* edited by U. Kamachi Mudali and Baldev Raj, New Delhi, India: Narosa.
5. A.K. Bhaduri, S.K. Albert, and Baldev Raj, 2008, *"Robust welding technologies for ferrous alloys".* In *Weld cracking in ferrous alloys: Welding Technology and Design to Prevent Weld Cracking (Part 1).* edited by R Singh, 34-95, Cambridge, UK : Woodhead.
6. Chellapandi, and S.C. Chetal, 2008, *"Design against cracking in ferrous weldments",* In *Weld cracking in ferrous alloys: Welding Technology and Design to Prevent Weld Cracking (Part 1),* edited by R. Singh, Cambridge, UK : Woodhead.
7. Baldev Raj, K.V. Kasiviswanathan, N. Raghu, N.G. Muralidharan and V. Karthik, 2008, *"Lessons learnt from failures in ferrous weldments",* In *Weld cracking in ferrous alloys: Weld Crack Behaviour, Evaluation And Repair (Part 2),* edited by R Singh, Cambridge, UK : Woodhead.
8. Baldev Raj, T. Jayakumar and P. Palanichamy, 2008, *"Testing and evaluation of weld cracking in ferrous alloys",* In *Weld cracking in ferrous alloys: Weld Crack Behaviour, Evaluation and Repair (Part 2)***,** edited by R Singh, Cambridge, UK : Woodhead.
9. K. Bhanu Sankara Rao, M.D. Mathew, K. Laha, R. Sandhya and Baldev Raj, 2008, *"Mechanical behaviour of stainless steel, ferritic steels welds and weld joints",* In *Weld cracking in ferrous alloys : Weld Crack Behaviour, Evaluation And Repair (Part 2),* edited by R Singh, Cambridge, UK : Woodhead.
10. R.K. Dayal, Hasan Shaikh and N. Parvathavarthini, 2008, *"Corrosion issues in ferrous weldments",* In *Weld cracking in ferrous alloys: Environment-Assisted Weld Cracking (Part 3),* edited by R. Singh, Cambridge, UK: Woodhead.
11. S. Ningshen and U. Kamachi Mudali, 2008, *"Metallic and Oxide Coatings for Corrosion Protection",* In *Corrosion Science and Technology: Mechanism, Mitigation and Monitoring,* edited by U. Kamachi Mudali and Baldev Raj, 141-174, New Delhi, India: Narosa.

12. S.K.Ray and G.Sasikala, 2008, *"Fracture toughness: Considerations and evaluation for design and operation of ferrous weldments",* In *Weld Cracking in Ferrous Alloys : Weld Crack Behaviour, Evaluation and Repair (Part 2)***,** edited by R. Singh, 185-221, Cambridge, UK : Woodhead.

PATENTS

1. *An innovative cut and feed operation for enhancing the performance of ion exchange chromatographic separations*
   Inventors: C. Anand Babu, B.K. Sharma, G. Mohanakrishnan and Baldev Raj
   PCT International Application No.PCT/IN2008/ 000293 date :12/05/2008
2. *Process for making enhanced sensitization resistance in austenitic stainless steel through specific heat treatment*
   Inventors: R.K. Dayal, N. Parvathavarthini, Baldev Raj, S.V. Mulki and I. Samajdar
   PCT International Application No. 893/MUM/2008 dt. 21-04-2008
3. *Wash solution suitable for use in continuous reprocessing of nuclear fuel and a system thereof.*
   Inventors: P.Govindan, K.Dhamodharan, K.S.Vijayan, R.V.Subba Rao, M.Venkataraman and R.Natarajan
   PCT International application No. PCT/IN2008/00516 dated 18-08-08.
4. *A process for the treatment of cellulose based waste for the removal of hazardous materials and recovery of valuables*
   Inventors: Ch. Jagadeeswara Rao, K.A. Venkatesan, K.Nagarajan, T.G. Srinivasan and P.R. Vasudeva Rao
   712/ASA/PP-529/DAE
5. *A method and Apparatus for Block Encryption and Synchronous Stream Cipher*
   Inventors: T.Prasanth Kumar, S.A.V.Satya Murty, P.Swaminathan
   PCT/IN 08/644 dated 07.10.2008

COLLOQUIA, SEMINARS AND CONFERENCES - 2008

IGC COLLOQUIA

1. *Materials research at Hahn-Meitner-Institute, Berlin* by Dr. Christian Abromeit, Deputy Head, Department of Materials, Kahn-Meitner-Institute, Berlin on 7 January 2008.
2. *Aerosol Reactor Synthesis of Nanomaterials : Step Processes for Production of Oxide Nanoparticles* by Prof. Pratim Biswas, The Stifel and Quinette Jens Professor, Chairman, Department of Energy, Environmental and Chemical Engineering, Washington University, St. Louis, USA on 21 January 2008.
3. *Global Energy Systems - Opportunities and Challenges* by Dr. Rajan Gupta, Los Alamos National Laboratory, USA on 1 February 2008.
4. *Polymer Nanocomposites* by Dr. Anil K. Bhowmick, Rubber Technology Centre, IIT, Kharagpur on 12 February 2008.
5. *Fast Neutron Reactor: Past, Present and Future* by Dr. Casimir Pierre Zaleski, Executive Director, Centre for Geopolitics of Energy and Raw Materials University, Paris Dauphine, France on 15 February 2008.
6. *Monju Reactor Accidents and Related Materials Research* by Prof. Yoshio Monmo, Kochi University of Technology, Japan on 7 March 2008.
7. *From Nuclear Fuel to Materials Design and from Materials Design to Nuclear Commons* by Prof. Shuichi Iwata, The University of Tokyo, Japan on 11 March 2008.
8. *Science in Antartica* by Dr. Saurabh K. Verma, Consulting Scientist, DST Project, Scientist 'G' (Retd.), National Geophysical Research Institute (NGRI), Hyderabad on 16 April 2008.
9. *Indian Aerospace Engineering & Technology - Current Scenario* by Dr. R. Balasubramaniam, Head, Structures Division and Advisor (Retd.), National Aerospace Laboratories, Bengaluru on 17 April 2008.
10. *Psychology and Mental Health* by Dr. Shobini L. Rao, Head, Department of Mental Health and Social Psychology, National Institute of Mental Health and Neurosciences (NIMHANS), Bengaluru on 26 November 2008.

11. *Integrating Monitoring into Engineering Structures* by Prof. Christian Boller, Director, Fraunhofer Institute for NDT (IZFP) & Chair in NDT and Quality Assurance, Saarland University, Saarbruecken, Germany on 15 December 2008.

SPECIAL LECTURES

1. *Curie Memorial Lecture - Applications of Radiation and Radioisotoes in Food and Agriculture* by Dr. A.K. Sharma on 16 January 2008.
2. *Power of Sub-conscious Mind* by Dr. Pankaj Mehta on 10 April 2008.
3. *Diabetes: Prevention and Control* by Prof. A. Sundaresan, Kilpauk Medical College, Chennai on 25 April 2008.
4. *Scientists as Leaders / Leadership Providers* by Dr. Kinnera Murthy on 28 May 2008.
5. *Role of Engineers in Sustainable use of Natural Resources* by Dr. A. Jagadeesh, Director, Nayudamma Centre for Development Alternatives, Nellore on 15 September 2008.
6. *Seaborg Memorial Lecture - Uranium Mining in India : Present Scenario and Challenges Ahead* by Shri. Ramendra Gupta, Chairman & Managing Director, UCIL on 30 September 2008.
7. *Insights into Theories of Turbulence, Transport Phenomena and their Implications to Design of Reactors* by Prof. J.B. Joshi, Director, UICT, Mumbai on 17 November 2008.
8. *Curie Memorial Lecture - Role of Nuclear Technology in Food Security* by Dr. S.F. D'Souza, Head, Nuclear Agriculture and Biotechnology Division & Associate Director, Bio-Medical Group, BARC on 1 December 2008.

SEMINARS, WORKSHOPS AND MEETINGS

1. International Symposium on Sustaining Global Pressures : Women in Science and Engineering, 3-5 January 2008.
2. Sixteenth DAE-BRNS "National Symposium and Workshop on Thermal Analysis", 4-8 February 2008.
3. International Conference on Advances in Manufacturing Technology for Young Engineers, 6-8 February 2008.
4. DAE Anu Week Celebrations - 2008 at PSG College of Technology, Coimbatore, 15-19 February 2008.
5. Theme Meeting on "Small Specimen Mechanical Testing" on 25 February 2008.
6. BRNS sponsored Workshop on "Physics and Mechanics of Advanced Structural Materials", 27-29 March 2008.
7. Theme Meeting on "Structure and Thermodynamics of Emerging Materials", 17-18 April 2008.
8. Theme Meeting on "Recent Advances in Post-Irradiation Examination", 22-24 May 2008.
9. Conference on "Role of IT-Enabled Knowledge Management in Growth of India", 24-26 July 2008.
10. SERC School on "Chemical Thermodynamics", 18-23 August 2008.
11. Electrochemistry & Corrosion Camp, 12-13 September 2008.
12. Discussion Meet on "Seismic Reevaluation", 17-18 September 2008.
13. IGCAR-CEA Workshop on "Materials and Design Issues for Fusion and Fission Reactors", 23 September 2008.
14. 5th International Conference on "Creep, Fatigue and Creep-Fatigue Interaction", 24-26 September 2008.
15. IGCAR-KAERI Workshop on "High-Temperature Materials, Design and Assessment", 29 September 2008.
16. Quality Circle Annual Meet - 2008 on 16-17 October 2008.
17. Symposium on "Operational and Environmental Issues Concerning the use of Water as a Coolant in Power Plants and Industries" (OPENWAC-2008), 15-16 December 2008.
18. 25th DAE Safety & Occupational Health Professionals Meet, 18-20 December 2008.

NURTURING ACTIVITIES

1. BITS Practice School from 26 May 2008 to 4 July 2008.
2. Summer Training Programme in Physics and Chemistry (STIPAC 2008), a six weeks training programme for final year M.Sc., (Physics/Chemistry) students from 26 May 2008 to 4 July 2008.

NEWS AND EVENTS

Eminent visitors to IGCAR

❖ A delegation from United States Nuclear Regulatory Commission (USNRC) visited Kalpakkam during 3-4 March, 2008. This visit is a part of bilateral exchange of visits between USNRC and AERB. The team was interested to know about project management and safe work culture while executing major nuclear reactor projects and expressed their appreciation of approach in managing the BHAVINI project.

Team members of the USNRC delegation with Shri S.C.Chetal, Director, REG

❖ Prof. Siegfried Hecker, Co-Director, Centre for International Security and Cooperation, Stanford University, Dr.Gordon Jarvinen, Deputy Director, Seaborg Institute, Los Alamos National Laboratory and Dr. Chaim Braun, Science fellow, Stanford University visited the Centre during 20-21 March 2008 and held discussions with senior scientists and made presentations on Fundamental Physics and Metallurgy of Plutonium and Plutonium Alloys (Prof. Hecker), Fundamental Chemistry of Separations and bonding (Dr.Jarvinen) and Advanced Reactor Programmes from Industry Perspective (Dr. Braun). The delegates also visited various facilities at the Centre.

Dr. Gordon Jarvinen, Dr.Baldev Raj, Distinguished Scientist and Director, IGCAR, Dr. Chaim Braun, Prof. Siegfried Hecker, Dr. P.R.Vasudeva Rao, Director, CG &MMG, Dr.C.S.Sundar, Head, MSD, MMG and Dr.M.Sai Baba, Head, SIRD and S&HRPS after the presentations at Ramanna Auditorium

❖ A Norwegian - Swedish delegation visited Kalpakkam during 28-29 March, 2008. During the visits there were presentations by the visiting team on Thorium Utilisation, Swedish Waste Management Programme and Titanium Production. From the Indian Side, Shri S.C.Chetal, Director, Reactor Engineering Group gave an overview of status of FBRs in the country and Dr.P. Mohanakrishnan, Head, RPD, REG, elaborated on the Thorium utilization in Fast Breeder Reactors. The delegation visited Fast Breeder Test Reactor, BHAVINI, Safety Group and Fast Reactor Technology Group. The delegation has an ambitious plan of utilizing the thorium resources.

Senior scientists from IGCAR holding discussions with the visiting Norwegian-Swedish Delegation

❖ Dr. Bernard Bigot, Dr. Claude Guet & Dr. Hugues De Longevialle from CEA, France visited the Centre during 13-14 April, 2008. The team held discussions with Director, IGCAR and senior colleagues of the Centre on the status of R&D related to FBR in India and France. They also

Dr. Bernard Bigot, Dr. Claude Guet & Dr. Hugues De Longevialle from CEA, France during discussions with Dr.Baldev Raj, Director, IGCAR

visited various facilities at IGCAR. Dr.Bigot also put forward the strategies adopted to attract young talent towards Nuclear programmes in his country. He addressed the student community of IGCAR comprising of Trainee Scientific Officers and Research Scholars.

❖ Dr. A.P.J. Abdul Kalam, Former President of India, visited IGCAR on 24th April 2008. Dr. Anil Kakodkar, Chairman, AEC and Dr. S. Banerjee, Director, BARC accompanied him during the visit. Dr. A.P.J. Abdul Kalam showed keen interest during the visit to various facilities at IGCAR. He was briefed on the status of operations at

Dr. Baldev Raj, Director, IGCAR, explaining the status of Fast Breeder Test Reactor to Dr. A.P.J. Abdul Kalam. Dr. Anil Kakodkar, Chairman, AEC and Dr. S. Banerjee, Director, BARC join the discussion

FBTR. At the hot cells in the Post-Irradiation Examination Division, he was explained about some of the experimental programmes on irradiated fuel bundle and about new robotic instruments developed in-house. He was shown unconventional and innovative Non Destructive Evaluation Techniques being pursued at the Centre and the sensors and instrumentation developed in-house. At the CORAL facility, he was explained the progress in R&D relating to dissolution of high burn-up high plutonium content mixed carbide fuel and reprocessing of advanced carbide fuel. Dr. Kalam has made a special mention about the same in his address on the occasion of "National Technology Day Celebrations - 2008".

Dr. A.P.J. Abdul Kalam's passion towards youngsters, especially students, is well known and it was reflected in the interaction session with the student community of IGCAR comprising the Trainee Scientific Officers and Research Scholars. In his address to the students he said. "Everyone especially the students should do a SWOT analysis in life. The four main points which one should ponder towards achieving success in any endeavor are: aim, acquiring knowledge, hard work and perseverance. To be successful, one has to become a captain and defeat the problem"

While touching upon the great strides our country is taking towards economic growth, he stressed upon the necessity to be self-reliant and to push the GDP from the present level of 8% to 10%. He envisaged the following areas (1) Education and Health Care (2) Agriculture and Agro products (3) Nuclear Technology and (4) Information Technology to be the key players in leading India to the forefront in the international arena.

With his exceptional experience in scientific research and technology management, Dr. Kalam gave several tips to the students to tackle scientific problems and achieve outstanding results. He enthusiastically answered the volley of the questions put forth by the intriguing students.

Dr. A.P.J. Abdul Kalam addressing the students

Air Marshal Shri S.C.Mukul, Commanding-in-Chief of Southern command and other officers from Air Force Station holding discussion with Dr.Baldev Raj, Director, IGCAR and senior colleagues of the Centre

- Commanding-in-Chief of southern command Air Marshal Shri S.C. Mukul visited the Centre on 6 August, 2008. He held discussions with Dr.Baldev Raj, Director, IGCAR and other senior colleagues of the Centre on safety and security related issues. Later on, he visited FBTR, MAPS and BHAVINI.
- Shri Jayaram Ramesh, Hon'ble Minister of State for Commerce and Power, Government of India visited the Centre on 12 July, 2008 and held discussions with Dr.Baldev Raj, Director,IGCAR, Shri S.K.Jain, CMD, NPCIL and other senior colleagues from various units of DAE. Director, IGCAR made a presentation on the status of the programmes in the Centre. Shri Jayaram Ramesh interacted with the Trainee Scientific officers and research scholars.
- Shri T.K.Rangarajan, Hon'ble Member of Parliament visited the Centre on 12 August, 2008 and held discussions with Dr. Baldev Raj, Director, IGCAR. He has also visited various facilities at the Centre and the project site of BHAVINI.

Shri T.K.Rangarajan, Hon'ble Member of Parliament discussing with Dr. Baldev Raj, Director, IGCAR.

Shri Jayaram Ramesh, Hon'ble Minister of State for Commerce and Power, Govt. of India during discussion with Dr.Baldev Raj, Director, IGCAR, Shri S.K.Jain, CMD, NPCIL and other senior colleagues of the Centre

Delegation from Japan Atomic Industrial Forum headed by Mr.Takuya Hattori, President, Japan Atomic Industrial Forum along with Dr.P.R.Vasudeva Rao, Director, Chemistry, Metallurgy and Materials Groups and other senior colleagues of the Centre and NPCIL

- The Japan Atomic Industrial Forum headed by its President, Mr.Takuya Hattori, visited the Centre during November 27-29, 2008 to hold discussions with the Director and other senior colleagues of the Centre.The team visited various facilities at the Centre.

- Prof. Georges Vendryes, former Executive Director, CEA, Francet and Mrs.Inge Vendryes visited the Centre during December, 2008. They were taken around the Centre and BHAVINI. The student community of IGCAR comprising of Trainee Scientific Officers and Research Scholars had an opportunity to interact with Prof. Vendryes and Mrs Vendryes at Training School Hostel premises at Sadras East.

BITS Practice School
May 26 – July 4, 2008

Twenty four students from BITS Pilani (Pilani and Goa campuses) underwent BITS Practice school for seven weeks at our Centre. Dr. Baldev Raj inaugurated the BITS practice School at IGCAR on May 26, 2008 along with the STIPAC courses. The BITS practice school bridges the professional world with the educational world. The course aims at exposing the students to industrial and research environments, on how the organizations work, to follow and maintain work ethics, study the core subjects and their application in the organization, participate in some of the assignments given to them in the form of projects. The students were from various Engineering disciplines namely, Mechanical Engineering, Electrical & Electronics Engineering, Electronics & Instrumentation Engineering, Computer Science Engineering and other disciplines like Mathematics, Physics and Economics. Students carried out challenging projects from various divisions in line with their discipline. During the period of their stay they visited various facilities at IGCAR, BHAVINI and MAPS. Group discussions, seminars, project work presentation and report writing formed the practice school curriculum. On completion of the practice school, Shri S.C.Chetal Director REG, had an interaction session with the students and distributed certificates to the students.

Prof. Georges Vendryes and Mrs.Vendryes at Training School Hostel premises on December 5, 2008.

Shri S.C.Chetal, Director, REG with BITS students along with senior colleagues of IGCAR

Summer Training Programme in Physics (STIPAC)

May 26 - July 4, 2008

A summer Training Programme in Physics and Chemistry for the year 2008 (STIPAC-2008) with a theme focused on "Physics and Chemistry of Nanomaterials" got up to a jubilant start with Dr. Baldev Raj, Director, IGCAR inaugurating the programme on 26 May, 2008.

During the inaugural session Dr. Baldev Raj exhorted the students to undertake science and technology based research career to build a stronger scientific frontier that would effectively counter several challenging problems bordering environment and energy. This years programme, in which nineteen students from physics and twenty students from chemistry participated, continued till 4 July, 2008. Although the theme was on nanomaterials, the core areas of physics and chemistry were covered by experts in the respective fields including introductory lectures on nuclear reactors. In the afternoon hours the students were imparted hands on experience through project work. In order to enthuse the student participants to take up a career in science, special lectures by eminent educationalists and scientists from leading institutes were arranged. STIPAC 2008 had an interesting additional feature, viz., two lectures that were delivered by former STIC students. The valedictory function held on July 4, 2008 and was presided over by Dr. P. R. Vasudeva Rao, Director, Chemistry and Metallurgy & Materials Groups who emphasized the need for synergy between physics and chemistry in the context of nanotechnology. Prof. P. T. Manoharan, Chief Guest of the function dwelt on some interesting and current research on nanotechnology and distributed the certificates to the students.

Students of Summer Training Programme in Physics and Chemistry with Dr. Baldev Raj, Director, IGCAR and other colleagues of the Centre

Dr. P.S.Goel, President, INAE and former Secretary, Department of Earth Sciences, Dr.Anil Kakodkar, Chairman, Atomic Energy Commission & Secretary, Department of Atomic Energy, Dr.Baldev Raj, Director, IGCAR during the Graduation Day

Graduation Function of the 2nd Batch of BARC Training School at IGCAR

August 30, 2008

The graduation function of the 2nd batch of BARC Training School at IGCAR was held on August 30, 2008 at Sarabhai Auditorium, Homi Bhabha Building, IGCAR. Forty five trainees graduated after successful completion of their training. Dr. P.S. Goel, President, Indian National Academy of Engineering and former Secretary, Department of Earth Sciences graced the occasion as Chief Guest and Dr. Anil Kakodkar, Chairman, Atomic Energy Commission & Secretary, DAE presided over the function. Dr. M. Sai Baba, Head, Strategic and Human Resources Planning Section and Head, BARC Training School at IGCAR welcomed the gathering. Dr. Baldev Raj, Director, IGCAR addressed the gathering. A souvenir featuring the 2nd year of the training programme at IGCAR was released by Dr. Anil Kakodkar and Dr. P.S. Goel received the first copy. In his address Dr. Anil Kakodkar mentioned that human resources development is the most important activity in DAE. He mentioned that Training School program was also bringing the people together from varied backgrounds and binding them together as a family. Some of the Trainee Scientific Officers from 2nd batch voiced their feedback about the courses and their stay at the hostel. Dr. P.S. Goel gave away the prestigious 'Homi Bhabha Prize' to the meritorious toppers from each of the disciplines. He also gave away the course completion certificates to all the graduates passing out. Dr. P.S. Goel also gave away the course completion certificates to "Operation and Maintenance Trainee Scientific Officers" of BHAVINI who have successfully completed their training at BARC Training School at IGCAR. Dr. P.S. Goel addressed the gathering with a very inspiring and thought provoking lecture highlighting the aspects of global warming and emphasized the need for scientists and engineers to work together to achieve breakthroughs. Dr. Vidya Sundararajan, S&HRPS proposed the vote of thanks.

Dr. Anil Kakodkar, Chairman, Atomic Energy Commission & Secretary, Department of Atomic Energy, with BARC Trainees at IGCAR

CEA-DAE Mid year review Meeting

September 11, 2008

A French delegation led by Mr.Y.Kalunzy, Senior Vice-President, International Relations and Cooperation, Nuclear Energy Division, CEA, Franvce visited the Centre to participate in the "CEA-DAE Mid year review meeting" held at IGCAR on 11 September, 2008. Dr.Baldev Raj, Director, IGCAR gave a perspective on the collaborative programmes. There were presentations by senior colleagues on design and safety aspects of Fast Reactors. There were discussions on the status of collaborative projects and areas where bilateral participations are likely. The team also visited various facilities at the Centre and BHAVINI.

French delegation led by Mr.Y.Kalunzy, Senior Vice-President, International Relations and Cooperation, Nuclear Energy Division, CEA, France with Dr. Baldev Raj, Director, IGCAR and other senior colleagues of the Centre

CEA-DAE Coordination meeting

December 2-3, 2008

The 6th CEA-DAE Coordination meeting was held at IGCAR, Kalpakkam during 2-3 December, 2008. The CEA delegation was led by Dr.Alain Bugat, Chairman, CEA and the Indian delegation was led by Dr.Anil Kakodkar, Chairman, AEC. The CEA team visited Fast Breeder Test Reactor, facilities in Safety Group, Fast Reactor Technology Group, Laboratories in Materials Science Division, Structural Mechanics Laboratory, Nuclear Desalination Development Plant and the construction site of Prototype Fast Breeder Reactor. Dr. Alain Bugat, Chairman,CEA and Dr.Anil Kakodkar, Chairman,AEC jointly interacted with the student community of IGCAR comprising of Trainee Scientific Officers and Research Scholars during the visit.

Dr.Alain Bugat, Chairman,CEA, Dr.Anil Kakodkar, Chairman, AEC, Dr. Baldev Raj, Director, IGCAR, Dr. S. Banerjee, Director, BARC and senior colleagues of the Centre with the visiting French delegation

Dr. Alain Bugat, Chairman, CEA, Dr. Anil Kakodkar, Chairman, AEC and Dr. Baldev Raj, Director, IGCAR during the interaction session with students

IGC COUNCIL

Chairman

Dr. Baldev Raj

Dr. Baldev Raj, BE, Ph.D; Distinguished Scientist & Director, Indira Gandhi Centre for Atomic Research is a Member, German National Academy of Sciences, Fellow, Third World Academy of Sciences, Fellow of all Engineering and Science Academies in India. His specializations include materials characterization, testing and evaluation using non-destructive evaluation methodologies, materials development and performance assessment and technology management. He has more than 700 publications in leading refereed journals and books. He has co-authored 12 books and co-edited 30 books and special journal volumes. He has 5 Indian Standards and 16 patents to his credit. He is on the editorial boards of national and international journals. He is Editor-in-Chief of two series of books: one related to NDE Science & Technology and another related to Metallurgy & Materials. He is the past-President of International Committee on NDT. He is currently on the Board of Directors of International Institute of Welding. He has won many awards and honours, notable among them being Life Time Achievement Award of Indian Society for Nondestructive Testing (2004), Indian Welding Society (2004), Jaeger Lecture Award of International Institute of Welding (2004), International Researcher Award of International Committee on NDT (2000-2004), Indian Nuclear Society Award (2004). He is recipient of Padma Shri from Govt. of India (a Civilian honour), Distinguished Alumni Award (2007) of Indian Institute of Science, Prof. Jai Krishna Memorial Award-2008 of Indian National Academy of Engineering, Distinguished Materials Scientist for the year 2009 from MRSI, FICCI Annual Award for Outstanding Research in Materials Science (2007-08), etc.. He is member, Global Energy International Prize Committee (Russia), National Nanotechnology Advisory Board of South Africa; Chairman of India-Brazil-South Africa Initiative on Nano Science & Technology. His interest includes technology management, heritage, philosophy, religion and education.

Members

Dr. P. Chellapandi

Dr. P. Chellapandi, B.E (Hons), M.Tech, Ph.D is Outstanding Scientist and Director, Safety Group and Associate Director, Nuclear Engineering Group. He joined Department of Atomic Energy in 1978 through BARC Training School. He has been engaged in the design and development activities of 500 MWe Prototype Fast Breeder Reactor (PFBR) since its inception. He has contributed significantly for PFBR over a wide spectrum of design activities, viz., conceptualization, consolidation of failure modes, development of sophisticated computer codes and analysis methodologies, detailed analysis, design confirmation and validation of components, preparation of preliminary safety analysis reports, execution of R&D activities ensuring the robustness of design. His activities include specification of manufacturing tolerances based on detailed analysis and development of innovative design features for the future fast breeder reactors beyond PFBR, planned by the department. He has 380 publications to his credit. He is a Fellow of Indian National Academy of Engineering. He has received the Homi Bhabha Science and Technology Award for the year 1997, Indian Nuclear Society Award and National Design Award in Mechanical Engineering in 2006, DAE Group achievement award for Design of PFBR Main Vessel and Safety, 2006, Agni Award for Excellence in Self-reliance - DRDO-2007 and DAE Group Achievement Award for Seismic Design and Qualification of PFBR Components,2007 for his outstanding contributions in the design of Fast Breeder Reactor Components. He is also a Professor of Homi Bhabha National Institute.

Shri S.C. Chetal

Shri S.C. Chetal graduated in Mechanical Engineering from Delhi College of Engineering in 1970. After graduating from the 14th Batch of BARC Training School, he joined IGCAR in 1971. Since 1971, he has been engaged in the field of fast reactor engineering. He has made contributions towards design of FBTR sodium systems and components. At present, he is Distinguished Scientist & Director, Reactor Engineering Group, IGCAR. He has made contributions towards the material selection, manufacturing technology, R&D, design and construction of 500 MWe Prototype Fast Breeder Reactor. He is member of many professional institutions and fellow of Indian National Academy of Engineering. He is a recipient of Indian Nuclear Society INS Award 2003 for contributions towards nuclear related high technology, National Design Award-2007 by Institution of Engineers, 2003 VASVIK Award, Agni Award for Excellence in Self-reliance by DRDO for titanium sponge production, and Certification of Appreciation by IAEA towards fast reactor technology. His interests include pressure vessel and materials technology. He has to his credit 350 publications in Journals/Symposium/ Conferences. He is on the Board of BHAVINI.

Shri R.N. Jayaraj

Shri R.N. Jayaraj, a Mechanical Engineer graduated from Osmania University, is presently the Chief Executive of Nuclear Fuel Complex (NFC), Hyderabad. After successful completion of one-year orientation course in Nuclear Engineering from the 17th batch of BARC Training School, he joined Atomic Fuels Division of BARC and contributed in the production of metallic uranium fuel assemblies for CIRUS reactor and development of fuel assemblies for DHRUVA reactor. After his transfer to NFC, he played a key role in establishing the assembly plant and successfully fabricated all the core sub-assemblies, for the first time in India, required for FBTR. He was instrumental in scaling up of production of fuel bundles required for all the nuclear power reactors, thus consistently meeting the requirements of Nuclear Power Corporation of India Limited (NPCIL). He has to his credit the indigenous development of various equipment for critical processes involving welding, machining centers and assembly stations, thus creating a strong base for establishing self-reliance in nuclear fuel manufacturing. He played pioneering role in standardizing the manufacturing processes for the fuel bundles required for 540 MWe Pressurized Heavy Water Reactors (PHWR). He served the Department for the last 34 years in various capacities and gained rich experience in development and production of fuel for Thermal Research Reactors and Power Reactors. Shri Jayaraj, besides being a Member of IGC Council, is also on the Boards of Uranium Corporation of India Limited (UCIL) and Indian Rare Earths Limited (IREL). He is also the Chairman of the Hyderabad Chapters of Indian Nuclear Society (INS) and Indian Society for Non-Destructive Testing (ISNT). He is recipient of 'Engineer of the Year' Award - 1994 from Institution of Engineers and Indian Nuclear Society Award - 2006.

Shri H.S. Kamath

Shri H.S. Kamath,B.E (Metallurgy), is a Distinguished Scientist and Director of the Nuclear Fuels Group in BARC. He has been associated with the development of plutonium bearing nuclear fuels for the last 35 years, which started with the fabrication of fuel for 'PURNIMA' in 1970-1972. His main area of work is in the development of uranium-plutonium mixed oxide (MOX) fuels for nuclear power programme. He has made important contributions in this field both in laboratory scale as well as industrial scale activities. His most important contribution has been the setting up of the industrial scale MOX fuel fabrication plant at Tarapur. Shri Kamath is the recipient of Indian Nuclear Society Award for the year 2003 in recognition of his outstanding contributions in the field of nuclear fuel fabrication. Shri H.S. Kamath is the recipient of DAE Lifetime Achievement Award for the year 2007.

Prof P.K. Kaw

Prof P.K. Kaw, Ph.D (Physics) from IIT Delhi, is the Director of Institute for Plasma Research, Gandhinagar since 1986. The Institute has pioneered plasma physics research in India which includes design, development and fabrication of two tokamaks, ADITYA and SST 1, research work on a large number of fundamental plasma physics experiments and work on industrial applications of plasma physics. ADITYA was the first tokamak to discover intermittency in edge and SOL turbulence. The Institute also spearheaded India's case for participation in ITER and is now the nodal domestic agency for ITER. Prof. Kaw's personal research work in this period includes physics of intermittency, drift waves and anomalous transport, MARFES, solitons, laser fusion, anomalous stopping effects, dusty plasmas, nonneutral plasmas, quark gluon plasmas, etc. Earlier he had held positions like Princeton University Plasma Physics Laboratory Research Staff and Professor at Physical Research Laboratory, Ahmedabad before taking over as Director, Plasma Physics Program in 1982. He played a key role in initiating tokamak physics program in India. He has more than 294 research papers to his credit in international journals. He has several honours and delivered important lectures. Artsimovitch Memorial lecture at the IAEA Fusion Energy Conference in 1992, Invited talk on International Energy Research at the APS Centennial celebrations (1999) in Atlanta, Georgia and a presentation on the International impact of USDOE Fusion Theory Program to the NSF-NRC Panel Chaired by C F Kennel, San Diego are just a few of them to name. Prof Kaw was also the Chairman of the International Fusion Research Council (IFRC) of IAEA from 2000 to 2007 and is currently the Chairman of the Science & Technology Advisory Committee [STAC] of the ITER Governing Council.

Shri H.S. Kushwaha

Shri H.S. Kushwaha, B.Sc., M.Tech.(IIT, Kanpur), is presently the Director of Health, Safety and Environment Group at BARC. He has made significant and important contributions in the design and analysis of nuclear structures, components and piping of Indian Pressurised Heavy Water Reactors (PHWR). He has done pioneering work in the area of seismic design and analysis of 540 MWe PHWR being built at Tarapur, Maharashtra. He has developed several finite element computer programmes in the field of structural mechanics, heat transfer and fluid mechanics. He has developed an improved finite element method using upwinding schemes to solve three dimensional advection-diffusion equation. He is an active member of Project Design Safety Committee of PHWRs/FBR, Civil Engineering Safety Committee and Safety Review Committee for Operating Plants (SARCOP) constituted by AERB, Mumbai. He has published around 400 papers/reports in national and international journals.

Shri Y.C. Manjunatha

Shri Y.C. Manjunatha, Director, Engineering Services Group of Indira Gandhi Centre for Atomic Research, Kalpakkam, is a M.Tech. in Electrical Engineering from IIT, Madras and belongs to the 16th batch of BARC Training School, Department of Atomic Energy. He steers one of the largest multidisciplinary groups in the Centre which focuses on providing reliable and robust services through cutting edge technologies and methodologies. Some of his major contributions are development and sustenance of infrastructural works of IGCAR & GSO involving civil, electrical, air conditioning and ventilation, communication, workshop and QA activities. He has published more than 10 papers.

Shri S.D. Misra

Shri S.D. Misra, B.E (Electrical & Mechanical Engineering) is presently the Director of Nuclear Recycle Group at BARC. He is from 13th Batch of BARC Training School and has been involved in the Back End activities of Nucler Fuel Cycle. He was a member of the team that pioneered setting up of the first Vitrification Plant in the country. Shri Misra was responsible for design and construction of vitrification plants at Trombay & Kalpakkam. He was also instrumental in solving all the problems faced in the first resin fixation facility at Narora Atomic Power Project and made it operational. Shri Misra has participated in a number of symposia and seminars on radioactive waste management and has also worked as an expert on various technical committees of International Atomic Energy Agency. Presently he is a Member of International Radioactive Waste Technical Committee (WATEC) of IAEA. He has also served as Director, Purchase & Stores, DPS. In this capacity, he has successfully overcome the problems of technology control regime and made available some of the critical stores for the programmes of the Department. Presently, as Director, Nuclear Recycle Group, he is holding the responsibility of setting up and operation of Reprocessing and Waste Management Plants at various sites in the country.

Dr. Prasenjit Mukherjee

Dr. Prasenjit Mukherjee, IAS had his early education in Orissa. He passed his B.A. Honors in English in 1974, securing the First position in first Class with Distinction in other subjects. He was awarded the University Gold Medal by the Utkal University for securing the First position in M.A. English in 1976. From 1977 to 1980 he served as a Lecturer in Berhampur University, Orissa. He appeared for the Civil Services examination and was selected to the Indian Audit & Accounts Service in 1980. In 1991, he went on deputation to Government of India in the Ministry of Commerce where he worked as Director (Finance & West Europe). Under the Colombo Plan, he was selected and deputed to the University of Manchester Institute of Science & Technology (UMIST) in U.K. in 1995 from where he successfully completed his M.Sc. degree in Project Management. On reversion to the department, he served as Accountant General (Audit) II, Lucknow, U.P., from November 1996 to June 2000, and as Accountant General (A & E), Karnataka, Bangalore from July 2000 to December 2004. In December 2004, he went on deputation to the Department of Space as Joint Secretary (Finance) and in April 2008, he joined the Department of Atomic Energy as Joint Secretary (R & D). Recently, Dr. Mukherjee was awarded the Ph.D. degree from the National Law School of India University at Bangalore on the subject of disinvestment in India.

Shri R. Natarajan

Shri R. Natarajan, a Chemical Engineer from the Annamalai University, joined the Department of Atomic Energy in 1975. He is presently the Director, Reprocessing Group in IGCAR. Under his leadership, the CORAL facility, for establishing the process technology for the reprocessing of fast reactor fuels, was designed, erected and commissioned. He led the team which has successfully completed the reprocessing of fast reactor spent fuel, with a burn-up of as high as 155 GWd/t with Plutonium rich fuels, for the first time in the world. As Director of Reprocessing Group, he is responsible for the R&D activities of fast reactor fuel reprocessing and setting up of Demonstration as well as the commercial PFBR fuel reprocessing plants. His specialization is in the design process flow sheets and plant design. He has also experiences in the design and operation of Thorium-Uranium cycles. He has participated in the irradiated thorium fuel reprocessing campaigns at the Reprocessing Development Laboratory and the Uranium-233 recovered is used as fuel for the reactor KAMINI. He has interests in solvent extraction process modeling, extraction equipment design, design of feed clarification systems of high active solutions, acid recovery systems, system designs of radioactive offgas circuits and ventilation design of radiochemical plants. He has over ninety five technical presentations and publications to his credit. He has won prestigious NOCIL Award for Excellence in Design and Development of Process Plant and Equipment for the year 2005 for his contribution in the development of fast reactor fuel reprocessing. He is also the recipient of Indian Nuclear Society's INS award for the year 2006 for his contributions in Nuclear Fuel Cycle technologies.

Shri A.L.N. Rao

Shri A.L.N. Rao, B.E.(Electrical), is presently the Chairman & Chief Executive of the Heavy Water Board. He joined Bhabha Atomic Research Centre as 15th batch trainee in the year 1971. He was awarded Junior License Certificate in 1974 and took independent charge of the unit consisting reactor, turbine, generator and associated utilities and control systems of TAPS. Shri A.L.N. Rao participated in the first refuelling operations which consisted of transferring the irradiated fuel bundles from the reactor core to fuel storage pool and loading the fresh fuel bundles from storage pool into the reactor under 60 feet of water. He had also replaced the core components which was a challenging task. In the year 1978, he obtained Senior License Certificate and took independent charge of the complete plant in shifts. Shri A.L.N. Rao moved from Nuclear Power Board to Heavy Water Board in the year 1984. He closely followed up the project activities of the Captive Power Plant of Heavy Water Plant (Manuguru). In the year 1987 he took over as Operation Manager of Captive Power Plant having capacity to generate 265 x 3 T/hr of superheated steam and 3 x 30 MWe of electricity generation. He assumed charge as General Manager of the complete Heavy Water Plant (Manuguru), which is the largest heavy water producing plant in India, in the year 1998. He became Associate Director (Projects/Energy & Services) in the year 2003 at the Central Office and took charge as Director (Energy & Services/Operation) in the year 2004. In 2005 he was designated as Executive Director (Projects/Energy & Services). During this period, he formed Energy Cells at every Plant with common monitoring at Corporate office. The Specific Energy Consumption had come down to 32 GJ/Kg. of Heavy Water produced during this period. He discharged the duties as the Secretary of the Heavy Water Board. He coordinated all activities related to export of Heavy Water to South Korea and the Republic of China. As Management Representative for Quality Management Systems as per ISO 9001, he followed up all the activities and obtained ISO 9001 Certificate for Board Office.

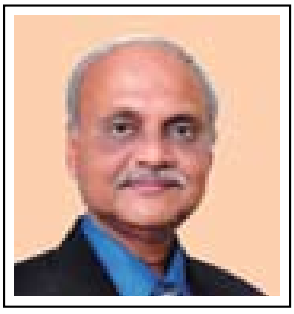

Shri R.K. Sinha

Shri R.K. Sinha, B.E (Mechanical Engineering), is presently a Distinguished Scientist, Director of Reactor Design and Development Group, and Director of Design Manufacturing and Automation Group at BARC. He is a nationally and internationally recognised expert in the area of nuclear reactor technology. He has handled several major assignments relating to the Indian research and power reactors. In particular, he has specialised in design, development and safety related activities relating to coolant channels of heavy water reactors. He is currently guiding the design and development of the innovative Advanced Heavy Water Reactor and Compact High Temperature Reactor. Shri Sinha has received several awards and honours including the Homi Bhabha Science and Technology Award, VASVIK Award, Indian Nuclear Society Award and DAE Special Contributions Award. He is a Fellow of the Indian National Academy of Engineering.

Shri G. Srinivasan

Shri.G. Srinivasan is a mechanical engineer from the 18th batch of BARC Training School. He joined FBTR project as a designer in 1975, and participated in the design, fabrication and installation of Reactor Assembly Components. He moved over to O&M in 1983. After holding the positions of Senior Engineer (Planning) & Senior Engineer (Technical), he took over as Technical Services Superintendent and later as AD (O&M). He is Director, ROMG since Sep 2008.

Shri P. Swaminathan

Shri P. Swaminathan graduated with honours degree in Electronics & Communication Engineering from Regional Engineering College, Tiruchirapalli in 1971. He has obtained Gold medal from University of Madras. After undergoing one year course in Nuclear Science & Engineering from BARC Training School. Shri P. Swaminathan joined Indira Gandhi Centre for Atomic Research in 1972. He further underwent one year course in Main frame system from International Honeywell Bull Training Institute, Paris. Shri P. Swaminathan is the main architect for the design, development, installation and commissioning of Fault Tolerant Safety Critical Real Time Computer System for Fast Breeder Test Reactor. As Director of Electronics & Instrumentation Group, Shri P. Swaminathan is actively engaged in the development of Safety Instrumentation, Full scope Training Simulator and Knowledge Management System for Fast Breeder Reactor Programe. Shri P. Swaminathan is a Fellow of Institution of Engineers and also holds Master Degree in Management Science. He actively interacts with project students and is also Distinguished visiting professor of INAE. He has over 50 publications in International journals/seminars. Also as Chairman, Hospital Management Committee, Shri P. Swaminathan ensures the smooth functioning of Health Care System.

Shri Umesh Chandra

Shri Umesh Chandra is Senior Executive Director (Safety and Knowledge Management) in NPCIL. His areas of responsibilities include Reactor Safety & Analysis of design, Health, Safety & Environment of nuclear power plants in operation and construction, Software Quality Assurance, Training Simulators, Knowledge Management, IT infrastructure and Communications. He has been responsible for establishing R&D infrastructure and activities in NPCIL, including setting up an R&D Centre at Tarapur and a computer based C&I lab at NPCIL HQ. He has been responsible for design of Control and Instrumentation of 540 MWe PHWRs at Tarapur. Earlier at BARC, he has been a developer of computer based control and monitoring systems of several nuclear power plants. He has also been responsible for establishment of a group engaged in Independent Verification and Validation of Digital Systems in NPCIL. He has contributed in preparation of safety guides of AERB for safety systems and computer based I&C systems and also in safety reviews of projects. Shri Umesh Chandra is a Distinguished Scientist and a graduate of IIT, Kanpur.

Shri G. Vaidyanathan

Shri. G. Vaidyanathan, graduated in Engineering from Delhi University in 1971 and joined IGCAR in 1972 after completion of one year orientation course in BARC Training School. Later he acquired a Post Graduate Degree in Operation Management. Presently he is an Outstanding Scientist and Heads the Fast Reactor Technology Group at IGCAR as Group Director. Since 1972, he has been actively involved in the field of Fast reactor design, thermal hydraulic analysis and experiments. He has made significant contributions to numerical simulation of heat transfer and fluid flow processes in sodium cooled fast reactors. He has meticulously planned and carried out R&D for the thermal hydraulics of Fast Reactors. He has also contributed significantly as member of the IGCAR safety committee. He was instrumental in setting up the Steam Generator Test Facility at IGCAR . He has to his credit about 185 publications in journals/conferences and has co-authored one book.

Dr. P.R. Vasudeva Rao

Dr. P.R. Vasudeva Rao, is a Distinguished Scientist and presently Director of Chemistry Group as well as Metallurgy and Materials Group in IGCAR. He obtained his Doctorate degree in Inorganic Chemistry from Bombay University in 1979. He has played an active role in shaping the Radiochemistry Programme of IGCAR to its current status. His research interests cover a wide range of areas such as development of alternate extractants and resins for actinide recovery solvent extraction, third phase formation, thermodynamics, applications of photochemistry in actinide separations, development of pyrochemical and other non-aqueous processes for recovery of actinides and rare earths, thermochemical studies on nuclear materials, application of microwaves in synthesis of nuclear fuels and other ceramic materials, nuclear fuel cycle, fuel behaviour in reactors, burn-up measurements, and non-destructive assay. He has published more than 150 papers in reputed international journals apart from guiding several research scholars for their doctorate degrees. He is a life member of Indian Nuclear Society, Materials Research Society of India, Society for Advancement of Electrochemical Science and Technology, Indian Association of Nuclear Chemists and Allied Scientists (IANCAS), and President of the Southern Regional Chapter - IANCAS. He has been awarded the MRSI Medal in 1998 and the INS award for the year 2007. He is also a Fellow of Tamil Nadu Academy of Sciences. He is a member of the International Advisory Board of the Journal of Nuclear Materials.

Dr. V. Venugopal

Dr. V. Venugopal, M.Sc.,Ph.D, is presently an Outstanding Scientist and the Director of Radiochemistry and Isotope Group at BARC, Mumbai, and Officer-in-charge, Nuclear Material Accounting and Control (NUMAC) cell of DAE. He is currently a member of Standing Advisory Group for Safeguard Implementation (SAGSI) to advice Director General IAEA on Safeguards Matters. He is a specialist in the field of thermal/ thermodynamics of plutonium based fuels at high temperature, chemical quality control of fuel, X-ray and solid state chemistry and oversees Radioisotope and Radiation Technology Programs at BARC. He is the chairman of Radiation Technology and Applications Committee (RTAC) of BRNS and a member of BRIT board. He is a member of safety committees such as OPSRC and CFSRC under BSC at BARC. He has to his credit more than 300 publications in international journals. Widely acclaimed as an expert in the area of thermodynamics, Dr. Venugopal is the President of Indian Thermal Analysis Society (ITAS) and Vice President and editor, INS news of Indian Nuclear Society (INS). He is also a member of several professional bodies IANCAS, NAARRI, ISAS, ISEAS, ISMAS, MRSI and Hindi Vigyan Parishad. He has received many awards including the Netzsch-ITAS award in 2001, ISCAS silver medal in 2002 and MRSI medal for 2003-04 and INS award for 2005.

Members of IGCSC and Activities of Various Groups

Chairman

Dr. Baldev Raj
Director, IGCAR

Chemistry Group

Dr. P.R. Vasudeva Rao
Director

Dr. T. Gnanasekaran
Head, LM&SCD

Dr. V. Ganesan
Head, MCD

Shri K.C. Srinivas
Head, CFD

Dr. T.G. Srinivasan
Head, FChD

The Chemistry Group is responsible for carrying out R & D to provide inputs with respect to all the chemistry aspects of the fast reactor and its fuel cycle. Besides the R & D activities, the Chemistry Group also provides extensive analytical support using a wide range of analytical techniques to all the programmes at Kalpakkam. The Chemistry Group has also specialized in setting up of facilities for experiments with radioactive or air-sensitive materials, and in indigenous development of chemical instrumentation. The areas of R & D in Chemistry Group include sodium chemistry, chemistry of un-irradiated as well as irradiated fuel materials, development of fuel cycle, high temperature chemistry, analytical chemistry, spectroscopy and more recently, boron chemistry. Chemistry Group also has been developing instrumentation in support of the R & D programme. Development of sensors for PFBR and sensors for environmental applications, cover gas purification system for PFBR, development of radionuclide traps for PFBR, development of cleaning and decontamination techniques for fast reactor components, development of Laser Induced Breakdown Spectroscopy and X-ray absorption based techniques for on-line monitoring of plutonium streams in reprocessing plants, development of technology for production of plutonium rich fuels and minor actinide containing fuels through sol-gel route and development of sodium bonding for metallic fuels are some of the R & D programmes on the anvil. Recent achievements include successful testing of the electrochemical hydrogen sensor in Phenix reactor in France and production of enriched elemental boron.

Electronics and Instrumentation Group

Shri P. Swaminathan
Director

Shri S. Ilango Sambasivan
Head, EID

Shri N. Murali
Head, RTSD

Shri B. Saha
Head, IIS

Dr. M. Sai Baba
Head, SIRD

Shri S.A.V. Satya Murty
Head, CD

Dr. A. Vijaya
Head, MD

The Electronics and Instrumentation Group is actively engaged in the development of Strategic Safety Instrumentation Systems for Fast Breeder Reactor Programme such as Real Time Computer Systems, Safety Logic Systems, Expert systems, Distributed Digital Control Systems etc. Unique Instrumentation systems such as Electromagnetic Time Domain Survey System is also being developed to detect deeply buried uranium ore. Highly reliable Instrumentation systems are being developed using modern VLSI design tools, thermal design tools, EMI/EMC design tools etc. Application software packages are being developed using powerful CASE TOOL. Development process is ISO certified. A Full scope Replica Type Training Simulator is being developed for training the operators of Prototype Fast Breeder Reactor. Walk-through of different areas of the reactor is being developed using PDMS package. State of the art Visualisation center with stereoscopic projection is being set up. Intranet based Knowledge Management System is being managed. Simplicity in instrumentation is being realised through the innovative programme on creation of pulsating sensors for diverse parameters, enabling development of completely indigenous plant monitoring and surveillance systems, rapid analytical and diagnostic tools. Security electronics systems are constantly being updated for Kalpakkam site. Biometric hand geometry based attendance system is recently commissioned. The group has Scientific Information Resource Division which is in pursuance of its objective of providing efficient and effective information service to the Scientists, Engineers, TSOs and Research Scholars at Kalpakkam Campus. The group is also responsible to ensure satisfactory health services to the residents of Kalpakkam and Anupuram Townships.

Engineering Services Group

Shri Y.C. Manjunatha
Director

Shri A. Jyothish Kumar
Head, ESD

Shri K. Manoharan,
Deputy Director, GSO

Shri A.S.L.K. Rao
Head, AC&VSD and CWD

Shri C. Sivathanu Pillai
ACE, Civil

Dr. B. Venkatraman
Head, QAD

Shri N. Vijayan Varier
Head, TC & QCS

Engineering Services Group is responsible for providing quality services pertaining to Civil Engineering, Electrical Engineering, Voice Communication Systems, Air-conditioning & Ventilation Systems, Material Handling Equipments, Central Workshop activities, Quality Control & Quality Assurance and Testing. The Group also coordinates the telecommunication requirements of the Centre. The Group has a mandate to establish additional infrastructure requirements so as to meet Design, R&D and operational objectives of IGCAR. The Group has expert teams with capability to design, engineer and execute systems under their jurisdiction. Electricity, water, quality-air and other services are being extended to other units of DAE located at Kalpakkam. The nature of work involves interaction with several State Government and Central Government Organizations.

Fast Reactor Technology Group

Shri G. Vaidyanathan
Director

Shri P. Kalyanasundaram
Associate Director, FRTG

Shri K.K. Rajan
Head, SFD

Dr. C. Anand Babu
Head, ST&THD

Shri B. Krishnakumar
Head, C&IDD

The Fast Reactor Technology Group is actively involved in development and testing of scaled models, prototype components for PFBR, sodium pumps and instrumentation and process development for boron enrichment and separation technologies. The Group has sodium and water test facilities, 5.5 MWt steam generator test facility and boron enrichment plant. FRTG carries out heat and mass transfer studies in water loops, liquid sodium and cover gas and development of sodium components like cold trap, sodium level and flow sensors and leak detectors. FRTG also carries out testing of control rod mechanisms, inflatable seals and full scale fuel handling machines in air and sodium. Further studies are carried out for pressure drop and cavitation in fuel and other subassemblies and reactor assembly flow patterns. The steam generator test facility is used for carrying out detailed temperature measurements, study of transient response and thermo hydraulic instability of sodium heated once-through steam generator. The Group is also responsible for vibration testing of steam generator, intermediate heat exchanger, rotating machinery etc. In short, the Group is working on all engineering aspects of FBRs.

Metallurgy and Materials Group

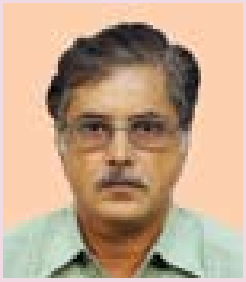

Dr. P.R. Vasudeva Rao
Director

Shri K.V. Kasiviswanathan
Associate Director,
GRIP and Head, PIED

Dr. K. Bhanu Sankara Rao
Associate Director
MDCG and Head, MMD

Dr. S. Venugopal
Head, RIRD

Dr. T. Jayakumar
Head, NDED

Dr. C.S. Sundar
Head, MSD

Dr. A.K. Bhaduri
Head, MTD

Dr. R.K. Dayal
Head, CSTD

Dr. M. Vijayalakshmi
Head, PMD

Metallurgy and Materials Group, IGCAR has a comprehensive R&D programme on various facets of Materials Science & Engineering ranging from basic research in materials science to pursuit of advanced materials technologies in areas that have a direct bearing on FBRs and associated fuel cycle technologies. The R&D programs on Materials Technologies include the development of special alloys and welding consumables, optimisation of fabrication routes, characterisation of microstructural and mechanical properties using a variety of techniques, corrosion and bio-fouling studies, development and application of specialised NDE techniques, irradiation experiments, and development of technologies for robotics and remote handling.

Basic studies in materials science encompasses a spectrum of activities that include studies on structural, electronic, optical, superconducting and magnetic properties of novel materials at low temperature, high pressures and magnetic fields; ion beam simulation of radiation damage to structural materials using accelerators; computational materials science; studies on nanomaterials, and the development and applications of SQUIDs based sensors.

Some of the recent significant contributions of the Group include PIE of FBTR fuel pins at high burn-up (155 GWd/t), development of activated flux TIG welding process, indigenous development of ODS alloys and welding consumables, and the commissioning of an unique MEG facility. The research contributions of the Group are well recognised in fields as diverse as life prediction under creep and creep-fatigue conditions, characterisation of microstructures by NDE techniques, welding science and technology, and basic research in materials science.

Reactor Engineering Group

Shri S.C. Chetal
Director

Dr. P. Chellapandi
Associate Director, NEG

Shri P. Puthiyavinayagam
Head, RCD

Shri P. Selvaraj
Head, MHD

Shri S. Raghupathy
Head, CH & MD

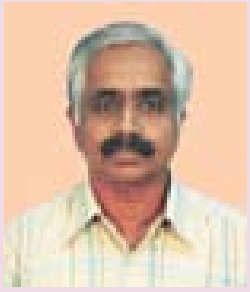

Shri V. Balasubramaniyan
Head, HTSD

Shri K. Madhusoodanan
Head,PPCD

Dr. P. Mohanakrishnan
Head, RPD

Shri C. Sivathanu Pillai
Head, CED

Reactor Engineering Group (REG) is responsible for the design of 500 MWe Prototype Fast Breeder Reactor. Design of Nuclear Steam Supply System is carried out in-house. For Balance of Plant, design coordination is carried out by REG while the consultants are assigned the design work. REG is responsible for getting the design clearance of 500 MWe FBR from AERB. R&D coordination towards FBR and execution of R&D for structural mechanics is also the responsibility of the Group. REG provides the design support to FBTR. REG has acquired expertise in design of fast reactor. As a spin-off, structural mechanics expertise is being provided for non-reactor activities. REG is presently engaged in preparation of the blueprint for the future FBRs to provide enhanced safety and improved economics. This includes safety criteria, innovative design features, R&D needs and manufacturing technology needs.

Reactor Operations and Maintenance Group

Shri G. Srinivasan
Director

Dr. V. Ramanathan
Associate Director, O&M

Shri K.V. Suresh Kumar
Head, ROD

Shri B. Ananthapadmanaban
Head, RMD

Ms. S. Usha
Head, TSD

Shri P.R. Swaminathan
Head, PPD

ROMG is responsible for safe operation of Fast Breeder Test Reactor (FBTR) and KAMINI reactor within the limits given in technical specification documents. The group also takes part in the operational safety review of PFBR Project documents. The Training section of the group, besides training O&M staff of FBTR and KAMINI, is also responsible for training the O&M staff of PFBR and future FBR's. Progressive modifications in FBTR to increase its availability and for gaining newer experience in operation, utilizing the reactor for irradiation of advanced fuels and materials for fast reactors and conducting safety related experiments form a major part of ROMG's activities

Reprocessing Group

Shri R. Natarajan
Director

Shri. V. Sundararaman
Head, FRPD

Dr. S. B. Koganti
Head, RRDD

Shri M. Venkataraman
Head, RPOD

Shri P. Ramkumar
Head, RPSD

Shri A. Ravishankar
Head, RPDD

The Reprocessing Group (RpG) of IGCAR is responsible for the development of Fast reactor fuel reprocessing technology and construction of the reprocessing plants. RDL has two hot cell facilities: In one of them,U-233 was recovered from irradiated thorium rods on campaign basis and used as fuel in KAMINI reactor and in FBTR (as PFBR test fuel). The other hot cell facility, called, CORAL (COmpact facility for Reprocessing Advanced fuels in Lead cells) commissioned in 2003, is a test bed for validating the process flow sheet and scaling up of equipment designs for fast reactor fuel reprocessing, by processing the FBTR fuel itself. CORAL has already processed in several campaigns mixed carbide fuels irradiated in FBTR with 25, 50, 100 and 155 GWd/t burn ups. This has provided valuable experience to the design of Demonstration Fast Reactor Fuel Reprocessing Plant, DFRP, in which the FBTR fuels will be reprocessed on a regular basis. DFRP, which will also demonstrate the reprocessing of PFBR fuel subassemblies, is slated for commissioning by 2009. RpG is also carrying out the design of the reprocessing plant, FRP, for reprocessing spent fuels of PFBR on commercial basis. Various R&D activities are being carried in the Reprocessing Development Laboratory. Engineering scale testing of equipment and systems are done here before installing in for hot cell. Chopper, dissolver, feed clarification equipment, centrifugal extractors are few of the important equipment developed at RDL. Apart from equipment development, research is undertaken for understanding and solving various process and chemistry problems of fast reactor fuel reprocessing such as, mathematical modeling of solvent extraction of the complex U-Pu system, efficient solvent management, development of online monitoring of Pu for process control, liquid flow metering in high radioactive fields etc.

Safety Group

Dr. P. Chellapandi
Director

Dr. R. Indira
Head, RSD

Shri N. Kasinathan
Head, SED

Safety Group consists of Safety Engineering Division, Radiological Safety Division and Environmental & Industrial Safety Section.

Safety Engineering Division is engaged in the simulated experimental studies and development of computer codes for severe accident analysis specific to Fast Breeder Reactor situations. This includes investigation of core disruptive accident scenarios, sodium fire, molten fuel coolant interaction, core catcher, post accident heat removal capabilities and fire hazard analysis.

Radiological Safety Division is mainly responsible for the research and development activities in radiation safety. The division provides health physics services for all the radioactive facilities in IGCAR. Studies on criticality safety, radiological safety, shield design, bio-dosimetry, concrete ageing, environmental impact, atmospheric dispersion, aerosol transport, meteorological measurement and development of radiation detectors, pulsed neutron generator for actinide assay and decision support system for radiological emergencies are some of the key areas of research being carried out presently.

Environmental & Industrial Safety Section provides industrial safety services to all the facilities at IGCAR. The section also carries out R&D in the domain of biodiversity, biofouling, sediment characterization, Phytoplankton (plants) and Zooplankton (animals) studies.

The group organizes public awareness programs on radiation safety and nuclear energy. It also carries out training and awareness programs on industrial, radiation and fire safety to occupational workers.

Fast Reactor Fuel Cycle Facility

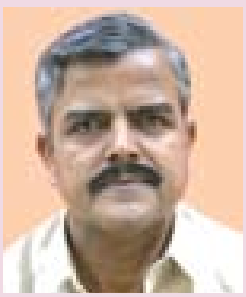

Shri P.V. Kumar
Project Director

Work on design of the Fast Reactor Fuel Cycle Facility (FRFCF) to close the fuel cycle of Prototype Fast Breeder Reactor (PFBR) is in progress. The work is being piloted by IGCAR with technical support from BARC and NFC. Revised financial sanction for the preparatory project for development of site infrastructure and engineering of FRFCF has been obtained and the work is in progress. Approval of AERB for the site has been obtained. Technical investigations of the site like geotechnical investigations, hydro-geological studies and estimation of design basis flood level have been completed. Basic infrastructure like approach roads, construction power supply system, and storage/construction office space is being created at the site to reduce the lead time required to commence the construction work once the FRFCF project is sanctioned. Review of the preliminary safety analysis report by Project Design Safety Committee for FRFCF and specialist working groups is in progress. The detailed project report and detailed design are planned to be prepared with assistance from consultants. Process of appointment of consultants is in progress. Detailed project report for FRFCF is planned to be submitted for financial sanction during the year 2009-10.

Planning Division

Smt. Uma Seshadri
Head, PD

Planning Division is responsible for budget monitoring and control of Capital projects of the Centre under R&D, I&M and Power Sectors. Being the nodal agency it has to closely coordinate between Project Coordinators, Accounts, Purchase and Stores for meeting the financial milestones. In addition, it interacts regularly with DAE for the matters related to approvals, financial sanctions, clarifications, reports and also provide inputs to DAE for queries raised in Parliament, Planning Commission, Finance Ministry and Department of Science and Technology etc. It also coordinates with BARC, NFC, RRCAT & VECC for obtaining their support for the capital projects executed by them for the Centre. In order to ease the work functions in Administration and Accounts wings, several online services were made available in the intranet for use by the officials of the Centre. With a view to implementing integrated approach towards office automation of financial, purchase, stores and administration and accounts activities, a work flow automation system has been designed and action for the procurement & installation of the system is in progress.

Strategic and Human Resources Planning Section

Dr. M. Sai Baba
Head, S &HRPS

The section has the mandate of planning for the Strategic and Human Resource needs of the Centre which involve: Planning and running the training school programs at Training School; Collaborative projects with various R&D Organizations and Academic Institutes; Compilation of technical reports on important activities of the Centre; interacting and coordinating with National and International delegations; Assessing and projecting the human resource needs of the Centre for effective deployment and utilization; Interacting with the research scholars at the Centre; Planning and organizing meetings related to human resource and personality development.

Madras Regional Purchase Unit

Shri K. Balachander
Regional Director, MRPU

Material Management activities for IGCAR and General Services Organisation are taken care by Madras Regional Purchase Unit which comes under Directorate of Purchase & Stores of Department of Atomic Energy. Procurement and payment to suppliers are carried out at Chennai and inventory and accounting are carried out by Central Stores at Kalpakkam. Total expenditure for purchase of material and equipment in the calendar year 2008 has crossed 100 Crores. Some of the major equipment for which orders have been placed are Neutron Generator (Linac), Scanning Electron Microscopes and Thermal Ionisation Mass Spectrometer. Timely action taken by MRPU has resulted in excellent compliance of expenditure budget targets.

Administration and Accounts

Shri V. Dayalan
Chief Administrative Officer

Shri S. Mani
Joint Controller (Finance & Accounts)

Shri R.G. Raghavan
AO(R&SR), Secretary, IGCSC

LIST OF IMPORTANT ABBREVIATIONS

AERB	*Atomic Energy Regulatory Board*
BARC	*Bhabha Atomic Research Centre*
BARCF	*BARC Facilities*
BHAVINI	*Bharatiya Nabhikiya Vidyut Nigam Limited*
C&IDD	*Components & Instrumentation Development Division*
CDPS	*Central Data Processing System*
CERMON	*Continuous Environmental Radiation Monitoring Network*
CG	*Chemistry Group*
CORAL	*COmpact facility for Reprocessing Advanced fuels in Lead cell*
CSTD	*Corrosion Science and Technology Division*
CWD	*Central Workshop Division*
DFRP	*Demonstration Fast Breeder Reprocessing Plant*
EID	*Electronics & Instrumentation Division*
EIG	*Electronics and Instrumentation Group*
ESG	*Engineering Services Group*
FBR	*Fast Breeder Reactor*
FBTR	*Fast Breeder Test Reactor*
FChD	*Fuel Chemistry Division*
FRFCF	*Fast Reactor Fuel Cycle Facility*
FRTG	*Fast Reactor Technology Group*
IDEAS	*Innovative Design, Engineering and Synthesis*
IIS	*Innovative Instrumentation Section*
LMFBR	*Liquid Metal Cooled Fast Breeder Reactor*
M&HD	*Mechanics & Hydraulics Division*
MAPS	*Madras Atomic Power Station*
MCD	*Materials Chemistry Division*
MMD	*Mechanical Metallurgy Division*
MD	*Medical Division*
MMG	*Metallurgy and Materials Group*
MSD	*Materials Science Division*
MTD	*Materials Technology Division*
NDED	*Non-Destructive Evaluation Division*
NFC	*Nuclear Fuel Complex*
NICB	*Nuclear Island Connected Buildings*
NPCIL	*Nuclear Power Corporation of India Limited*
NSSS	*Nuclear Steam Supply System*
PD	*Planning Division*
PFBR	*Prototype Fast Breeder Reactor*
PFRP	*PFBR Fuel Reprocessing Plant*
PHWR	*Pressurized Heavy Water Reactor*
PIED	*Post Irradiation Examination Division*
PMD	*Physical Metallurgy Division*
QAD	*Quality Assurance Division*
REG	*Reactor Engineering Group*
RIRD	*Remote Handling, Irradiation Experiments & Robotics Division*
RMD	*Reactor Maintenance Division*
ROMG	*Reactor Operation and Maintenance Group*
RPD	*Reactor Physics Division*
RpG	*Reprocessing Group*
RRDD	*Reprocessing Research and Development Division*
RSD	*Radiological Safety Division*
S&HRPS	*Strategic & Human Resources Planning Section*
SED	*Safety Engineering Division*
SG	*Safety Group*
SGTF	*Steam Generator Test Facility*
SIRD	*Scientific Information Resource Division*
SOWART	*Sodium Water Reaction Test facility*
ST&HD	*Separation Technology & Thermal Hydraulics Division*